Photophysical Properties of Chromophores studied by Multimodal Fluorescence Spectroscopy

Inaugural-Dissertation

zur Erlangung des Doktorgrades

der Mathematisch-Naturwissenschaftlichen Fakultät

der Heinrich-Heine-Universität Düsseldorf

vorgelegt von

Dragana Sretenović

aus Čačak, Republik Serbien

Düsseldorf, April 2024

aus dem Institut für Physikalische Chemie II
der Heinrich-Heine-Universität Düsseldorf

Gedruckt mit der Genehmigung der
Mathematisch-Naturwissenschaftlichen Fakultät der
Heinrich-Heine-Universität Düsseldorf

Berichterstatter:

1. Prof. Dr. Claus A. M. Seidel

2. Prof. Dr. Peter Gilch

Tag der mündlichen Prüfung: 21.12.2023

Affidavit

I declare in lieu of an oath that the dissertation has been written by me independently and without any inadmissible outside help, in compliance with the "Principles for Ensuring Good Scientific Practice at the Heinrich Heine University Düsseldorf". The dissertation has not been submitted to any other institution in the form presented or in a similar form and I have not made any unsuccessful attempts at a doctorate to date.

Place, date

Dragana Sretenović

To my parents and my brother

Abstract

Although the phenomenon of thermally activated delayed fluorescence (TADF) was already known several decades ago, it gained significant attention in recent years in the field of organic electronics because of its capability to harvest triplet excitons in organic light-emitting diodes (OLEDs) through fluorescence. Concerning that, the research training group ModISC was formed to study the processes responsible for TADF: intersystem crossing (ISC) and reverse intersystem crossing (rISC). This thesis is a result of collaborative work within this graduate school. Three families of chromophores divided into three project areas were investigated: **A.** Organic donor-acceptor conjugates, **B.** Organometallic donor-acceptor complexes of copper(I) and **C.** Organic compounds that are derivatives of flavins. The first two compound families are investigated with respect to TADF. One of the main goals of this thesis was to establish ultrasensitive fluorescence methods for the detection of TADF and find a correlation between structure and photophysical properties.

In project class **A**, five organic donor-acceptor conjugates were designed with a twisted conformation and the steric demand on the linker between the donor and acceptor was controlled to study the influence of the resulting torsion angle on the TADF properties of the chromophores. The diffusion-controlled quenching effect of oxygen was tremendous in our study, and special care had to be taken to ensure that oxygen was efficiently removed and that the deoxygenated samples were preserved for an extended period of time, which was achieved by extensive bubbling with inert gas and storage in hermetically sealed glass ampoules. The TADF properties are verified by temperature-dependent time-resolved measurements and time-resolved emission spectroscopy, which confirmed the same origin of the prompt and delayed emission. The compound with the highest steric torsion was proven to be the most efficient TADF emitter.

In project class **B**, the photophysical properties of four copper(I) complexes bearing an anionic diamido-N-heterocyclic carbene ligand and and pyridine-based ligands were investigated. Due to chemical instabilities in solution, all fluorescence measurements were performed in cyclohexane suspension which allowed the use of standard cuvettes. Validation of the employed approach was obtained through fluorescence measurements of neat powders. Complexes with pyridine and lutidine ligands exhibit luminescence characteristics for locally-excited states, namely fluorescence and phosphorescence. However, the situation changes when the respective ligands are tuned in the electron-withdrawing direction by the addition of formyl groups. In this case, charge-transfer states are stabilized, which opens a pathway to TADF. Temperature-dependent time-resolved measurements and time-resolved emission spectroscopy are conducted across three distinct time regimes (nanoseconds, microseconds and milliseconds) in the temperature range from 10 K to 270 K to study luminescence properties and establish their relation with the nature of the excited states predicted by quantum chemical calculations.

Moreover, our research extended beyond TADF: an example of that is project class **C** which includes fluorinated flavin derivatives chosen for their significance in biological systems. Their photophysical properties strongly depend on the applied fluorination pattern. Theoretical calculations enabled the synthesis of a derivative with strengthened fluorescence properties, which are further increased by using deuterated solvents, i.e., D_2O instead of H_2O.

Overall, this thesis provides joint synthetic and theoretical efforts in the rational design of novel chromophores, with particular reference to detailed spectroscopic characterization and investigation of their photophysical properties.

This thesis is based on the following articles and manuscripts:

Published articles

- Philipp Schmeinck, **Dragana Sretenović**, Jasper Guhl, Ralf Kühnemuth, Claus A. M. Seidel, Christel M. Marian, Markus Suta, Christian Ganter. Luminescent Copper(I)-Complexes with an Anionic NHC obtained via a Coordination Polymer as Versatile Precursor. *European Journal of Inorganic Chemistry* **2023**, 26, e202300416. DOI: 10.1002/ejic.202300416. A previous version of this manuscript has been deposited on ChemRxiv, DOI: 10.26434/chemrxiv-2023-3k5bl.
  (Chapter 7.2)

- Mira K. Kubitz, Wiebke Haselbach, **Dragana Sretenović**, Mario Bracker, Martin Kleinschmidt, Ralf Kühnemuth, Claus A. M. Seidel, Peter Gilch, Constantin Czekelius. Increasing the Fluorescence Quantum Yield and Lifetime of the Flavin Chromophore by Rational Design. *ChemPhotoChem* **2023**, 7, e202200334. DOI: 10.1002/cptc.202200334
  (Chapter 7.4)

Manuscripts in preparation

- **Dragana Sretenović**, Laura N. Kloeters, Jeremy M. Kaminski, Tobias Böhmer, Philipp Schmeinck, Gereon A. Sommer, Mina Chalani, Suren Felekyan, Ralf Kühnemuth, Guido J. Reiß, Christoph Janiak, Claus A. M. Seidel, Christel M. Marian, Thomas J.J. Müller. The effect of conformation constraints and oxygen quenching on TADF in donor-acceptor systems. *Manuscript in preparation for Chemical Science*.
  (Chapter 7.1)

- Jasper Guhl,[†] **Dragana Sretenović,**[†] Philipp Schmeinck, Suren Felekyan, Ralf Kühnemuth, Christian Ganter, Claus A. M. Seidel, Christel M. Marian, Markus Suta. How to tune luminescent Cu(I) complexes with strong donor carbenes towards TADF? *Manuscript was submitted to Journal of Materials Chemistry C on 11.04.2024.*
  (Chapter 7.3)

[†] These authors contributed equally.

Contributions

Chapter 7.1

The effect of conformation constraints and oxygen quenching on TADF in donor-acceptor systems

Dragana Sretenović, Laura N. Kloeters, Jeremy M. Kaminski, Tobias Böhmer, Philipp Schmeinck, Gereon A. Sommer, Mina Chalani, Suren Felekyan, Ralf Kühnemuth, Guido J. Reiß, Christoph Janiak, Claus A. M. Seidel, Christel M. Marian, Thomas J.J. Müller

D. S.: Sample preparation, fluorescence measurements, experimental data analysis, data interpretation, visualization of the experimental data and writing-original draft and writing-review and editing. L. N. K.: Synthesis and sample characterization, and writing-original draft. J. M. K.: Quantum chemical calculations, theoretical data analysis and interpretation, visualization of the theoretical data and writing-original draft. T. B.: Quantum chemical calculations, theoretical data analysis and interpretation, visualization of the theoretical data and writing-original draft. P. S.: Sample preparation (ampoules) and writing-review and editing. G. A. S.: Establishment of the synthetic routes, sample characterization. M. C.: Experimental data analysis. S. F.: Design and software writing for automating temperature-dependent time-resolved fluorescence measurements, software writing for the analysis of time-resolved fluorescence data, data analysis. R. K.: Research design of fluorescence experiment, data analysis and interpretation, and writing-review and editing. G. J. R.: Measurement and refinement of the X-ray diffraction data. C. J.: Refinement of the X-ray diffraction data and writing-original draft. C. A. M. S.: Research design of fluorescence experiments, data analysis and interpretation, writing-original draft and writing-review and editing, project administration, and funding acquisition. C. M. M.: Research design of quantum chemical calculations, writing-original draft and writing-review and editing, project administration, and funding acquisition. T. J. J. M.: Conceptualization of project, research design of chemical synthesis and characterization, writing-original draft and writing-review and editing, project administration, and funding acquisition.

Chapter 7.2

Luminescent Copper(I)-Complexes with an Anionic NHC obtained via a Coordination Polymer as Versatile Precursor

Philipp Schmeinck, **Dragana Sretenović**, Jasper Guhl, Ralf Kühnemuth, Claus A. M. Seidel, Christel M. Marian, Markus Suta, Christian Ganter

Conceptualization: C. M. M., C. G.; Methodology: P. S., **D. S.**, J. G., R. K., M. S.; Validation: P. S., **D. S.**, J. G.; Formal analysis: P. S., **D. S.**, J. G., R. K., M. S.; Investigation: P. S., **D. S.**, J. G., M. S.; Data curation: P. S., **D. S.**, J. G.; Writing – original draft preparation: P.S., **D. S.**, J. G., M. S.; Writing – review and editing: P. S., C. A. M. S., C. M. M., M. S., C. G.; Visualization: P. S., **D. S.**, J. G.; Project administration: C. A. M. S., C. M. M., M. S., C. G., Funding acquisition: C. A. M. S., C. M. M., M. S., C. G. All authors have given approval to the final version of the manuscript.

Chapter 7.3

How to tune luminescent Cu(I) complexes with strong donor carbenes towards TADF?

Jasper Guhl,† **Dragana Sretenović,**† Philipp Schmeinck, Suren Felekyan, Ralf Kühnemuth, Christian Ganter, Claus A. M. Seidel, Christel M. Marian, Markus Suta

Conceptualization: C. M. M. and M. S.; Methodology: J. G., **D. S.**, P. S., S. F., R. K., M. S.; Validation: J. G., **D. S.**, P. S.; Formal analysis: J. G., **D. S.**, P. S., S. F., M. S.; Investigation: J. G., **D. S.**, P. S. M. S; Data curation: J. G., **D. S.**, P. S., S. F.; Writing – original draft preparation: J. G., **D. S.**, P. S., C. M. M., M. S.; Writing – review and editing: J. G., **D. S.**, P. S., R. K., C. G., C. A. M. S., C. M. M., M. S.; Visualization: J. G., **D. S.**, P. S.; Project administration: C. G., C. A. M. S., C. M. M., M. S.; Funding acquisition: C. G., C. A. M. S., C. M. M., M. S.

Chapter 7.4

Increasing the Fluorescence Quantum Yield and Lifetime of the Flavin Chromophore by Rational Design

Mira K. Kubitz, Wiebke Haselbach, **Dragana Sretenović**, Mario Bracker, Martin Kleinschmidt, Ralf Kühnemuth, Claus A. M. Seidel, Peter Gilch, Constantin Czekelius

M. K. K.: Sample preparation and characterization, and writing-original draft and writing-review and editing. W. H.: Steady-state measurements, nanosecond transient absorption measurements, data analysis, visualization of the experimental data and writing-original draft. **D. S.**: Time-resolved fluorescence measurements by TCSPC, FCS measurements, data analysis, writing-original draft. M. B.: Quantum chemical calculations, theoretical data analysis, and visualization of the theoretical data. M. K.: Writing-original draft, project administration, and funding acquisition. R. K.: FCS measurements, data analysis and interpretation, and writing-review and editing. C. A. M. S.: conceptualization, research design, data interpretation, writing-review and editing, project administration, and funding acquisition. P. G.: conceptualization, research design, data interpretation, writing-review and editing, project administration, and funding acquisition. C. C.: conceptualization, research design, sample preparation, writing-original draft and writing-review and editing, project administration, and funding acquisition.

Acknowledgement

I would like to express my gratitude to Prof. Dr Claus A. M. Seidel for providing me with the opportunity to conduct my doctoral thesis in his research group and for his support throughout this journey. I am also thankful to my second supervisor, Prof. Dr Peter Gilch, for being available for discussions and for offering valuable advice on my projects.

I thank all the members of the Seidel group for their kindness and the great working atmosphere. Special thanks go to my office colleague, Dr Suren Felekyan, for developing software that has greatly increased my working efficiency and for his willingness to always help, and to Dr Ralf Kühnemuth for his technical support and constructive feedback that has encouraged me to delve deeper into my research.

I am happy to have had the opportunity to be a part of the research training group ModISC and to participate in many interesting projects that have led to this thesis. Regular scientific meetings and networking events within this school have been of great importance for my scientific and personal development. Many thanks go to all the members, especially to my collaborators and Dr Martina Holz for her great administrative work for this school.

I am grateful to my colleague and friend, Milana Popara, who has taken care of me since my first day in Germany and who always had an answer for my questions.

I thank Philipp's family for making me feel at home.

I extend my gratitude to my uncle's family and my grandaunt for their continuous support throughout my studies.

Special thanks go to my friends, whose support and encouragement over the years have been invaluable.

I am thankful to my parents, Vesna and Ljuban, for investing in my and my brother's education and for teaching us to be patient and persistent in pursuit of our long-term goals. I appreciate their trust and support in allowing me to make my own decisions from an early age.

My brother Duško deserves thanks for encouraging me to confront my fears.

Finally, I would like to thank Philipp for his creative ideas in our shared projects, as well as for proofreading this thesis. I also thank him for all the wonderful moments we have shared together.

Table of Contents

List of Abbreviations

ch	channel
CT	charge-transfer
DACs	donor-acceptor conjugates
DCN	1,4-dicyanobenzene
DF	delayed fluorescence
DFG	Deutsche Forschungsgemeinschaft
FCS	fluorescence correlation spectroscopy
FWHM	full width at half maximum
IC	internal conversion
IRF	instrument response function
ISC	intersystem crossing
LC	ligand-centered
LE	locally-excited
LLCT	ligand-to-ligand charge-transfer
MCS	multichannel scaling
MIA	10-methyl-isoalloxazine
MLCT	metal-to-ligand charge transfer
ModISC	modulation of intersystem crossing
NHC	N-heterocyclic carbene
OLED	organic light-emitting diodes
PF	prompt fluorescence
rISC	reverse intersystem crossing
SOC	spin-orbit coupling
TAA	triarylamine
TADF	thermally activated delayed fluorescence
TCSPC	time-correlated single photon counting
TRES	time-resolved emission spectroscopy
UV-Vis	ultraviolet-visible

Chapter 1. Introduction

Electronic excitations and transitions play a significant role in various fields, spanning from fundamental scientific research (photophysics,[1] photochemistry,[2,3] photobiology[4]) to practical applications in everyday life (e.g., electronic devices[5,6]). When molecules absorb light, they are excited from the electronic ground state to an excited state. Once in the excited state, they can undergo various transitions, including radiative and non-radiative deactivation pathways. Intersystem Crossing (ISC) is a non-radiative transition between electronic states with different spin multiplicities, such as singlet and triplet states. The lifetimes of the triplet states are typically significantly longer than those of singlet states as the radiative transition to the ground singlet state S_0 is spin forbidden.[2] This condition makes the triplet states more susceptible to environmental effects like quenching and in that way, the energy is lost by non-radiative deactivation. Thus, ISC is a key process in photochemistry and photophysics. The efficiency and kinetics of ISC can render electronically excited molecules photo-labile or -stable, emissive or dark. Gaining a deeper understanding of photophysical processes and potentially controlling the longevity of the triplet states represents a great challenge in fundamental scientific research.

This doctoral thesis is embedded in the collaborative research program of the DFG-funded research training group ModISC. ModISC was established to study and modulate ISC in molecules by varying their substituents and their molecular environment. ModISC aims at a deeper understanding of emission enhancement by controlling ISC from singlet to triplet and its reverse (rISC). Notably, rISC to S_1 results in delayed fluorescence,[7] which depends on the energy gap ΔE_{ST} between the S_1 and T_1 states and hence is temperature-dependent (Figure 1.1).

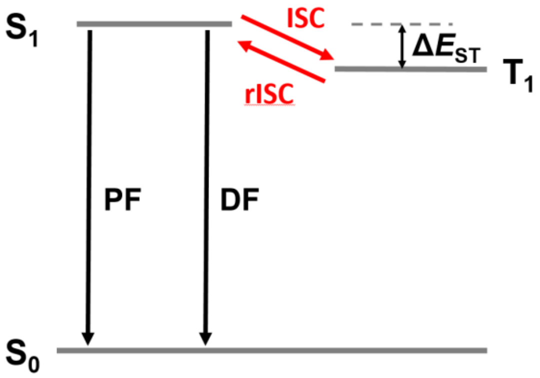

Figure 1.1. Simplified Jablonski diagram. Prompt Fluorescence (PF) and delayed fluorescence (DF) are denoted. The ratio of the rate constants of the intersystem crossing (ISC) and reverse intersystem crossing (rISC) depends on the energy gap ΔE_{ST}.

This process, known as thermally activated delayed fluorescence (TADF), has attracted substantial attention in the field of organic electronics as its potential to harvest both singlet and triplet excitons has been recognized in the third generation of organic light-emitting diodes (OLEDs).[6,8]

In this thesis, three classes of newly designed chromophores are investigated to study ISC and their spectral and temporal emission properties. Each chapter of the thesis explores a close interplay between theoretical predictions by quantum chemical calculations, novel synthetic strategies, and distinct modern spectroscopic methods to examine the photophysical properties of these chromophores in detail (Figure 1.2). Rationally designed chromophores (Figure 1.3) could be later used for practical applications, such as emitters for OLEDs[5,9] and reporters for bioanalytical applications.[10]

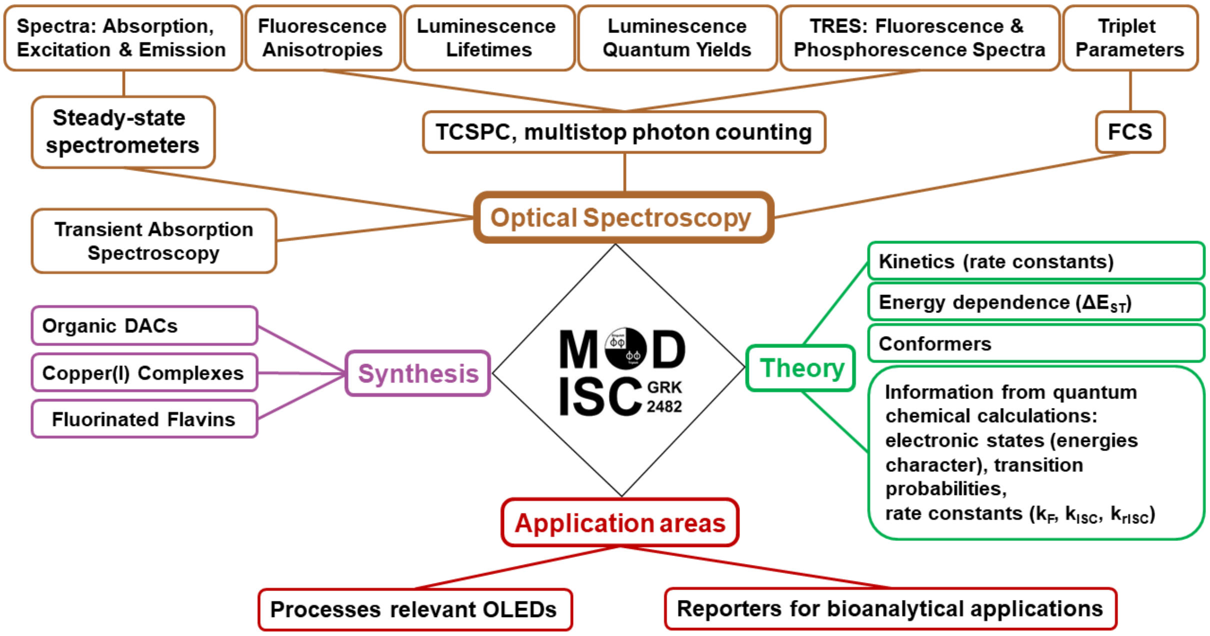

Figure 1.2. Interdisciplinary character of the research training group ModISC involved in all projects presented in this thesis.

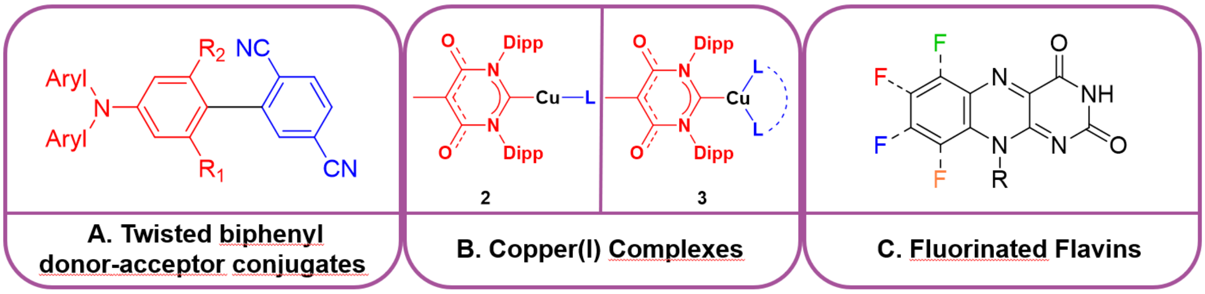

A. Twisted biphenyl donor-acceptor conjugates

B. Copper(I) Complexes

C. Fluorinated Flavins

Figure 1.3. General chemical formulas of the three investigated chromophore families. **A.** Organic donor-acceptor conjugates (DACs): twisted biphenyl chromophores (*p*TAA-DCN) with a triarylamine (TAA) donor and a 1,4-dicyanobenzene (DCN) acceptor moiety (Figure 2.1); **B.** Copper(I) complexes bearing an anionic diamido N-heterocyclic carbene (NHC) and pyridine-based ligand L: **2** linear and **3** trigonal-planar class (Figure 3.1); and **C.** Fluorinated flavin derivatives (Figure 4.1).

All three model chromophores feature interesting photophysical properties associated with their triplet states. One of the primary objectives of this thesis is to establish a correlation between chemical structure and photophysical property. Chromophore family **A** includes organic chromophores which are donor-acceptor conjugates (organic DACs). In these chromophores, a torsional twist in the linker connecting the donor and acceptor moieties causes a conformational separation that minimizes the spatial overlap of hole and electron densities of the excited charge-transfer (CT) state.[11] This leads to a small energy gap (ΔE_{ST}) between the singlet and triplet states,[12] enabling reverse intersystem crossing (rISC) from the triplet to the singlet state if sufficient thermal energy is available. Twisted biphenyl chromophores with a triarylamine (TAA) donor and a 1,4-dicyanobenzene (DCN) acceptor moiety represent the chromophore family **A** and are promising candidates for TADF. Chromophore family **B** is comprised of organometallic compounds, specifically copper(I) complexes.[13] These compounds are also donor-acceptor conjugates. They contain a donating anionic carbene and either one or two pyridine-based ligands whose acceptor strength is varied to tune the TADF properties. Chromophore family **C** includes fluorinated flavin derivatives that are important in biological systems.[14] Depending on the fluorination pattern predicted by quantum chemistry,[15] the fluorescence quantum yield and lifetime of these chromophores can be significantly increased.

For studying TADF, we established ultrasensitive fluorescence detection methods with very low irradiances per pulse (between 0.1 and 2 W/cm^2) at average irradiances of $5.3 \cdot 10^{-5}$ W/cm^2 and low concentrations (<10 µM down to the single-molecule level). In this way, unwanted photochemical reactions such as triplet-triplet annihilation and triplet self-quenching are avoided as they can complicate the analysis of TADF.[16] The ultrasensitive methods include high-precision time-correlated single photon counting (TCSPC) for detecting prompt fluorescence (PF), newly built time-gated multistop TCSPC for resolving slower processes such as TADF in the microsecond time range, and multichannel scaling (MCS) for recording luminescence decay in the time range from nanoseconds to milliseconds without gating. Gating is particularly beneficial when fast and slow processes (e.g., PF and phosphorescence) are recorded together, as it can be difficult to extract the slower process from the overall signal, which mainly originates from the faster process.[17] To analyse the signal decay, the data are fitted by a model function with a series of exponential functions with characteristic lifetimes and a constant offset to account for detector dark counts and afterpulsing.

Singlet and triplet dynamics are studied with respect to environmental parameters, such as temperature, solvent polarity and the presence of a quencher. To study the temperature dependence of delayed fluorescence, the TCSPC spectrometer was equipped with a custom-designed cryostat powered by a closed helium compressing cycle providing an operation range of temperatures from 10 K to 350 K. Oxygen played a considerable role in this study as it is an efficient triplet and singlet quencher.[3] Substantial efforts were made to establish and validate a procedure for extensive bubbling with inert gas to achieve efficient removal of oxygen traces in the solution.

Chapter 2. Compound Class A – Organic Donor-Acceptor Conjugates

Overview of the Project

In this chapter, the TADF properties of a series of organic donor-acceptor conjugates with distinct torsion angles (compound series **5a-5d**) and increased donor strength (compound **5e**) were investigated (Figure 2.1). The steric torsion was varied by introducing different alkyl-substituents in the phenylene linker between the donor and acceptor moieties. The methyl-substituted derivative (**5b**) has already been reported as a TADF emitter.[18,19]

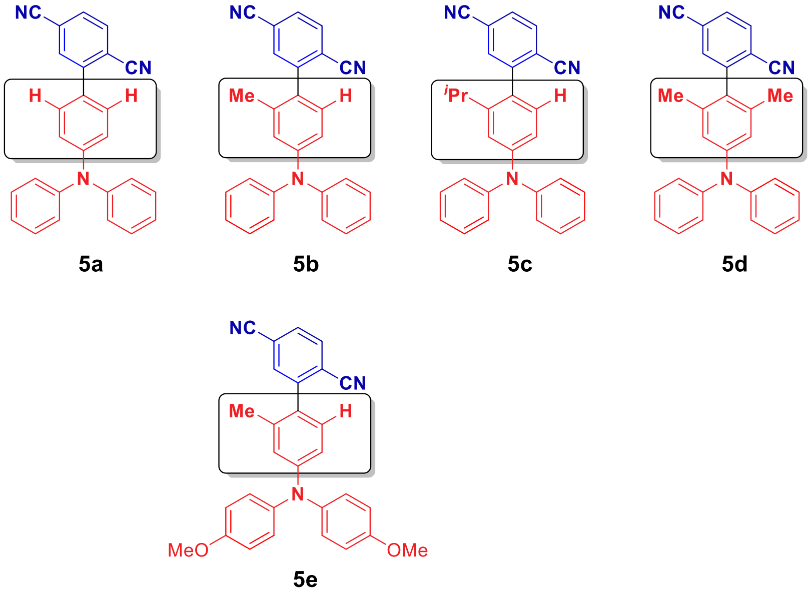

5a **5b** **5c** **5d**

5e

Figure 2.1. Chemical structures of twisted biphenyl chromophores (*p*TAA-DCN) with a triarylamine (TAA) donor and a 1,4-dicyanobenzene (DCN) acceptor moiety investigated in this study.

Compounds **5a-5e** were measured in air-saturated and nitrogen-purged toluene solutions. The prompt fluorescence lifetime is significantly increased in nitrogen-purged toluene solution (Figure 2.2, Table 2.1), suggesting that singlet states are quenched to a certain extent by oxygen. Molecular oxygen is known to be a very efficient quencher of excited states.[1,3] The ground state of molecular oxygen ($^3O_2$) is a triplet state ($^3\Sigma_g^-$), and two singlet states ($^1\Delta_g$ and $^1\Sigma_g^+$) are located above the triplet ground state, with energies of 95 kJ mol^{-1} and 158 kJ mol^{-1}, respectively.[20] The upper $^1\Sigma_g^+$ singlet state is rapidly deactivated to the lower $^1\Delta_g$ singlet state, known as singlet oxygen ($^1O_2$). The mechanism of singlet quenching involves energy transfer from an excited sensitizer molecule ($^1S^*$) to $^3O_2$. If the singlet-triplet energy gap (ΔE_{ST}) of the sensitizer is larger than the $^3\Sigma_g^-$ - $^1\Delta_g$ energy gap of oxygen of 95 kJ mol^{-1}, $^1O_2$ will be formed [reaction (1a)]. Otherwise, an oxygen-catalyzed ISC takes place [(1b)].[2,3,21]

$$^{1}S^{*} + {}^{3}O_2 \rightarrow {}^{3}S^{*} + {}^{1}O_2 \tag{1a}$$

$$^{1}S^{*} + {}^{3}O_2 \rightarrow {}^{3}S^{*} + {}^{3}O_2 \tag{1b}$$

The mechanism of triplet quenching by oxygen is also an energy transfer [reaction (2)].[22]

$$^{3}S^{*} + {}^{3}O_2 \rightarrow {}^{1}S + {}^{1}O_2 \tag{2}$$

However, for reasons of spin statistics, only one out of nine collisions leads to the product with singlet multiplicity.[23]

In addition to the energy transfer mechanism proposed initially by Kautsky,[22] several other mechanisms for oxygen quenching have been discussed,[24] including electron transfer[25] and enhanced ISC.[26] Weiss[25] suggested that quenching occurs by electron transfer [reaction (3)]. However, it is unlikely that this process takes place in non-polar solvents.[27]

$$D^{*} + O_2 \rightarrow D^{+} + O_2^{-} \tag{3}$$

where D* is an excited donor molecule.

The quenching mechanism known as the inhomogeneous magnetic field effect, in which the paramagnetic nature of oxygen causes mixing of the singlet and triplet states,[26] is a form of enhanced ISC.[24] However, this effect has proven to be negligible.[27] Overall, the mechanism of energy transfer is considered more important than enhanced ISC.[24]

Moreover, triplet states are more sensitive to oxygen quenching because they have a longer lifetime compared to singlet states and therefore the probability of collisions leading to quenching is higher.[22] For compounds **5a**-**5e**, TADF was not even detected in the air-saturated toluene solutions. On the other hand, in nitrogen-purged solution, substantial variations in the TADF lifetimes were observed depending on the deoxygenation procedure used during sample preparation. This finding could be explained by the Stern-Volmer equation,[28] which predicts that for longer lifetimes small changes in quencher concentration may cause larger deviations in measured lifetimes (Figure 7.5). To prevent the ingress of oxygen, all samples were stored in sealed glass ampoules after being thoroughly bubbled with nitrogen and subjected to the freeze-thaw cycle (Figure 7.6). Nonetheless, compound **5a** did not exhibit TADF under these conditions. The longest lifetimes obtained in this study are represented in Figure 2.2 and Table 2.1.

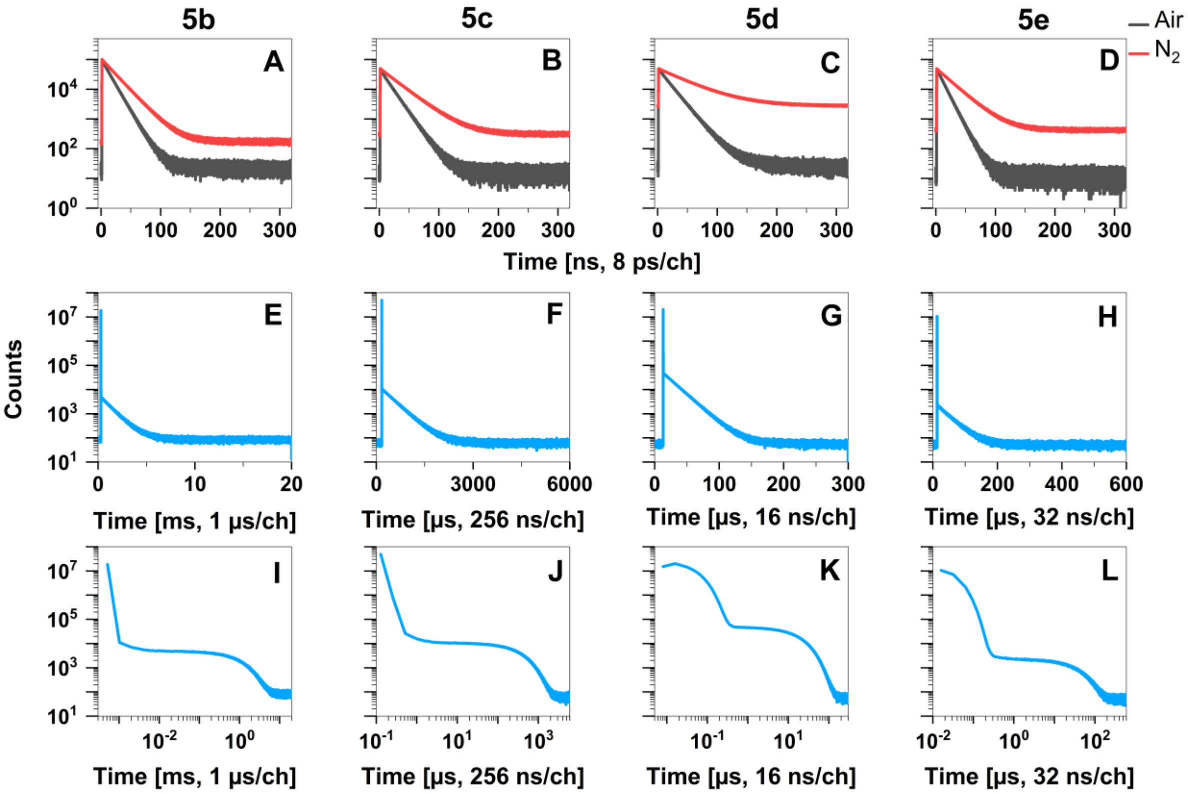

Figure 2.2. Time-resolved decays of compounds **5b**-**5e**. Compound **5a** was omitted in this representation as no TADF was observed for this compound. **A**-**D**: Prompt fluorescence in air-saturated and nitrogen-purged solutions in toluene measured by TCSPC. The repetition rate was 3.12 MHz for all four compounds. Prompt and delayed fluorescence data are represented in two formats: **E**-**H**: Logarithmic y-axis and linear x-axis, and **I**-**L**: Logarithmic y- and x- axes (log-log data representation). The repetition rates in these measurements were: 0.05 kHz, 0.15 kHz, 3.33 kHz, and 1.67 kHz for **5b**-**5e** respectively. Samples were excited at 375 nm and detected at 495 nm (**5b**-**5d**) and 560 nm (**5e**).

As the torsion angle increases within the series from **5a** to **5d**, the spatial overlap of hole and electron densities increases, resulting in a decrease in the energy gap ΔE_{ST} between singlet and triplet excited states. Temperature-dependent measurements and the energy gaps derived from Arrhenius plots confirmed the trend predicted by quantum chemical predictions. The measured absorption coefficients $\varepsilon_{\mathrm{exp}}$ also demonstrate agreement with the calculated S_0-S_1 oscillator strengths. Moreover, the quantum yield and the amplitude of TADF are increasing from **5b** to **5d**, and the delayed fluorescence lifetime becomes shorter. Compound **5e**, despite possessing nearly identical torsion angle as **5b**, demonstrates enhanced TADF characteristics due to its increased donor strength. Table 2.1 summarizes the most important findings.

Table 2.1. Spectroscopic and photophysical parameters of compounds **5a**-**5e** in toluene. The wavelength maxima of the 1st band with the lowest absorption energies (λ_{max}), absorption coefficients (ε), and fluorescence emission maxima (λ_{em}) refer to the spectra in the wavelength domain.

Parameters	**5a**	**5b**	**5c**	**5d**	**5e**
1st λ_{max} [nm]	391	382	381	377	401
1st ε_{max} [M^{-1} cm^{-1}]	10309	4586	2289	941	5750
S_0-S_1 f **[a]**	0.237	0.077	0.047	0.002	0.081
λ_{em} [nm]	493	497	492	497	558
Φ_{PF}^{Air} **[b]**	0.59	0.36	0.29	0.20	0.16
$\Phi_{PF}^{N_2}$ **[c]**	0.76	0.60	0.56	0.53	0.36
Φ_{DF} **[d]**	0.00	0.07	0.10	0.33	0.04
Φ_{TF} **[e]**	0.76	0.67	0.67	0.86	0.40
$\langle\tau\rangle_F^{Air}$ [ns] **[f]**	7.3	12.3	14.7	17.5	10.8
$\langle\tau\rangle_F^{N_2}$ [ns] **[f]**	9.4	20.4	28.5	46.5	24.6
τ_{DF} at 300 K [µs]	no TADF	1074.8	357.5	18.4	35.5
ΔE_{ST} [meV], exp. **[g]**	no TADF	102	75	23	34
ΔE_{ST} ad. [meV], theory	501	438	428	333	228
ΔE_{ST} vert. [meV], theory	341	192	162	73	157

[a] Calculated S_0-S_1 oscillator strengths f.

[b] Quantum yield of prompt fluorescence measured in an air-saturated toluene (Φ_{PF}^{Air}) was determined using the relative method with Rhodamine 6G in ethanol as a reference (Φ_F^r = 0.94).[29]

[c] Quantum yield of prompt fluorescence for a nitrogen-purged solution (Φ_{PF}^{N2}) was calculated according to: $\Phi_{PF}^{N_2} = \Phi_{PF}^{air} \cdot \frac{\langle\tau\rangle_F^{N_2}}{\langle\tau\rangle_F^{Air}}$.

[d] Quantum yield of delayed fluorescence determined by the TCSPC offset analysis.

[e] Total fluorescence quantum yield obtained as: $\Phi_{TF} = \Phi_{PF}^{N2} + \Phi_{DF}$.

[f] Fluorescence-weighted lifetimes of prompt fluorescence in air and nitrogen measured by TCSPC.

[g] Singlet-triplet energy gaps (ΔE_{ST}) were determined experimentally from the Arrhenius plots (Figure 7.8).

To determine the singlet-triplet energy gap (ΔE_{ST}), Arrhenius plots were constructed based on the temperature-dependent time-resolved measurements in the temperature range from 180 K to 300 K. Additionally, the spectral overlap between prompt and delayed fluorescence was confirmed by the time-resolved emission spectroscopy (TRES). Our research extended beyond TADF: prompt fluorescence and phosphorescence properties were also investigated at low temperatures to answer the question which deactivation pathways are operative in these systems. Upon photoexcitation, three deactivation channels take place: prompt fluorescence (k_F), intersystem crossing (k_{ISC}) and reverse intersystem crossing (k_{rISC}). Brightness losses are caused by non-radiative transitions, ISC and internal conversion (IC). In contrast to IC, brightness losses due to ISC can be recovered by rISC. Both IC and ISC losses are suppressed at lower temperatures, as it has been observed that the prompt fluorescence lifetime increases for all compounds at low temperatures: 9 ns (300 K) to 11 ns (200 K) for **5a**, 20 ns (300 K) to 24 ns (200 K) for **5b,** 28 ns (300 K) to 35 ns (200 K) for **5c**, and finally, from 46 ns (300 K) to 61 ns (200 K) for **5d**.

In relation to electroluminescence considered in OLEDs, where the harvesting of triplet excitons and the efficiency of rISC are of particular importance, compound **5d** stands out as the most promising candidate in the investigated series (quantum yield $\Phi_{DF} = 0.28$ and the shortest lifetime $\tau_{DF} = 18.4$ µs).

Chapter 3. Compound Class B – NHC Copper(I) complexes

Overview of the Project

Quantum chemical calculations enabled the rational design of novel copper(I) complexes of donor-acceptor design principle shown in Figure 3.1. All complexes possess the same donor, namely an anionic diamido N-heterocyclic carbene (NHC). The acceptor is varied to tune the complexes' TADF properties. The parent ligand pyridine is substituted with methyl and formyl groups in order to fine tune the electronic and steric properties. The goal is a larger spatial separation of hole and electron densities of the excited CT state, leading to a smaller energy gap ΔE_{ST} and potentially TADF.

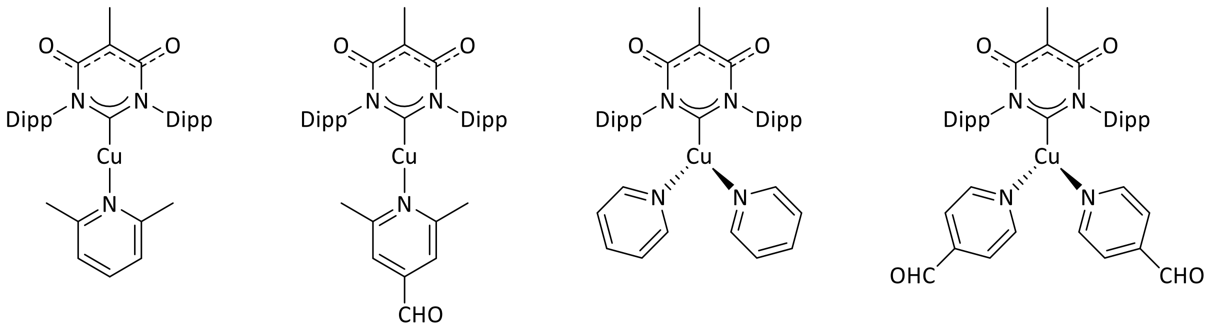

2a **2b** **3a** **3b**

Figure 3.1. Chemical structures of selected copper(I) complexes featuring an anionic carbene ligand. The numbers **2** and **3** denote the coordination numbers of copper(I) within these complexes. Linear complexes are labelled with the number **2**, and trigonal-planar complexes have the label **3**. Additionally, the labels **a** and **b** are related to the formyl groups: **b** indicates the presence of a formyl group on the ligand. Compound **2a** bears a 2,6-lutidine ligand, while compound **2b** contains a 4-formyl-2,6-lutidine ligand. Compounds **3a** and **3b** contain two pyridine ligands and two 4-formyl pyridine ligands, respectively.

However, by increasing the acceptor strength, the overall stability of the complexes decreased as they tend to dissociate in solution to a 1D coordination polymer and free ligand (Figure 3.2). This coordination polymer is composed of only the NHC ligand and copper(I), and it is highly insoluble. Considering this equilibrium present in solution of these complexes, a meaningful spectroscopic characterization could only be carried out in solid-state. Since our measuring device is only compatible with standard cuvettes, we performed the measurements in cyclohexane suspensions of the microcrystalline compounds. Cyclohexane was chosen because it: (i) is inert; (ii) does not dissolve the compounds; and (iii) has a high melting point of 6.5 °C, which allows measurements over a wide temperature range without undergoing phase transitions. However, luminescence of the dissociated ligand was observed in cyclohexane. In order to minimize the dissociation effect, the samples were shock-frozen in an acetone/liquid nitrogen bath and all time-resolved measurements were carried out in solid suspensions at temperatures below 270 K. Additional verification of the obtained results came from the selected measurements on the neat powder samples where the sample dissociation does not occur.

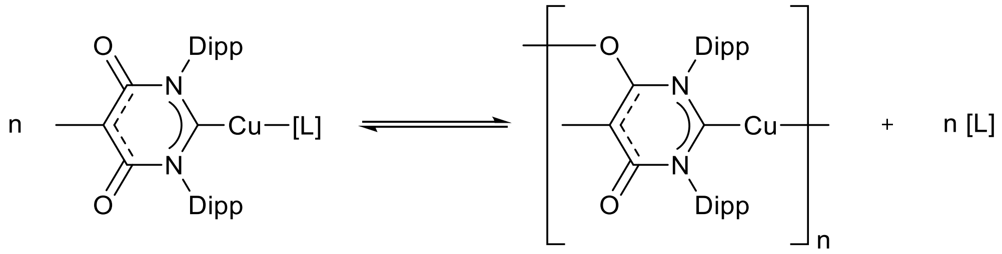

Figure 3.2. Complexes in equilibrium with polymer and free ligand in solution.

The linear lutidine complex **2a** and the trigonal pyridine complex **3a** are studied with respect to their luminescence performance across three distinct time regimes (nanoseconds, microseconds, and milliseconds) and at four selected temperatures (10 K, 60 K, 160 K, and 260 K). In addition to the donating NHC carbene, these two complexes have two relatively weak pyridine-based electron acceptors ligands. Thus, CT-type emission and TADF were not anticipated in these complexes. Strong fluorescence in nanoseconds and a weak portion of phosphorescence in milliseconds are observed for **2a** (Figure 3.3, A and B), in agreement with theory which predicts that the luminescence stems primarily from the ligand-centred (LC) states. In the case of **3a**, the trigonal coordination pattern causes an energetic increase of the corresponding ligand-field orbital and mixing with the metal-to-ligand charge-transfer (MLCT) states. This admixture leads to a strong spin-orbit coupling (SOC) between the MLCT and ligand-to-ligand charge-transfer (LLCT) states, which in turn means higher ISC rate constants. Phosphorescence from the ^{3}LC state is dominant in this case, which is confirmed by the time-resolved measurements (Figure 3.3, C and D).

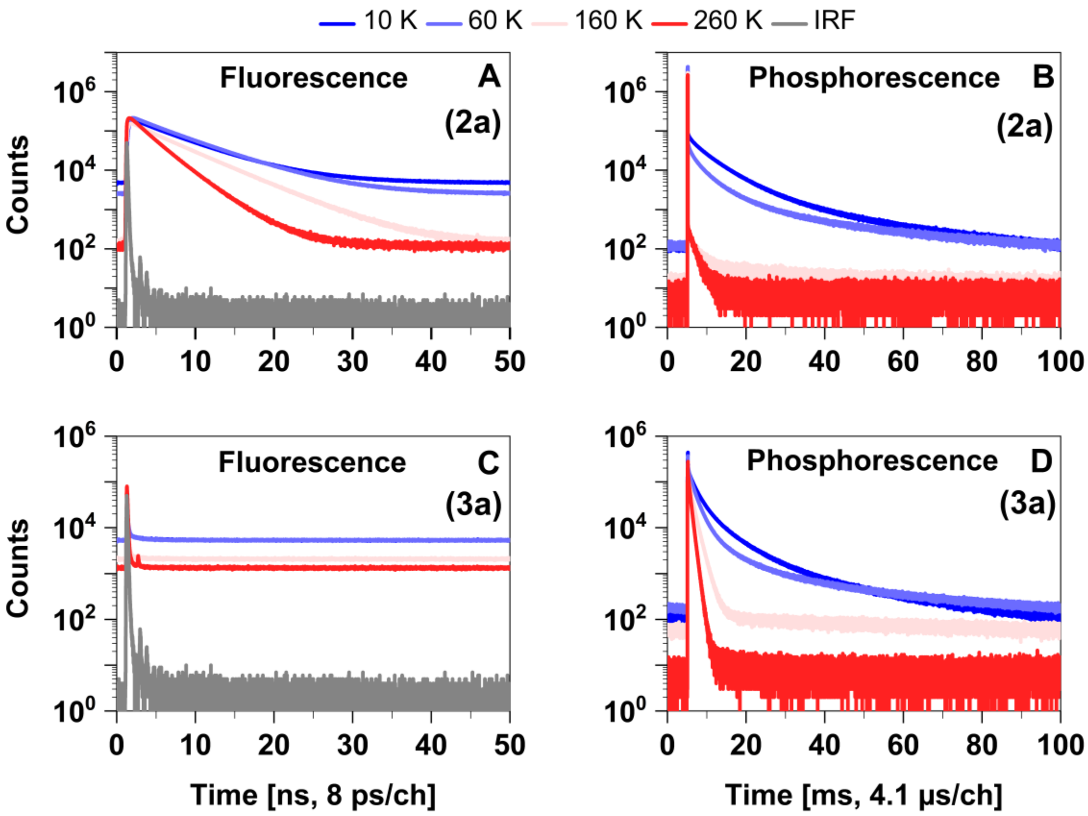

Figure 3.3. Time-resolved luminescence measurements of the linear lutidine complex **2a** and the trigonal pyridine complex **3a** in cyclohexane suspension. **A.** Fluorescence of **2a**. Theory predicts emission from the ^{1}LC state. **B.** Phosphorescence of **2a** from the ^{3}LC state. **C.** Fluorescence of **3a** in the sub-nanosecond time regime. **D.** Phosphorescence of **3a** from the ^{3}LC state as predicted by quantum chemical calculations.

More detailed steady-state and time-resolved studies were performed on the linear formyl lutidine complex **2b** and the trigonal formyl pyridine complex **3b** in the temperature range spanning from 10 K to 270 K. The steady-state spectrum of **3b** exhibits a notable bathochromic shift upon cooling (Figure 3.4D), while the spectrum of **2b** remains almost constant in the range from 270 K to 100 K (Figure 3.4A). The prompt fluorescence emission of **2b** is well resolved in the TCSPC measurements in contrast to **3b** (Figure 3.4, B and E). The prompt fluorescence of **3b** looks very similar to that of **3a**, presumably due to the very fast ISC. The complexes **2b** and **3b** were designed with the electron-withdrawing formyl groups on the lutidine and pyridine moieties to stabilize LLCT and MLCT type of emission and give rise to TADF. Indeed, a significant portion (56%) of the luminescence emission of **3b** at 270 K is delayed. However, the emission in microsecond time range is not assigned only to TADF, but also to phosphorescence (Figure 3.4, C and F). TADF is a dominant process at higher temperatures, while phosphorescence takes over at lower temperatures. Moreover, luminescence of the free ligands of the complexes is observed in cyclohexane suspension, despite all efforts to minimize sample dissociation. The luminescence of the free ligands of the complexes occurs in the millisecond range and is only particularly pronounced below 100 K. This made it possible to distinguish their signal from the signal of the complexes.

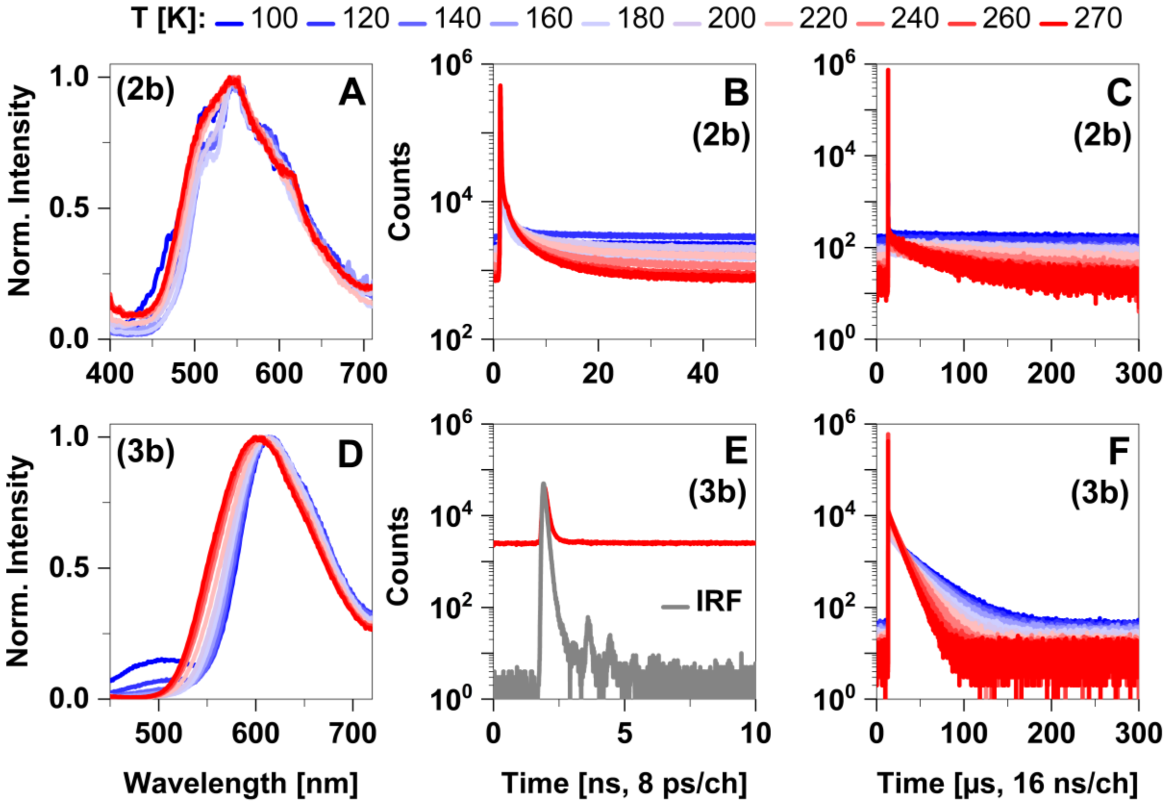

Figure 3.4. Steady-state and time-resolved luminescence measurements of **2b** and **3b** in cyclohexane suspension the temperature range from 100 K to 270 K. Steady-state spectra are shown in panels **A** (**2b**) and **D** (**3b**), time-resolved measurements in: nanoseconds - panels **B** (**2b**) and **E** (**3b**), and microseconds - panels **C** (**2b**) and **F** (**3b**). For the sake of comparison, the nanosecond decay of **3b** is presented with the instrument response function (IRF) with the full width at half maximum (FWHM) of 112 picoseconds (panel **E**).

Chapter 4. Compound Class C – Fluorinated Flavins

Overview of the Project

In this chapter, the excited state properties of fluorinated flavin derivatives in aqueous solution are investigated. The quantum chemical computations and the spectroscopic observations explain the distinct fluorescence quantum yields by specifically changing rate constants of intersystem crossing. As it was shown previously,[30] fluorination at 6-, 7-, and 8-positions (Figure 4.1A) of the 10-methyl-isoalloxazine (**MIA**) had a significant impact on the photophysical properties depending on the position of fluorination. Quantum chemical studies[15] enabled the rational design of the derivative 7,8-difluoro-10-methyl-isoalloxazine (**7,8-dF-MIA**) which was predicted to have an increased fluorescence quantum yield and lifetime. In this study, this novel di-fluorinated derivative was synthesized together with its ribityl derivative, as well as **9-F-MIA** for the sake of comparison (Figure 4.1).

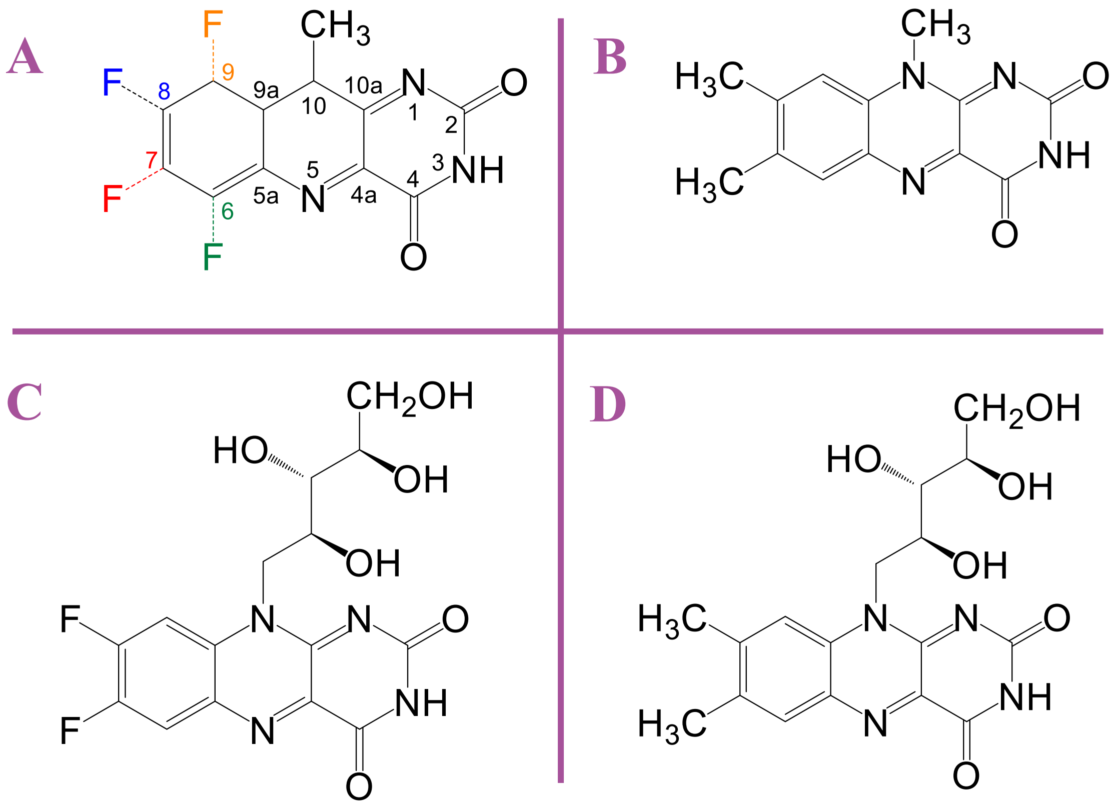

Figure 4.1. Chemical structures of fluorinated flavin derivatives investigated in this study: **A.** 10-methylisoalloxazine (**MIA**) with labelled fluorine substitution positions, **B.** 7,8,10-tri-methyl-isoalloxazine (lumiflavin), **C.** 7,8-difluor-10-ribityl-isoalloxazine (**7,8-dF-RIA**), and **D.** 7,8-dimethyl-10-ribityl-isoalloxazine (riboflavin).

The compounds are characterized by steady-state, time-resolved and fluorescence correlation spectroscopy (FCS). The experiments confirmed the quantum chemical predictions regarding the fluorescence performance. Remarkably, **7,8-dF-MIA** had the highest fluorescence quantum yield (0.42 in H_2O) and sensitivity (4669 M^{-1} cm^{-1}) of all fluorinated derivatives. Moreover, switching from H_2O to D_2O as solvent is shown to significantly increase the fluorescence quantum yields and lifetimes of all fluorinated flavin derivatives. Full fluorescence correlation spectroscopy (full-FCS)[31] (Figure 4.2C) showed that the rate constants of intersystem crossing are not strongly affected. In agreement with Maillard et al.,[32] D_2O for flavin derivatives mainly reduces the rate constant of internal conversion by suppressing water quenching.

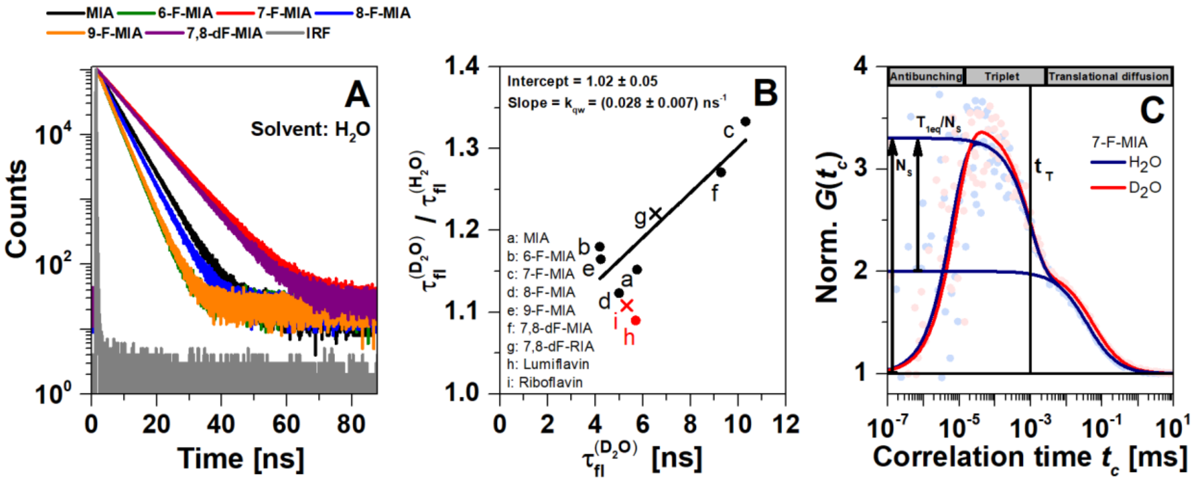

Figure 4.2. A. Fluorescence decays in H_2O measured by TCSPC; **B**. Stern-Volmer plot: the ratio of fluorescence lifetimes in D_2O over H_2O is plotted against the lifetimes in D_2O; **C**. Normalized and averaged full correlation curves $G(t_c)$ of **7-F-MIA** in air-saturated H_2O and D_2O at nanomolar concentrations.

Chapter 5. Conclusion

An in-depth photophysical assessment of three compound families is presented in this thesis. We have demonstrated successful rational design of organic and organometallic compounds. With respect to TADF, we have shown that both classes of compounds have in common intramolecular charge transfer achieved by the spatial separation of hole and electron densities, leading to a small ΔE_{ST} energy gap and efficient rISC. This study draws special attention to oxygen quenching and provides solutions for sensitive TADF detection. It shows the advantages of employing quantum chemical studies in predicting and describing photophysical behavior of compounds. ISC was successfully modulated in all three classes of compounds, and the tailored photophysical properties were confirmed by sophisticated time-resolved spectroscopic measurements.

To achieve this, we went through a technical journey which resulted in our instruments being equipped with modern up-to-date technology and established measurement routines. The time-correlated single photon counting spectrometer was complemented with an extension which enabled multi-photon counting and the detection of longer-lived processes, such as delayed fluorescence and phosphorescence. As most of the investigated samples absorbed in the UV region, a diode laser with the excitation wavelength of 375 nm was purchased and used extensively in this study. Furthermore, to investigate temperature-dependent processes, a cryostat unit with a closed helium cycle was installed, enabling measurements in the temperature range from 10 K to 350 K. Last but not least, software was created to facilitate measurements and data analysis.

Chapter 2 – Compound Class A – Organic Donor-Acceptor Conjugates

The main outcomes of this chapter are:

- **Oxygen quenching played a major role in this study**

TADF was not detected in air-saturated solutions of compounds **5a**-**5e**, indicating that the triplet states were completely quenched by oxygen. However, this is not always the case, as photoluminescence lifetimes in the microsecond range have been reported for some organometallic complexes in air-saturated solution. The bulky ligands in these complexes sterically shield the metal centers against oxygen.[33]

In our study, not only the triplet states but also the singlet states were quenched to a certain extent by oxygen. Quenching of the singlet states was observed in our time-resolved measurements of prompt fluorescence in air-saturated and nitrogen-purged toluene solutions (Figure 2.2, Table 2.1). A known approach[34] to estimate the quantum yield of delayed fluorescence from the steady-state data encompassed a comparison of the integrals of the fluorescence emission spectra of oxygenated and deoxygenated samples; their difference was used to estimate the quantum yield of delayed fluorescence, under the assumption that delayed fluorescence is completely quenched in air-saturated solution. However, this approach is not completely correct if the singlet states are quenched by oxygen. The total increase in steady-state emission of deoxygenated samples does not only arise from the delayed fluorescence but also from the enhanced prompt fluorescence, as quenching of singlet states is suppressed by deoxygenation. Thus, the quantum yield of prompt fluorescence in nitrogen ($\Phi_{\mathrm{PF}}{}^{\mathrm{N}_2}$) has to be considered when estimating the yield of delayed fluorescence within the context of the overall increase in emission in absence of oxygen, eq. (1).

$$\Phi_{DF} = \Phi_{TF} - \Phi_{\mathrm{PF}}^{N_2} \qquad \text{eq. (1)}$$

where Φ_{DF} is the quantum yield of the delayed fluorescence, Φ_{TF} is the total fluorescence quantum yield in absence of oxygen, $\Phi_{\mathrm{PF}}{}^{\mathrm{N}_2}$ is the prompt fluorescence quantum yield in nitrogen, which is estimated according to eq. (2).

$$\Phi_{\mathrm{PF}}^{N_2} = \Phi_{\mathrm{PF}}^{\mathrm{air}} \cdot \frac{\langle\tau\rangle_{\mathrm{F}}^{N_2}}{\langle\tau\rangle_{\mathrm{F}}^{\mathrm{Air}}} \qquad \text{eq. (2)}$$

where $\Phi_{\mathrm{PF}}{}^{\mathrm{Air}}$ is the prompt fluorescence quantum yield in air, and $\langle\tau\rangle_{\mathrm{F}}{}^{\mathrm{N}_2}$ and $\langle\tau\rangle_{\mathrm{F}}{}^{\mathrm{Air}}$ are the intensity-weighted prompt fluorescence lifetimes in nitrogen and air, respectively.

- **Efficiency of deoxygenation procedures often underestimated in the literature**

The efficiency of the applied deoxygenation procedures are very often not described in detail in literature. In our study, the measured delayed fluorescence lifetime strongly depended on the deoxygenation conditions. Samples were prepared in highly diluted form and deoxygenated by bubbling with nitrogen for approximately 30 minutes. However, the used teflon stoppers proved to be insufficiently tight in terms of oxygen permeability, as the delayed fluorescence lifetimes decreased after a few hours due to oxygen ingress and quenching. Thus, we designed sealed glass ampoules which ensured constant measurement conditions for each sample (Figure 7.6). The absorbance of the sample was determined by UV-Vis spectroscopy after each deoxygenation procedure.

- **Influence of steric torsion on TADF properties**

To shed light on the TADF properties, we conducted a series of temperature-dependent time-resolved measurements. Steric demand on the linker between donor and acceptor had a strong influence on the fluorescence performance. In terms of photoluminescence, the compound with the lowest steric demand on the linker connecting donor and acceptor exhibited the highest fluorescence quantum yield (Φ_{PF}), which was a consequence of the strong prompt fluorescence from the singlet state. Delayed fluorescence was not observed for this compound. However, for practical applications which involve electroluminescence, the compound with the highest steric hindrance and torsional angle exhibited the best TADF performance and the highest total fluorescence quantum yield (Φ_{TF}) among all five compounds (Table 2.1).

- **Limitations of the Arrhenius equation**

Moreover, this study also shows the limitations in the determination of the singlet-triplet energy gap ΔE_{ST} via the Arrhenius equation, eq. (3).

$$k_{TADF} = Ae^{-\frac{\Delta E_{ST}}{RT}} \qquad \text{eq. (3)}$$

where k_{TADF} is the TADF rate constant, A is a constant, ΔE_{ST} is the singlet-triplet energy gap, R is the ideal gas constant, and T is the temperature.

This equation employs k_{TADF} calculated as $1/\tau_{\mathrm{TADF}}$; however, experimentally determined lifetimes and derived rate constants are determined by all processes which depopulate the triplet state, including oxygen quenching and phosphorescence, and not only the TADF. This influences the slope of the Arrhenius plot and thus, the determined energy gap will not necessarily correspond to the actual energy gap in the molecules. Nevertheless, in this study, we observed a general trend for the ΔE_{ST} of all four compounds which aligns with theoretical predictions.

Another way to assess the ΔE_{ST} energy gap involves the equilibrium constant[35] [eq. (4)], which can be derived from the ratio of the amplitudes of delayed and prompt fluorescence [eq. (5)].[36]

$$K_{eq} = \frac{[S_1]}{[T_1]} = \frac{k_{rISC}}{k_{ISC}} = \frac{1}{3} e^{-\frac{\Delta E_{ST}}{k_B T}} \qquad \text{eq. (4)}$$

$$K_{eq} = \frac{A_r}{\phi_T^2} = \frac{A_d}{(A_p + A_d) \cdot \phi_T^2} \qquad \text{eq. (5)}$$

where K_{eq} is the constant for the $T_1 \rightleftarrows S_1$ equilibrium, k_{rISC} and k_{ISC} are the rate constants of the rISC and ISC, ΔE_{ST} is the singlet-triplet energy gap, k_{B} is the Boltzmann constant, T is the temperature, A_{r} is the amplitude ratio, A_{d} and A_{p} are the amplitudes of the prompt and delayed fluorescence, and Φ_{T} is the triplet quantum yield. The factor of ⅓ refers to the three-fold degeneracy of the triplet state.[37]

The main advantage of this method is that the amplitude ratio A_{r} is not affected by oxygen quenching and remains constant at different oxygen concentrations.

- **TRES as a powerful method to determine the spectral properties of luminescence**

We obtained additional conformation for TADF through time-resolved emission spectroscopy (TRES). This method employs time-resolved data to construct emission spectra of different types of luminescence which can give valuable insight into the origin of the emission. All four compounds showed spectral overlap between prompt and delayed fluorescence.

Chapter 3 – Compound Class B – NHC Copper(I) complexes

Main outcomes of this chapter are:

- **Development of the methodology for optical measurements**

At the beginning of this study, we encountered difficulties with the solutions of the evaluated complexes, as we observed white precipitates as soon as the complexes are dissolved. It was determined by single crystal X-ray diffraction experiments that the white precipitate is a 1D coordination polymer consisting of the carbene ligand briding between linearly coordinated copper(I) ions. When in solution, the complexes are in an equilibrium with the polymer and free ligand (Figure 3.2). The free ligand features its own emission behaviour which becomes prominent at very low temperatures (below 100 K) and complicates the photophysical analysis of the complexes. Thus, cyclohexane suspensions of the complexes were employed in this study instead of solutions, and measurements of powders validated the applied approach. Steady-state spectroscopy was performed in liquid cyclohexane suspension at room temperature with constant sample stirring. The contribution of the scattered light to the measured absorption spectra was taken into account. The emission wavelengths of these complexes ranged from blue (450 nm) to orange (590 nm) on the spectrum of visible light, upon excitation at 375 nm. Time-resolved measurements were conducted in frozen cyclohexane suspensions.

- **Luminescence behaviour of donor-acceptor copper(I) complexes with weak ligand-acceptor strength**

Copper(I) complexes in family **a**, the linear lutidine complex **2a** and the trigonal pyridine complex **3a**, consist of electron-rich carbenes and pyridine-based ligands, which are weak acceptors. This condition does not favor the stabilization of charge-transfer states and thus TADF emission, but rather the luminescence from the states that are locally-excited (LE) in their character. As predicted by theory, fluorescence in nanoseconds and phosphorescence in milliseconds were observed for these complexes, but not TADF.

- **Luminescence behaviour of donor-acceptor copper(I) complexes with increased ligand-acceptor strength**

Copper(I) complexes in family **b**, the linear formyl lutidine complex **2b** and the trigonal formyl pyridine complex **3b**, consist of electron-rich carbenes and electron-withdrawing pyridine-based ligands. This situation favors the stabilization of the excited states, which have a charge-transfer character, and opens a path to TADF. However, it was quite complicated to verify TADF experimentally, as it mixes with phosphorescence in the microsecond time range. In these complexes, TADF is a dominant process at higher and phosphorescence at lower temperatures.

Chapter 4 – Compound Class 3 – Fluorinated Flavins

Main outcomes of this chapter are:

- **Specific fluorination position on the flavin chromophore matters**

Quantum chemical calculations provided detailed insights into the fluorescence behaviour of fluorinated flavin derivatives.[15] A novel di-fluorinated derivative, **7,8-dF-MIA**, was synthesized with improved characteristics: increased fluorescence quantum yield (0.42) and prolonged fluorescence lifetime (7.31 ns) compared to the **MIA** derivative with a fluorescence quantum yield of 0.22 and fluorescence lifetime of 5 ns.[30] Moreover, a derivative **9-F-MIA** showed the opposite trend: its fluorescence performance subsided with a fluorescence quantum yield of 0.12 and fluorescence lifetime of 3.64 ns.

- **Deuterated solvents improved fluorescence performance**

In this study, we showed that the fluorescence is quenched in H_2O in comparison with D_2O. From the examination of the full-FCS correlation curve, we could deduce that the triplet times remain almost unchanged when changing from H_2O to D_2O, suggesting that the intersystem crossing rate constants were not affected by the H_2O quenching. However, the internal conversion rate constants were.

- **The ribityl group quenched fluorescence**

In both synthesized ribityl derivatives, the ribityl group caused quenching of fluorescence. Further investigation of the full-FCS curves revealed additional internal conversion pathways that facilitate the quenching process.

Chapter 6. References

[1] J. B. Birks, *Photophysics of aromatic molecules*, Wiley-Interscience, **1970**.

[2] N. J. Turro, *Modern molecular photochemistry*, University Science Books, **1991**.

[3] P. Klán, J. Wirz, *Photochemistry of organic compounds: from concepts to practice*, Wiley-Blackwell, **2009**.

[4] L. O. Björn, *Photobiology: The Science of Life and Light*, Springer: New York, **2007**.

[5] H. Sasabe, J. Kido, *J. Mater. Chem.* C **2013**, *1*, 1699-1707.

[6] Y. Tao, K. Yuan, T. Chen, P. Xu, H. Li, R. Chen, C. Zheng, L. Zhang, W. Huang, *Adv. Mater.* **2014**, *26*, 7931–7958.

[7] C. A. Parker, C. G. Hatchard, *Trans. Faraday Soc.* **1961**, *57*, 1894-1904.

[8] a) H. Uoyama, K. Goushi, K. Shizu, H. Nomura, C. Adachi, *Nature* **2012**, *492*, 234–238.

b) C. Adachi, *Jpn. J. Appl. Phys.* **2014**, *53*, 060101.

c) G. Hong, X. Gan, C. Leonhardt, Z. Zhang, J. Seibert, J. M. Busch, S. Bräse, *Adv. Mater.* **2021**, *33*, 2005630.

[9] a) C. W. Tang, S. A. VanSlyke, *Appl. Phys. Lett.* **1987**, *51*, 913–915.

b) J. Kido, M. Kimura, K. Nagai, *Science* **1995**, *267*, 1332-1334.

[10] a) A. Losi, *Photochem. Photobiol.* **2007**, *83*, 1283–1300.

b) A. Losi, W. Gärtner, *Annu. Rev. Plant Biol.* **2012**, *63*, 49–72.

c) L. Jullien, A. Gautier, *Methods Appl. Fluoresc.* **2015**, *3*, 042007.

[11] H. Beens, A. Weller, *Acta Phys. Pol.* **1968**, *34*, 593-602.

[12] a) Q. Zhang, H. Kuwabara, W. J. Potscavage Jr, S. Huang, Y. Hatae, T. Shibata, C. Adachi, *J. Am. Chem. Soc.* **2014**, *136*, 18070–18081.

b) T. J. Penfold, *J. Phys. Chem.* C **2015**, *119*, 13535–13544.

c) P. L. Santos, J. S. Ward, P. Data, A. S. Batsanov, M. R. Bryce, F. B. Dias, A. P. Monkman, *J. Mater. Chem.* C **2016**, *4*, 3815-3824.

---

[13] a) R. Czerwieniec, M. J. Leitl, H. H. H. Homeier, H. Yersin, *Coord. Chem. Rev.* **2016**, *325*, 2-28.

b) E. Cariati, E. Lucenti, C. Botta, U. Giovanella, D. Marinotto, S. Righetto, *Coord. Chem. Rev.* **2016**, *306*, 566 – 614.

c) A. Steffen, B. Hupp, in *Comprehensive Coordination Chemistry III*, eds. E. C. Constable, G. Parkin, L. Jr Que, Elsevier, **2021**, pp. 466-502.

[14] E. Silva, A. M. Edwards, *Flavins: Photochemistry and Photobiology*, The Royal Society of Chemistry: Cambridge, UK, **2006**.

[15] M. Bracker, F. Dinkelbach, O. Weingart, M. Kleinschmidt, *Phys. Chem. Chem. Phys.* **2019**, *21*, 9912-9923.

[16] A. Monguzzi, R. Tubino, F. Meinardi, *Phys. Rev.* B **2008**, *77*, 155122.

[17] Edinburgh Instruments, *Benefits of Using a Gated PMT Detector in the FLS1000*, Technical Note, **2020**. Retrieved from: https://www.edinst.com/benefits-of-time-gating-the-pmt-in-the-fls1000/.

[18] G. A. Sommer, L. N. Mataranga-Popa, R. Czerwieniec, T. Hofbeck, H. H. H. Homeier, T. J. J. Müller, H. Yersin, *J. Phys. Chem. Lett.* ***2018***, *9*, 3692-3697.

[19] W. Haselbach, J. M. Kaminski, L. N. Kloeters, T. J. J. Müller, O. Weingart, C. M. Marian, P. Gilch, B. E. Nogueira de Faria, *Chem. Eur. J.* **2023**, *29*, e202202809.

[20] a) G. Herzberg, *Molecular Spectra and Molecular Structure*, Vols I-III Van Nostrand, Toronto, **1966**.

b) D. R. Kearns, *Chem. Rev.* **1971**, *71*, 395–427.

c) H. H. Wasserman, R. W. Murray, *Singlet Oxygen*, Academic press, New York, **1979**.

[21] R. Potashnik, C. R. Goldschmidt, M. Ottolenghi, *Chem. Phys. Letters* **1971**, *9*, 424-425.

[22] H. Kautsky, *Trans. Faraday Soc.* **1939**, *35*, 216-219.

[23] O. L. J. Gijzeman, F. Kaufman, G. Porter, *J. Chem. Soc.*, *Faraday Trans. 2*, **1973**, *69*, 708-720.

[24] K. Kawaoka, A. U. Khan, D. R. Kearns, *J. Chem. Phys.* **1967**, *46*, 1842–1853.

[25] J. Weiss, *Trans. Faraday Soc.* **1939**, *35*, 48-56.

[26] D. F. Evans, *J. Chem. Soc.* **1957**, 1351-1357.

[27] H. Tsubomura, R. S. Mulliken, *J. Am. Chem. Soc.* **1960**, *82*, 5966–5974.

[28] J. R. Lakowicz, *Principles of Fluorescence Spectroscopy*, 3rd edition, Springer, **2006**.

[29] M. Fischer, J. Georges, *Chem. Phys. Lett.* **1996**, *260*, 115-118.

[30] A. Reiffers, C. Torres Ziegenbein, A. Engelhardt, R. Kühnemuth, P. Gilch, C. Czekelius, *Photochem. Photobiol.* **2018**, *94*, 667-676.

[31] S. Felekyan, R. Kühnemuth, V. Kudryavtsev, C. Sandhagen, W. Becker, C. A. M. Seidel, *Rev. Sci. Instrum.* **2005**, *76*, 083104.

[32] J. Maillard, K. Klehs, C. Rumble, E. Vauthey, M. Heilemann, A. Fürstenberg, *Chem. Sci.* **2021**, *12*, 1352-1362.

[33] a) L. Stein, C. Wang, C. Förster, U. Resch-Genger, K. Heinze, *Dalton Trans.* **2022**, *51*, 17664-17670.

b) N. Sawicka, C. J. Craze, P. N. Horton, S. J. Coles, E. Richards, S. J. A. Pope, *Chem. Commun.* **2022**, *58*, 5733–5736.

c) C. Wang, W. R. Kitzmann, F. Weigert, C. Förster, X. Wang, K. Heinze, U. Resch-Genger, *ChemPhotoChem* **2022**, *6*, e202100296.

[34] F. B. Dias, T. J. Penfold, A. P. Monkman, *Methods Appl. Fluoresc.* **2017**, *5*, 012001.

[35] a) R. Hamze, S. Shi, S. C. Kapper, D. S. Muthiah Ravinson, L. Estergreen, M.-C. Jung, A. C. Tadle, R. Haiges, P. I. Djurovich, J. L. Peltier, R. Jazzar, G. Bertrand, S. E. Bradforth, M. E. Thompson, *J. Am. Chem. Soc.* **2019**, *141*, 8616–8626.

b) D. S. Muthiah Ravinson, M. E. Thompson, *Mater. Horiz.* **2020**, *7*, 1210-1217.

[36] a) P. Gilch, *Kinetics of TADF*, seminar of the research training group ModISC, Heinrich-Heine-Universität Düsseldorf, **2021**.

b) Y. Tsuchiya, S. Diesing, F. Bencheikh, Y. Wada, P. L. dos Santos, H. Kaji, E. Zysman-Colman, I. D. W. Samuel, C. Adachi, *J. Phys. Chem.* A **2021**, *125*, 8074-8089.

[37] P. F. Jones, A. R. Calloway, *Chem. Phys. Lett.* **1971**, *10*, 438–443.

Chapter 7. Associated Manuscripts

7.1 Compound Class A – Organic Donor-Acceptor Conjugates

The effect of conformational constraints and oxygen quenching on TADF in donor-acceptor systems

Dragana Sretenović,[a] Laura N. Kloeters,[b] Jeremy M. Kaminski,[c] Tobias Böhmer,[c] Philipp Schmeinck,[d] Gereon A. Sommer,[b] Mina Chalani,[a] Suren Felekyan,[a] Ralf Kühnemuth,[a] Guido J. Reiß,[d] Christoph Janiak,[d] Claus A. M. Seidel,*[a] Christel M. Marian,*[c] and Thomas J. J. Müller*[b]

[a] D. Sretenović, M. Chalani, Dr. S. Felekyan, Dr. R. Kühnemuth,
Prof. Dr. C. A. M. Seidel
Institut für Physikalische Chemie
Heinrich-Heine-Universität Düsseldorf
Universitätsstr. 1, 40225 Düsseldorf, Germany
E-mail: cseidel@hhu.de

[b] Dr. L. N. Kloeters, Dr. G. A. Sommer, Prof. Dr. T. J. J. Müller
Institut für Organische Chemie und Makromolekulare Chemie
Heinrich-Heine-Universität Düsseldorf
Universitätsstr. 1, 40225 Düsseldorf, Germany
E-mail: ThomasJJ.Mueller@uni-duesseldorf.de

[c] J. M. Kaminski, T. Böhmer, Prof. Dr. C. M. Marian
Institut für Theoretische Chemie und Computerchemie
Heinrich-Heine-Universität Düsseldorf
Universitätsstr. 1, 40225 Düsseldorf, Germany
E-mail: christel.marian@hhu.de

[d] P. Schmeinck, Dr. G. J. Reiß, Prof. Dr. C. Janiak
Institut für Anorganische Chemie und Strukturchemie
Heinrich-Heine-Universität Düsseldorf
Universitätsstr. 1, 40225 Düsseldorf, Germany

Manuscript stage: In preparation for *Chemical Science.* Changes can still be made to the current version, such as adding or removing text or figures and author contributions.

7.1.1 Introduction

TADF (thermally activated delayed fluorescence) has become an important design principle of metal free dyes and their applications range from non-doped organic light-emitting diodes (OLEDs),[1] over biomedicine[2] to photocatalysis.[3] In particular, increasing the energy efficiency of emitters in OLEDs takes enormous effort and has become the major interdisciplinary challenge for devising novel emissive molecules by synthesis, photophysics and theory.[4,5] One decisive key factor for enabling high internal quantum efficiency of TADF emitters is the singlet-triplet energy difference (ΔE_{ST}).[6] Small ΔE_{ST} values allow for efficient reverse intersystem crossing (rISC) that leads to the depopulation of non-emissive triplet states T_1 into emissive singlet states S_1. In donor-acceptor conjugates with steric distortion, spatial separation of hole and electron densities leads to intramolecular charge transfer and small ΔE_{ST}.[7] This steric distortion is achieved by conformational fixation with the aromatic linkers, for instance in *spiro* systems or by bis-*ortho* disubstitution.

However, at complete orthogonalization of the donor and acceptor units, the emission transition dipole moment might reduce to zero, which causes a dramatic loss of emission quantum yield. Therefore, fine-tuning of ΔE_{ST} by conformational constraint of the angle between donor and acceptor parts warranting a small energy gap with a concomitant sufficiently large fluorescence rate constant appears to be an option for modulating singlet-triplet transitions.[8] Besides this approach based upon conformational design, the presence of oxygen as a quencher of both singlet and triplet state might also affect the TADF characteristics of donor-acceptor dyes. Herein, we report the investigation of conformational effects on the photophysics as well as on TADF properties of a TADF system that we chose as a meaningful model.[9,10] Introducing substituents with different steric demand on the phenylene bridge of the reference system causes a conformational constraint in the ground state and this effect on the TADF properties is scrutinized by experimental and computational approaches. Photophysical measurements consider the effects of oxygen quenching on the delayed fluorescence lifetimes.

7.1.2 Results and Discussion

Synthesis

Five donor-acceptor systems including the primordial system that already has been shown to possess TADF properties[9,10] are accessible by a concise two-step sequence. Starting from *para*-bromo anilines **1** and aryl iodides **2**, the brominated triphenylamine donor substrates **3** are synthesized by Ullmann coupling in the presence of catalytic amounts of copper iodide and 1,10-phenanthroline and potassium *tert*-butoxide as a base in 31–86% yield (Scheme 7.1).[11] The donor substrates **3** subsequently react in a bromine-lithium exchange-borylation-Suzuki (BLEBS) sequence[12] with 2-iodoterephthalonitrile (**4**) as an acceptor component to give after workup and purification by flash chromatography on silica gel the target compounds **5** in 14-99% yield.[10] While this one-pot sequence proceeds smoothly with $Pd(PPh_3)_4$ for monosubstituted phenyl bridges, the sterically demanding donor substrate **3d** with *ortho,ortho'*-disubstitution requires the catalyst system $Pd_2(dba)_3$/2-biphenyl)-dicyclohexylphosphane (CyJohnPhos) and K_3PO_4 as a base in the Suzuki step to give the desired product **5d** in low yield. The molecular structures of the title compounds **5** were unambiguously assigned by comprehensive ^{1}H and ^{13}C NMR spectroscopy and the molecular composition was determined by combustion analysis and/or mass spectrometry (see chapter 7.1.4, Supplementary Information).

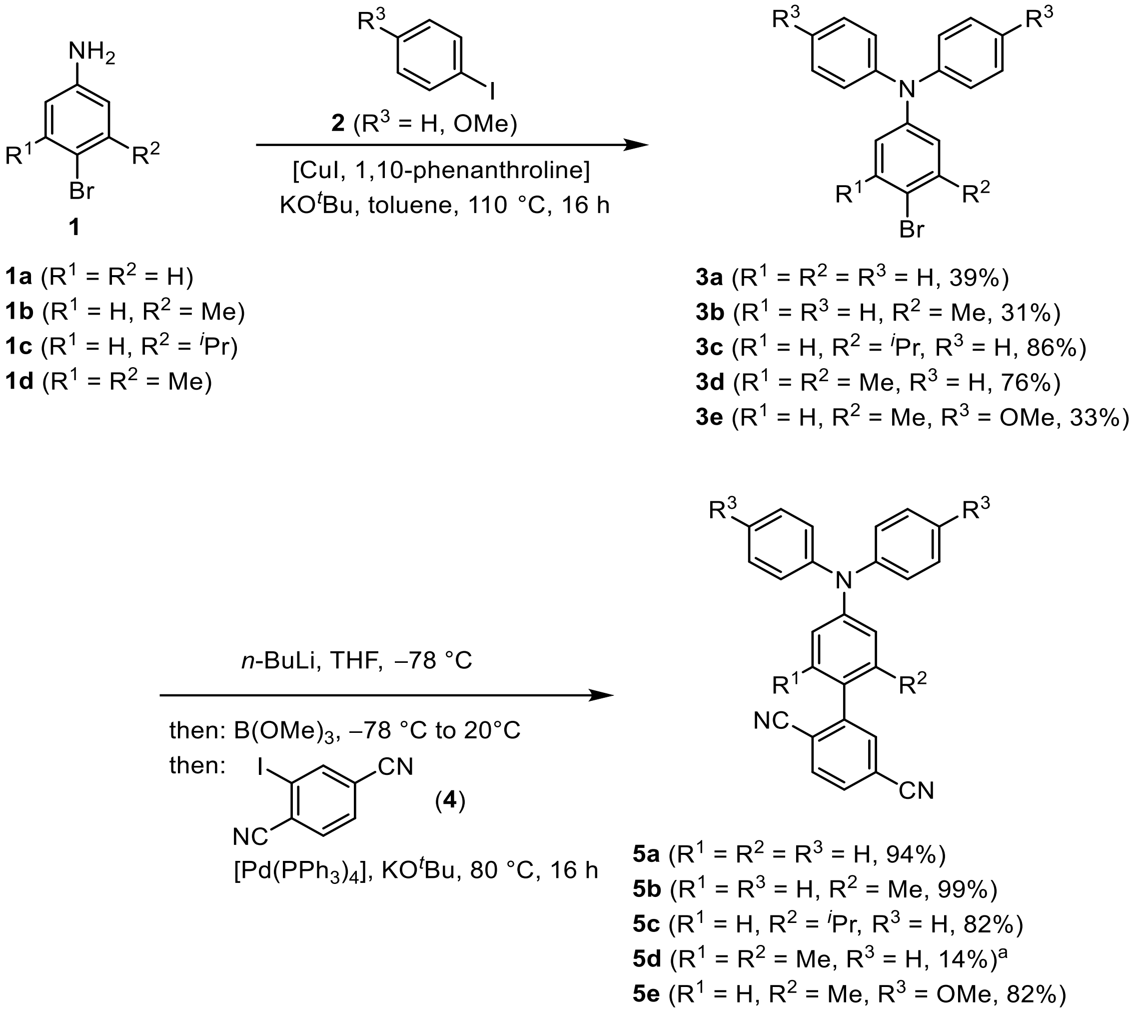

Scheme 7.1. Synthesis of donor-acceptor systems **5** with torsionally constrained phenylene-bridge via Ullmann arylation and one-pot bromine-lithium-exchange-borylation-Suzuki coupling (BLEBS) sequence [^{a}Pd$_2$(dba)$_3$/2-biphenyl)dicyclohexylphosphane (CyJohnPhos) and K$_3$PO$_4$ are employed in the Suzuki step].

Placing *ortho*-substituents on the phenylene bridge adjacent to the terephthalonitrile acceptors causes significant torsion of the donor-acceptor axes as seen in the crystal structure (see chapter 7.1.4, Supplementary Information). This causes an increased conformational strain and eventually hindered rotation around the donor-acceptor ligating sigma bond (Figure 7.1). A criterion for estimating restricted rotation around an aryl-aryl CC-bond[13] is reflected by the hindered rotation of isopropyl groups,[14] where the methyl groups become diastereotopic as a result of the formation of atropisomeric conformer at a coalescence temperature T_c that corresponds to the energy barrier of rotation.

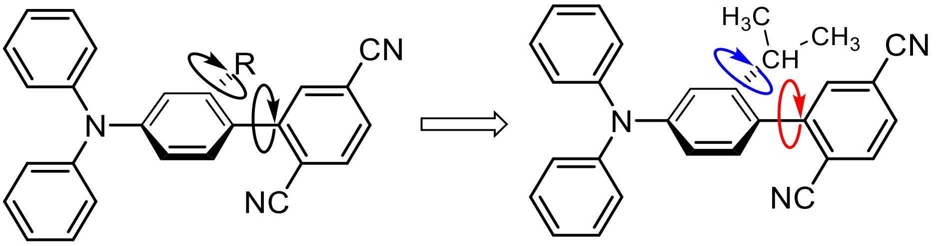

Figure 7.1. Restricted rotation around the aryl-aryl CC-bond in dyes **5** (left) and *iso*-propyl substituted model (right) with two interfering rotations of the *iso*-propyl (blue) and the biaryl rotation (red).

The expected doublet for the methyl protons of the *iso*-propyl group of dye **5c** for free rotation splits at lower temperature into two doublets at δ 1.01 and 0.96 with coupling constants of 6.77 and 6.82 Hz. Indeed, on the proton NMR time scale the rotation of the iso-propyl group is very slow at room temperature in DMSO-d^6. Variable temperature (VT) NMR spectra were recorded at 298, 328, 343, and 373 K to estimate the rotational barrier (Figure S7.27). At 343 K the *iso*-propyl protons are broadened indicating the coalescence temperature T_c. In the VT ^{1}H NMR spectrum above 343 K the methyl groups of the *iso*-propyl protons of compound **3d** are isochronous by free rotation and the signal appears as a doublet at δ 0.99 (J = 6.8 Hz). From the coalescence temperature (T_c = 343 K) the rate constant k_{T_c} and thereby the Gibbs free enthalpy of activation for rotation of the isopropyl group can be calculated to $\Delta Gc^{\ddagger}$ = 74 kJ/mol (for details, see Supplementary Information).[15] This value lies within the same order of magnitude for hindered isopropyl rotations[14] as well as for hindered *ortho,ortho'*-biaryl rotations.[13] As a consequence, in solution and at room temperature the rotational degrees of freedom around the biaryl σ-bond are restricted and, therefore, these systems can be considered to be conformationally constrained in the electronic ground state.

Spectroscopy

We examined two factors influencing the photophysical properties in our study: the influence of steric torsion variations within the linker between the donor and acceptor (compound series **5a-5d**), and the increased donor strength (compound **5e**). The effect of enhanced donor strength and the resulting changes in the photophysical properties of compound **5e** are addressed separately.

Compounds 5a-5d: Impact of varied steric torsion on the photophysical properties

Compound **5a** has the smallest torsion angle, which results in the closest spatial proximity of its hole and electron densities. Thus, this compound has the highest absorption coefficient for its lowest-energy absorption maximum among all four compounds. From **5a** to **5d**, the increasing torsion angle leads to a more significant decoupling of the donor and acceptor, and consequently lower absorption coefficients (Figure 7.2A). The calculated S_0-S_1 oscillator strengths (*f*) follow this trend (Figure 7.2B). Additionally, compound **5a** shows three, while compounds **5b-5d** show two bands in the UV region. The lowest-energy absorption maximum shifts hypsochromically, from 391 nm (**5a**) to 377 nm (**5d**) (Table 7.1).

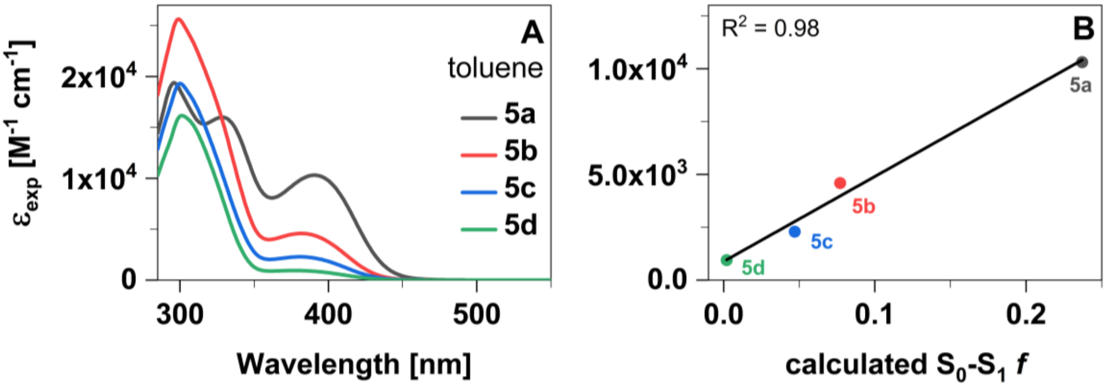

Figure 7.2. A. Absorption spectra of compounds **5a-5d** in toluene. Experimental absorption coefficients (ε_{exp}) derived from absorption spectra are shown. **B.** The correlation between the experimental absorption coefficients (ε_{exp}) and the calculated oscillator S_0-S_1 strengths *f*.

The fluorescence emission maxima for all four compounds in toluene are in the range of 490 nm to 500 nm. We derived several values from the corrected steady-state spectra, including the 0-0 energy ($\tilde{\nu}_{00}$), the full width at half maximum (FWHM) of the emission band, Stokes shift ($\Delta\tilde{\nu}_s$), and radiative rate constants calculated according to the Strickler-Berg method (k_F^{SB}) (Table 7.1). Both the absorption and fluorescence spectra were transformed into the transition dipole moment representation for analysis (Figure S7.33). The 0-0 energies ($\tilde{\nu}_{00}$)

were determined as the intersection point between the corrected absorption and fluorescence emission spectra and ranged from 22472 cm^{-1} (**5a**) to 22676 cm^{-1} (**5c**). To calculate the FWHM of the emission band, we measured the distance in wavenumber units between two points with a normalized intensity of 0.5. Compound **5d** exhibited the widest fluorescence band in toluene, with a FWHM of 4106 cm^{-1}. The Stokes shift was determined as the distance between the first absorption maxima and the fluorescence maxima. To find the first absorption maximum, we deconvoluted the absorption spectra using a Gaussian fit. The calculated Stokes shift increased from 5421 cm^{-1} for **5a** to 6385 cm^{-1} for **5d**. These Stokes shift values were used in the Lippert-Mataga analysis[16,17] to determine the difference in the dipole moments between the excited and ground states (μ_E-μ_G) (Table 7.1). To generate Lippert-Mataga plots (Figure S7.36), we measured compounds **5a-5d** in toluene, methyl *tert*-butyl ether (tBuMeEther), anisole, chlorobenzene, ethyl acetate, tetrahydrofuran (THF), dichloromethane (DCM), dimethylformamide (DMF), and acetonitrile (MeCN). The measurements revealed a positive solvatochromic effect (Figure 7.3), typically associated with charge-transfer states and TADF.

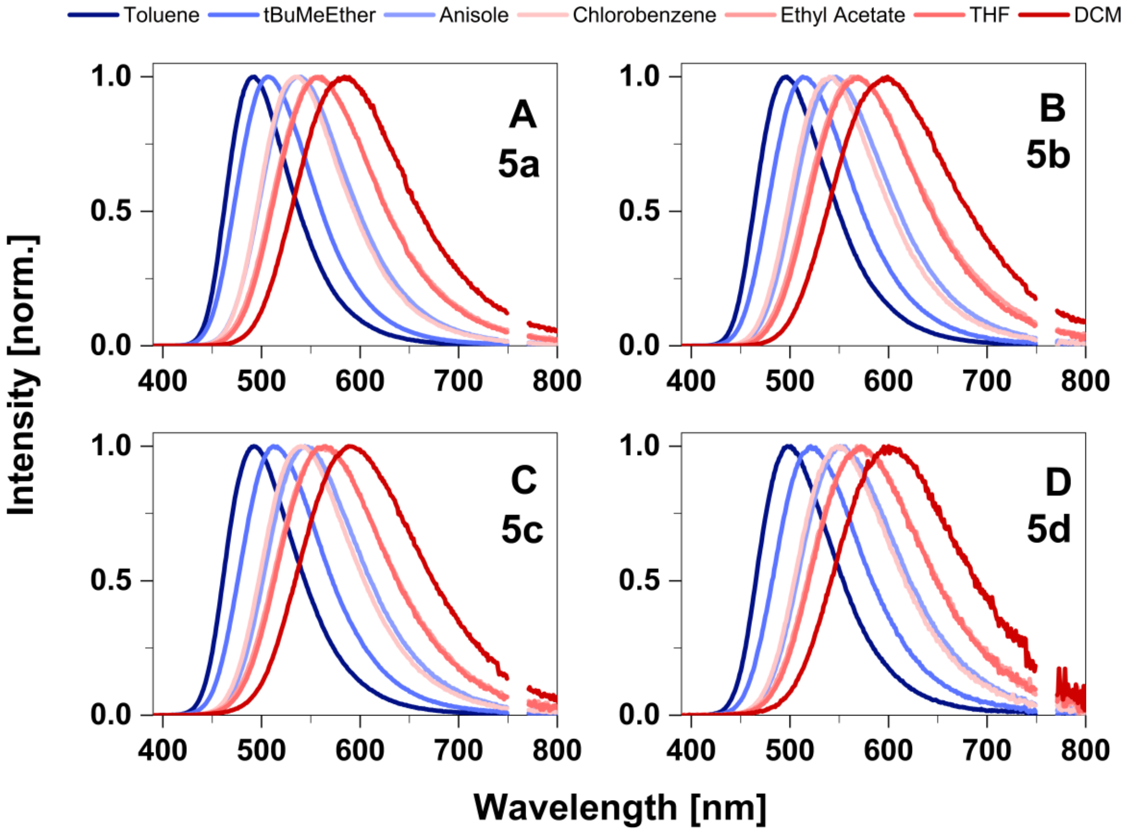

Figure 7.3. Fluorescence emission spectra of **5a-5d** (**A-D**) in solvents labeled in the legend above the figure. Samples were excited at 375 nm. The range between 750 and 770 nm is excluded due to the presence of second-order diffracted laser light.

Modifications to the substituents on the linker between donor and acceptor had a significant impact on the fluorescence quantum yields. The fluorescence quantum yields in air-saturated toluene ($\Phi_{\mathrm{PF}}{}^{\mathrm{Air}}$) were determined in relation to Rhodamine 6G in ethanol as a reference ($\Phi_{\mathrm{F}}{}^{\mathrm{r}} = 0.94$).[18,19] Compound **5a** had the highest $\Phi_{\mathrm{PF}}{}^{\mathrm{Air}}$ of 60%. From **5a** to **5d**, the $\Phi_{\mathrm{PF}}{}^{\mathrm{Air}}$ decreases and reaches 20% for compound **5d**. To determine the prompt fluorescence quantum yield in nitrogen ($\Phi_{\mathrm{PF}}{}^{\mathrm{N_2}}$), we multiplied the quantum yield in air ($\Phi_{\mathrm{PF}}{}^{\mathrm{Air}}$) by the ratio of the fluorescence-weighted prompt fluorescence lifetimes in nitrogen and air, $\langle\tau\rangle_{\mathrm{F}}{}^{\mathrm{N_2}}$ and $\langle\tau\rangle_{\mathrm{F}}{}^{\mathrm{Air}}$ [eq. (1), Table 7.1].

$$\Phi_{\mathrm{PF}}^{N_2} = \Phi_{\mathrm{PF}}^{\mathrm{air}} \cdot \frac{\langle\tau\rangle_{\mathrm{F}}^{N_2}}{\langle\tau\rangle_{\mathrm{F}}^{\mathrm{Air}}} \tag{1}$$

One approach to determine the delayed fluorescence quantum yield (Φ_{DF}) uses steady-state data. In an air-saturated solution, only prompt fluorescence is observed due to the quenching of triplet states by oxygen. In a nitrogen-purged solution, both prompt and delayed fluorescence are operative. Thus, the integral of the steady-state fluorescence spectrum in air is proportional to Φ_{PF}, while in nitrogen is $\Phi_{\mathrm{PF}} + \Phi_{\mathrm{DF}}$.[20] However, the quantum yield of delayed fluorescence cannot be simply calculated as the difference between the steady-state fluorescence integrals in air and nitrogen as indicated in Ref. [20], since singlet states are also quenched by oxygen to a certain extent (see Figure 7.4, Table 7.1). The increase in the steady-state emission signal in nitrogen is therefore not only due to the delayed fluorescence, but also to the enhanced prompt fluorescence. To obtain an estimate of the delayed fluorescence quantum yield, it is important to consider the prompt fluorescence quantum yield in nitrogen ($\Phi_{\mathrm{PF}}{}^{\mathrm{N_2}}$) and not in air ($\Phi_{\mathrm{PF}}{}^{\mathrm{Air}}$) in the context of the total fluorescence emission in absence of oxygen (Φ_{TF}), eq. (2).

$$\Phi_{TF} = \Phi_{\mathrm{PF}}^{N_2} + \Phi_{DF} \tag{2}$$

By combining equations (1) and (2), the delayed fluorescence quantum yield is calculated from the following equation:

$$\Phi_{DF} = \Phi_{TF} - \Phi_{\mathrm{PF}}^{\mathrm{air}} \cdot \frac{\langle\tau\rangle_{\mathrm{F}}^{N_2}}{\langle\tau\rangle_{\mathrm{F}}^{\mathrm{Air}}} \tag{3}$$

Another method to assess the quantum yields of delayed fluorescence involves integrating the time-resolved decays recorded within the nanosecond time range (Figure 7.4, Table 7.1). The region within the decay offset in nitrogen is important because it contains long lifetime components such as delayed fluorescence [eqs. (4) and (5)]. The quantum yield of delayed fluorescence is estimated by comparing the TCSPC decay offsets obtained under air and nitrogen in the nanosecond time range [see eqs. (6) and (7)].

$$offset\ (Air) = dark\ counts + afterpulses \tag{4}$$

$$offset\ (N_2) = dark\ counts + afterpulses + F_{DF} \tag{5}$$

$$F_{DF} = \int offset\ (N_2) - \int offset\ (Air) \tag{6}$$

$$\Phi_{DF} = \frac{F_{DF}}{F_{PF}} \cdot \Phi_{\mathrm{PF}}^{N_2} \tag{7}$$

where F_{DF} and F_{PF} are the integral fractions of delayed and prompt fluorescence.

The radiative rate constants ($k_{\mathrm{F}}^{\mathrm{SB}}$) were determined using the Strickler-Berg method,[21] by integrating the absorption and fluorescence spectra. To compute the absorption integral, we focused on the absorption band with the lowest energy, identifying it through comparison with the corresponding corrected fluorescence spectrum. This fluorescence spectrum was mirrored at the 0-0 energy point and scaled to match the height of the corrected absorption spectrum.[22] The calculated rate constants decreased from $7.4 \cdot 10^7$ s^{-1} for **5a** to $0.7 \cdot 10^7$ s^{-1} for **5d**. Furthermore, fluorescence lifetimes ($\tau_{\mathrm{F}}^{\mathrm{SB}}$) were estimated based on the radiative rate constant, accounting for the fluorescence quantum yields [eqs. (8) and (9), Table 7.1].

$$\tau_{\mathrm{F}}^{\mathrm{SB\ air}} = \frac{\phi_{\mathrm{PF}}^{\mathrm{air}}}{k_{\mathrm{F}}^{\mathrm{SB}}} \tag{8}$$

$$\tau_{\mathrm{F}}^{\mathrm{SB}\ N_2} = \frac{\phi_{\mathrm{PF}}^{N_2}}{k_{\mathrm{F}}^{\mathrm{SB}}} \tag{9}$$

However, the calculated values do not align with those measured by TCSPC, which is presumably due to the non-Condon effect.[10,23] As the torsion angle increases in the series **5a-5d**, the discrepancies in lifetimes also grow, ranging from 9% for **5a** to 66% for **5d**. This discrepancy is quantified as the ratio of the measured and Strickler-Berg calculated radiative rate constant, denoted as k_{F} / $k_{\mathrm{F}}^{\mathrm{SB}}$ in Table 7.1.

Table 7.1. Spectroscopic and photophysical parameters of compounds **5a-5e** in toluene. The wavelength maxima of the 1st and 2nd bands with the lowest absorption energies (λ_{max}), absorption coefficients (ε), and fluorescence emission maxima (λ_{em}) refer to the spectra in the wavelength domain. 0-0 energies ($\tilde{\nu}_{00}$), full widths at half maxima of the emission bands (emission FWHM), and Stokes shift ($\Delta\tilde{\nu}_{S}$) were derived from the corrected absorption and fluorescence emission spectra (Figure S7.33).[24]

Parameters	**5a**	**5b**	**5c**	**5d**	**5e**
1st λ_{max} [nm]	391	382	381	377	401
1st ε_{max} [M^{-1} cm^{-1}]	10309	4586	2289	941	5750
S_0-S_1 ***f*** [a]	0.237	0.077	0.047	0.002	0.081
λ_{em} [nm]	493	497	492	497	558
2nd λ_{max} [nm]	330	299	300	301	298
2nd ε_{max} [M^{-1} cm^{-1}]	15979	25648	19324	16166	33333
$\tilde{\nu}_{00}$ [cm^{-1}]	22472	22624	22676	22624	20790
Emission FWHM [cm^{-1}]	3606	3990	3916	4106	4417
$\Delta\tilde{\nu}_{S}$ [cm^{-1}]	5421	6022	6077	6385	7090
μ_E-μ_G [D], exp. [b]	14.1	13.9	14.5	14.4	14.1
μ_E-μ_G [D], theory [b]	19.1	22.9	22.7	24.0	25.3
Φ_{PF}^{Air} [c]	0.59	0.36	0.29	0.20	0.16
$\Phi_{PF}^{N_2}$ [d]	0.76	0.60	0.56	0.53	0.36
Φ_{DF} [e]	0.00	0.07	0.10	0.33	0.04
Φ_{TF} [f]	0.76	0.67	0.67	0.86	0.40
k_F^{SB} [10^7 s^{-1}] [g]	7.4	3.4	1.7	0.7	3.2
$\tau_F^{SB\ Air}$ [ns] [g]	8.0	10.6	17.0	29.1	5.1
$\tau_F^{SB\ N_2}$ [ns] [g]	10.3	17.6	33.0	77.1	11.6
$\langle\tau\rangle_F^{Air}$ [ns] [h]	7.3	12.3	14.7	17.5	10.8
$\langle\tau\rangle_F^{N_2}$ [ns] [h]	9.4	20.4	28.5	46.5	24.6
k_F / k_F^{SB} [i]	1.1	0.9	1.2	1.7	0.5
τ_{DF} at 300 K [μs]	-	1074.8	357.5	18.4	35.5
ΔE_{ST} [meV], exp. [j]	-	102	75	23	34
ΔE_{ST} ad. [meV], theory	501	438	428	333	228
ΔE_{ST} vert. [meV], theory	341	192	162	73	157

[a] Calculated S_0-S_1 oscillator strengths ***f***. **[b]** The difference between the dipole moments of the excited and ground states (μ_E-μ_G) was experimentally determined via the Lippert-Mataga analysis (Figure S7.36). Theoretical values are based on the toluene implicit solvent model. **[c]** The quantum yield of prompt fluorescence measured in an air-saturated toluene (Φ_{PF}^{Air}) was determined using the relative method with Rhodamine 6G in ethanol as a reference (Φ_F^r = 0.94).[18] **[d]** The quantum yield of prompt fluorescence for a nitrogen-purged solution (Φ_{PF}^{N2}) was calculated according to eq. (1). **[e]** The quantum yield of delayed fluorescence determined by the TCSPC offset analysis, eq. (7). **[f]** The total fluorescence quantum yield calculated according to eq. (2). **[g]** The radiative rate constants (k_F^{SB}) predicted by Strickler-Berg analysis.[21] The fluorescence lifetimes were estimated according to eqs. (8) and (9). **[h]** The fluorescence-weighted lifetimes of prompt fluorescence measured by TCSPC. Individual decay times and species fractions are compiled in the Supplementary Information. **[i]** The ratio of the measured and Strickler-Berg calculated radiative rate constant, k_F / k_F^{SB}. **[j]** The singlet-triplet energy gaps (ΔE_{ST}) were determined experimentally from the Arrhenius plot (Figure 7.8).

Prompt fluorescence lifetimes of compounds **5a-5d** were measured in both air-saturated and nitrogen-purged toluene solutions (Figure 7.4). All decays were characterized using bi-exponential fit functions (see chapter 7.1.4, Supplementary Information). The prompt fluorescence lifetime shows a significant increase from **5a** to **5d**. The decoupling of the donor and acceptor apparently influences non-radiative deactivation pathways, resulting in a prolonged lifetime of the bright state S_1. Additionally, a significant increase in prompt fluorescence lifetime was observed when the toluene solution is purged with nitrogen. These results suggest that singlet states are quenched by oxygen.

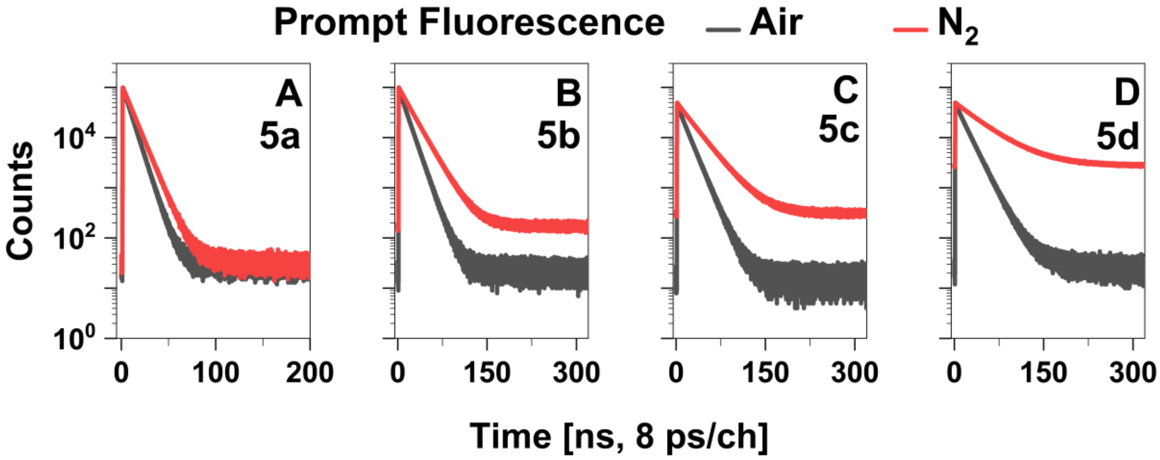

Figure 7.4. Prompt fluorescence of compounds **5a-5d** (**A-D**) in air-saturated and nitrogen-purged solutions in toluene measured by TCSPC. The samples were excited at 375 nm, and the detection wavelength was 490 nm. The repetition rate was 4.88 MHz for compound **5a**, and 3.12 MHz for compounds **5b-5d**. The bin size was 8 picoseconds for all compounds.

By applying the Stern-Volmer equation [eq. (10)], we predicted the prompt fluorescence lifetimes in air-saturated solutions [$\langle\tau\rangle^{\mathrm{Air}}$] based on the measured prompt fluorescence lifetimes under nitrogen [$\langle\tau\rangle^{\mathrm{N_2}}$] and a quenching constant derived from diffusion ($k_{\mathrm{q,diff.}}$), since oxygen quenching is a diffusion-controlled process.[25]

$$\langle\tau\rangle^{air} = \frac{\langle\tau\rangle^{N_2}}{1 + k_{q,diff.} \cdot \langle\tau\rangle^{N_2} \cdot [O_2]} \tag{10}$$

The oxygen concentration $[O_2]$ in toluene is 1.8 mM at 20 °C and an O_2 partial pressure of 0.213 bar.[26] The quenching constant ($k_{\mathrm{q,diff.}}$) is calculated according to eq. (11).

$$k_{q,diff.} = 4\pi N_A \left(r_{dye} + r_{O_2}\right)\left(D_{dye} + D_{O_2}\right) \tag{11}$$

where N_A is the Avogadro constant, r_{dye} and r_{O2} are the radii of the fluorescent dye and oxygen, and D_{dye} and D_{O2} are the diffusivites of the fluorescent dye and oxygen, respectively. The dye radius, r_{dye}, is estimated in *PyMol* (Figure S7.34) and via time-resolved anisotropy (Figure S7.35). The oxygen diffusivity in toluene is $D_{O2} = 4.38 \cdot 10^{-9}$ m^2/s.[27] The dye diffusivity, D_{dye}, is calculated using eq. (12).

$$D_{dye} = \frac{k_B T}{6\pi\eta r_{dye}} \tag{12}$$

where k_B is the Boltzmann constant, T is the temperature, η is the toluene viscosity.

Finally, the quenching constant derived from diffusion is $k_{q,diff.} = 2.1 \cdot 10^{10}$ M^{-1} s^{-1}. The predicted and measured air-saturated prompt fluorescence lifetimes are in excellent agreement (Table 7.2). Furthermore, we calculated the experimental quenching constants, $k_{q,exp.}$, by using the measured lifetimes, and they are quite similar for all four compounds (around $2 \cdot 10^{10}$ M^{-1} s^{-1}, Table 7.2) and in good agreement with the previously determined $k_{q,diff}$.

Table 7.2. Predicted air-saturated prompt fluorescence lifetimes by the Stern-Volmer equation [eq. (10)] and experimental quenching constants ($k_{q,exp}$) for compounds **5a-5d**. The species-averaged lifetimes, $\langle\tau\rangle_x$ (see Supplementary Information), are used in eq. (10). The ratio of predicted to the measured air-saturated prompt fluorescence lifetimes is equal to 1 for all four compounds.

Compound	Species-averaged lifetime, $\langle\tau\rangle_x$ [ns]			Ratio predicted / measured	$k_{q,exp.}$ [$\cdot 10^{10}$ M^{-1}s^{-1}]
	Air (measured)	N_2 (measured)	**Air (predicted)**		
5a	7.1	9.1	6.8	1.0	1.7
5b	11.2	20.2	11.5	1.0	2.2
5c	13.0	28.2	13.7	1.1	2.3
5d	16.2	46.0	16.9	1.0	2.2

In addition to the prompt fluorescence observed in the nanosecond time range, compound **5b** also shows delayed fluorescence in the microsecond time range.[9,10] Our aim was to study how different substituents on the phenylene bridge between the donor and acceptor affect TADF properties in the series of compounds **5a-5d**. However, our findings indicate that oxygen plays a crucial role, and TADF properties are highly dependent on the oxygen concentration in the toluene solution. It is known that oxygen efficiently quenches triplet states,[28] with longer lifetimes being more susceptible to quenching than shorter ones,[29] but the observed effect in our study was quite dramatic. This can be effectively illustrated by the Stern-Volmer[19] plots [eq. (10), Figure 7.5]. We calculated air-saturated lifetimes (τ^{Air}) for different oxygen concentrations with respect to specific oxygen-free lifetimes (denoted as τ^{N_2}). The oxygen-free lifetimes include examples of (i): fast (21 ns, as prompt fluorescence of compound **5b**, Figure 7.5A), (ii): slow (30 µs, Figure 7.5B), and (iii): very slow (300 µs, Figure 7.5C) processes. It becomes evident from Figure 7.5A that for fast processes such as prompt fluorescence, oxygen has limited time to act, and saturation is reached relatively quickly. Consequently, there is no difference in measured lifetimes if the concentration of oxygen in the solution is 10^{-5} M or 10^{-7} M, as both cases yield a lifetime of 21 ns. However, the scenario changes when observing slower processes, such as delayed fluorescence in the microseconds. Minor changes in oxygen concentration can lead to significant changes in measured lifetimes (Figure 7.5B and C). In an air-saturated toluene solution, with a standard oxygen concentration of 1.8 mM,[26] we have not detected any delayed fluorescence for this particular compound series. Standard deoxygenation methods, such as bubbling or freeze-thaw procedures, can reach oxygen concentrations in the range of 10^{-6} M to 10^{-7} M.[30] However, even when reaching an oxygen concentration of 10^{-7} M in the solution, we are limited by diffusion, and only lifetimes of approximately 1 ms can be experimentally measured. At lower temperatures, this limit is exceeded since diffusion is considerably slower.

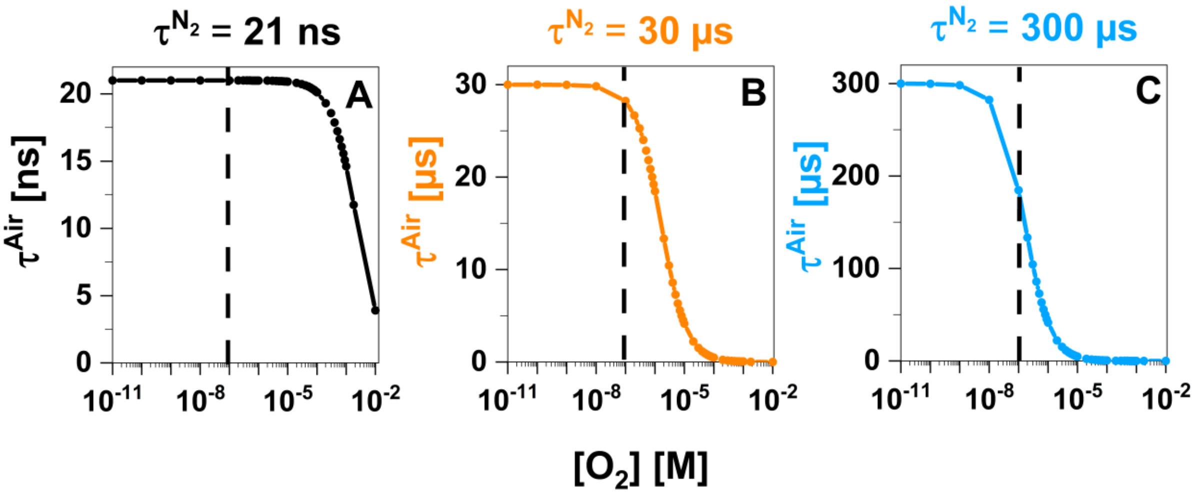

Figure 7.5. Oxygen quenching predicted by Stern-Volmer equation. Air-saturated lifetimes (τ^{Air}) are calculated for various oxygen concentrations in relation to specific oxygen-free lifetimes (τ^{N_2}) using the Stern-Volmer equation. The selected oxygen-free lifetimes represent different process speeds: **A.** τ^{N_2} = 21 ns; **B.** τ^{N_2} = 30 µs and **C.** τ^{N_2} = 300 µs.

We observed substantial variations in the delayed fluorescence lifetimes within this compound series. After successfully reproducing the previously reported delayed fluorescence lifetime of 30 μs for **5b**,[9,10] we observed that the same compound could yield dramatically longer lifetimes depending on the specific deoxygenation procedure used during sample preparation. Thus, sample preparation was one of the most challenging aspects of this study.

The experimental setup used for deoxygenation is shown in Figure 7.6. In the first step, the cryogenic UV-quartz cuvette [labelled (I)] was filled with the sample solution. One additional millilitre of solvent was added to the prepared sample to ensure that the concentration does not increase beyond the range suitable for fluorescence measurements during deoxygenation via inert gas bubbling. For this, nitrogen N5 (Air Liquide) was passed through the capillary in the sample [(II) to (III)] until the solvent level reached the initial value in the cuvette (approximately 30 min). The setup was then pressurized with nitrogen to 0.2 bar above ambient pressure and cooled to 77 K in a liquid nitrogen bath. The valve to the inert gas inlet [(II)] was closed, and the valve to the Schlenk line [(IV)] was opened. A high dynamic vaccum ($5 \cdot 10^{-6}$ bar) was applied and the cuvette was flame sealed using a propane torch at the tapered position of the attached Duran glass tube [(V)].

The exact concentration of the deoxygenated sample was then determined by UV-Vis absorption. The oxygen impermeability of the resulting ampoules was verified by an unchanged lifetime of the delayed fluorescence even over a storing period of several months.

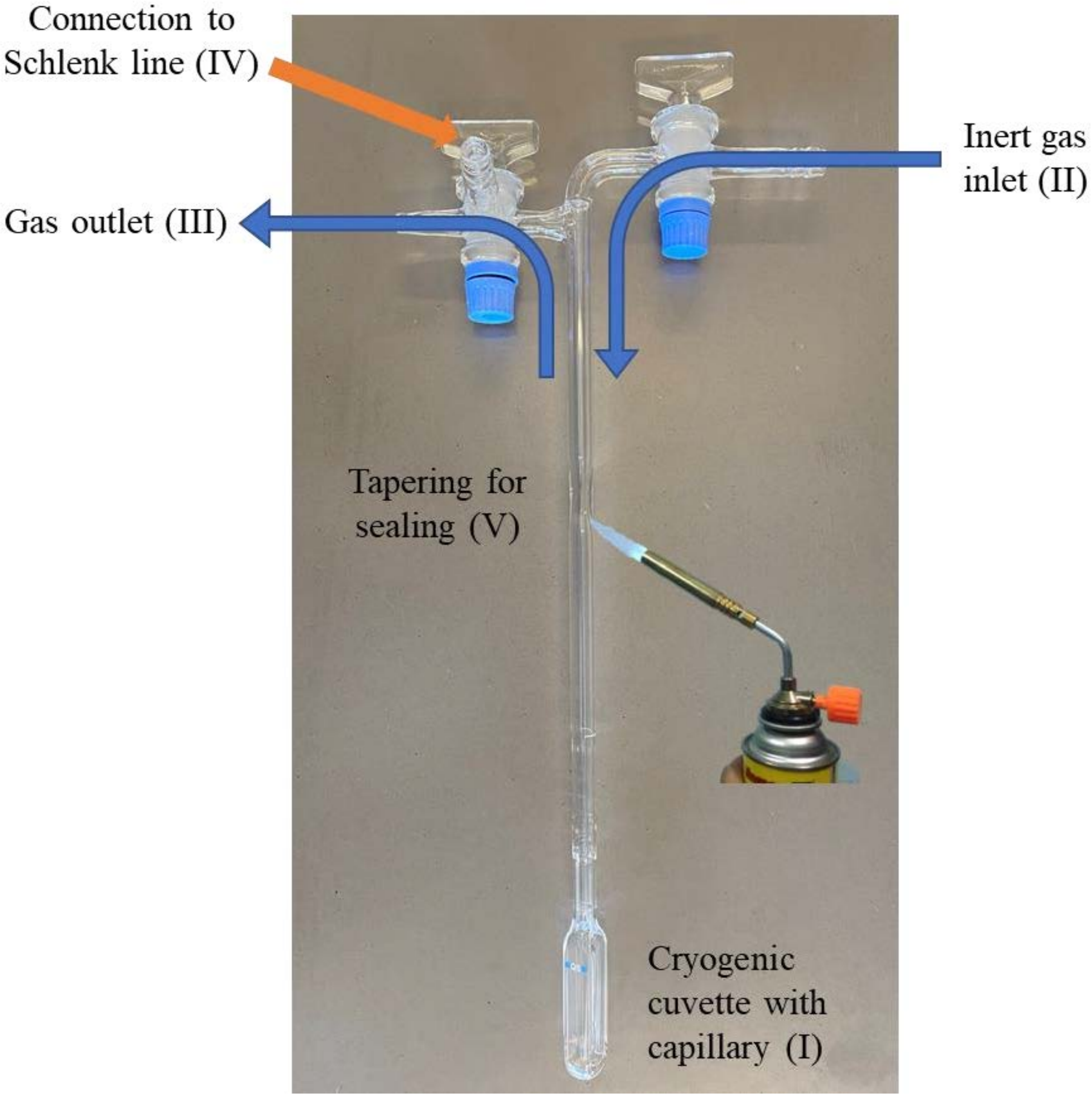

Figure 7.6. Setup used for degassing and sealing of the samples.

The delayed fluorescence lifetimes (Table 7.1) and all related results presented in the following are based on the longest lifetimes recorded for compounds **5a-5d** in this study (Figure 7.7).

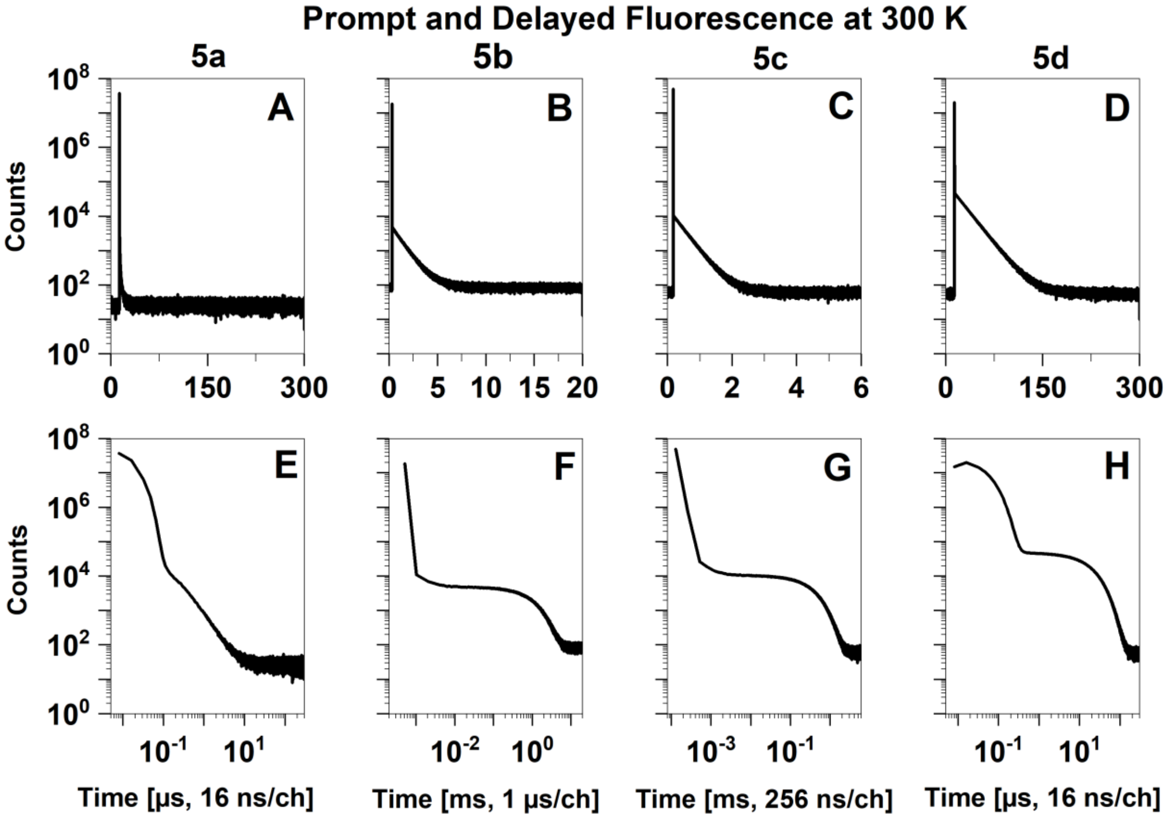

Figure 7.7. Prompt and delayed fluorescence of compounds **5a-5d** in nitrogen-purged toluene solutions. Data are represented in two formats: **A**-**D**: Logarithmic y-axis and linear x-axis, and **E**-**H**: Logarithmic y- and x-axes (log-log data representation). Samples were excited at 375 nm and detected at 495 nm. Repetition rates were: 3.33 kHz for compounds **5a** and **5d**, 0.05 kHz for **5b**, and 0.15 kHz for **5c**. Bin sizes were 16 ns for **5a** and **5d**, 1 μs for **5b**, and 256 ns for **5c**.

For compound **5a** TADF was not observed in our measurements (Figure 7.7 A and E). From **5b** to **5d**, the torsion angle increases, and we observe an increase in the quantum yield and the amplitude of delayed fluorescence. Additionally, the lifetime of delayed fluorescence becomes shorter (Table 7.1). To confirm the temperature dependency of the delayed fluorescence, we conducted a series of time-resolved measurements in a temperature range from 182 K to 300 K (Figure 7.8 A-C). We wanted to avoid phase transitions and conducted measurement only in liquid solutions, considering the melting point of toluene at 178.1 K. For all compounds, temperature series were firstly conducted from a lower to a higher temperature (i.e. from 200 K to 300 K) and then reversely (from 300 K to 182 K) to check the reproducibility of the measured data (see Table S7.8, Table S7.9, Table S7.10). The selected temperatures (labeled in the legend above above Figure 7.8 A-C) were chosen to be equidistant in the reciprocal temperature scale and refer to the silicon diode sensor at the cold head of the cryostat. The temperatures of the samples differed slightly (see Table S7.8, Table S7.9, Table S7.10) and were used for all Arrhenius analyses (Figure 7.8 D-F).

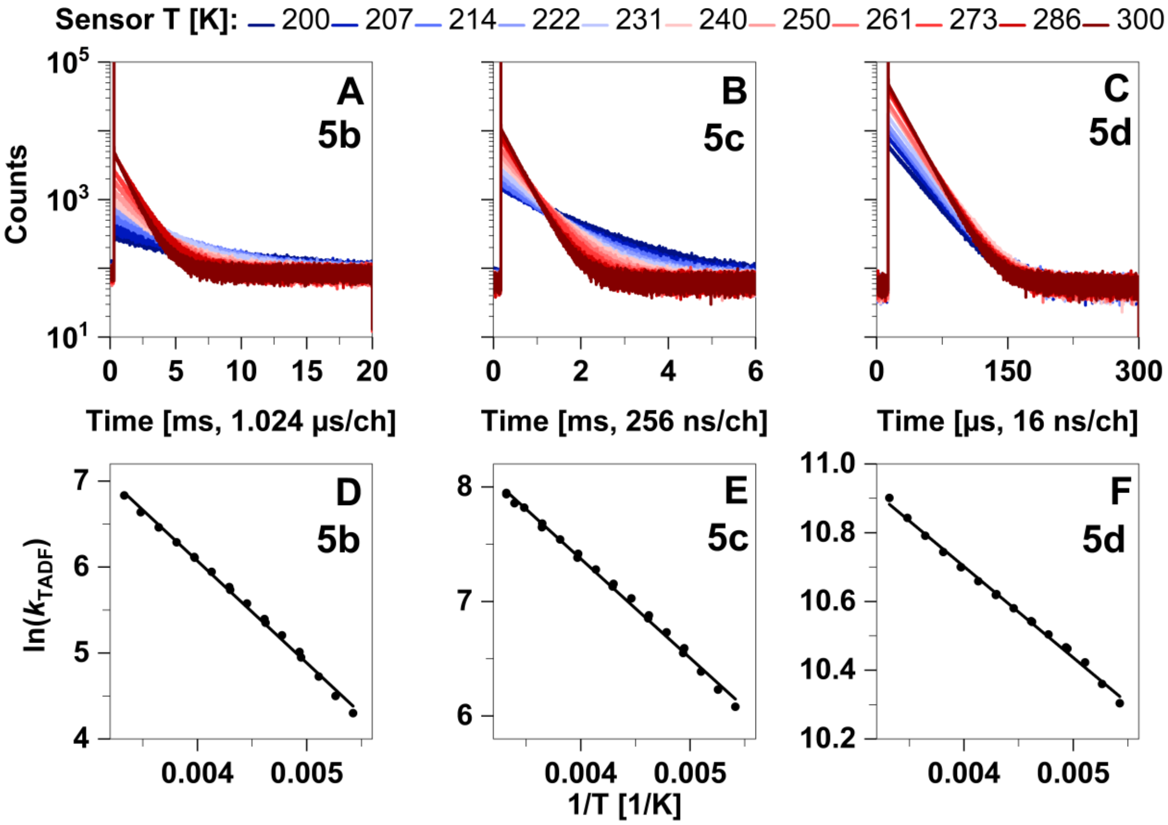

Figure 7.8. A-C: Temperature-dependent time-resolved measurements of compounds **5b-5d** in toluene. The selected temperatures are indicated in the labels above panels A-C and refer to the silicon diode sensor at the cold head of the cryostat. The prompt fluorescence peak has been truncated in order to emphasize the amplitude of the delayed fluorescence. **D-F**: The natural logarithm of the TADF rate constant [ln(k_{TADF})] is plotted against the reciprocal sample temperature (1/T) for compounds **5b-5d** in toluene (see Table S7.8, Table S7.9, Table S7.10). The TADF rate constants k_{TADF} were calculated from the exponential fits of the decays displayed in panels A-C, as: $k_{\mathrm{TADF}} = 1/\tau_{\mathrm{TADF}}$, where τ_{TADF} is the fitted TADF lifetime. Singlet-triplet energy gaps (ΔE_{ST}) were determined from the slope of the linear fit (Table 7.1), according to the Arrhenius equation [Eq. (13)].

$$k_{TADF} = Ae^{-\frac{\Delta E_{ST}}{RT}} \tag{13}$$

where k_{TADF} is the TADF rate constant, A is a constant, ΔE_{ST} is the singlet-triplet energy gap, R is the ideal gas constant, and T is the temperature.

Upon cooling, the amplitudes of delayed fluorescence decrease (Figure 7.8 A-C). This observation is a typical characteristic of TADF. Moreover, the delayed fluorescence lifetimes increase with decreasing temperature due to the reduced efficiency for overcoming the energy barrier when less thermal energy is available. We determined the experimental singlet-triplet energy gaps (ΔE_{ST} in Table 7.1) from the slopes of the Arrhenius plots (Figure 7.8 D-F) according to eq. (13). However, it is important to keep in mind that the absolute numbers may not accurately represent the actual ΔE_{ST} of the molecules. The measured TADF rate constant is affected by processes that depopulate triplet states, such as oxygen quenching and phosphorescence. Given that our molecules are prone to oxygen quenching, and despite our efforts to minimize oxygen concentrations to experimental minima, the measured TADF rate constant is a result of joint depopulation of the triplet state by both TADF and oxygen quenching, rather than TADF alone. Nonetheless, the data can be interpreted qualitatively, focusing on a general trend observed from **5b** to **5d**, which agrees well with the theoretical predictions (Table 7.1).

We have also employed a different approach based on kinetics to experimentally determine the ΔE_{ST} energy gaps [equations (14) and (15)].[31]

$$K_{eq} = \frac{[S_1]}{[T_1]} = \frac{k_{rISC}}{k_{ISC}} = \frac{1}{3} e^{-\frac{\Delta E_{ST}}{k_B T}} \qquad \text{eq. (14)}$$

$$K_{eq} = \frac{A_r}{\phi_T^2} = \frac{A_d}{(A_p + A_d) \cdot \phi_T^2} \qquad \text{eq. (15)}$$

where K_{eq} is the constant for the $T_1 \rightleftarrows S_1$ equilibrium, k_{rISC} and k_{ISC} are the rate constants of the rISC and ISC, ΔE_{ST} is the singlet-triplet energy gap, k_{B} is the Boltzmann constant, T is the temperature, A_{r} is the amplitude ratio, A_{d} and A_{p} are the amplitudes of the prompt and delayed fluorescence, and Φ_{T} is the triplet quantum yield. The factor of ⅓ comes from the three-fold degeneracy of the triplet state.[32]

Oxygen quenching influences the measured k_{TADF} rate constant involved in the Arrhenius equation, but not the amplitude ratio A_{r}. For compound **5b**, this ratio is estimated as the average of ten measurements at the same temperature, including the correction for $A_{\mathrm{p}}+A_{\mathrm{d}}$ in channel zero. Based on the previous results,[9] the triplet quantum yield of compound **5b** is estimated to be about 0.2. Thus, the ΔE_{ST} energy gap for **5b** estimated with this method is 193 meV. This value differs significantly from the value determined by the Arrhenius analysis (Table 7.1).

To further investigate the spectral properties of delayed fluorescence, we conducted time-resolved emission spectroscopy (TRES) measurements. A spectral overlap between prompt and delayed fluorescence confirms that both types of emission originate from the same excited state (S_1). We integrated the specific areas under the time-resolved decay curves in microseconds to obtain the spectra of both prompt and delayed fluorescence. These spectra overlap for all three compounds (Figure 7.9 A-C), giving an additional verification to TADF.

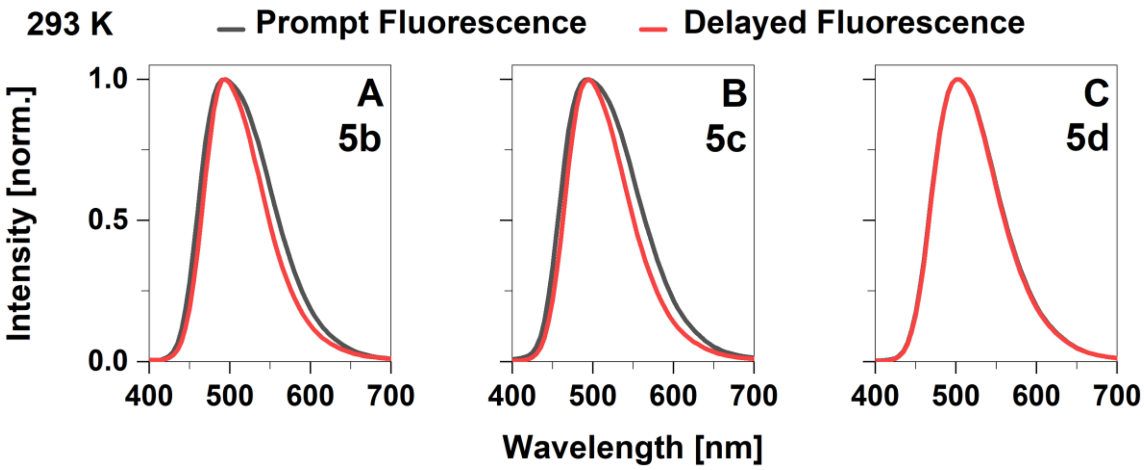

Figure 7.9. Time-resolved emission spectra of compounds **5b-5d** (**A**-**C**) in toluene at 293 K. Spectral overlap between prompt and delayed fluorescence is observed for all three compounds, implying that both emissions originate from the same excited state.

Compound 5e: Impact of the increased donor strength on photophysical properties

The absorption spectrum of **5e** in toluene contains three bands in the UV region, as predicted by theory (Figure 7.10 A and B). The variation in the donor already significantly influences the fluorescence emission spectrum, shifting it batochromically in comparison with its counterpart **5b** (dashed magenta and grey lines respectively, Figure 7.10 A). Photophysical parameters of this compound are compiled in Table 7.1.

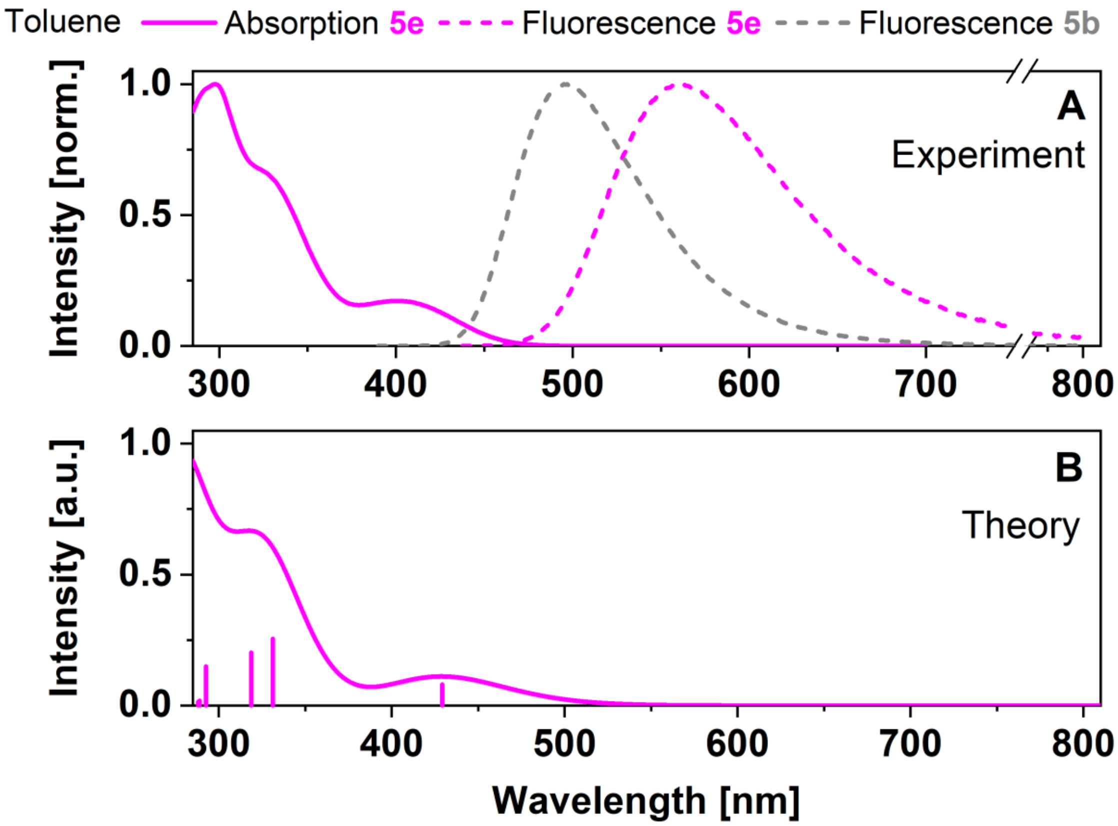

Figure 7.10. Compound **5e** in toluene. **A.** Experimental absorption (full magenta line) and fluorescence emission spectra (dashed magenta line). For comparison, experimental fluorescence emission spectra of **5b** are shown (dashed grey line). The range between 750 and 770 nm is excluded due to the presence of second-order diffracted laser light. **B.** Theoretical absorption spectra with spectral lines broadened with Gaussians of 4400 cm^{-1}.

Both prompt and delayed fluorescence were detected for compound **5e**. As in the previous series (**5a-5d**), the prompt fluorescence lifetime is significantly increased in nitrogen-purged toluene solution (Figure 7.11A). Delayed fluorescence was not detected in air-saturated but in nitrogen-purged toluene solution with its maximal lifetime of 35.5 µs (Table 7.1 and Figure 7.11 B and C). In comparison with **5b** which has a similar torsion angle (Table S7.1), increased donor strength in **5e** significantly enhanced the TADF properties: the quantum yield and the amplitude of delayed fluorescence are larger and the lifetime is shorter. However, due to the very low prompt fluorescence quantum yield of **5e**, compound **5b** remains brighter under nitrogen where both prompt and delayed fluorescence are operative (see Φ_{TF} in Table 7.1).

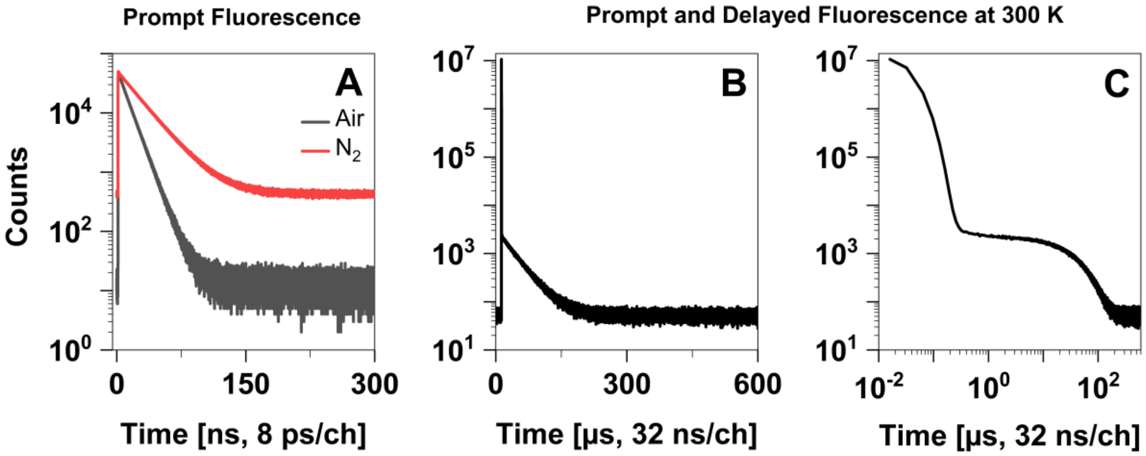

Figure 7.11. Compound **5e** in toluene. **A.** Prompt fluorescence measured by TCSPC in air-saturated and nitrogen-purged toluene solutions. **B.** and **C.** Prompt and delayed fluorescence measured in nitrogen-purged solution at 300 K presented in two formats: logarithmic y-axis and linear x-axis, and logarithmic y- and x-axes (log-log data representation).

To confirm the presence of TADF, we conducted temperature-dependent time-resolved measurements in range of 182 K to 300 K in the microsecond time range (Figure 7.12A). Upon cooling, the delayed fluorescence amplitude decreases, and the lifetime becomes longer. The singlet-triplet energy gap (ΔE_{ST} in Table 7.1) was determined from the slope of the Arrhenius plot (Figure 7.12B, Table S7.11). Finally, the TRES measurements confirmed that prompt and delayed fluorescence have the same spectral properties (Figure 7.12C).

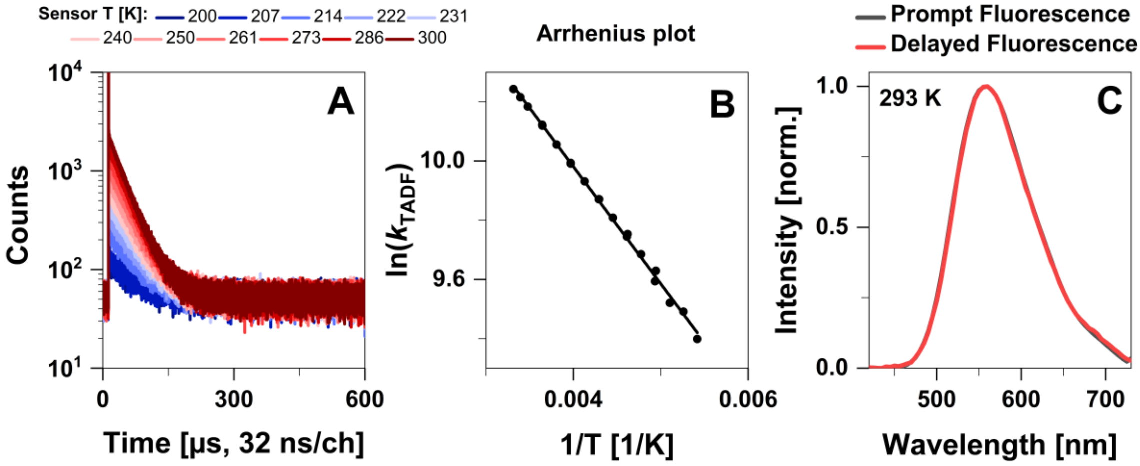

Figure 7.12. Compound **5e** in toluene. **A.** Time-resolved temperature dependent measurements in the microsecond time range. **B.** Arrhenius plot (see Table S7.11). **C.** Time-resolved emission spectra of prompt and delayed fluorescence at 293 K.

Computational Results

Due to helical structure of the triarylamine (TAA) donors, **5a-5e** occur in two enantiomeric forms. All calculations were performed for the (-) enantiomer, i.e., a left-handed helix. For **5a**, our geometry optimizations find two distinct conformers in the electronic ground state with donor–acceptor dihedral angles of about 50° and 130°, respectively (Figure 7.13, left). Their adiabatic energy difference is small (7 meV). The comparably high barrier for the interconversion of the two conformers (ca. 60 meV from 1 to 2, 53 meV in the other direction) is not caused solely by steric effects. The energy profile rather suggests an interplay of electronic π-conjugation and steric repulsion of the hydrogen atoms at small interplanar angles. Sterically more demanding substituents, such as Me (**5b**, **5d**, **5e**) or ^{i}Pr (**5c**) prevent nearly coplanar arrangements of the donor and acceptor moieties where the π-conjugation is at its maximum. Two conformers with donor–acceptor angles of about 70° and 110° can be observed for **5b**, separated only by a low barrier (ca. 15 meV / 2 meV) which should be easily overcome in solution at ambient conditions. The shallow torsional potential can also explain the large impact of a crystal environment on the interplanar angle which differs by ca. 14° between the computed value for conformer 1 in solution and the experimental X-ray structure (Table S7.1).

A simple one-dimensional pathway along the torsional coordinate is not sufficient to locate distinguishable conformers of **5c**: The energy profile, presented in Figure 7.13 (left) shows a single minimum. However, including the rotation of the ^{i}Pr group reveals a second conformer, in agreement with the NMR analysis (Figure S7.27). For the sake of a better visualization and simplicity, we created a heat map (Figure 7.13, right) which clearly shows that two different conformers can be identified. The more stable conformer has a donor–acceptor dihedral angle of approximately 75° and an isopropyl rotation angle of –5°. The second conformer, which is about 110 meV less favorable in terms of energy, exhibits a donor–acceptor angle of 95° and an ^{i}Pr rotation angle of 190°. The transition state lies only 27 meV above the minimum of conformer 2. The intrinsic minimum reaction path for the interconversion of conformer 2 to conformer 1 initially runs nearly parallel to the y-axis until the ^{i}Pr substituent adopts a rotation angle of about 30°. Concerted rotations of the donor and acceptor moieties and of the ^{i}Pr group are necessary to eventually reach the minimum of conformer 1. The one-dimensional pathway does not show a second conformer for **5d** which incorporates two Me substituents. With a donor–acceptor torsional angle of about 87°, its minimum nuclear arrangement exhibits an orientation which is almost perpendicular.

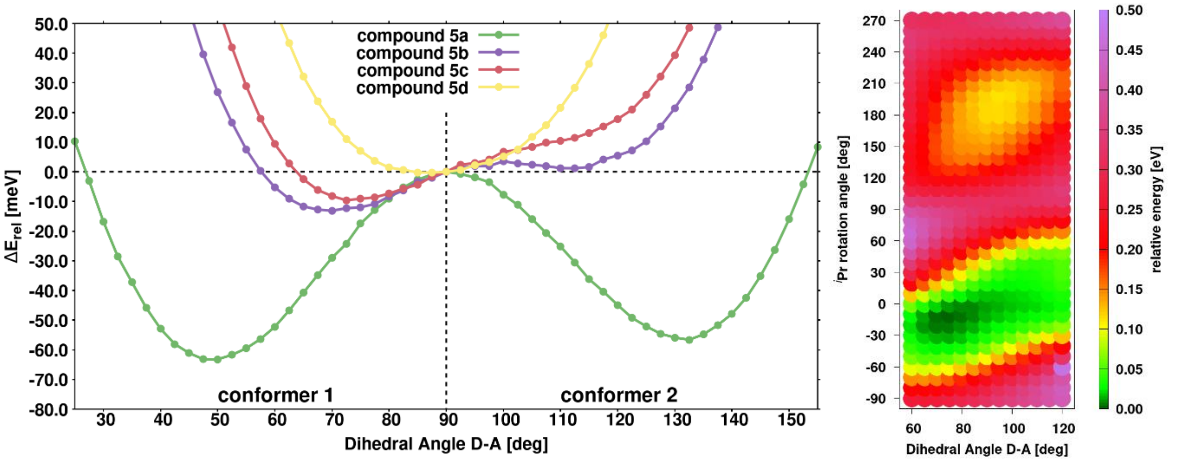

Figure 7.13. Left: Relaxed KS-DFT scan of the ground-state potential energy surfaces of **5a-5d** along the donor–acceptor dihedral angle. Right: Heat map of a relaxed two-dimensional scan of the ground-state potential energy surface of **5d**. Plotted are the individual single-point energies for a variation of the donor–acceptor torsional angle (x-axis) and the rotation angle of the isopropyl group (y-axis). The data points were coloured according to their energy with respect to the minimum of conformer 1, as shown in the colour box.

We observe excellent agreement between the measured and computed absorption spectra in toluene solution (Figure 7.2 and Figure 7.10), both in position and intensity of the peaks. This agreement lends, on the one hand, confidence to our computational protocol, and allows, on the other hand, the assignment and interpretation of the experimental spectra.

The intensity of the first absorption band in this series and the donor–acceptor torsional angle of ground-state equilibrium structure of the compound are clearly correlated: The larger this angle, the higher is the charge-transfer (CT) character and the weaker is the oscillator strength of the $S_0 \rightarrow S_1$ HOMO–LUMO transition. Its absorption wavelength experiences only a small blue shift when moving from **5a** to **5d**. Note that the CT contributions to the corresponding T_1 states are markedly smaller, save for **5d** with nearly orthogonal donor and acceptor orientation. The analysis of the second and third singlet transitions is not as straight forward. The oscillator strength of the $S_0 \rightarrow S_2$ absorption decreases from roughly 0.42 in **5a** to approximately one tenth of this value in **5d** although the locally-excited (LE) character of the transition increases from 41 to 85 % in this series. A closer look reveals that the direction of transition dipole is decisive for the intensity of the transition as well. In **5a**, the $S_0 \rightarrow S_2$ transition dipole vector points in the direction of the long molecular axis whereas it runs almost perpendicular to it in **5d**. The opposite is true for the $S_0 \rightarrow S_3$ transition. Accordingly, the absorption spectrum of **5a** has a distinct peak at 330 nm whereas the absorption spectra of **5b** and **5c** exhibit at most a shoulder at 315 and 320 nm, respectively.

Table 7.3. DFT/MRCI-R2016 computed electric dipole oscillator strengths f (in length form), vertical absorption wavelengths λ_{abs} [nm] and wave function composition [%] of low-lying electronic states at the respective ground-state geometry of conformer 1.

		Compound			
Transition	Property	**5a**	**5b**	**5c**	**5d**
$S_0 \rightarrow S_1$	λ_{abs} / f	410 / 0.2369	400 / 0.0774	400 / 0.0468	396 / 0.0021
$S_0 \rightarrow S_2$	λ_{abs} / f	331 / 0.4166	319 / 0.2892	315 / 0.2261	307 / 0.0435
$S_0 \rightarrow S_3$	λ_{abs} / f	312 / 0.0220	307 / 0.1633	306 / 0.2308	302 / 0.4360
$S_0 \rightarrow T_1$	λ_{abs}	462	426	422	405
$S_0 \rightarrow T_2$	λ_{abs}	385	375	374	375
$S_0 \rightarrow S_1$	CT/$\mathrm{LE_{TAA}}$/$\mathrm{LE_{TPN}}$	70/10/09	80/06/04	82/05/04	87/02/02
$S_0 \rightarrow S_2$	CT/$\mathrm{LE_{TAA}}$/$\mathrm{LE_{TPN}}$	40/41/09	31/59/02	26/64/02	07/85/02
$S_0 \rightarrow S_3$	CT/$\mathrm{LE_{TAA}}$/$\mathrm{LE_{TPN}}$	04/86/00	09/82/01	12/80/01	15/77/01
$S_0 \rightarrow T_1$	CT/$\mathrm{LE_{TAA}}$/$\mathrm{LE_{TPN}}$	45/28/18	59/22/11	65/16/11	86/03/02
$S_0 \rightarrow T_2$	CT/$\mathrm{LE_{TAA}}$/$\mathrm{LE_{TPN}}$	29/44/19	22/66/07	16/74/05	05/90/00

Relaxed TDDFT/ωB97X-D scans of the energy profiles of the first excited singlet and triplet states along the torsional coordinate are shown exemplarily for **5b** in Figure 7.14 (left). For comparison, the energy profile of the electronic ground state, computed at the DFT/ωB97X-D level of theory, is drawn at the same scale. Three peculiarities of the excited-state potentials of **5b** are immediately eye-catching: i) The minima of the T_1 PES are located at much smaller torsional angles than for the S_1 state, ii) the barrier for interconversion of the conformers in the T_1 state is much higher and iii) the singlet–triplet gap does not approach zero for a perpendicular orientation of the donor and acceptor moieties. The underlying reasons become apparent when looking at Figure 7.14 (right) where the static electric dipole moments of the S_0, S_1 and T_1 states along these paths are displayed. The static electric dipole moment of the S_1 state is large across the considered range of torsional angles, reaching its maximum at 90° as may be expected for a through-bond CT donor–acceptor emitter. For T_1, the variation of the static electric dipole moment is much more pronounced. At torsional angles close to planarity, its wavefunction exhibits substantial contributions from a locally excited configuration on the triarylamine donor moiety, $^3\mathrm{LE_{TAA}}$, leading in total to a reduced static electric dipole moment in comparison to S_1. With growing interplanar donor–acceptor angle, the percentage of HOMO-to-LUMO CT excitation in the T_1 wavefunction and hence the static electric dipole moment increases until it suddenly drops as the torsional angle approaches 85°, indicating a major change in the excited-state electronic structure. Between 85° and 95°, the lowest triplet state originates from a local excitation on the terephthalonitrile (TPN) acceptor moiety, $^3\mathrm{LE}_{\mathrm{TPN}}$. A two-state equilibrium model of the ISC and rISC processes, underlying the Arrhenius analysis of the prompt and delayed fluorescence decay times, is therefore not considered appropriate for describing the kinetic scheme of **5b**. The analysis of the excited-state energy profiles of **5a**, **5c** and **5d** suggests that these compounds exhibit similar excited-state decay characteristics. Interestingly, **5e** behaves differently in this respect. The two methoxy substituents in the backbone enhance the donor strength of the TAA moiety of this compound to an extent that the T_1 state retains its CT characteristics in the perpendicular donor–acceptor arrangement.

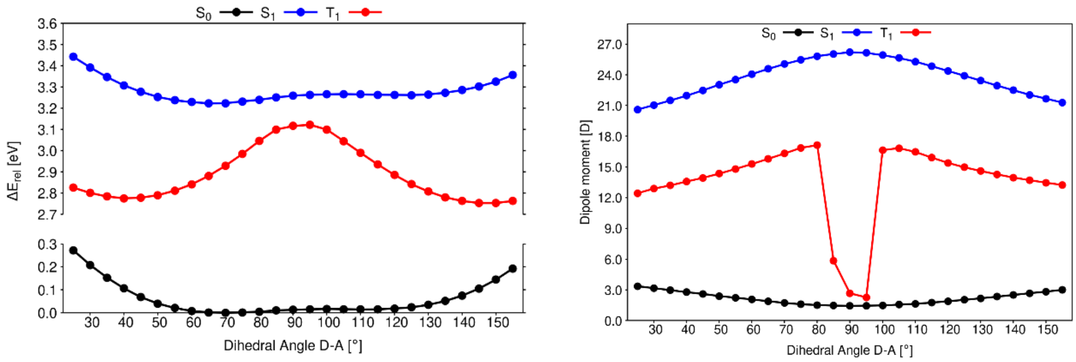

Figure 7.14. Left: Relaxed (TD)DFT/ωB97X-D scan of the potential energy profiles of the S_0, S_1 and T_1 states of compound **5b** along the donor–acceptor dihedral angle (relaxed scans). Right: Static electric dipole moments of the S_0, S_1 and T_1 states (DFT/MRCI-R2016) along these paths.

The differences between the computed static dipole moments of the S_1 and S_0 states in their respective equilibrium nuclear arrangements are considerably larger than those derived from Lippert–Mataga analyses of Stokes shifts (Table 7.1, Figure S7.36). The computed dipole moment differences follow the expected trends, i.e., they increase from ca. 19 D in **5a** over 23 D in **5b**, **5c** and 24 D in **5d** to 25 D in **5e**, whereas fits to the Lippert–Mataga data yield a nearly constant value of approximately 14 D for all compounds. The reason for this discrepancy is unclear. The PCM solvent model used in this work does not take account of the solvent reorganization in the excited state and is therefore prone to underestimate the polarity of the CT excited state, not to overestimate it. Another reason could be that the simple Lippert-Mataga model is not applicable in the present case: The underlying equations assume that the solvent cavity is spherical, which is far from true for the molecular structures of compounds **5a-5e**.

The commonly used adiabatic Hessian (AH) method[33] results in featureless and very broad emission spectra. Due to large-amplitude motions in low-frequency modes, here mainly the above-mentioned torsional coordinate, the harmonic oscillator model, which uses the respective equilibrium geometry as offset for the Taylor expansion of the PES, is not appropriate. The newly implemented vertical Hessian (VH) method for the computation of vibronic spectra yields emission bands with spectral origins and peak maxima in excellent agreement with experiment. Because the harmonic approximation tends to overestimate the Franck–Condon (FC) factors between the initial vibrational level in the electronically excited state and higher vibrational quanta of torsional modes in the electronic ground state, the computed spectra are merely somewhat broader than their experimental counterparts. The emission spectra of **5a**, **5b** and **5c** are almost superimposable with emission maxima at 482 nm, 484 nm and 490 nm, respectively. In comparison, the emission spectrum of the dimethylated compound **5d** is slightly redshifted to about 513 nm. Methoxy substituents in the backbone of the TAA donor (**5e**) further increases the CT character of the transition and shifts the emission maximum to about 539 nm according to the VH calculations.

The ability of a molecule to emit TADF depends critically on the singlet–triplet energy gap ΔE_{ST}. In earlier work,[9] a value of 980 cm^{-1} (120 meV) had been derived for the energy difference between the S_1 and T_1 states of **5b** on the basis of an Arrhenius plot. In the same work,[9] a quantum chemically determined energy separation of 840 cm^{-1} (100 meV) was reported. Note, however, that the single-point TDDFT/B3-LYP calculations had been performed at the optimized S_0 geometry and that this vertical energy gap is not directly comparable to the 0-0 energy difference underlying the Arrhenius equations.

Table 7.4. DFT/MRCI-R2016 computed $S_1 - T_1$ energy differences ΔE_{ST} [meV] and $S_1 - S_0$ static electric dipole moment differences $\Delta\mu$ [D] of conformer 1 in toluene solution.

	Compound				
Property	**5a**	**5b**	**5c**	**5d**	**5e**
$\Delta E_{\mathrm{ST},\ \textit{vertical at}\ S_0\ \textit{minimum}}$	341	192	162	73	157
$\Delta E_{\mathrm{ST},\ \textit{adiabatic}}$	501	438	428	333	228
$\Delta E_{\mathrm{ST},\ \textit{0–0}}$	510	481	463	322	243
$\Delta\mu$	19.1	22.9	22.7	24.0	25.3

The vertical $S_1 - T_1$ DFT/MRCI-R2016 energy differences, computed in the present work for **5a-5d** at their respective S_0 equilibrium structures, apparently match the experimental trends (Table 7.4) very well. However, TADF is not an instantaneous process that proceeds on the sub-picosecond time scale. Upon electronic excitation, the nuclear coordinates therefore have the time to adapt to the electronic potentials of the S_1 and T_1 states, respectively. Relaxed scans reveal that the torsional angles of the S_1 and S_0 equilibrium structures are similar, whereas T_1 has its minimum at markedly reduced values of the torsional coordinate. As a consequence, geometry relaxation in the excited state increases the ΔE_{ST} values. Zero-point vibrational energy corrections of the adiabatic ΔE_{ST} values change the overall picture only slightly. We therefore have to face the situation that the computed $S_1 - T_1$ 0–0 energy gaps are significantly larger than the ones derived from Arrhenius plots of the measured fluorescence decay times. This may have a variety of reasons which are analyzed and discussed in the following.

In liquid solutions, the initially excited solute does not only relax internal nuclear degrees of freedom. For all but ultrafast processes, the reorganization of the solvent environment has to be taken into consideration as well. Solvent reorganization effects on spectroscopic properties are notoriously difficult to model. The corrected linear response (cLR)[34] model works extremely well for CT transitions in polar transition metal compounds, e.g., which reduce the static dipole moment of the molecule.[35] Applied to the $S_1 \rightarrow S_0$ emission of **5b**, the cLR corrections lower the emission energy in toluene solution by more than 600 meV in comparison to a PCM environment. The good agreement of the latter model with the experimental emission spectrum speaks against the applicability of the cLR model in the present case. Recently, Mewes and co-workers advertised a state-specific ROKS/PCM approach,[36] which appears to work well for many organic donor–acceptor compounds but fails to reproduce the published experimental ΔE_{ST} value of 120 meV for **5b**.[9] The adiabatic energy gaps of **5b** in toluene, reported by Mewes et al., are much larger and rather resemble the computational results of the present work. Implicit solvent models do not provide a possibility to form exciplexes with surrounding toluene molecules. When two quantum-chemically treated explicit toluene molecules are placed close to the donor, the CT excitations are stabilized and the ΔE_{ST} gap decreases, but not to an extent that makes it compatible with the data extracted from the Arrhenius plots. Therefore, the question arises which other causes could lead to the apparent mismatch.

The Arrhenius equations are based on a two-state model in which the state populations equilibrate according to Boltzmann statistics. The energy profile and the course of the static dipole moment in the T_1 state (Figure 7.14) indicate, however, that a two-state equilibrium model might not be sufficient. Close to the transition state for the conformer interconversion, the ^{3}CT ^{3}LE$_{TPN}$ PESs undergo a conical intersection. For torsional angles between ca. 85° and 95°, the T_1 state adopts a ^{3}LE$_{TPN}$ electronic structure whereas the S_1 state keeps its ^{1}CT character. Therefore, the ^{1}CT and ^{3}LE$_{TPN}$ PESs must intersect as well in the neighborhood. The leading configurations of the ^{1}CT and ^{3}LE$_{TPN}$ states share the electron accepting orbital on the TPN moiety, but the hole orbitals are different. This means that the S_1 and ^{3}LE$_{TPN}$ states are singly excited with respect to one another, an important property in view of the effective one-electron nature of the spin–orbit coupling (SOC) operator. The PES crossing is reflected in a sudden increase of the mutual $S_1 - T_1$ SOC close to an orthogonal donor–acceptor arrangement. The Condon approximation for evaluating ISC and rISC rate[37] is therefore not valid in the present case. Earlier work on organic donor–acceptor TADF emitters, exhibiting a low-lying ^{3}LE state energetically close to the ^{3}CT and ^{1}CT states, suggests two principal approaches to include spin-vibronic interactions in the calculations:[38] nonadiabatic quantum dynamics and a Herzberg–Teller (HT) like expansion of the coupling. In our laboratory, the latter ansatz was employed successfully to explain, for example, the complicated excited-state decay behavior of the through-space CT TADF emitter TpAT-tFFO[39] and of the well-known through-bond CT TADF emitter DMAC-TRZ.[40]

Going beyond the FC approximation in the case of **5b** increases the rISC rate constant at room temperature merely to $9 \cdot 10^{-2}$ s^{-1}, a value much too small to explain the experimentally observed TADF. The fact that the delayed fluorescence is blue-shifted with respect to prompt fluorescence points toward a kinetic scheme in which the population transfer between the S_1 and T_1 surfaces and the radiative decay of the S_1 population to the S_0 potential occur at different points in space.[41] The ΔE_{ST} gap is smallest for an orthogonal donor–acceptor orientation (Figure 7.14, left) and therefore rISC is fastest here. In contrast, the electric dipole transition probability is very low at 90°, but increases appreciably as the torsional angle gets smaller. Fluorescence is therefore preferentially emitted in less twisted conformations. A similar mechanism was postulated for linear carbene metal amides. In these compounds, the torsional motion plays a key role for the understanding of its photophysics as well.[42,35]

To mimic the dynamic behavior of the ISC and rISC processes in **5b**, we applied a VH approach to compute rate constants at fixed torsional angles of the relaxed S_1 path. The VH method is well established for computing absorption and emission spectra,[43] but it has – to our knowledge – so far not been applied to determine vibrational densities of states for nonradiative transitions such as ISC and rISC. Briefly, this method uses the gradients and Hessians of the initial and final electronic states at the fixed geometry of the initial state to extrapolate the course of the PES of the final state and to compute FC factors. In the limit of strictly parabolic PESs, the VH and AH methods are supposed to yield identical results. In the strong coupling case, which is characterized by large geometric displacements of the minima in at least one vibrational coordinate,[44] we expect the VH model to be more realistic, especially in cases in which these displacements are related to low-frequency modes. Details of the method and its implementation will be presented in a forthcoming paper.

Application of the VH method to the $S_1 \rightarrow T_1$ ISC in **5b** yields rate constants ranging between 10^6 and 10^7 s^{-1} upon variation of the torsional angle. Interestingly, the highest value is obtained for 60º, close to the equilibrium geometry of the S_1 state. In contrast, the reverse $T_1 \rightarrow S_1$ ISC process speeds up dramatically as the torsional angle increases. Starting from values of the order of 1 s^{-1} at the T_1 minimum, the rISC rate constant grows roughly exponentially to about $5 \cdot 10^3$ s^{-1} for an angle of 80º. The sudden jump of the rISC rate constant to values between 10^6 and 10^7 s^{-1} for torsional angles between 85 and 90º is only partially caused by the diminishing S_1 –T_1 energy. A large portion of this increase is due to the $^3LE_{TPN}$ electronic structure in the T_1 state and the concomitant enhancement of the SOC.

7.1.3 Experimental Section

Spectroscopic conditions

Absorption spectra were measured on a Cary 4000 UV-Vis spectrophotometer (Agilent Technologies, USA), while fluorescence spectra were recorded on a Horiba Fluorolog FL3-22 spectrophotometer. Time-resolved measurements were conducted with a fluorescence lifetime and steady-state spectrometer FT300 (PicoQuant, Germany) equipped with a ColdEdge cryostat powered by a Sumitomo CH-204 cold head and HC-4E Helium compressor (Cryoandmore, Germany). Temperatures were regulated by a temperature controller, Model 335 (Lake Shore Cryotronics, USA), using a silicon diode sensor at the cold head. Sample temperatures were measured independently with a second diode (Model 540 group B, Scientific Instruments, USA; accuracy: ± 0.5 K) and used for all analyses. All samples were measured in UV Quartz Type Hellma QS 221.001 Fluorescence Cuvette Cells with a nozzle made of Quartz/Duran glass mixture and a light path of 10 mm. For the steady-state and time-resolved measurements in the nanosecond time regime, samples were excited with a supercontinuum laser excitation source (EXW-12 with EXTEND-UV spectral extension unit, NKT Photonics, Denmark). An excitation wavelength of 375 nm was set by tuning the frequency doubler. Time-correlated single photon counting (TCSPC) was achieved with HydraHarp 400 electronics (PicoQuant, Germany). The time bin was 8 ps. For the time-resolved measurements in the microsecond and millisecond time ranges, samples were excited with a modulated continuous wave diode laser (Cobolt 375 nm MLD laser, Series 06-01, Hübner Photonics, Germany). In both cases, the excitation wavelength was 375 nm. A TCSPC and MCS board, Time Harp 260 (PicoQuant, Germany), provided photon counting and timing. Signal detection was achieved with a hybrid PMT detector (PicoQuant, Germany). Emission was detected under magic angle conditions (excitation polarizer 0°, emission polarizer 54.7°). The detection wavelength was 495 nm for compounds **5a-5d**, and 560 nm for **5e**. All time-resolved measurements were conducted with a scripted measurement routine. A home-built software was used for data analysis. All emission spectra were subsequently corrected for wavelength-dependent detection efficiencies of the instrument.

Computational Details

Molecular geometries and vibrational frequencies were determined with Gaussian 16[45] employing the optimally tuned, range-separated ωB97X-D density functional[37] and the split-valence double zeta def2-SV(P) basis set.[46] The optimal tuning procedure followed the scheme recommended in Ref. [47], yielding a value of ω=0.15 for the range separation parameter. Test calculations performed with the larger def2-TZVP basis set[35] gave only slightly varying results. Geometries of singlet excited state were optimized with time-dependent density functional theory (TDDFT). For triplet states, the Tamm-Dancoff approximation (TDA) was employed. Unless noted otherwise, the polarizable continuum model (PCM)[48] was used to mimic the toluene solvent environment. Excitation energies and excited-state properties were determined with the combined density functional theory and multireference configuration interaction (DFT/MRCI) method[49] using the tight R2016[50] parameter set. Spin–orbit coupling matrix elements were computed in atomic mean-field approximation using SPOCK.[51] Temperature dependent vibronic spectra and (r)ISC rate constants were calculated with a recent extension of the VIBES program[52] enabling the use of internal coordinates and the application of the vertical Hessian (VH) method[33,53] which are better suited for a pair of potential energy surfaces with large displacements in a dihedral angle than Cartesian coordinates and the adiabatic Hessian (AH) approach. Numerical derivatives of the electric dipole transition moments and of the spin–orbit coupling matrix elements with respect to the normal coordinates, required for computing radiative or (r)ISC rate constants in Herzberg–Teller approximation, were generated with the GRADIENATOR toolbox.[54] A detailed analysis of the CT and LE contributions to the DFT/MRCI transition densities was carried out with a local version of the THEODORE program.[55]

7.1.4 Supplementary Information

Synthesis

All reactions were carried out in Schlenk or multi-neck flasks under nitrogen atmosphere and using the septum and syringe technique, unless otherwise indicated. Dried THF was taken from the MB-SPS 800 solvent drying system (M. Braun). The reaction temperature was adjusted for reactions not conducted at ambient temperature using silicone oil baths preheated to the indicated temperatures or cooling baths (ice/water for 0 °C or dry ice/isopropanol for -78°C). Column chromatography was carried out on silica gel M60 (mesh 230 - 400, Macherey-Nagel, Düren, Germany). The column chromatographic separations were performed using the flash technique (overpressure of about 2 bars of compressed air). Silica coated aluminum foils (60 F254 Merck) were used for thin layer chromatography. Evaluation was performed under UV light (λ_{exc} = 254 and 356 nm) and staining with iodine.^{1}H-, ^{13}C-, and DEPT-135-NMR spectra were recorded at 293 K on Bruker Avance III 600 (600 MHz), Bruker Avance DRX 500 (500 MHz), and Bruker Avance III 300 (300 MHz) instruments, respectively, unless otherwise noted. DMSO-d_6 served as solvent. As an internal standard, the residual proton signal of the corresponding solvents was lured when recording the ^{1}H NMR spectra and ^{13}C NMR spectra (DMSO-d_6, H 2.50, C 39.52). Spin multiplicities are abbreviated as follows: s: singlet; d: doublet, dd: doublet of doublet; ddd: doublet of doublet of doublet; dt: doublet of a triplet; t: triplet, q: quintet; sp: septet; and m: multiplet. The quaternary carbon nuclei (C_{quat}) and the carbon nuclei of methine (CH), methylene (CH_2), and methyl (CH_3) groups were assigned based on DEPT-135 spectra. Melting points (uncorrected) were measured on the Büchi B545 instrument. EI mass spectra were measured on the TSQ 7000 triple quadrupole mass spectrometer (Finnigan MAT). Indicated are all peaks with an intensity > 10% of the base peak, the mole peak, and any characteristic fragment peaks with an intensity < 10%. IR spectra were measured on the IRAffinity-1 instrument (Shimadzu) (single reflection ATR unit with diamond ATR crystal, wavenumber range: 4000 - 600 cm^{-1}). The intensities of the absorption bands are given as s (strong), m (medium), and w (weak). The elemental analyses were measured on the Perkin Elmer Series II Analyzer 2400 at the Institute of Pharmaceutical Chemistry, Heinrich Heine University.

4-Bromo-*N*,*N*-diphenylaniline (3a)

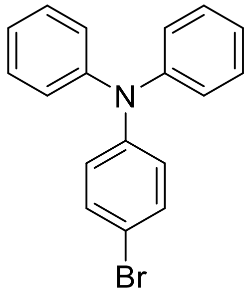

$C_{18}H_{14}BrN$
324.22

In a Schlenk vessel with magnetic stir bar 4-bromoaniline (**1a**) (1.72 g, 10.0 mmol), copper(I) iodide (190 mg, 1.00 mmol), phenanthroline (180 mg, 1.00 mmol), and potassium hydroxide (1.964 g, 35.00 mmol) were placed under nitrogen atmosphere and then dissolved in dry THF (50 mL). Then, iodobenzene (**2a**) (5.85, 25.0 mmol) was added, and the reaction mixture was heated in at 110 °C (oil bath) for 19 h. The reaction mixture was cooled to room temp and extracted with dichloromethane (3 x 60 mL). The combined organic fractions were washed with brine (30 mL) and dried (anhydrous sodium sulfate). The organic solution was adsorbed on Celite® and purified by column chromatography on silica gel (*n*-hexane/ethyl acetate (20:1). After purification a red oil was obtained, which was then crystallized in ethanol and then dried under vacuum until weight constancy to give compound **3a** (1.27 g, 39%) as a brownish solid, Mp 98-103 °C. R$_f$: 0.84 (*n*-hexane/ethyl acetate = 20:1).

^{1}H NMR: (300 MHz, DMSO-d_6) δ = 7.42 (d, ^3J = 8.9 Hz, 2H), 7.37 – 7.26 (m, 4H), 7.05 (dd, ^3J = 19.7 Hz, ^4J = 7.4 Hz, 6H), 6.89 (d, ^3J = 9.0 Hz, 2H). **^{13}C NMR:** (75 MHz, DMSO-d_6) δ = 146.7 (C$_{quat}$), 132.2 (CH), 129.7 (CH), 124.6 (CH), 124.2 (CH), 123.5 (CH), 113.8 (C$_{quat}$). **MS(EI)** *m/z* (%): 326 (17), 325 ([M-Br^{81}]$^+$, 96), 324 (28), 323 ([M-Br^{79}]$^+$, 100), 261 (14), 245 (40), 244 (50), 243 (84), 242 (26), 241 (19), 167 (47), 166 (52), 142 (10), 141 (27), 140 (17), 139 (19), 121 (27), 120 (19), 115 (22), 77 ([C_6H_5]$^+$, 24), 51 (22).

4-Bromo-3-methyl-*N*,*N*-diphenylaniline (3b)

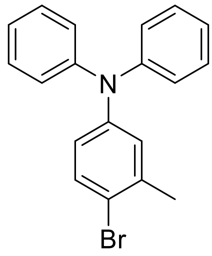

$C_{19}H_{16}BrN$
338.25

In a Schlenk vessel with magnetic stir bar 4-bromo-3-methylaniline (**1b**) (1.86 g, 10.0 mmol), copper(I) iodide (381 mg, 2.00 mmol), phenanthroline (360 mg, 2.00 mmol), and potassium hydroxide (1.964 g, 35.00 mmol) were placed under nitrogen atmosphere and then dissolved in dry THF (30 mL). Then, iodobenzene (**2a**) (3.40 mL, 30.0 mmol) was added, and the reaction mixture was heated in at 130 °C (oil bath) for 24 h. The reaction mixture was cooled to room temp and extracted with dichloromethane (3 x 60 mL). The combined organic fractions were washed with brine (30 mL) and dried (anhydrous sodium sulfate). The organic solution was adsorbed on Celite® and purified by column chromatography on silica gel (*n*-hexane/ethyl acetate (20:1). After purification a red oil was obtained, which was then crystallized in ethanol and then dried under vacuum until weight constancy to give compound **3b** (1.05 g, 31%) as a red solid, Mp 143.6 °C. R_f: 0.78 (*n*-hexane/ethyl acetate = 20:1).

^{1}H NMR: (300 MHz, DMSO-d_6) δ = 7.45 (d, ^3J = 8.6 Hz, 1H), 7.30 (dd, ^3J = 8.5, ^4J = 7.4 Hz, 4H), 6.92-7.11 (m, 7H), 6.72 (dd, ^3J = 8.6, ^4J = 2.8 Hz, 1H), 2.23 (s, 3H). **^{13}C NMR:** (75 MHz, DMSO-d_6) δ = 146.9 (C_{quat}), 146.9 (C_{quat}), 138.2 (C_{quat}), 132.9 (CH), 129.6 (CH), 125.5 (CH), 124.0 (CH), 123.3 (CH), 122.7 (CH), 117.0 (C_{quat}), 22.5 (CH_3). **MS(EI)** *m/z* (%): 340 (8), 339 ([M-Br^{81}]$^+$, 96), 338 (25), 337 ([M-Br]$^+$, 100), 258 ($C_{19}H_{16}N^{\bullet}$, 17), 257 (51), 257 (51), 256 (19), 243 ($C_{18}H_{13}N^{2\bullet}$, 40), 242 (15), 180 (26), 167 (10), 166 (11), 155 (11), 153 (11), 152 (12), 129 (15), 128 (20), 127 (11), 120 (14), 115 (11), 77 (26), 51 (16).

4-Bromo-3-isopropyl-*N*,*N*-diphenylaniline (3c)

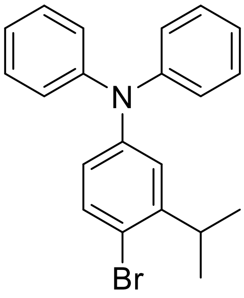

$C_{21}H_{20}BrN$
366.30

In a 20 mL Schlenk flask with magnetic stir bar 3-isopropylaniline (5.0 mL, 37 mmol) was cooled to 0 °C (ice bath) before a solution of acetic anhydride (5.2 mL, 56 mmol) and acetic acid (5.3 mL, 93 mmol) was added dropwise. Then, the mixture was heated to 60 °C (oil bath) for 1 h. After cooling to room temp, the reaction mixture was cooled down to -20 °C (ice/sodium chloride) and bromine (5.6 g, 37 mmol)) was carefully added dropwise. The reaction mixture was stirred for 10 min. The pinkish solid was filtered and washed with cold water (50 mL). Then, the pinkish solid was stirred with 6 N KOH in water/methanol (1:1) (100 mL) at 90 °C for 2 h. Then, the reaction mixture was cooled to room temp and washed dichloromethane (3 x 50 mL). The combined organic layers were washed brine (50 mL), dried (anhydrous sodium sulfate) and solvents were removed *in vacuo* and the residue was dried to weight constancy to give 4-bromo-3-isopropylaniline (**1c**) (5.7 g, 99%) as a red-brownish oil, **R$_f$:** 0.37 (*n*-hexane/ethyl acetate = 4:1).

^{1}H NMR: (300 MHz, DMSO-*d$_6$*) δ = 7.12 (d, ^3J = 8.5 Hz, 1H), 6.57 (d, ^4J = 2.7 Hz, 1H), 6.34 (dd, ^3J = 8.5 Hz, ^4J =2.7 Hz, 1H), 5.16 (s, 2H), 3.10 (hept, ^3J = 6.9 C$_{quart}$ Hz, 1H), 1.15 (s, 3H), 1.12 (s, 3H). **^{13}C NMR:** (75 MHz, DMSO-*d$_6$*) δ = 148.6 (C$_{quat}$), 146.5 (C$_{quat}$), 132.4 (CH), 113.6 (CH), 112.1 (CH), 108.2 (C$_{quat}$), 32.2 (CH), 22.7(CH$_3$). **MS(ESI)** *m/z* (%): 216 ([M-Br^{81}]$^+$, 100), 214 ([M-Br^{79}]$^+$, 90).

In a Schlenk vessel with magnetic stir bar 4-bromo-3-isopropylaniline (**1c**) (2.14 g, 10.0 mmol), copper(I) iodide (38 mg, 0.20 mmol), phenanthroline (72 mg, 0.04 mmol), and potassium hydroxide (3.366 g, 30.00 mmol) were placed under nitrogen atmosphere and then dissolved in dry THF (20 mL). Then, iodobenzene (**2a**) (2.79 mL, 25.0 mmol) was added, and the reaction mixture was heated in at 110 °C (oil bath) for 16 h. The reaction mixture was cooled to room temp and extracted with dichloromethane (3 x 60 mL). The combined organic fractions were washed with brine (30 mL) and dried (anhydrous sodium sulfate). The organic solution was adsorbed on Celite® and purified by column chromatography on silica gel (*n*-hexane/ethyl acetate (40:1). After purification a red oil was obtained, which was then crystallized in ethanol and then dried under vacuum until weight constancy to give compound **3c** (3.05 g, 83%) as a yellow solid, Mp 75-83 °C. R$_f$: 0.75 (*n*-hexane/ethyl acetate = 20:1).

^{1}H NMR: (300 MHz, DMSO-*d$_6$*) $\delta = 7.43$ (d, $^3J = 8.6$ Hz, 1H), 7.24 – 7.35 (m, 4H), 6.97 – 7.11 (m, 6H), 6.95 (d, $^4J = 2.8$ Hz, 1H), 6.69 (dd, $^3J = 8.6$ Hz, $^4J = 2.8$ Hz, 1H), 3.16 (hept, $^3J = 6.8$ Hz, 1H), 1.07 (s, 3H), 1.05 (s, 3H). **^{13}C NMR:** (75 MHz, DMSO-*d$_6$*) $\delta = 147.3$ (C_{quat}), 147.2 (C_{quat}), 146.8 (C_{quat}), 133.2, (CH) 129.6 (CH), 124.1 (CH), 123.4 (CH), 122.3 (CH), 121.1 (CH), 115.8 (C_{quat}), 32.4 (CH), 22.4 (CH_3). **MS(EI)** *m/z* (%): 368 (20), 367 ([M-Br^{81}]$^+$, 99), 366 (23), 365 ([M-Br^{79}]$^+$, 100), 287 (26), 285 (14), 272 (14), 271 (53), 270 (25), 256 (14), 254 (13), 245 (13), 244 (29), 243 (40), 242 (14), 241 (12), 168 (13), 167 (33), 166 (20), 165 (11), 128 (12), 127 (16), 121 (10), 115 (12), 77 ([C_6H_5]$^+$, 21).

4-Bromo-3,5-dimethyl-*N*,*N*-diphenylaniline (3d)

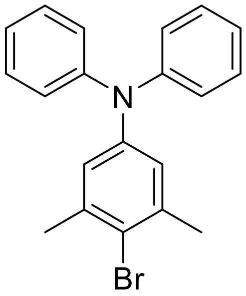

$C_{20}H_{18}BrN$
352.28

In a Schlenk vessel with magnetic stir bar 4-bromo-3,5-dimethylaniline (**1d**) (2.00 g, 10.0 mmol), copper(I) iodide (38 mg, 0.20 mmol), phenanthroline (72 mg, 0.04 mmol), and potassium hydroxide (3.4 g, 30 mmol) were placed under nitrogen atmosphere and then dissolved in dry THF (20 mL). Then, iodobenzene (**2a**) (3.4 mL, 30 mmol) was added, and the reaction mixture was heated in at 110 °C (oil bath) for 16 h. The reaction mixture was cooled to room temp and extracted with dichloromethane (3 x 60 mL). The combined organic fractions were washed with brine (30 mL) and dried (anhydrous sodium sulfate). The organic solution was adsorbed on Celite® and purified by column chromatography on silica gel (*n*-hexane/ethyl acetate (40:1). After purification a red oil was obtained, which was then crystallized in ethanol and then dried under vacuum until weight constancy to give compound **3d** (2.60 g, 76%) as yellow crystals, Mp 175.6 °C. R_f: 0.75 (*n*-hexane/ethyl acetate = 20:1), R_f: 0.74 (*n*-hexane/ethyl acetat = 20:1).

^{1}H NMR: (600 MHz, DMSO-d_6, 80 °C) $\delta = 7.29$ (t, $^3J = 7.9$ Hz, 4H), 7.04 (t, $^3J = 8.0$ Hz, 2H), 7.00 (d, $^3J = 9.7$ Hz, 4H), 6.81 (s, 2H), 2.26 (s, 6H). **^{13}C NMR:** (150 MHz, DMSO-d_6, 80 °C) $\delta = 146.7$ (C_{quat}), 145.8 (C_{quat}), 138.2 (C_{quat}), 129.1 (CH), 123.5 (CH), 123.2 (CH), 122.7 (CH), 119.8 (C_{quat}), 22.9 (CH_3). **MS(EI)** *m/z* (%): 354 (19), 353 ([M-Br^{81}]$^+$, 99), 352 (20), 351 ([M-Br^{79}]$^+$, 100), 272 (14), 271 (46), 257 (47), 256 (27), 180 (10), 169 (17), 136 (15), 128 (15), 127 (11), 127 (23), 121 (16), 77 ([C_6H_5]$^+$, 14). **Anal. calcd.** for $C_{20}H_{18}BrN$ (352.3): C 68.19, H 5.15, N 3.98; found: C 68.47, H 5.02, N 3.86. **IR:** $\tilde{v}$ [cm^{-1}] = 1574 (m), 1481 (m), 1466 (m), 1454 (w), 1433 (w), 1408 (w), 1377 (w), 1343 (m), 1323 (w), 1308 (w), 1292 (m), 1279 (m), 1233 (m), 1177 (w), 1155 (w), 1074 (w), 1028 (w), 1017 (w), 984 (w), 961 (w),867 (w), 858 (m), 831 (w), 806 (w), 758 (m), 694 (s), 658 (w), 637 (m), 617 (w).

4-Bromo-*N*,*N*-bis(4-methoxyphenyl)-3-methylaniline (3e)

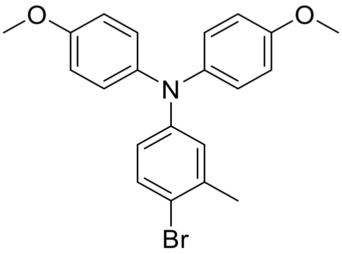

$C_{21}H_{20}BrNO_2$
398.30

In a Schlenk vessel with magnetic stir bar 4-bromo-3-methylaniline (**1b**) (1.86 g, 10.0 mmol), copper(I) iodide (190 mg, 1.00 mmol), phenanthroline (180 mg, 1.00 mmol), and potassium hydroxide (1.964 g, 35.00 mmol) were placed under nitrogen atmosphere and then dissolved in dry THF (50 mL). Then, *para*-iodoanisole (**2b**) (5.85 g, 25.0 mmol) was added, and the reaction mixture was heated in at 110 °C (oil bath) for 19 h. The reaction mixture was cooled to room temp and extracted with dichloromethane (3 x 60 mL). The combined organic fractions were washed with brine (30 mL) and dried (anhydrous sodium sulfate). The organic solution was adsorbed on Celite® and purified by column chromatography on silica gel (*n*-hexane/ethyl acetate (20:1). After purification a red oil was obtained, which was then crystallized in ethanol and then dried under vacuum until weight constancy to give compound **3e** (1.31 g, 33%) as a brown solid, Mp 145.9 °C. R_f: 0.42 (*n*-hexane/ethyl acetate = 20:1).

^{1}H NMR: (300 MHz, DMSO-d_6) δ = 7.32 (d, ^3J = 8.7 Hz, 1H), 7.00 (d, ^3J = 9.0 Hz, 4H), 6.90 (d, ^3J = 9.1 Hz, 4H), 6.72 (d, ^4J = 2.7 Hz, 1H), 6.50 (dd, ^3J = 8.7 Hz, ^4J = 2.8 Hz, 1H), 3.73 (s, 6H), 2.17 (s, 3H). **^{13}C NMR:** (75 MHz, DMSO-d_6) δ = 155.9 (C_{quat}), 148.1 (C_{quat}), 139.8 (C_{quat}), 137.5 (C_{quat}), 132.4 (CH), 126.7 (CH), 121.4 (CH), 118.8 (CH), 115.0 (CH), 113.9 (C_{quat}), 55.2 (CH_3), 22.6 (CH_3). **MS(EI)** *m/z* (%): 400 (21), 399 ([M-Br^{81}]$^+$, 94), 398 (24), 397 ([M-Br^{79}]$^+$, 100), 385 (14), 384 ($C_{20}H_{17}Br^{81}NO_2^{\bullet}$, 64), 383 (16), 382 ($C_{20}H_{17}Br^{79}NO_2^{\bullet}$, 68), 198 (12), 159 (12), 151 (12), 142 (10), 115 (14), 90 (11), 89 (12).

2-Iodoterephthalnitrile (4)

In a 2L three-necked round bottom flask with KPG-stirrer and reflux dimethyl 2-aminoterephthalate (21 g, 0.1 mol) was suspended in cold water (320 mL) and concentrated sulfuric acid (62 mL) was slowly added. The reaction mixture was cooled to 0 °C (ice bath) for 15 min. Then, sodium nitrite (6.9 g, 0.100 mol) dissolved in ice water (40 mL) was added via a dropping funnel to mixture at 0 °C over 1 h. The resulting suspension was additionally stirred at 0 °C for 1 h before potassium iodide (16.6 g, 0.10 mol) dissolved in water (60 mL) was added via a dropping funnel at 0 °C over 20 min. The solution was stirred at 0 °C until the gas evolution ceased. Then, the dark red suspension was heated at 60 °C (oil bath) for 2 h. The dark brown reaction mixture was then filtered and the obtained dark brownish solid was recrystallized in methanol (300 mL). Then, the crystallized product was purified by column chromatography on silica gel (*n*-hexane/ethyl acetate 10:1) and dried under vacuum to weight constancy to give dimethyl 2-iodoterephthalate (28.49 g, 89%) as a yellow solid Mp 78 °C, R*f*: 0.19 (*n*-hexane/ethyl acetate = 10:1).

^{1}H NMR: (300 MHz, DMSO-*d*$_6$) δ = 8.44 (d, ^3J = 1.6 Hz, 1H), 8.03 (dd, ^3J = 8.2 Hz, ^4J = 1.6 Hz, 1H), 7.81 (d, ^3J = 7.9 Hz, 1H), 3.89 (s, 3H), 3.88 (s, 3H). **^{13}C NMR:** (75 MHz, DMSO-*d*$_6$) δ = 166.5 (C_{quat}), 166.2 (C_{quat}), 140.5 (CH), 132.9 (C_{quat}), 130.2 (CH), 128.7 (CH), 94.1 (C_{quat}), 52.8 (CH_3). **MS(EI)** *m/z* (%): 320 ($[M]^+$, 65), 289 ($[M – OMe]^+$, 100), 261 ($[M – CO_2Me]^+$,14), 246 ($[M – CO_2Me – Me]^+$, 12), 229 ($[M – (CO_2Me)_2]^+$,6), 119 (14),104 (13), 103 (24), 76 (18), 75 (22), 74 (29), 63 (11).

Dimethyl-2-iodoterephthalate (7.04 g, 22.0 mmol) was suspended in a 25% aqueous ammonia solution (35 mL) in a Schlenk vessel with magnetic stir bar under nitrogen atmosphere and the reaction mixture was then refluxed at 100 °C (oil bath) for 4 h. After cooling to room temp the colorless precipitate was filtered and washed with ice cold water (100 mL) and dried under vacuum until weight constancy to give 2-iodoterephthalamide (2.81 g, 55%) as a colorless transparent solid, Mp 295.2 °C.

^{1}H NMR: (300 MHz, DMSO-*d*$_6$) δ = 8.32 (d, ^4J = 1.6 Hz, 1H), 8.10 (s, 1H), 7.91 – 7.85 (m, 2H), 7.60 (s, 1H), 7.51 (s, 1H), 7.39 (d, ^3J = 7.9 Hz, 1H). **^{13}C NMR:** (75 MHz, DMSO-*d*$_6$) *δ* = 170.1 (C_{quat}), 165.8 (C_{quat}), 145.4 (C_{quat}), 137.9 (CH), 135.8 (C_{quat}), 127.4 (CH), 127.0 (CH), 92.7 (C_{quat}). **MS(EI)** *m/z* (%): 320 (70), 289 ($[M]^+$, 100), 261 (15), 246 (12), 149 (13), 119 (10), 105 (12), 104 (10), 103 (17), 77 (11), 75 (29), 74 (21), 73 (13), 69 (10), 60 (16), 57 (20), 55 (16).

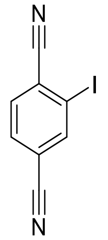

$C_8H_3IN_2$
254.03

2-Iodoterephthalamide (3.164 g, 10.91 mmol) was suspended in phosphoryl chloride (8.0 mL, 84 mmol) in a dry Schlenk flask with magnetic stir bar under nitrogen atmosphere and then heated at 130 °C (oil bath) for 6 h. After cooling to room temp and the residual phosphoryl chloride was carefully hydrolyzed with ice water under external cooling (ice bath). The precipitate was filtered and washed with ice water and then dried under vacuum until weight constancy to give 2-iodoterephthalnitrile (**4**) (2.55 g, 92%) as a sand colored solid, Mp 219 °C, R_f: 0.13 (*n*-hexane/ethyl acetate = 4:1).

^{1}H NMR: (300 MHz, DMSO-*d*$_6$) δ = 8.60 (dd, ^4J = 1.4 Hz, ^5J = 0.6 Hz, 1H), 8.02 – 8.11 (m, 2H). **^{13}C NMR:** (75 MHz, DMSO-*d*$_6$) δ = 142.1 (CH), 135.0 (CH), 132.2 (CH), 123.5 (C_{quat}), 118.6 (C_{quat}), 116.5 (C_{quat}), 116.3 (C_{quat}),101.0 (C_{quat}). **Anal. calcd.** for $C_8H_3IN_2$ (254.0): C 37.82, H 1.19, N 11.03, found: C 37.81, H 1.13, N 11.03. **MS(EI)** *m/z* (%): 254 ([M]$^+$, 100), 127 ([M – I]$^+$,80), 100 ([M – I – CN]$^+$, 34), 75 (12). **IR:** $\tilde{\nu}$ [cm^{-1}] = 1508 (w), 1452 (s), 1437 (w), 1379 (w), 1300 (w), 1281 (w), 1244 (s), 1196 (w), 1163 (w), 1155 (w), 1140 (w), 1123 (w), 1032 (w), 963 (w), 905 (w), 866 (w), 851 (m), 831 (m), 801(m), 721 (w), 623 (s).

4'-(Diphenylamino)-[1,1'-biphenyl]-2,5-dicarbonitrile (5a)

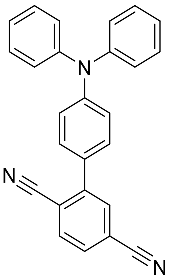

$C_{26}H_{17}N_3$
371.44

In a dry Schlenk vessel with magnetic stir bar 4-bromo-*N*,*N*-diphenylaniline (**3a**) (972 mg, 3.00 mmol) were dissolved in dry THF (10 mL) under nitrogen atmosphere. The solution was cooled -78 °C (isopropanol/dry ice) for 10 min. At -78 °C freshly titrated *n*-BuLi (1.59 M) (2.14 mL, 3.40 mmol) was added dropwise to the reaction mixture and stirring was continued for 5 min. Then, trimethyl borate (1.18 mL, 3.60 mmol) was added at -78 °C. Then, the reaction mixture was allowed to come to room temp and stirring was continued for 20 min. Then, $Pd(PPh_3)_4$ (173 mg, 0.15 mmol), 2-iodoterephthalnitrile (**4**) (505 mg, 4.50 mmol), and KO^{t}Bu (762 mg, 3.00 mmol) were added before the reaction mixture was heated at 80 °C (oil bath) for 18 h. After cooling to room temp ethyl acetate (2 mL) was added and then adsorbed on Celite®. The solvents were removed *in vacuo* and the residue was purified by column chromatography on silica gel (*n*-hexane/ethyl acetate 10:1) to give after two crystallizations from ethanol (20 mL) and then dried under vacuum until weight constancy to give compound **5a** (453 mg, 44%) as a yellow solid. Mp 175 – 189 °C. R_f: 0.51 (*n*-hexane/ethyl acetate = 4:1).

^{1}H NMR: (600 MHz, DMSO-d_6) δ = 8.14 (d, ^3J = 7.9 Hz, 2H), 7.99 (dd, ^3J = 7.9 Hz, ^4J =1.7 Hz, 1H), 7.56 (d, ^3J = 9.0 Hz, 2H), 7.44 – 7.32 (m, 4H), 7.22 – 7.09 (m, 6H), 7.02 (d, J = 8.9 Hz, 2H). **^{13}C NMR:** (150 MHz, DMSO-d_6) δ = 148.5 (C_{quat}), 146.5 (C_{quat}), 144.8 (C_{quat}), 134.9 (CH), 133.3 (CH), 130.8 (CH), 130.0 (CH), 129.8 (CH), 128.5 (C_{quat}), 125.2 (CH), 124.2 (CH), 121.0 (CH), 117.6 (C_{quat}), 117.5 (C_{quat}), 115.9 (C_{quat}), 113.9 (C_{quat}). **MS(HR-ESI)** *m/z* (%): 374.1562 ([M]$^+$), 373.1529, 372 ([M]$^+$).1498 ([M]$^+$, 100), 371.3257 ([M]$^+$). **Anal. calcd.** for $C_{26}H_{17}N_3$ (371.4): C 84.07, H 4.61, N 11.31, found: C 83.97, H 4.64, N 11.15. **IR:** $\tilde{\nu}$ [cm^{-1}] = 1587 (m), 1545 (w), 1512 (w), 1481 (m), 1451 (w), 1420 (w), 1391 (w), 1327 (w), 1317 (w), 1273 (m), 1259 (m), 1196 (w), 1179 (w), 1157 (w), 1115 (w), 1076 (w), 1042 (w), 1028 (w), 1013 (w), 1001 (w), 959 (w), 924 (w), 912 (w), 897 (w), 870 (w), 835 (m), 750 (m), 729 (w), 694 (s), 662 (w), 637 (w), 623 (m).

4'-(Diphenylamino)-2'-methyl-[1,1'-biphenyl]-2,5-dicarbonitrile (5b)

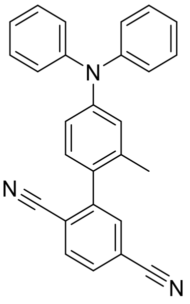

$C_{27}H_{19}N_3$
385.47

In a dry Schlenk vessel with magnetic stir bar 4-bromo-3-methyl-*N*,*N*-diphenylaniline (**3b**) (338 mg, 1.00 mmol) were dissolved in dry THF (5 mL) under nitrogen atmosphere. The solution was cooled -78 °C (isopropanol/dry ice) for 10 min. At -78 °C freshly titrated *n*-BuLi (1.59 M) (0.77 mL, 1.20 mmol) was added dropwise to the reaction mixture and stirring was continued for 20 min. Then, trimethyl borate (0.46 mL, 3.60 mmol) was added at -78 °C. Then, the reaction mixture was allowed to come to room temp and stirring was continued for 20 min. Then, Pd(PPh$_3$)$_4$ (58 mg, 0.05 mmol), 2-iodoterephthalnitrile (**4**) (278 mg, 1.10 mmol), and KO^{t}Bu (427 mg, 2.40 mmol) were added before the reaction mixture was heated at 80 °C (oil bath) for 18 h. After cooling to room temp ethyl acetate (2 mL) was added and then adsorbed on Celite®. The solvents were removed *in vacuo* and the residue was purified by column chromatography on silica gel (*n*-hexane/ethyl acetate 10:1) to give after crystallization from ethanol (10 mL) and then dried under vacuum until weight constancy to give compound **5b** (385 mg, 99%) as a yellow solid. Mp 164.9 °C. R$_f$: 0.14 (*n*-hexane/ethyl acetate = 10:1).

^{1}H NMR: (600 MHz, DMSO-d_6) δ = 8.17 (d, ^3J = 8.4 Hz, 1H), 8.05 (m, 2H), 7.39 – 7.32 (m, 4H), 7.17 (d, ^3J = 8.3 Hz, 1H), 7.13 – 7.07 (m, 6H), 6.93 (d, ^3J = 2.1 Hz, 1H), 6.85 (dd, ^3J = 8.3 Hz, ^4J = 2.3 Hz, 1H), 2.04 (s, 3H). **^{13}C NMR:** (150 MHz, DMSO-d_6) δ = 148.1 (C_{quat}), 146.8 (C_{quat}), 145.4 (C_{quat}), 136.7 (C_{quat}), 134.2 (CH), 134.1 (CH), 131.5 (CH), 130.8 (CH), 129.7 (C_{quat}), 129.65 (CH), 124.69 (CH), 123.73 (CH), 123.22 (CH), 119.43 (CH), 117.45 (C_{quat}), 116.98 (C_{quart}), 116.35 (C_{quat}), 115.54 (C_{quat}), 19.67 (CH_3). **MS(EI)** *m/z* (%): 386 (22), 385 ([M]$^+$, 100), 166 (10). **Anal. calcd.** for $C_{27}H_{19}N_3$ (385.47): C 84.13, H 4.97, N 10.90, found: C 84.02, H 4.89, N 10.77. **IR:** $\tilde{\nu}$ [cm^{-1}] = 1607 (w), 1586 (m), 1477 (m), 1456 (m), 1418 (m), 1373 (m), 1337 (m), 1308 (m), 1271 (m), 1252 (s), 1192 (w), 1171 (w), 1126 (w), 1107 (w), 1067 (m), 1005 (m), 928 (w), 866 (w), 822 (m), 802 (m), 777 (m), 758 (s), 748 (m), 729 (m), 700 (s), 640 (m), 623 (s), 611 (m).

4'-(Diphenylamino)-2'-isopropyl-[1,1'-biphenyl]-2,5-dicarbonitrile (5c)

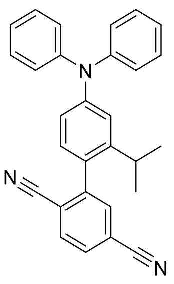

$C_{29}H_{23}N_3$
413.52

In a dry Schlenk vessel with magnetic stir bar 4-bromo-3-isopropyl-*N*,*N*-diphenylaniline (**3c**) (972 mg, 2.40 mmol) were dissolved in dry THF (10 mL) under nitrogen atmosphere. The solution was cooled -78 °C (isopropanol/dry ice) for 10 min. At -78 °C freshly titrated *n*-BuLi (1.59 M) (0.75 mL, 1.20 mmol) was added dropwise to the reaction mixture and stirring was continued for 5 min. Then, trimethyl borate (0.43 mL, 1.30 mmol) was added at -78 °C. Then, the reaction mixture was allowed to come to room temp and stirring was continued for 20 min. Then, $Pd(PPh_3)_4$ (116 mg, 0.05 mmol), 2-iodoterephthalnitrile (**4**) (254 mg, 1.00 mmol), and KO^{t}Bu (135 mg, 1.20 mmol) were added before the reaction mixture was heated at 80 °C (oil bath) for 18 h. After cooling to room temp ethyl acetate (2 mL) was added and then adsorbed on Celite$^{®}$. The solvents were removed *in vacuo* and the residue was purified by column chromatography on silica gel (*n*-hexane/ethyl acetate 10:1) to give after two crystallizations from ethanol (20 mL) and then dried under vacuum until weight constancy to give compound **5c** (339 mg, 82%) as a yellow solid. Mp 132 – 148 °C. R_f: 0.62 (*n*-hexane/ethyl acetate = 4:1).

^{1}H NMR: (300 MHz, DMSO-d_6) δ = 8.18 (dd, ^3J = 7.8 Hz, ^4J = 0.9 Hz, 1H), 8.04 – 8.10 (m, 2H), 7.31 – 7.42 (m, 4H), 7.05 – 7.18 (m, 6H), 7.02 (d, ^4J = 2.4 Hz, 1H), 6.81 (dd, ^3J = 8.4 Hz, ^4J = 2.4 Hz, 1H), 2.58 (hep, ^3J = 6.8 Hz, 1H), 1.08 – 0.79 (m, 6H). **^{13}C NMR:** (75 MHz, DMSO-d_6) δ = 148.3 (C_{quat}), 147.2 (C_{quat}), 146.7 (C_{quat}), 145.6 (C_{quat}), 134.2 (CH), 133.9 (CH), 131.7 (CH), 130.7 (CH), 129.7 (CH), 128.7 (C_{quat}), 124.6 (CH), 123.8 (CH), 119.1 (CH), 118.5 (CH), 117.5 (C_{quat}), 116.9 (C_{quat}), 116.8 (C_{quat}), 115.5 (C_{quat}), 29.7 (CH), 23.8 (CH_3), 23.0 (CH_3). **MS(HR-ESI)** *m/z* (%): 416.2029 ([M]$^+$), 415.1998 ([M]$^+$), 414.1967 ([M]$^+$). **Anal. calcd.** for $C_{29}H_{23}N_3$ (413.5): C 84.23, H 5.61, N 10.16, found: C 84.45, H 5.40, N 9.97. **IR:** ṽ [cm^{-1}] = 1607 (w), 1589 (m), 1553 (w), 1476 (m), 1447 (w), 1424 (w), 1398 (w), 1383 (w), 1350 (w), 1331 (m), 1304 (w), 1265 (m), 1256 (m), 1204 (w), 1153 (w), 1130 (w), 1113 (w), 1074 (w), 1024 (w), 990 (w), 970 (w), 951 (w), 924 (w), 893 (w), 862 (w), 824 (m), 804 (w), 791 (w), 760 (m), 747 (w), 704 (s), 685 (w), 658 (w), 631 (m), 619 (w).

4'-(Diphenylamino)-2',6'-dimethyl-[1,1'-biphenyl]-2,5-dicarbonitrile (5d)

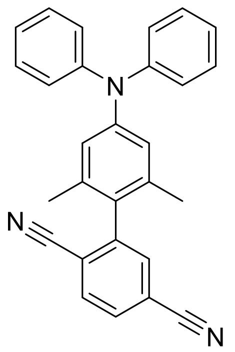

$C_{28}H_{21}N_3$
399.50

In a dry Schlenk vessel with magnetic stir bar 4-bromo-3,5-dimethyl-*N*,*N*-diphenylaniline (**3d**) (176 mg, 0.50 mmol) were dissolved in dry THF (5 mL) under nitrogen atmosphere. The solution was cooled -78 °C (isopropanol/dry ice) for 10 min. At -78 °C freshly titrated *n*-BuLi (1.59 M) (0.93 mL, 1.50 mmol) was added dropwise to the reaction mixture and stirring was continued for 5 min. Then, trimethyl borate (0.54 mL, 1.65 mmol) was added at -78 °C. Then, the reaction mixture was allowed to come to room temp and stirring was continued for 20 min. Then, $Pd_2(dba)_3$ (46 mg, 0.05 mmol), (2-biphenyl)dicyclohexylphosphane (CyJohnPhos) (17.5 mg, 0.05 mmol), 2-iodoterephthalnitrile (**4**) (127 mg, 0.50 mmol), and K_3PO_4 (159 mg, 0.75 mmol) were added before the reaction mixture was heated at 80 °C (oil bath) for 18 h. After cooling to room temp ethyl acetate (2 mL) was added and then adsorbed on Celite®. The solvents were removed *in vacuo* and the residue was purified by column chromatography on silica gel (*n*-hexane/ethyl acetate 10:1) to give after two crystallizations from ethanol (20 mL) and then dried under vacuum until weight constancy to give compound **5d** (28 mg, 14%) as a yellow solid. Mp 188 °C. R_f: 0.62 (*n*-hexane/ethyl acetate = 4:1).

^{1}H NMR: (300 MHz, DMSO-d_6) δ = 7.88 (d, ^3J = 7.9 Hz, 1H), 7.75 (d, ^3J = 8.1 Hz, 1H), 7.65 (d, ^4J = 1.5 Hz, 1H), 7.30 (d, ^3J = 8.5 Hz, 4H), 7.14 (d, ^3J = 8.5 Hz, 4H), 7.11 – 7.01 (m, 2H), 6.83 (s, 2H), 1.90 (s, 6H). **^{13}C NMR:** (75 MHz, DMSO-d_6) δ = 148.6 (C_{quat}), 147.6 (C_{quat}), 147.2 (C_{quat}), 136.7 (C_{quat}), 134.6 (CH), 133.8 (CH), 130.7 (CH), 129.5 (CH), 125.1 (CH), 123.43, 122.1 (CH), 118.3 (C_{quat}),117.4 (C_{quat}), 116.79, 116.6 (C_{quat}), 20.7 (CH_3). **MS(HR-ESI)** *m/z* (%): $(C_{28}H_{21}N_3+H)^+$ *m/z*: 400.1808; Found: 400.1812. **IR:** ṽ [cm^{-1}] = 3078 (s), 3057 (s), 2235 (s), 1589 (m), 1570 (s), 1487 (m), 1473 (s), 1396 (s), 1340 (s), 1317 (s), 1290 (m), 1280 (m), 1226 (s), 1178 (s), 1151 (s), 842 (m), 759 (m), 750 (m), 686 (s), 667 (m), 653 (s), 636 (s).

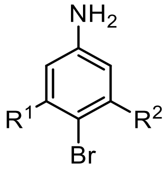

1

1a ($R^1 = R^2 = H$)
1b ($R^1 = H$, $R^2 = Me$)
1c ($R^1 = H$, $R^2 = {}^iPr$)
1d ($R^1 = R^2 = Me$)

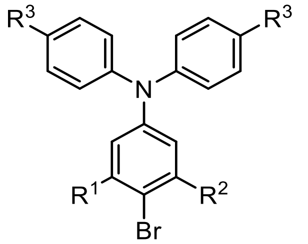

3a ($R^1 = R^2 = R^3 = H$, 39%)
3b ($R^1 = R^3 = H$, $R^2 = Me$, 31%)
3c ($R^1 = H$, $R^2 = {}^iPr$, $R^3 = H$, 86%)
3d ($R^1 = R^2 = Me$, $R^3 = H$, 76%)
3e ($R^1 = H$, $R^2 = Me$, $R^3 = OMe$, 33%)

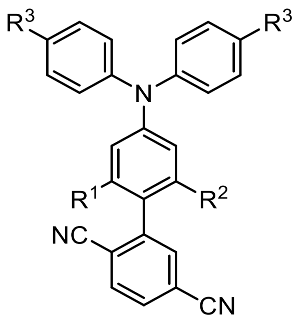

5a ($R^1 = R^2 = R^3 = H$, 94%)
5b ($R^1 = R^3 = H$, $R^2 = Me$, 99%)
5c ($R^1 = H$, $R^2 = {}^iPr$, $R^3 = H$, 82%)
5d ($R^1 = R^2 = Me$, $R^3 = H$, 14%)[a]
5e ($R^1 = H$, $R^2 = Me$, $R^3 = OMe$, 82%)

4'-(Bis(4-methoxyphenyl)amino)-2'-methyl-[1,1'-biphenyl]-2,5-dicarbonitrile (5e)

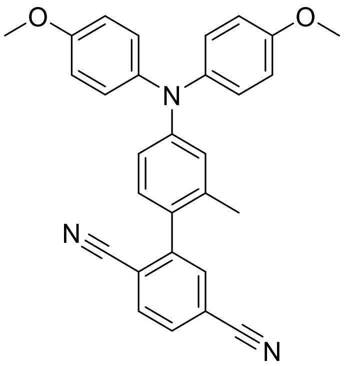

$C_{29}H_{23}N_3O_2$
445.52

In a dry Schlenk vessel with magnetic stir bar 4-bromo-*N*,*N*-bis(4-methoxyphenyl)-3-methylaniline (**3e**) (971 mg, 2.40 mmol) were dissolved in dry THF (30 mL) under nitrogen atmosphere. The solution was cooled -78 °C (isopropanol/dry ice) for 10 min. At -78 °C freshly titrated *n*-BuLi (1.59 M) (2.49 mL, 3.12 mmol) was added dropwise to the reaction mixture and stirring was continued for 5 min. Then, trimethyl borate (0.70 mL, 3.00 mmol) was added at -78 °C. Then, the reaction mixture was allowed to come to room temp and stirring was continued for 20 min. Then, $Pd(PPh_3)_4$ (139 mg, 0.12 mmol), 2-iodoterephthalnitrile (**4**) (610 mg, 2.40 mmol), and KO^tBu (592 mg, 5.28 mmol) were added before the reaction mixture was heated at 80 °C (oil bath) for 18 h. After cooling to room temp ethyl acetate (2 mL) was added and then adsorbed on Celite®. The solvents were removed *in vacuo* and the residue was purified by column chromatography on silica gel (*n*-hexane/ethyl acetate 10:1) to give after crystallization from ethanol (10 mL) and then dried under vacuum until weight constancy to give compound **5e** (874 mg, 82%) as a yellow solid, Mp 174.5 °C. R_f: 0.38 (*n*-hexane/ethyl acetate = 4:1).

^{1}H NMR: (300 MHz, DMSO-*d*$_6$) δ = 8.14 (dd, ^3J = 7.9 Hz, ^4J = 0.6 Hz, 1H), 7.97 – 8.06 (m, 2H), 7.08 – 7.15 (m, 4H), 7.06 (d, ^3J = 8.4 Hz, 1H), 6.91 – 6.99 (m, 4H), 6.68 (d, ^4J = 2.3 Hz, 1H), 6.61 (dd, ^3J = 8.4 Hz, ^4J = 2.4 Hz, 1H), 3.75 (s, 6H), 2.00 (s, 3H). **^{13}C NMR:** (75 MHz, DMSO-*d*$_6$) δ = 156.4 (C_{quat}), 149.3 (C_{quat}), 145.72 (C_{quat}), 139.5 (C_{quat}), 136.2 (C_{quat}), 134.4 (CH), 134.1 (CH), 131.3 (CH), 130.6 (CH), 127.5 (CH), 127.0 (C_{quat}), 119.0 (CH), 117.5 (C_{quat}), 117.1 (C_{quat}), 116.4 (C_{quat}), 115.5 (C_{quart}), 115.4 (CH), 115.1 (CH), 55.2 (CH_3), 19.81 (CH_3). **MS(EI)** *m/z* (%): 446 ([M+H$^+$]$^+$, 32), 445 ([M]$^+$, 100), 431 (23), 430 (77). **Anal. calcd.** for $C_{29}H_{23}N_3O_2$ (445.52): C 78.18, H 5.20, N 9.43, found: C 78.16, H 5.17, N 9.29. **IR:** ṽ [cm^{-1}] = 1601 (w), 1505 (m), 1481 (w), 1456 (m), 1441 (m), 1418 (w), 1393 (w), 1337 (w), 1298 (w), 1279 (w), 1242 (s), 1167 (w), 1140 (w), 1101 (w), 1036 (m), 922 (w), 872 (w), 822 (s), 779 (w), 745 (w) 723 (w), 712 (w), 633 (w).

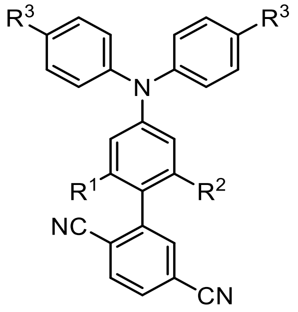

5a (R^1 = R^2 = R^3 = H, 94%)
5b (R^1 = R^3 = H, R^2 = Me, 99%)
5c (R^1 = H, R^2 = ^{i}Pr, R^3 = H, 82%)
5d (R^1 = R^2 = Me, R^3 = H, 14%)[a]
5e (R^1 = H, R^2 = Me, R^3 = OMe, 82%)

4-Bromo-*N*,*N*-diphenylaniline (3a)

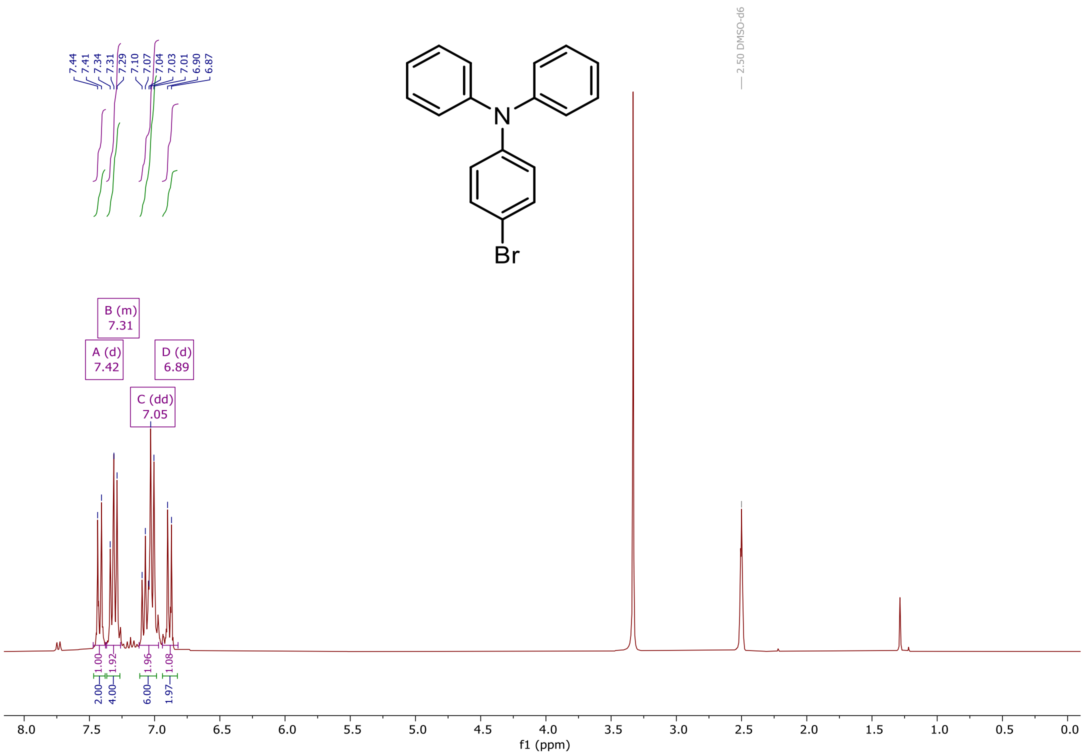

Figure S7.1. ^{1}H NMR spectrum of compound **3a** in DMSO-d_6 (T = 298 K, 300 MHz).

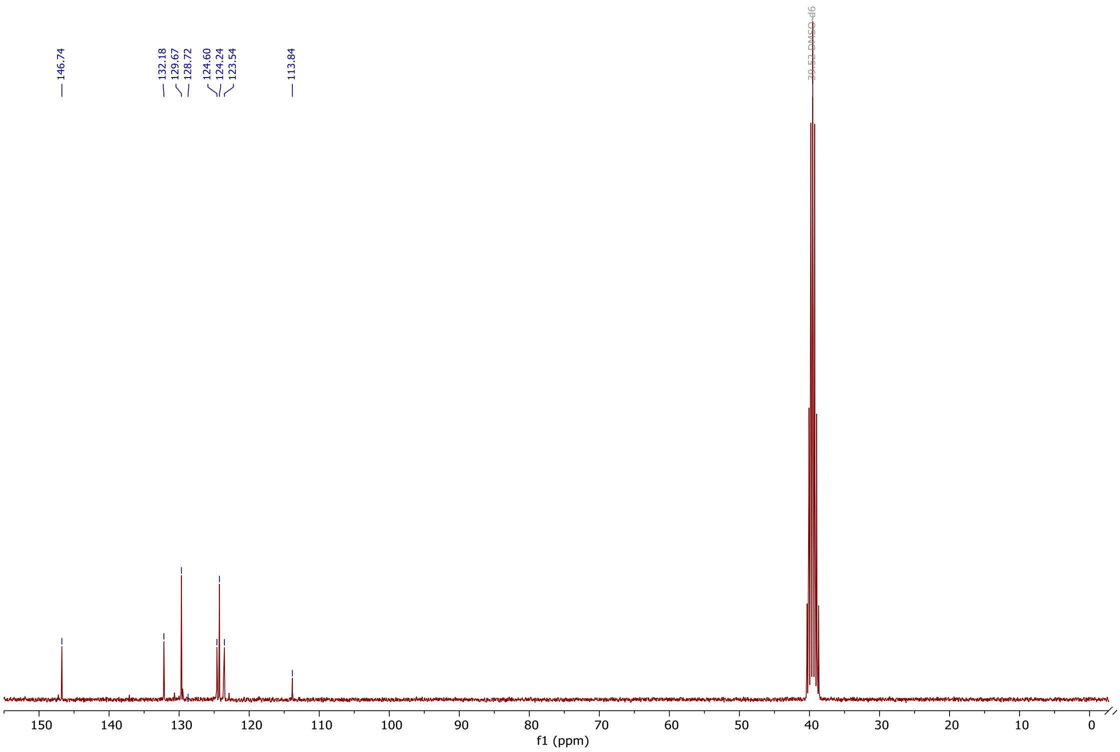

Figure S7.2. ^{13}C NMR spectrum of compound **3a** in DMSO-d_6 (T = 298 K, 75 MHz).

4-Bromo-3-methyl-*N*,*N*-diphenylaniline (3b)

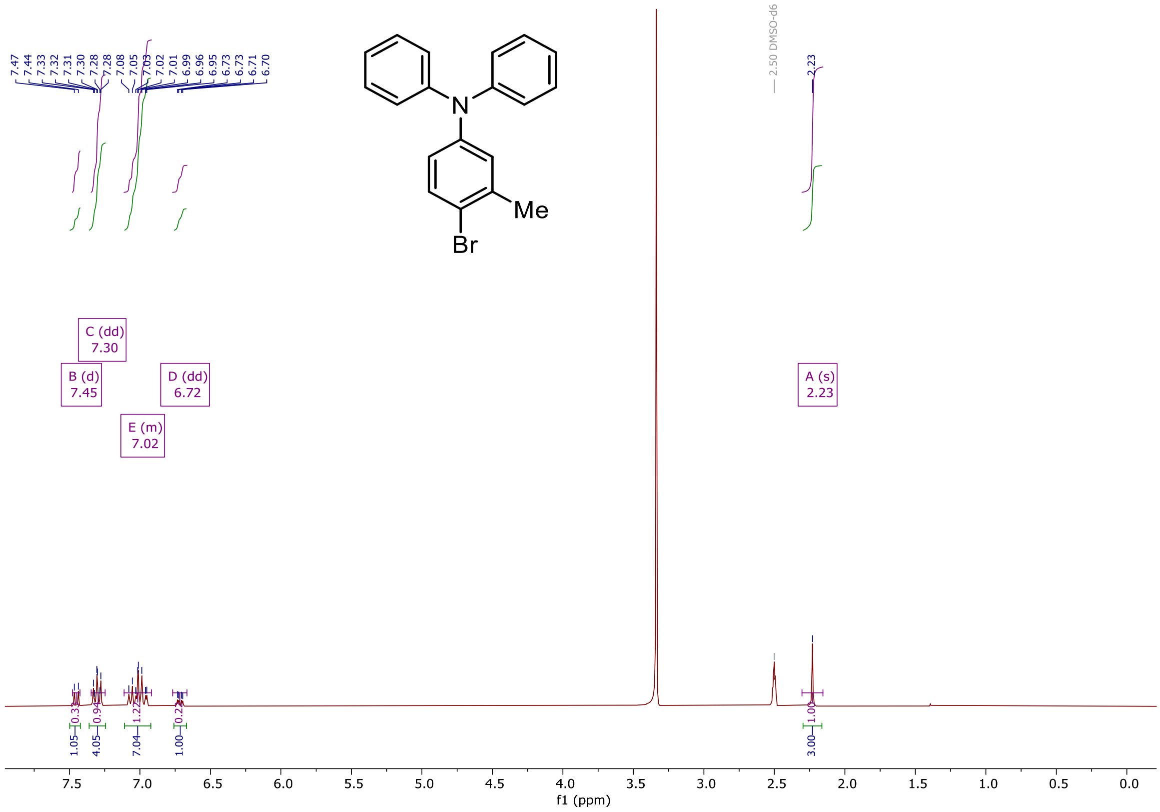

Figure S7.3. ^{1}H NMR spectrum of compound **3b** in DMSO-d$_6$ (T = 298 K, 300 MHz).

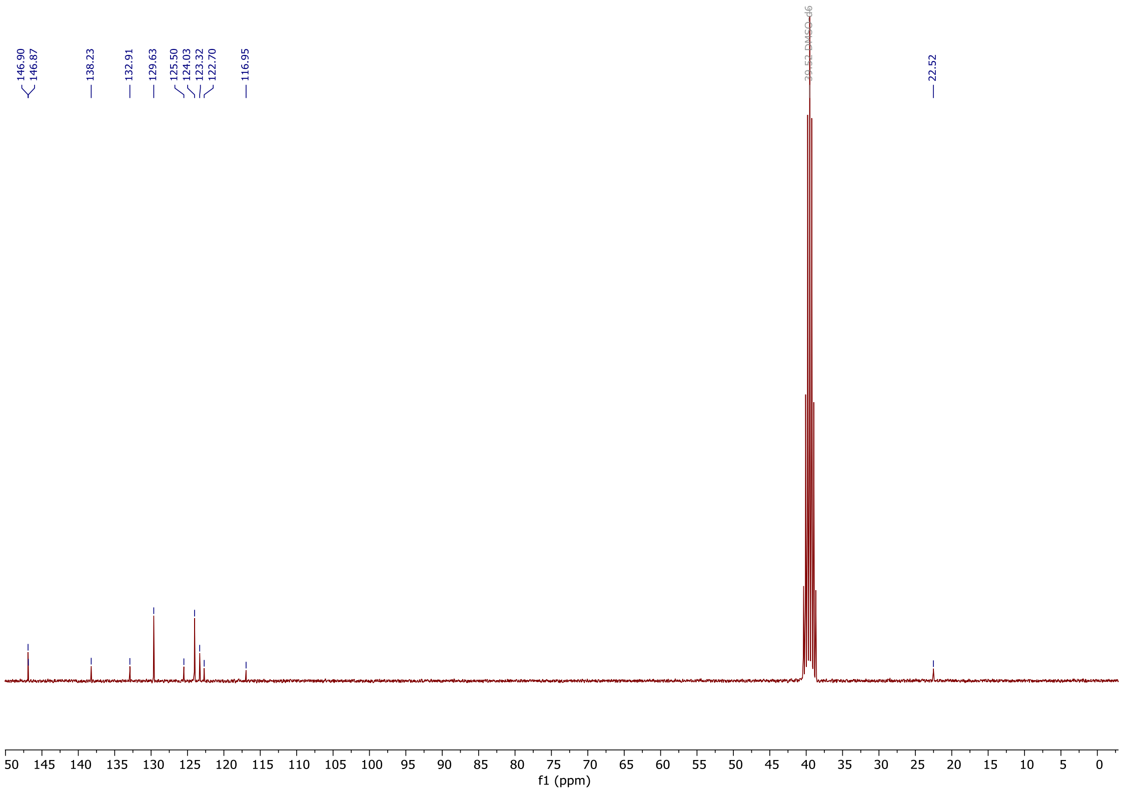

Figure S7.4. ^{13}C NMR spectrum of compound **3b** in DMSO-d$_6$ (T = 298 K, 75 MHz).

4-Bromo-3-isopropyl-N,N-diphenylaniline (3c)

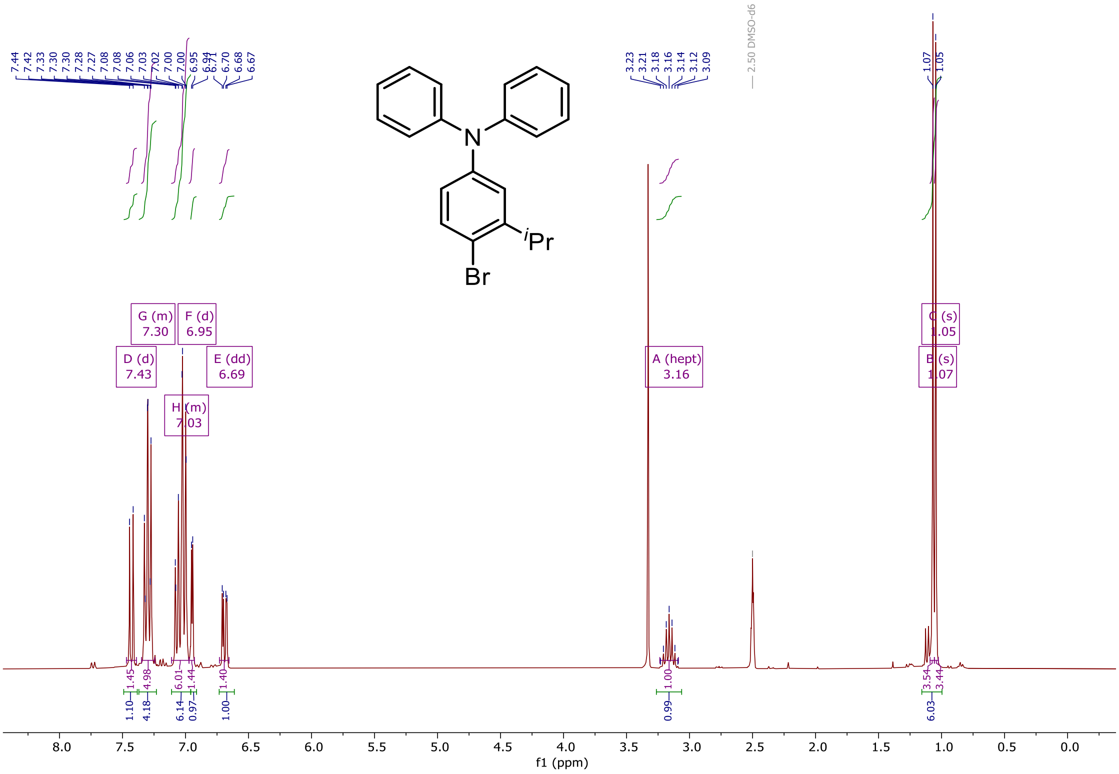

Figure S7.5. ^{1}H NMR spectrum of compound **3c** in DMSO-d$_6$ (T = 298 K, 300 MHz).

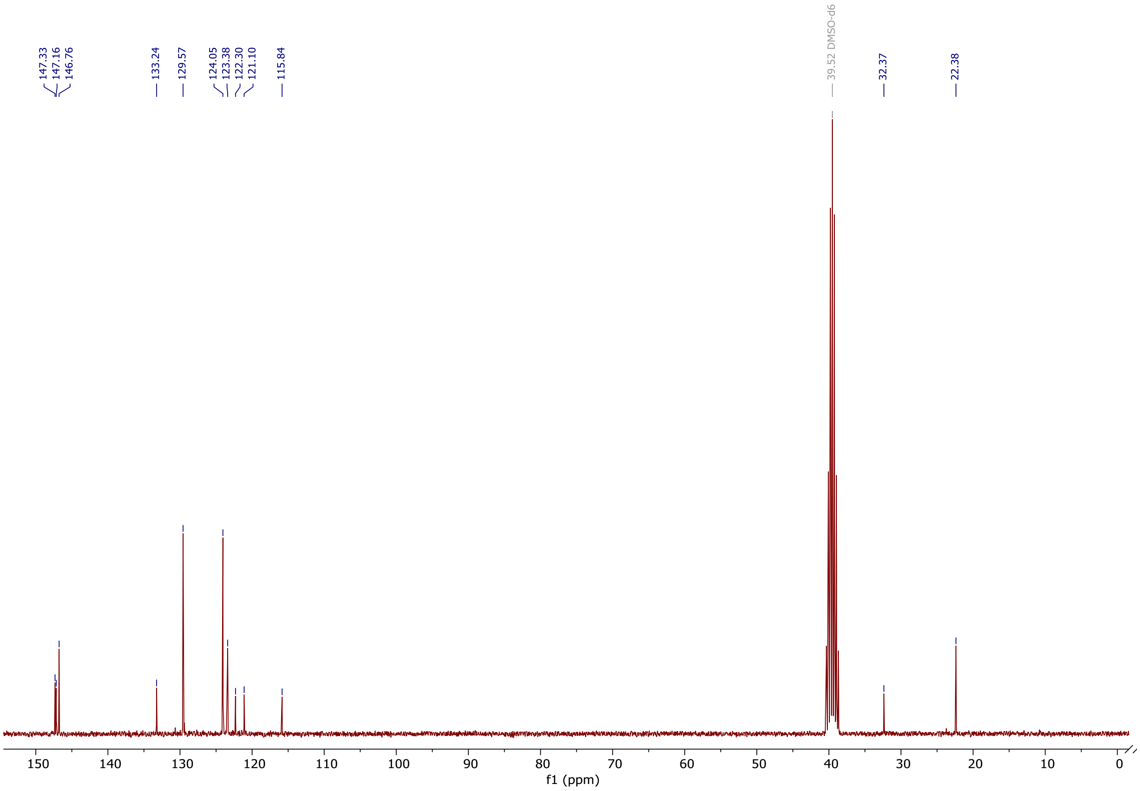

Figure S7.6. ^{13}C NMR spectrum of compound **3c** in DMSO-d$_6$ (T = 298 K, 75 MHz).

4-Bromo-3,5-dimethyl-*N*,*N*-diphenylaniline (3d)

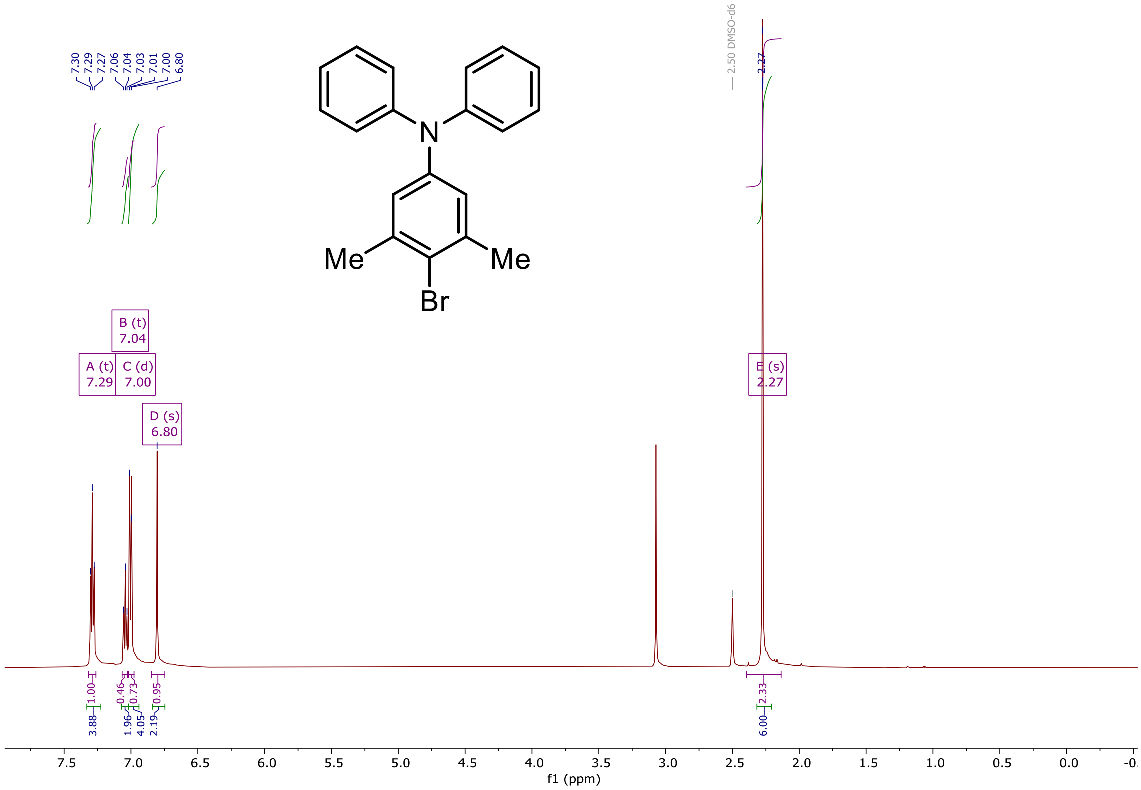

Figure S7.7. ^{1}H NMR spectrum of compound **3d** in DMSO-d$_6$ (T = 298 K, 300 MHz).

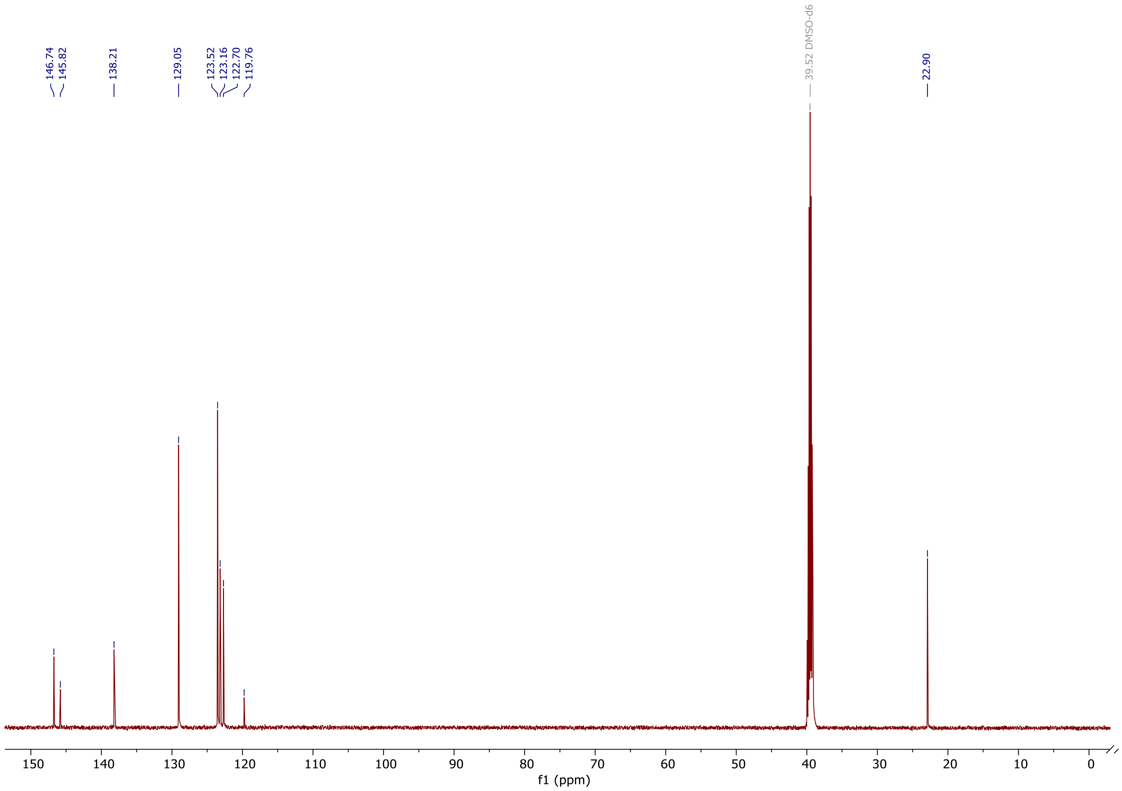

Figure S7.8. ^{13}C NMR spectrum of compound **3d** in DMSO-d$_6$ (T = 298 K, 75 MHz).

4-Bromo-*N*,*N*-bis(4-methoxyphenyl)-3-methylaniline (3e)

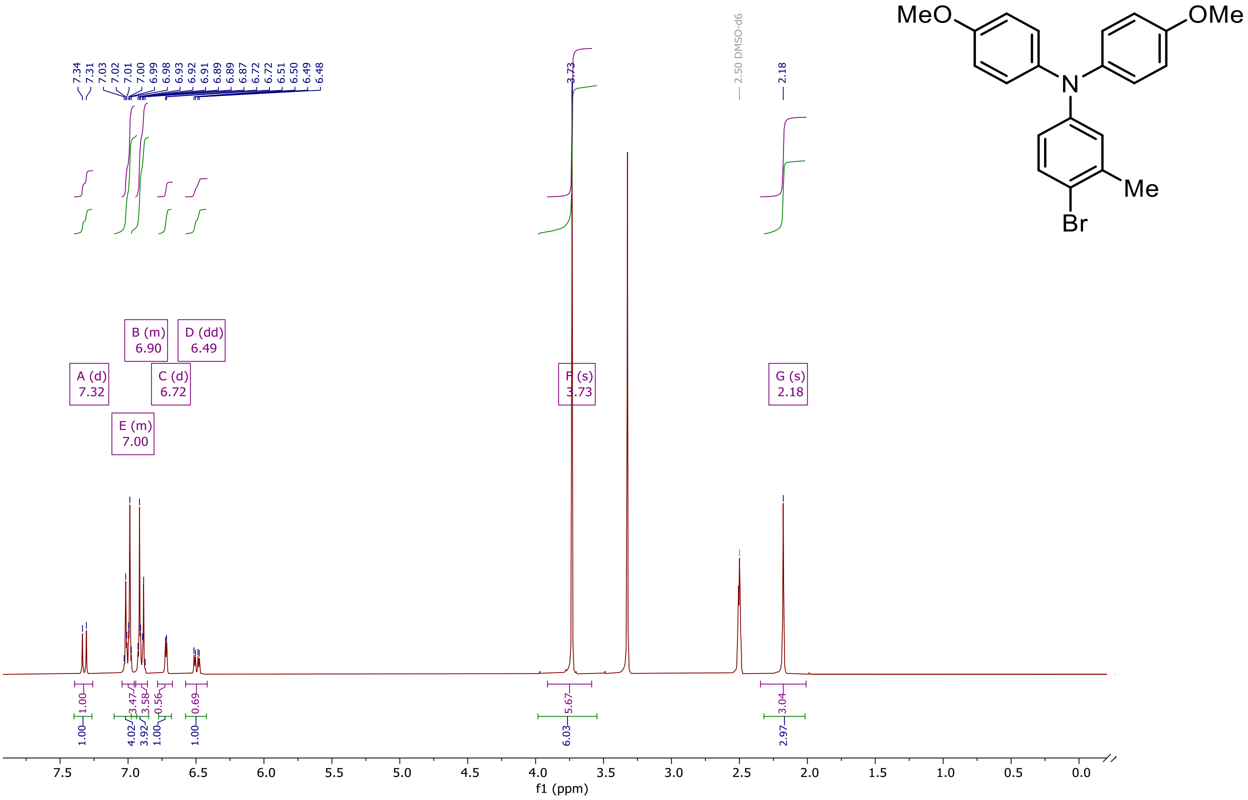

Figure S7.9. ^{1}H NMR spectrum of compound **3e** in DMSO-d$_6$ (T = 298 K, 300 MHz).

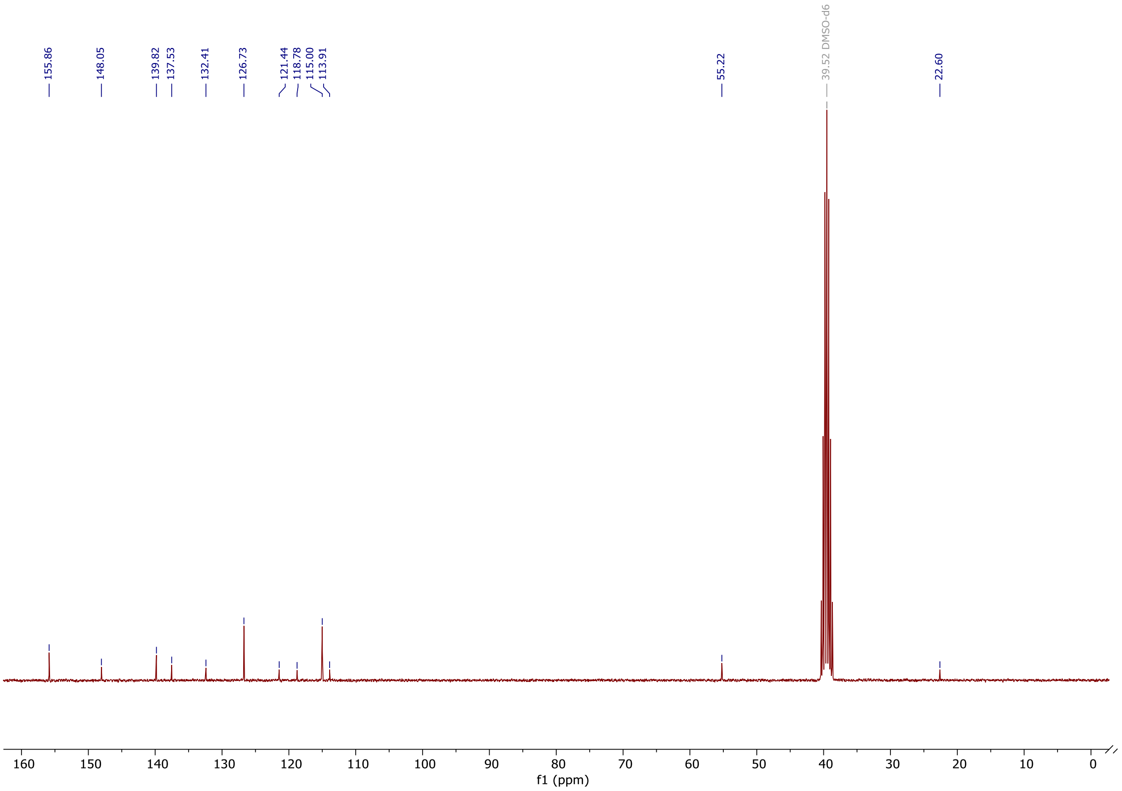

Figure S7.10. ^{13}C NMR spectrum of compound **3e** in DMSO-d$_6$ (T = 298 K, 75 MHz).

Dimethyl-2-iodoterephthalate

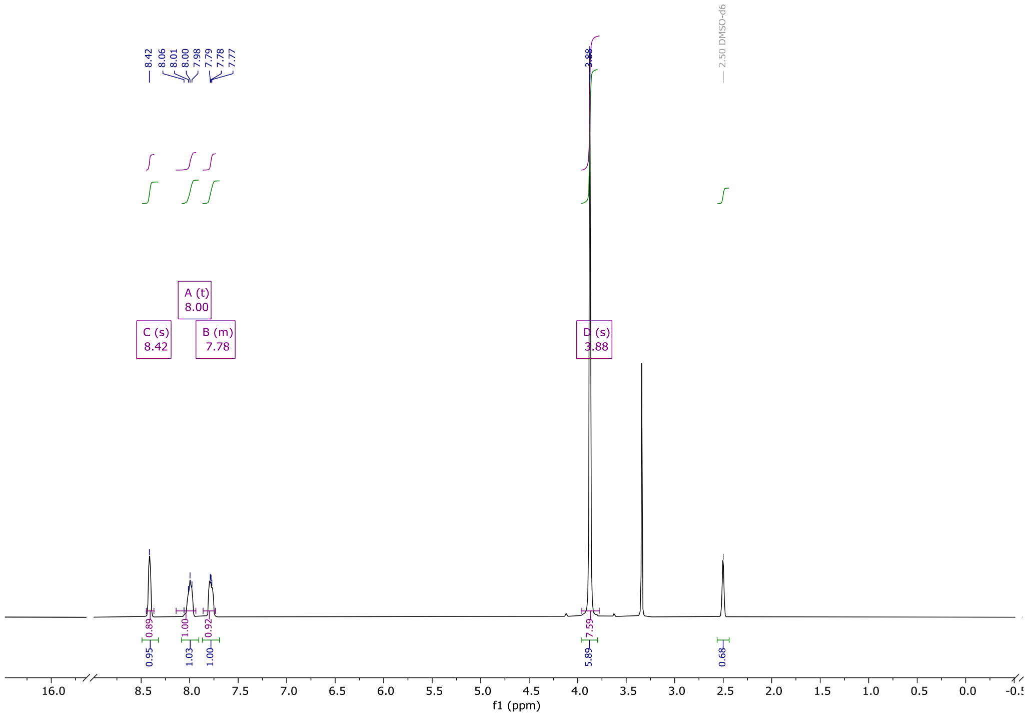

Figure S7.11. ^{1}H NMR spectrum of dimethyl-2-iodoterephthalate in DMSO-d_6 (T = 298 K, 300 MHz).

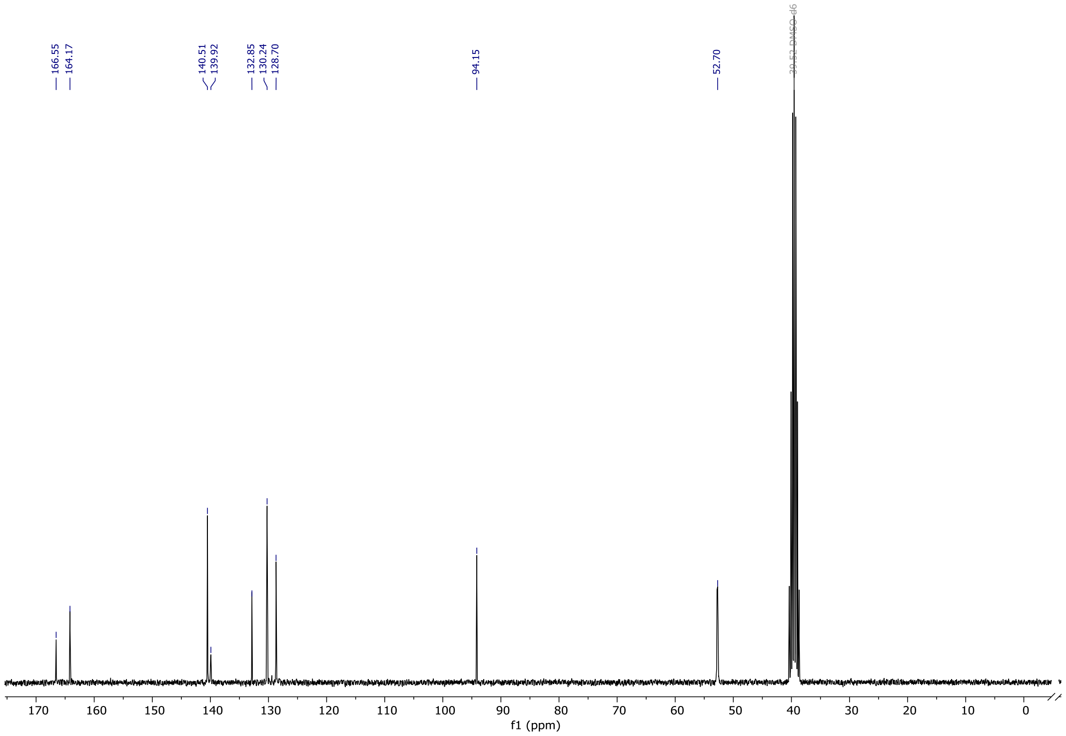

Figure S7.12. ^{13}C NMR spectrum of dimethyl-2-iodoterephthalate in DMSO-d_6 (T = 298 K, 75 MHz).

2-Iodoterephthalamide

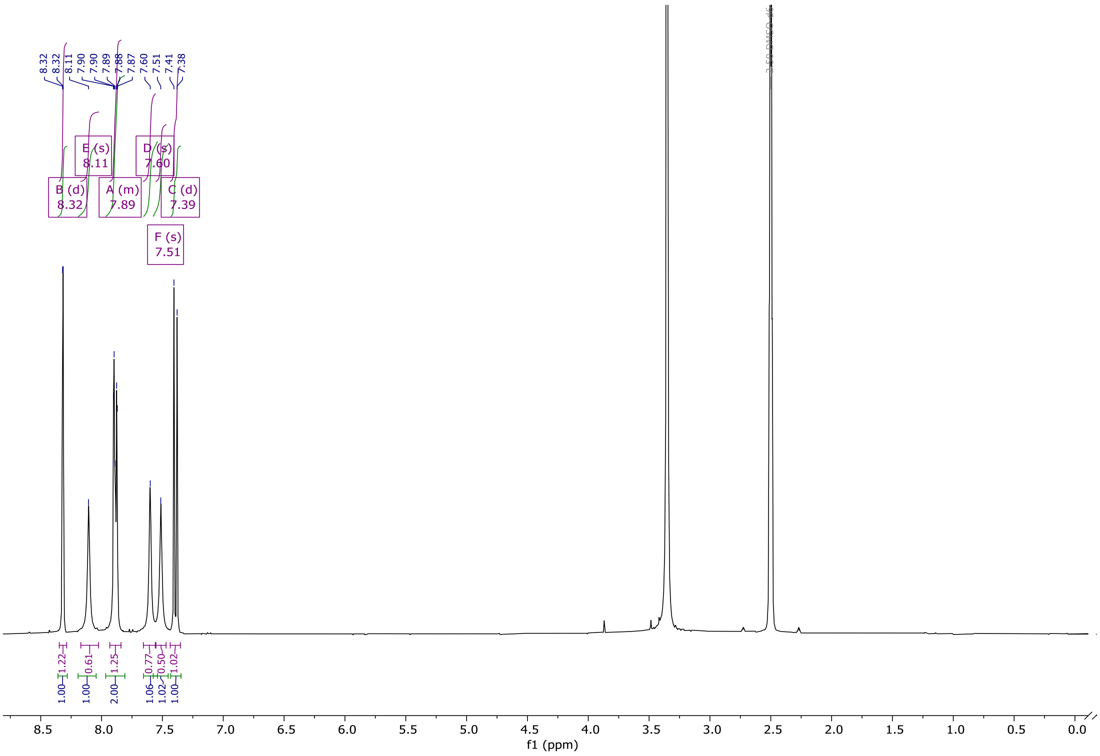

Figure S7.13. ^{1}H NMR spectrum of 2-iodoterephthalamide in DMSO-d$_6$ (T = 298 K, 300 MHz).

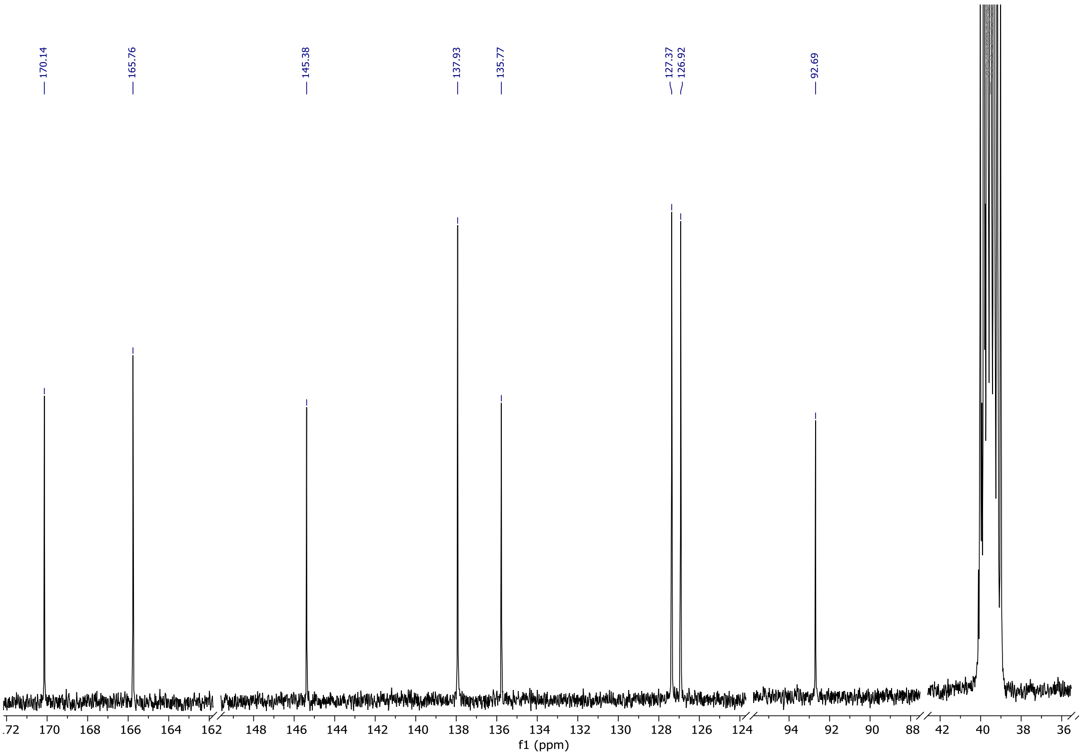

Figure S7.14. ^{13}C NMR spectrum of 2-iodoterephthalamide in DMSO-d$_6$ (T = 298 K, 75 MHz).

2-Iodoterephthalnitrile (4)

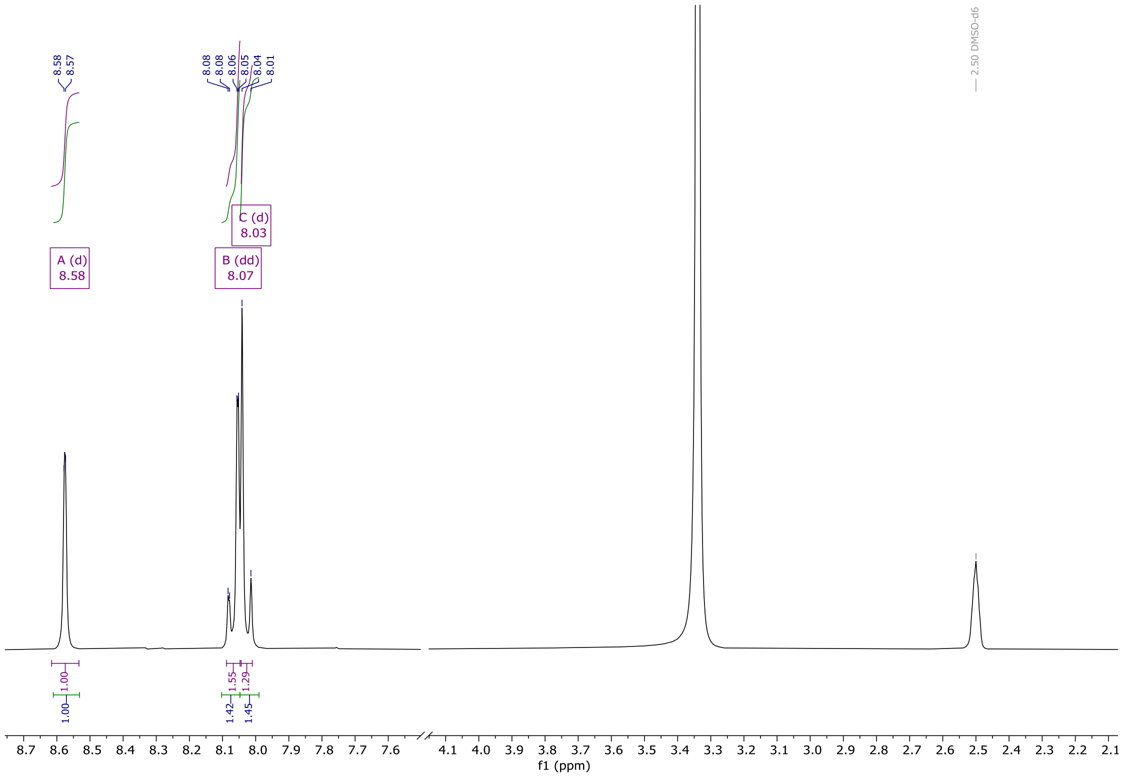

Figure S7.15. ^{1}H NMR spectrum of compound **4** in DMSO-d$_6$ (T = 298 K, 300 MHz).

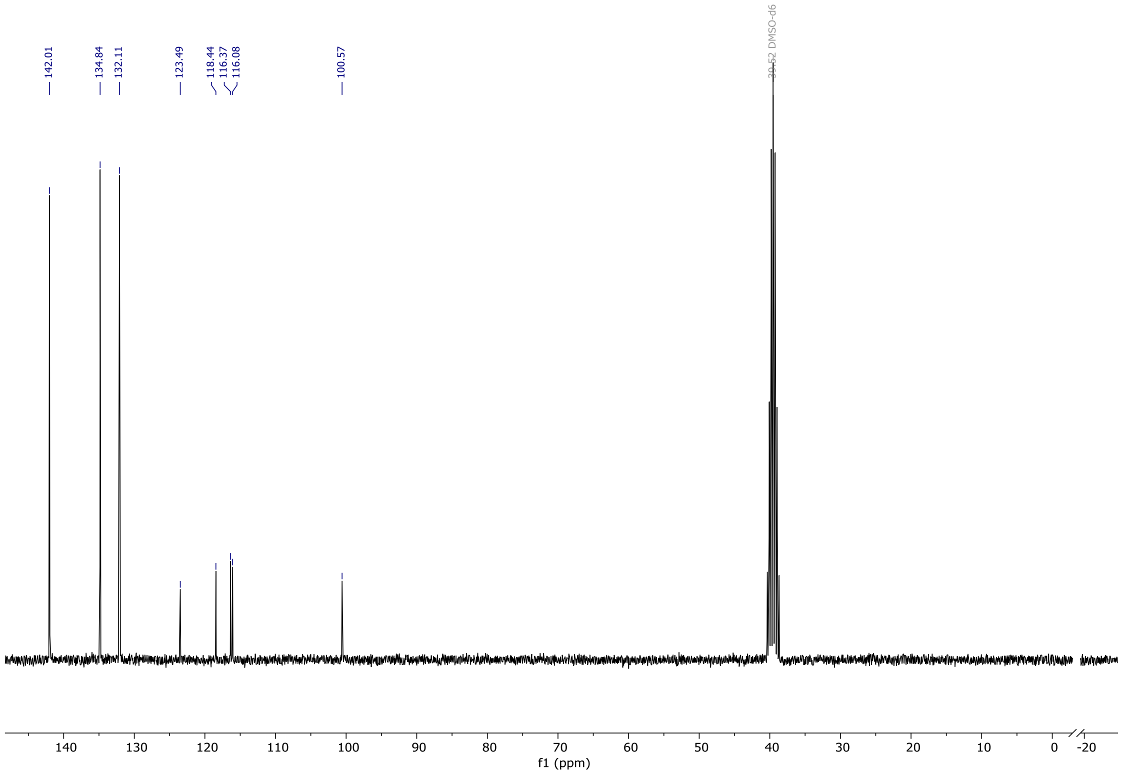

Figure S7.16. ^{13}C NMR spectrum of compound **4** in DMSO-d$_6$ (T = 298 K, 75 MHz).

4'-(Diphenylamino)-[1,1'-biphenyl]-2,5-dicarbonitrile (5a)

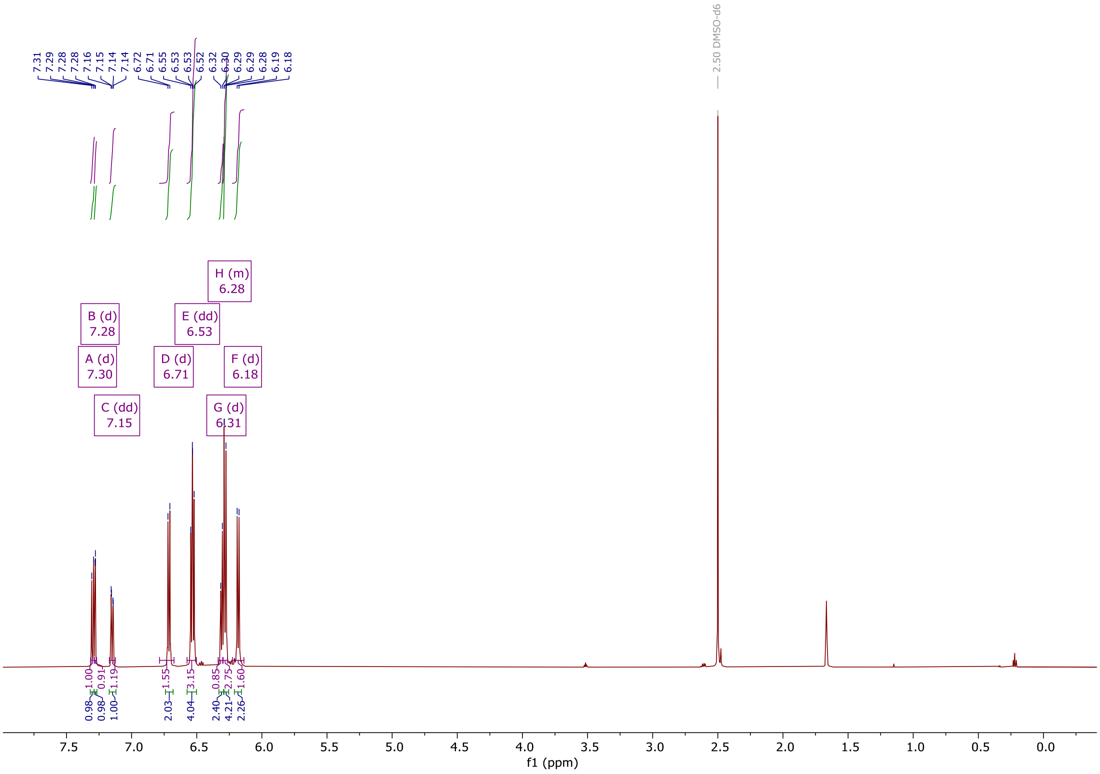

Figure S7.17. ^{1}H NMR spectrum of compound **5a** in DMSO-d$_6$ (T = 298 K, 600 MHz).

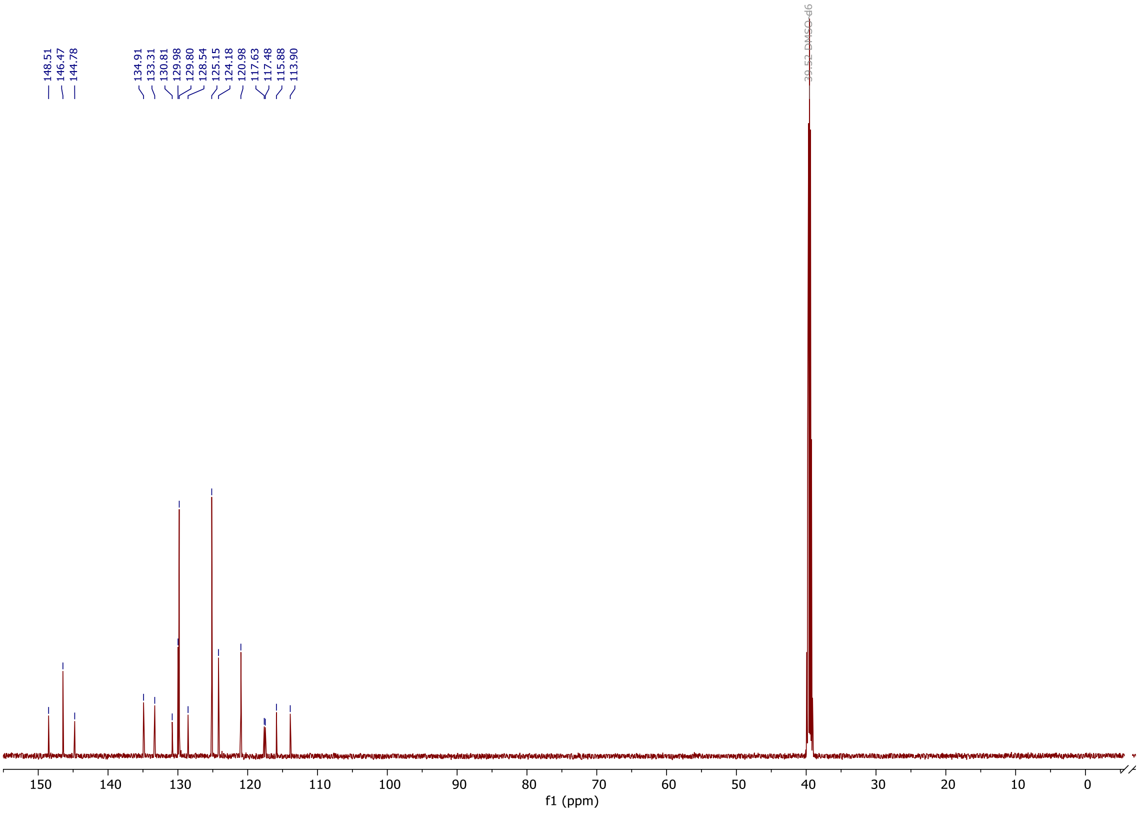

Figure S7.18. ^{13}C NMR spectrum of compound **5a** in DMSO-d$_6$ (T = 298 K, 150 MHz).

4'-(Diphenylamino)-2'-methyl-[1,1'-biphenyl]-2,5-dicarbonitrile (5b)

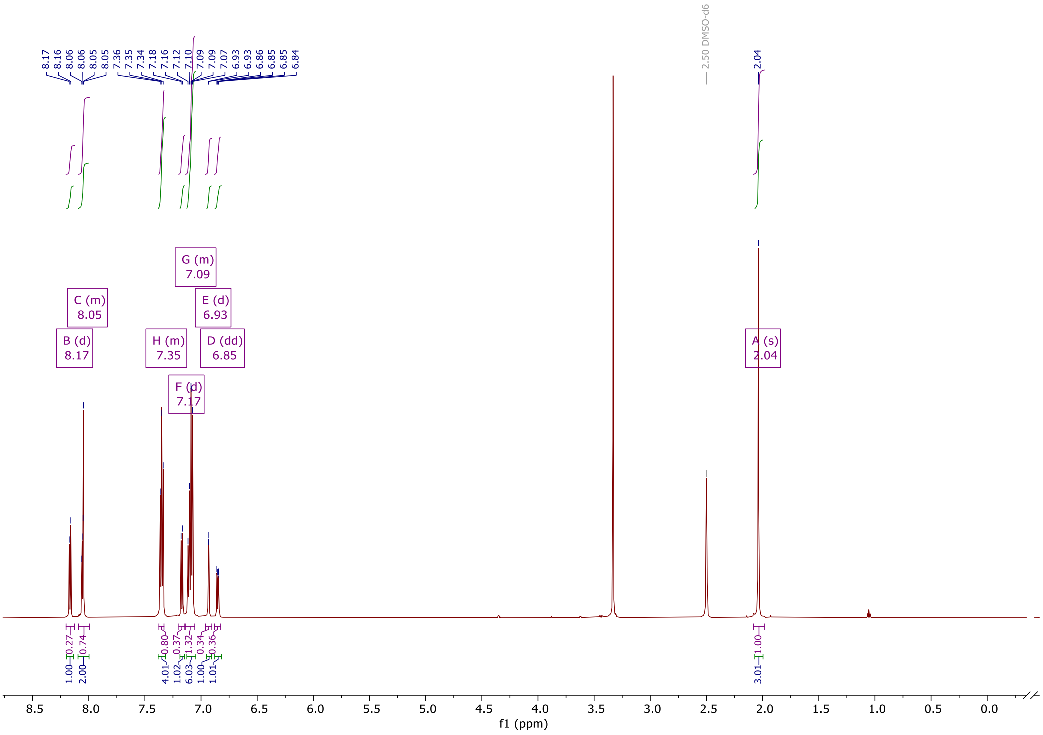

Figure S7.19. ^{1}H NMR spectrum of compound **5b** in DMSO-d$_6$ (T = 298 K, 600 MHz).

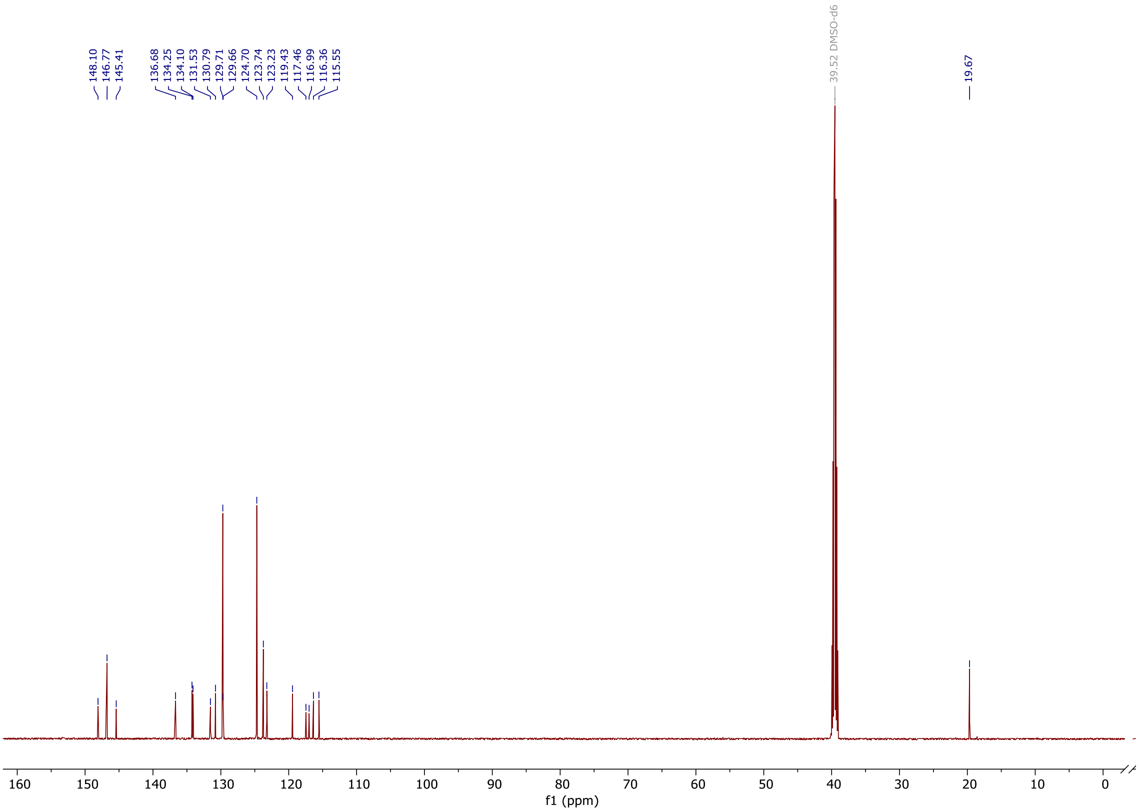

Figure S7.20. ^{13}C NMR spectrum of compound **5b** in DMSO-d$_6$ (T = 298 K, 150 MHz).

4'-(Diphenylamino)-2'-isopropyl-[1,1'-biphenyl]-2,5-dicarbonitrile (5c)

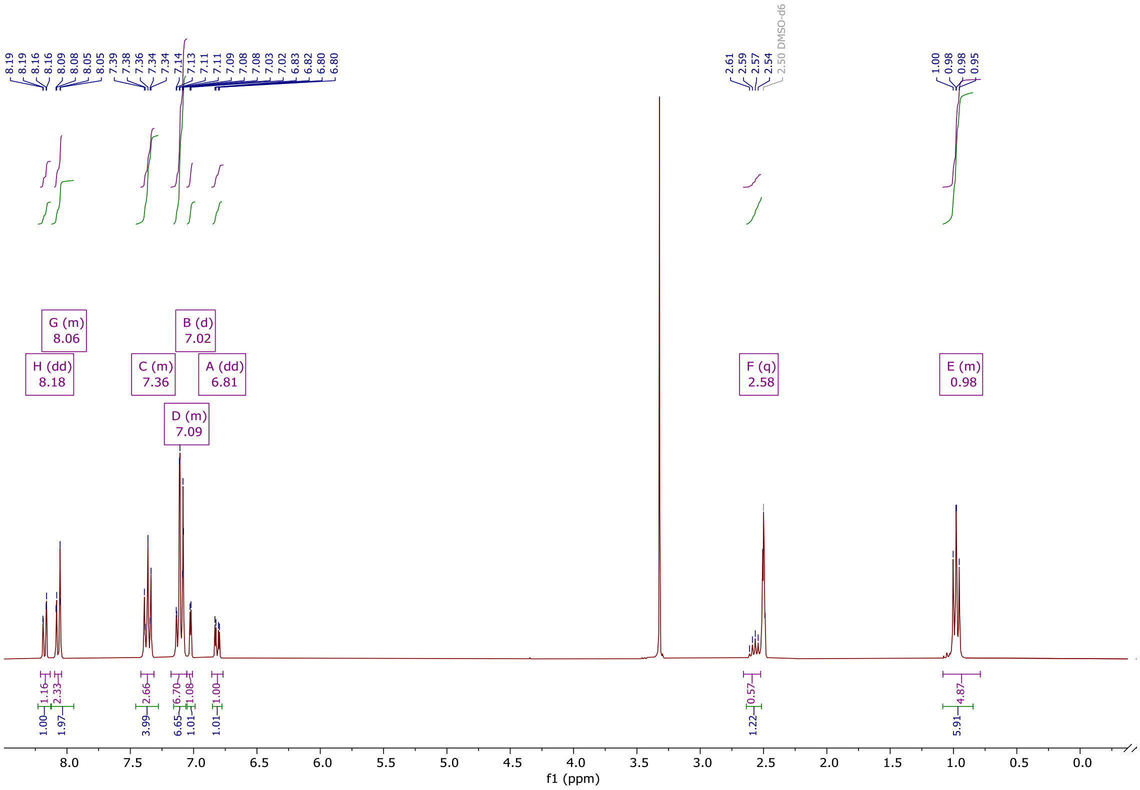

Figure S7.21. ^{1}H NMR spectrum of compound **5c** in DMSO-d$_6$ (T = 298 K, 600 MHz).

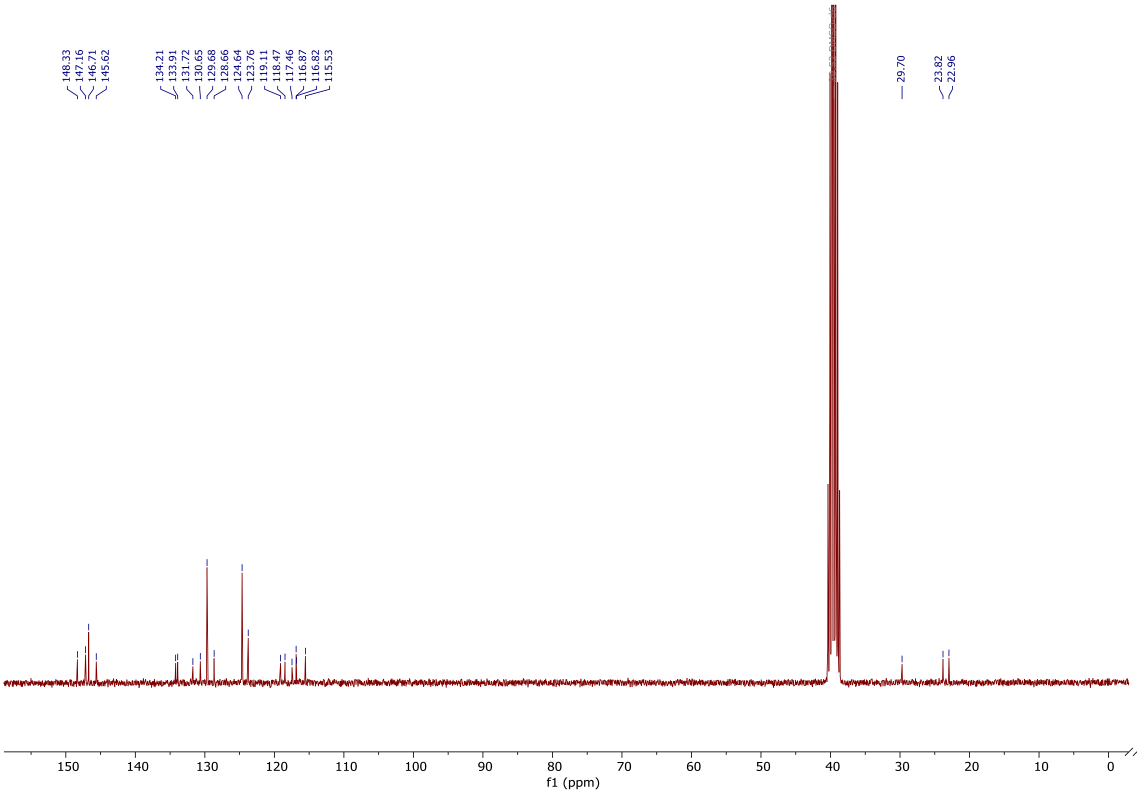

Figure S7.22. ^{13}C NMR spectrum of compound **5c** in DMSO-d$_6$ (T = 298 K, 150 MHz).

4'-(Diphenylamino)-2',6'-dimethyl-[1,1'-biphenyl]-2,5-dicarbonitrile (5d)

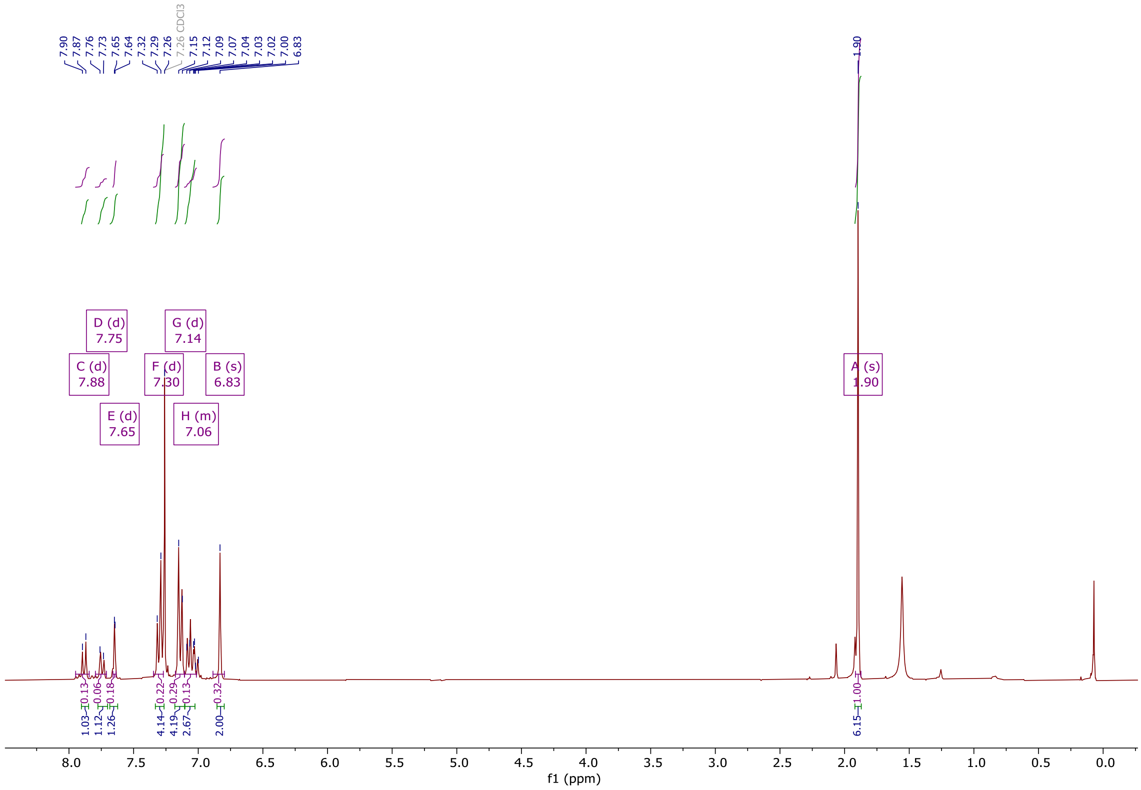

Figure S7.23. ^{1}H NMR spectrum of compound **5d** in DMSO-d$_6$ (T = 298 K, 600 MHz).

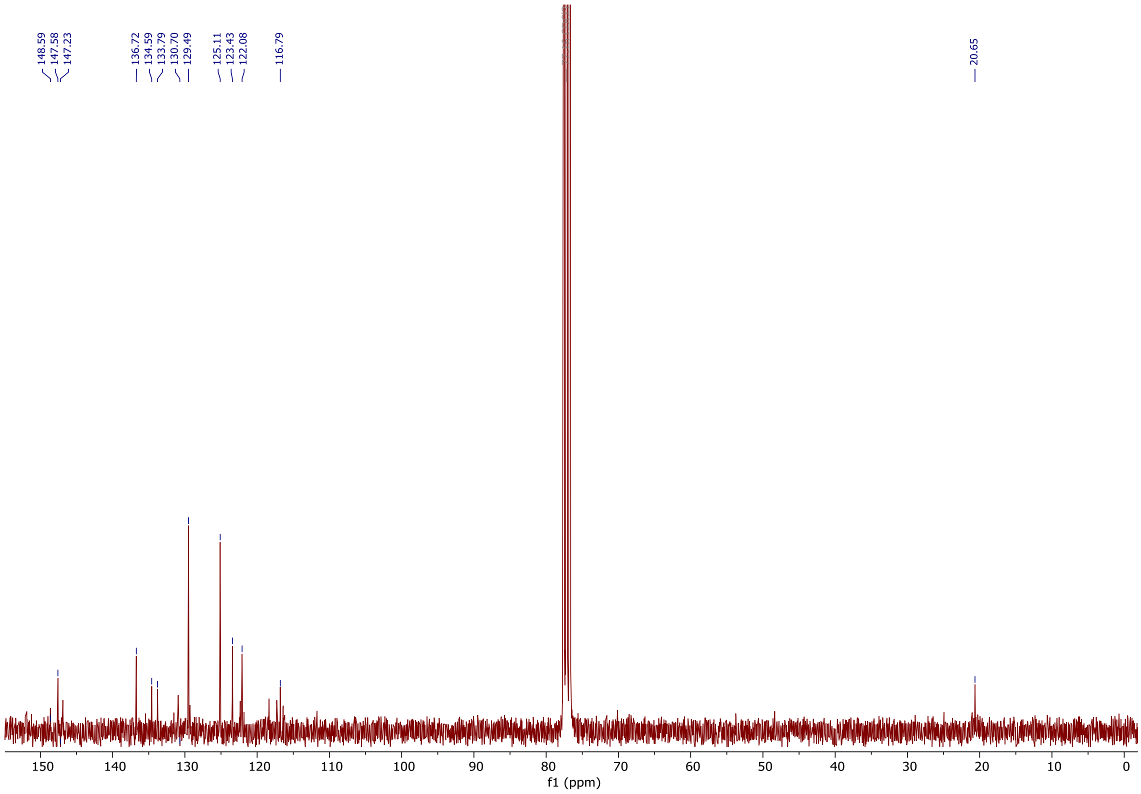

Figure S7.24. ^{13}C NMR spectrum of compound **5d** in DMSO-d$_6$ (T = 298 K, 150 MHz).

4'-(Bis(4-methoxyphenyl)amino)-2'-methyl-[1,1'-biphenyl]-2,5-dicarbonitrile (5e)

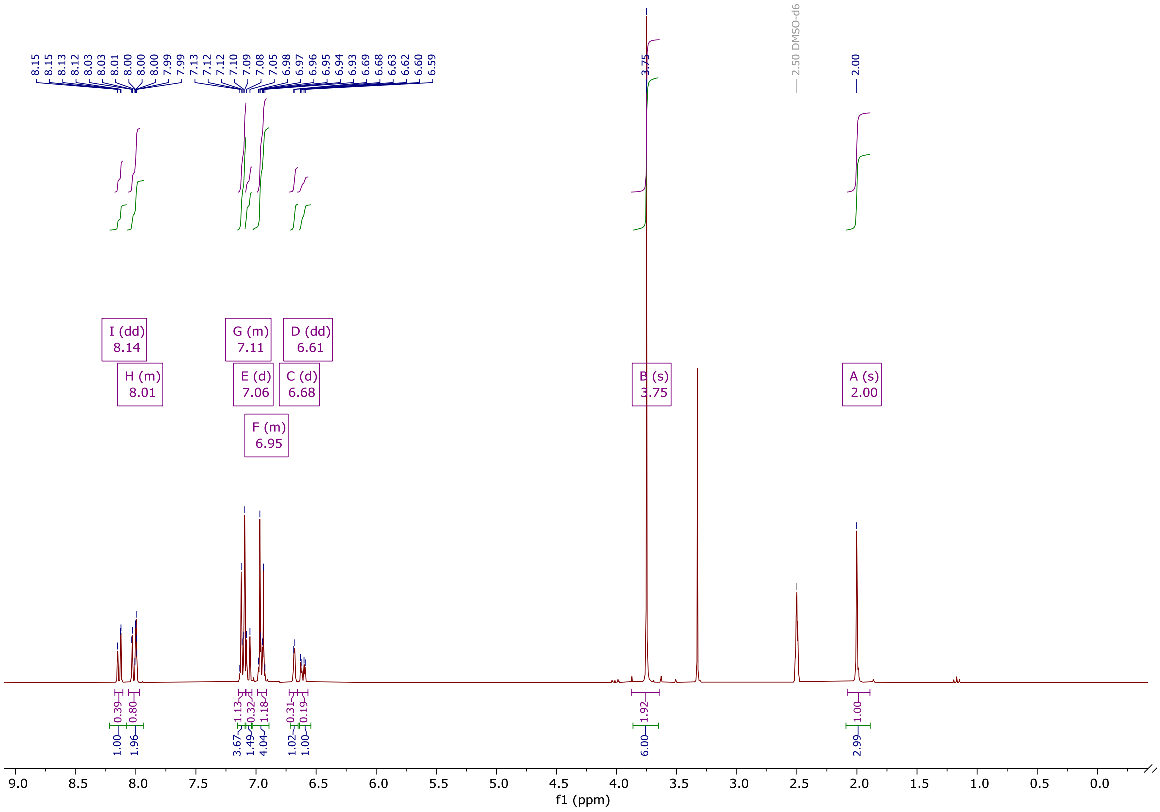

Figure S7.25. ^{1}H NMR spectrum of compound **5e** in DMSO-d$_6$ (T = 298 K, 600 MHz).

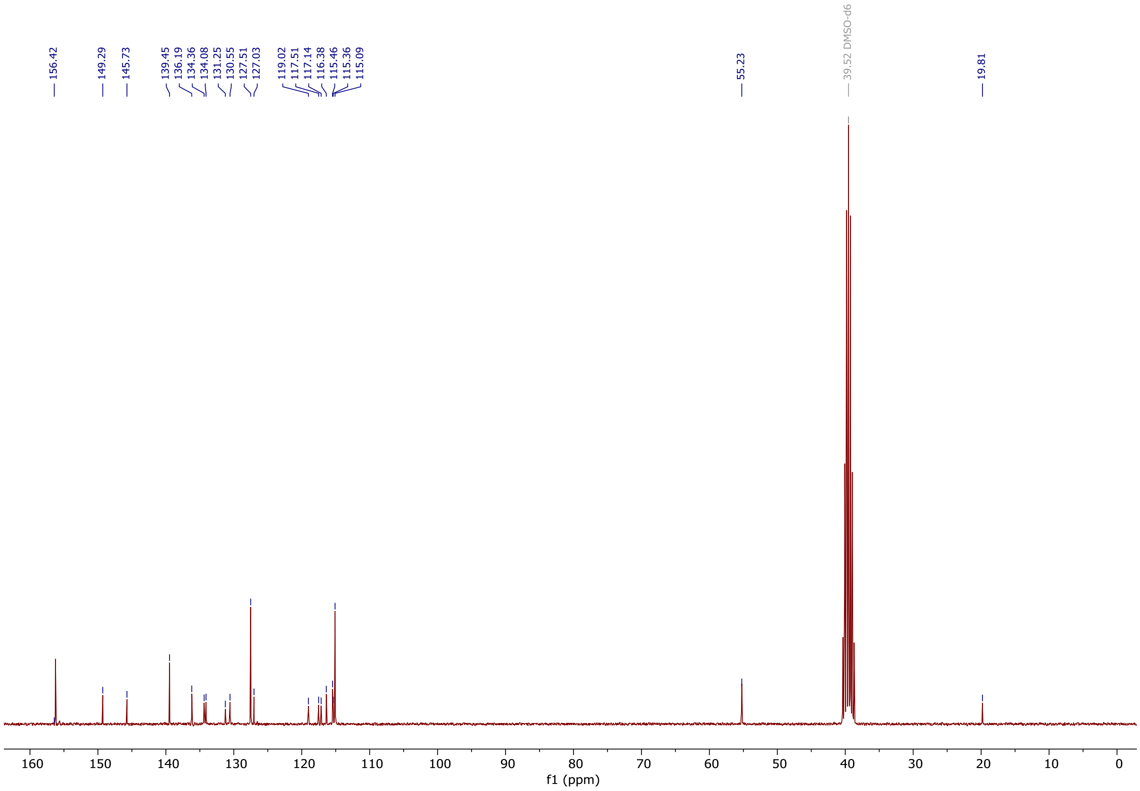

Figure S7.26. ^{13}C NMR spectrum of compound **5e** in DMSO-d$_6$ (T = 298 K, 150 MHz).

VT-NMR and determination of the activation barrier for isopropyl rotation

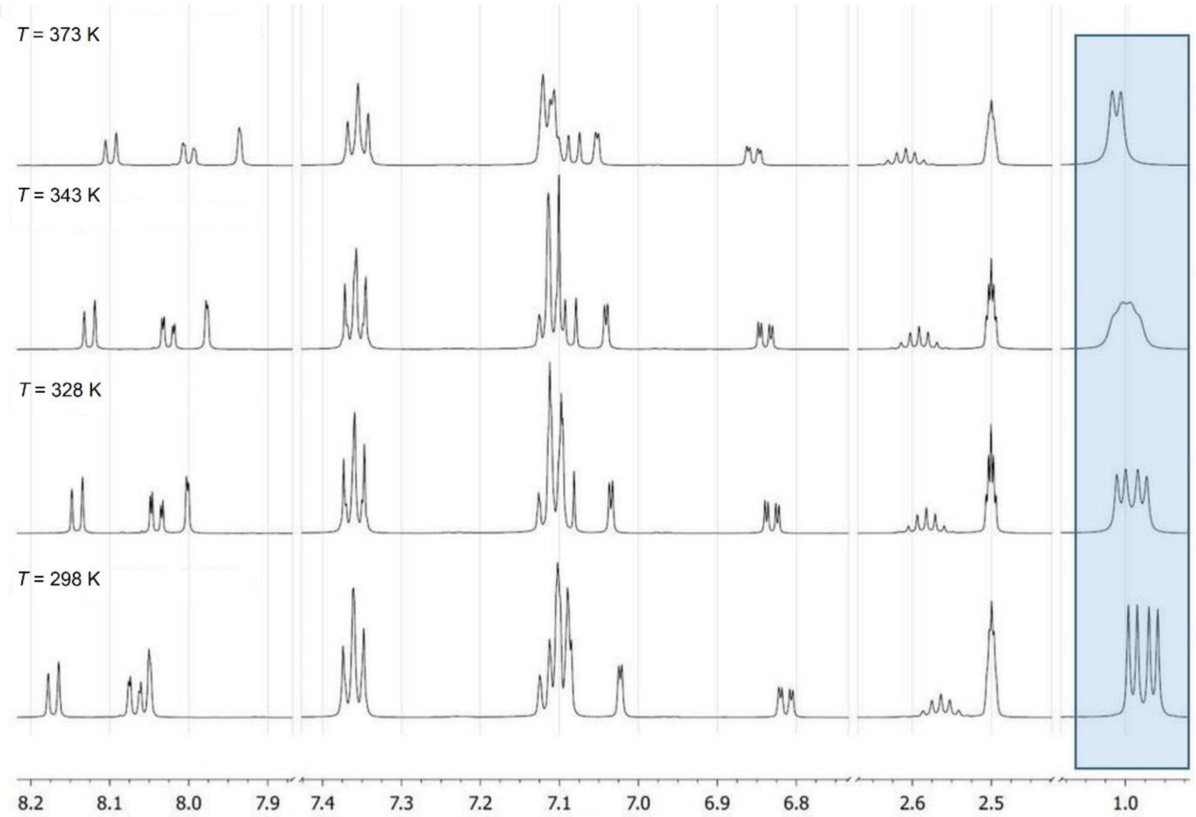

Figure S7.27. Sections of VT-^{1}H NMR spectra of compound **5c** at T = 298, 328, 343 and 373 K (DMSO-d^6, 600 MHz) with coalescence of the isopropyl methyl signals.

With the help of the coalescence temperature T_c and the difference of the chemical shifts of the signals of the respective methyl groups at measurements as far as possible below the coalescence temperature, the free activation enthalpy for the rotation around the corresponding bond can be estimated.[56] The process considered here is one with first-order kinetics A⇄B, with k as the rate constant. For the rate constant, Eyring states:

$$k = \frac{RT}{N_A \cdot h} \cdot e^{-\frac{\Delta G^{\neq}}{RT}} \qquad \text{Eq. S1}$$

At the coalescence point, k:

$$k_{T_c} = \frac{\pi}{\sqrt{2}} |\nu_A - \nu_B| \qquad \text{Eq. S2}$$

This relationship inserted into the Eyring equation gives the following relationship:

$$\frac{\pi}{\sqrt{2}} |\nu_A - \nu_B| = \frac{RT}{N_A \cdot h} \cdot e^{-\frac{\Delta G^{\neq}}{RT_c}} \text{ resp. } \Delta G^{\neq} = RT_c \cdot ln \frac{RT_c\sqrt{2}}{\pi \cdot N_A \cdot h |\nu_A - \nu_B|} \qquad \text{Eq. S3}$$

With the T_c in K and the absorption ν in Hz, the free activation enthalpy in kJ/mol is obtained. In summary, this results in:

$$\Delta G^{\neq} = 1.91 \cdot 10^{-2} \cdot T_c \cdot (9.97 + \log T_c - \log|\Delta\nu|) \qquad \text{Eq. S4}$$

Entering the values of the process at hand here, one obtains

$$\Delta G^{\neq} = 1.91 \cdot 10^{-2} \cdot 343.15\, K \cdot (9.97 + \log 343.15 - \log|16|) = 74\, \frac{kJ}{mol} \qquad \text{Eq. S5}$$

Thus, the estimated Gibbs free enthalpy of activation for the rotation of the isopropyl group is about 74 kJ/mol.

Crystallographic Data

The structures and interplanar dihedral angles of dyes **5b**, **5c**, **5d**, and **5e** were corroborated by X-ray crystal structure analyses (Figure S7.28, Figure S7.29, Figure S7.30, Figure S7.31, Table S7.1).

Compound **5b** crystallizes in the form of colourless needles in the monoclinic, non-centrosymmetric space group *C*2. All investigated crystals were found to be twinned. Finally, a crystal was used for data collection whose twin components are about the same size. The twin law is a 180° rotation about the following axes: reciprocal space: -0.530 -0.001 0.848 direct space: 0 0 1 in direct space (transformation matrix: 0.000 -0.001 1.000 1.000 -0.006 -1.238 0.000 -0.996 -0.001 0.000 -0.002 0.997. There are two crystallographically independent molecules in the asymmetric unit (Figure S7.28). The dihedral angle between the central phenyl ring and the phenyl ring of the benzodinitrile moiety is 55.1(2)° for molecule A and 54.7(2)° for molecule B. The dihedral angle of the C-N-C plane to the central phenyl ring is 24.6(3)° (molecule A) and 29.8(4)° (molecule B).

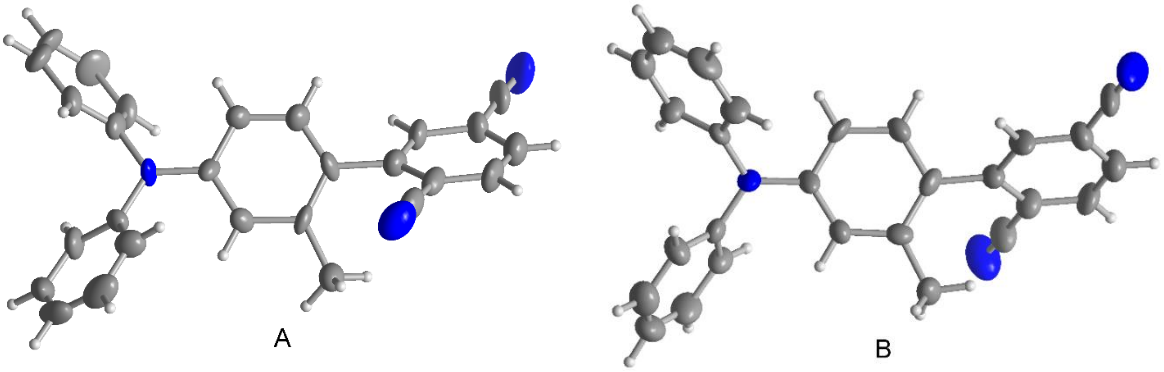

Figure S7.28. Molecular structure of the two symmetry-independent molecules (A and B) in the crystal of **5b** (50% thermal ellipsoids, H atoms with arbitrary radii).

Compound **5c** crystallizes as needles (monoclinic space group *Cc*). The asymmetric unit contains two symmetry independent molecules (A and B) (Figure S7.29). The dihedral angle between the central phenyl ring and the phenyl ring of the terephtalodinitrile unit is 69.51(7)° for molecule A and 68.3(2)° for molecule B. The geometry around the diphenyl-N atoms is nearly planar with angle sums of 359.9° (A) and 359.4° (B). The dihedral angle of the C-N-C plane to the central phenyl ring is 13.5(1)° (A) and 12.1 (B). Both conformers A and B are almost superimposable with only minor angle differences (Figure S7.32).

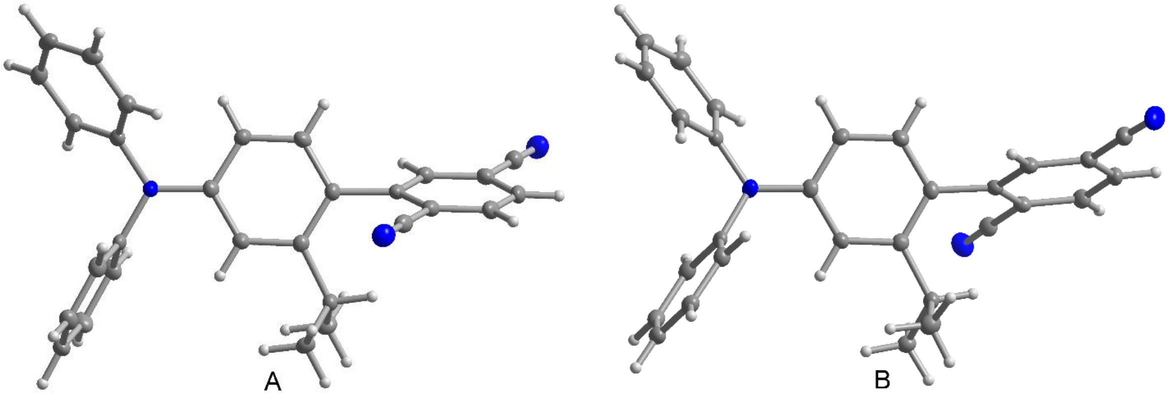

Figure S7.29. Molecular structures of the two symmetry-independent molecules (A and B) in the crystal of **5c** (50% thermal ellipsoids, H atoms with arbitrary radii).

Compound **5d** crystallizes as thin large platelets in the orthorhombic, centrosymmetric space group *Pbca*. The dihedral angle between the central aryl ring and the phenyl ring of the benzodinitrile moiety is 73.10(7)°. The geometry around the diphenyl-N atom is nearly planar (Figure S7.30). The dihedral angle of the C-N-C plane to the central phenyl ring is 58.77(16)°.

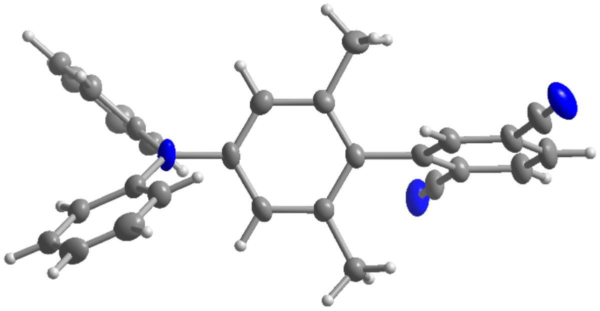

Figure S7.30. Molecular structure of **5d** (50% thermal ellipsoids, H atoms with arbitrary radii).

Compound **5e** crystallizes as needles (triclinic space group *P*-1). The dihedral angle between the central phenyl ring and the phenyl ring of the benzodinitrile unit is 58.2(1)°. The geometry around the dianisyl-N atom is nearly planar with an angle sum of 359.3° (Figure S7.31). The dihedral angle of the C-N-C (or C4-N1-C7) plane to the central phenyl ring is 21.1(1)°.

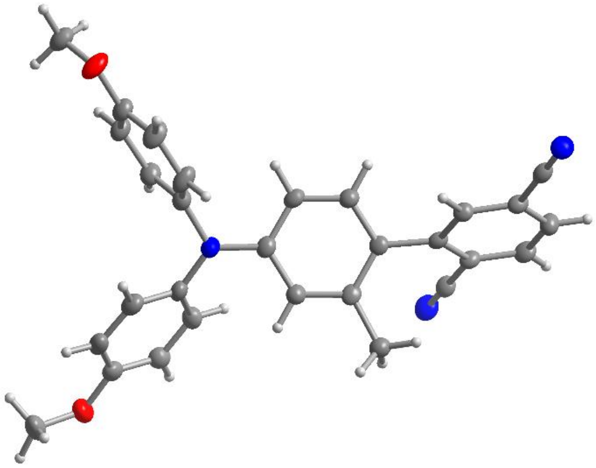

Figure S7.31. Molecular structure of **5e** (50% thermal ellipsoids, H atoms with arbitrary radii).

Table S7.1. Interplanar dihedral angles θ of the structures **5b-5e** extracted the crystal structure analyses.

	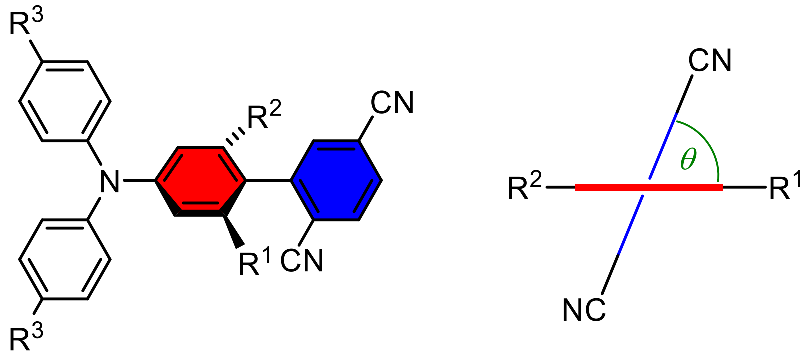			
structure	R^1	R^2	R^3	interplanar dihedral angle θ
5b	H	Me	H	55.1(2)°[a] / 54.7(2)°[b]
5c	H	iPr	H	69.51(7)°[a] / 68.3(2)°[b]
5d	Me	Me	H	73.10(7)°
5e	H	Me	OMe	58.2(1)°

[a] Molecule A. [b] Molecule B.

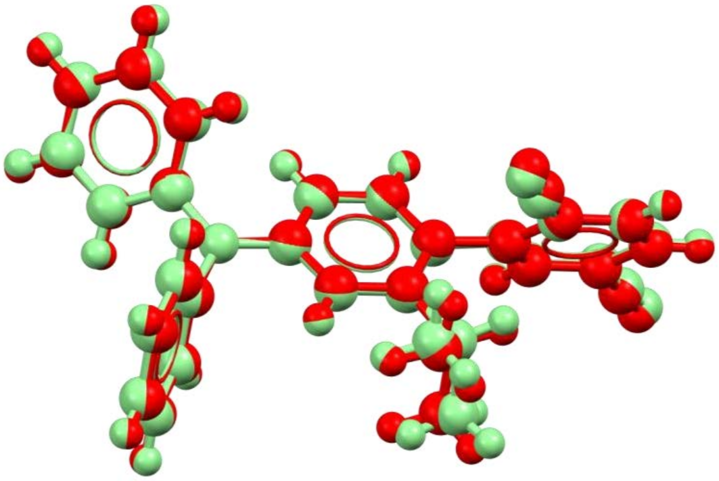

Figure S7.32. Overlay of the two symmetry-independent molecules A (green) and B (red) in **5c** prepared with the program Mercury.[57]

Spectroscopy

Absorption and Steady-State Fluorescence Emission Spectra

Absorption and fluorescence spectra were redrawn in wavenumber scale ($\tilde{\nu}$). The absorption spectra were corrected by dividing the extinction coefficient by the wavenumber: $\varepsilon(\tilde{\nu})/\tilde{\nu}$, and the fluorescence spectra by dividing the fluorescence intensity by $\tilde{\nu}^3$.[24] Subsequently, both the corrected absorption and fluorescence spectra were normalized to their respective maximum (Figure S7.33).

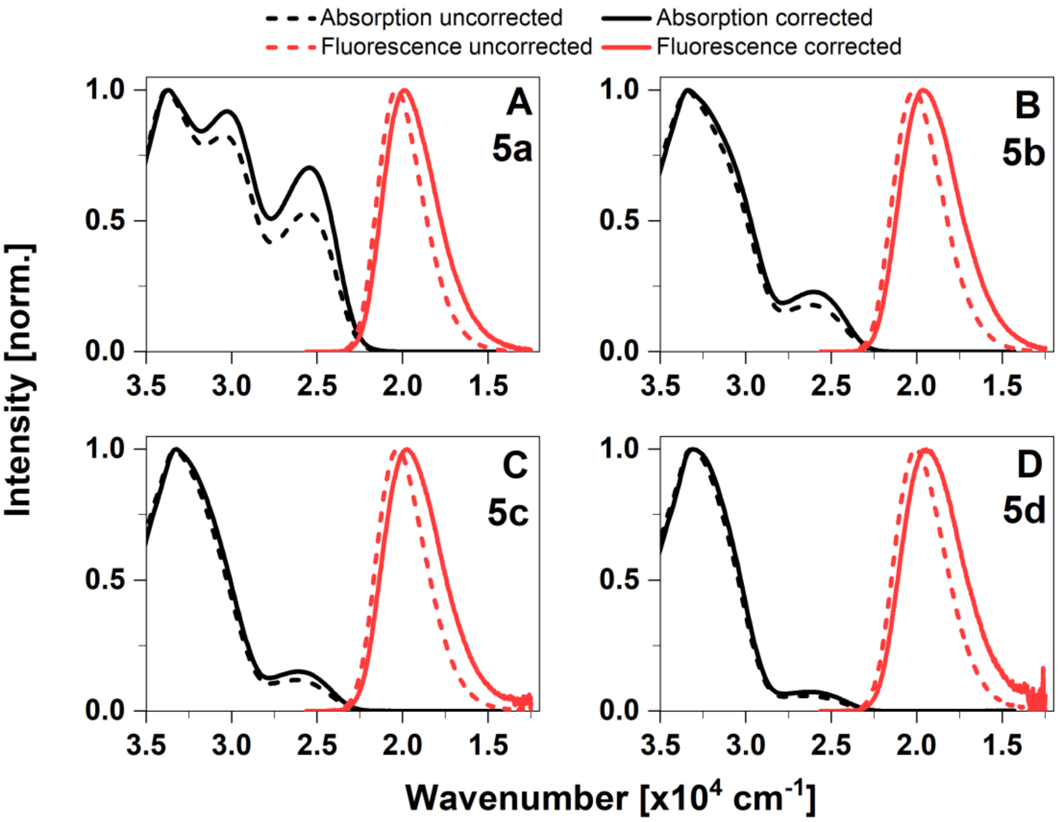

Figure S7.33. Absorption and fluorescence emission spectra of compounds **5a**-**5d** presented with and without corrections for comparison.

Lippert-Mataga analysis

Lippert-Mataga analysis is based on the Lippert-Mataga equation (eq. S6).[16,17]

$$\tilde{\upsilon}_A - \tilde{\upsilon}_F = \frac{2}{hc}\frac{(\mu_E - \mu_G)^2}{r^3} \cdot \Delta f + constant \qquad \text{Eq. S6}$$

In this equation, $\tilde{\nu}_A$ and $\tilde{\nu}_F$ represent the wavenumbers (cm^{-1}) of the absorption and emission, h is Planck's constant, c the speed of light, μ_G and μ_E indicate the dipole moments of the ground and excited states, and r corresponds to the radius of the cavity in which the fluorophore is situated.[19] The orientation polarizability is defined as:

$$\Delta f = \frac{\varepsilon - 1}{2\varepsilon + 1} - \frac{n^2 - 1}{2n^2 + 1} \qquad \text{Eq. S7}$$

where ε is the dielectric constant, and *n* is the refractive index of the solvent.

Table S7.2. The solvents employed in this study with their corresponding refractive indexes (*n*), dielectric constants (ε) and calculated orientation polarizabilities (Δ*f*).

Solvent	***n***	**ε**	**Δ*f***
Toluene	1.496	2.38	0.014
Methyl tert-butyl ether (MTBE)	1.369	2.60	0.074
Anisole	1.517	4.33	0.112
Chlorobenzene	1.525	5.62	0.143
Ethyl Acetate	1.372	6.08	0.201
THF	1.407	7.58	0.210
DCM	1.424	8.93	0.217
DMF	1.431	36.7	0.274
Acetonitrile	1.344	37.5	0.305

The radius of the molecule is determined in *PyMol* and by comparison with the time-resolved anisotropy data. However, it is clear that the assumed spherical shape of the molecules is not completely justified for compounds **5a**-**5e**.

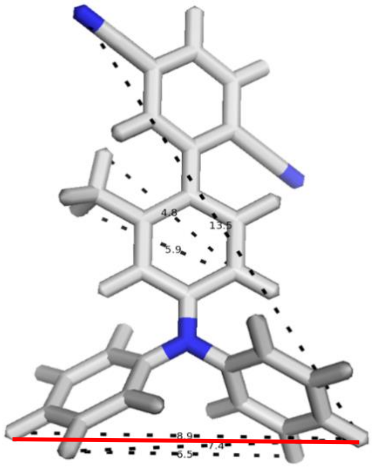

Figure S7.34. Compound **5b** was visualized in *PyMol*. A radius of 4.45 Å was used for calculations for compounds **5a**-**5d**, assuming rotational movement around the red-marked axis with a length of 8.9 Å. Similarly, a radius of 4.7 Å was estimated for compound **5e**.

An additional support for the estimation of molecule radius was obtained by time-resolved anisotropy. The molecule is assumed to be a spherical rotator with a radius (r). Anisotropy under pulsed excitation is described by the equation:

$$r(t) = r_0 e^{-t/\rho} \qquad \text{Eq. S8}$$

By fitting the experimental data (Figure S7.35), we determined a rotational correlation time ρ of 68 ps.

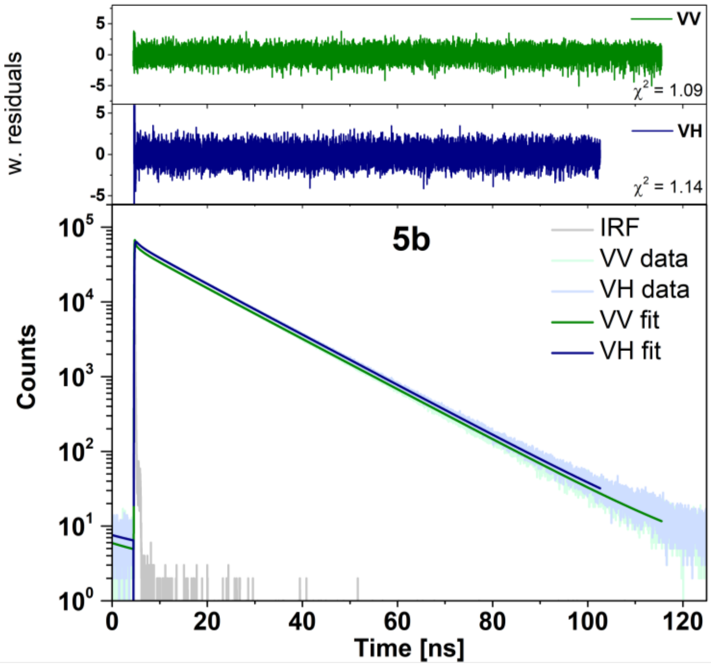

Figure S7.35. Time-resolved anisotropy measurement of **5b** in toluene.

Subsequently, the volume (V) is estimated (Eq. S9), and finally, the radius of the molecule (Eq. S10):

$$V = \frac{\rho k_B T}{\eta} \qquad \text{Eq. S9}$$

$$r = \sqrt[3]{\frac{3V}{4\pi}} = 4.8\ \text{Å} \qquad \text{Eq. S10}$$

where η is the viscosity, k_B the Boltzmann constant, and T is the temperature.

We determined the difference of the absorption and emission maxima in wavenumbers by measuring the respective spectra in toluene, methyl tert-butyl ether (tBuMeEther), anisole, chlorobenzene, ethyl acetate, tetrahydrofuran (THF), dichloromethane (DCM), dimethylformamide (DMF), and acetonitrile (MeCN).

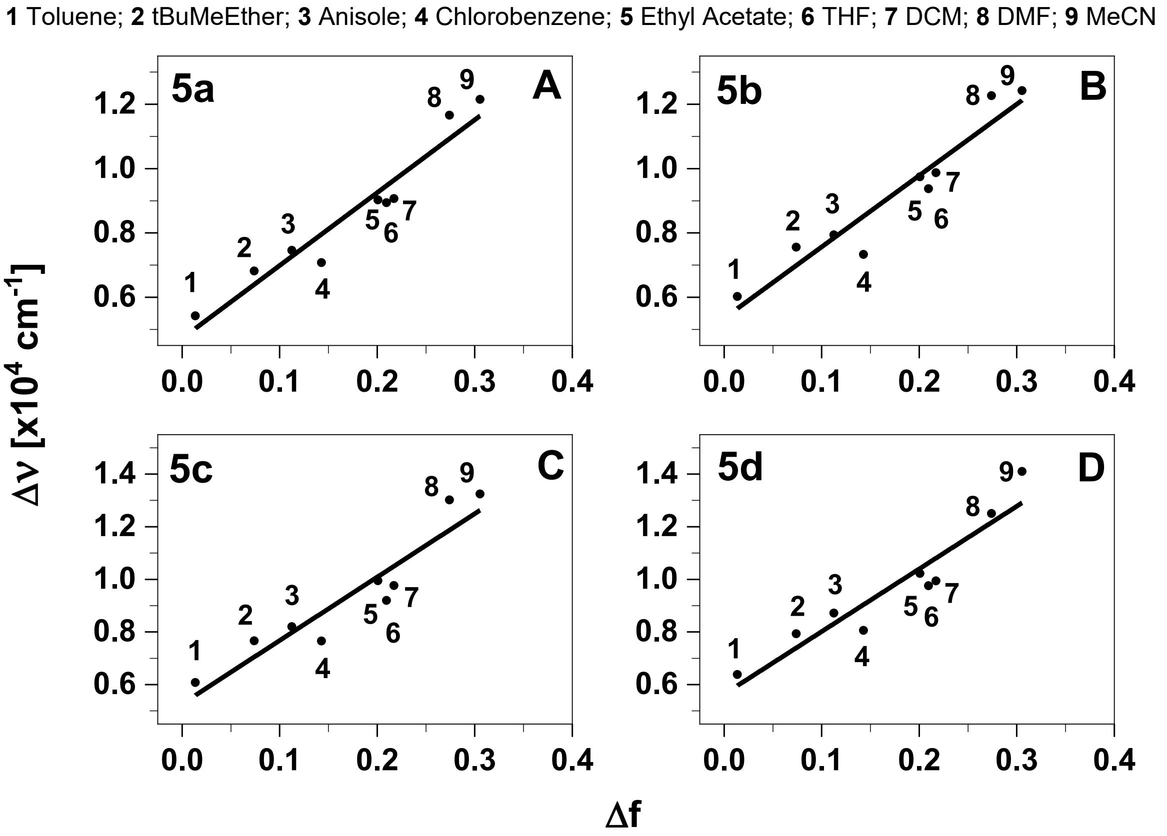

Figure S7.36. Lippert-Mataga plots for compounds **5a-5d** (**A-D**). The labels 1-9 corresponding to the used solvents are provided above the figure. A linear regression is applied, and the difference in dipole moments is extracted from the slope (Eq. S11, Table 7.1).

From the slope of the linear regression $\Delta\tilde{\nu}$ against Δf (Figure S7.36), we determined the difference between the dipole moments of the ground and excited states (Eq. S11). Results are given in Table 7.1 in the main text.

$$\mu_E - \mu_G = \sqrt{\frac{slope \cdot hc \cdot r^3}{2}} \qquad \text{Eq. S11}$$

Compound ***5e***

The fluorescence of **5e** is quenched in polar solvents such as DMF or acetonitrile. Thus, the difference in the dipole moments between the excited and ground states is obtained from the Lippert-Mataga plot which does not include these two points (Figure S7.37). The calculated difference between the dipole moments of the ground and excited states is given in Table 7.1.

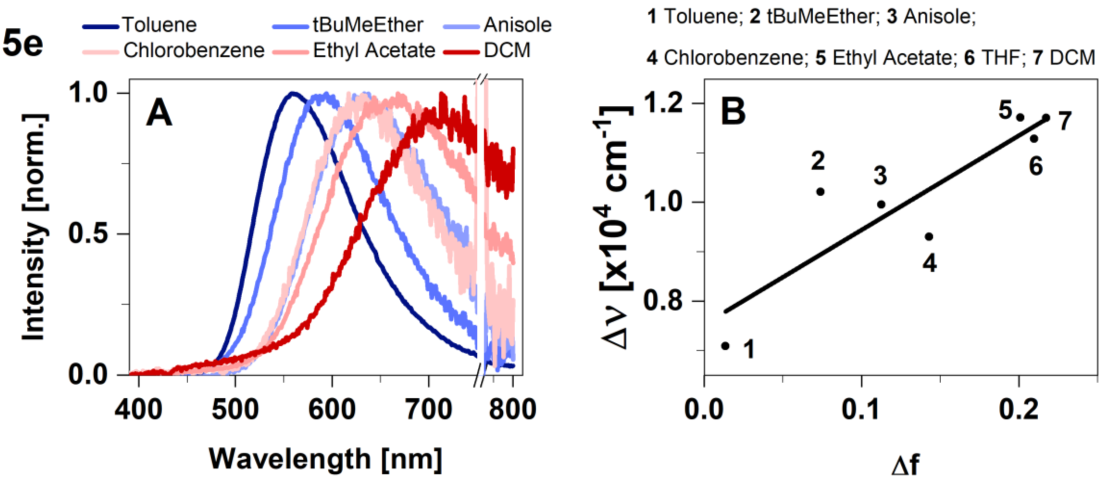

Figure S7.37. Compound **5e**: **A.** Fluorescence spectra in toluene, methyl tert-butyl ether (tBuMeEther), anisole, chlorobenzene, ethyl acetate, and dichloromethane (DCM). The excitation wavelength was 375 nm. The range between 750 and 770 nm is omitted due to the second-order diffraction. **B.** Lippert-Mataga plot.

Prompt Fluorescence

A bi-exponential fit function is applied to characterize the experimental TCSPC data. Each emissive species is presented with its fraction (x_i) and lifetime (τ_i). Species-averaged lifetime $\langle\tau\rangle_x$ (Eq. S12) and intensity-weighted lifetime $\langle\tau\rangle_F$ (Eq. S13) are given, as well as the reduced χ_r^2 value as a measure of the goodness of the fit.

$$\langle\tau\rangle_x = \sum_{i=1}^{2} x_i\tau_i \qquad \text{Eq. S12}$$

$$\langle\tau\rangle_F = \frac{\sum_{i=1}^{2} x_i\tau_i^2}{\sum_{i=1}^{2} x_i\tau_i} \qquad \text{Eq. S13}$$

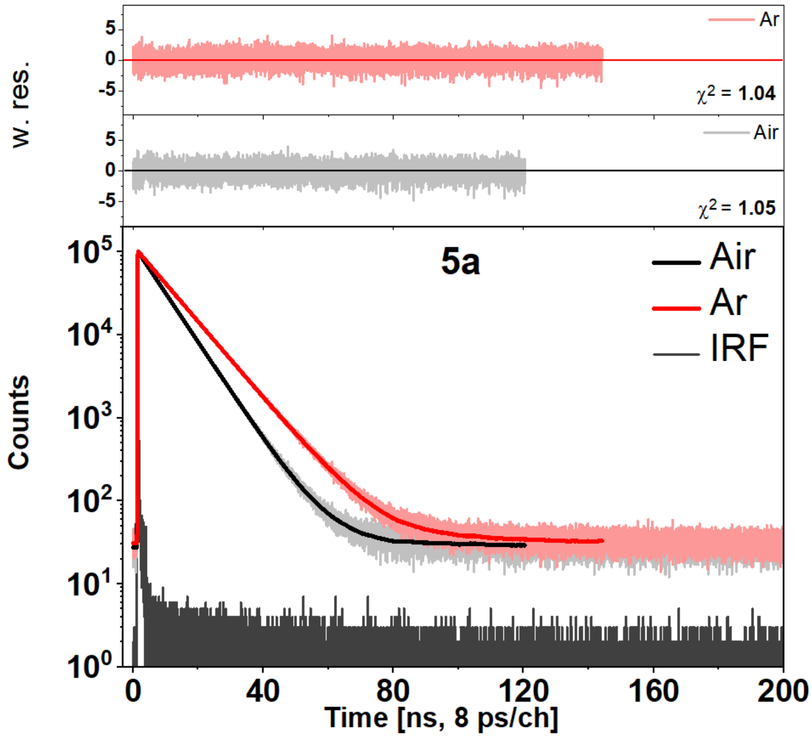

Figure S7.38. Prompt fluorescence of compound **5a** in air-saturated and nitrogen-purged solutions in toluene measured by TCSPC. Lifetime fit results with fixed lifetime fractions are shown in Table S7.3.

Table S7.3. Prompt fluorescence lifetime fit for compound **5a** with fixed lifetime fractions.

5a	**x_1**	**τ_1 [ns]**	**x_2**	**τ_2 [ns]**	**$\langle\tau\rangle_x$ [ns]**	**$\langle\tau\rangle_F$ [ns]**	**χ_r^2**
Air	0.96	7.37	0.04	0.76	7.09	7.34	1.05
Ar	0.96	9.44	0.04	0.17	9.06	9.44	1.04

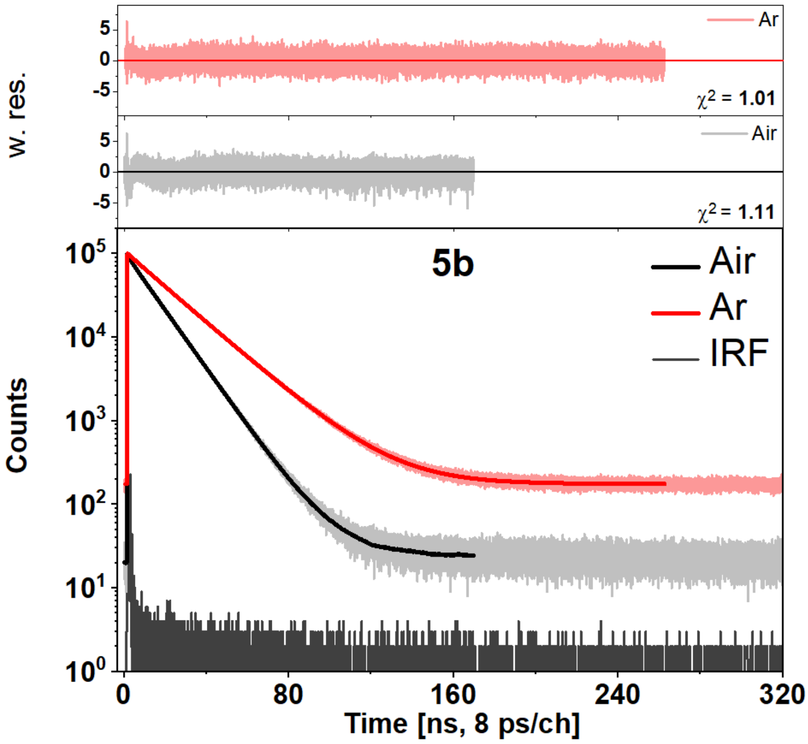

Figure S7.39. Prompt fluorescence of compound **5b** in air-saturated and nitrogen-purged solutions in toluene measured by TCSPC. Lifetime fit results with fixed lifetime fractions are shown in Table S7.4.

Table S7.4. Prompt fluorescence lifetime fit of compound **5b** with fixed lifetime fractions.

5b	**x_1**	**τ_1 [ns]**	**x_2**	**τ_2 [ns]**	**$\langle\tau\rangle_x$ [ns]**	**$\langle\tau\rangle_F$ [ns]**	**χ_r^2**
Air	0.89	12.46	0.11	1.50	11.22	12.29	1.11
Ar	0.89	20.91	0.11	14.83	20.23	20.41	1.01

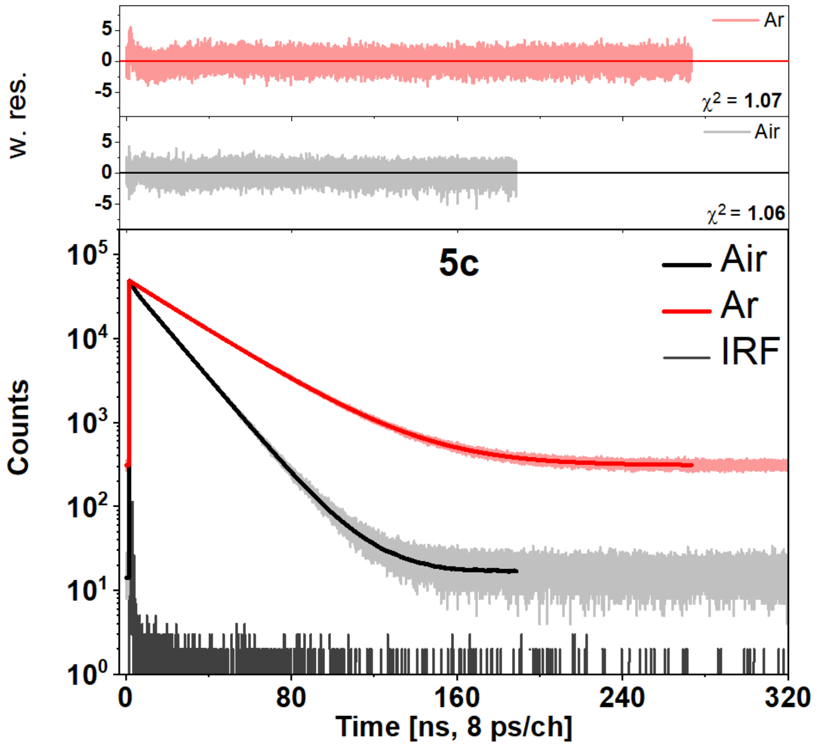

Figure S7.40. Prompt fluorescence of compound **5c** in air-saturated and nitrogen-purged solutions in toluene measured by TCSPC. Lifetime fit results with fixed lifetime fractions are shown in Table S7.5.

Table S7.5. Prompt fluorescence lifetime fit of compound **5c** with fixed lifetime fractions.

5c	**x_1**	**τ_1 [ns]**	**x_2**	**τ_2 [ns]**	**$\langle\tau\rangle_x$ [ns]**	**$\langle\tau\rangle_F$ [ns]**	**χ_r^2**
Air	0.85	14.96	0.15	1.66	13.01	14.71	1.06
Ar	0.85	29.40	0.15	21.09	28.18	28.49	1.07

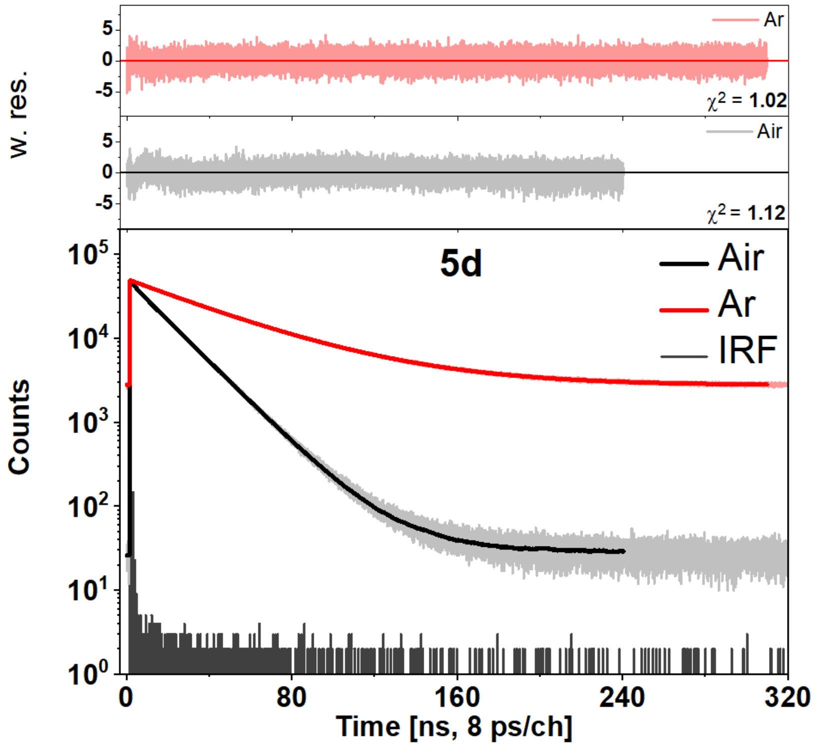

Figure S7.41. Prompt fluorescence of compound **5d** in air-saturated and nitrogen-purged solutions in toluene measured by TCSPC. Lifetime fit results with fixed lifetime fractions are shown in Table S7.6.

Table S7.6. Prompt fluorescence lifetime fit of compound **5d** with fixed lifetime fractions.

5d	**x_1**	**τ_1 [ns]**	**x_2**	**τ_2 [ns]**	**$\langle\tau\rangle_x$ [ns]**	**$\langle\tau\rangle_F$ [ns]**	**χ_r^2**
Air	0.90	17.74	0.10	2.22	16.20	17.53	1.12
Ar	0.90	47.64	0.10	30.74	45.96	46.52	1.02

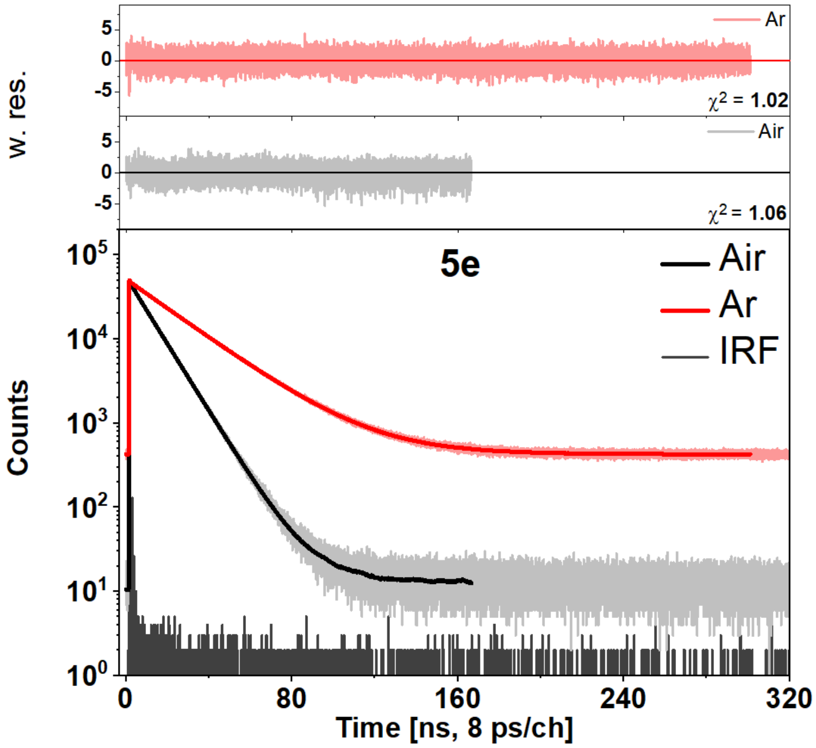

Figure S7.42. Prompt fluorescence of compound **5e** in air-saturated and nitrogen-purged solutions in toluene measured by TCSPC. Lifetime fit results with fixed lifetime fractions are shown in Table S7.7.

Table S7.7. Prompt fluorescence lifetime fit of compound **5e** with fixed lifetime fractions.

5e	**x_1**	**τ_1 [ns]**	**x_2**	**τ_2 [ns]**	**$\langle\tau\rangle_x$ [ns]**	**$\langle\tau\rangle_F$ [ns]**	**χ_r^2**
Air	0.91	10.87	0.09	0.95	9.94	10.78	1.06
Ar	0.91	24.60	0.09	0.39	22.34	24.56	1.02

Delayed Fluorescence: Data for Arrhenius analysis

Table S7.8. Data for the determination of the ΔE_{ST} energy gap by Arrhenius analysis for compound **5b**. The table contains the temperatures of the sensor and the sample (sensor T and sample T), the reciprocal sample temperature (Sample T^{-1}), the lifetime fit result of the measured delayed fluorescence lifetime (τ_{TADF}), and the natural logarithm of the delayed fluorescence rate constant [$\ln(k_{\mathrm{TADF}})$]. The delayed fluorescence rate constant is calculated as: $k_{\mathrm{TADF}} = 1/\tau_{\mathrm{TADF}}$. In the Arrhenius plots, $\ln(k_{\mathrm{TADF}})$ is plotted against the reciprocal of the sample temperature (see Figure 7.8 D).

Sensor T [K]	**Sample T [K]**	**Sample T^{-1} [$\cdot 10^{-3}$ K^{-1}]**	**τ_{TADF} [µs]**	**$\ln(k_{\mathrm{TADF}})$**
200.0	202.7	4.9	6661.1	5.0
206.9	209.5	4.8	5485.7	5.2
214.3	216.8	4.6	4537.1	5.4
222.2	224.6	4.5	3782.7	5.6
230.8	233.1	4.3	3124.6	5.8
240.0	242.2	4.1	2617.4	5.9
250.0	251.9	4.0	2203.2	6.1
260.9	262.6	3.8	1856.6	6.3
272.7	274.4	3.6	1562.4	6.5
285.7	287.3	3.5	1309.0	6.6
300.0	300.4	3.3	**1076.0**	6.8
272.7	274.3	3.6	1559.3	6.5
250.0	251.7	4.0	2220.2	6.1
230.8	232.6	4.3	3232.1	5.7
214.3	216.3	4.6	4741.3	5.4
200.0	202.1	4.9	7096.9	4.9
193.5	195.7	5.1	8849.0	4.7
187.5	190.0	5.3	11112.3	4.5
181.8	184.4	5.4	13552.5	4.3

Table S7.9. Data for the determination of the ΔE_{ST} energy gap by Arrhenius analysis for compound **5c**. The table contains the temperatures of the sensor and the sample (sensor T and sample T), the reciprocal sample temperature (Sample T^{-1}), the lifetime fit result of the measured delayed fluorescence lifetime (τ_{TADF}), and the natural logarithm of the delayed fluorescence rate constant [$\ln(k_{TADF})$]. The delayed fluorescence rate constant is calculated as: $k_{TADF} = 1/\tau_{TADF}$. In the Arrhenius plots, $\ln(k_{TADF})$ is plotted against the reciprocal of the sample temperature (see Figure 7.8 E).

Sensor T [K]	**Sample T [K]**	**Sample T^{-1} [$\cdot 10^{-3}$ K^{-1}]**	**τ_{TADF} [µs]**	**$\ln(k_{TADF})$**
200.0	202.2	4.9	1370.9	6.6
206.9	209	4.8	1193.1	6.7
214.3	216.3	4.6	1029.1	6.9
222.2	224.1	4.5	888.0	7.0
230.8	232.6	4.3	782.5	7.2
240.0	241.7	4.1	690.6	7.3
250.0	251.6	4.0	601.5	7.4
260.9	262.5	3.8	530.6	7.5
272.7	274.2	3.6	462.0	7.7
285.7	287.2	3.5	402.0	7.8
300.0	301.4	3.3	**354.0**	7.9
300.0	301.4	3.3	**357.7**	7.9
293.0	294.7	3.4	386.8	7.9
272.7	274.5	3.6	477.3	7.6
250.0	252	4.0	622.7	7.4
230.8	233.1	4.3	800.7	7.1
214.3	216.6	4.6	1057.4	6.9
200.0	202.6	4.9	1430.5	6.5
193.5	196.1	5.1	1681.6	6.4
187.5	190.3	5.3	1967.7	6.2
181.8	184.7	5.4	2285.1	6.1

Table S7.10. Data for the determination of the ΔE_{ST} energy gap by Arrhenius analysis for compound **5d**. The table contains the temperatures of the sensor and the sample (sensor T and sample T), the reciprocal sample temperature (Sample T^{-1}), the lifetime fit result of the measured delayed fluorescence lifetime (τ_{TADF}), and the natural logarithm of the delayed fluorescence rate constant [ln(k_{TADF})]. The delayed fluorescence rate constant is calculated as: $k_{TADF} = 1/\tau_{TADF}$. In the Arrhenius plots, ln(k_{TADF}) is plotted against the reciprocal of the sample temperature (see Figure 7.8 F).

Sensor T [K]	**Sample T [K]**	**Sample T^{-1} [$\cdot 10^{-3}$ K^{-1}]**	**τ_{TADF} [µs]**	**ln(k_{TADF})**
200.0	202.7	4.9	28.5	10.5
206.9	209.5	4.8	27.4	10.5
214.3	216.7	4.6	26.4	10.5
222.2	224.5	4.5	25.4	10.6
230.8	233.1	4.3	24.4	10.6
240.0	242.1	4.1	23.5	10.7
250.0	251.9	4.0	22.5	10.7
260.9	262.5	3.8	21.6	10.7
272.7	274.3	3.6	20.6	10.8
285.7	287.2	3.5	19.5	10.8
300.0	301.5	3.3	**18.4**	10.9
272.7	274.3	3.6	20.6	10.8
250.0	251.7	4.0	22.6	10.7
230.8	232.7	4.3	24.4	10.6
214.3	216.3	4.6	26.4	10.5
200.0	202.2	4.9	28.6	10.5
193.5	195.8	5.1	29.7	10.4
187.5	190.0	5.3	31.7	10.4
181.8	184.3	5.4	33.5	10.3

Table S7.11. Data for the determination of the ΔE_{ST} energy gap by Arrhenius analysis for compound **5e**. The table contains the temperatures of the sensor and the sample (sensor T and sample T), the reciprocal sample temperature (Sample T^{-1}), the lifetime fit result of the measured delayed fluorescence lifetime (τ_{TADF}), and the natural logarithm of the delayed fluorescence rate constant [$\ln(k_{TADF})$]. The delayed fluorescence rate constant is calculated as: $k_{TADF} = 1/\tau_{TADF}$. In the Arrhenius plots, $\ln(k_{TADF})$ is plotted against the reciprocal of the sample temperature (see Figure 7.12 B).

Sensor T [K]	**Sample T [K]**	**Sample T^{-1} [$\cdot 10^{-3}$ K^{-1}]**	**τ_{TADF} [µs]**	**$\ln(k_{TADF})$**
200.0	202.7	4.9	68.1	9.6
206.9	209.5	4.8	62.2	9.7
214.3	216.8	4.6	58.6	9.7
222.2	224.6	4.5	55.0	9.8
230.8	233.1	4.3	51.6	9.9
240.0	242.2	4.1	48.6	9.9
250.0	252	4.0	45.7	10.0
260.9	262.6	3.8	42.9	10.1
272.7	274.4	3.6	40.3	10.1
285.7	287.5	3.5	37.8	10.2
293.0	294.7	3.4	36.6	10.2
300.0	301.7	3.3	**35.6**	10.2
272.7	274.5	3.6	40.2	10.1
250.0	251.9	4.0	45.8	10.0
230.8	232.8	4.3	51.7	9.9
214.3	216.4	4.6	58.1	9.8
200.0	202.3	4.9	65.8	9.6
193.5	195.9	5.1	73.3	9.5
187.5	190.1	5.3	75.5	9.5
181.8	184.6	5.4	82.8	9.4

7.1.5 References

---

[1] a) Y.-Z. Shi, H. Wu, K. Wang, J. Yu, X.-M. Ou, X.-H. Zhang, *Chem. Sci.* **2022**, *13*, 3625-3651.

b) X.-K. Chen, D. Kim, J.-L. Brédas, *Acc. Chem. Res.* **2018**, *51*, 2215-2224.

c) C. Adachi, *Jpn. J. Appl. Phys.* **2014**, *53*, 060101.

[2] F. Fang, L. Zhu, M. Li, Y. Song, M. Sun, D. Zhao, J. Zhang, *Adv. Sci.* **2021**, 8, 2102970.

[3] M. A. Brydena, E. Zysman-Colman, *Chem. Soc. Rev.* **2021**, *50*, 7587-7680.

[4] S.-J. Zou, Y. Shen, F.-M. Xie, J.-D. Chen, Y.-Q. Li, J.-X. Tang, *Mater. Chem. Front.* **2020**, *4*, 788-820.

[5] J. Bauri, R. B. Choudhary, G. Mandal, *J. Mater. Sci.* **2021**, *56*, 18837-18866.

[6] M. Zheng, Y. Li, Y. Wei, L. Chen, X. Zhou, S. Liu, *J. Phys. Chem. Lett.* **2022**, *13*, 2507-2515.

[7] Paras, Angat Dhiman, C. N. Ramachandran, *Chem. Phys. Lett.* **2022**, *801*, 139711.

[8] P. Stachelek, J. S. Ward, P. L. dos Santos, A. Danos, M. Colella, N. Haase, S. J. Raynes, A. S. Batsanov, M. R. Bryce, A. P. Monkman, *ACS Appl. Mater. Interfaces* **2019**, *11*, 27125-27133.

[9] G. A. Sommer, L. N. Mataranga-Popa, R. Czerwieniec, T. Hofbeck, H. H. H. Homeier, T. J. J. Müller, H. Yersin, *J. Phys. Chem. Lett.* ***2018**, 9*, 3692-3697.

[10] W. Haselbach, J. M. Kaminski, L. N. Kloeters, T. J. J. Müller, O. Weingart, C. M. Marian, P. Gilch, B. E. Nogueira de Faria, *Chem. Eur. J.* **2023**, *29*, e202202809.

[11] C. Sambiagio, S. P. Marsden, A. J. Blacker, P. C. McGowan, *Chem. Soc. Rev.* **2014**, *43*, 3525-3550.

[12] A. W. Franz, T. J. J. Müller, *Synthesis* **2008**, *7*, 1121-1125.

---

[13] M. S. Sundar, G. Singh, R. S. Ampapathi, A. V. Bedekar, *J. Mol. Struct.* **2017**, *1147*, 495-501.

[14] E. Rochlin, Z. Rappoport, *J. Org. Chem.* **1994**, *59*, 3857-3870.

[15] J. Sandström, *Dynamic NMR Spectroscopy*, Academic Press, London, **1982**.

[16] E. Lippert, *Z. Electrochem.* **1957**, *61*, 962–975.

[17] N. Mataga, Y. Kaifu, M. Koizumi, *Bull. Chem. Soc. Jpn.* **1956**, *29*, 465-470.

[18] M. Fischer, J. Georges, *Chem. Phys. Lett.* **1996**, *260*, 115-118.

[19] J. R. Lakowicz, *Principles of Fluorescence Spectroscopy*, 3rd edition, Springer, **2006**.

[20] F. B. Dias, T. J. Penfold, A. P. Monkman, *Methods Appl. Fluoresc.* **2017**, *5*, 012001.

[21] S. J. Strickler, R. A. Berg, *J. Chem Phys.* **1962**, *37*, 814-822.

[22] A. Reiffers, C. Torres Ziegenbein, A. Engelhardt, R. Kühnemuth, P. Gilch, C. Czekelius, *Photochem. Photobiol.* **2018**, *94*, 667-676.

[23] Y. Yoneda, H. Sotome, R. Mathew, Y. A. Lakshmanna, H. Miyasaka, *J. Phys. Chem.* A **2020**, *124*, 265–271.

[24] W. W. Parson, *Modern optical spectroscopy*, Vol. 2, Springer, **2007**.

[25] W. R. Ware, *J. Phys. Chem.* **1962**, *66*, 455–458.

[26] M. Montalti, A. Credi, L. Prodi, M. T. Gandolfi, *Handbook of Photochemistry*, 3rd edition, Taylor & Francis Group, CRC Press, **2006**.

[27] A. Schumpe, P. Lühring, *J. Chem. Eng. Data* **1990**, *35*, 24-25.

[28] P. Klán, J. Wirz, *Photochemistry of organic compounds: from concepts to practice*, Wiley-Blackwell, **2009**.

[29] H. Kautsky, *Trans. Faraday Soc.* **1939**, *35*, 216-219.

[30] N. J. Turro, *Modern Molecular Photochemistry*, University Science Books, **1991**.

[31] a) P. Gilch, *Kinetics of TADF*, seminar of the research training group ModISC, Heinrich-Heine-Universität Düsseldorf, **2021**.

b) Y. Tsuchiya, S. Diesing, F. Bencheikh, Y. Wada, P. L. dos Santos, H. Kaji, E. Zysman-Colman, I. D. W. Samuel, C. Adachi, *J. Phys. Chem.* A **2021**, *125*, 8074-8089.

c) R. Hamze, S. Shi, S. C. Kapper, D. S. Muthiah Ravinson, L. Estergreen, M.-C. Jung, A. C. Tadle, R. Haiges, P. I. Djurovich, J. L. Peltier, R. Jazzar, G. Bertrand, S. E. Bradforth, M. E. Thompson, *J. Am. Chem. Soc.* **2019**, *141*, 8616–8626.

[32] P. F. Jones, A. R. Calloway, *Chem. Phys. Lett.* **1971**, *10*, 438–443.

[33] J. P. Götze, B. Karasulu, W. Thiel, *J. Chem. Phys.* **2013**, *139*, 234108.

[34] M. Caricato, B. Mennucci, J. Tomasi, F. Ingrosso, R. Cammi, S. Corni, G. Scalmani, *J. Chem. Phys.* **2006**, *124*, 124520.

[35] J. F ller, C. M. Marian, *J. Phys. Chem. Lett.* **2017**, *8*, 5643-5647.

[36] T. Froitzheim, S. Grimme, J. M. Mewes, *J. Chem. Theory Comput.* **2022**, *18*, 7702-7713.

[37] a) J.-D. Chai, M. Head-Gordon, *J. Chem. Phys.* **2008**, *128*, 084106.

b) J.-D. Chai, M. Head-Gordon, *Phys. Chem. Chem. Phys.* **2008**, *10*, 6615-6620.

[38] T. J. Penfold, E. Gindensperger, C. Daniel, C. M. Marian, *Chem. Rev.* **2018**, *118*, 6975 – 7025.

[39] a) J. M. Kaminski, A. Rodríguez-Serrano, F. Dinkelbach, H. Miranda-Salinas, A. P. Monkman, C. M. Marian, *Chem. Sci.* **2022**, *13*, 7057-7066.

b) H. Miranda-Salinas, A. Rodriguez-Serrano, J. M. Kaminski, F. Dinkelbach, N. Hiromichi, Y. Kusakabe, H. Kaji, C. M. Marian, A. P. Monkman, *J. Phys. Chem. C* **2023**, *127*, 8607-8617.

[40] a) R. Dhali, D. K. A. P. Huu, F. Bertocchi, C. Sissa, F. Terenziani, A. Painelli, *Phys. Chem. Chem. Phys.* **2021**, *23*, 378-387.

b) K. Stavrou, L. G. Franca, T. Böhmer, L. M. Duben, C. M. Marian, A. P. Monkman, *Adv. Func. Mat.* **2023**, *33*, 2300910.

---

[41] J. Eng, T. J. Penfold, *Chem. Rec.* **2020**, *20*, 831-856.

[42] S. Thompson, J. Eng, T. J. Penfold, *J. Chem. Phys.* **2018**, *149*, 014304.

[43] a) J. Cerezo, F. Santoro, *J. Comp. Chem.* **2023**, *44*, 626-643.

b) F. J. A. Ferrer, F. Santoro, *Phys. Chem. Chem. Phys.* **2012**, *14*, 13549-13563.

[44] R. Englman, J. Jortner, *Mol. Phys.* **1970**, *18*, 145-164.

[45] Gaussian 16, Revision A.03, M. J. Frisch, G. W. Trucks, H. B. Schlegel, G. E. Scuseria, M. A. Robb, J. R. Cheeseman, G. Scalmani, V. Barone, G. A. Petersson, H. Nakatsuji, X. Li, M. Caricato, A. V. Marenich, J. Bloino, B. G. Janesko, R. Gomperts, B. Mennucci, H. P. Hratchian, J. V. Ortiz, A. F. Izmaylov, J. L. Sonnenberg, D. Williams-Young, F. Ding, F. Lipparini, F. Egidi, J. Goings, B. Peng, A. Petrone, T. Henderson, D. Ranasinghe, V. G. Zakrzewski, J. Gao, N. Rega, G. Zheng, W. Liang, M. Hada, M. Ehara, K. Toyota, R. Fukuda, J. Hasegawa, M. Ishida, T. Nakajima, Y. Honda, O. Kitao, H. Nakai, T. Vreven, K. Throssell, J. A. Montgomery, Jr., J. E. Peralta, F. Ogliaro, M. J. Bearpark, J. J. Heyd, E. N. Brothers, K. N. Kudin, V. N. Staroverov, T. A. Keith, R. Kobayashi, J. Normand, K. Raghavachari, A. P. Rendell, J. C. Burant, S. S. Iyengar, J. Tomasi, M. Cossi, J. M. Millam, M. Klene, C. Adamo, R. Cammi, J. W. Ochterski, R. L. Martin, K. Morokuma, O. Farkas, J. B. Foresman, D. J. Fox, Gaussian, Inc., Wallingford CT, **2016**.

[46] a) A. Schäfer, H. Horn, R. Ahlrichs, *J. Chem. Phys.* **1992**, *97*, 2571-2577.

b) F. Weigend, R. Ahlrichs, *Phys. Chem. Chem. Phys.* **2005**, *7*, 3297-3305.

c) F. Weigend, *Phys. Chem. Chem. Phys.* **2006**, *8*, 1057-1065.

[47] O. S. Bokareva, G. Grell, S. I. Bokarev, O. Kühn, *J. Chem. Theory Comput.* **2015**, *11*, 1700-1709.

[48] a) S. Miertuš, E. Scrocco, J. Tomasi, *Chem. Phys.* **1981**, *55*, 117-129.

b) U. Chandra Singh, P. A. Kollman, *J. Comput. Chem.* **1984**, *5*, 129-145.

c) M. Cossi, V. Barone, *J. Chem. Phys.* **2001**, *115*, 4708-4717.

d) R. Cammi, S. Corni, B. Mennucci, J. Tomasi, *J. Chem. Phys.* **2005**, *122*, 104513.

e) J. Tomasi, B. Mennucci, R. Cammi, *Chem. Rev.* **2005**, *105*, 2999-3094.

f) G. Scalmani, M. J. Frisch, B. Mennucci, J. Tomasi, R. Cammi, V. Barone, *J. Chem. Phys.* **2006**, *124*, 094107.

[49] a) S. Grimme, M. Waletzke, *J. Chem. Phys.* **1999**, *111*, 5645-5655.

b) C. M. Marian, A. Heil, M. Kleinschmidt, *WIREs Comput. Mol. Sci.* **2019**, *9*, e1394.

c) M. Kleinschmidt, C. M. Marian, M. Waletzke, S. Grimme, *J. Chem. Phys.* **2009**, *130*, 044708.

[50] I. Lyskov, M. Kleinschmidt, C. M. Marian, *J. Chem. Phys.* **2016**, *144*, 034104.

[51] a) M. Kleinschmidt, J. Tatchen, C. M. Marian, *J. Comput. Chem.* **2002**, *23*, 824-833.

b) M. Kleinschmidt, C. M. Marian, *Chem. Phys.* **2005**, *311*, 71-79.

c) M. Kleinschmidt, J. Tatchen, C. M. Marian, *J. Chem. Phys.* **2006**, *124*, 124101.

[52] a) M. Etinski, J. Tatchen, C. M. Marian, *Phys. Chem. Chem. Phys.* **2014**, *16*, 4740-4751.

b) M. Etinski, J. Tatchen, C. M. Marian, *J. Chem. Phys.* **2011**, *134*, 154105.

c) M. Etinski, V. Rai-Constapel, C. M. Marian, *J. Chem. Phys.* **2014**, *140*, 114104.

[53] C. R. Jacob, Edited by V. Barone, *Chem. Phys. Chem.* **2012**, 13, 3231-3231.

[54] a) A. Rodriguez-Serrano, F. Dinkelbach, C. M. Marian, *Phys. Chem. Chem. Phys.* **2021**, *23*, 3668-3678.

b) F. Dinkelbach, M. Bracker, M. Kleinschmidt, C. M. Marian, *J. Phys. Chem.* A **2021**, *125*, 10044-10051.

[55] F. Plasser, *J. Chem. Phys.* **2020**, *152*, 084108.

[56] M. Hesse, H. Meier, B. Zeeh, *Spektroskopische Methoden in der organischen Chemie,* Georg Thieme Verlag, Stuttgart, **2005**, p 103.

[57] C. F. Macrae, I. Sovago, S. J. Cottrell, P. T. A. Galek, P. McCabe, E. Pidcock, M. Platings, G. P. Shields, J. S. Stevens, M. Towler, P. A. Wood, *J. Appl. Crystallogr.* **2020**, *53*, 226–235.

7.2 Compound Class B – NHC Copper(I) complexes: Manuscript I

Luminescent Copper(I)-Complexes with an Anionic NHC obtained via a Coordination Polymer as Versatile Precursor

Philipp Schmeinck,[a] Dragana Sretenović,[b] Jasper Guhl,[c] Ralf Kühnemuth,[b] Claus A. M. Seidel,*[b] Christel M. Marian,*[c] Markus Suta,*[a] and Christian Ganter*[a]

[a] P. Schmeinck, Jun.-Prof. Dr. M. Suta, Prof. Dr. C. Ganter
Institute of Inorganic and Structural Chemistry
Heinrich Heine University Düsseldorf
Universitätsstr. 1, 40225 Düsseldorf, Germany
E-mail: markus.suta@hhu.de, christian.ganter@hhu.de

[b] D. Sretenović, Dr. R. Kühnemuth, Prof. Dr. C. A. M. Seidel
Institute of Physical Chemistry
Heinrich Heine University Düsseldorf
Universitätsstr. 1, 40225 Düsseldorf, Germany
E-mail: cseidel@hhu.de

[c] J. Guhl, Prof. Dr. C. M. Marian
Institute of Theoretical and Computational Chemistry
Heinrich Heine University Düsseldorf
Universitätsstr. 1, 40225 Düsseldorf, Germany
E-mail: christel.marian@hhu.de

This article has been published in *European Journal of Inorganic Chemistry* **2023**, *26*, e202300416.

DOI: 10.1002/ejic.202300416.

A previous version of this manuscript has been deposited on ChemRxiv:

DOI: 10.26434/chemrxiv-2023-3k5bl.

7.2.1 Abstract

The anionic diamido *N*-heterocyclic carbene **1** is used to prepare a series of linear as well as trigonal, heteroleptic $\mathrm{Cu^I}$ complexes with small molecular ligands such as pyridine derivatives or triphenylphosphine. A key role lies in the versatile precursor for these complexes, a moisture- and air-stable 1D coordination polymer **[1·Cu]$_n$** composed of only the NHC ligand and $\mathrm{Cu^I}$, such that the copper is linearly coordinated by the carbene carbon atom and one oxygen atom of the backbone of the carbene. This polymer can easily be cleaved into monomeric complexes by addition of the desired ligand to dispersions of the polymer in dichloromethane. In solution, the complexes are in equilibrium with this highly insoluble polymer and free ligand. Thus, analytical and spectroscopical experiments with the compounds are limited to their crystalline state, characterized by single crystal X-ray diffraction experiments. Some of the complexes exhibit visible luminescence in the solid state upon irradiation with ultraviolet light. The spectral features (emission wavelength, Stokes shift, width of the emission band, vibrational fine structure) significantly differ among the complexes. Quantum mechanical computations reveal a subtle interplay of several factors such as coordination number and charge transfer character of the emissive state.

Abbreviations

CAAC	cyclic (alkyl)(amino)carbene
DMAP	4-Dimethylamino pyridine
DIPP	2,6-Diisopropylphenyl
HV	High vacuum
IPr	1,3-bis(2,6-diisopropylphenyl)imidazole-2-ylidene
ITr	1,3-bis(triphenylmethyl)imidazole-2-ylidene
NHC	N-heterocyclic carbene
OLED	Organic light emitting diode
PLQY	Photoluminescence quantum yield
TADF	Thermally activated delayed fluorescence
TEP	Tolman electronic parameter

7.2.2 Introduction

Cu^I is one of the most promising transition metal ions for employment in luminophores for various applications like, for example, organic light-emitting devices (OLEDs). Compared to commonly used heavy transition metals like Ir^{III}, Pt^{II} or Au^I, it is appreciated for its vast abundance and inexpensiveness.[1] Moreover, its d^{10} configuration limits metal-centred transitions at optically accessible energies, which can lead to non-radiative decay of excited states. In particular, 3rd generation OLEDs significantly benefit from the use of Cu^I-complexes, since many of them are established candidates for thermally activated delayed fluorescence (TADF), an elegant way to harvest 100 % of the electrically generated excitons in an OLED. Thermally induced reverse intersystem crossing back to an excited singlet state can boost the internal quantum efficiency to a theoretical limit of 1 compared to 0.25 in devices that rely on prompt fluorescence only.[2] Among those Cu^I compounds, complexes containing *N*-heterocyclic carbene ligands (NHCs) have attracted considerable interest during the last years.[3,4,5,6] Synthetically, such complexes are accessible via a couple of routes, the most common one employing the free NHC, either isolated or generated in situ, reacting with a Cu^I halide.[3] The generated $(NHC)Cu^IX$ complexes (X = Cl, Br, I) may serve as precursors for a wide range of other structures, often by substitution of the halide with other ligands.[7,8] Such manipulations usually produce inorganic salts as byproducts alongside the desired complexes which can be difficult to remove.

In a previous study we presented a linear complex of the type $[IPrCu(2\text{-picoline})]BF_4$ (IPr = 1,3-bis(2,6-diisopropylphenyl)imidazole-2-ylidene) that barely emits in single crystalline state or solution. However, after grinding or precipitation it reaches a luminescence quantum yield of up to 0.87, which is attributed to the coordination of the BF_4^- anion to the central Cu^I ion.[9] Moreover, trigonal bis(ligand) complexes $[IPrCu(2\text{-picoline})2]BF_4$ were formed that are brightly blue luminescent in the solid state but require an excess of ligand to be stable in solution. In a later publication, we extended this investigation by replacing the IPr carbene by the sterically much more demanding NHC 1,3-bis(triphenylmethyl)imidazole-2-ylidene (ITr), first reported by Rivard and co-workers.[10] The high buried volume of ITr prevented an interaction with the anion and also resulted in exclusively linear complexes (apart from chelating ligands like 2,2'-bipy).[11] Nevertheless, all the complexes we presented so far are salts composed of a copper containing cation and an appropriate anion and thus have a low vapor pressure, which is disadvantageous for manufacturing of OLEDs since the emitter layer is often generated by chemical vapor deposition of the luminophore.

Charge neutrality is usually achieved by anionic co-ligands. Such an approach was for example reported by Thompson and co-workers who synthesized and characterized complexes with a neutral (di)amido carbene, structurally related to the one used in this work, and anionic carbazolate derivatives coordinating to Cu^I. The emissions of these complexes covered a vast portion of the visible spectrum and reached photoluminescence quantum yields of up to unity.[7]

In this contribution we pursued the opposite approach in utilizing the anionic NHC derivate **1**, first reported by César and co-workers,[12,13] coordinated to a cationic Cu-L_m moiety (m = 1, 2), resulting in overall charge-neutral complexes. Photophysical investigations of this type of anionic carbene coordinating to coinage metals were earlier reported by Bochmann and co-workers, who synthesized a series of mixed NHC complexes with an additional cyclic (amino)alkyl carbene (CAAC) coordinating to Cu^I, Ag^I and Au^I.[14]

In this contribution, we report an air- and water-stable one-dimensional coordination polymer **[1·Cu]$_n$** consisting of only the anionic NHC ligand **1** and the metal ion. The NHC bridges the central Cu^I ions with its carbene-carbon and backbone-oxygen atoms, respectively. This coordination mode of the NHC ligand has previously been observed in a polymeric structure containing $Hg^{II}Cl$ moieties.[15] **[1·Cu]$_n$** is easily available, serves as a versatile starting material for a wide range of heteroleptic complexes and is, to the best of our knowledge, the first report on the synthetic use of a coordination polymer only consisting of an NHC and a metal ion. Its application circumvents the aforementioned problems of the formation of inorganic byproducts during the synthesis of the final complexes, which are depicted in Scheme 7.2.

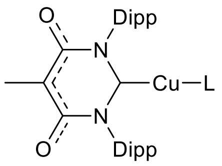

2

a: L = 2,6-lutidine
b: L = 4-formyl-2,6-lutidine
c: L = 4-dimethylamino pyridine
d: L = acridine
e: L = triphenyl phosphine

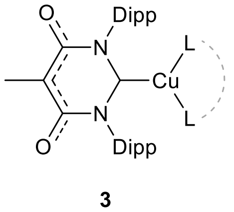

3

a: L = pyridine
b: L = 4-formyl pyridine
c: L = 4-acetyl pyridine
d: L^L = 2-acetyl pyridine
e: L^L = 2,2'-bipyridine

Scheme 7.2. Cu^I complexes investigated in this work.

7.2.3 Results and Discussion

Synthesis

The zwitterionic precursor **1·H** of the anionic six-membered diamido carbene **1** was synthesized according to a literature procedure reported by César and co-workers (see Scheme 7.3).[13] However, in our synthetic approach a recrystallization of **1·H** from ethyl acetate / *n*-hexane mixture proved more successful for larger quantities than column chromatography as described in the original preparation. The liberation and subsequent coordination of **1** to CuCl was also conducted as previously described. Thus, deprotonation of **1·H** with *n*-butyllithium in THF followed by addition of solid CuCl to the reaction mixture yields **Li[1·CuCl]**. Complexes of this type are well-established as precursors for heteroleptic Cu^I-complexes, since the chloride ligand can be easily exchanged.[9,11,13]

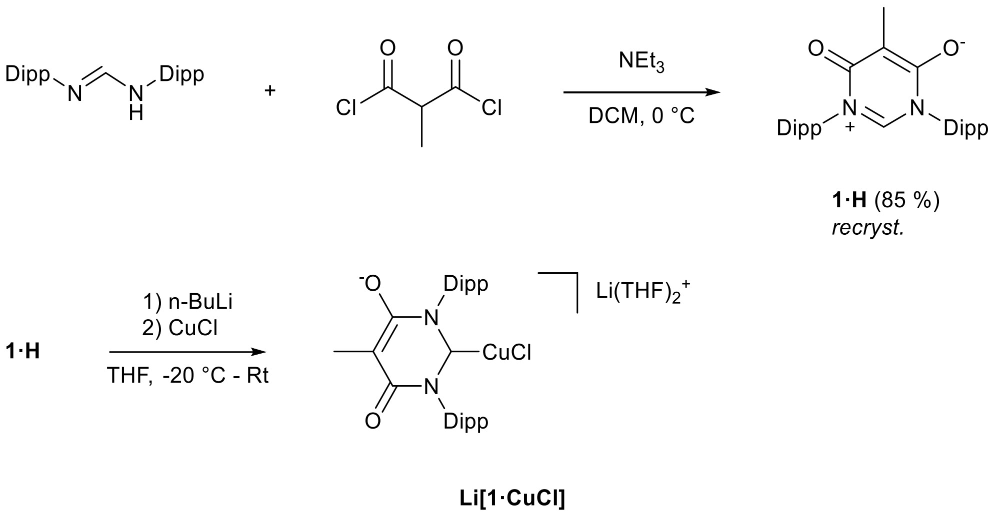

Scheme 7.3. Synthesis of carbene precursor **1·H** and subsequent coordination to CuCl.

However, we refrained from using **Li[1·CuCl]** as direct precursor for the complexes **2a-e** and **3a-e**. Attempts to remove the chloride as AgCl by treatment with $AgBF_4$ in the presence of the desired ligand resulted in products containing residual lithium salts that were difficult to remove. The products reproducibly incorporated sub-stoichiometric amounts of the desired ligand as could be proven by ^{1}H-NMR-spectroscopy. The deviation from the expected amount of ligand present is smaller for L = pyridine (~ 0.8 eq. pyridine per NHC in final product) than for L = 4-formyl pyridine. For the latter we detected the formation of a colourless precipitate after the AgCl was filtered off, which contained no 4-formyl pyridine at all. Only the signal set of **1** was present in the NMR spectrum recorded in acetonitrile-*d₃*. Intrigued by the nature of this unknown compound, we attempted to obtain single crystalline material of it, which was eventually achieved by slow evaporation of its saturated acetonitrile solutions. X-ray diffraction revealed **[1·Cu]ₙ**, a 1D coordination polymer, with the $\mathrm{Cu^I}$ centre linearly coordinated by the carbene carbon atom to one side and one oxygen atom of the carbene backbone to the other (Figure 7.15). Although a correct elemental analysis of the material could be obtained, the crystal quality was reproducibly poor and only low-quality diffraction data could be collected preventing a meaningful discussion of geometrical parameters. However, the X-ray diffraction measurements unequivocally prove the polymeric nature of the compound and the bridging coordination mode of the carbene ligand.

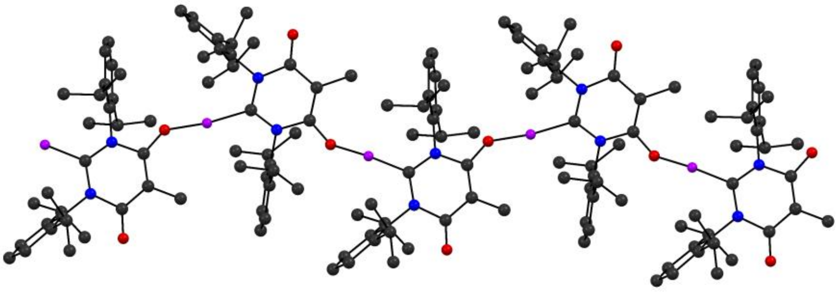

Figure 7.15. Ball-and-Stick representation of the constitution of **[1·Cu]ₙ**. Hydrogen atoms are omitted for clarity.

*Synthesis and use of **[1·Cu]ₙ*** – We attributed great potential to **[1·Cu]ₙ** since it is composed of only the NHC-Cu moieties intended to form the complexes **2 a-e** and **3 a-e** with the respective ligand. Depolymerization of **[1·Cu]ₙ** is possible by addition of a suitable ligand that binds more favourably to the $\mathrm{Cu^I}$ than the O atom from the carbene backbone. Thus, we successfully synthesized **[1·Cu]ₙ** just by addition of degassed water to a solution of **Li[1·CuCl]** in acetonitrile, precipitating the compound with an isolated yield of 60 % under concomitant removal of lithium chloride via the aqueous phase (see Scheme 7.4). **[1·Cu]ₙ** is obtained as a moisture- and air-stable, colourless powder which is highly insoluble in most standard organic solvents. Even in acetonitrile, it is only sparingly soluble with approximately 1 mg/ml under standard conditions. With the successful isolation of **[1·Cu]ₙ**, we then pursued the synthesis of the complexes **2a-e** and **3a-e**.

*Synthesis of **2a-e** and **3a-e*** – Addition of the appropriate amount of ligand to a suspension of **[1·Cu]ₙ** in dichloromethane leads to full dissolution and formation of the desired complex (see Scheme 7.4). In case of **2e**, a few drops of methanol were needed, because the product is insoluble in dichloromethane.

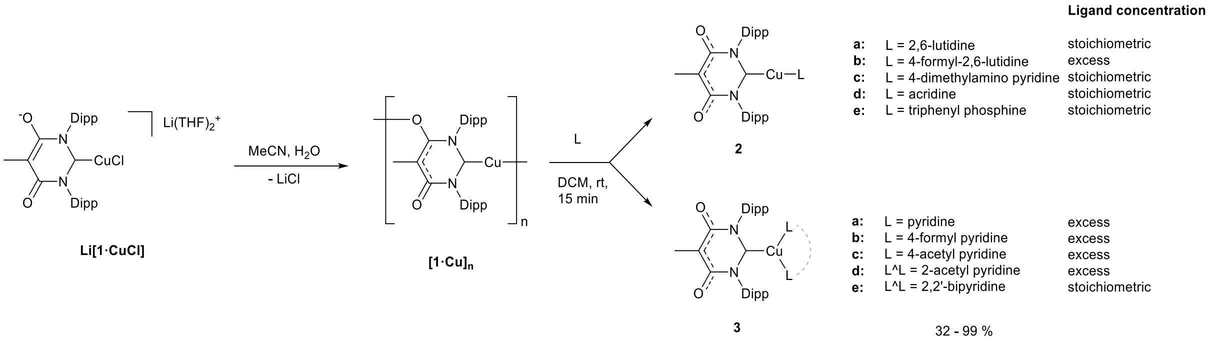

Scheme 7.4. Syntheses of **[1·Cu]ₙ** and complexes **2a-e** and **3a-e**.

Conveniently, the dissolution of **[1·Cu]ₙ** upon addition of ligand served as visual indication for the reaction progress, which we found to differ tremendously depending on the nature of the ligand. Products **2a,c-e** and **3e** are formed within only a few minutes upon addition of a stoichiometric amount of ligand and pure solutions of the desired compounds in dichloromethane are obtained without additional purification steps. In contrast, **2b** and **3a-d** do not form upon addition of a stoichiometric amount of ligand. In those cases, a complete conversion of the polymer requires the addition of 10 – 50 equivalents of ligand, providing the resulting complexes in analytically pure form after removal of the dichloromethane *in vacuo* and subsequent extraction of the resulting solid with diethyl ether in order to remove excess ligand. Consequently, the stoichiometric composition of the respective products cannot be controlled by the amount of added ligand. Thus, **3a-c** can only be obtained as the trigonal bis(ligand) complexes. Apart from stoichiometry, however, the composition can be controlled by other means. For example, the bulky acridine **(2d)**, 2,6-lutidines (**2a,b**) or triphenyl phosphine **(2e)** exclusively form the mono(ligand) complexes due to steric hindrance. In **2c**, electronic reasons prevent a second electron-rich DMAP from coordinating, presumably because of the already strongly electron-donating anionic carbene (TEP = 2043 cm^{-1}) resulting in an electronic mismatch.[16] All statements about the stoichiometric composition of these compounds are based on elemental analysis and their molecular structures determined by X-ray crystallography (see below for details). Although pyridines with electron withdrawing formyl substituents are detrimental for the chemical stability, they were considered promising ligands with respect to the luminescence properties as indicated by quantum chemical calculations (*vide infra*).

Recycling – Compounds **2a-e** and **3a-e** may be subjected to a simple recycling procedure by dissolving them in acetonitrile and precipitating **[1·Cu]$_n$** by addition of water in a fashion similar to its synthesis as described above. For water-insoluble ligands, the product needs to be washed with an appropriate solvent like diethyl ether before reusing it.

The situation in solution – The behaviour of the compounds **2a-e** and **3a-e** during their synthesis indicates an equilibrium between the mononuclear complexes and oligo- or polymeric material of **[1·Cu]$_n$** in solution and we carefully investigated the involved processes. We first tried to verify the existence of oligomeric material by MALDI mass spectrometry on the complexes in dichloromethane. Indeed, **2a-e** and **3a-e** show peaks of oligomeric species **[1·Cu]$_n$** with n = 2-4 besides the molecular ion peak of the parent molecule, if visible. The presence of a highly dynamic equilibrium between these species was verified by NMR spectroscopy, which revealed only one signal set indicative of ligand exchange processes that are fast on the NMR time scale. Furthermore, the NMR spectra of **3a** in acetonitrile-*d$_3$* were measured after subsequent additions of excess pyridine. The spectra show only one signal set for the pyridine with the chemical shifts approaching those of free pyridine in the case of a large excess of the ligand.

The complexes **2b** and **3b-d** containing pyridine moieties with electron withdrawing substituents are the most unstable in solution. These complexes dissociate instantaneously upon dissolution under formation of a white precipitate of **[1·Cu]$_n$**, indicating that the oligomers have a too high chain length to remain soluble. ^{1}H-NMR spectroscopy after removal of the precipitate shows strong peaks of the respective free pyridine ligand and only very weak signals for the carbene, indicating almost complete dissociation. Based on these observations, we deduce that the formation of **[1·Cu]$_n$** in solutions of **2a-e** and **3a-e** depends on electronic and steric properties of the respective secondary ligand. Overall, the stability of complexes **2a-e** and **3a-e** in solution is limited. Even for those complexes that do not visibly dissociate, oligomeric **[1·Cu]$_n$** species with variable chain length and length distribution are present as verified by MALDI MS.

Solid state – In the solid state, compounds **2a-e** and **3a-e** show remarkable stability and can be handled and stored under atmospheric conditions without detectable degree of decomposition. Suitable single crystals for structural analysis by X-ray diffraction were obtained by cooling saturated solutions, evaporating them slowly or diffusing an anti-solvent into them. In most crystallizations an excess of ligand was added to prevent polymer formation (see experimental section for detailed procedures). An overview of the molecular structures is depicted in Figure 7.16.

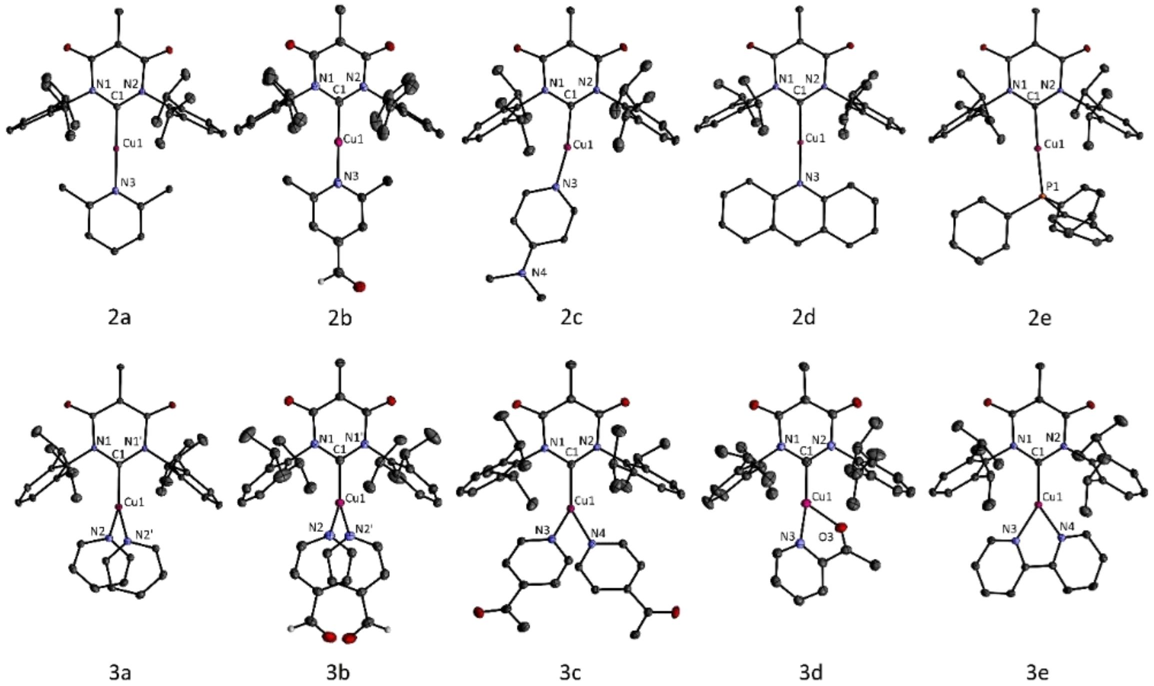
2a 2b 2c 2d 2e

3a 3b 3c 3d 3e

Figure 7.16. Thermal ellipsoid plots of the complexes **2a-e** and **3a-e**. Ellipsoids are drawn at the 30% probability level; hydrogen atoms (except formyl protons) and solvent molecules (if present) are omitted for clarity.

As summarized in Table 7.5, the distances between the Cu and the carbene carbon atoms as well as the contact atoms of the other ligands are in the range of previously reported related systems.[9,13] The angles around the Cu centre sum up to 360°, indicating trigonal-planar coordination for all triply coordinated molecules. Only in compound **3d** an angle sum of 357.3(2)° and a distorted T-shaped arrangement are found due to the chelating coordination mode of the 2-acetyl pyridine. Another structural feature is the coplanarity of the mean planes of the carbene and the DMAP ligand in **2c**, which stands out compared to the other linear complexes **2a,b,d**, in which torsion angles of ca. 10° between the mean planes of the carbene and the ligand are found.

Table 7.5. Selected distances and angles for complexes **2a-e** and **3a-e**.

Compound	NHC-Cu [Å]	L-Cu [Å]	Angle sum at Cu (trig.)	Angle at Cu (lin.)	Torsion NHC-pyridine
2a	1.918(3)	1.925(2)[a]	-	178.6(1)[a]	10.07(7)[a]
2b	1.901(4)	1.926(3)	-	178.5(1)	10.54(1)
2c	1.894(2)	1.880(2)	-	169.0(1)	0.00(0)
2d	1.905(2)	1.918(1)	-	177.9(1)	11.73(5)
2e	1.927(4)	2.203(1)	-	177.4(1)	-
3a	1.910(2)	2.046(1)	360.0(1)	-	-
3b	1.897(2)	2.031(1)	360.0(1)	-	-
3c	1.927(3)	2.054(1)[b]	360.0(2)	-	-
3d	1.889(3)	1.937(2)	357.3(2)	-	30.73(8)
3e	1.905(2)	2.046(2)[b]	360.0(1)	-	40.03(4)

[a] Average between the two independent molecules in the asymmetric unit; [b] Average between the two coordinating pyridine moieties.

Apart from the previously discussed features of the molecular structures, a relevant property common to all complexes **2a-e** and **3a-e** is the presence of classical as well as non-classical intermolecular hydrogen bonding in the crystal lattices as displayed in Figure 7.17.[17,18] A detailed discussion of the geometric parameters of these close contacts is given next. It should be noted that estimated standard deviations (ESDs) are not reasonable in this context, since all hydrogen atoms are fixed to geometric positions. Our data show that mostly the oxygen atoms of the carbene backbone or incorporated solvents are involved as Lewis basic sites. However, also the π systems of the dipp substituents may function as H bond acceptors. For example, the protons of the formyl groups attached to the pyridines in **3b** each form intermolecular two-electron-three-centre contacts with two carbon atoms of a dipp substituent. On the other hand, aromatic protons of pyridines or triphenyl phosphine can also form H bonds. For example, the H atoms in meta position pointing outward in **3b** interact with the backbone-oxygen of the carbene with a distance of 2.133 Å. In **2e**, an interaction between one meta proton of the triphenyl phosphine and the oxygen atom of an incorporated methanol molecule with a distance of 2.491 Å is observed (Figure 7.17). This behaviour highlights a strong intramolecular charge separation and consequently, high dipole moments in the electronic ground state. Similar observations have been reported by Weber and co-workers in the case of halogenated azaarene derivatives.[19]

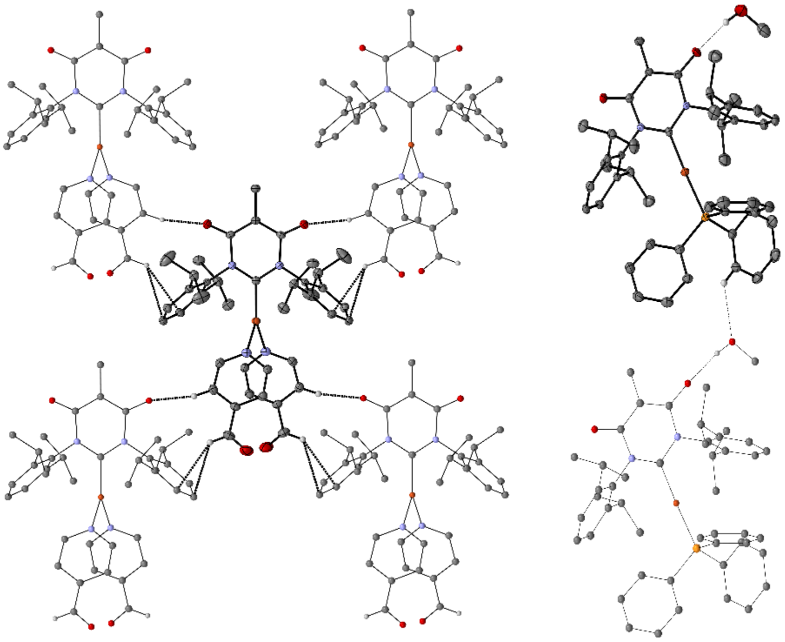

Figure 7.17. Hydrogen bonding patterns in the SC-XRD structures of **3b** (left) and **2e** (right). See the Supporting Information for details.

Interestingly, the crystal structure of **3b** was found to change upon heating a powder sample to 50 °C as indicated by the different powder X-ray diffraction patterns. Apparently, an irreversible phase change takes place, probably due to the breakdown of the intermolecular hydrogen bond network, while an elemental analysis indicated no change in the composition of the compound (See Supplementary Information for details).

Photophysical Properties

Some of the reported molecules exhibit visible luminescence in the solid state upon irradiation with ultraviolet light ($\lambda = 365$ nm). Four complementary complexes (**2a,b** and **3a,b**) were selected for detailed investigations of their photophysical properties. The set comprises two linearly (**2a,b**) and two trigonally-planar coordinated complexes (**3a,b**). One compound of each pair, respectively, contains pyridine ligands with an electron-withdrawing formyl group (**2b**,**3b**), while the carbene ligand is electron-rich. These features possibly result in interesting excited state photophysics compared to the work of Thompson et al.,[7] in which the opposite case of Cu^{I} complexes with an electron-poor NHC and electron-rich carbazolate ligands has been investigated. As pointed out above, all complexes are involved in ligand distribution equilibria in solution. Therefore, reliable photophysical measurements could only be performed in the solid state. In addition to luminescence spectra of powdered samples, a new technique was established by investigating suspensions of the microcrystalline solid in cyclohexane in standard cuvettes. Cyclohexane was chosen for several reasons. Firstly, all complexes are insoluble in this solvent and it was thus supposed to provide a non-reacting medium for the photophysical investigations without interference from solution equilibria (*vide supra*). Secondly, cyclohexane has a relatively high melting point of 6.5 °C under standard conditions, allowing photoluminescence measurements in a chemically inert, solid matrix at temperatures just below room temperature. It should be noted that absorption spectra were recorded for the suspensions in cyclohexane and corrected for scattering of the micro-crystals (see Methods), while photoluminescence excitation spectra were measured for the powdered samples. Figure 7.18 shows the normalized absorption and emission spectra in cyclohexane suspension as well as the normalized excitation and emission spectra obtained from powdered samples. Photoluminescence excitation spectra usually offer information about excited states with high sensitivity. This often even allows to detect transitions with low oscillator strengths, e.g., spin-forbidden excitations to the T_1 state. However, for transitions with high absorption cross sections, photoluminescence excitation spectra of highly concentrated species such as in powders usually suffer from non-linear self-absorption effects, which does not allow to readily use intensities as a measure for theoretically computed oscillator strengths anymore. Moreover, inhomogeneous broadening effects of aggregated species diminish the spectral resolution such that the appearance of photoluminescence spectra of the powdered species should be regarded with caution. In that regard, the absorption spectra of the suspended compounds in cyclohexane contain complementary information. As the photoluminescence excitation spectra are usually quickly saturated at a higher absorbance, excitation spectra are especially informative to identify the onset of the S_0-S_1 transition with high sensitivity while the overall intensities of the bands should be discussed with caution. In this view, the location of the S_0-S_1 transition and its relative oscillator strength are well resolved for all compounds. It is remarkable that only for **3b** in cyclohexane suspension the absorbance in the longest excitation band is very weak and below the detection limit of absorption spectroscopy.

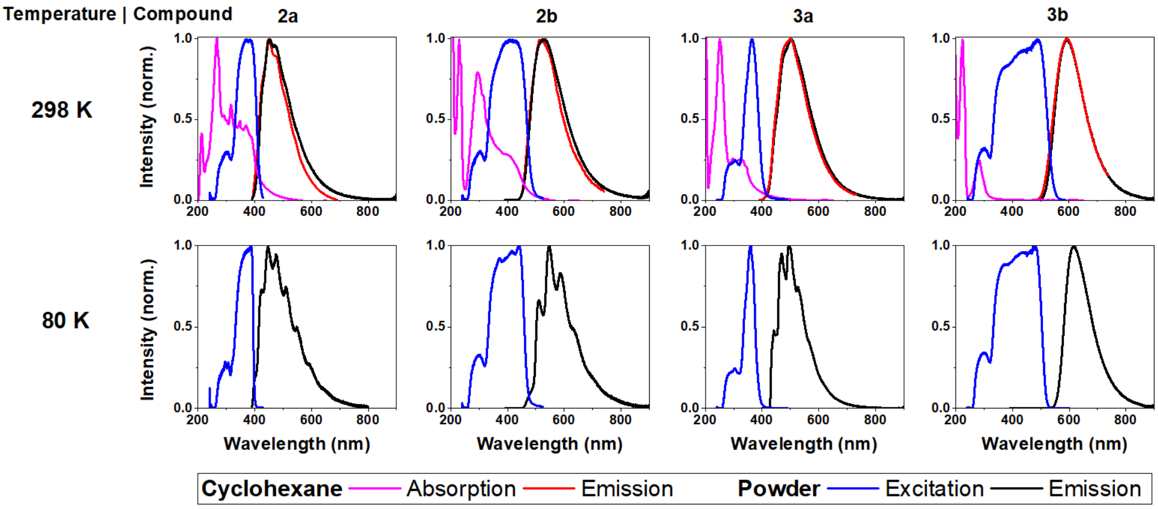

Figure 7.18. Absorption / excitation and emission spectra as described in methods. Top row: Excitation and emission spectra of powdered samples and absorption and emission spectra of samples suspended in cyclohexane at 298 K. Bottom row: Excitation and emission spectra of powdered samples at 80 K. All emission spectra were recorded at an excitation wavelength λ_{ex} = 375 nm. The excitation spectra were recorded for an emission wavelength of 450 nm **(2a)**, 540 nm **(2b)**, 500 nm **(3a)**, 598nm (**3b**, 298 K) and 615 nm (**3b**, 80 K). The photophysical parameters are compiled in Table 7.6.

Table 7.6. Optical properties of powdered samples **2a,b** and **3a,b**. Excitation and emission maxima, their FWHMs, Stokes shifts, the energy of the vibronic progressions at 298 K and 80 K, if applicable, as well as absolute photoluminescence quantum yields (PLQYs) at λ_{ex} = 350 nm and room temperature.

	λ_{max} Ex [nm]		**λ_{max} Em [nm]**		**App. Stokes shift [cm^{-1}]**[a]		**0-0 Energy [cm^{-1}]**[b]		**FWHM Emission [cm^{-1}]**		**Vibr. Prog. [cm^{-1}]**	**Φ_{PL}**
T [K]	80	298	80	298	80	298	80	298	80	298	80	298
2a	387	369	447	451	4915	4615	24975	23987	6580	7040	1350	0.04
2b	441	407	547	527	4301	4170	20572	20786	4600	5799	1250	0.01
3a	361	364	494	504	7690	7605	23337	23403	4380	5937	1200	0.02
3b	478	490	615	591	4520	3400	18467	18477	2835	3945	-	0.13

[a] Apparent Stokes shift is given as distance between the maxima of excitation and emission of powder. [b] Estimation by the intersection of excitation and emission spectra of powder.

To understand the apparent trends in the absorption / excitation spectra, quantum chemical calculations were performed employing a combination of Kohn-Sham density functional theory (KS-DFT) and multireference configuration interaction (MRCI) expansions. They reveal the presence of multiple electronic transitions in the considered wavelength regime

(Figure 7.19). With regard to the specific donor and acceptor properties of Cu^I and the ligands, we expect three types of excitations (or combinations thereof) to be energetically low-lying: Metal-to-ligand charge transfer (MLCT) states involving the pyridine moiety, ligand-to-ligand charge transfer (LLCT) states originating from a carbene-to-pyridine electron transfer and a local $\pi\pi^*$ excitation on the carbene ligand (Figure 7.19). In addition, the $n\pi^*$-type excitation on the formyl pyridine is energetically accessible in the wavelength region above 300 nm. The local $\pi\pi^*$ transition on the pyridine ring is known to peak at about 260 nm.[20] According to the calculations, the narrow band in the excitation spectrum of the linear complex **2a** is dominated by a strong LC(carbene) transition at about 350 nm and a weaker MLCT transition at about 330 nm. LLCT transitions do not play an important role in this compound. However, introduction of an electron-withdrawing formyl group in *para* position of the pyridine moiety increases the acceptor strength of this ligand, thus strongly stabilizing the LLCT and MLCT transitions in **2b**, while the energy of the LC(carbene) transition is similar to that of the respective transition in **2a**. The redshift is particularly pronounced for the LLCT state which forms the lowest excited state of this complex and therefore might qualify as potential TADF emitter according to the design principles suggested by Lüdtke et al.[21] While the electronic nature of the excitations is clearly assignable in the linear complexes **2a** and **2b**, states of mixed character are found for the trigonal complexes **3a** and **3b**. Introduction of an additional lutidine or 4-formyl pyridine ligand leads to a blueshift of the LC(carbene) states, an energetic splitting of corresponding MLCT transitions and a stabilization of the LLCT transitions in the trigonal complexes. The lower energy parts of the excitation spectra of **3a** and **3b** are thus composed of linear combinations of two LLCT and MLCT transitions.

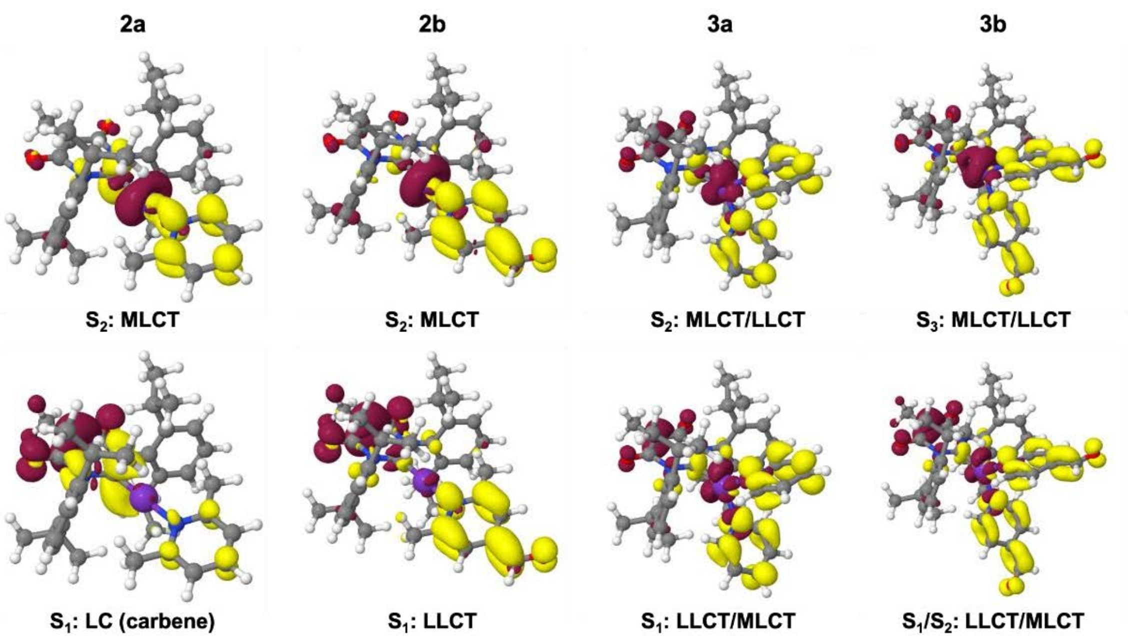

Figure 7.19. Differences of the electron densities (isosurface ± 0.002) between the low-lying excited singlet states and the electronic ground state in the Franck–Condon region. A loss of electron density upon electronic excitation is indicated in red, a gain in yellow.

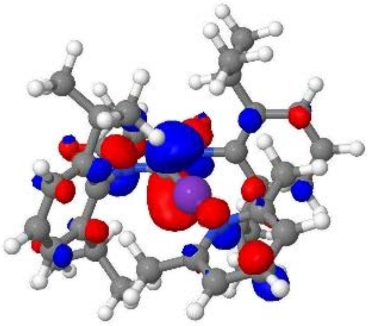

Figure 7.20. Lowest unoccupied molecular orbital on the carbene moiety of **2a** (isosurface 0.04). The π* character of the carbene C–N bonds is clearly visible. Similar π*(carbene) molecular orbitals are present in all compounds.

The steady state emission spectra are spread over a wide range (Figure 7.18) irrespective of the coordination environment. While **2b** and **3a** exhibit apparently similar emission bands with maxima of 527 nm and 504 nm, respectively, **2a** shows an emission maximum at 451 nm in the blue, and **3b** has the most red-shifted emission peak at 591 nm at room temperature (see Figure 7.18). A comparison between the emission FWHMs and Stokes shifts provides additional insight. For example, the apparent Stokes shift between excitation and emission maximum of **3a** is substantially larger than the emission band FWHM at both 80 K and room temperature (see Table 7.6). This implies a non-radiative relaxation process into a lower energetic state after excitation at 375 nm, from which radiative emission results. The observation of vibronic fine structure in the emission spectrum of **3a** at 80 K indicates a ligand centred localized excitation. By the same virtue, also **2a** and **2b** apparently show emission from a more localized electronic state at 80 K (see Figure 7.18). The similarity of the observable vibronic progression frequency ($\Delta\tilde{\nu} \approx 1300$ cm^{-1}) in the emission spectra of powdered **2a**, **2b** and **3a** at 80 K is compatible with coupling to a C-N stretching vibration of the carbene moiety commonly having this vibrational frequency due to the population of the C-N-antibonding π^* orbital (see Figure 7.20) in the common LC(carbene) state.

The trigonal-planar complex **3b** with two 4-formyl pyridine ligands shows a featureless emission band with small FWHM both at 80 K and room temperature in line with a low Stokes shift compared to all other compounds (see Table 7.6). Thus, despite an emissive state with apparently more delocalized electron density indicative for LLCT/MLCT-type transitions, the solid compound shows sufficient structural rigidity that limits substantial excited state relaxation. The hydrogen bonding network in solid **3b** (see Figure 7.17) can be a possible reason for this. The linear complex **2b** with one 4-formyllutidine ligand follows this trend and its luminescence spectra are characterized by similarly low Stokes shifts compared to **3b**. Both **2b** and **3b** are characterized by FWHMs of the emission bands at room temperature that are comparable to the respective Stokes shifts, which implies that the lowest energetic excitation bands in both compounds can be assigned to the emissive states at room temperature.

2a takes a special role among the four compounds. Its luminescence spectra are characterized by similar Stokes shifts compared to **2b** and **3b** in the powder both at 80 K and room temperature indicating a certain degree of structural rigidity in the solid, while the observable vibronic fine structure implies a localized emissive state. However, it shows the largest FWHM of the emission band among the four compared Cu^{I} complexes at both regarded temperatures (see Table 7.6). A possible explanation is simultaneous radiative emission from two thermally decoupled excited states with sufficiently large energy gap ($\Delta E > 0.25$ eV). Future detailed time-resolved and quantum chemical studies on these complexes will be necessary to additionally resolve these issues.

The introduction of electron-withdrawing formyl groups generally leads to a bathochromic shift of the emission in both cases (**2b** and **3b**). This is understandable given the complementary electron-donating nature of the carbene moiety that induces an overall charge-transfer type nature of the electronic transition. As a second general trend, we find that the trigonally-planar coordinated Cu(I) complexes emit at lower energies than the related linearly coordinated ones, i.e., **3a** emits at lower energy than **2a** and **3b** at lower energy than **2b**. This trend can be qualitatively understood as follows. In the trigonal planar complexes **3a** and **3b**, two pyridine ligands contribute with their π*-type orbitals instead of only one ligand as in **2a** and **2b**. The presence of two acceptor ligands results in a stronger pull effect and hence a stabilization of the CT states in the three-coordinated complexes. Moreover, the superposition of the two close-lying acceptor orbitals causes a perturbative energy splitting, thus shifting the emission even further to the red.

Despite their promising brightness upon UV irradiation, the overall absolute photoluminescence quantum yields (PLQYs) of all regarded powdered compounds **2a**, **2b**, **3a**, and **3b** are below 20% (see Table 7.6) and indicate that emission in the as-prepared solid Cu^I carbene complexes is strongly quenched at room temperature. The trigonal-planar complex **3b** with the electron-withdrawing 4-formyl pyridine moieties has the largest PLQY among the four compounds with around 13%. All measured PLQYs are much lower than what is known for e.g., Cu^I carbene complexes with electron-poor carbene moieties and electron-donating ligands, especially if the ligands are sterically demanding.[22]

7.2.4 Conclusion

We have reported a series of linear as well as trigonal Cu^I complexes incorporating the anionic diamido NHC **1**. The versatile precursor for these complexes is the water- and air-stable 1D coordination polymer **[1·Cu]$_n$** composed only of the NHC and Cu^I, with the copper being linearly coordinated by the carbene carbon atom and one oxygen atom from the carbene's backbone. This polymer forms monomeric complexes upon addition of suitable ligands. The composition of these complexes depends on the electronic and the steric properties of such ligands. Electron donating ligands such as DMAP lead to a fast and full conversion of the polymeric material to the respective linear complex upon addition of one equivalent of ligand. Electron withdrawing ligands, such as 4-formyl pyridine, on the other hand require a considerable excess in order to achieve full conversion, resulting in exclusively the trigonal complexes. For sterically demanding ligands like 2,6-lutdine, exclusively mono coordination is observed, regardless of the stoichiometry of added ligand. In line with this observation, the compounds are in an equilibrium with oligomeric material of **[1·Cu]$_n$** once solubilized. Electron withdrawing ligands favour full dissociation and lead to the precipitation of insoluble polymeric **[1·Cu]$_n$**. However, while attachment of an electron withdrawing formyl group to the pyridine weakens its binding strength to the copper ion, it is beneficial for lowering the energy of the LLCT excitation. Fundamental spectral properties were determined for four exemplary compounds. We observed light emission for all four compounds ranging from the blue region in **2a** to the orange region in **3b**. The spectral features (Stokes shift, width of the emission band, vibronic fine structure) in Table 7.6 differ significantly among the complexes. Quantum mechanical computations (Figure 7.19) reveal a subtle interplay of several factors such as coordination number and charge transfer character of the complex, structural rigidity as well as possible electronic transitions influencing photophysics and whether the lowest energetic excitation band can also be assigned to the emissive state at room temperature. While the excitation / absorption spectra of compound **2a**, **2b** and **3a** are featureless, the spectral signatures of compound **3b** imply a more complicated behavior of the excited states. Time-resolved emission studies are under way to shed light on the excited state relaxation processes.

7.2.5 Experimental Section

Synthesis. All manipulations were carried out under dry nitrogen using the Schlenk technique or under argon in a glovebox, unless otherwise stated. The oven dried glassware used was evacuated and flooded with dry nitrogen three times prior to any manipulation. All organic solvents were dried by storing them over freshly activated molecular sieve of the appropriate pore size three days prior to use. Subsequently, they were deoxygenated by low pressure and nitrogen overpressure cycles. Commercial copper(I)-chloride was purified according to a literature procedure.[23] All other chemicals were purchased commercially and used as received. 4-Formyl-2,6-lutidine was synthesized by performing a bromine-lithium-exchange reaction with n-butyl lithium and 4-bromo-2,6-lutidine and subsequent reaction with dry *N,N*-dimethyl-formamide and protic work-up. The NMR-spectra of this compound are in agreement with its literature characterization.[24]

Characterization. NMR spectra were recorded either on Bruker Avance III 300 or a Bruker Avance III 600. All ^{1}H and ^{13}C{^{1}H}-NMR spectra are referenced to the chemical shifts of residual proton signal (^{1}H) or the solvent signal (^{13}C). Mass spectra were obtained with an Ultraflex I of Bruker Daltonics (MALDI-TOF) or a Bruker Daltonics UHR-QTOF maXIS 4Gspectrometer (ESI). An Elementar Vario MICRO cube was used for elemental analyses. X-ray crystal structure data were collected on a Bruker Apex Duo diffractometer or a Rigaku XtaLAB-Synergy S diffractometer and refined using Olex2 by OlexSys Ltd. Thermal ellipsoid plots were generated with Mercury by the Cambridge Crystallographic Data Centre.[25]

NOTE: In some cases, analytical investigations that require solubilized compounds could not be performed due to the degradation processes in solution, which are described in the results and discussion part or due to their high insolubility. These instances are highlighted for the respective compounds below.

Optical measurements. Absorption spectra were recorded on a Cary 4000 UV-Vis spectrophotometer (Agilent Technologies, USA). Samples were prepared by suspending 0.24, 0.28, 0.17, and 0.22 mg of compounds **2a**, **2b**, **3a**, and **3b**, respectively, in a total volume of 3.0 ml of cyclohexane (HiPerSolv Chromanorm, for HPLC, VWR). Quartz Macro cell type 111-QS cuvettes (Hellma) with a light path of 10 mm were used. The samples were treated in an ultrasonic bath and immediately subjected to measurement. Constant mixing of the suspension during the measurement was achieved by Hellma cuv-o-stirr model 333. The extinction spectra of each sample were measured five times, and the averaged spectra were taken. To avoid saturation effects, we studied diluted suspensions with extinctions in the range of 0.15. The contributions to the extinction E_{corr} by scattered light and drift of the spectral baseline (slope and offset) were estimated for a spectral range with no absorbance of the complexes using the corresponding correction parameters a, b_1, and b_2 in eq. (1).

$$E_{\mathrm{corr}} = \frac{a}{\lambda^4} + b_1 \cdot \lambda + b_2 \tag{1}$$

The approximate contribution of the absorbance A by the complexes to the total measured extinction E_{tot} is computed by eq. (2).

$$A \approx E_{\mathrm{tot}} - E_{\mathrm{corr}} \tag{2}$$

The correction parameters a, b_1, and b_2 were determined from a system of three linear equations. Three different wavelengths were chosen from the averaged absorption spectra, such that the samples do not absorb at these wavelengths (i.e., 450, 550, and 650 nm).

The excitation and emission spectra of the suspensions were recorded on a Horiba Fluorolog FL3-22 spectrofluorometer. For this, Quartz Semi-Micro cuvettes (Hellma) with a light path of 10 mm and a sample volume of 1.5 ml were used. Samples were stirred all the time during the measurements. Excitation and emission spectra on solid samples were acquired on an Edinburgh Instruments FLS1000 spectrofluorometer with a 450 W Xe lamp, double grating Czerny-Turner monochromators in excitation and emission compartment and a thermoelectrically cooled Hamamatsu PMT-980 photomultiplier tube. All spectra were corrected for wavelength-dependent grating efficiency and detector sensitivity, while the excitation spectra were additionally corrected for potentially fluctuating lamp intensity. Luminescence spectra at 80 K were obtained by placing powdered sample into a liquid N_2-cooled Linkam THMS600 temperature cell (temperature precision ± 0.1 K) that was coupled to the spectrometer with optical fiber bundles. Absolute photoluminescence quantum yields were measured at room temperature with an integrating sphere coated with BenFlect®.

Quantum chemical calculations. All geometry optimizations were conducted with Gaussian 16[26] employing the PBE0[27,28] density functional and a def-SV(P)[29] basis set for all atoms except for copper, where a cc-pVDZ-PP[30] basis set was used in conjunction with a relativistic effective core potential.[31] Dispersion corrections were accounted for with the D3-method.[32] Dichloromethane (**3a**, **3b**) or 2-methyltetrahydrofurane (**2a**, **2b**) solvent environments were simulated by performing self-consistent reaction field calculations employing the PCM.[33,34] At the optimized geometries, single-point electronic structure calculations were performed with the DFT/MRCI program,[35,36] which is interfaced to the TURBOMOLE suite.[37,38] For the density functional theory (DFT) part, the BH-LYP functional was employed,[39,40] while the semiempirical R2018 Hamiltonian[41] in its tight parametrization was used for all multireference configuration interaction (MRCI) calculations. Herein, the solvent surrounding was accounted for by importing the point charges generated in the geometry optimization step. The MRCI equations were solved for the 20 lowest singlet and triplet states, respectively. To this end, the primary reference space, created by distributing 10 electrons in the first 10 frontier orbitals with at most double excitations, was refined in a second step by including all configurations with sizeable CI-coefficients from the first run in the final reference space.

Synthetic procedures

Preparation of [1·Cu]$_n$. Into a 250 ml Schlenk flask 1.12 mmol (500 mg, 1 eq.) **1·H** are added, dissolved in 50 ml THF and cooled to -20 °C. 1.175 mmol (470 µl, 1.05 eq.) *n*-butyllithium solution (2.5 M in n-pentane) is added dropwise and the cooling bath is removed. The resulting colourless solution is stirred for 15 min after which time, 1.13 mmol (112 mg, 1.01 eq.) of copper(I) chloride is added as a solid and the mixture is stirred for 1 h, until the solid dissolves. All volatiles are removed *in vacuo* and the residue is taken up in 20 ml of DCM. The suspension is filtered (Celite®, DCM) and the solvent is again removed *in vacuo*. The resulting white solid is dissolved in 10 ml of acetonitrile and the product is precipitated by addition of 100 ml of distilled water. It is collected by centrifugation and the supernatant is decanted. The solid is washed two times each with distilled water, methanol and diethyl ether. The product is obtained as a white powder after drying *in vacuo* overnight. Yield: 61 %, ^{1}H-NMR (300 MHz, CD_3CN) δ = 7,40 – 7,33 (m, 2H, $H_{Dipp, para}$), 7,27 – 7,21 (m, 4H, $H_{Dipp, meta}$), 2,87 (sept, $^3J_{HH}$ = 7,0 Hz, 4H, CH_{iPr}), 1,76 (s, 3H, $CH_{3\ apical}$), 1,20 (d, $^3J_{HH}$ = 6,9 Hz, 12H, CH_{3iPr}), 1,15 (d, $^3J_{HH}$ = 6,8 Hz, 12H, $CH_{3\ iPr}$) ppm, MS (ESI, CH_3CN) m/z = 550.3 (NHC-Cu-CH_3CN + H^+), Elem. anal. calcd. for $C_{29}H_{37}CuN_2O_2$: C 68,41; H 7,32; N 5,50, Found: C 68,20; H 7,32; N 5,43. NOTE: Due to the high insolubility of this compound, ^{13}C-NMR-spectroscopy data is not available.

General procedure A: Synthesis of complexes requiring a stoichiometric amount of ligand **[1·Cu]$_n$** is added to a 10 ml microwave vessel. In case of solid ligand, 1.02 equivalents of it are added at this point as well. The vessel is sealed with a crimp cap and 7 ml of dichloromethane are added via syringe through the septum. In case of liquid ligand, 1.02 equivalents of it are added via syringe at this point. The reaction mixture is treated in an ultrasonic bath, after which **[1·Cu]$_n$** is dissolved. The mixture is taken up with a syringe and filtered through a PTFE syringe filter into a Schlenk flask. The volatiles are removed in HV and the resulting solid washed once with diethyl ether and dried overnight in HV.

General procedure B: Synthesis of complexes requiring an excess of ligand **[1·Cu]$_n$** is added to a 10 ml microwave vessel. The vessel is sealed with a crimp cap and 7 ml of dichloromethane are added via syringe through the septum. The appropriate amount of ligand is added via syringe (see specific procedures) and the reaction mixture is treated in an ultrasonic bath, after which **[1·Cu]$_n$** is dissolved. The mixture is taken up with a syringe and filtered through a PTFE syringe filter into a Schlenk flask. The volatiles are removed in HV and the resulting solid washed five times with diethyl ether and dried overnight in HV.

1-Cu-(2,6-lutidine) (2a): Starting from 0.20 mmol **[1·Cu]$_n$** (102 mg) and following procedure A*, this complex is isolated in 54 % yield as a white solid. Crystals suitable for XRD studies were obtained by slow diffusion of 2-methylpropane into a saturated dichloromethane solution. ^{1}H-NMR (600 MHz, CD_2Cl_2) δ = 7,54 (t, $^3J_{HH}$ = 7,7 Hz, 1H, $H_{Lut, para}$), 7,44 – 7,40 (m, 2H, $H_{Dipp, para}$), 7,28 – 7,25 (m, 4H, $H_{Dipp, meta}$), 6,91 (d, $^3J_{HH}$ = 7,7 Hz, 2H, $H_{Lut, meta}$), 3,01 (sept, $^3J_{HH}$ = 6,9 Hz, 4H, CH_{iPr}), 1,94 (s, 3H, $CH_{3\ apical}$), 1,48 (s, 6H, $CH_{3\ Lut}$), 1,23 (d, $^3J_{HH}$ = 6,7 Hz, 12H, $CH_{3\ iPr}$), 1,17 (d, $^3J_{HH}$ = 6,9 Hz, 12H, $CH_{3\ iPr}$) ppm, ^{13}C-NMR (151 MHz, CD_2Cl_2) δ = 192,4 (s, carbene), 162,4 (s, C=O), 159,4 (s, $C_{Lut, ortho}$), 147,0 (s, C_{Lut}), 140,4 (s, Ar), 140,2 (s, Ar), 140,0 (s, C_{Lut}), 129,8 (s, Ar), 129,6 (s, Ar), 124,7 (s, Ar), 124,5 (s, Ar), 122,6 (s, Ar), 122,5 (s, Ar), 92,0 (s, C_{apical}), 29,0 (s, C_{iPr}), 24,6 (s, $C_{Lut, Methyl}$), 24,5 (s, $CH_{3\ iPr}$), 24,1 (s, $CH_{3\ iPr}$), 24,0 (s, $CH_{3\ iPr}$), 9,5 (s, $CH_{3\ apical}$) ppm, MS (MALDI-TOF, DCM) m/z = 509.2 (NHC-Cu-H$^+$), 616.3 (NHC-Cu-(2,6-lut)-H$^+$), 1124.5 ((NHC-Cu)$_2$-(2,6-lut)-H)$^+$, 1634.7((NHC-Cu)$_3$-(2,6-lut)-H$^+$), Elem. anal. calcd. for $C_{36}H_{46}CuN_3O_2$: C 70.16; H 7.52; N 6.82, Found: C 69.93; H 7.46; N 6.74. *The general procedure was modified in that the product was recrystallized by slow diffusion of 2-methylpropane into the obtained dichloromethane solution after filtration.

1-Cu-(4-formyl-2,6-lutidine) (2b): Starting from 0.20 mmol **[1·Cu]$_n$** (102 mg) and following procedure B* with 7 eq. of 4-formyl-2,6-lutidine, this complex is isolated in 56 % yield as a light-yellow solid. Crystals suitable for XRD studies were obtained by slow evaporation of a saturated dichloromethane solution with excess ligand. Elem. anal. calcd. for $C_{37}H_{46}CuN_3O_3$: C 68.97; H 7.20; N 6.52, Found C 68.61; H 7.28; N 6.38. *The general procedure was modified in that the resulting product solution in dichloromethane with excess of ligand was allowed to slowly evaporate, resulting in the product recrystallizing. NOTE: Due to fast degradation in solution, ^{1}H-NMR, ^{13}C-NMR and mass spectrometry data is not available.

1-Cu-(4-dimethylamino pyridine) (2c): Starting from 0.20 mmol **[1·Cu]$_n$** (102 mg) and following procedure A*, this complex is isolated in 32 % yield as a white solid. Crystals suitable for XRD studies were directly yielded by the synthetic procedure. ^{1}H-NMR (300 MHz, CD_3CN) δ = 7.47 – 7.39 (m, 2H, $H_{Dipp, para}$), 7.34 – 7.26 (m, 4H, $H_{Dipp, meta}$), 7.05 – 6.92 (m, 2H, $H_{DMAP, ortho}$), 6.46 – 6.38 (m, 2H, $H_{DMAP, meta}$), 2.97 – 2.86 (m, 10H, CH_{iPr} + $CH_{3\ DMAP}$), 1.82 (s, 3H, $CH_{3\ apical}$), 1.22 – 1.14 (d, 24H, $CH_{3\ iPr}$) ppm, ^{13}C-NMR (75 MHz, CD_2Cl_2) δ = 194.0 (s, carbene), 162.6 (s, CO), 146.7 (s, Dipp), 146.2 (s, DMAP), 139.9 (s, Dipp), 131.2 (s, DMAP), 129.2 (s, Dipp), 124.8 (s, DMAP), 124.2 (s, Dipp), 91.4 (s, C-Me_{apical}), 39.5 (s, N-$(CH_3)_2$), 29.0 (s, C-^{i}Pr), 24.4 (s, Dipp-CH_3), 24.3 (s, Dipp-CH_3), 9.6 (s, $CH_{3\ apical}$). MS (MALDI-TOF, DCM) m/z = 631.3 (NHC-Cu-(DMAP)-H$^+$), 1139.5 ((NHC-Cu)$_2$-(DMAP)-H$^+$), 1649.7 ((NHC-Cu)$_3$-(DMAP)-H$^+$), 2157.9 ((NHC-Cu)$_4$-(DMAP)-H$^+$), Elem. anal. calcd. for $C_{36}H_{47}CuN_4O_2$: C 68.49; H 7.50; N 8.87, Found C 68.25; H 7.23; N 8.80. *The general procedure was modified in that the product was recrystallized by cooling down its hot saturated acetonitrile solution.

1-Cu-(acridine) (2d): Starting from 0.14 mmol **[1·Cu]$_n$** (72 mg) and following procedure A, this complex is isolated in 88 % yield as a yellow solid. Crystals suitable for XRD studies were obtained by slow evaporation of a saturated dichloromethane solution. ^{1}H-NMR (300 MHz, CD_2Cl_2) δ = 8.96 (s, 1H, $Acr_{para\text{-}H}$), 8.03 – 7.99 (m, 2H, Acr), 7.70 – 7.64 (m, 2H, $Dipp_{paraH}$), 7.59 – 7.53 (m, 4H, Acr), 7.48 – 7.41 (m, 4H, $Dipp_{meta\text{-}H}$), 6.42 – 6.14 (m, 2H, Acr), 3.12 (sept, J_{HH} = 6.8 Hz, 4H, ^{iPr}CH), 1.99 (s, 3H, $CH_{3,\ apical}$), 1.28 (d, J_{HH} = 6.8 Hz, 12H, Dipp CH_3), 1.12 (d, J_{HH} = 6.9 Hz, 12H, Dipp CH_3) ppm, ^{13}C-NMR (75 MHz, CD_2Cl_2) δ = 192.1 (s, carbene), 162.4 (s, CO), 148.4 (brs, Acr), 147.5 (s, Dipp), 146.2 (brs, Acr), 139.5 (s, Dipp), 134.6 (brs, Acr), 130.2 (s, Acr para-C), 129.0 (brs, Acr), 127.1 (s, Dipp), 127.0 (brs, Acr), 126.2 (brs, Acr), 124.8 (s, Dipp), 92.2 (s, C_{apical}), 29.1 (s, ^{iPr}CH), 24.7 (s, CH_3, Dipp), 24.0 (s, CH_3, Dipp), 9.7 (s, $CH_{3,\ apical}$) ppm, MS (MALDI-TOF, DCM) m/z = 509.2 (NHC-Cu-H$^+$), 688.3 (NHC-Cu-(acr)-H$^+$), 1017.4 ((NHC-Cu)$_2$-H$^+$), 1196.5 ((NHC-Cu)$_2$-(acr)-H$^+$), Elem. anal. calcd. for $C_{42}H_{46}CuN_3O_2$: C 73.28; H 6.74; N 6.10, Found C 73.28; H 7.01; N 5.98.

1-Cu-(triphenyl phosphine) (2e): Starting from 0.093 mmol **[1·Cu]$_n$** (47 mg) and following procedure A*, this complex is isolated in 99 % yield as a white solid. Crystals suitable for XRD studies were obtained by slow evaporation of a saturated methanol solution. ^{1}H-NMR (300 MHz, CD_3OD) δ = 7.62 – 7.29 (brm, 21H, TPP + Dipp), 4.12 (sept, J_{HH} = 6.8 Hz, 4H, ^{iPr}CH), 1.96 (s, 3H, $CH_{3\ \mathrm{apical}}$), 1.23 (d, J_{HH} = 6.6 Hz, 12H, Dipp CH_3), 1.07 (d, J_{HH} = 6.6 Hz, 12H, Dipp CH_3) ppm, ^{13}C-NMR (75 MHz, CD_3OD) δ = 164.0 (s, CO), 147.4 (s, Dipp), 146.9 (s, Dipp), 139.1 (s, Dipp), 134.8 (s, Dipp), 134.6 (s, Dipp), 132.0 (s, TPP), 131.1 (s, TPP), 130.4 (s, TPP), 130.3 (s, TPP), 125.6 (s, Dipp), 125.5 (s, Dipp), 95.1 (s, C_{apical}), 30.1 (s, ^{iPr}C), 25.1 (s, Dipp CH_3), 24.2 (s, Dipp CH_3), 9.3 (s, $CH_{3,\ \mathrm{apical}}$) ppm, ^{31}P-NMR (121 MHz, CD_3OD) δ = 32.4 (s, TPP) ppm, MS (MALDI-TOF, DCM) m/z = 771.3 (NHC-Cu-(TPP)-H^+), 1281.5 ((NHC-Cu)$_2$-(TPP)-H^+), 1789.7 ((NHC-Cu)$_3$-(TPP)-H^+), 2298.0 ((NHC-Cu)$_4$-(TPP)-H^+), Elem. anal. calcd. for $C_{47}H_{52}CuN_2O_2P$: C 73.17; H 6.79; N 3.63, Found C 72.91; H 6.65; N 3.64. *The general procedure was modified in that 6 ml of dichloromethane and 1 ml of methanol was used as solvent.

1-Cu-(pyridine)$_2$ (3a): Starting from 0,20 mmol **[1·Cu]$_n$** (102 mg) and following procedure B with 10 eq. of pyridine, this complex is isolated in 91 % yield as a white solid. Crystals suitable for XRD studies were obtained by slow diffusion of diethyl ether in a saturated methanol solution containing excess pyridine. ^{1}H-NMR (300 MHz, CD_3CN) δ = 8,48 – 8,43 (m, 4H, $H_{\mathrm{Py,\ ortho}}$), 7,75 (tt, $^3J_{HH}$ = 7,7 Hz, $^4J_{HH}$ = 1,8 Hz, 2H, $H_{\mathrm{Py,\ para}}$), 7,40 – 7,30 (m, 6H, $H_{\mathrm{Dipp,\ para}}$ + $H_{\mathrm{Py,\ meta}}$), 7,27 – 7,22 (m, 4H, $H_{\mathrm{Dipp,\ meta}}$), 2,88 (sept, $^3J_{HH}$ = 6,7 Hz, 4H, CH_{iPr}), 1,78 (s, 3H, $CH_{3\ \mathrm{apical}}$), 1,19 (d, $^3J_{HH}$ = 6,8 Hz, 12H, $CH_{3\ \mathrm{iPr}}$), 1,15 (d, $^3J_{HH}$ = 6,9 Hz, 12H, $CH_{3\ \mathrm{iPr}}$) ppm, ^{13}C-NMR (75 MHz, CD_3CN) δ = 197,6 (s, Carbene), 163,7 (s, C=O), 150,4 (s, Ar), 146,5 (s, Ar), 139,2 (s, Ar), 137,3 (s, Ar), 129,8 (s, Ar), 124,8 (s, Ar), 124,7 (s, Ar), 93,8 (s, C_{apical}), 29,4 (s, CH_{iPr}), 24,7 ($CH_{3\ iPr}$), 24,3 (s, $CH_{3\ \mathrm{iPr}}$), 10,0 (s, $CH_{3\ \mathrm{apical}}$) ppm, MS (MALDI-TOF, DCM) m/z = 509.3 (NHC-Cu-H^+), 588.4 (NHC-Cu-Py-H^+), 1017.6 (NHC-Cu-H)$_2^+$, 1528.0 (NHC-Cu-H)$_3^+$, Elem. anal. calcd. for $C_{39}H_{47}CuN_4O_2$: C 70.19; H 7.10; N 8.40, Found: C 69,95; H 7,08; N 8,15.

1-Cu-(4-formyl pyridine)$_2$ (3b): Starting from 0.20 mmol **[1·Cu]$_n$** (102 mg) and following procedure B with 50 eq. of 4-formyl pyridine, this complex is isolated in 82 % yield as an orange solid. Crystals suitable for XRD studies were obtained by cooling down a saturated solution in dichloromethane with excess of ligand to -20 °C. Elem. anal. calcd. for $C_{41}H_{47}CuN_4O_4$: C 68.07; H 6.55; N 7.75, Found C 67.89; H 6.39; N 7.63. NOTE: Due to fast degradation in solution, ^{1}H-NMR, ^{13}C-NMR and mass spectrometry data is not available.

1-Cu-(4-acetyl pyridine)$_2$ (3c): Starting from 0.20 mmol **[1·Cu]$_n$** (102 mg) and following procedure B with 30 equivalents of 4-acetyl pyridine, this complex is isolated in 72 % yield as a yellow solid. Crystals suitable for XRD studies were obtained by slow evaporation of a saturated dichloromethane solution with excess ligand. Elem. anal. calcd. for $C_{43}H_{51}CuN_4O_4$: C 68.73; H 6.84; N 7.46, Found C 68.71; H 6.64; N 7.39. NOTE: Due to fast degradation in solution, ^{1}H-NMR, ^{13}C-NMR and mass spectrometry data is not available.

1-Cu-(2-acetyl pyridine) (3d): Starting from 0.10 mmol **[1·Cu]$_n$** (51 mg) and following procedure B* with 20 equivalents of 2-acetyl pyridine, this complex is isolated in 89 % yield as a dark-red solid. Crystals suitable for XRD studies were obtained by slow evaporation of a saturated dichloromethane solution with excess ligand and a few drops of methanol. MS (MALDI-TOF, DCM) m/z = 509.1 (NHC-Cu-H$^+$), 630.3 (NHC-Cu-(2-AcPy)-H$^+$), 1017.4 (NHC-Cu-H)$_2$$^+$, 1527.6 (NHC-Cu-H)$_3$$^+$, MS (HR-ESI, DCM) calcd. m/z = 630.2751, found m/z = 630.2755 (NHC-Cu-(2-acpy)-H)$^+$. *The general procedure was modified in that 6 ml of dichloromethane and 1 ml of methanol was used as solvent. NOTE: Due to fast degradation in solution, ^{1}H-NMR and ^{13}C-NMR data is not available.

1-Cu-(2,2'-bipyridine) (3e): Starting from 0.10 mmol **[1·Cu]$_n$** (51 mg) and following procedure A, this complex is isolated in 93 % yield as a yellow solid. Crystals suitable for XRD studies were obtained by layering a saturated dichloromethane solution with *n*-hexane. ^{1}H-NMR (300 MHz, CD_2Cl_2) δ = 7.92 (d, 2H, $^3J_{HH}$ = 8.1 Hz, NCH_{Bipy}), 7.82 (dt, J_{HH} = 7.7/1.6 Hz, Bipy), 7.42 – 7.35 (m, 2H, $H_{Dipp, para}$), 7.26 – 7.22 (m, 4H, $H_{Dipp, para}$), 7.21 – 7.16 (m, 2H, Bipy), 6.79 (d, J_{HH} = 4.9 Hz, N-C^C-CH_{Bipy}), 3.14 (sept, J_{HH} = 7.0 Hz, 4H, ^{iPr}CH), 1.94 (s, 3H, $CH_{3, apical}$), 1.22 (d, J_{HH} = 6.9 Hz, 12H, $CH_{3, Dipp}$), 1.05 (d, J_{HH} = 6.9 Hz, 12H, $CH_{3, Dipp}$) ppm, ^{13}C-NMR (75 MHz, CD_2Cl_2) δ = 163.1 (s, CO), 151.4 (s, Bipy), 150.8 (s, Bipy), 147.0 (s, Bipy), 141.6 (s, Dipp), 139.3 (s, Dipp), 128.8 (s, Bipy), 125.6 (s, Dipp), 124.4 (s, Dipp), 121.0 (s, Bipy), 91.5 (s, C_{apical}), 28.9 (s, ^{iPr}C), 24.2 (s, $CH_{3, Dipp}$), 23.9 (s, $CH_{3, Dipp}$), 9.7 (s, $CH_{3, apical}$) ppm, MS (MALDI-TOF, DCM) m/z = 665.2 (NHC-Cu-(bipy)-H)$^+$, 1173.5 ((NHC-Cu)$_2$-(bipy)-H)$^+$, Elem. anal. calcd. for $C_{39}H_{45}CuN_4O_2$: C 70.40; H 6.82; N 8.42, Found C 70.44; H 6.89; N 8.41.

7.2.6 Supplementary Information

NMR-Data

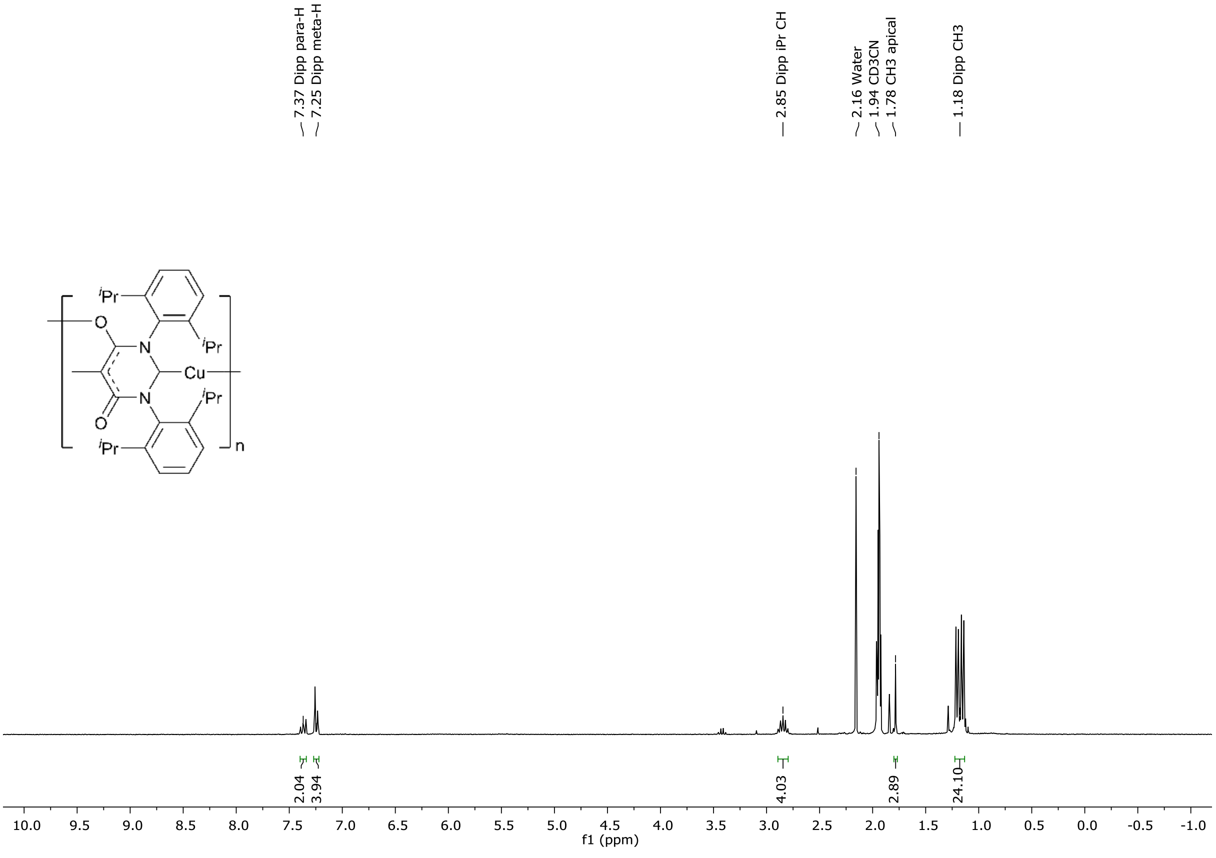

Figure S7.43. ^{1}H NMR spectrum of **[1·Cu]$_n$** in CD$_3$CN.

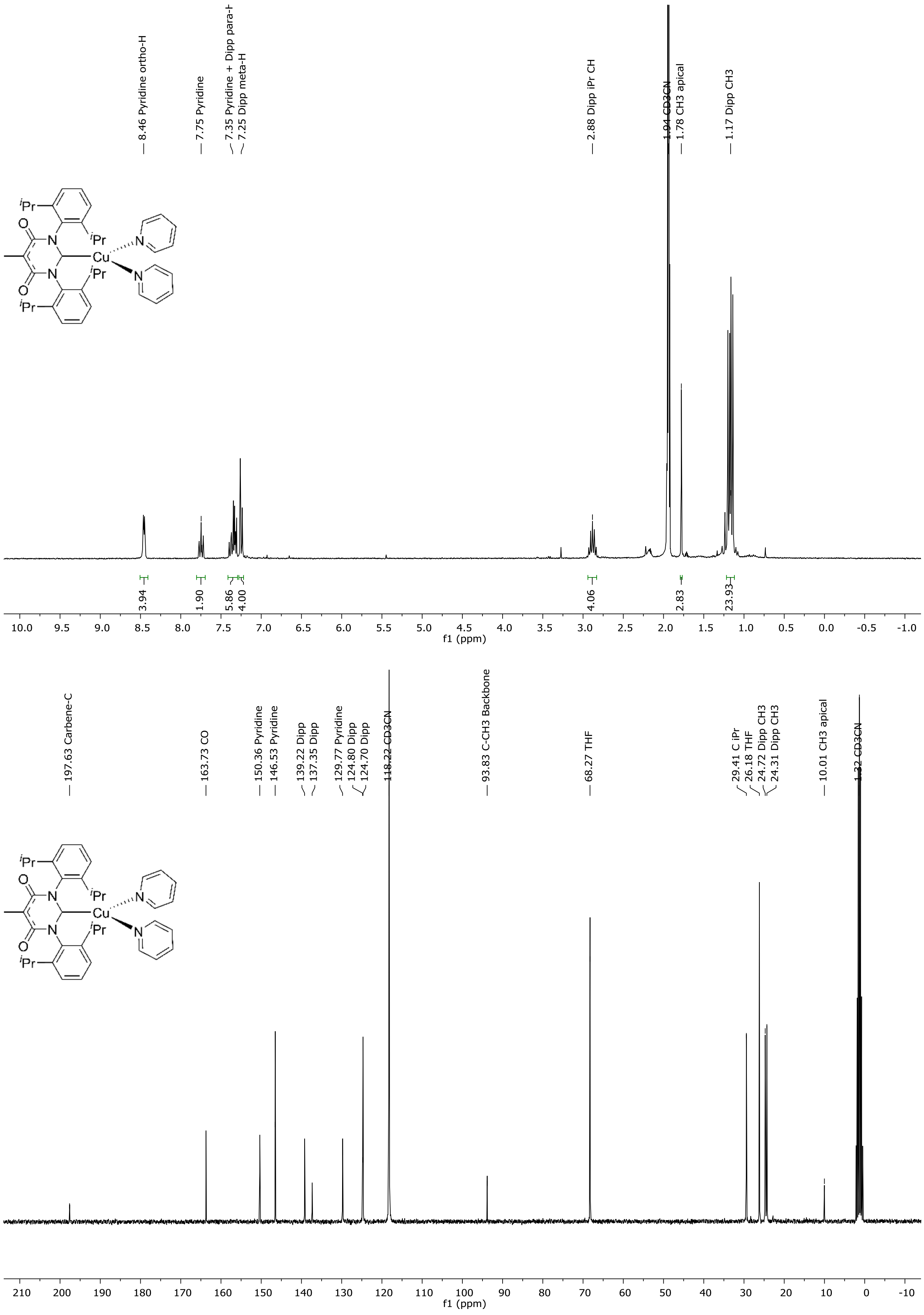

Figure S7.44. ^{1}H NMR spectrum (top) and $^{13}C\{^{1}H\}$ NMR spectrum (bottom) of **3a** in CD_3CN.

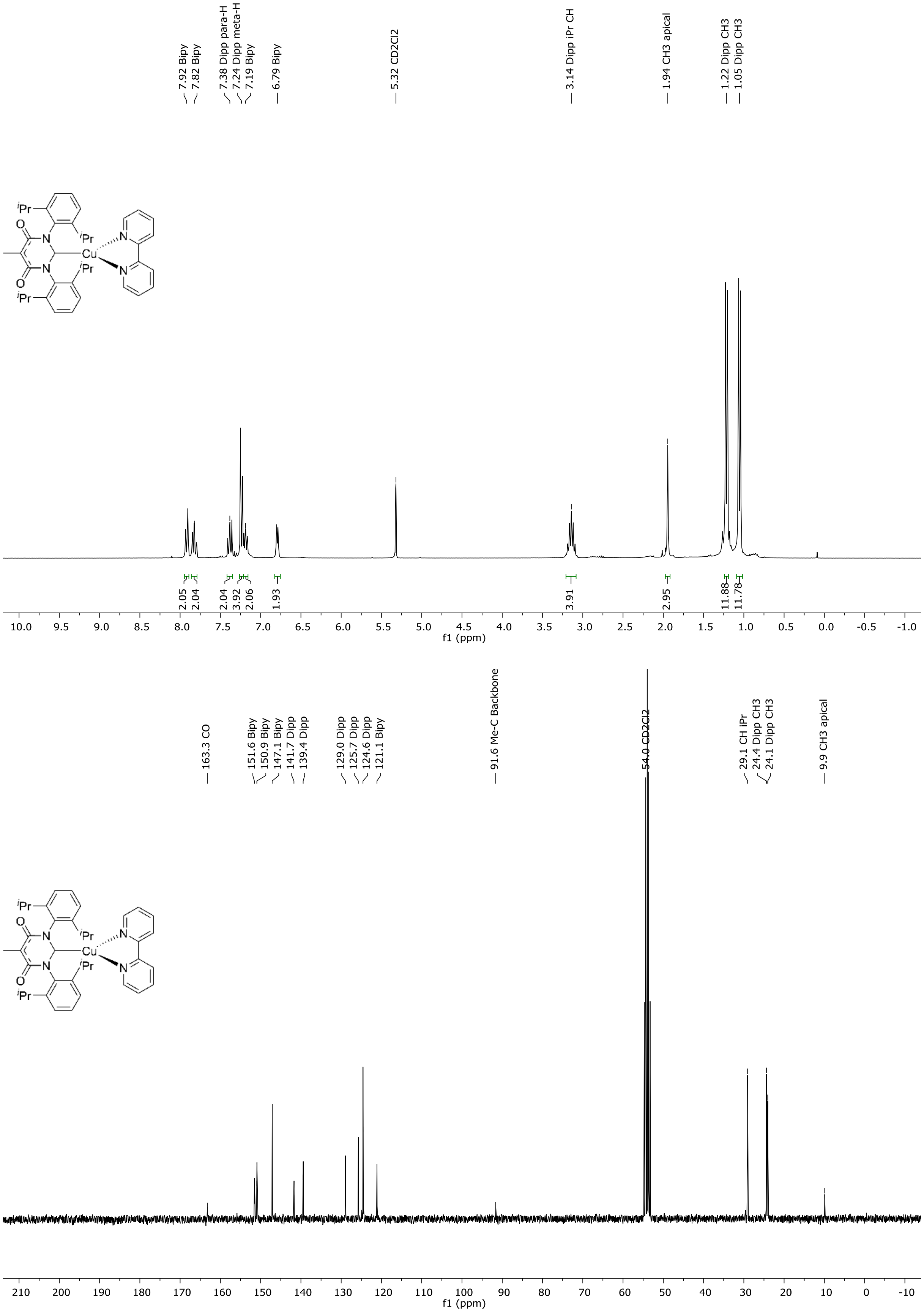

Figure S7.45. ^{1}H NMR spectrum (top) and ^{13}C{^{1}H} NMR spectrum (bottom) of **3e** in CD_2Cl_2.

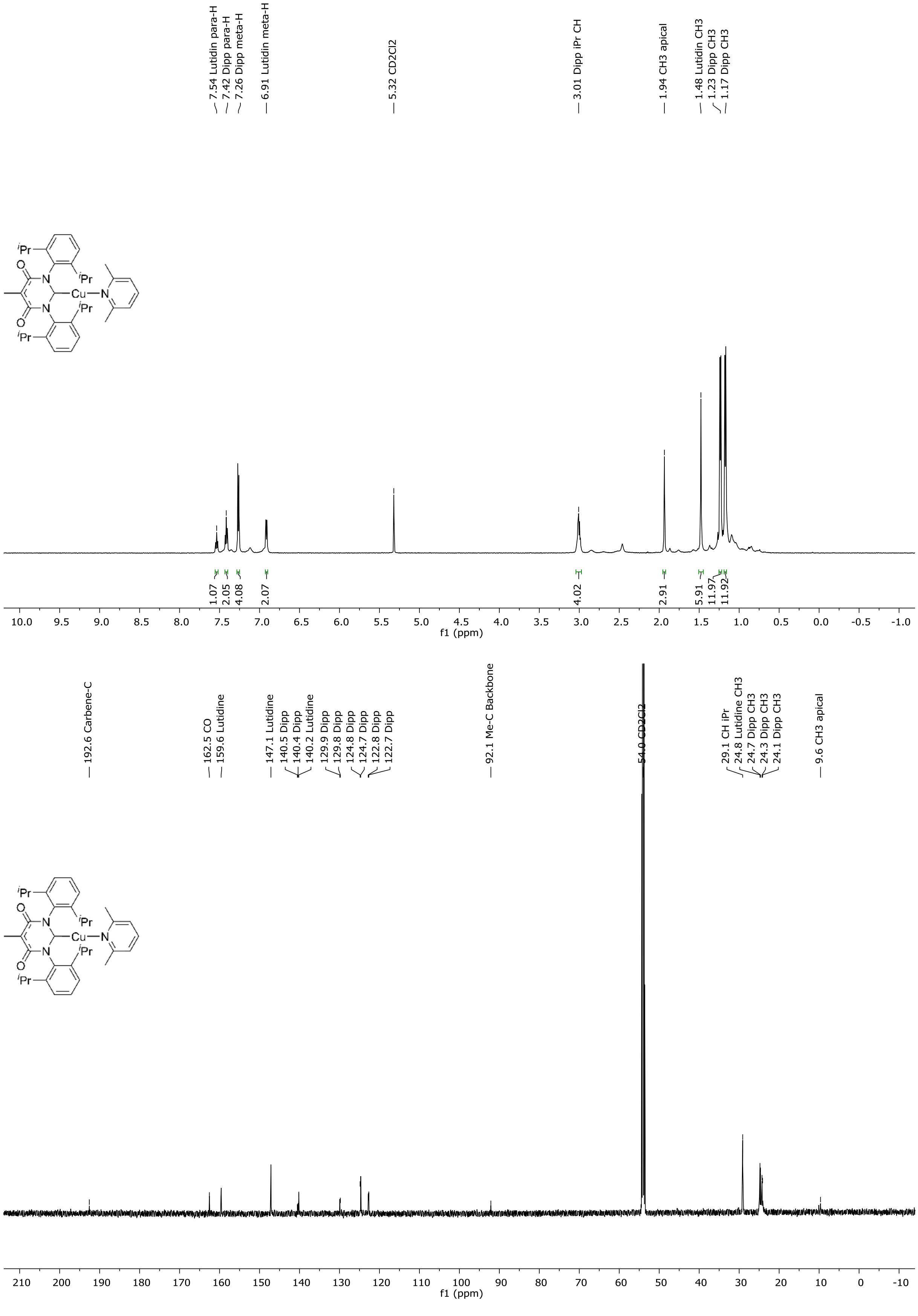

Figure S7.46. ^{1}H NMR spectrum (top) and ^{13}C{^{1}H} NMR spectrum (bottom) of **2a** in CD_2Cl_2.

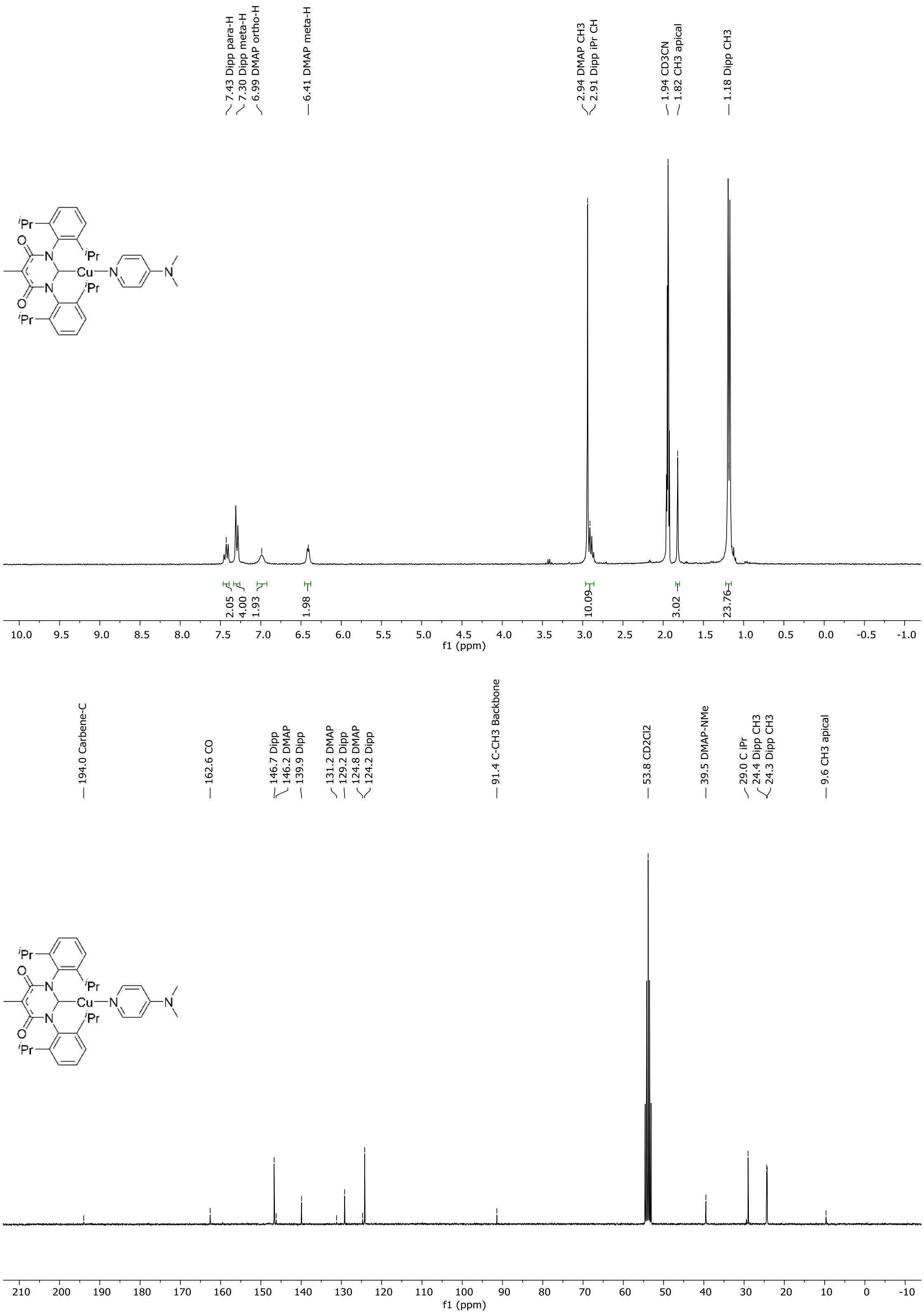

Figure S7.47. ^{1}H NMR spectrum (top) in CD_3CN and $^{13}C\{^1H\}$ NMR spectrum (bottom) in CD_2Cl_2 of **2c**.

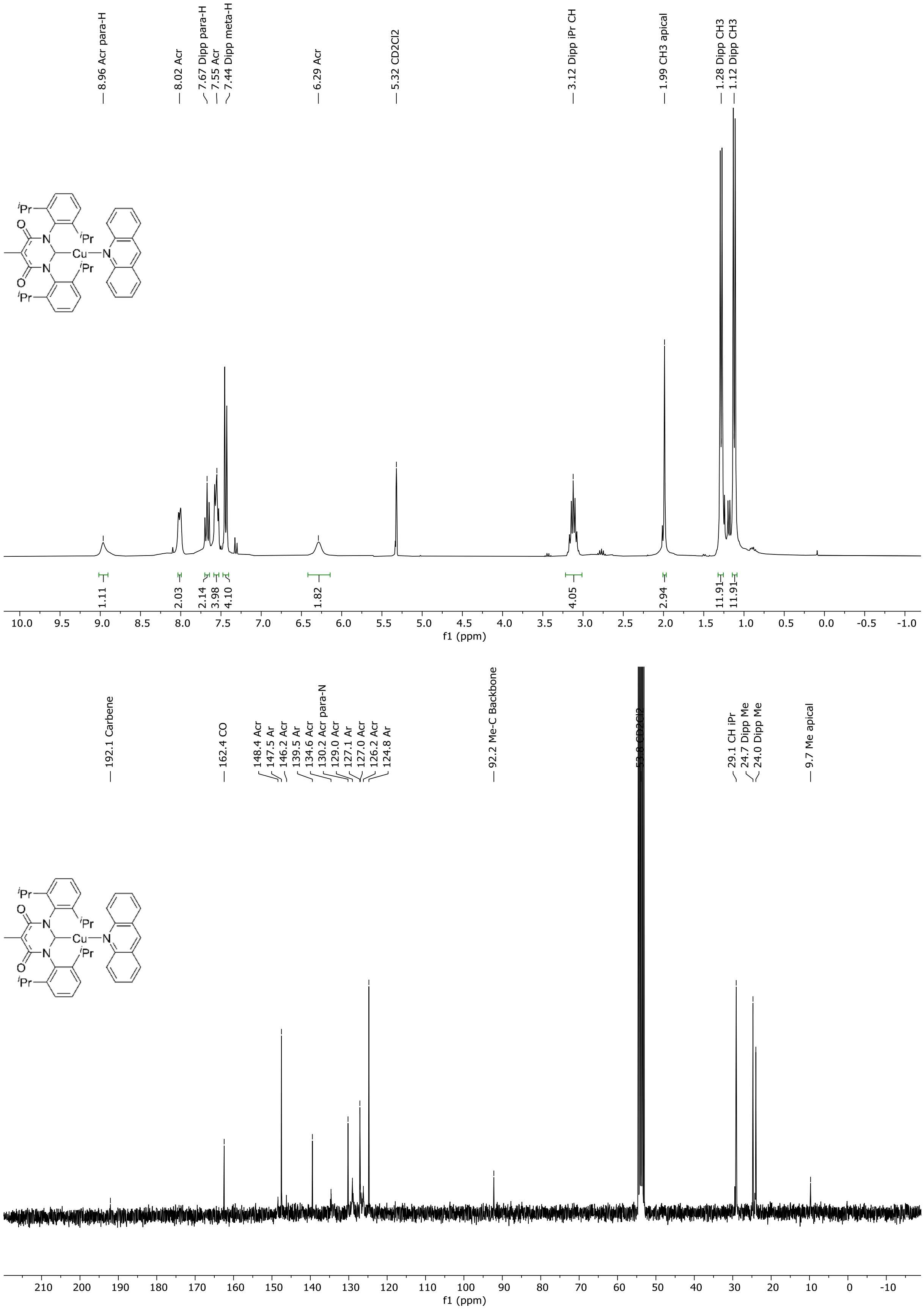

Figure S7.48. ^{1}H NMR spectrum (top) and $^{13}C\{^1H\}$ NMR spectrum (bottom) of **2d** in CD_2Cl_2.

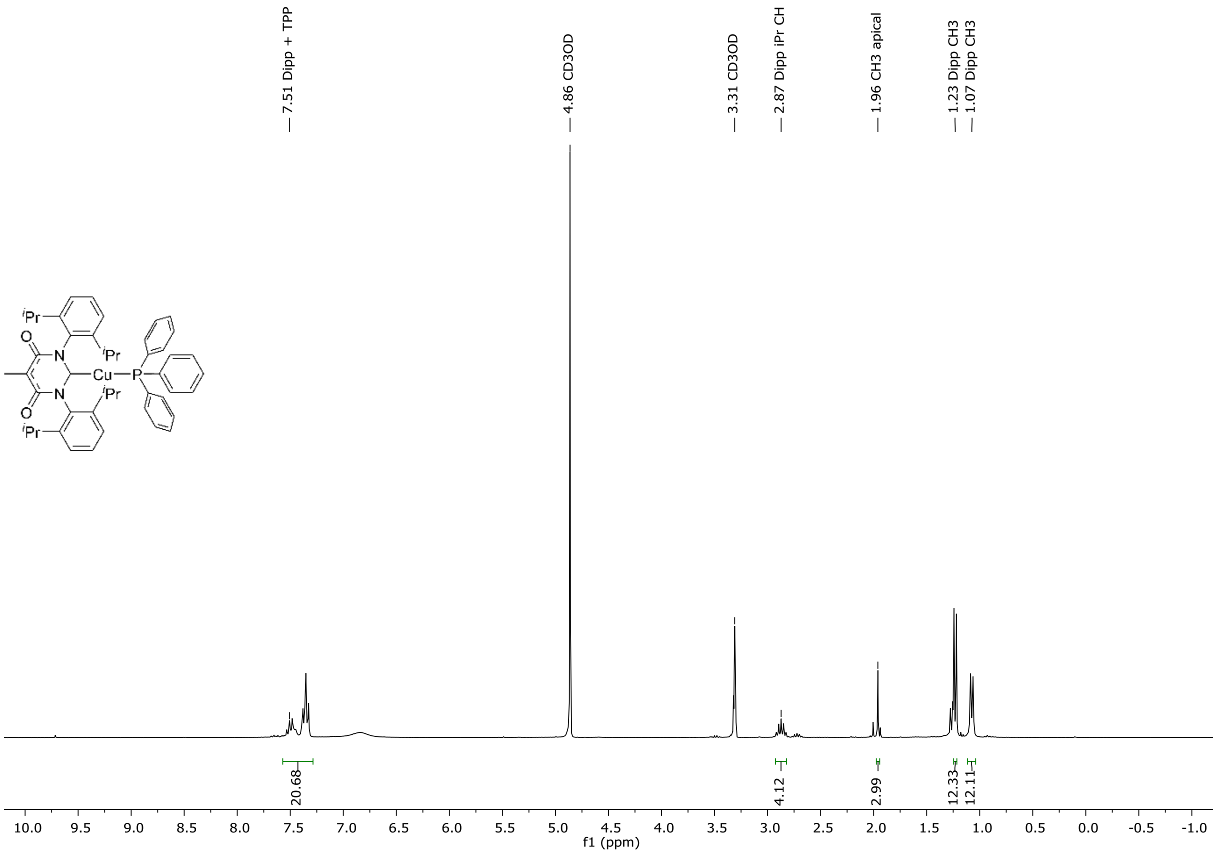

7.51 Dipp + TPP
4.86 CD3OD
3.31 CD3OD
2.87 Dipp iPr CH
1.96 CH3 apical
1.23 Dipp CH3
1.07 Dipp CH3
20.68
4.12
2.99
12.33
12.11
10.0
9.5
9.0
8.5
8.0
7.5
7.0
6.5
6.0
5.5
5.0
4.5
4.0
3.5
3.0
2.5
2.0
1.5
1.0
0.5
0.0
-0.5
-1.0
f1 (ppm)
^{i}Pr
O
N
Cu
P
^{i}Pr
N
^{i}Pr
O
^{i}Pr

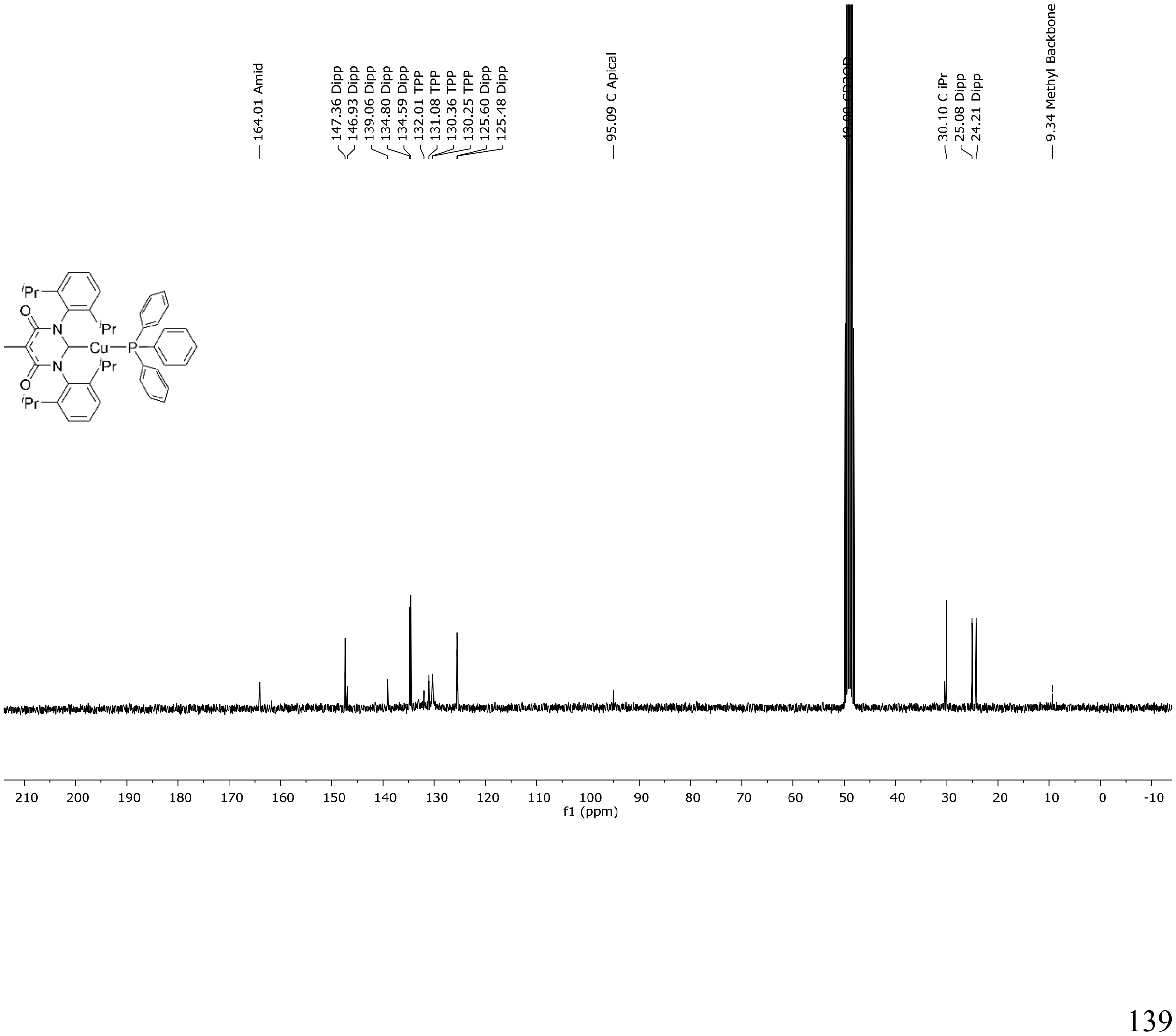

164.01 Amid
147.36 Dipp
146.93 Dipp
139.06 Dipp
134.80 Dipp
134.59 Dipp
132.01 TPP
131.08 TPP
130.36 TPP
130.25 TPP
125.60 Dipp
125.48 Dipp
95.09 C Apical
49.00 CD3OD
30.10 C iPr
25.08 Dipp
24.21 Dipp
9.34 Methyl Backbone
210
200
190
180
170
160
150
140
130
120
110
100
90
80
70
60
50
40
30
20
10
0
-10
f1 (ppm)
^{i}Pr
O
N
Cu
P
^{i}Pr
N
^{i}Pr
O
^{i}Pr

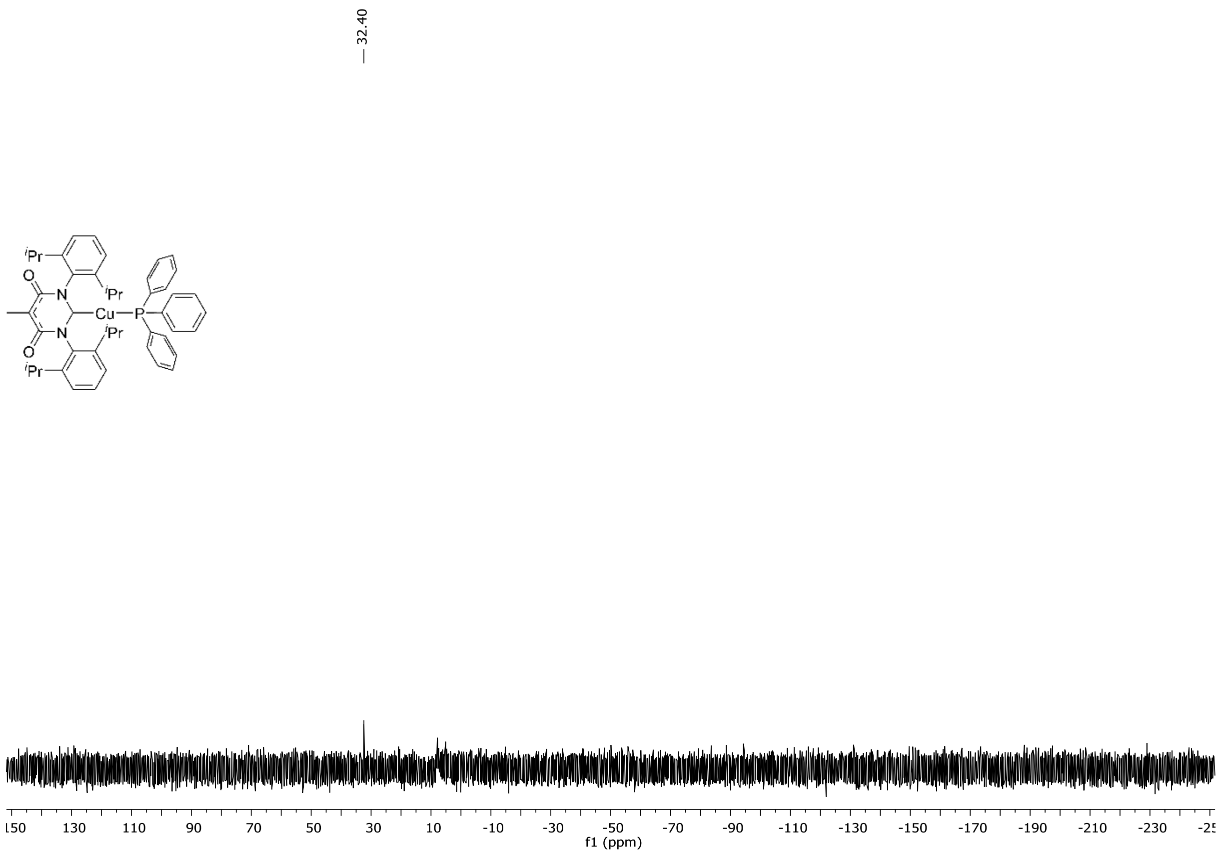

Figure S7.49. ^{1}H NMR spectrum (top), ^{13}C{^{1}H} NMR spectrum (middle) and ^{31}P{^{1}H} NMR spectrum (bottom) of **2e** in CD_3OD.

Crystallographic Data

Compound	**3a**	**3b**	**3c**	**3d**
Ligand	**pyridine**	**4-formyl pyridine**	**4-acetyl pyridine**	**2-acetyl pyridine**
CCDC No.	2256219	2256220	2256222	2256223
Empirical formula	$C_{19.5}H_{23.5}Cu_{0.5}N_2O$	$C_{20.5}H_{23.5}Cu_{0.5}N_2O_2$	$C_{43}H_{51}CuN_4O_4$	$C_{36}H_{44}CuN_3O_3$
Formula weight [g/mol]	333.67	361.68	751.41	630.28
Crystal shape and colour	block, colourless	block, yellow	block, yellow	block, yellow
Size [mm^3]	0.1 × 0.1 × 0.05	0.1 × 0.05 × 0.05	0.3 × 0.1 × 0.1	0.1 × 0.1 × 0.1
Temperature [K]	140	100	100	100
Crystal system	monoclinic	monoclinic	orthorhombic	monoclinic
Space group	$C2/c$	$C2/c$	$P2_12_12_1$	$P2_1/c$
Lattice parameters [Å]	a = 15.7393(13) b = 13.6942(11) c = 15.9958(14)	a = 14.8386(2) b = 16.4904(3) c = 15.9004(3)	a = 10.10330(10) b = 18.36820(10) c = 21.4085(2)	a = 14.2718(3) b = 10.7805(2) c = 21.8146(4)
	β = 97.987(4)	β = 101.238(2)		β = 98.305(2)
Volume [Å^3]	3414.2(5)	3816.14(12)	3972.98(6)	3321.13(11)
Z	8	8	4	4
ρ_{calc} [g/cm^3]	1.298	1.259	1.256	1.261
Abs. coeff. [mm^{-1}]	0.680	1.163	1.135	1.224
F(000)	1416.0	1528.0	1592.0	1336.0
2Θ range [°]	3.96 to 57.066	8.102 to 157.15	6.34 to 158.306	6.258 to 157.168
Index ranges	$-21 \leq h \leq 21$ $-18 \leq k \leq 18$ $-21 \leq l \leq 21$	$-16 \leq h \leq 18$ $-19 \leq k \leq 19$ $-19 \leq l \leq 20$	$-12 \leq h \leq 12$ $-21 \leq k \leq 23$ $-25 \leq l \leq 26$	$-21 \leq h \leq 21$ $-18 \leq k \leq 18$ $-21 \leq l \leq 21$
Reflections collected	27050	14598	72398	24404
Independent reflections	4284	3754	8012	6551
Final R-value ($I>2\sigma(I)$)[a]	R_1 = 0.0438 wR_2 = 0.1142	R_1 = 0.0349 wR_2 = 0.0950	R_1 = 0.0347 wR_2 = 0.0948	R_1 = 0.0545 wR_2 = 0.1423
R-value (whole data)[a]	R_1 = 0.0540 wR_2 = 0.1191	R_1 = 0.0373 wR_2 = 0.0969	R_1 = 0.0355 wR_2 = 0.0955	R_1 = 0.0623 wR_2 = 0.1465
Completeness	99.5	100	100	99.8
Data/restraints/ parameters	4284/0/215	3754/0/233	8012/139/481	6551/0/398
Flack parameter	-	-	-0.022(6)	-
Goodness-of-fit on F^2[b]	1.068	1.083	1.041	1.048

Compound	3e	2a	2b	2c*
Ligand	**2,2'-bipyridine**	**2,6-lutidine**	**4-formyl-2,6-lutidine**	**4-dimethylamino pyridine**
CCDC No.	2256224	2256225	2256226	2256227
Empirical formula	$C_{39}H_{45}CuN_4O_2 \cdot CH_2Cl_2$	$C_{72}H_{92}Cu_2N_6O_4$	$C_{37}H_{46}CuN_3O_3$	$C_{18}H_{23.5}Cu_{0.5}N_2O$
Formula weight [g/mol]	750.25	1232.59	644.31	148.54
Crystal shape and colour	block, yellow	block, colourless	plate, yellow	block, colourless
Size [mm^3]	0.31 × 0.16 × 0.12	0.05 × 0.05 × 0.05	0.2 × 0.2 × 0.05	0.1 × 0.1 × 0.05
Temperature [K]	100	100	100	100
Crystal system	monoclinic	triclinic	monoclinic	orthorhombic
Space group	$P2_1/n$	P-1	$P2_1/c$	Pbcm
Lattice parameters [Å]	a = 11.21210(10) b = 21.4513(3) c = 16.3875(2)	a = 11.0787(2) b = 11.1412(2) c = 28.2628(4)	a = 11.4918(3) b = 14.1551(3) c = 21.1762(5)	a = 13.6625(2) b = 20.2132(2) c = 13.88800(10)
	β = 99.5840(10)	α = 90.1010(10) β = 90.8170(10) γ = 106.0810(10)	β = 92.579(2)	
Volume [Å^3]	3886.41(8)	3351.58(10)	3441.19(14)	3835.35(7)
Z	4	2	4	8
ρ_{calc} [g/cm^3]	1.282	1.221	1.244	1.093
Abs. coeff. [mm^{-1}]	2.355	1.177	1.192	1.047
F(000)	1576.0	1312.0	1368.0	1344.0
2Θ range [°]	6.848 to 158.336	6.256 to 158.276	7.514 to 140	6.47 to 158.214
Index ranges	$-8 \le h \le 14$ $-26 \le k \le 24$ $-20 \le l \le 19$	$-13 \le h \le 13$ $-14 \le k \le 14$ $-36 \le l \le 29$	$-13 \le h \le 13$ $-12 \le k \le 17$ $-25 \le l \le 25$	$-17 \le h \le 16$ $-24 \le k \le 25$ $-17 \le l \le 7$
Reflections collected	29297	44491	21990	25518
Independent reflections	7791	13496	6354	4196
Final R-value ($I>2\sigma(I)$)[a]	$R_1 = 0.0378$ $wR_2 = 0.1026$	$R_1 = 0.0603$ $wR_2 = 0.1477$	$R_1 = 0.0683$ $wR_2 = 0.1727$	$R_1 = 0.0380$ $wR_2 = 0.0952$
R-value (whole data)[a]	$R_1 = 0.0404$ $wR_2 = 0.1044$	$R_1 = 0.0657$ $wR_2 = 0.1493$	$R_1 = 0.0838$ $wR_2 = 0.1843$	$R_1 = 0.0392$ $wR_2 = 0.0958$
Completeness	100	99.2	98.9	100
Data/restraints/ parameters	7791/2/471	13496/0/779	6354/0/408	4196/0/237
Flack parameter	-	-	-	-
Goodness-of-fit on F^2[b]	1.086	1.233	1.129	1.124

*__2c__ contained a heavily distorted molecule of acetonitrile. Its electron density was squeezed during refinement.

Compound	**2d**	**2e**
Ligand	**acridine**	**triphenylphosphine**
CCDC No.	2256228	2256230
Empirical formula	$C_{42}H_{46}CuN_3O_2$ • CH_2Cl_2	$C_{47}H_{52}CuN_2O_2P$ • 2 CH_3OH
Formula weight [g/mol]	773.28	835.50
Crystal shape and colour		
Size [mm^3]	0.3 × 0.1 × 0.05	0.1 × 0.05 × 0.05
Temperature [K]	100	100
Crystal system	monoclinic	orthorhombic
Space group	$P2_1/c$	$Pna2_1$
Lattice parameters [Å]	a = 9.0341(2) b = 22.8317(4) c = 19.2670(4)	a = 25.4211(2) b = 12.74610(10) c = 13.64160(10)
	β = 98.822(2)	
Volume [$Å^3$]	3927.07(14)	4420.15(6)
Z	4	4
ρ_{calc} [g/cm^3]	1.308	1.256
Abs. coeff. [mm^{-1}]	2.340	1.390
F(000)	1624.0	1776.0
2Θ range [°]	6.044 to 157.986	6.954 to 158.304
Index ranges	$-11 \le h \le 7$ $-28 \le k \le 25$ $-23 \le l \le 24$	$-31 \le h \le 32$ $-15 \le k \le 16$ $-17 \le l \le 17$
Reflections collected	28594	144848
Independent reflections	7667	9182
Final R-value (I>2σ(I))[a]	$R_1 = 0.0344$ $wR_2 = 0.0868$	$R_1 = 0.0479$ $wR_2 = 0.0865$
R-value (whole data)[a]	$R_1 = 0.0401$ $wR_2 = 0.0898$	$R_1 = 0.0528$ $wR_2 = 0.0876$
Completeness	99.8	100
Data/restraints/ parameters	7667/0/499	9182/1/538
Flack parameter	-	-0.013(8)
Goodness-of-fit on F^2[b]	1.033	1.051

[a] $R_1 = \sum||F_o| - |F_c|| / \sum|F_o|$;

$wR_2 = [\sum w(F_o^2 - F_c^2)2 / \sum wF_o^2]^{1/2}$;

$w = 1 / [\sigma^2 F_o^2 + (aP)^2 + bP]$ with $P = (F_o^2 + 2F_c^2) / 3$.

[b] GooF = $[\sum w(F_o^2 - F_c^2)^2 / (N_R - N_P)]^{1/2}$

with N_R = Number of reflexes and N_P = Number of parameters.

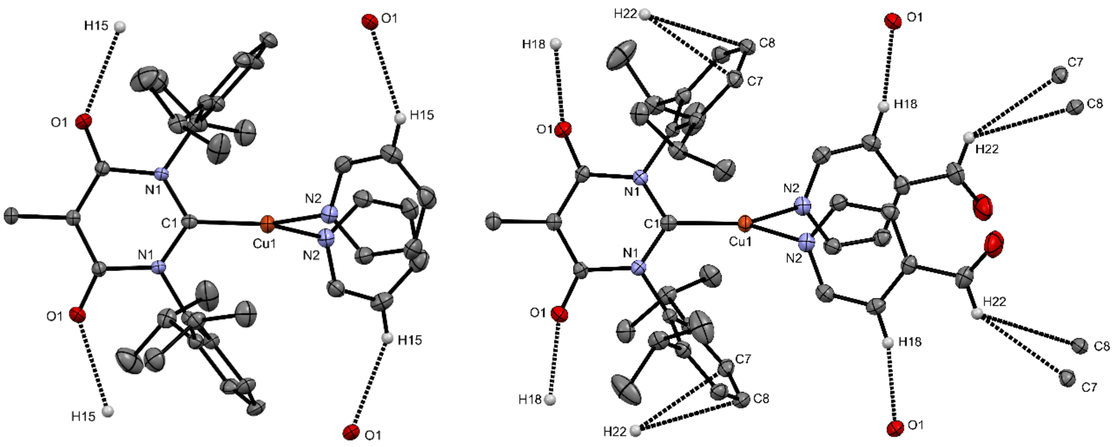

Figure S7.50. Molecular structures of **3a** (left) and **3b** (right) with indication of their involvement in intermolecular close contacts. Non-interacting H-atoms are omitted for clarity, thermal displacement ellipsoids are drawn at the 30 % probability level. Selected bond and contact lengths, the latter are given in *italic* format and without ESD values, since all hydrogen atoms are fixed to geometric positions:

Bond / *Contact*	**in 3a [Å]**	**in 3b [Å]**
C1-Cu1	1.910(2)	1.897(2)
Cu1-N2	2.0462(14)	2.0306(13)
O1-Hx	*H15: 2.474*	*H18: 2.133*
C7-H22	-	*2.745*
C8-H22	-	*2.843*

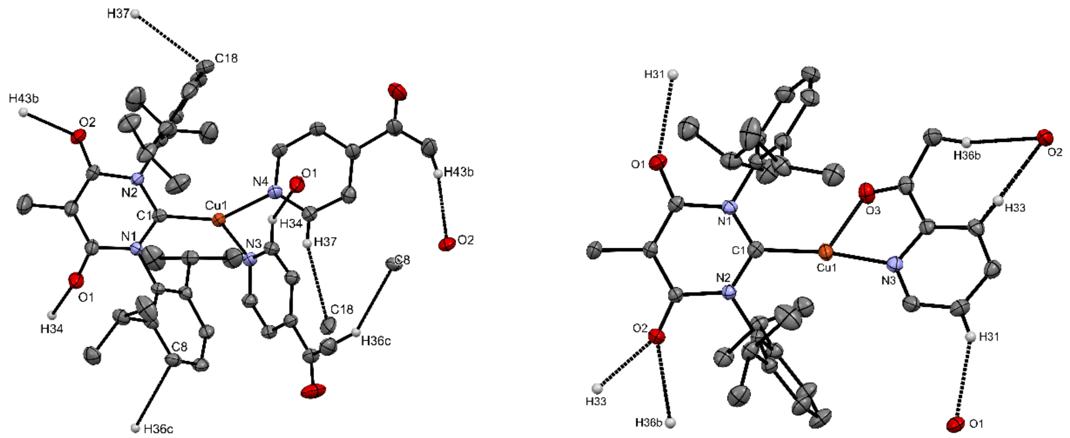

Figure S7.51. Molecular structures of **3c** (left) and **3d** (right) with indication of their involvement in intermolecular close contacts. Non-interacting H-atoms are omitted for clarity, thermal displacement ellipsoids are drawn at the 30% probability level. Selected bond and contact lengths, the latter are given in *italic* format and without ESD values, since all hydrogen atoms are fixed to geometric positions:

Bond / *Contact*	**in 3c [Å]**	**in 3d [Å]**
C1-Cu1	1.927(3)	1.889(3)
Cu1-N3	2.074(2)	1.937(2)
Cu1-N4	2.034(2)	-
Cu1-O3	-	2.2722(19)
O1-Hx	*H34: 2.580*	*H31: 2.399*
O2-Hx	*H43b: 2.303*	*H33: 2.137, H36b: 2.461*
C18-H37	*2.781*	-
C8-H36c	*2.772*	-

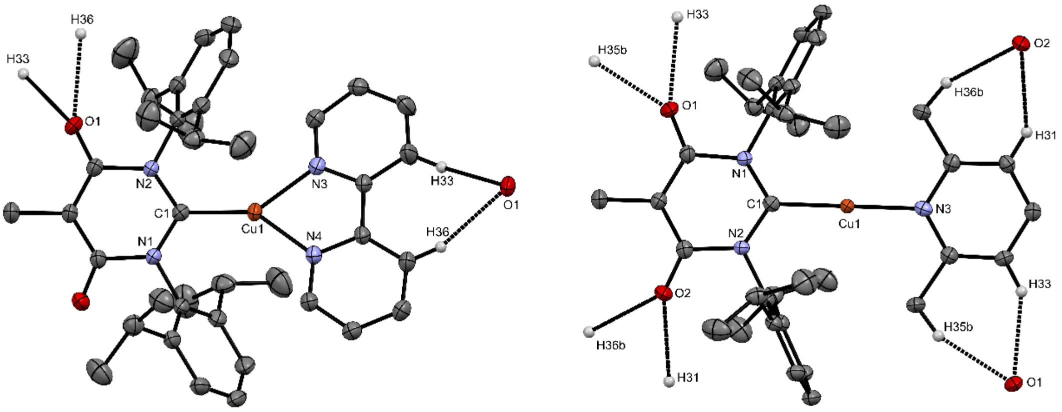

Figure S7.52. Molecular structures of **3e** (left) and **2a** (right, one of two independent molecules is considered) with indication of their involvement in intermolecular close contacts. Non-interacting H-atoms and solvent molecules are omitted for clarity, thermal displacement ellipsoids are drawn at the 30 % probability level. Selected bond and contact lengths, the latter are given in *italic* format and without ESD values, since all hydrogen atoms are fixed to geometric positions:

Bond / *Contact*	**in 3e [Å]**	**in 2a [Å]**
C1-Cu1	1.9051(15)	1.918(3)
Cu1-N3	2.0403(13)	1.928(3)
Cu1-N4	2.0511(13)	-
O1-Hx	*H33: 2.145, H36: 2.352*	*H33: 2.352, H35b: 2.260*
O2-Hx	-	*H31: 2.377, H36b: 2.346*

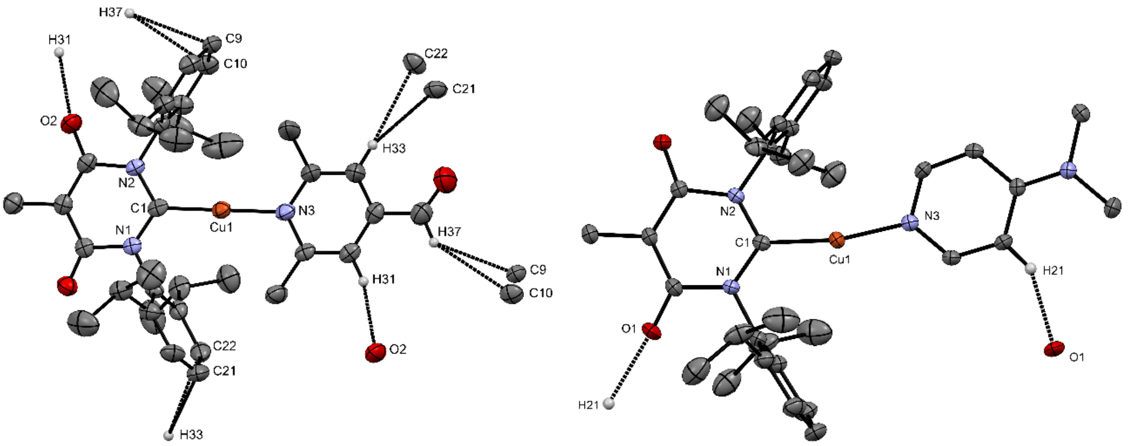

Figure S7.53. Molecular structures of **2b** (left) and **2c** (right) with indication of their involvement in intermolecular close contacts. Non-interacting H-atoms are omitted for clarity, thermal displacement ellipsoids are drawn at the 30 % probability level. Selected bond and contact lengths, the latter are given in *italic* format and without ESD values, since all hydrogen atoms are fixed to geometric positions:

Bond / *Contact*	**in 2b [Å]**	**in 2c [Å]**
C1-Cu1	1.901(4)	1.894(2)
Cu1-N3	1.926(3)	1.8804(19)
O1-H21	-	*2.096*
O2-H31	*2.149*	-
C9-H37	*2.644*	-
C10-H37	*2.767*	-
C21-H33	*2.753*	-
C22-H33	*2.675*	-

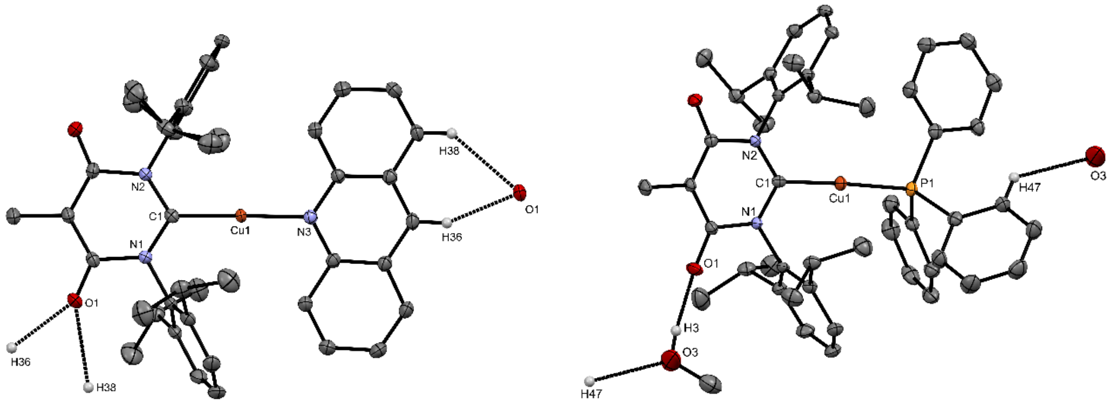

Figure S7.54. Molecular structures of **2d** (left) and **2e** (right) with indication of their involvement in intermolecular close contacts. Non-interacting H-atoms and solvent molecules are omitted for clarity, thermal displacement ellipsoids are drawn at the 30% probability level. Selected bond and contact lengths, the latter are given in *italic* format and without ESD values, since all hydrogen atoms are fixed to geometric positions:

Bond / *Contact*	**in 2d [Å]**	**in 2e [Å]**
C1-Cu1	1.9045(16)	1.927(4)
Cu1-N3	1.9183(13)	-
Cu1-P1	-	2.2027(11)
O1-Hx	*H36: 2.174, H38: 2.488*	*H3: 1.922*
O3-H47	-	*2.491*

PXRD-Data

We investigated the temperature-dependent phase transitions exemplary by obtaining PXRD data on compound **3b** after synthesis and after heating it to 50 °C for 30 min (Figure S7.55). They reveal that the crystal structure must have irreversibly changed upon heating, while an elemental analysis indicated no change in the composition of the compound. We assign this observation to the cleavage of the weak intermolecular contacts.

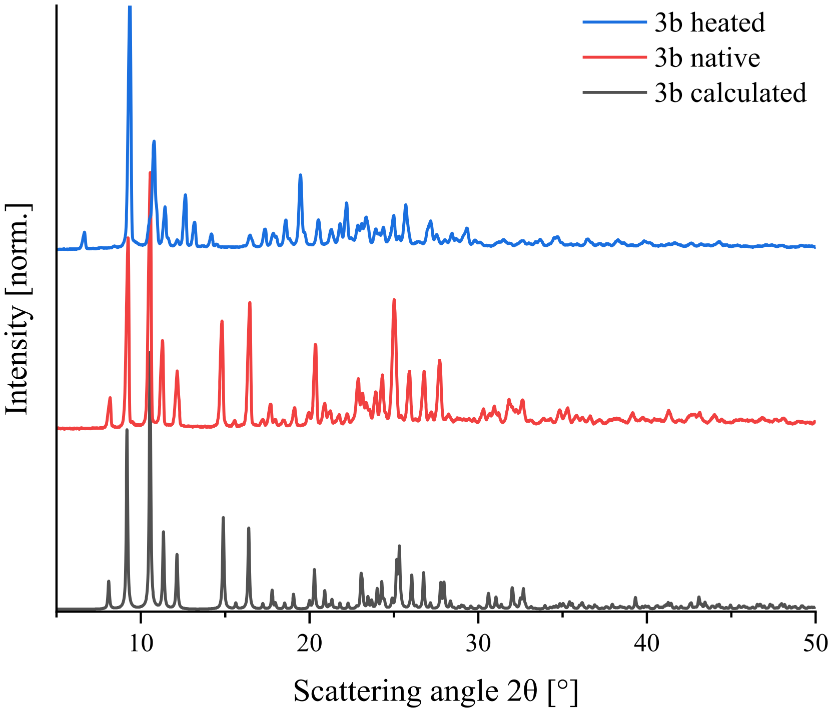

Figure S7.55. PXRD patterns of the same powder samples of **3b** directly after synthesis (red) and after heating it to 50 °C for 30 min (blue), acquired with Cu K_α radiation, in comparison to the simulated pattern according to single crystal structure data (black).

Computational chemistry

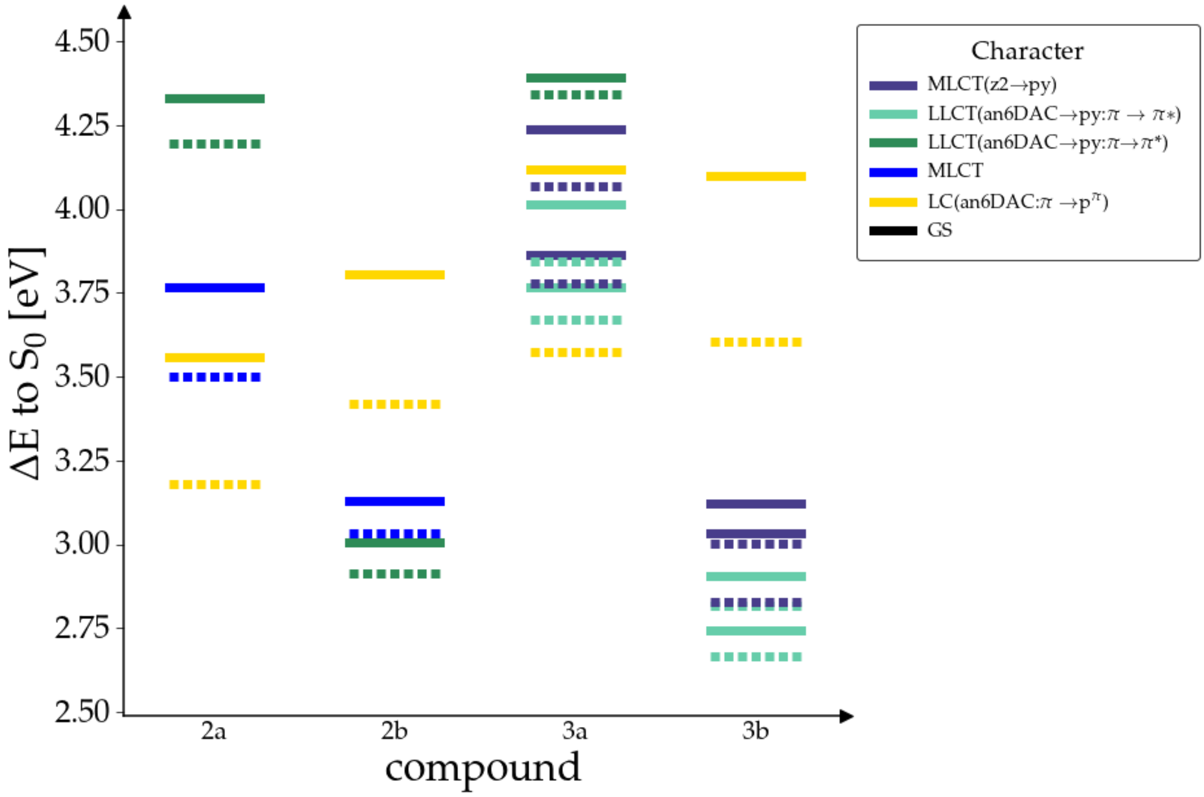

Figure S7.56. Selected vertical excitation energies of the four complexes. In the trigonal complexes, the excited states are strongly mixed. This is indicated with colours close to the pure states (mint green & green / lavender & blue).

Table S7.12. Singlet states and their properties at the ground state geometry of **2a**. The sign of the static electric dipole moment of the states corresponds to the sign of the z-component. The z-axis roughly co-aligns with the C-Cu bond.

state	E [eV]	λ_{abs} [nm]	osc. strength	μ [D]	character
S_0				-19.21	S_0
S1	3.56	349	0.09251	-4.79	LC(NHC)
S2	3.77	329	0.02394	-14.76	MLCT(→py+NHC)
S3	4.33	286	0.00585	6.41	LLCT
S4	4.41	281	0.00218	-15.07	MLCT(→NHC+py)
S5	4.73	262	0.09399	-18.05	LC(py: $\pi\pi$*)
S6	4.73	262	0.00529	-17.22	LC(Ph→Ph*)
S7	4. 80	258	0.00483	-19.16	LC(Ph→Ph*)
S8	4.87	255	0.01983	-12.71	LC(NHC:nπ*)
S9	4.90	253	0.05730	-12.21	LC(NHC:$\pi\pi$*)
S10	5.02	247	0.10468	-13.32	MLCT(→NHC+py)

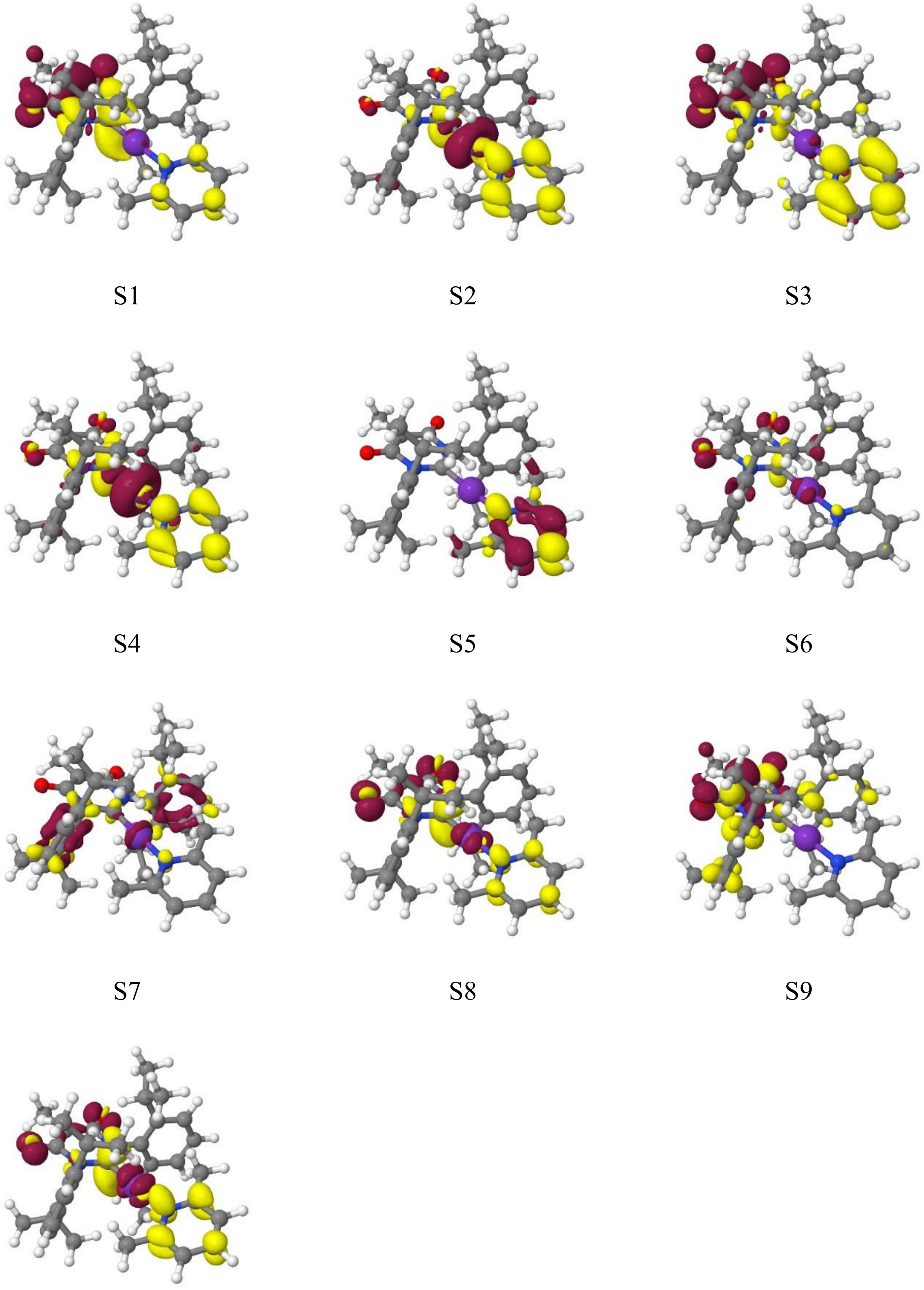

S1 S2 S3

S4 S5 S6

S7 S8 S9

S10

Figure S7.57. Differences of the electron densities (isosurface ± 0.002) between the low-lying excited singlet states and the electronic ground state of **2a** in the Franck–Condon region. For the difference density of the S7, a cut-off of ±0.001 was chosen. For colour codes, see Figure 7.19.

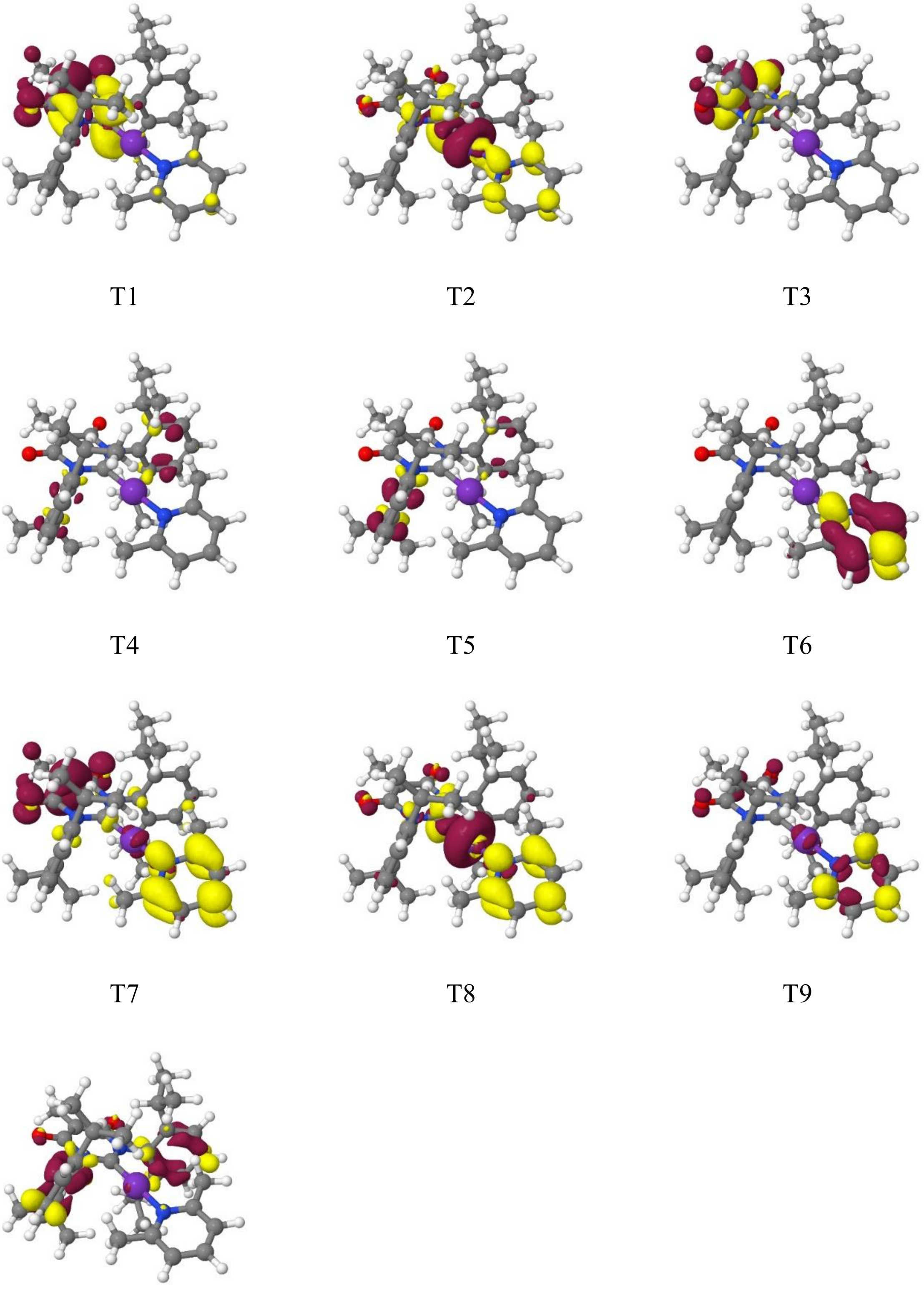

T1 T2 T3

T4 T5 T6

T7 T8 T9

T10

Figure S7.58. Differences of the electron densities (isosurface ± 0.002) between the low-lying excited triplet states and the electronic ground state of **2a** in the Franck–Condon region. For the difference density of the T10, a cut-off of ±0.001 was chosen. For colour codes, see Figure 7.19.

Table S7.7. Singlet states and their properties at the ground state geometry of **2b**. The sign of the static electric dipole moment of the states corresponds to the sign of the z-component. The z-axis roughly coaligns with the C-Cu bond.

state	E [eV]	λ_{abs} [nm]	osc. strength	μ [D]	character
S_0				-16.4	S_0
S1	3.01	412	0.03057	16.47	LLCT
S2	3.13	396	0.00801	2.48	MLCT(→fpy)
S3	3.56	348	0.00000	-21.42	LC(py:nπ*)
S4	3.81	326	0.08037	-4.03	LC(NHC)
S5	4.05	306	0.0951	-11.46	LC(py:ππ*)
S6	4.20	295	0.01486	-18.55	MLCT(→NHC)
S7	4.26	291	0.04309	4.65	LLCT
S8	4.38	283	0.02636	9.06	LLC(Ph→py)
S9	4.39	282	0.01382	13.36	LLC(Ph→py)
S10	4.49	276	0.07359	1.96	MLCT+LC(py)

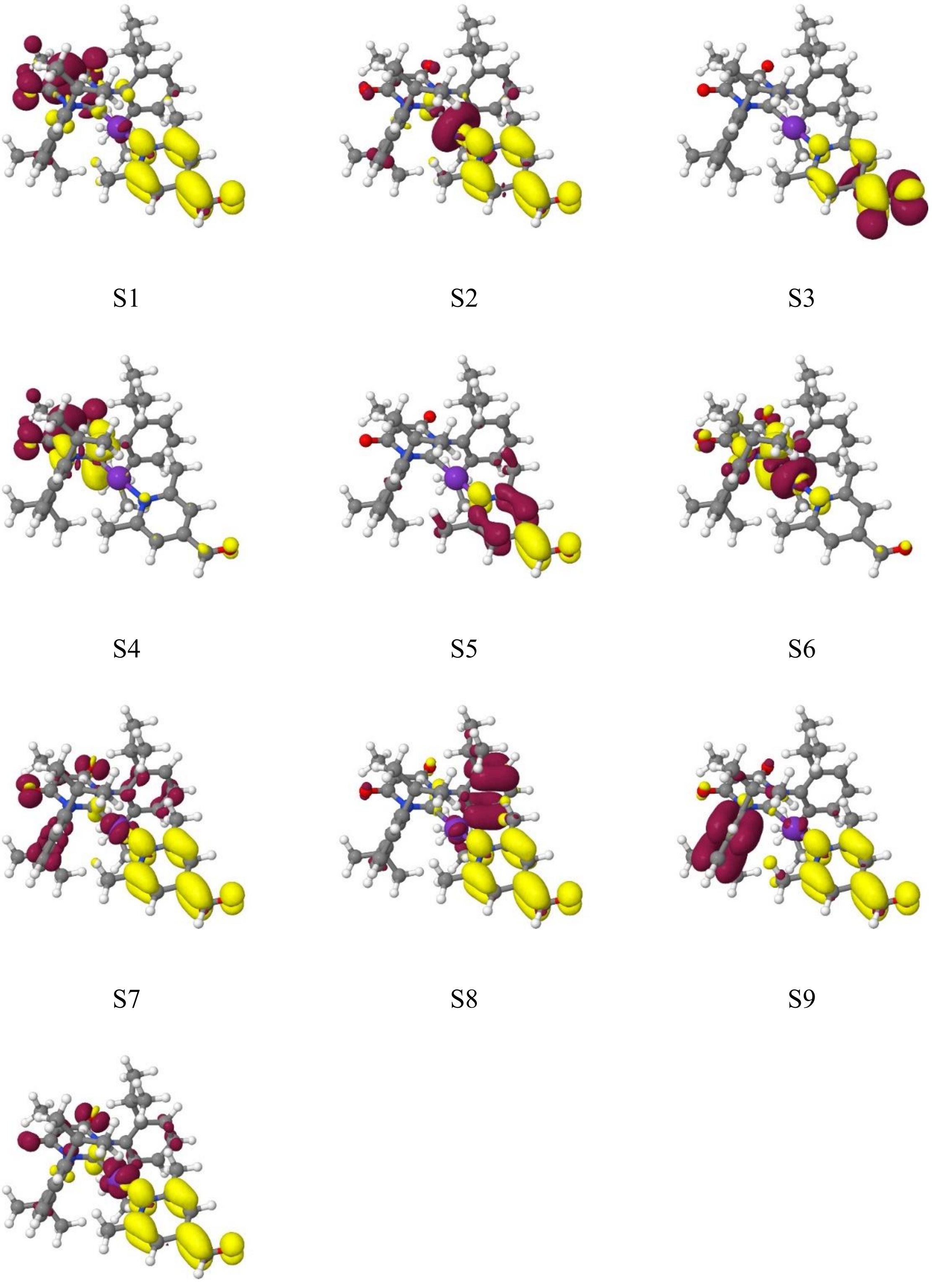

S1 S2 S3

S4 S5 S6

S7 S8 S9

S10

Figure S7.59. Differences of the electron densities (isosurface ± 0.002) between the low-lying excited singlet states and the electronic ground state of **2b** in the Franck–Condon region. For colour codes, see Figure 7.19.

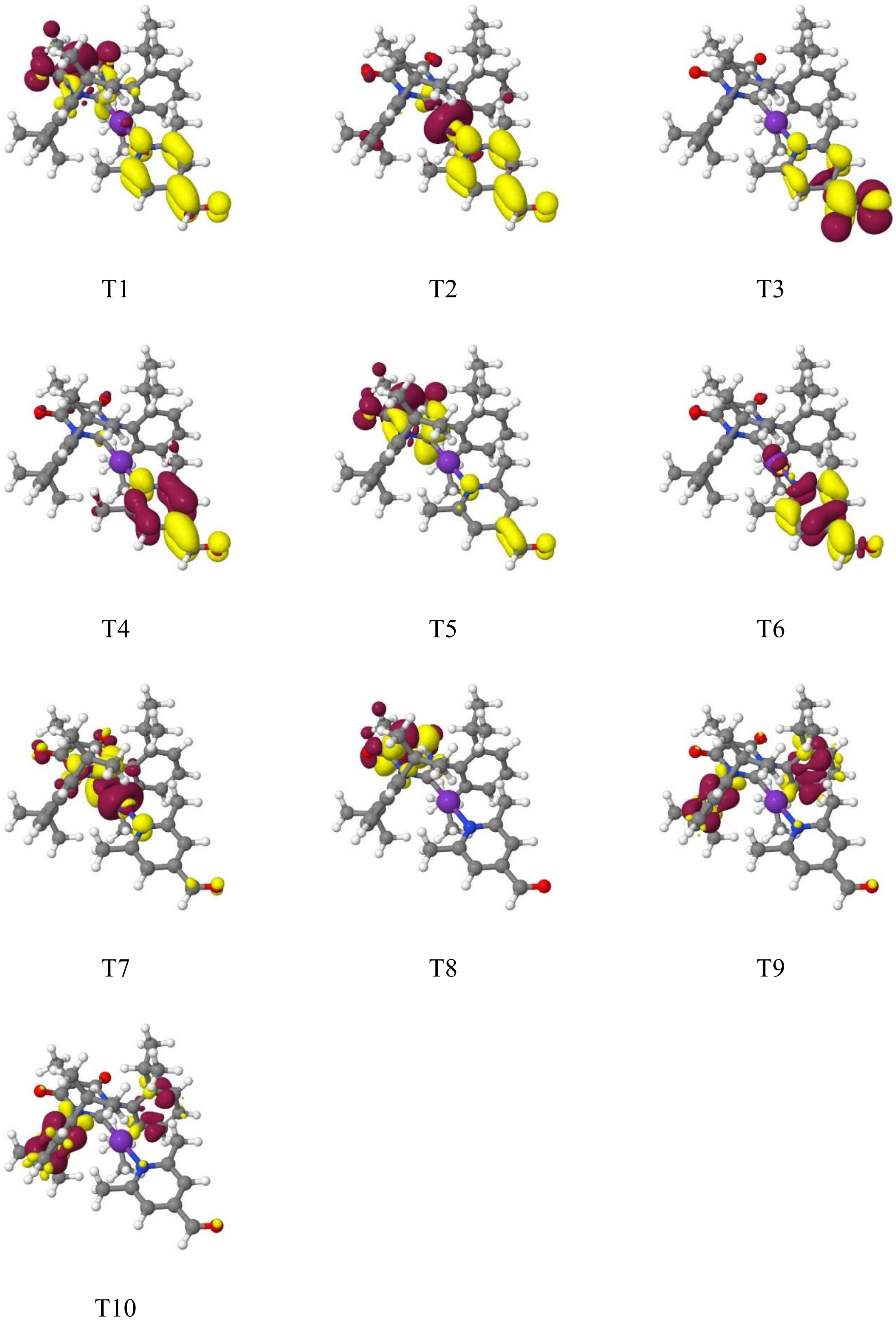

T1 T2 T3

T4 T5 T6

T7 T8 T9

T10

Figure S7.60. Differences of the electron densities (isosurface ± 0.002) between the low-lying excited triplet states and the electronic ground state of **2b** in the Franck–Condon region. For the difference density of the T9 and T10, a cut-off of ±0.001 was chosen. For colour codes, see Figure 7.19.

Table S7.8. Singlet states and their properties at the ground state geometry of **3a**. The sign of the static electric dipole moment of the states corresponds to the sign of the z-component. The z-axis roughly co-aligns with the C-Cu bond.

state	E [eV]	λ_{abs} [nm]	osc. strength	μ [D]	character
S_0				-23.01	S_0
S1	3.77	329	0.00916	-9.41	LLCT+MLCT
S2	3.86	321	0.14889	-12.74	MLCT+LLCT
S3	3.96	313	0.05833	-21.73	MLCT(→NHC)
S4	4.01	309	0.08989	-10.29	LLCT+MLCT
S5	4.12	301	0.02919	-13.1	LC(NHC)
S6	4.24	292	0.01188	-18.09	MLCT+LLCT
S7	4.39	282	0.00707	0.49	LLCT
S8	4.49	276	0.00007	-8.07	LLCT
S9	4.55	273	0.01124	-3.71	LLCT
S10	4.61	269	0.00258	-12.72	MLCT(py)

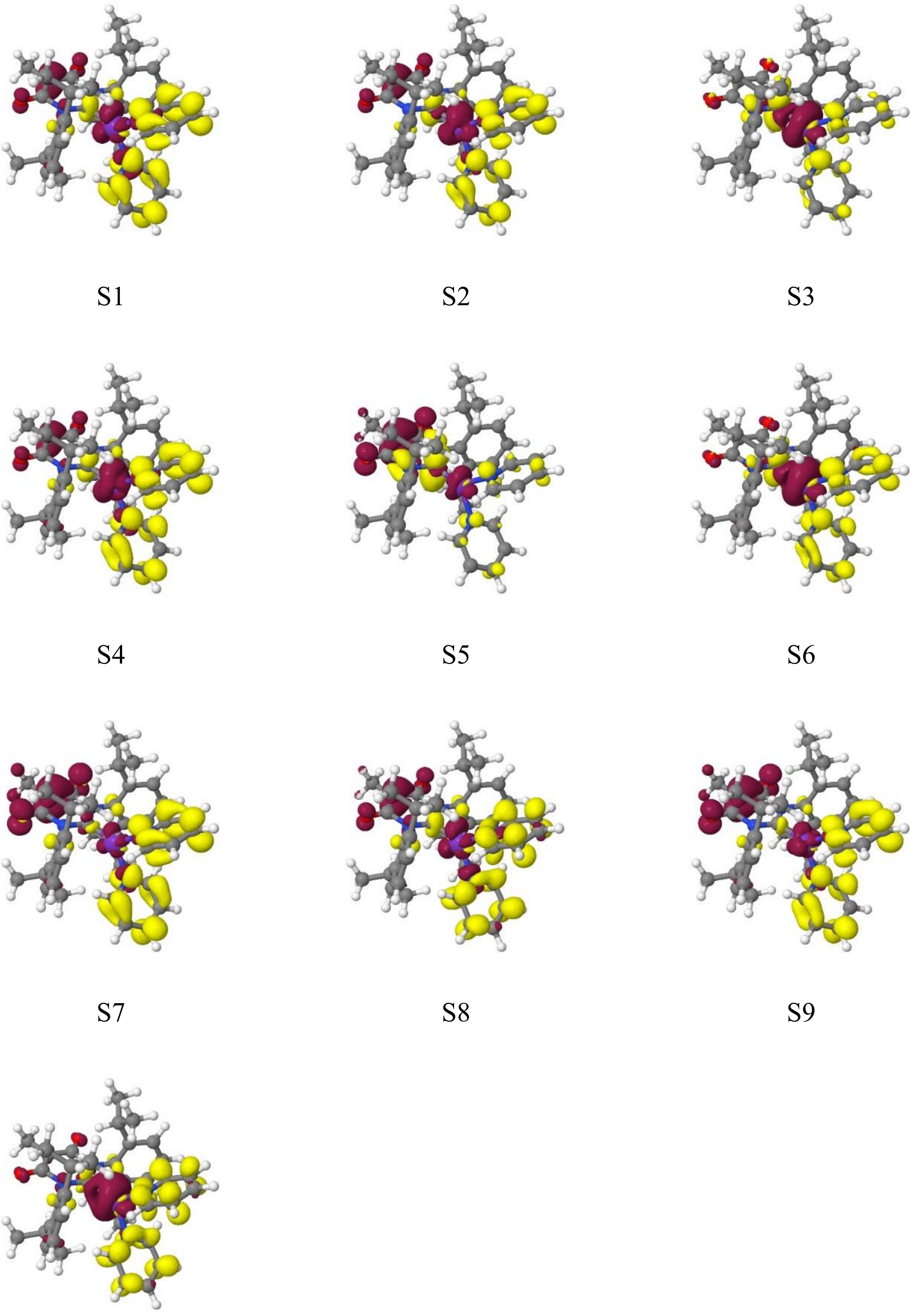

S1 S2 S3

S4 S5 S6

S7 S8 S9

S10

Figure S7.61. Differences of the electron densities (isosurface ± 0.002) between the low-lying excited singlet states and the electronic ground state of **3a** in the Franck–Condon region. For colour codes, Figure 7.19.

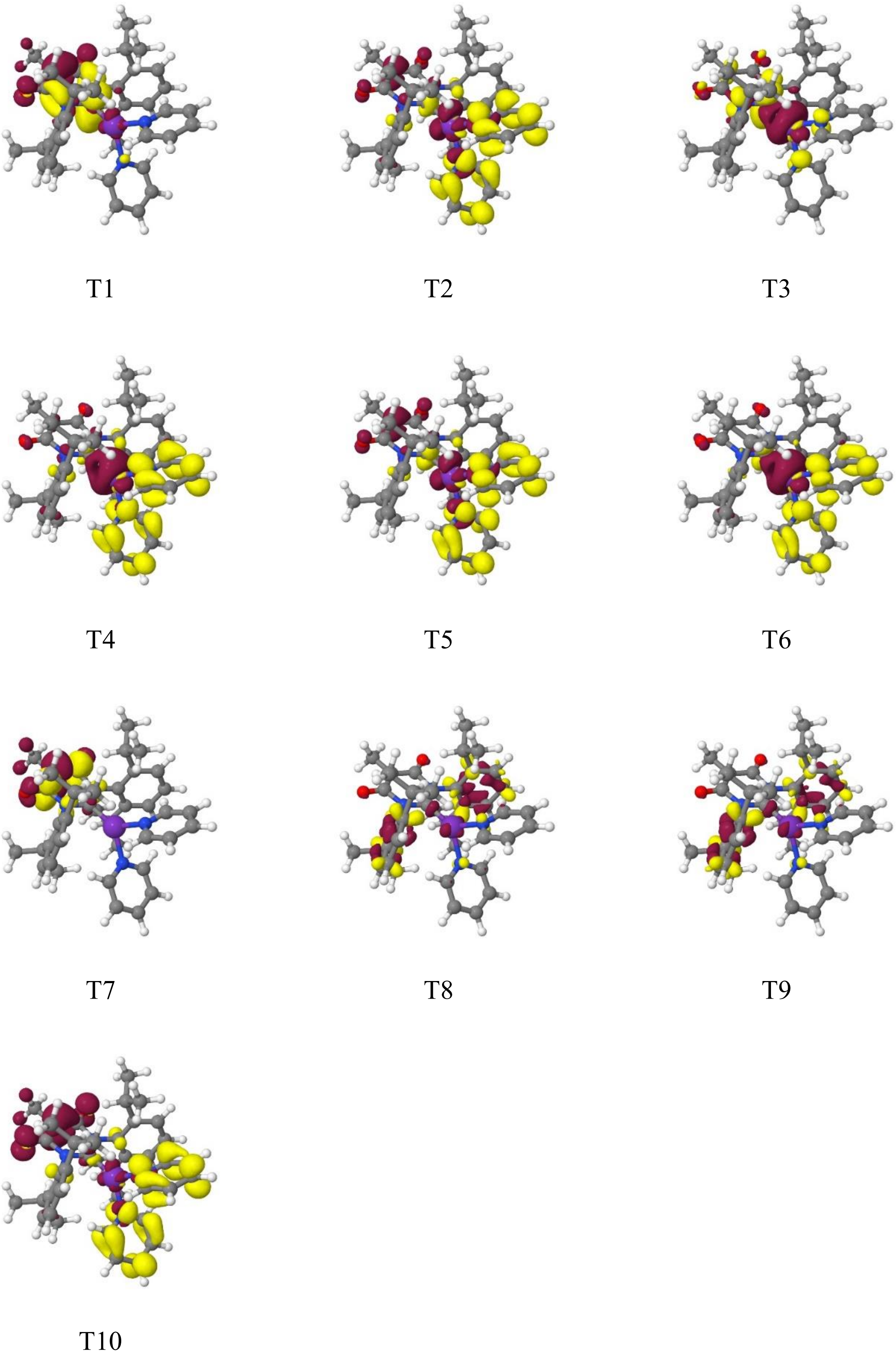

T1

T2

T3

T4

T5

T6

T7

T8

T9

T10

Figure S7.62. Differences of the electron densities (isosurface ± 0.002) between the low-lying excited triplet states and the electronic ground state of **3a** in the Franck–Condon region. For the difference density of the T8 and T9, a cut-off of ±0.001 was chosen. For colour codes, see Figure 7.19.

Table S7.9. Singlet states and their properties at the ground state geometry of **3b**. The sign of the static electric dipole moment of the states corresponds to the sign of the z-component. The z-axis roughly coaligns with the C-Cu bond.

state	E [eV]	λ_{abs} [nm]	osc. strength	μ [D]	character
S_0				-18.94	S_0
S1	2.75	452	0.01507	0.20	LLCT+MLCT
S2	2.91	427	0.00305	0.13	LLCT+MLCT
S3	3.03	409	0.13578	-3.86	MLCT+LLCT
S4	3.12	397	0.07613	-11.11	MLCT+LLCT
S5	3.25	381	0.01202	-4.30	LLCT
S6	3.40	365	0.00421	5.45	LLCT
S7	3.50	354	0.00043	-22.72	LC(fpy:nπ*)
S8	3.51	353	0.00126	-21.87	LC(fpy:nπ*)
S9	3.77	329	0.04002	-5.57	MLCT(→fpy)
S10	3.93	316	0.02047	-5.22	MLCT(→fpy)
S11	4.10	303	0.11954	-9.59	LC(NHC)

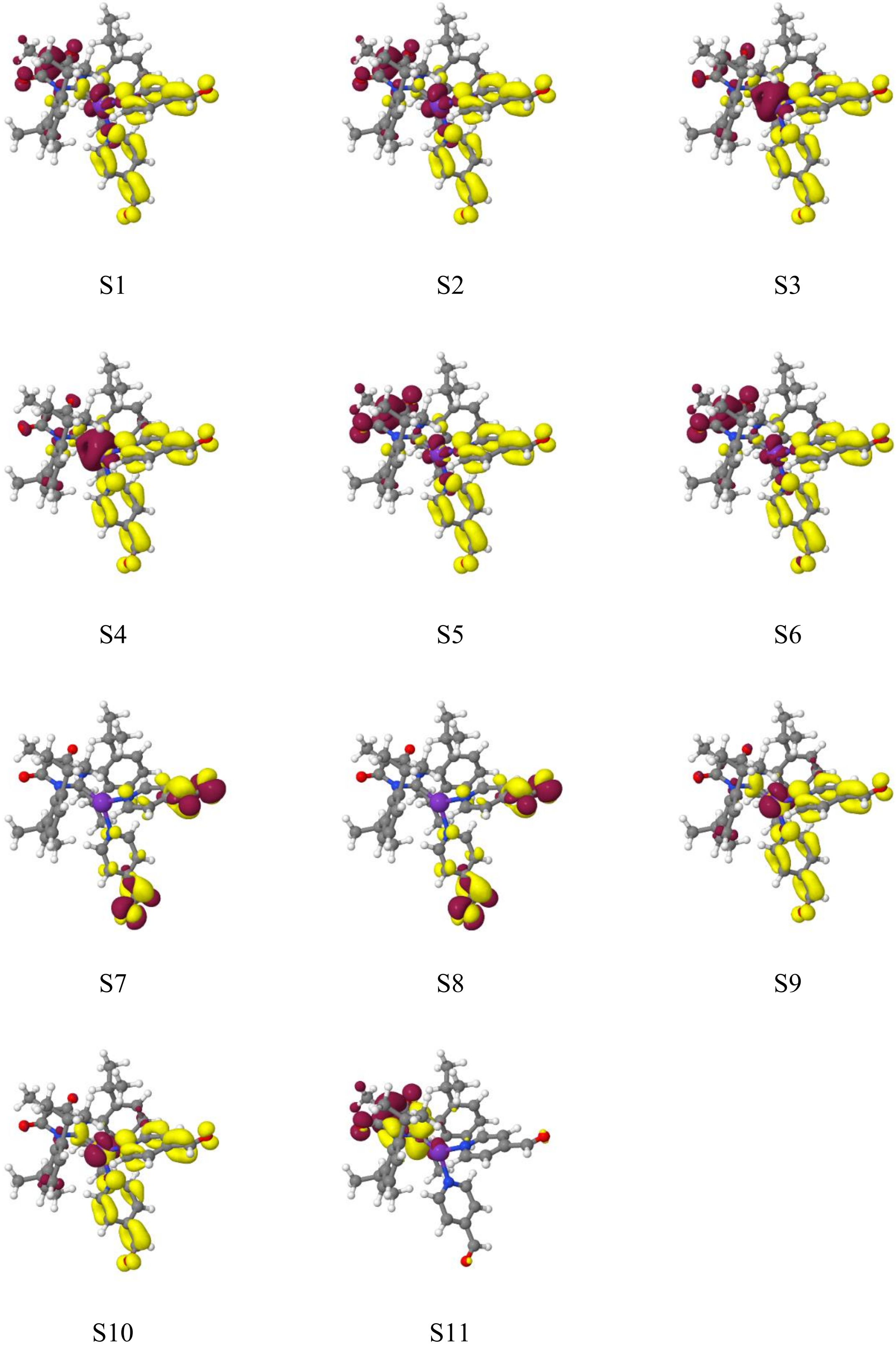

S1 S2 S3

S4 S5 S6

S7 S8 S9

S10 S11

Figure S7.63. Differences of the electron densities (isosurface ± 0.002) between the low-lying excited singlet states and the electronic ground state of **3b** in the Franck–Condon region. For colour codes, see Figure 7.19.

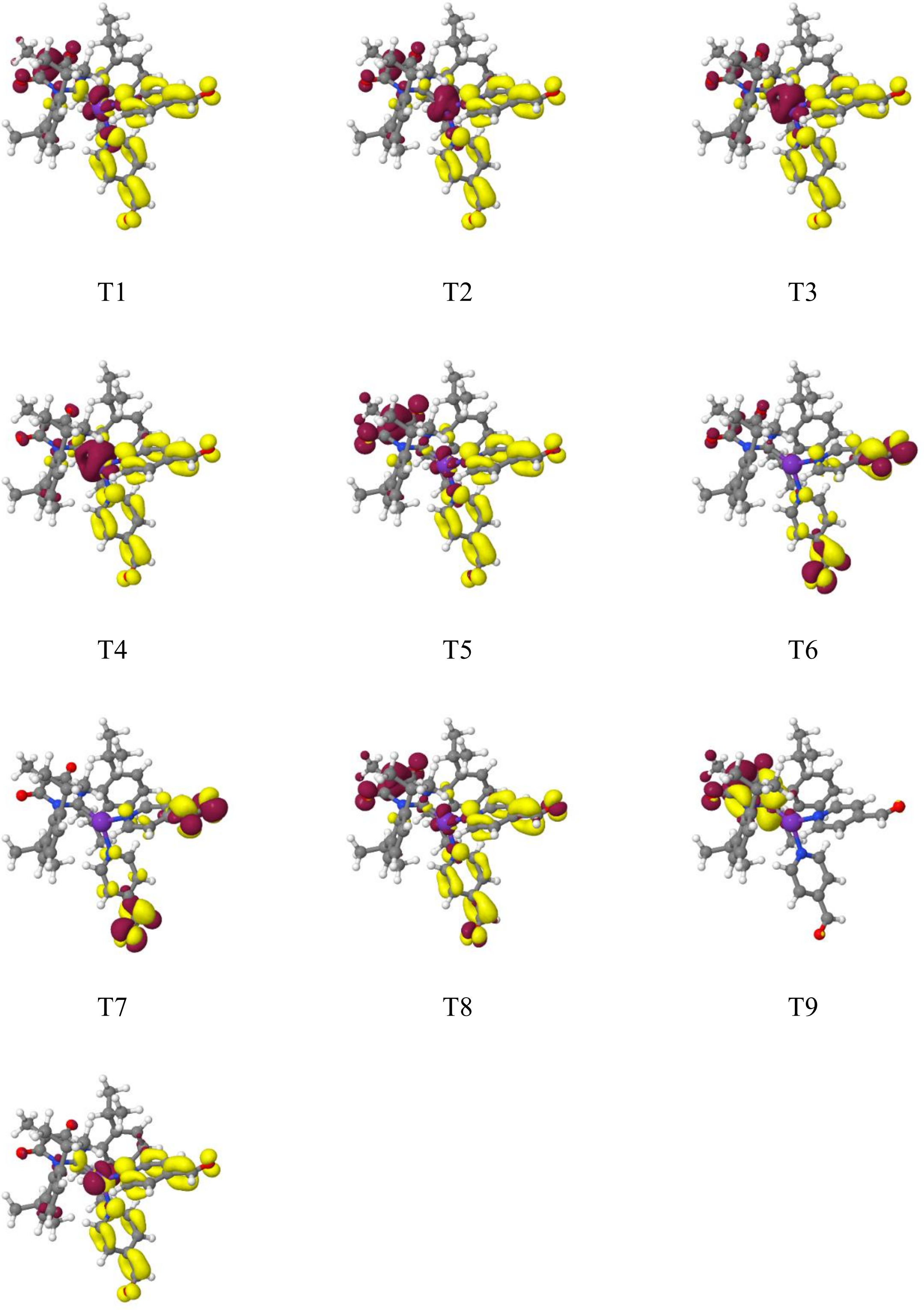

T1 T2 T3

T4 T5 T6

T7 T8 T9

T10

Figure S7.64. Differences of the electron densities (isosurface ± 0.002) between the low-lying excited triplet states and the electronic ground state of **3b** in the Franck–Condon region. For colour codes, see Figure 7.19.

7.2.7 References

---

[1] L. P. Ravaro, K. P. S. Zanoni, A. S. S. de Camargo, *Energy Rep.* **2020**, *6*, 37–45.

[2] J. Eng, T. J. Penfold, *Chem. Rec.* **2020**, *20*, 831–856.

[3] A. A. Danopoulos, T. Simler, P. Braunstein, *Chem. Rev.* **2019**, *119*, 3730-3961 and references cited therein.

[4] V. A. Krylova, P. I. Djurovich, M. T. Whited, M. E. Thompson, *Chem. Commun.* **2010**, *46*, 6696-6698.

[5] V. A. Krylova, P. I. Djurovich, J. W. Aronson, R. Haiges, M. T. Whited, M. E. Thompson, *Organometallics* **2012**, *31*, 7983-7993.

[6] V. A. Krylova, P. I. Djurovich, B. L. Conley, R. Haiges, M. T. Whited, T. J. Williams, M. E. Thompson, *Chem. Comm.* **2014**, *50*, 7176-7179.

[7] S. Shi, M. C. Jung, C. Coburn, A. Tadle, D. M. R. Sylvinson, P. I. Djurovich, S. R. Forrest, M. E. Thompson, *J. Am. Chem. Soc.* **2019**, *141*, 3576-3588.

[8] R. Hamze, M. Idris, D. Sylvinson, M. Ravinson, M.C. Jung, R. Haiges, P. Djurovich, M. E. Thompson, *Front. Chem.* **2020**, *8*, 401.

[9] A. Liske, L. Wallbaum, T. Hölzel, J. Föller, M. Gernert, B. Hupp, C. Ganter, C. Marian, A. Steffen, *Inorg. Chem.* **2019**, *58*, 5433-5445.

[10] M. M. D. Roy, P. A. Lummis, M. J. Ferguson, R. McDonald, E. Rivard, *Chem. Eur. J.* **2017**, *23*, 11249-11252.

[11] T. Hölzel, A. Belyaev, M. Terzi, L. Stenzel, M. Gernert, C. M. Marian, A. Steffen, C. Ganter, *Inorg. Chem.* **2021**, *60*, 18529-18543.

[12] V. César, N. Lugan, G. Lavigne, *J. Am. Chem. Soc.* **2008**, *130*, 11286-11287.

[13] V. César, C. Barthes, Y. C. Farré, S. V. Cuisiat, B. Y. Vacher, R. Brousses, N. Lugan, G. Lavigne, *Dalton Trans.* **2013**, *42*, 7373-7385.

[14] F. Chotard, A. S. Romanov, D. L. Hughes, M. Linnolahti, M. Bochmann, *Eur. J. Inorg. Chem.* **2019**, 4234-4240.

[15] C. Dash, A. Das, H. V. R. Dias, *Molecules* **2020**, *25*(16), 3741.

[16] M. Ruamps, N. Lugan, V. César, *Eur. J. Inorg. Chem.* **2017**, 4167-4173.

[17] G. R. Desiraju, T. Steiner, *The Weak Hydrogen Bond In Structural Chemistry and Biology*, Oxford University Press, New York, **1999**.

[18] J. S. Murray, G. Resnati, P. Politzer, *Faraday Discuss.* **2017**, *203*, 113-130.

[19] J. Hübscher, W. Seichter, E. Weber, *CrystEngComm.* **2017**, *19*, 3026-3036.

[20] O. Nolden, J. Kremper, W. Haselbach, M. Morshedi, J. Guhl, P. Schmeinck, C. M. Marian, C. Ganter, P. Gilch, *ChemPhotoChem* **2023**, *7*, e202200231.

[21] N. Lüdtke, J. Föller, C. M. Marian, *Phys. Chem. Chem. Phys.* **2020**, *22*, 23530-23544.

[22] R. Hamze, J. L. Peltier, D. Sylvinson, M. Jung, J. Cardenas, R. Haiges, M. Soleilhavoup, R. Jazzar, P. I. Djurovic, G. Bertrand, M. E. Thompson, *Science* **2019**, *363*, 601-606.

[23] J. Österlof, *Acta Chem. Scand.* **1950**, *4*, 374-385.

[24] K. J. Arm, W. Leslie, J. A. G. Williams, *Inorg. Chim. Acta* **2006**, *359*, 1222-1232.

[25] C. F. Macrae, I. Sovago, S. J. Cottrell, P. T. A. Galek, P. McCabe, E. Pidcock, M. Platings, G. P. Shields, J. S. Stevens, M. Towler, P. A. Wood, *J. Appl. Cryst.* **2020**, *53*, 226-235.

[26] Gaussian 16, Revision A.03, M. J. Frisch, G. W. Trucks, H. B. Schlegel, G. E. Scuseria, M. A. Robb, J. R. Cheeseman, G. Scalmani, V. Barone, G. A. Petersson, H. Nakatsuji, X. Li, M. Caricato, A. V. Marenich, J. Bloino, B. G. Janesko, R. Gomperts, B. Mennucci, H. P. Hratchian, J. V. Ortiz, A. F. Izmaylov, J. L. Sonnenberg, D. Williams-Young, F. Ding, F. Lipparini, F. Egidi, J. Goings, B. Peng, A. Petrone, T. Henderson, D. Ranasinghe, V. G. Zakrzewski, J. Gao, N. Rega, G. Zheng, W. Liang, M. Hada, M. Ehara, K. Toyota, R. Fukuda, J. Hasegawa, M. Ishida, T. Nakajima, Y. Honda, O. Kitao, H. Nakai, T. Vreven, K. Throssell, J. A. Montgomery Jr., J. E. Peralta, F. Ogliaro, M. J. Bearpark, J. J. Heyd, E. N. Brothers, K. N. Kudin, V. N. Staroverov, T. A. Keith, R. Kobayashi, J. Normand, K. Raghavachari, A. P. Rendell, J. C. Burant, S. S. Iyengar, J. Tomasi, M. Cossi, J. M. Millam, M. Klene, C. Adamo, R. Cammi, J. W. Ochterski, R. L. Martin, K. Morokuma, O. Farkas, J. B. Foresman, D. J. Fox, Gaussian Inc., Wallingford CT, **2016**.

[27] J. P. Perdew, K. Burke, M. Ernzerhof, *Phys. Rev. Lett.* **1996**, *77*, 3865-3868.

[28] C. Adamo, V. Barone, *J. Chem. Phys.* **1999**, *110*, 6158-6170.

[29] A. Schäfer, H. Horn, R. Ahlrichs, *J. Chem. Phys.* **1992**, *97*, 2571-2577.

[30] K. A. Peterson, C. Puzzarini, *Theor. Chem. Acc.* **2005**, *114*, 283-296.

[31] D. Figgen, G. Rauhut, M. Dolg, H. Stoll, *Chem. Phys.* **2005**, *311*, 227-244.

[32] S. Grimme, J. Antony, S. Ehrlich, H. Krieg, *J. Chem. Phys.* **2010**, *132*, 154104.

[33] E. Cancès, B. Mennucci, J. Tomasi, *J. Chem. Phys.* **1997**, *107*, 3032-3041.

[34] B. Mennucci, E. Cancès, J. Tomasi, *J. Phys. Chem.* B **1997**, *101*, 10506-10517.

[35] S. Grimme, M. Waletzke, *J. Chem. Phys.* **1999**, *111*, 5645-5655.

[36] C. M. Marian, A. Heil, M. Kleinschmidt, *WIREs Comput. Mol. Sci.* **2019**, *9*, 1.

[37] R. Ahlrichs, M. Bär, M. Häser, H. Horn, C. Kölmel, *Chem. Phys. Lett.* **1989**, *162*, 165-169.

[38] TURBOMOLE V7.1 2017, a development of University of Karlsruhe and Forschungszentrum Karlsruhe GmbH, 1989-2007, TURBOMOLE GmbH, since **2007** available from http://www.turbomole.com.

[39] A. D. Becke, *J. Chem. Phys.* **1993**, *98*, 1372-1377.

[40] C. Lee, W. Yang, R. G. Parr, *Phys. Rev.* B **1988**, *37*, 785-789.

[41] A. Heil, M. Kleinschmidt, C. M. Marian, *J. Chem. Phys.* **2018**, *149*, 164106.

7.3 Compound Class B – NHC Copper(I) complexes: Manuscript II

How to tune luminescent Cu(I) complexes with strong donor carbenes towards TADF?

Jasper Guhl,†[a] Dragana Sretenović,†[b] Philipp Schmeinck,[c] Suren Felekyan,[b] Ralf Kühnemuth,[b] Christian Ganter,[c] Claus A. M. Seidel,*[b] Christel M. Marian,*[a] and Markus Suta*[c]

† These authors contributed equally.

[a] J. Guhl, Prof. Dr. C. M. Marian
Institute of Theoretical and Computational Chemistry
Heinrich Heine University Düsseldorf
Universitätsstr. 1, 40225 Düsseldorf, Germany
E-mail: christel.marian@hhu.de

[b] D. Sretenović, Dr. S. Felekyan, Dr. R. Kühnemuth, Prof. Dr. C. A. M. Seidel
Institute of Physical Chemistry
Heinrich Heine University Düsseldorf
Universitätsstr. 1, 40225 Düsseldorf, Germany
E-mail: cseidel@hhu.de

[c] P. Schmeinck, Prof. Dr. C. Ganter, Jun.-Prof. Dr. M. Suta
Institute of Inorganic and Structural Chemistry
Heinrich Heine University Düsseldorf
Universitätsstr. 1, 40225 Düsseldorf, Germany
E-mail: markus.suta@hhu.de

Manuscript stage: This version of the manuscript was submitted to *Journal of Materials Chemistry C* on 11.04.2024.

7.3.1 Abstract

Cu(I) carbene complexes are common emitters of current emerging interest for next-generation OLED technology based on their often encountered thermally activated delayed fluorescence (TADF) properties. However, general molecular design principles for successfully observable TADF properties of such complexes usually rely on electron-withdrawing N-heterocyclic carbene (NHC) ligands, while Cu(I) carbene complexes with strongly electron-donating NHC ligands are still scarce. Based on a simple synthetic approach reported by us earlier (P. Schmeinck et al., *Chem. Eur. J.* **2023**, *26*, e202300416) that offers large-scale access to this class of Cu(I) carbene complexes, we aim to elucidate design principles to enhance their TADF properties. In this work, we combined temperature-dependent time-resolved luminescence spectroscopy on different time scales (ns, µs, ms) with high-level DFT/MRCI calculations on a number of representative Cu(I) NHC complexes with An6DAC as an anionic carbene and additional pyridine-derived ligands. Good agreement between experiment and theory with respect to the electronic nature of the optical transitions, the energy levels of the electronic states as well as the kinetics of interconversion controlled by the respective energy gaps was found. We conclude that both the electron-rich or electron-poor nature of the pyridine ligands and the coordination geometry (linear, trigonal planar) play a significant role for the outcome of the optical properties of these complexes. While electron-rich pyridine moieties induce decoupled prompt fluorescence and phosphorescence with connected low photoluminescence quantum yields (PLQYs), electron-poor pyridine moieties enhance a "push-pull" effect mediated by Cu(I) that favours TADF properties so that the luminescence is increased by 1-2 orders of magnitude if the complex is trigonal. In the trigonal formyl pyridine complex, theory predicts high MLCT contributions to the electronic wavefunctions, so that the T_1 states should exhibit large SOCMEs with several excited singlet states. Indeed, in temperature dependent luminescence measurements, the electronic states behave as an intimately coupled ensemble. At 270 K, 56% of its luminescence can be attributed to TADF. However, while the internal PLQYs are higher for the trigonal complexes, the chemical Cu-pyridine bond is also more labile. Overall, this study provides a detailed overview of the possibilities of targeted molecular design to selectively address desirable optical properties in organometallic compounds for potential applications in lighting.

7.3.2 Introduction

Since the pioneering work of Tang et al.[1] on organic electroluminescent diodes in the 1980s, we have witnessed the evolution of four generations of small-molecule organic light-emitting diodes (OLEDs).[2–5] Currently, there is still no end of this evolution in sight: The first generation was based on fluorescent emitters and can therefore exploit at most 25% of the electrically generated excitons. The second generation made use of heavy-metal complexes based on, e.g., $\mathrm{Ir^{III}}$ or $\mathrm{Pt^{II}}$ that enhance spin-orbit coupling by the heavy-atom effect and thus, lead to dominant phosphorescence. Due to ultrafast intersystem crossing from the excited singlet state to the triplet manifold, this approach harvests both singlet and triplet excitons and increased the theoretically expected internal quantum efficiency of electroluminescence (IQE) to 100%. The third (exploiting thermally activated delayed fluorescence, TADF) and fourth (hyperfluorescence, combination of a TADF emitter with a narrow-band emitting fluorescent emitter) generations use less expensive materials and can in principle achieve 100% IQE as well. Despite those promising features, there are still several shortcomings to be tackled. With typical electroluminescence decay times in the microsecond regime, phosphorescent OLEDs (PhOLEDs) and OLEDs based on TADF are prone to photochemical side reactions in the excited state, which are detrimental to the operational durability of the device.[6] In particular, blue light emitting OLEDs are known to suffer from degradation of the emitter material.[7] TADF emitters have the advantage over PhOLED emitters that their synthesis does not rely on any precious heavy metals but are composed of earth-abundant elements and thus, less expensive. Besides purely organic donor–acceptor systems, complexes of the coinage metals, in particular $\mathrm{Cu^{I}}$, have been used.[8–10] The preference for d^{10} elements in TADF emitting transition metal complexes is related to the lack of energetically accessible metal-centered (MC) $d \rightarrow d^*$ excitations that are known to cause predissociation of metal–ligand bonds in phosphorescent $\mathrm{Ir^{III}}$ and $\mathrm{Pt^{II}}$ complexes,[11] for example.

The energetic proximity of metal-to-ligand charge transfer (MLCT), ligand-to-ligand charge-transfer (LLCT) and ligand-centered (LC) excitations in $\mathrm{Cu^{I}}$ complexes is both bless and curse - a bless because it forms the basis for a rich photochemistry and photophysics,[10] and a curse because low-lying ^{3}LC states tend to act as dark traps for the excited state population with the tendency for non-radiative relaxation.[12,13] Dependent on the particular case, the population of MLCT states can be advantageous or disadvantageous for the luminescence properties of $\mathrm{Cu^{I}}$ complexes involving triplet states. On the one hand, the hole in the Cu d shell enhances spin–orbit coupling (SOC) and thus increases the probability of intersystem crossing

(ISC) and reverse ISC (rISC) processes that are necessary for harvesting the triplet excitons in OLEDs.[10,14,15] On the other hand, the pseudo Jahn–Teller effect on the d^9 electronic structure in an MLCT state causes large geometrical displacements which can be detrimental to the electro- or photoluminescence quantum yields (Φ_{EL} or Φ_{PL}) of MLCT states and requires chemical ligand design strategies to sterically limit the distortion in the excited state.[16–23] In cationic Cu^I complexes carrying an N-heterocyclic carbene (NHC) and an aromatic ligand, moreover the torsional orientation of the carbene and π-systems has an impact on the S–T energy gap, ΔE_{ST}, and hence, the ability of these complexes to show phosphorescence or TADF.[24,25] Generally, ΔE_{ST} tends to be larger for MLCT states than for LLCT states.[19] For this reason, 2-coordinate linear Cu^I complexes with MLCT-type S_1 and T_1 states are often phosphorescent, whereas complexes with energetically low-lying LLCT states are more promising candidates for TADF if admixture of energetically close MLCT states is possible.

Among the linear coinage metal complexes, carbene metal amides stand out: Depending on the π-acceptor strength of the carbene, the color of the LLCT emission can be tuned from blue to the NIR region and many of these complexes are TADF-active with high luminescence quantum yields.[21–23,25–32] Their ISC and rISC mechanism have been studied in great detail revealing solvent reorganization as well as vibronic coupling effects.[19,33–37] The direction of the CT is less obvious in cationic linear carbene Cu^I complexes incorporating neutral aromatic imine ligands instead of an amide. Here, the carbene as well as the imine may adopt the role of the acceptor. Studies employing classical NHC and pyridine-based ligands revealed that the steric demand of the NHC and the presence of electron-withdrawing substituents in *para*-position of the pyridine ligand are important factors favoring luminescence involving the triplet state either directly or via TADF.[12,38]

Another class of efficient OLED emitters are zwitterionic mixed carbene coinage metal complexes combining an anionic malonate-derived NHC unit and a classical neutral NHC. Such complexes were reported to show bluish-white phosphorescence.[39] The overall charge neutrality of this class of compounds is advantageous for the fabrication of OLED devices due to their appreciable vapor pressure. Zwitterionic carbene Cu(I) units may alternatively be combined with neutral pyridine-based ligands and are also overall charge neutral. Specifically, in a recent paper we reported on a series of such complexes, comprising, *inter alia*, the linear derivatives **2a,b** and the trigonal compounds **3a,b** (Scheme 7.5). In the present contribution we analyse the photophysical properties of these four complexes in depth with both, experimental and theoretical methods. The aim was to eventually establish a design principle for efficient TADF performance.

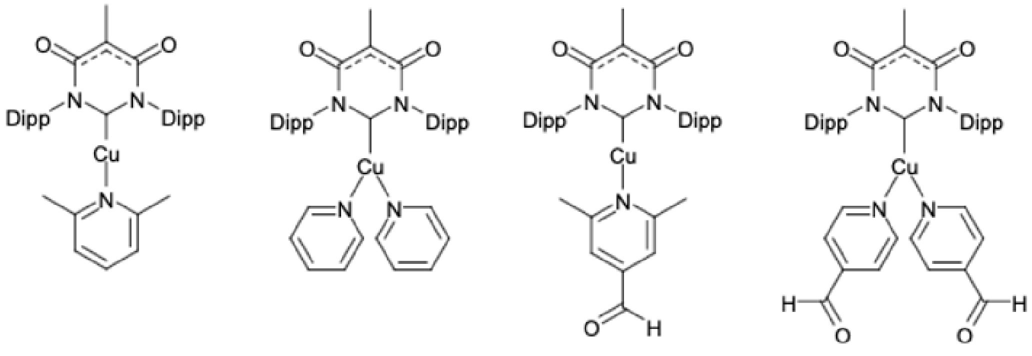

2a **3a** **2b** **3b**

Scheme 7.5. Chemical structures of the complexes investigated in this work.

Preliminary scans of the energy level scheme by quantum chemistry (Figure 7.21) revealed that the acceptor properties of pyridine are insufficient for making the carbene-to-pyridine LLCT states the lowest singlet and triplet excited states.[40] In the linear complex with unsubstituted pyridine, S_1 and T_1 arise predominantly from local excitations on the carbene ligand. With a ΔE_{ST} value of 0.394 eV, the singlet–triplet energy gap is too large enabling TADF at room temperature. Test calculations suggest that fluorination is not sufficient to increase the acceptor strength of the pyridine ligand, as F exerts a +M effect in addition to a -I effect. Possible substituents combining -I with -M effects are nitrile and formyl groups. Previous work on related cationic carbene pyridine Cu(I) complexes revealed, however, that a nitrile functionality in *para*-position of the pyridine ligand tends to coordinate to a Cu atom of a neighbouring linear complex, thus forming a coordination polymer.[38] When a formyl group was employed as an electron-withdrawing substituent instead, this complication did not arise. In the present case, S_1 and T_1 adopt LLCT character if 4-formylpyridine is used as a ligand in the neutral linear copper carbene complex which reduces ΔE_{ST} to merely 0.092 eV (Figure 7.21). Moreover, MLCT states are found energetically close-by, thus promoting SOC. Thus, this linear 4-formylpyridine Cu^I complex with an anionic donor carbene could be considered an ideal candidate for an efficient TADF emitter if it were not for the known problem that sterically unprotected electron-deficient Cu centers are susceptible to bond formation with further coordinating molecules.[12,25,26,41,42] To prevent the accidental formation of trigonal complexes, we introduced additional methyl groups in *ortho*-position of the pyridine ring which increase the steric demand of the ligand, yielding the linear lutidine and 4-formyllutidine complexes **2a** and **2b**, respectively.[43] An alternative approach to increase the “pull” effect is the introduction of a second acceptor ligand resulting in the bis(formylpyridine) complex **3b**, for which lower energies of the LLCT and MLCT states in comparison to the LC states are calculated (Figure 7.21). Moreover, it leads to a mixture of LLCT and MLCT character in the lowest electronically excited singlet and triplet states, resulting in an even smaller ΔE_{ST} value and larger mutual SOC in comparison to the respective linear complex (Figure 7.21). For the reasons outlined above, the four complexes **2a,b** and **3a**,**b** (Scheme 7.5) were selected for our in-depth analysis of the photophysical properties.

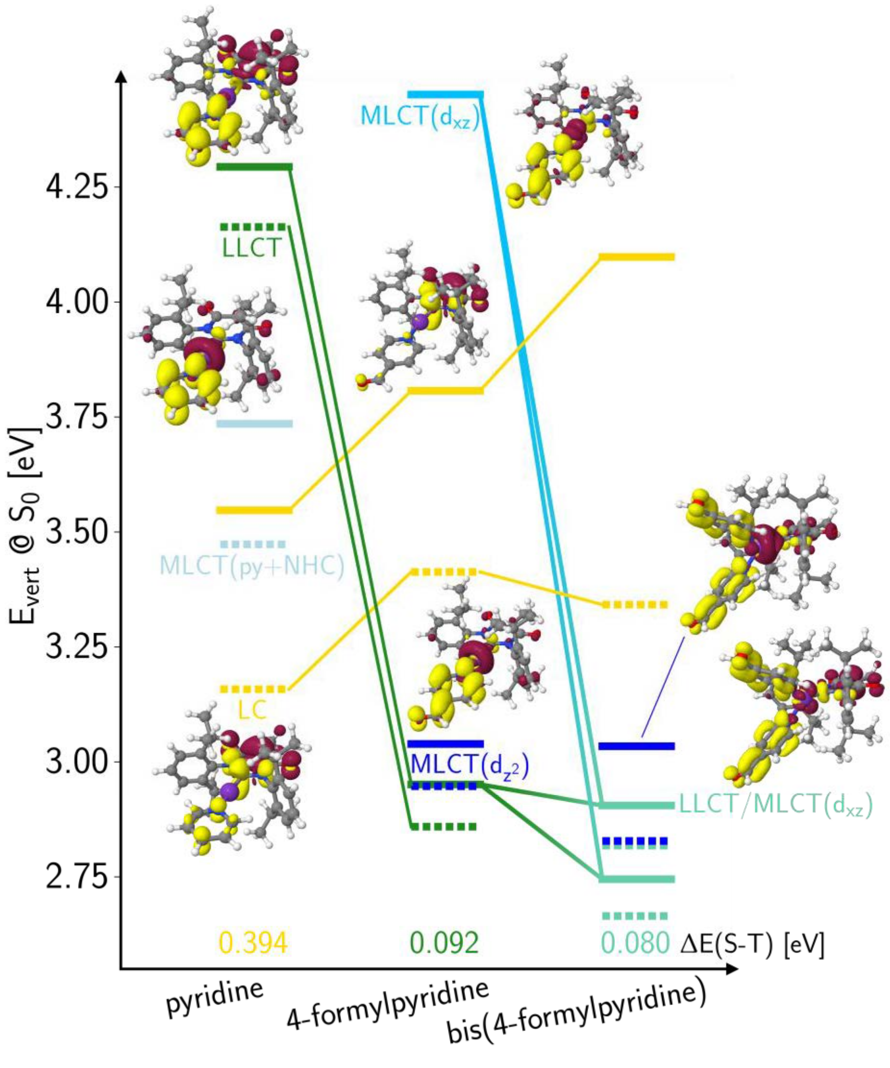

Figure 7.21. DFT/MRCI energy level scan of the linear complexes with a pyridine or 4-formylpyridine ligand, respectively, and the bis(4-formylpyridine) complex **3b** at the ground-state geometry in dichloromethane solution and assignment of the electronic structures of the excited states.

Our synthesis started from a moisture and air-stable one-dimensional coordination polymer to generate linear or trigonal complexes, dependent on the particular substitution pattern of the pyridine ligand.[43] In addition to structural characterization of the synthesized compounds, excitation, absorption and steady-state emission spectra of four luminescent complexes were presented in that work, but the electronic nature of the emitting states, and their luminescence decay times with the corresponding temperature dependence had not yet been determined.

We combine quantum chemical methods and time-resolved spectroscopy in suspensions of microcrystallites and the solid state in a temperature range between 10 K and 298 K. Due to chemical lability of the complexes in solution, the spectroscopy was carried out in cyclohexane suspensions of microcrystalline compounds. This method allowed for the preparation of sufficiently stable solid-state samples in standard cuvettes, thereby enabling absorption experiments, among other benefits. The validity of the collected data is supported by selected experiments on the neat powdered samples (Figure S7.67).

7.3.3 Results and discussion

The linear lutidine complex 2a

In this complex, an electron-rich carbene is combined with a relatively electron-rich pyridine moiety. Consequently, CT-type emission is not readily expected in **2a** and the luminescence should be governed by ligand-centred (LC) states. The excitation and emission spectra of this complex in Figure 7.22 confirm this idea. At the excitation wavelength of the luminescence experiments (375 nm), primarily the S_1 state is populated. Our quantum chemical calculations indicate that its wavefunction is dominated by a ^{1}LC(carbene) character with small ^{1}LLCT(carbene-to-lutidine) contributions (vertical excitation wavelength 349 nm, oscillator strength $f = 0.093$). Below S_1, the corresponding ^{3}LC(carbene) and a ^{3}MLCT(d_{z2}-to-lutidine) state are found in the vertical energy spectrum, respectively. The latter state is practically degenerate with S_1 in the Franck–Condon (FC) region, but does not play an essential role in the emission process. Occupation of the C-N-antibonding π* orbital in the S_1 state leads to a substantial elongation of the carbene C-N bonds which stabilizes the LC(carbene) contributions to the S_1 wavefunction. Blue emission with a maximum at $\lambda_{max} \approx 450$ nm is observed in the luminescence spectrum at room temperature. The excitation and emission spectra of the powdered samples are in excellent agreement with those measured in cyclohexane suspension (Figure 7.22A). However, the measured excitation spectrum in cyclohexane suspension does not completely overlap with the absorption spectrum (Figure 7.22B). This discrepancy is quantified by the ratio of excitation and absorption values, normalized at the excitation wavelength of 375 nm (Figure 7.22B top). The normalized excitation/absorption ratio at longer wavelengths indicates the presence of additional non-luminescent species in suspension. Despite the observed discrepancy, the theoretically predicted spectrum agrees well with the longest excitation band.

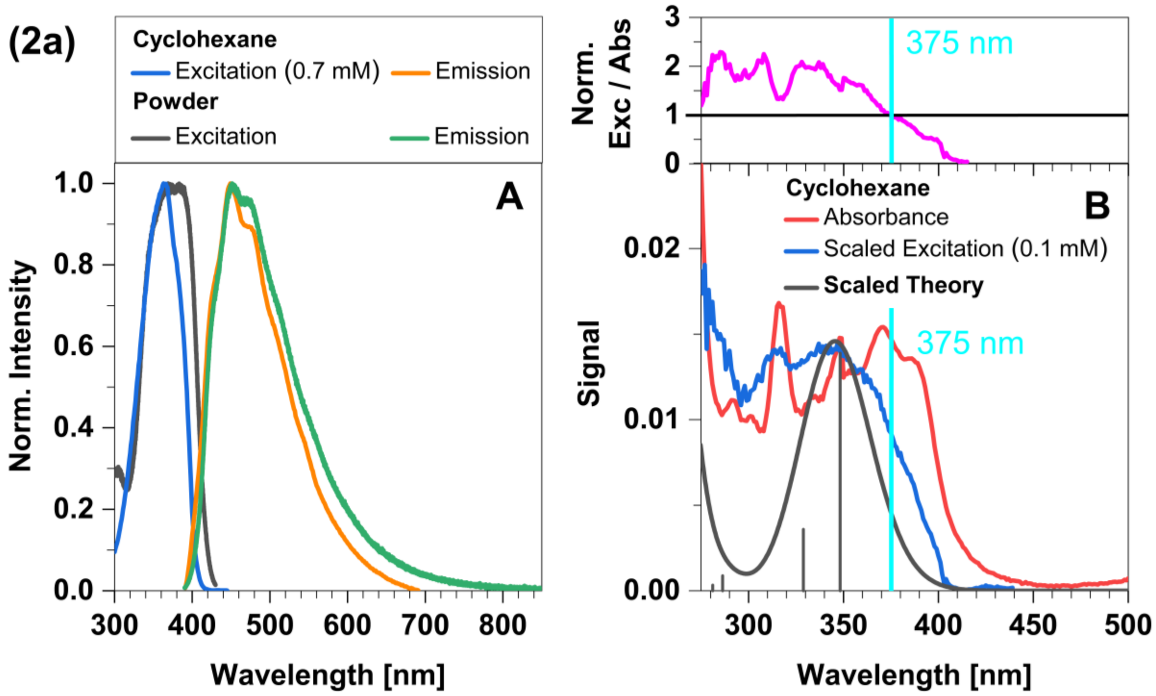

Figure 7.22. Spectra of compound **2a** at 298 K. The excitation spectra were recorded by monitoring luminescence at the respective emission maximum (450 nm). An excitation wavelength of 375 nm was used for the emission spectra. **A.** Excitation and emission spectra in liquid cyclohexane and powder. A concentrated cyclohexane suspension (0.7 mM) was used to mimic the conditions in powder form. **B.** Absorbance corrected for baseline and Mie scattering [see Experimental and Theoretical Procedures, eq. (3)]. A diluted sample (0.1 mM) and a semi-microcuvette (optical path length of 4 mm) are used to minimize inner-filter effects while recording the excitation spectra in cyclohexane. Both excitation in cyclohexane and the DFT/MRCI line spectra broadened with a Gaussian of 0.175 meV FWHM are scaled to the absorbance spectrum for qualitative comparison. The ratio of excitation and absorbance is normalized at 375 nm.

Despite a mutual spin–orbit coupling matrix element (SOCME) below 1 cm^{-1} and an adiabatic S_1-T_1 energy separation $\Delta E_{\mathrm{ST,adiab}} \approx 0.65$ eV, theoretically expected S_1-T_1 ISC appears to be competitive to prompt fluorescence (Table 7.12) and gives rise to a weak portion of phosphorescence. Time-resolved measurements of **2a** in cyclohexane suspension were performed at four different temperatures (10, 60, 160, and 260 K) (see Figure 7.23) to verify this kinetic scheme experimentally. The measured intensity-averaged decay time $\langle \tau_{ns} \rangle_I$ of prompt fluorescence in the nanosecond regime agrees well with the estimate for the upper limit of the fluorescence lifetime of state (i), $\tau_{PF,lim}^{(i)}$ (Table 7.12), considering only k_F and k_{ISC}. Thus, internal conversion (IC) is not a main modulator of the fluorescence properties, which holds true for most of the other compounds with the exception of **2b**. From the resulting decay times and amplitudes, intensity-weighted averages, $\langle\tau_{ns}\rangle_I$, have been generated. Their temperature dependence was approximated by a simple exponential behavior with temperature-independent activation energy E_A and rate constants k_A and k_S [Eq. (1)].

$$\langle\tau_{ns}\rangle_I(T) = \left(k_S + k_A \cdot exp\left(-\frac{E_A}{k_B T}\right)\right)^{-1} \tag{1}$$

Possible temperature-dependent processes affecting singlet state lifetimes are internal conversion, intersystem crossing (ISC), diffusion-controlled quenching etc., but for the studied samples the assumption of one process was sufficient to fit the data within the experimental noise level (Figure 7.23B). Fit results of all compounds in the nanoseconds range are given in Table S7.24.

The computed vertical emission wavelength at the S_1 minimum (443 nm) is also in good agreement with the experimental observations ($\lambda_{max} \approx 450$ nm). The vibronic progression frequency ($\Delta\tilde{\nu} \approx 1350$ cm^{-1}), observable in the emission spectrum of powdered **2a** at 77 K (see Figure S7.67), is compatible with the coupling of the electronic transition to a C-N stretching vibration of the carbene moiety and indicates luminescence from a LC state. Due to the large S_1-T_1 energy gap of $\Delta E_{ST} \approx 0.46$ eV, delayed fluorescence is not detected in this compound within the regarded temperature range. The observed phosphorescence in the millisecond time regime (see Table S7.14) is in line with the LC nature of the T_1 excitation, associated with a low radiative rate constant (calculated value $k_P \approx 10^1$ s^{-1}). As expected, phosphorescence becomes efficiently quenched at elevated temperatures (see Figure 7.23D). Overall, the appearance of the photoluminescence spectra of the linear lutidine complex **2a** can be interpreted as conventional fluorescence and energetically separated weak phosphorescence. The photoluminescence properties of powdered **2a** agree very well with those measured in the cyclohexane suspension.

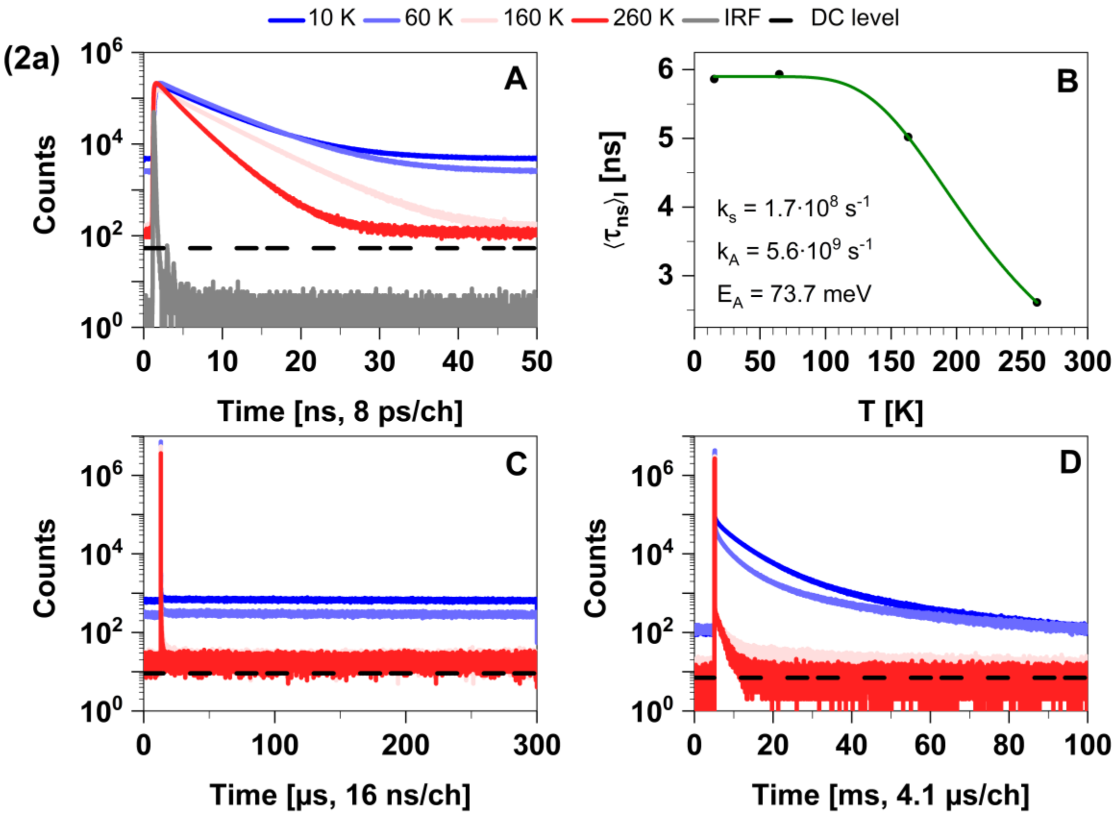

Figure 7.23. Time-resolved luminescence measurements of compound **2a** in solid cyclohexane suspension at temperatures of 10 K, 60 K, 160 K, 260 K, in three distinct time regimes. **A.** Decays in nanoseconds. **B.** Temperature-dependence of the intensity-weighted prompt fluorescence lifetime $\langle \tau_{ns} \rangle_I$. The green line represents the fit of the experimental data according to eq. (1). All fit results with their respective errors are shown in Table S7.24. **C.** Microseconds with no decay component. **D.** Decays in milliseconds. All luminescence decays exhibit multi-exponential behaviour. The intensity-averaged luminescence lifetimes $\langle \tau \rangle_I$ are listed in Table 7.11, the individual decay times and species fractions are compiled in Table S7.13 and Table S7.14. The excitation wavelength was at 375 nm, and the detection wavelength 460 nm. The counts that correspond to the dark count (DC) rate of the detector (95 Hz) are marked with a black dashed line.

Table 7.10. Experimental steady-state spectroscopic parameters of complexes **2a**, **2b**, **3a** and **3b**, powdered and in liquid cyclohexane suspension at 298 K. The tables include excitation ($\lambda_{exc,m}$) and emission maxima ($\lambda_{em,m}$), apparent Stokes shifts ($\Delta\tilde{v}_S$), 0-0 energies ($\tilde{v}_{00}$), emission band full widths at half maximum (FWHM emission), and relative quantum yields in cyclohexane (rel. Φ_{PL}).

Compound	**2a**		**3a**		**2b**		**3b**	
Condition	**powder**	**cyclohexane**	**powder**	**cyclohexane**	**powder**	**cyclohexane**	**powder**	**cyclohexane**
$\lambda_{exc,m}$ [nm]	369	363	364	368	407	386	490	395
$\lambda_{em,m}$ [nm]	451	449	504	502	527	521	591	590
$\Delta\tilde{v}_S$ [cm^{-1}]	4615	5001	7605	7450	4170	4122	3400	3800
$\tilde{v}_{00}$ [cm^{-1}]	23987	24938	23403	24570	20786	21692	18477	19493
FWHM emission [cm^{-1}]	7040	5651	5937	5240	5799	4687	3945	3607
rel. Φ_{PL} (λ_{exc} = 375 nm)	-	0.08	-	0.01	-	0.02	-	1.00

Table 7.11. Experimental time-resolved luminescence decay parameters (intensity-averaged luminescence lifetime $\langle\tau\rangle_I$) of complexes **2a**, **2b**, **3a** and **3b,** powdered (298 K and 80 K) and in frozen cyclohexane suspension at 260 K and 60 K (see Methods). All decays are multi-exponential, individual decay times and species fractions are provided in the Supplementary Information (see Table S7.13 to Table S7.23). No em.: no decay component in this time range.

Powder								
Compound	**2a**		**3a**		**2b**		**3b**	
T [K]	**298**	**80**	**298**	**80**	**298**	**80**	**298**	**80**
$\langle\tau_{ns}\rangle_I$ [ns]	1.7	5.9	no em.	no em.	3.5	22.3	no em.	no em.
$\langle\tau_{\mu s}\rangle_I$ [μs]	no em.	no em.	no em.	no em.	1.7	no em.	7.6	27.4
$\langle\tau_{ms}\rangle_I$ [ms]	1.2	2.2	0.4	1.3	no em.	0.04	no em.	no em.
Solid cyclohexane suspension								
T [K]	**260**	**60**	**260**	**60**	**260**	**60**	**260**	**60**
$\langle\tau_{ns}\rangle_I$ [ns]	2.6[a]	5.9[a]	0.5[c]	1.2[c]	1.6[f]	10.1[f]	0.4[i]	1.1[i]
$\langle\tau_{\mu s}\rangle_I$ [μs]	no em.	no em.	338.0[d]	208.6[d]	55.4[g]	267.3[g]	10.0[j]	28.3[j]
$\langle\tau_{ms}\rangle_I$ [ms]	2.4[b]	14.2[b]	0.6[e]	9.0[e]	0.18[h]	4.5[h]	no em[k]	no em[k]

a: see Table S7.13. **b**: see Table S7.14. **c**: see Table S7.15. **d**: see Table S7.16. **e**: see Table S7.17 (For 260 K, within error the emission presumably is the same as in microseconds). **f**: see Table S7.18. **g**: see Table S7.19. **h**: see Table S7.20. **i**: see Table S7.21. **j**: see Table S7.22. **k**: The detected emission in the millisecond time range (see Table S7.23) does not originate from the compound, but from its free ligand (for more details, see Figure S7.73).

Table 7.12. Computed photophysical data of the complexes **2a**, **3b**, **3a**, **3b**.

Property	Compound			
	2a	**3a**	**2b**	**3b**
λ_{abs} (S$_1$) [nm]	349 (LC/LLCT)	329 (LLCT/MLCT(d$_{xz}$))	412 (LLCT)	452 (LLCT/MLCT(d$_{xz}$))
f_{abs} (S$_1$)	0.09251	0.00916	0.03057	0.01507
$\lambda_{\mathrm{em,vert}}$ ^{a} [nm]	443 (^{1}LC)^b 664 (^{3}LC)	606 (^{1}LC) 665 (^{3}LC)	563 (^{1}LLCT) 591 (^{3}LLCT) 615 (^{3}LC)	704 (^{1}LLCT) 728 (^{3}LLCT) 707 (^{1}MLCT) 748 (^{3}MLCT)
k_{F} [s^{-1}]	4.0×10^7 (^{1}LC)	1.0×10^7 (^{1}LC)	6.3×10^6 (^{1}LLCT)	4.2×10^5 (^{1}LLCT) 2.6×10^6 (^{1}MLCT)
k_{ISC} (298 K) [s^{-1}]	8×10^7 (^{1}LC-^{3}LC)	1.5×10^9 (^{1}LC-^{3}LC)	2.7×10^6 (^{1}LLCT-^{3}LLCT) 8.5×10^5 (^{1}LLCT-^{3}LC)	2.3×10^7 (^{1}LLCT-^{3}LLCT) 9.1×10^{10} (^{1}LLCT-^{3}MLCT) 2.7×10^{10} (^{1}MLCT-^{3}MLCT) 2.8×10^{11} (^{1}MLCT-^{3}LLCT)
$\tau_{PF,lim}^{(i)}$ (298 K) [ns] ^{c}	8.3	0.7	101.5	0.010 (^{1}LLCT) 0.004 (^{1}MLCT)
k_{rISC} (298 K) [s^{-1}]	-	5.1×10^{-2} (^{3}LC-^{1}LC)	1.0×10^5 (^{3}LLCT-^{1}LLCT) 1.8×10^3 (^{3}LC-^{1}LLCT)	3.1×10^5 (^{3}LLCT-^{1}LLCT) 2.1×10^9 (^{3}MLCT-^{3}LLCT) 5.7×10^8 (^{3}MLCT-^{1}MLCT) 2.4×10^8 (^{3}LLCT-^{1}MLCT)
k_{P} (77K) [s^{-1}]	1.1×10^1 (^{3}LC)	8.6×10^1 (^{3}LC)	7.6×10^1 (^{3}LLCT) 2.7×10^1 (^{3}LC)	1.4×10^4 (^{3}LLCT) 7.9×10^3 (^{3}MLCT)
$\Delta E_{\mathrm{ST,ad.}}$ [eV]	0.645 (LC)	0.464 (LC)	0.046 (LLCT) -0.001 (^{1}LLCT-^{3}LC)	0.058 (LLCT) 0.095 (MLCT)

^{a} Multiple entries indicate that more than one minimum was found on the S$_1$ or T$_1$ potential energy hypersurface, respectively. Adiabatic excitation energies and photophysical properties at these minima are given in the Supplementary Information.

^{b} The ^{1}LC state was optimised with the constrained inter-ligand dihedral angle of the ^{3}LC state. It does not constitute a proper minimum on the S$_1$ potential energy hypersurface. A proper minimum could not be obtained with the PBE0 functional.

^{c} Estimate for the upper limit of the fluorescence lifetime of state (i) with several ISC channels to n triplet states: $\tau_{PF,lim}^{(i)} = 1/\left(k_F^{(i)} + \sum_n k_{ISC,n}^{(i)}\right)$ based on the computed rate constants in this table. For this estimate, internal conversion is not considered.

The trigonal pyridine complex 3a

Like in complex **2a**, an electron-donating carbene ligand is combined with two slightly electron-rich pyridine moieties. This design is also not expected to readily give rise to TADF but rather conventional decoupled fluorescence and phosphorescence. The trigonal coordination pattern should, however, effectively decrease the S_1-T_1 energy gap ΔE_{ST} and also the energies of the lowest excited states compared to the energies in **2a**. Previous experimental and quantum chemical studies on cationic NHC Cu^I pyridine complexes[12,13] had shown that association of a second pyridine ligand shifted the relative energies of LC, LLCT and MLCT states such that trapping of the photoexcitation in a long-lived ^{3}LC state was suppressed. This effect enhances the luminescence efficiency of the complexes. In the present case, trigonal complexes are formed as well when the sterically less demanding pyridine instead of 2,6-lutidine is added to the zwitterionic NHC Cu^I coordination polymer in excess.[43]

The agreement between cyclohexane and powder spectral data is quite good (Figure 7.24A). Although the apparent absorbances of **2a** and **3a** (Figure 7.22 and Figure 7.24), measured in cyclohexane suspensions of microcrystallites, and their excitation spectra slightly differ, their excitation maxima at around 367 nm are similar (Table 7.10). Remarkably, the peak width of the first excitation band of **3a** is much narrower than the one of **2a**. Simultaneously, the emission maximum of **3a** is significantly red-shifted compared to that of **2a** (Figure 7.24). Among the four complexes, **3a** exhibits the largest apparent Stokes shift of 7605 cm^{-1}.[43] Like in **2a**, a vibronic progression ($\Delta\tilde{\nu} \approx 1200$ cm^{-1}) is observable in the emission spectrum of the powder at 77 K[43] (Figure S7.67), which indicates an LC state as the emitting state.

The predicted theoretical spectrum is clearly blue-shifted compared to the absorption and excitation spectra in cyclohexane (Figure 7.24B). The deviations are particularly pronounced around the excitation wavelength of 375 nm. A quantum chemical analysis of the vertical excitation energies and electronic structures of the low-lying singlet and excited states in the FC region[43] had shown that the LC(carbene) and MLCT(d_{z2}) dominated states of **3a** are blue shifted compared to their **2a** congeners whereas the states exhibiting mainly LLCT(carbene-to-pyridine) or MLCT(d_{xz}) character are stabilized by the coordination of a second pyridine ligand. The ^{1}LC state, which was primarily excited in **2a**, is hardly accessible in **3a** at the excitation wavelength (λ_{ex} = 375 nm) used to record the emission spectra. The lowest-lying excited singlet state rather possesses mixed ^{1}LLCT and ^{1}MLCT(d_{xz}) character. The ^{3}LC state is blue-shifted as well, but remains the lowest excited triplet state. Admixture of

MLCT(d_{xz}) contributions causes an untypically large oscillator strength of the $T_1 \leftarrow S_0$ absorption. Intensity is mainly borrowed from the spin-allowed $S_3 \leftarrow S_0$ transition exhibiting MLCT(d_{z2}) character. Therefore, theory suggests that the long wavelength tail of the excitation spectrum stems from the spin-forbidden T_1 absorption. This interpretation is in line with the observation that the origins of the excitation and phosphorescence emission spectra overlap (Figure 7.24). According to the calculations, the emission of **3a** is thus expected to have a dominant character of phosphorescence. Another intriguing experimental observation is the large Stokes shift of the emission of **3a** (Figure 7.24). Inspection of the energy schemes (Figure S7.228) reveals that the nuclear arrangement at the relaxed T_1 geometry of **3a** is very unfavourable for the S_0 state. The observed large Stokes shift is thus a consequence of the simultaneous lowering of the T_1 and steep rise of the S_0 state potential energies. The normalized excitation/absorption ratio at shorter wavelengths indicates the presence of additional non-luminescent species in suspension (Figure 7.24B).

(3a)

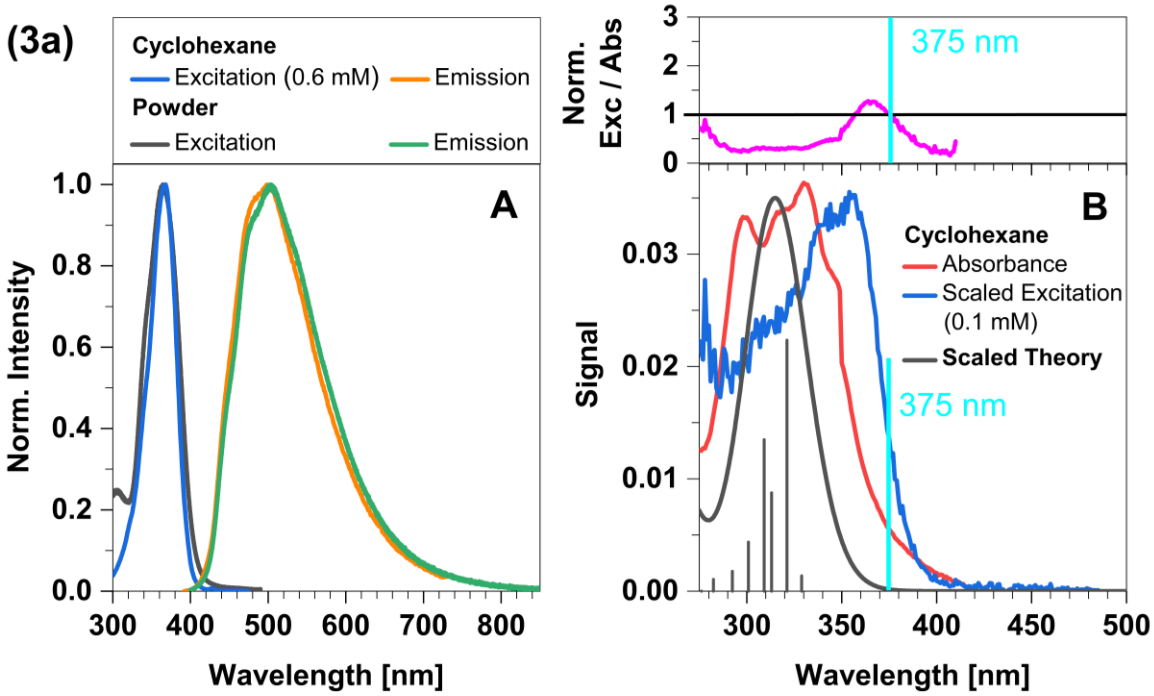

Figure 7.24. Spectra of compound **3a** at 298 K. The excitation spectra were recorded by monitoring luminescence at the respective emission maximum (500 nm). An excitation wavelength of 375 nm was used for the emission spectra. A. Excitation and emission spectra in liquid cyclohexane and powder. A concentrated cyclohexane suspension (0.6 mM) was used to mimic the conditions in powder form. B. Absorbance corrected for baseline and Mie scattering [see Experimental and Theoretical Procedures, eq. (3)]. A diluted sample (0.1 mM) and a semi-micro cuvette (optical path length of 4 mm) are used to minimize inner-filter effects while recording the excitation spectra in cyclohexane. Both excitation in cyclohexane and the DFT/MRCI line spectra broadened with a Gaussian of 0.175 meV FWHM are scaled to the absorbance spectrum for qualitative comparison. The ratio of excitation and absorbance is normalized at 375 nm.

Quickly decaying fluorescence was observed in our time-resolved spectroscopy experiments of **3a** in solid cyclohexane suspension alongside phosphorescence in the late microsecond and early millisecond time regime (Figure 7.25).

(3a)

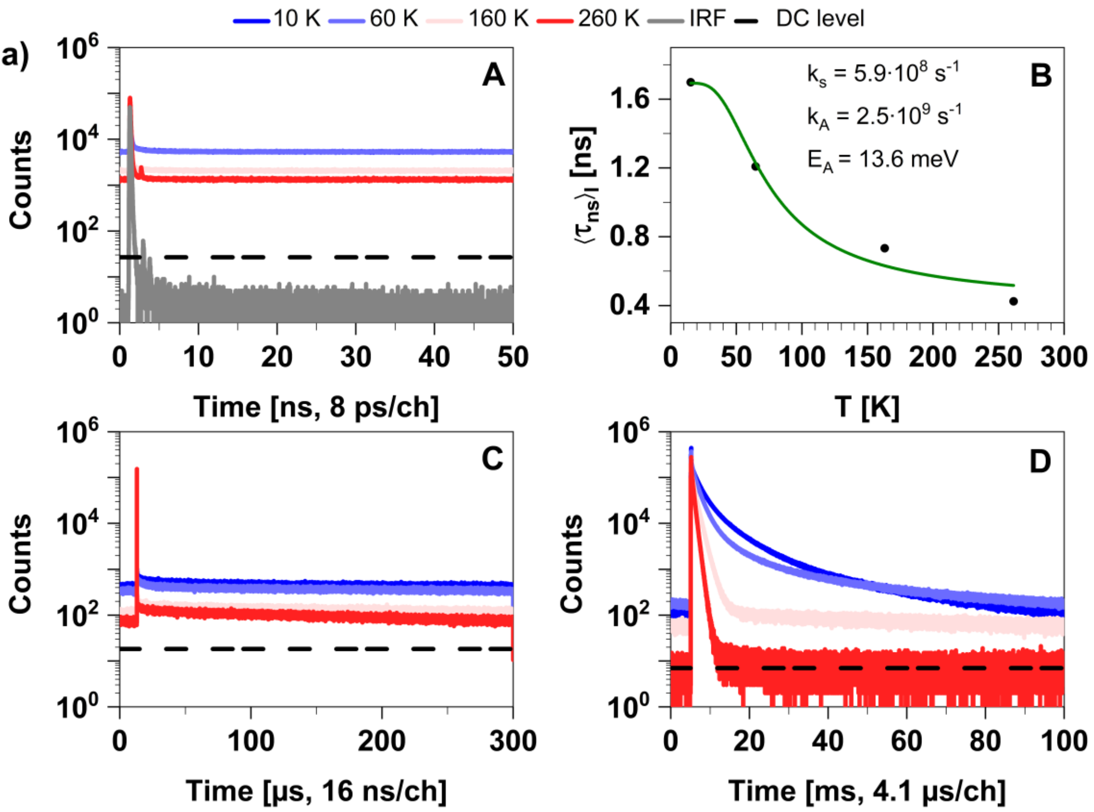

Figure 7.25. Time-resolved luminescence measurements of compound **3a** in solid cyclohexane suspension at temperatures of 10 K, 60 K, 160 K, 260 K, in three distinct time regimes. **A.** Decays in nanoseconds. **B.** Temperature-dependence of the intensity-weighted prompt fluorescence lifetime $\langle\tau_{ns}\rangle_I$. The green line represents the fit of the experimental data according to eq. (1). All fit results with their respective errors are shown in Table S7.24. **C.** Decays in microseconds. **D.** Decays in milliseconds. All luminescence decays exhibit multi-exponential behaviour. The intensity-averaged luminescence lifetimes $\langle\tau\rangle_I$ are listed in Table 7.11, the individual decay times and species fractions are compiled in Table S7.15-Table S7.17. The excitation wavelength was at 375 nm, and the detection wavelength 495 nm. The counts that correspond to the dark count (DC) rate of the detector (95 Hz) are marked with a black dashed line.

This characterization agrees well with the time-resolved data in Table 7.11 and Table 7.12. We attribute the apparent sub-nanosecond decay of the S_1 population to a competition between fluorescence and efficient ISC due to MLCT contributions to the singlet and triplet wavefunctions. This agrees with the estimated upper limit of the fluorescence lifetime $\boldsymbol{\tau_{PF,lim}^{(i)}}$(298 K) = 0.7 ns (see Table 7.12). The MLCT admixture is reduced upon geometry optimization of the T_1 state, resulting in a relatively low radiative rate constant (calculated value

$k_P \approx 10^2$ s^{-1}). This is compatible with measured phosphorescence decay times in the 100 µs – 10 ms regime at $\Phi_{PL} \approx 2\%$.[43] Like in **2a**, the phosphorescence is efficiently thermally quenched by increasing temperature from 10 K to 260 K. Thus, the trigonally coordinated complex **3a** is dominated by phosphorescence from a ^{3}LC state in the regarded temperature range based on an efficient ISC from the excited S_1 state.

The linear formyl lutidine complex 2b

In order to favour TADF in the regarded Cu^I complexes, electron-withdrawing lutidine or pyridine ligands are necessary that stabilize LLCT-type instead of LC states. For this purpose, we now consider a modified version of **2a** with an electron-withdrawing formyl substituent in *para* position of the lutidine ligand that gives rise to the linear Cu^I complex **2b**. Moreover, the steric bulk of the methyl groups in *ortho* position limits the torsional flexibility in the formyl lutidine complex **2b**. Considering the isolated complex, we only found one stable conformer with a ligand twist angle of approx. 26° in the electronic ground state in the calculations, compared to about 10° in a crystalline environment as determined by X-ray diffraction.[43] According to our quantum chemical studies, the ligand twist angles at the excited-state minima range from about 20° for the lowest LLCT(NHC-to-formyl lutidine) states over 23° in the ^{3}LC(formyl lutidine nπ*) and 31° in the LC (NHC) to about 51° in the MLCT(d_{z2}-to-formyl lutidine) states. As intended, the S-T energy gaps of the LLCT and MLCT states are much smaller than for the LC(NHC) state (Figure 7.24).

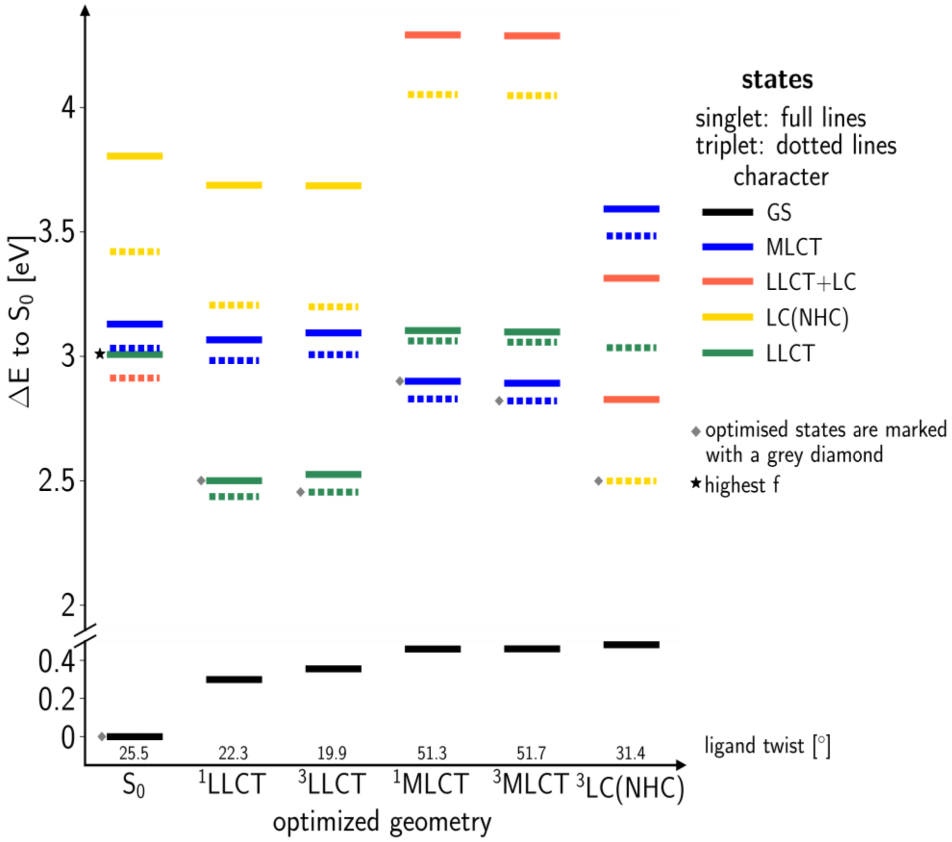

Figure 7.26. Overview over the computed vertical DFT/MRCI energy levels at optimized geometries of low-lying states of complex **2b**. The S$_0$ energy at the optimized ground-state geometry serves as common energy offset.

Excitation with a wavelength of 375 nm (approx. 3.3 eV) addresses a mixture of LLCT and MLCT states which are energetically close at the ground-state geometry (Figure 7.26). The ^{1}LLCT state exhibits higher absorbance than ^{1}MLCT and is therefore preferentially populated. The ^{1}LC(NHC) state lies energetically much higher in the FC region and cannot be reached with the chosen excitation wavelength. The LLCT, LC (NHC) and MLCT(d$_{z2}$) states of **2b** form minima on the S$_1$ or T$_1$ potential energy surfaces, respectively (Figure 7.26). The barrier separating the MLCT minima from the lower-lying LLCT minima is easily overcome. Direct emission from the MLCT minima is therefore not likely to occur in this complex.

Quantum chemistry predicts larger displacements of the nuclear coordinates between the minimum structures of the ^{3}LC and ^{3}LLCT states, which are adiabatically nearly degenerate (Figure 7.26). The ^{3}LC(NHC) state is long-lived as the equilibration with the other triplet potential wells is kinetically hindered by high reorganization energies. Their populations are interconvertible at room temperature, but a small portion appears to get trapped in the ^{3}LC potential well at lower temperatures and decays via ^{3}LC phosphorescence. These findings match the experimentally recorded low $\Phi_{PL} \approx 1\%$.[43]

The broad and structureless emission band (Figure 7.27) matches the predicted LLCT character of the emissive state. The absorption spectrum agrees well with that from theory (Figure 7.27B). The normalized excitation/absorption ratio at shorter wavelengths indicates small constributions of additional non-luminescent species in suspension (Figure 7.27B).

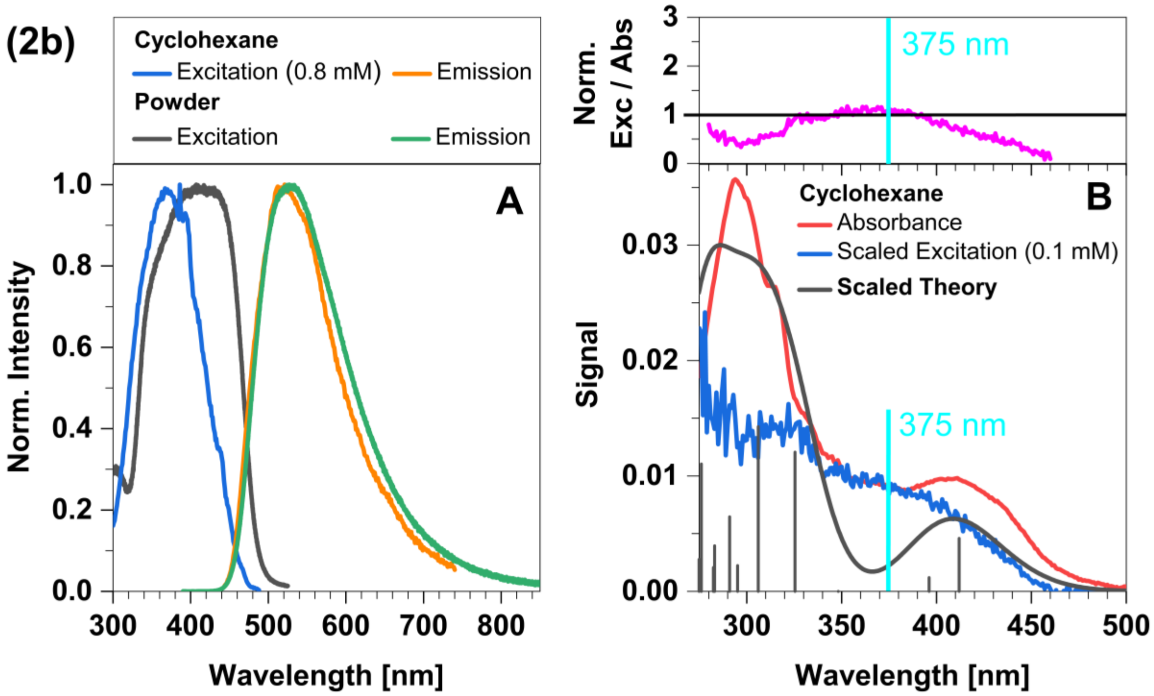

Figure 7.27. Spectra of compound **2b** at 298 K. The excitation spectra were recorded by monitoring luminescence at the respective emission maximum (540 nm). An excitation wavelength of 375 nm was used for the emission spectra. **A.** Excitation and emission spectra in liquid cyclohexane and powder. A concentrated cyclohexane suspension (0.8 mM) was used to mimic the conditions in powder form. **B.** Absorbance corrected for baseline and Mie scattering [see Experimental and Theoretical Procedures, eq. (3)]. A diluted sample (0.1 mM) and a semi-micro cuvette (optical path length of 4 mm) are used to minimize inner-filter effect while recording the excitation spectra in cyclohexane. Both excitation in cyclohexane (diluted suspension) and the DFT/MRCI line spectra broadened with Gaussian of 0.175 meV FWHM are scaled to the absorbance spectrum for qualitative comparison. The ratio of excitation and absorbance is normalized at 375 nm.

Vibronic coupling between the MLCT and LLCT states is expected to enhance the ISC and rISC between the ^{1}LLCT and ^{3}LLCT states. The small ΔE_{ST} value of the LLCT states and the admixture of small amounts of MLCT(d_{xz}) character (Figure S7.180 and Figure S7.188) suggest that thermally activated up-conversion to the corresponding singlet potential well is possible. Thus, we expect a multiexponential luminescence decay.

In the temperature range from 270 K to 100 K, the mean emission position red-shifts as phosphorescence takes over. However, as the temperature decreases below 100 K, we observe the opposite trend and the emission maximum shifts to shorter wavelengths (Figure 7.28A). This probably occurs due to small portions of the sample dissociating and emission of the free ligand (4-formyl-2,6-lutidine). The spectrum of the free ligand was compared with the spectrum of the sample at 10 K (Figure 7.28B).

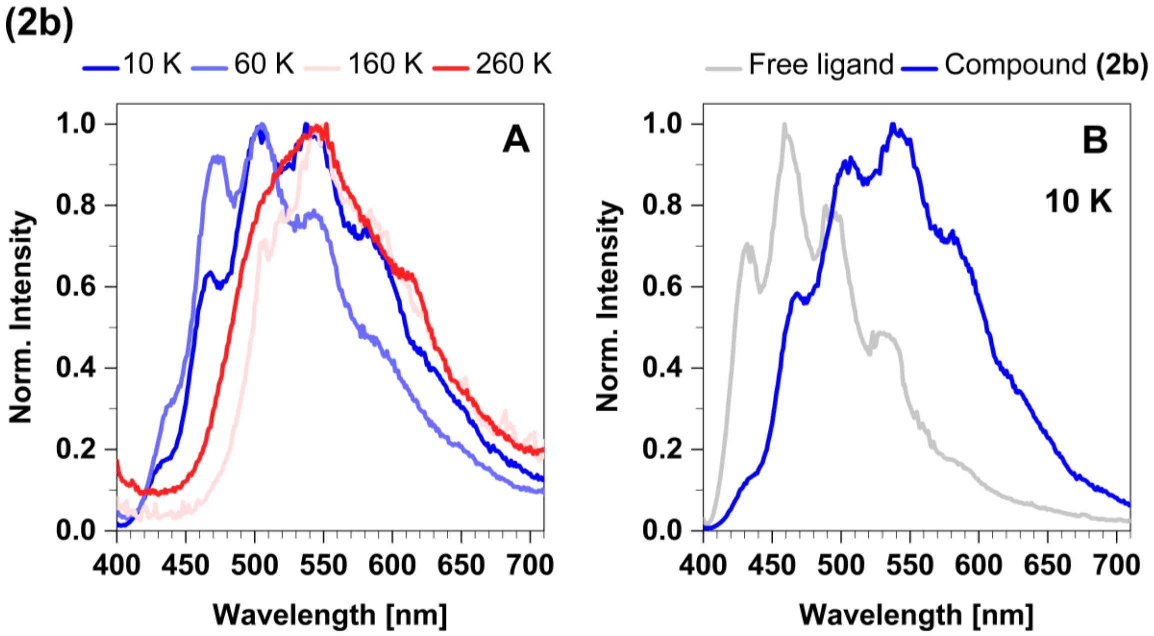

Figure 7.28. A. Steady-state luminescence spectra of **2b** in cyclohexane suspension at selected temperatures of 10 K, 60 K, 160 K, and 260 K. **B.** Comparison of the steady-state spectrum of **2b** with the free ligand spectrum obtained in cyclohexane solution at 10 K. The excitation wavelength was 375 nm.

In time-resolved measurements within the nanosecond time regime, we observe a significant increase of the offset fraction upon cooling. This observation implies slowly decaying emissive states at all temperatures (Figure 7.29A). The temperature dependence of the slow components does not follow a simple single barrier model anymore as implied by eq.

(1). To include the predicted fast equilibration of the LLCT and MLCT populations, we fitted the temperature-dependent behaviour of the delayed luminescence decay times to the following equation assuming Boltzmann thermalization among the involved states:

$$\boldsymbol{\tau_{fit}(T) = \frac{2 + exp\left(-\frac{E_1}{k_BT}\right) + 3exp\left(-\frac{E_2}{k_BT}\right) + exp\left(-\frac{E_3}{k_BT}\right) + exp\left(-\frac{E_4}{k_BT}\right)}{2k_0 + k_1 exp\left(-\frac{E_1}{k_BT}\right) + 3k_2 exp\left(-\frac{E_2}{k_BT}\right) + k_3 exp\left(-\frac{E_3}{k_BT}\right) + k_4 exp\left(-\frac{E_4}{k_BT}\right)}} \tag{2}$$

where the factors 2 and 3 account the state degeneracies of the triplet sublevels. k_0 and k_1 refer to the T_1 state, split by E_1, while k_2 and E_2 represent T_2. k_3(E_3) and k_4(E_4) are rate constants (energies) associated with the singlet states S_1 and S_2, respectively. For details, see section 7.3.5 (Experimental and Theoretical Procedures).

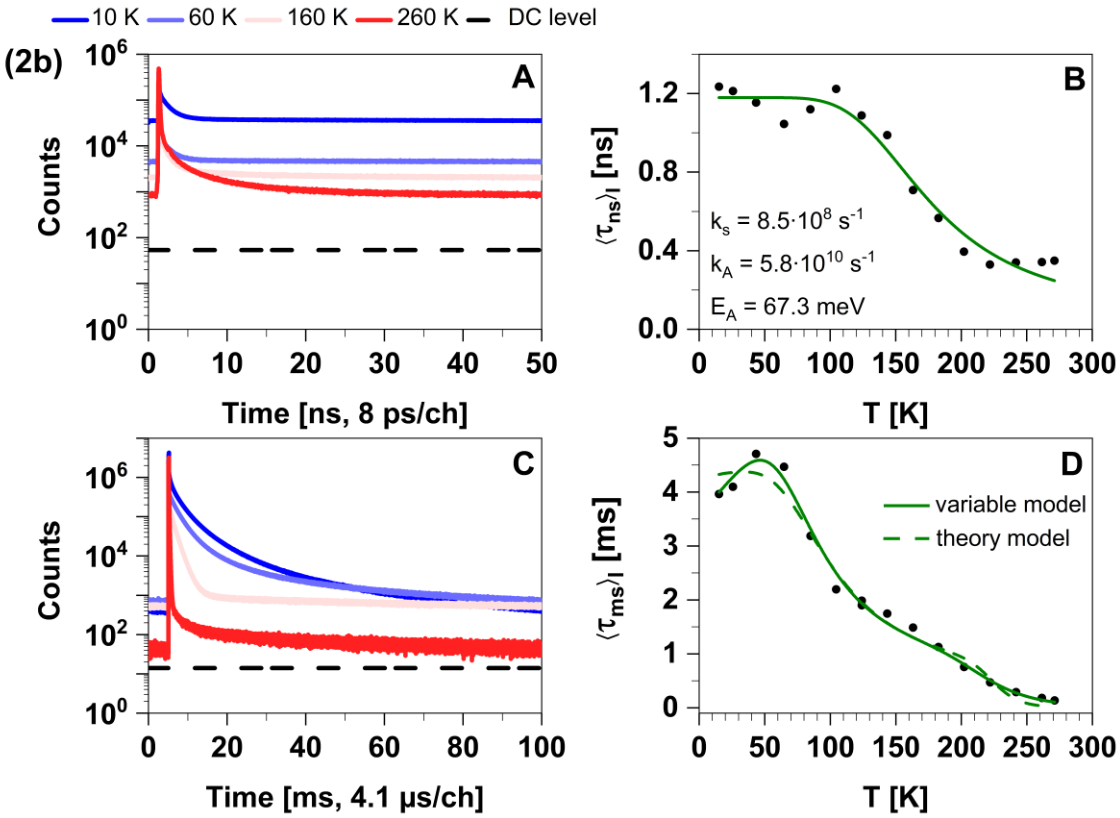

Figure 7.29. Time-resolved luminescence measurements of compound **2b** in solid cyclohexane suspension at selected temperatures of 10 K, 60 K, 160 K, 260 K, in two distinct time regimes. Related decay components recorded in the temperature range from 10 K to 270 K are provided in Figure S7.68. The excitation wavelength was 375 nm, and the detection emission wavelength 540 nm. **A.** Decay curves in nanoseconds. **B.** Temperature dependence of the intensity-weighted prompt fluorescence lifetime $\langle \tau_{ns} \rangle_I$. The green line represents the fit of the experimental data according to eq. (1). All fit results with their respective errors are shown in Table S7.24. **C.** Decays in milliseconds. **D.** Temperature-dependence of the intensity-weighted luminescence lifetime $\langle \tau_{ms} \rangle_I$ with all parameters compiled in Table S7.25 and Table S7.26. The green lines represent least-squares fits of eq. (2) to the experimental data. Solid line (variable model, Table S7.25): E_1 and E_4 are free parameters while E_2 and E_3 are fixed to theoretically computed zero-point vibrational energy corrected adiabatic values of 28.5 meV and 52.2 meV, respectively. Dashed line (theory model, Table S7.26): all energies are fixed to theoretically computed zero-point vibrational energy corrected adiabatic values (Table S7.27). The intensity-averaged luminescence lifetimes $\langle \tau_{\mu s} \rangle_I$ are listed in Table 7.11, the individual decay times and species fractions are compiled in Table S7.18-Table S7.20. The counts that correspond to the dark count (DC) rate of the detector (95 Hz) are marked with a black dashed line.

To further investigate the TADF properties, we measured time-resolved emission spectra (TRES) at 270 K, 220 K, 180 K, and 10 K (Figure 7.30A-D). At the highest temperature (270 K), we observed that the spectra in the nanosecond and microsecond time regimes strongly overlap which can be attributed to the simultaneous presence of TADF and phosphorescence. As **2b** is cooled down, the spectral overlap decreases and two separate emission bands can be resolved. The emission in the nanosecond time regime exhibits a blue shift from 535 nm to 520 nm, while the emission in the microsecond time regime shifts towards longer wavelengths and even overlaps with the emission in milliseconds. Furthermore, the emission in both the microsecond and millisecond time regimes feature vibronic fine structure at low temperatures, which is typical for LC-related emission. In contrast, the emission band in the ns time range is broad and barely shows any fine structure implying emission from CT-type states. This observation suggests that phosphorescence from a ^{3}LC state is involved in the microsecond time range and becomes the dominant process at lower temperatures. Luminescence within the millisecond time range displays intricate multi-exponential characteristics (Figure S7.72). Upon careful spectral analysis, we deduced that the predominant source of luminescence arises from compound **2b**, with a minor contribution originating from leached ligand (Figure S7.74).

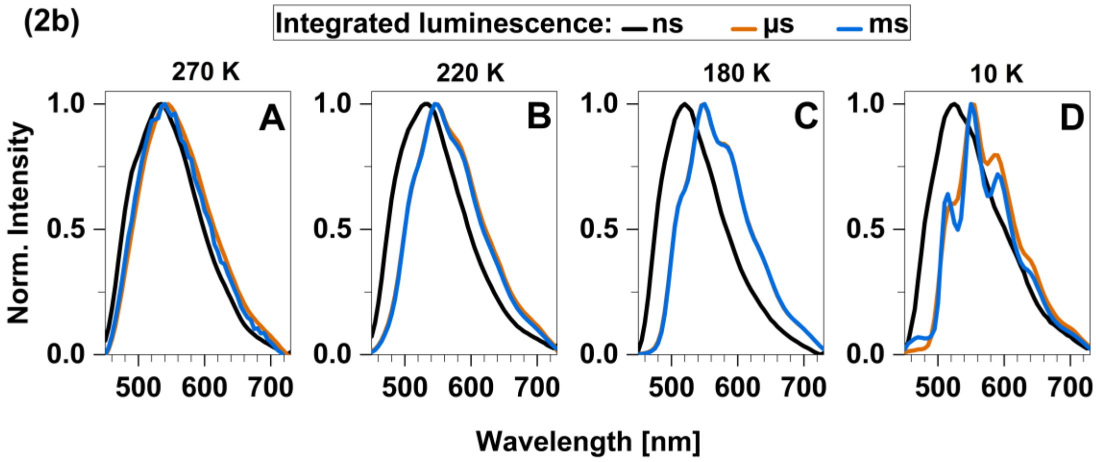

Figure 7.30. Time-resolved emission spectra (TRES) of **2b** in solid cyclohexane suspension obtained at four different temperatures: **A.** 270 K, **B.** 220 K, **C.** 180 K and **D.** 10 K.

In the temperature range from 100 K to 270 K, we observed a non-linear dependence of the logarithmic rate constant on the reciprocal temperature, which is indicative for limited thermal coupling in that temperature range. This implies that the rISC rate of **2b** cannot compete with the decay rate of T_1 in that temperature range yet and thus, must be at most of similar order of magnitude of k_P. It also matches the fact that phosphorescence can be experimentally distinguished from fluorescence at low temperatures while TADF only becomes relevant at temperatures above 220 K. Overall, TADF in **2b** is based on ISC and rISC between ^{1}LLCT and ^{3}LLCT states that admix with MLCT states. Additionally, the quasi-degeneracy between the ^{3}LLCT and a ^{3}LC state (Figure 7.24) leads to the observation of phosphorescence with vibronic fine structure at low temperatures ($T < 200$ K, Figure 7.30).

The trigonal formyl pyridine complex 3b

Replacement of the pyridine ligand in **3a** with the electron-withdrawing 4-formylpyridine results in complex **3b**. Similarly to **2b**, this leads to an energetic stabilization of the LLCT and MLCT(d_{z2}) states, with the easier accessibility of MLCT(d_{xz}) states caused by the energetic increase of the corresponding ligand-field orbital due to the trigonal coordination. Consequently, TADF properties should also be expected in this case. In the FC region, the lowest excited singlet and triplet states emerge from an LLCT excitation with large contributions from an MLCT(d_{xz}) configuration as may be clearly seen from the difference density of the S_1 state plotted in Figure 7.31 (left). The singlet and triplet MLCT(d_{z2}) states (Figure 7.31, right) only have marginally higher excitation energies at the ground state geometry. The $S_0 \rightarrow S_1$ and $S_0 \rightarrow S_3$ transitions both contribute to the excitation spectrum and should result in emission. With vertical singlet–triplet energy gaps of $\Delta E_{ST} \approx 807$ cm^{-1} (0.1 eV), S_1 and S_3 appear predestined for TADF, provided that their electronic structures and energy splittings do not change dramatically upon geometry relaxation. An overview over the energetic positions of the electronic states at various minimum geometries is provided in Figure 7.32.

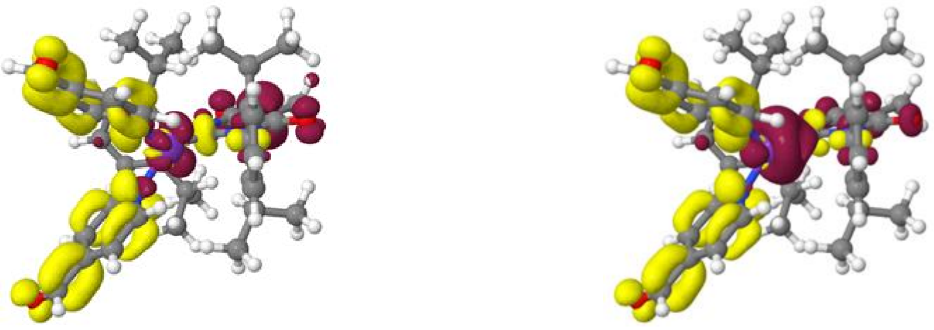

S_1 (LLCT/ MLCT(d_{xz})) S_3 (MLCT(d_{z2}))

Figure 7.31. Difference densities (isovalues ±0.002) of the S_1 (LLCT/ MLCT(d_{xz})) and S_3 (MLCT(d_{z2})) states of **3b** at the optimized S_0 geometry. Red colour signals electron loss, yellow colour electron gain with respect to the electronic ground state density.

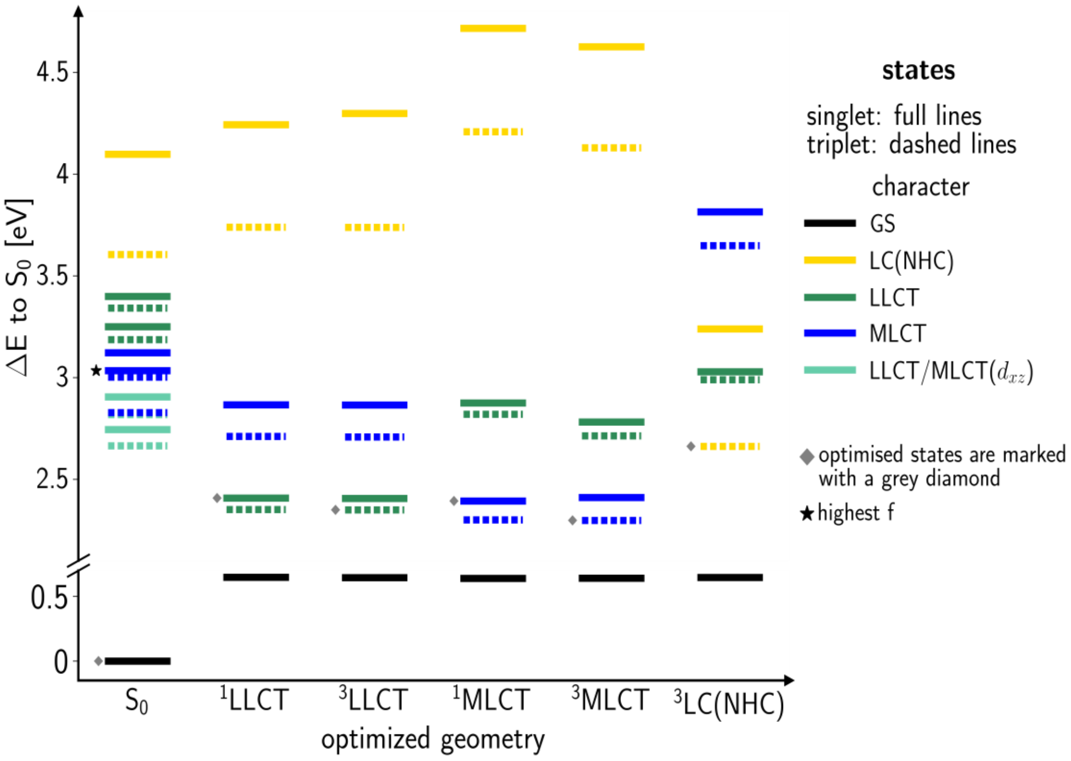

Figure 7.32. Overview over the computed vertical DFT/MRCI energy levels at optimized geometries of low-lying states of complex **3b**. The S_0 energy at the optimized ground-state geometry serves as common energy offset.

The absorption maximum predicted by theory of compound **3b** is at 405 nm and is related to the $S_3 \leftarrow S_0$ transition (Figure 7.32). The respective $S_1 \leftarrow S_0$ transition is only observable as a shoulder (excitation spectrum) or weak band (absorbance spectrum) (Figure 7.33B). However, the measured absorption and excitation spectra in cyclohexane are blue-shifted compared to the theoretically predicted spectrum (Figure 7.33B). The normalized excitation/absorption ratio at shorter wavelengths indicates the presence of additional non-luminescent species in suspension (Figure 7.33B).

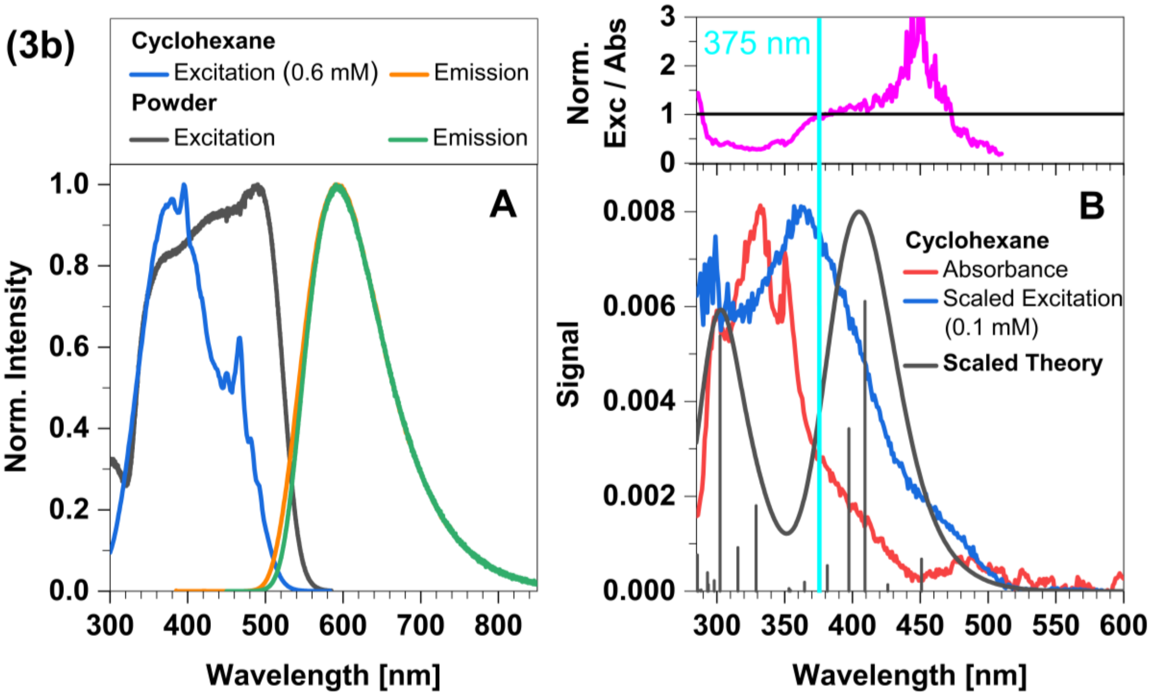

Figure 7.33. Spectra of compound **3b** at 298 K. The excitation spectra were recorded by monitoring luminescence at the respective emission maximum (595 nm). An excitation wavelength of 375 nm was used for the emission spectra. **A.** Excitation and emission spectra in liquid cyclohexane and powder. A concentrated cyclohexane suspension (0.6 mM) was used to mimic the conditions in powder form. **B.** Absorbance corrected for baseline and Mie scattering [see eq. (3)] and absorbance of the free ligand (see Experimental and Theoretical Procedures). A diluted sample (0.1 mM) and a semi-micro cuvette (optical path length of 4 mm) are used to minimize inner-filter effects while recording the excitation spectra in cyclohexane. Both excitation in cyclohexane and the DFT/MRCI line spectra broadened with a Gaussian of 0.175 meV FWHM are scaled to the absorbance spectrum for qualitative comparison. The ratio of excitation and absorbance is normalized at 375 nm.

The emission spectra in cyclohexane and powder overlap completely (Figure 7.33A). The maximum in the steady-state emission spectrum shows a blue-shift from 613 nm at 100 K to 599 nm at 270 K (Figure 7.34A), which allows to estimate a value of ΔE_{ST} = 381 cm^{-1}

(48 meV). At temperatures below 100 K, the maximum does not show any additional shift, but an additional band is observed. This band is assigned to luminescence of leached free ligand 4-formyl pyridine (Figure 7.34B), which was dissociated from the surface of the microcrystals before freezing. Another confirmation of this interpretation is the absence of this band in the respective solid-state measurements, indicating that this process only occurs with measurable significance in suspension. Concerning the chemical stability of this compound, this is an expected observation, since complex **3b** proved to be the least stable of the four investigated compounds.[43]

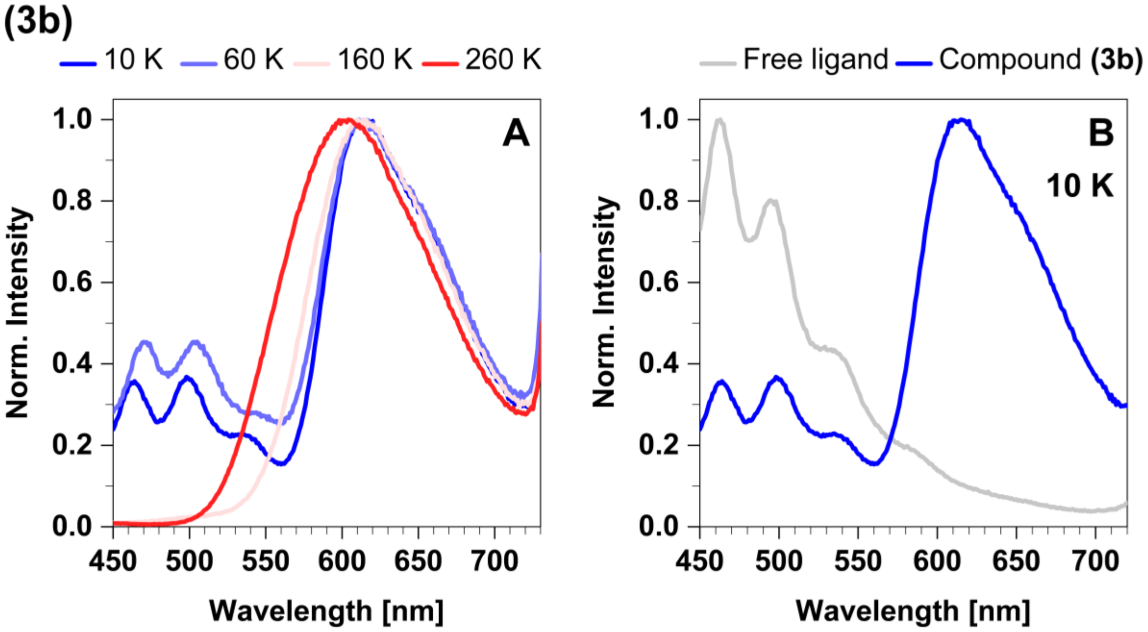

Figure 7.34. A. Steady-state luminescence spectra of **3b** in cyclohexane suspension at selected temperatures of 10 K, 60 K, 160 K, and 260 K. **B.** Comparison of the steady-state spectrum of **3b** with the spectrum of the free ligand (4-formyl pyridine) obtained in cyclohexane solution at 10 K. The excitation wavelength was 375 nm.

The energetic proximity of MLCT(d_{z2}) and MLCT(d_{xz}) states promises enhanced SOC. According to El-Sayed's rule,[44] the rate of ISC is relatively large if the non-radiative transition involves a change of orbital type. Although this rule was originally formulated for heterocyclic organic compounds, it can be extended to include transition metal complexes as well.[14] This extended version states that fast ISC is expected if the states are singly excited with respect to each other, the local orbital angular momentum $\boldsymbol{l}$ is conserved and the magnetic quantum number $\boldsymbol{m_l}$ changes by 0, ±1 unless $\boldsymbol{m_l = 0}$ where $\Delta\boldsymbol{m_l} = \pm 1$ is required. In the present context of **3b**, this means that strong SOC is expected between MLCT(d_{z2}) and MLCT(d_{xz}) or

MLCT(d_{yz}) configurations with a common ligand acceptor orbital. The large calculated rate constants for the ISC and rISC transitions between these pairs of states (Figure 7.35) suggest that their populations fully equilibrate at room temperature at higher rates than radiative decay, which, in turn, appears to be the rate-determining step (microseconds) in this complex. We therefore mainly expect delayed fluorescence under these conditions. Indeed, time-resolved spectroscopy measurements show that the prompt fluorescence of **3b** decays at the sub-nanosecond time scale (Figure 7.36A), which agrees well with the theoretical predictions. Presumably, a mixture of TADF and phosphorescence is observed in the microsecond time range. This assumption is confirmed by analysis of the temperature dependence of the luminescence decay times (Figure 7.36D). Given the El-Sayed allowed ISC process in **3b**, there is also an expectedly strong spin admixture between the ^{1}MLCT and ^{3}MLCT states, which should lead to radiative decay times in the order of microseconds. This qualitative line of argument proves true considering the values of the computed phosphorescence rate constants of the ^{3}LLCT and ^{3}MLCT states which are both of the order of $k_P \approx 10^4$ s^{-1} (Table 7.12).

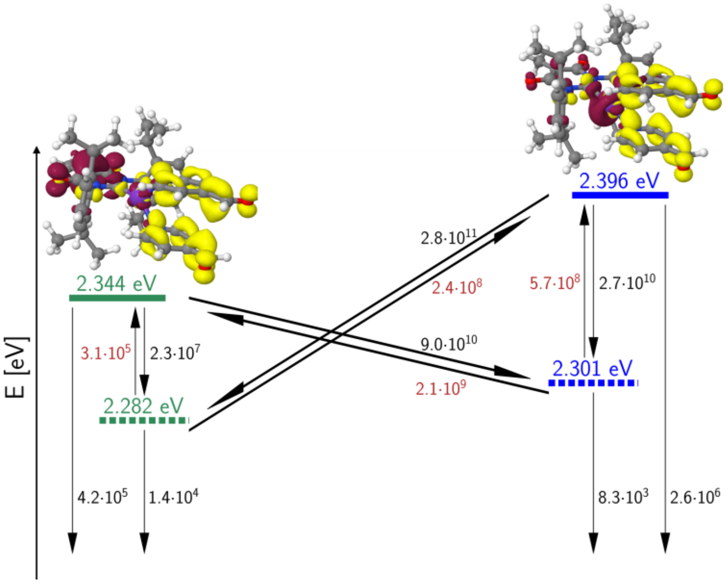

Figure 7.35. Calculated 0–0 energies of the LLCT/ MLCT(d_{xz}) (green) and MLCT(d_{z2}) (blue) states of **3b**. Singlet states are symbolized by solid line, triplet states by dashed lines. ISC and rISC rate constants [s^{-1}] were determined in Condon approximation for a temperature of 298 K. Rate constants of thermally activated processes are given in red. The fluorescence and phosphorescence rate constants [s^{-1}] were computed according to the Einstein formula and do not include FC factors. The insets depict difference densities (isovalues ±0.002) of the ^{1}LLCT (left) and ^{1}MLCT(d_{z2}) states at their respective minimum geometries. For colour codes, see Figure 7.31.

This expected time scale is experimentally confirmed. In the microsecond time regime, the decays are characterized by a multi-exponential fit function in the entire temperature range from 10 K to 270 K. The intensity-averaged decay times increases from 8.87 μs at 270 K to almost 40 μs at 10 K (Figure 7.36D, Table S7.22). We monitor three characteristic temperature regions: between 270-200 K (Figure S7.70A), the emission amplitude of delayed emission decreases, which is a characteristic observation for TADF. Between 200-100 K (Figure S7.70B), this amplitude remains constant. However, upon further cooling (between 100-10 K, Figure S7.70C), the amplitude rises again, indicating the presence of an alternative process distinct from TADF. The temperature dependence of the corresponding amplitudes and lifetimes is shown in Figure S7.71. This is anticipated because the thermal energy is not sufficient to overcome the computed energy gap of ΔE_{ST} = 62 meV. This value is close to the one derived from the spectral shift observed in the steady-state data (47 meV). Additionally, the observed spectral red-shift in the steady-state emission spectra upon cooling provides further evidence of phosphorescence becoming the dominant emission source at lower temperatures. An important experimental hint for this tightly coupled ensemble of excited states (red box in Figure 7.37) is the fit of the microsecond time domain temperature-dependent decay times to eq. (2). Using the theoretically predicted energy gaps between the relevant ^{1}LLCT, ^{3}LLCT, ^{1}MLCT, and ^{3}MLCT states of **3b** and optimizing the five corresponding rate constants, the agreement between theory and experiment is striking. Notably, the fitted rate constants are close to the theoretically predicted values (Table S7.28).

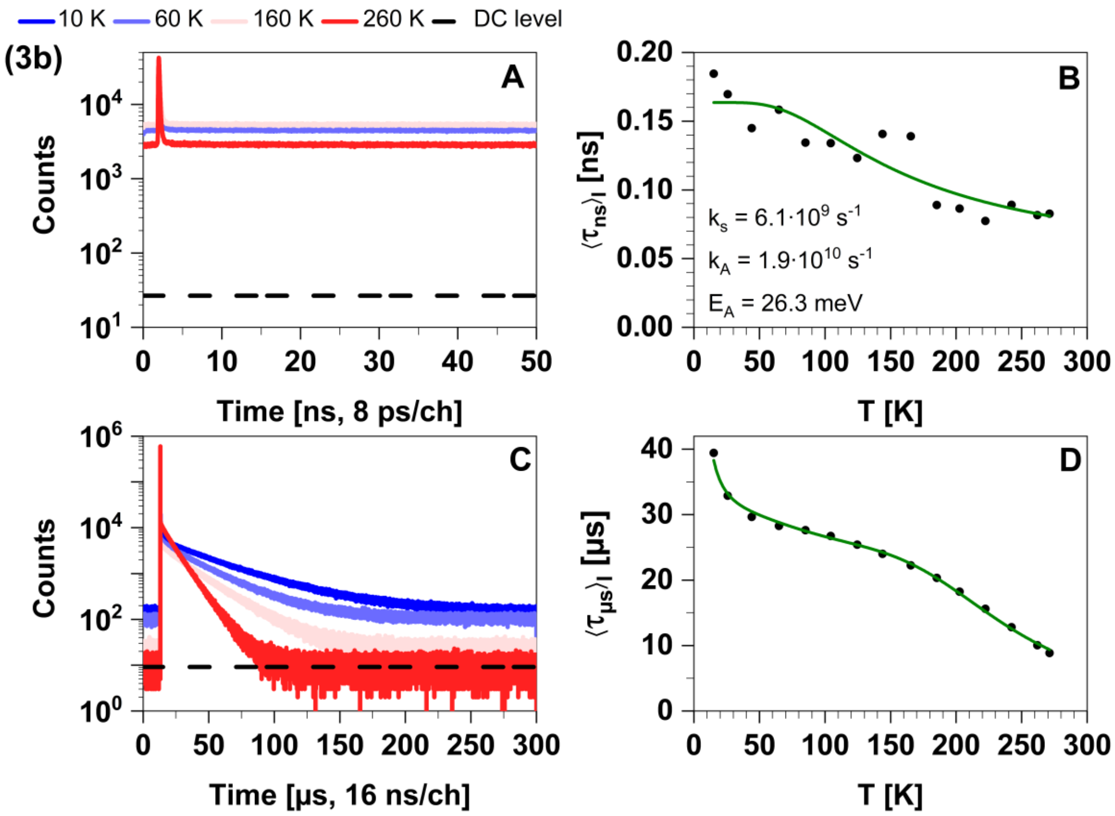

Figure 7.36. Time-resolved luminescence measurements of compound **3b** in solid cyclohexane suspension at selected temperatures of 10 K, 60 K, 160 K, 260 K, in two distinct time regimes. Related decay components recorded in the temperature range from 10 K to 270 K are provided in Figure S7.69 and Figure S7.70. The excitation wavelength was at 375 nm, and the detection wavelength 595 nm. **A.** Decay curves in nanoseconds. **B.** Temperature-dependence of the intensity-weighted prompt fluorescence lifetime $\langle \tau_{ns} \rangle_I$. The green line represents the fit of the experimental data according to eq. (1). All fit results with their respective errors are shown in Table S7.24. **C.** Decays in microseconds. **D.** Temperature-dependence of the intensity-weighted luminescence lifetime $\langle \tau_{\mu s} \rangle_I$ with all parameters compiled in Table S7.28. The green line represents the fit of eq. (2) to the experimental data: E_1 to E_4 were fixed to the theoretically computed zero-point vibrational energy corrected adiabatic values and k_0 to k_4 were optimized. The intensity-averaged luminescence lifetimes $\langle \tau_{\mu s} \rangle_I$ are listed in Table 7.11, the individual decay times and species fractions are compiled in Table S7.21-Table S7.23. The counts that correspond to the dark count (DC) rate of the detector (95 Hz) are marked with a black dashed line.

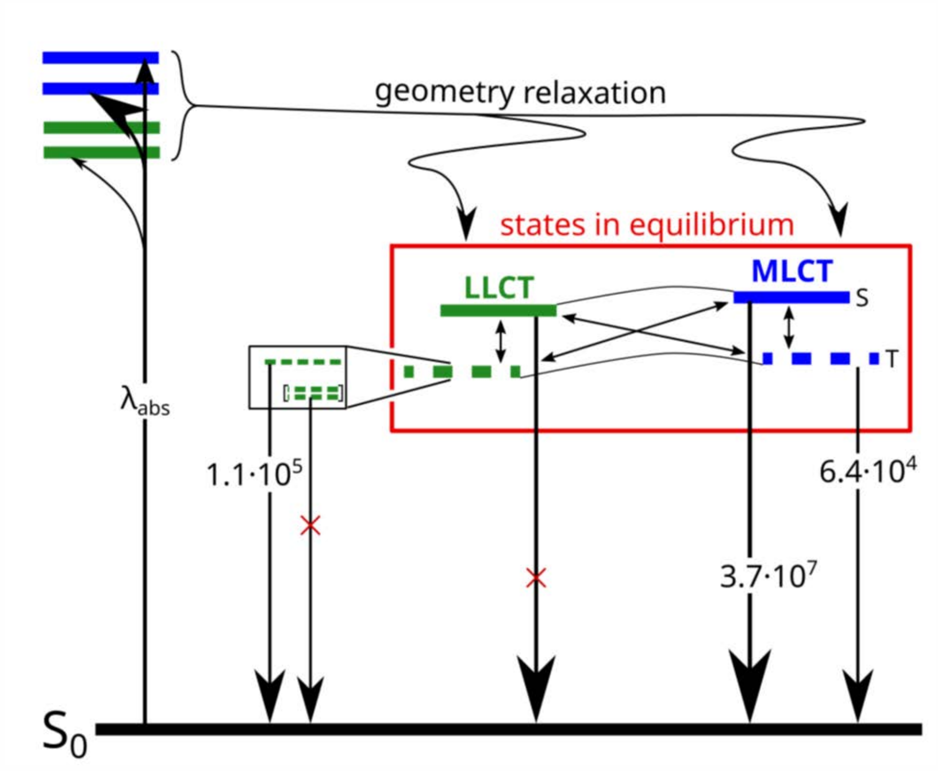

Figure 7.37. Kinetic scheme of the photo excitation decay of **3b.** The rate constants of the radiative transitions were obtained by fitting the temperature-dependent decay times to eq. (2) using fixed theoretical energy separations. Solid horizontal lines indicate singlet states, dashed lines triplet states. The zero-field splittings of the triplet sublevels are not drawn to scale.

Due to the high MLCT contributions to their electronic wavefunctions, the T_1 states exhibit large SOCMEs with several excited singlet states with high oscillator strengths from which the spin-forbidden transitions borrow intensity. The calculated spin-component averaged phosphorescence rate constants are of the order of $k_P \approx 10^4$ s^{-1}. Considering that only a small portion of the excited molecules radiatively decays ($\Phi_{PL} = 0.13$ was measured in the solid state at room temperature,[43] these kinetic constants are consistent with the measured decay times of roughly 10-40 µs (Table S7.22) for the slow component.

All-in-all, complex **3b** appears to be well suited for harvesting singlet as well as triplet excitons in an OLED. In the solid state, it emits orange luminescence with a PLQY of $\boldsymbol{\Phi}_{PL} = 0.13$, which is approximately 3 to 10 higher than the three other regarded complexes. In suspension, the increase of the PLQY of **3b** with respect to the other complexes is even more pronounced: 12 to 100 times (Table 7.10). It should be noted, however, that **3b** is chemically labile in solution unless 4-formylpyridine is added in excess. Thus, decomposition products might slightly have affected the determination of the relative quantum yields. Obviously, the formyl substituent in *para* position does not only increase the π-acceptor strength, it also reduces the σ-donor strength of the pyridine ligand. Thus, work is underway to synthesize trigonal complexes with two π-accepting ligands tethered together, which should enhance their chemical stability.

7.3.4 Summary and Conclusions

The aim of this work was the design of electrically neutral linear or trigonal TADF emitting Cu^I complexes with an electron donating carbene ligand and one or two electron accepting ligands to enable thin-film processing of the emitter in OLED technologies. For this purpose, we have combined temperature-dependent time-resolved photoluminescence spectroscopy with DFT/MRCI calculations to shed light on the expected optical performance of a number of selected neutral Cu^I complexes with pyridine-based acceptor ligands. They are easily accessible in large scales from a coordination polymer intermediate in a straightforward synthetic approach. All investigated complexes show luminescence in the visible range. A clear design pattern towards TADF properties can be extracted from our combined study. If the electron-donating carbene is combined with electron-rich pyridine-derived ligands, carbene ligand-centered states form the first excited singlet and triplet states with substantial S–T energy gap, which rather leads to the observation of dominantly decoupled prompt fluorescence and phosphorescence (compounds **2a** and **3a**). In contrast, electron-poorer pyridine ligands in such a Cu^I complex lead to an energetic stabilization of LLCT and MLCT states. This stabilization poses a leverage towards TADF (Figure 7.38) as observed in compounds **2b** and **3b**. Trigonal coordination with electron-poor pyridine ligands also greatly enhances the quantum yield but in the same instance, the Cu-ligand bonds become more labile, which limits the kinetic stability of such complexes in solution.

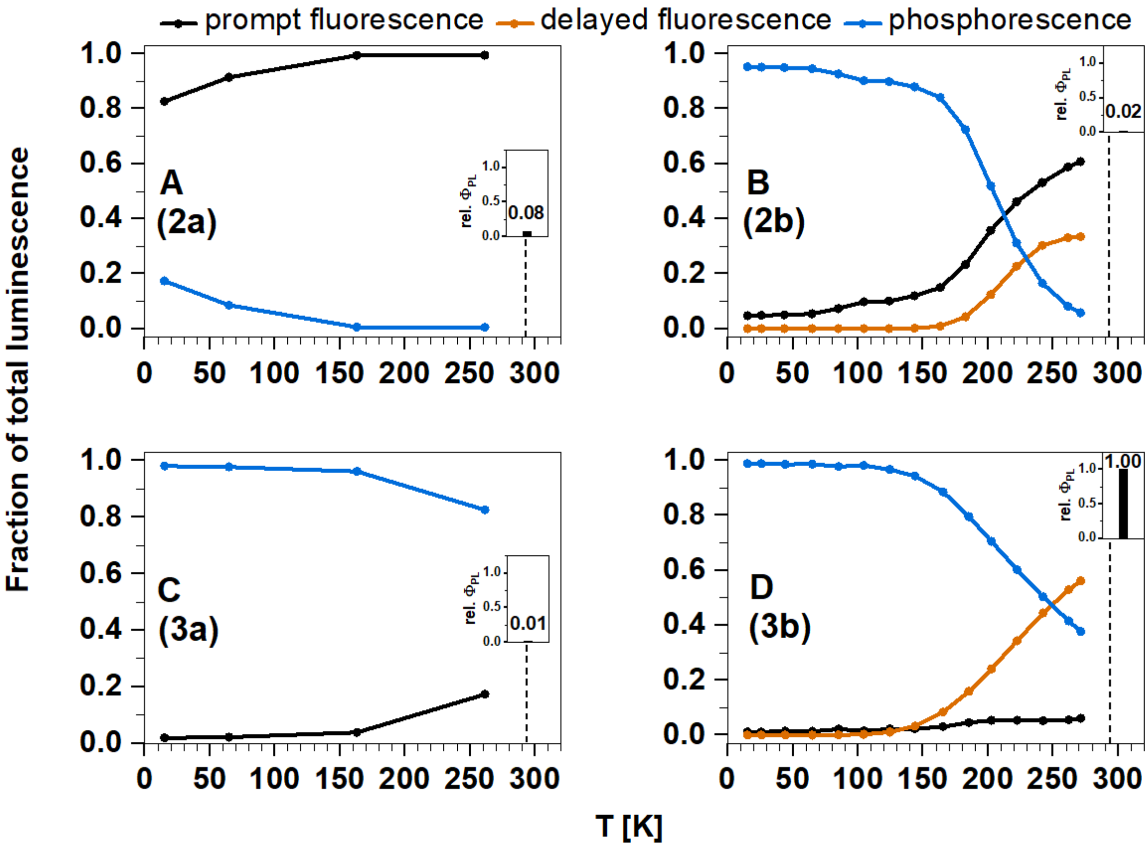

Figure 7.38. Temperature-dependent fractions of prompt (black), delayed (brown) fluorescence, and phosphorescence (blue) in the investigated Cu^{I} complexes derived by integration of the nanosecond range decay curves and, for **2b** and **3b**, the fitting results of the delayed luminescence according to eq. (2). For details, see chapter 7.3.5 (Experimental and Theoretical Procedures).

Trigonal coordination strongly favours ISC while slightly red-shifting the emission band compared to a linearly coordinated analogue. However, usage of electron-poorer pyridine ligands additionally renders the Cu-ligand bonds labile and thus, makes the respective complexes dynamic in solution or suspension. This sets a general limitation to the PLQYs. One strategy to circumvent this fundamental dilemma is to tether two π-accepting ligands together leading to a trigonal complex with enhanced chemical stability due to the chelate effect. Experiments in that direction are currently pursued in our laboratory. Overall, the present studies offer a detailed overview of the possibilities of targeted molecular design to selectively address desirable optical properties in organometallic compounds.

7.3.5 Experimental and Theoretical Procedures

Materials

Synthesis and characterization of the compounds. The complexes were prepared and characterized as described in our preceding publication.[43] In short, the coordination polymer **[1·Cu]ₙ** was obtained by treating an acetonitrile solution of the literature known Li[NHC-Cu-Cl] complex[45] with water. Subsequently, this polymer was reacted with an excess of the desired ligands in dichloromethane solution. Removing the solvent *in vacuo* and washing of the residue with diethyl ether yielded the desired compounds **2a**, **2b**, **3a** and **3b**.

Spectroscopy

Absorption spectra. Absorption spectra were recorded on a Cary 4000 UV-Vis spectrophotometer (Agilent Technologies, USA). To minimize artefacts, absorption spectra were measured for diluted samples. Samples were prepared by suspending 0.24 mg, 0.28 mg, 0.17 mg, and 0.22 mg of compounds **2a**, **2b**, **3a** and **3b**, respectively, in a total volume of 3.0 ml of cyclohexane (HiPerSolv Chromanorm for HPLC, VWR Chemicals). The samples were treated in an ultrasonic bath before the measurement. Constant stirring of the suspension during the measurement was achieved by Hellma cuv-o-stirr model 333. The spectrum of each compound was measured five times and averaged. The measured data were corrected for the baseline drifts and strong scattering of the suspensions at short wavelengths. To this end a correction function A_{corr} was generated and subtracted from the measured spectra. The baseline drift as observed in the absorption-free region of the spectrum (>550 nm) was approximated by a straight line. To model the scattering of the suspension of particles with a broad size distribution, a combination of Rayleigh and Mie-scattering was assumed. We used the approximation of Graaff et al.[46] where a scattering intensity proportional to $\nu^{0.37}$ was found for particles with diameter $d > \lambda$. Scattering of smaller particles we described with the well-known ν^4 dependence [Eq. (3)]:

$$\boldsymbol{A_{\text{corr}} = a + b\lambda + c/\lambda^4 + d/\lambda^{0.37}} \qquad (3)$$

with free parameters *a-d* to be optimized for the respective spectrum. Notably, corrections did not remove or add new peaks (see comparison between raw and corrected data in Figure S7.65).

Due to partial dissociation of the ligands, the spectra of the suspensions contained, to a different degree, contributions by absorption of free ligand. In order to enable proper comparison with excitation spectra this contribution was compensated by subtraction of independently measured corresponding (baseline corrected) absorbance spectra of free ligand in cyclohexane. The respective spectral contribution of free ligand was estimated around 250 nm, where the complexes showed only small absorption. This correction was required for the trigonal complexes **3a** (pyridine) and **3b** (formyl pyridine).

Excitation spectra. The excitation and emission spectra were recorded on a Horiba Fluorolog FL3-22 spectrofluorometer equipped with double monochromators and a cooled PMT. The excitation spectra of diluted suspensions were measured in semi-micro cuvettes (Hellma) with a light path of 4 mm. Samples were stirred all the time during the measurements. The measured data were corrected for inner filter effects in the excitation path using the measured absorbance of the samples in the relevant spectral range. Raman scattering of the solvent and in one case (**3b**) the second order diffraction signal of the excitation light was subtracted (see comparison between raw and corrected data in Figure S7.66).

Time-resolved spectroscopy in the solid state. Excitation and emission spectra on solid samples were acquired on an Edinburgh Instruments FLS1000 spectrofluorometer with a 450 W Xe lamp, double grating Czerny-Turner monochromators in excitation and emission compartment and a thermoelectrically cooled Hamamatsu PMT-980 photomultiplier tube. All spectra were corrected for wavelength-dependent grating efficiency and detector sensitivity, while the excitation spectra were additionally corrected for potentially fluctuating lamp intensity. Luminescence spectra at 80 K were obtained by placing powdered sample into a liquid N_2-cooled Linkam THMS600 temperature cell (temperature precision ± 0.1 K) that was coupled to the spectrometer with optical fiber bundles. Absolute photoluminescence quantum yields were measured at room temperature with an integrating sphere coated with BenFlect®. Time-resolved luminescence in the ns range was measured using time-correlated single photon counting (TCSPC) and a pulsed, mode-locked EPL-375 laser diode (Edinburgh Instruments, λ_{em} = 375 nm, temporal pulse width ~75 ps, wavelength range ~10 nm, incident average laser power < 0.1 mW) with variable repetition rates (20 MHz to 20 kHz) as the excitation source. Measurements in the µs and ms range were performed with single photon multi-channel scaling (MCS) and a pulsed VPL-420 laser diode (Edinburgh Instruments, λ_{em} = 423.2 nm, variable temporal pulse width (0.1 µs…1 ms), wavelength range ~10 nm, incident average laser power 70 mW) and variable trigger frequency (0.1 Hz to 5 MHz).

Time-resolved spectroscopy in cyclohexane suspensions. Steady-state and time-resolved measurements of cyclohexane suspensions were measured with a fluorescence lifetime and steady-state spectrometer (FT300 with hybrid PMT detector, PicoQuant, Germany) equipped with a custom designed ColdEdge cryostat powered by a Sumitomo CH-204 cold head and HC-4E Helium compressor (Cryoandmore, Germany). Temperatures were regulated by a temperature controller, Model 335 (Lake Shore Cryotronics, USA), using a silicon diode sensor at the cold head. Sample temperatures were measured independently with a second diode (Model 540 group B, Scientific Instruments, USA; accuracy: ± 0.5 K) and used for all analyses. All samples were measured in UV Quartz Type 65FL Macro Cryogenic Fluorescence Cuvette with PTFE Stopper with a light path of 10 mm. For the steady-state and time-resolved measurements in the nanosecond time regime, samples were excited with a supercontinuum laser excitation source (EXW-12 with EXTEND-UV spectral extension unit, NKT Photonics, Denmark). An excitation wavelength of 375 nm was set by tuning the frequency doubler. Time-correlated single photon counting (TCSPC) was achieved with HydraHarp 400 electronics (PicoQuant, Germany). The time bin was 8 ps. For the time-resolved measurements in the microsecond and millisecond time ranges, samples were excited with a modulated continuous wave diode laser (Cobolt 375 nm MLD laser, Series 06-01, Hübner Photonics, Germany). A TCSPC and MCS board, Time Harp 260 (PicoQuant, Germany), provided photon counting and timing. Time bins were 16 ns and 32 ns for repetition rates of 3330 Hz and 1670 Hz, respectively, and 4.1 μs for a repetition rate of 10 Hz. Emission was detected under magic angle conditions. In temperature series measurements, detection wavelengths were set to 460 nm, 540 nm, 495 nm, and 595 nm for **2a**, **2b**, **3a**, and **3b**, respectively. Both temperature series and time-resolved emission spectroscopy measurements were conducted with a scripted measurement routine. All emission spectra were subsequently corrected for wavelength-dependent detection efficiencies of the instrument.

Fitting and analysis of luminescence decays. The millisecond (**ms**) decays in cyclohexane of **2a**, **3a** and **2b**, as well as the free ligands of **2b** and **3b**, were analysed using an in-house written Python script applying a multiexponential model (up to six exponents) and a fixed offset, taking into account the independently measured dark-counts of the detector. The instrument response function (IRF) was approximated by a rectangular function of 100 μs width and used in an iterative reconvolution process to minimize χ_r^2. The fit range covered the full range after the excitation pulse. Decay times from the microsecond (**μs**) experiments were extracted by tail-fitting a biexponential model to the data using a custom-written LabView script. This model included a free offset to account for the fraction of signal decaying in the millisecond time regime or slower. For **3b**, the photon fraction generating this offset was between 0.07 and 3.4%.

From the fit results, photon number weighted average decay times were calculated. Here, the slowest component found in the experiments on **2b** (τ = 50-240 ms, 5-22% of total signal) was excluded as the corresponding state, due to its long lifetime, is unlikely to be sufficiently thermally equilibrated with the other states.

The averaged lifetimes thus derived for compounds **2b** and **3b** each in general consisted of one dominating component, justifying the assumption of approximate thermal equilibrium populations of the corresponding emissive states that were included in the averaging. Thermal equilibrium between multiple emissive states allows analysis of its temperature dependent luminescence lifetimes with well-established models,[47,48] assuming that the individual emission rate constants k_i are temperature independent. The resulting overall decay time under this condition is the inverse weighted sum of the individual emission rates of the contributing states [Eq. (4)]:

$$\tau(T) = \sum_{i=0}^{n} g_i\, exp\left(-\frac{E_i}{k_B T}\right) \Big/ \sum_{i=0}^{n} g_i\, k_i\, exp\left(-\frac{E_i}{k_B T}\right) = 1 \Big/ \sum_{i=0}^{n} x_i(T)\, k_i \qquad (4)$$

Here g_i is the degeneracy of state i, and E_i is the energy difference between state i and the lowest excited state.

Adapted to our systems, we used a model for the excited states consisting of two low-lying triplets with two energetically close singlets. To account for the experimentally observed changes in τ at very low temperatures (indicating correspondingly small involved activation energies), for the lowest triplet state zero-field splitting was included [Eq. (2)]. Fits were performed using OriginPro 8.6 (OriginLab Corporation, USA).

Prompt fluorescence as detected on the nanosecond (**ns**) time scale was analysed by a multiexponential model (up to 4 exponents) and a variable offset. The IRF was measured using scattered light from a Ludox® solution. To extract lifetime parameters, in-house Python scripts (*ChiSurf* [49]) were employed. From the resulting decay times and amplitudes photon-weighted averages have been generated. Their temperature dependence was approximated by a simple exponential process [Eq. (1)].

In the context of the model for the millisecond and microsecond decays as discussed above, detection of nanosecond decays can only be possible when thermal equilibration is not fully established on that time scale. For **3b** the measured singlet decay time (0.3 – 2.7 ns) is at least 10 times (compared to the fitted rate from the model above) or 100 times (compared to theory output) faster and therefore should not significantly affect the thermal equilibrium.

Luminescence fractions. The ratio of prompt (within nanoseconds after excitation) arriving photons to the offset in the nanosecond experiments allowed us to determine the fraction of prompt fluorescence in the total emission. Fit results from eq. (2) were then employed to separate the temperature dependent contributions of thermally activated delayed fluorescence and phosphorescence [Eq. (5)]:

$$f_i(T) = g_i k_i \, exp\left(-\frac{E_i}{k_B T}\right) \Big/ \sum_{i=0}^{n} g_i \, k_i \, exp\left(-\frac{E_i}{k_B T}\right) \tag{5}$$

The total phosphorescence and delayed fluorescence contributions were then obtained by adding $f_0(T) + f_1(T) + f_2(T)$ and $f_3(T) + f_4(T)$, respectively. For compound **2b**, the slow decay component that was not included in the averaged decay time was added to the fraction of phosphorescence. Due to its small total fraction (in average ca. 10%) the effect on the general appearance of the system was minor.

Theory

Quantum chemical methods. For the geometry optimization of the electronically excited singlet states, time-dependent density functional theory (TDDFT), as implemented in Gaussian 16,[50] was used employing the same basis sets, effective core potentials and density functionals as in previous work.[43] For triplets, the Tamm-Dancoff approximation (TDA) was applied. The corresponding analytical second derivatives were used to generate vibrational frequencies and wavefunctions, required for the computation of FC spectra as well as ISC and rISC rate constants. The effect of an electrostatic environment was mimicked by PCM[51,52] point charges resulting from self-consistent reaction field calculations for a relative permittivity 6.97 (**2a**, **2b**) or 8.93 (**3a**, **3b**). Singlet and triplet excitation energies and wavefunctions were obtained from multireference configuration interaction (MRCI) calculations at the DFT/MRCI level of theory[53–55] utilizing the same technical parameters as in previous work.[43] Spin–orbit coupling matrix elements (SOCMEs) were computed with SPOCK[56] employing a spin–orbit effective core potential on Cu[57] and the Breit–Pauli spin–orbit operator in atomic mean-field approximation on all other atoms. Temperature-dependent ISC and rISC rate constants were computed in Condon approximation employing a Fourier transform approach.[58,59] Before numerical integration, the time correlation function was multiplied by a Gaussian damping function. Its width, the time interval and the number of grid point varied from case to case to reach convergence. The final parameter sets are listed in Table S7.33. Fluorescence rate constants were computed according to the Einstein formula for spontaneous emission based on transition dipole moments and energies from DFT/MRCI wavefunctions. The electric transition dipole moments for computing the probabilities of the spin-forbidden radiative transitions were obtained from DFT/ multireference spin–orbit configuration interaction (DFT/MRSOCI) calculations using the appropriate SPOCK modules.[60] The resulting individual phosphorescence rate constants were then thermally averaged over all triplet spin substates.

7.3.6 Supplementary Information

Spectral Properties

Correction of Absorption Spectra

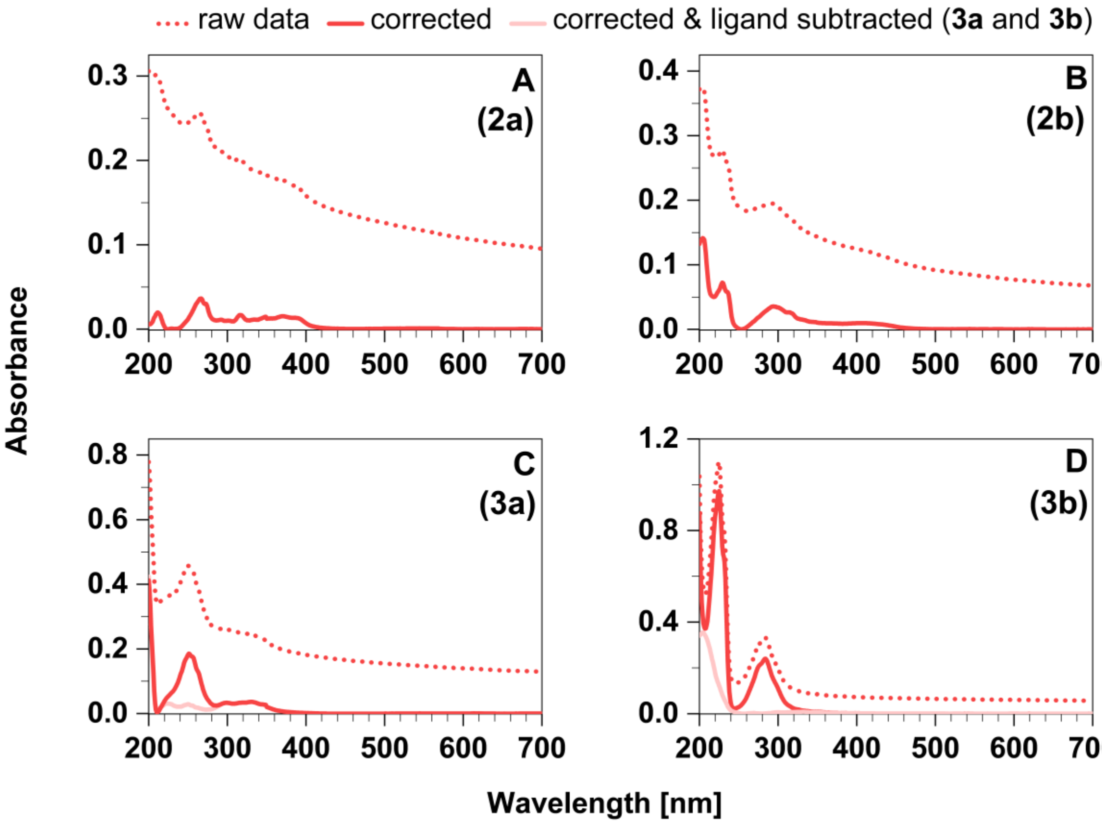

Figure S7.65. Comparison between raw and corrected absorption spectral data. The applied corrections were described in more detail in the main text under section 7.3.5 (Experimental and Theoretical Procedures).

Correction of Excitation Spectra

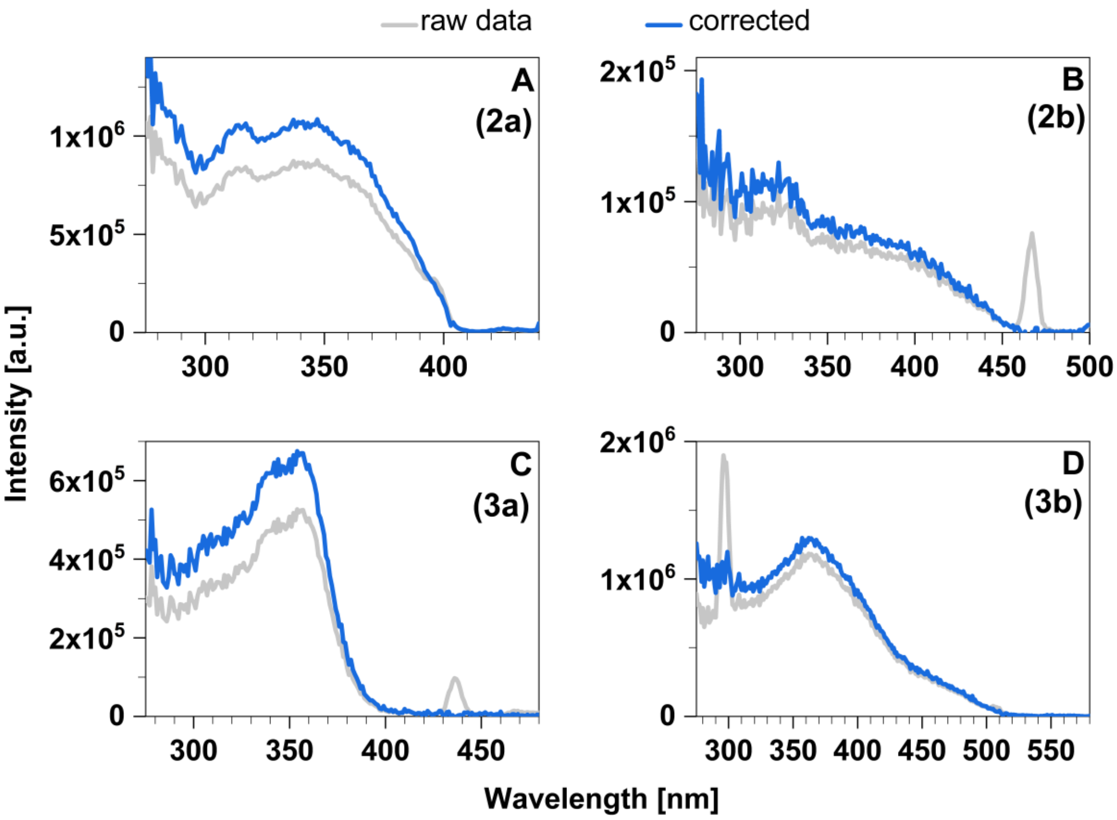

Figure S7.66. Comparison between raw and corrected excitation spectra. The measured data were corrected for inner filter effect (see section 7.3.5, Experimental and Theoretical Procedures) and Raman scattering of the solvent. Additionally, the second order diffraction signal of the excitation light was subtracted for **3b**.

Excitation and Emission Spectra of Powdered Samples at 80 K

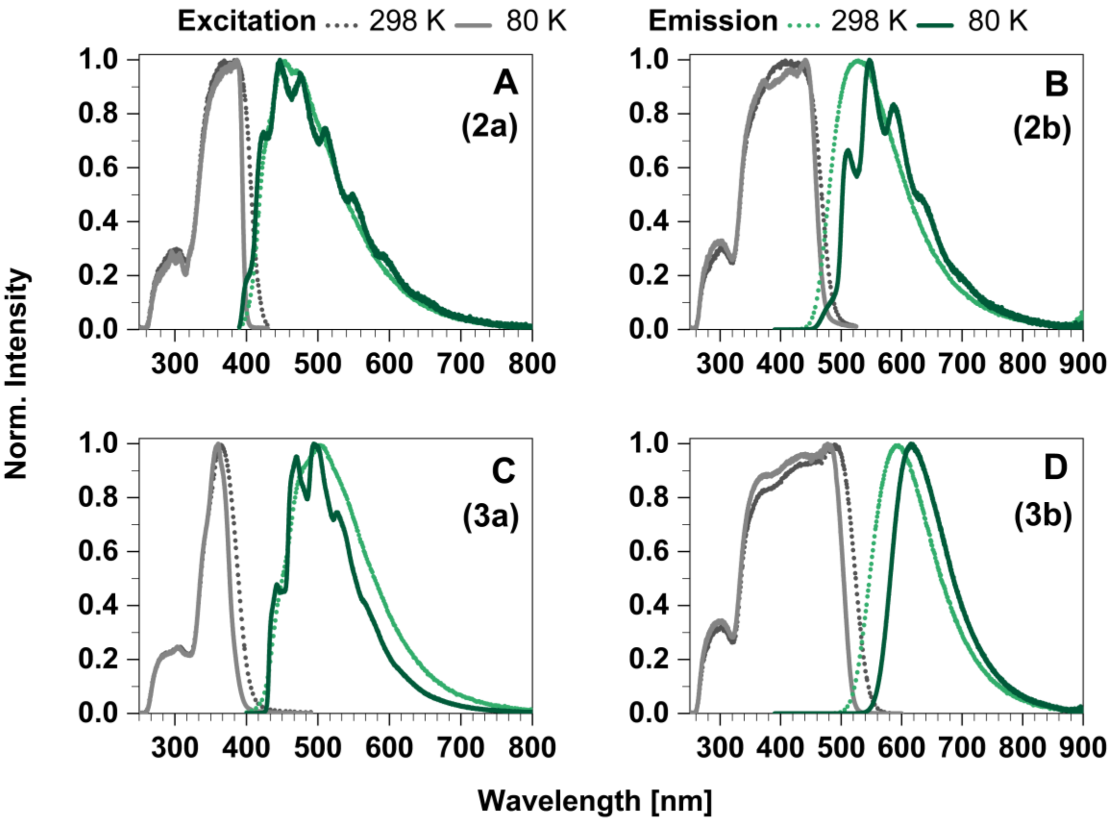

Figure S7.67. Comparison of the excitation and emission spectra of powdered samples at 298 K and 80 K. The excitation spectra were recorded at emission wavelength of 450 nm (**2a**), 540 nm (**2b**), 500 nm (**3a**), 598 nm (**3b**, 298 K) and 615 nm (**3b**, 80 K). The excitation wavelength was 375 nm for all compounds.

Luminescence decays: Temperature series from 10 K to 270 K

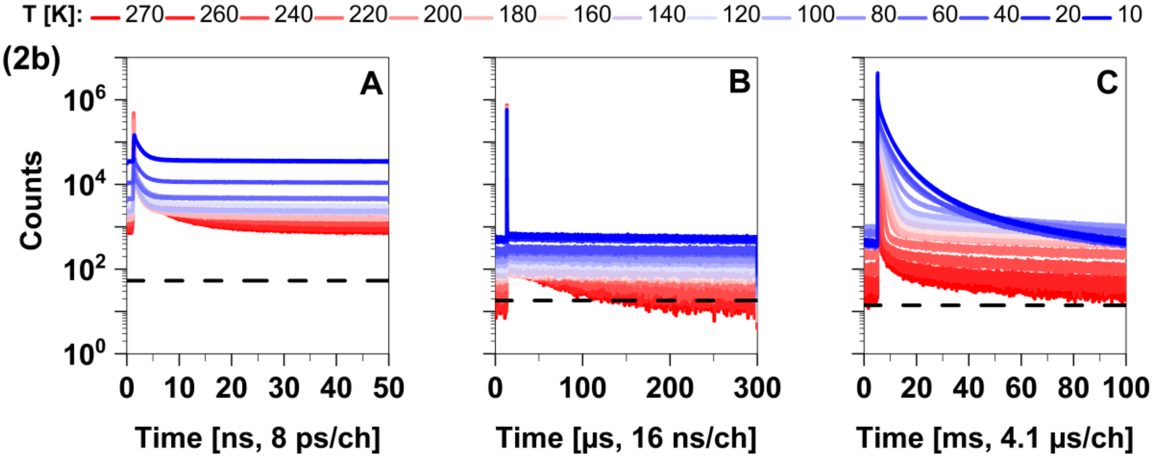

Figure S7.68. Time-resolved measurements of compound **2b** in solid cyclohexane suspension in the temperature range from 10 K to 270 K, in three distinct time regimes: **A.** nanoseconds, **B.** microseconds, and **C.** milliseconds.

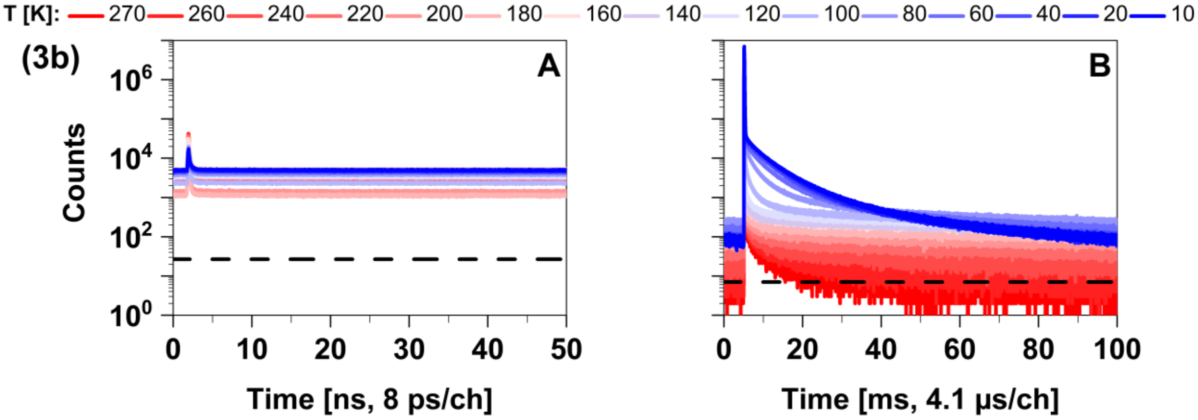

Figure S7.69. Time-resolved measurements of compound **3b** in solid cyclohexane suspension in the temperature range from 10 K to 270 K, in two distinct time regimes: **A.** nanoseconds, and **B.** milliseconds. The luminescence in milliseconds is assigned to the free ligand (see Figure S7.73). Decays in microseconds are presented in more detail in Figure S7.70.

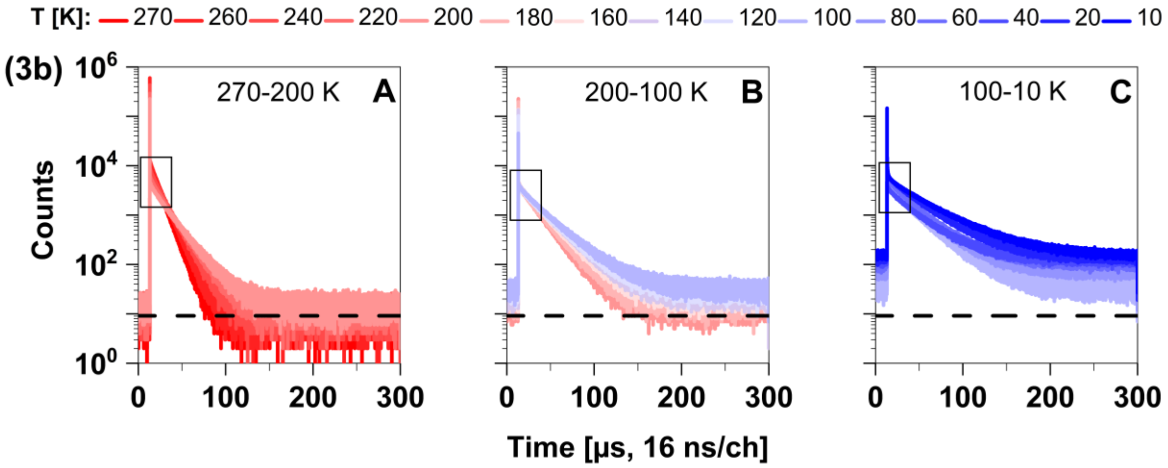

Figure S7.70. Time-resolved measurements of compound **3b** in solid cyclohexane suspension in microseconds in three characteristic temperature ranges: **A.** 270-200 K, **B.** 200-100 K, and **C.** 100-10 K. In the first temperature range (270-200 K), the amplitude of the delayed emission (its region is marked with a black rectangle) decreases, as is typical for TADF; in the second (200-100 K) it remains constant; while in the third (100-10 K) increases, presumably due to phosphorescence and ligand dissociation.

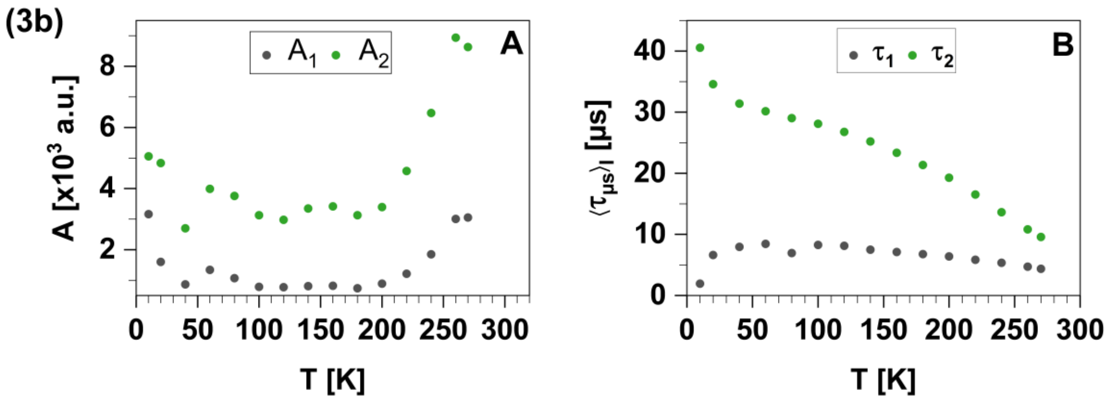

Figure S7.71. Temperature dependence of **A.** amplitude and **B.** lifetime in the microsecond time range of compound **3b** in solid cyclohexane suspension.

Fitting of luminescence decays

A multi-exponential model function (eq. S1) was used to describe the data. For fitting, the model function was convoluted with the instrumental function and, after adding a variable offset, iteratively optimized. For more details, see section 7.3.5 (Experimental and Theoretical Procedures). Each emissive species is presented with its amplitude (A_i) and/or fraction (x_i) (eq. S2), and lifetime (τ_i). Intensity-weighted lifetime $\langle\tau\rangle_I$ (eq. S3) is given, as well as the reduced χ_r^2 value (eq. S4) as a measure of the goodness of the fit. The value $\chi_r^2 = 1$ is obtained with an optimal fit.

$$F(t) = F(0)\sum_{i=1}^{6} x_i e^{-t/\tau_i} \qquad \text{(eq. S1)}$$

$$\sum_{i=1}^{6} x_i = 1 \qquad \text{(eq. S2)}$$

$$\langle\tau\rangle_I = \frac{\sum_{i=1}^{6} x_i\tau_i^2}{\sum_{i=1}^{6} x_i\tau_i} \qquad \text{(eq. S3)}$$

$$\chi_r^2 = \sum_{i=1}^{n} \frac{1}{(n-p)} \times (w.res.)^2 \qquad \text{(eq. S4)}$$

n: number of time channels, p: degrees of freedom

All fit results are given in Table S7.13-Table S7.23.

The linear lutidine complex 2a

Table S7.13. Lifetime fit results of **2a** in cyclohexane suspension in the nanosecond time regime.

T [K]	x_1	**τ_1 [ns]**	x_2	**τ_2 [ns]**	$\langle\tau\rangle_I$ [ns]	χ_r^2
261.3	0.35	**3.30**	0.65	**2.00**	2.61	1.18
163.0	0.48	**5.63**	0.52	**4.28**	5.02	1.14
64.7	0.20	**3.32**	0.80	**6.28**	5.94	1.12
15.1	0.26	**3.55**	0.74	**6.32**	5.87	1.17

Table S7.14. Lifetime fit results of **2a** in cyclohexane suspension in the millisecond time regime.

T [K]	x_1 $\cdot 10^{-3}$	**τ_1 [ms]**	x_2	**τ_2 [ms]**	x_3	**τ_3 [ms]**	x_4	**τ_4 [ms]**	x_5	**τ_5 [ms]**	$\langle\tau\rangle_I$ [ms]	χ_r^2
261.3	5.9	**13.2**	0.13	**2.27**	0.52	**1.21**	0.34	**0.06**			2.39	1.13
163.0	9.9	**74.4**	0.03	**7.95**	0.17	**1.58**	0.79	**0.08**			43.22	1.06
64.7	8.0	**59.2**	0.07	**11.4**	0.35	**3.73**	0.30	**1.19**	0.28	**0.21**	14.23	1.02
15.1	12.6	**39.1**	0.14	**10.3**	0.49	**4.77**	0.19	**1.37**	0.17	**0.25**	9.96	1.02

The trigonal pyridine complex 3a

Table S7.15. Lifetime fit results of **3a** in cyclohexane suspension in the nanosecond time regime.

T [K]	x_1	**τ_1 [ns]**	x_2	**τ_2 [ns]**	$\langle\tau\rangle_I$ [ns]	χ_r^2
261.4	0.03	**1.18**	0.97	**0.08**	0.45	1.72
163.3	0.04	**1.70**	0.96	**0.11**	0.73	1.15
64.7	0.09	**2.04**	0.91	**0.16**	1.19	1.12
15.2	0.12	**2.47**	0.88	**0.17**	1.70	1.04

Table S7.16. Lifetime fit results of **3a** in cyclohexane suspension in the microsecond time regime.

T [K]	A_1	x_1	**τ_1 [µs]**	A_2	x_2	**τ_2 [µs]**	$\langle\tau\rangle_I$ [µs]	χ_r^2
261.4	112.2	0.67	**341.20**	55.5	0.33	**6.55**	338.05	1.03
163.3	41.9	0.52	**273.49**	39.3	0.48	**4.12**	269.74	1.01
64.7	79.8	0.33	**219.59**	163.0	0.67	**5.84**	208.57	1.00
15.2	111.5	0.45	**98.68**	138.0	0.55	**6.00**	92.19	1.04

Table S7.17. Lifetime fit results of **3a** in cyclohexane suspension in the millisecond time regime.

T [K]	x_1 $\cdot 10^{-3}$	**τ_1 [ms]**	x_2	**τ_2 [ms]**	x_3	**τ_3 [ms]**	x_4	**τ_4 [ms]**	x_5	**τ_5 [ms]**	x_6	**τ_6 [ms]**	$\langle\tau\rangle_I$ [ms]	χ_r^2
261.4	0.1	**10.13**	0.48	**0.66**	0.39	**0.44**	0.13	**0.12**					0.58	1.07
163.3	0.3	**165.95**	<0.01	**9.05**	0.55	**1.24**	0.30	**0.62**	0.15	**0.12**			8.59	1.04
64.7	1.5	**73.29**	0.01	**12.69**	0.07	**3.85**	0.49	**1.46**	0.15	**0.45**	0.28	**0.06**	9.01	1.02
15.2	1.8	**42.39**	0.02	**9.82**	0.09	**4.28**	0.26	**1.68**	0.09	**0.29**	0.54	**0.04**	6.76	1.02

The linear formyl lutidine complex 2b

Table S7.18. Lifetime fit results of **2b** in cyclohexane suspension in the nanosecond time regime.

T [K]	x_1 $\cdot 10^{-3}$	**τ_1 [ns]**	x_2 $\cdot 10^{-3}$	**τ_2 [ns]**	x_3	**τ_3 [ns]**	x_4	**τ_4 [ns]**	$\langle\tau\rangle_I$ [ns]	χ_r^2
271.1	0.8	**7.26**	3.3	**1.61**	0.01	**0.39**	0.99	**0.02**	1.57	1.67
261.5	0.8	**7.64**	3.2	**1.61**	0.01	**0.38**	0.99	**0.02**	1.62	1.61
241.7	0.8	**8.53**	3.4	**1.58**	0.01	**0.37**	0.99	**0.02**	1.85	1.65
221.9	0.8	**9.11**	3.5	**1.54**	0.01	**0.38**	0.99	**0.02**	2.01	1.50
202.1	1.0	**10.55**	4.6	**1.61**	0.01	**0.42**	0.98	**0.03**	2.58	1.36
182.6	2.1	**12.13**	9.9	**1.76**	0.03	**0.51**	0.96	**0.04**	3.67	1.04
163.2	7.8	**12.29**	40.6	**1.51**	0.13	**0.54**	0.82	**0.07**	4.59	1.06
143.5	9.0	**18.01**	43.7	**2.12**	0.25	**0.66**	0.69	**0.08**	6.74	1.01
124.0	8.8	**23.42**	32.7	**2.47**	0.34	**0.80**	0.62	**0.05**	8.82	1.03
104.5	6.4	**39.51**	10.8	**4.78**	0.36	**1.01**	0.62	**0.16**	13.85	1.72
84.9	8.6	**24.61**	4.6	**3.87**	0.37	**1.09**	0.62	**0.06**	8.62	1.08
64.7	8.1	**26.64**	0.1	**1.42**	0.30	**1.17**	0.70	**0.07**	10.13	1.08
43.4	11.1	**26.59**	350.1	**1.11**	0.02	**2.21**	0.62	**0.05**	10.97	1.03
25.8	11.0	**43.89**	38.4	**2.37**	0.40	**1.05**	0.56	**0.06**	21.33	1.01
15.1	10.0	**45.60**	32.1	**2.52**	0.37	**1.06**	0.59	**0.05**	22.35	1.02

Table S7.19. Lifetime fit results of **2b** in cyclohexane suspension in the microsecond time regime.

T [K]	A_1	x_1	**τ_1 [µs]**	A_2	x_2	**τ_2 [µs]**	$\langle\tau\rangle_I$ [µs]	χ_r^2
271.1	111.5	0.56	**50.53**	86.9	0.44	**5.57**	46.97	1.09
261.5	99.5	0.55	**58.45**	81.6	0.45	**4.19**	55.43	1.06
241.7	72.6	0.50	**92.32**	73.1	0.50	**2.82**	89.66	1.05
221.9	57.8	0.40	**124.05**	88.1	0.60	**1.57**	121.73	1.03
202.1	47.4	0.36	**168.66**	84.5	0.64	**1.56**	165.96	1.01
182.6	22.6	0.34	**233.64**	43.2	0.66	**2.31**	229.37	1.02
163.2	18.8	0.35	**272.99**	34.4	0.65	**3.14**	267.41	1.00
143.5	16.9	0.32	**184.00**	35.6	0.68	**2.47**	179.00	1.00
124.0	26.7	0.22	**154.32**	94.3	0.78	**0.48**	152.64	1.00
104.5	30.9	0.13	**194.53**	202.3	0.87	**0.21**	193.15	1.02
84.9	29.4	0.07	**223.40**	381.1	0.93	**0.13**	221.69	1.01
64.7	31.2	0.06	**269.36**	517.1	0.94	**0.13**	267.28	1.02
43.4	32.4	0.05	**393.98**	585.8	0.95	**0.13**	391.60	1.00
25.8	71.8	0.05	**173.95**	1410.4	0.95	**0.13**	171.47	1.02
15.1	110.7	0.06	**202.15**	1855.2	0.94	**0.12**	200.14	1.00

Table S7.20. Lifetime fit results of **2b** in cyclohexane suspension in the millisecond time regime.

T [K]	$x_1 \cdot 10^{-3}$	**τ_1 [ms]**	$x_2 \cdot 10^{-3}$	**τ_2 [ms]**	$x_3 \cdot 10^{-2}$	**τ_3 [ms]**	x_4	**τ_4 [ms]**	x_5	**τ_5 [ms]**	x_6	**τ_6 [ms]**	$\langle\tau\rangle_I$ (2-6) [ms]	χ_r^2
271.1	0.02	**85.6**	0.04	**8.6**	0.02	**1.45**	0.05	**0.11**	0.47	**0.06**	0.47	**0.03**	0.14	1.03
261.5	0.03	**104.8**	0.06	**10.1**	0.03	**1.71**	0.09	**0.15**	0.45	**0.08**	0.46	**0.03**	0.18	1.02
241.7	0.06	**150.4**	0.11	**11.0**	0.05	**1.83**	0.19	**0.27**	0.41	**0.14**	0.40	**0.05**	0.29	1.02
221.9	0.15	**196.4**	0.23	**10.3**	0.65	**1.10**	0.30	**0.47**	0.37	**0.20**	0.32	**0.06**	0.47	1.01
202.1	0.29	**224.8**	0.37	**11.1**	12.13	**1.03**	0.36	**0.62**	0.29	**0.24**	0.22	**0.06**	0.76	1.01
182.6	0.58	**238.4**	0.64	**13.3**	25.93	**1.29**	0.35	**0.77**	0.22	**0.28**	0.18	**0.06**	1.13	1.00
163.2	0.96	**230.2**	0.95	**15.8**	33.49	**1.55**	0.33	**0.96**	0.17	**0.31**	0.16	**0.06**	1.49	0.98
143.5	1.23	**214.2**	1.32	**15.1**	41.29	**1.66**	0.20	**0.93**	0.12	**0.24**	0.26	**0.03**	1.75	1.00
124.0	1.23	**199.9**	1.59	**15.0**	44.61	**1.78**	0.16	**0.95**	0.13	**0.23**	0.26	**0.04**	1.90	1.00
124.0	1.41	**200.6**	1.78	**15.8**	41.64	**1.79**	0.16	**0.99**	0.13	**0.24**	0.29	**0.05**	1.99	1.01
104.5	1.57	**177.3**	3.17	**14.7**	34.61	**2.02**	0.27	**1.31**	0.17	**0.35**	0.21	**0.08**	2.19	1.00
84.9	1.99	**145.6**	8.75	**15.5**	7.01	**3.70**	0.60	**1.78**	0.17	**0.54**	0.15	**0.11**	3.19	1.00
64.7	2.61	**97.2**	19.30	**15.3**	13.29	**4.85**	0.61	**2.02**	0.13	**0.72**	0.10	**0.13**	4.47	1.02
43.4	2.99	**64.7**	27.70	**13.4**	21.90	**4.91**	0.58	**2.07**	0.09	**0.67**	0.08	**0.10**	4.71	0.99
25.8	1.94	**52.3**	21.40	**11.7**	15.90	**4.73**	0.52	**2.00**	0.09	**0.45**	0.21	**0.06**	4.10	0.99
15.1	1.59	**47.7**	23.80	**10.3**	13.23	**4.27**	0.29	**1.88**	0.27	**0.48**	0.28	**0.12**	3.96	0.99

The trigonal formyl pyridine complex 3b

Table S7.21. Lifetime fit results of **3b** in cyclohexane suspension in the nanosecond time regime.

T [K]	$x_1 \cdot 10^{-3}$	**τ_1 [ns]**	x_2	**τ_2 [ns]**	x_3	**τ_3 [$\cdot 10^{-2}$ ns]**	$\langle\tau\rangle_I$ [ns]	χ_r^2
271.5	0.77	**6.10**	0.03	**0.28**	0.97	**5.48**	0.48	1.22
261.6	1.11	**4.69**	0.06	**0.20**	0.94	**4.87**	0.42	1.06
241.8	0.96	**5.44**	0.02	**0.31**	0.97	**6.26**	0.44	1.27
222.0	2.76	**1.53**	0.04	**0.19**	0.95	**5.98**	0.14	1.20
202.2	3.11	**1.90**	0.79	**0.09**	0.21	**0.01**	0.21	1.26
183.1	4.69	**1.28**	0.68	**0.09**	0.31	**0.01**	0.17	1.07
163.3	4.97	**2.17**	0.74	**0.14**	0.25	**0.01**	0.30	1.04
143.6	10.82	**1.27**	0.64	**0.14**	0.35	**0.01**	0.24	1.38
124.1	14.30	**1.09**	0.77	**0.12**	0.22	**0.01**	0.24	1.39
104.6	26.60	**1.10**	0.78	**0.13**	0.19	**0.01**	0.32	1.12
85.0	5.27	**3.16**	0.68	**0.13**	0.31	**0.01**	0.56	1.53
64.8	6.23	**4.78**	0.69	**0.16**	0.30	**0.01**	1.11	1.11
43.5	6.96	**2.57**	0.54	**0.15**	0.45	**0.01**	0.54	1.28
25.8	21.60	**2.43**	0.81	**0.17**	0.17	**0.01**	0.77	1.15
15.0	4.53	**6.19**	0.13	**0.34**	0.87	**5.95**	1.46	1.44

Table S7.22. Lifetime fit results of **3b** in cyclohexane suspension in the microsecond time regime.

T [K]	A_1	x_1	**τ_1 [µs]**	A_2	x_2	**τ_2 [µs]**	$\langle\tau\rangle_I$ [µs]	χ_r^2
271.3	8634.6	0.74	**9.59**	3051.7	0.26	**4.38**	8.87	1.14
262.0	8941.3	0.75	**10.84**	3006.7	0.25	**4.73**	10.05	1.13
242.3	6474.1	0.78	**13.64**	1846.9	0.22	**5.37**	12.81	1.11
222.4	4575.9	0.79	**16.52**	1212.4	0.21	**5.84**	15.60	1.08
202.7	3391.8	0.79	**19.26**	887.5	0.21	**6.41**	18.23	1.06
185.3	3129.6	0.81	**21.36**	737.1	0.19	**6.78**	20.35	1.05
165.4	3419.2	0.81	**23.36**	819.7	0.19	**7.11**	22.25	1.04
143.8	3345.3	0.81	**25.19**	809.4	0.19	**7.50**	24.00	1.02
124.6	2978.6	0.79	**26.76**	769.9	0.21	**8.12**	25.40	1.03
104.4	3125.3	0.80	**28.09**	783.9	0.20	**8.28**	26.73	1.03
85.1	3758.0	0.78	**29.03**	1064.7	0.22	**6.94**	27.62	1.07
64.8	3990.4	0.75	**30.14**	1338.4	0.25	**8.45**	28.28	1.06
44.1	2701.7	0.76	**31.41**	863.4	0.24	**7.97**	29.65	1.06
25.8	4832.6	0.75	**34.57**	1597.2	0.25	**6.62**	32.90	1.14
15.1	5054.4	0.62	**40.55**	3160.9	0.38	**1.94**	39.42	1.58

Table S7.23. Lifetime fit results of **3b** in cyclohexane suspension in the millisecond time regime.

T [K]	x_1	**τ_1 [ms]**	x_2	**τ_2 [ms]**	x_3	**τ_3 [ms]**	x_4	**τ_4 [ms]**	$\langle\tau\rangle_I$ [ms]	χ_r^2
271.3	-	**-**	0.13	**10.04**	0.31	**2.30**	0.56	**0.64**	6.31	1.15
262.0	0.06	**38.93**	0.13	**8.13**	0.34	**1.96**	0.47	**0.53**	23.52	1.05
242.3	0.07	**106.53**	0.09	**15.58**	0.29	**3.04**	0.55	**0.77**	80.85	1.05
222.4	0.08	**180.92**	0.09	**14.01**	0.31	**2.56**	0.51	**0.67**	156.86	1.01
202.7	0.07	**295.96**	0.10	**22.27**	0.34	**2.66**	0.49	**0.56**	258.03	1.01
185.3	0.10	**253.31**	0.09	**15.85**	0.35	**2.39**	0.46	**0.49**	231.42	1.02
165.4	0.09	**244.89**	0.09	**16.03**	0.28	**2.51**	0.54	**0.51**	223.24	1.00
143.8	0.07	**228.72**	0.07	**15.66**	0.23	**2.32**	0.63	**0.42**	205.90	0.99
124.6	0.04	**207.14**	0.05	**13.54**	0.17	**2.05**	0.75	**0.44**	177.20	1.01
104.4	0.01	**170.11**	0.03	**11.52**	0.23	**2.00**	0.72	**0.52**	115.25	1.03
85.1	0.01	**123.07**	0.06	**11.69**	0.40	**2.91**	0.52	**0.88**	50.31	1.03
64.8	0.01	**79.65**	0.10	**11.86**	0.57	**3.90**	0.32	**1.35**	21.06	1.01
44.1	0.01	**61.87**	0.09	**12.45**	0.64	**4.66**	0.25	**1.95**	13.24	1.03
25.8	0.01	**51.94**	0.12	**11.03**	0.68	**4.58**	0.19	**1.48**	11.26	1.01
15.1	0.01	**46.68**	0.18	**9.47**	0.51	**4.17**	0.30	**1.01**	10.99	1.03

Analysis of luminescence decays

Temperature dependence of prompt fluorescence lifetimes in nanoseconds was approximated according to eq. (1). For more details, see section 7.3.5 (Experimental and Theoretical Procedures). Fit results are given in Table S7.24.

Table S7.24. Obtained parameters k_S, k_A and E_A from the fit of temperature-dependent prompt fluorescence lifetimes according to eq. (1).

ns decays	**2a**		**3a**		**2b**		**3b**	
	fit	error [%]	fit	error [%]	fit	error [%]	fit	error [%]
k_S [s^{-1}]	$1.7\cdot10^{8}$	0.6	$5.9\cdot10^{8}$	7.6	$8.5\cdot10^{8}$	2.8	$6.1\cdot10^{9}$	5.2
k_A [s^{-1}]	$5.6\cdot10^{9}$	15.7	$2.5\cdot10^{9}$	36.3	$5.8\cdot10^{10}$	57.1	$1.9\cdot10^{10}$	48.6
E_A [meV]	73.7	4.3	13.6	26.2	67.3	14.2	26.3	32.2
χ^2	0.0026		0.0152		0.0061		0.0002	
Fraction of total luminescence [%]	99.5		16.9		71.4		6.0	

Temperature dependence of delayed luminescence decay times was approximated according to eq. (2). For **2b**, two models were applied: in the first model, E_2 and E_3 are fixed to theoretically computed zero-point vibrational energy corrected adiabatic values of 28.5 meV and 52.2 meV respectively, while E_1 and E_4 are free parameters (solid line in Figure 7.29D, Table S7.25), and in the second model, all four energies E_1-E_4 are fixed (dashed line in Figure 7.29D, Table S7.26). Theoretically computed zero-point vibrational energy corrected adiabatic values are provided in Table S7.27. Zero-field splitting of ^{3}LLCT is <0.09 meV and not relevant in measured temperature range.

Table S7.25. Obtained fit parameters from temperature-dependent delayed luminescence decay of **2b** in milliseconds according to eq. (2). Fit is depicted as a solid green line in Figure 7.29D.

2b	Fit	Standard error	Theory	Unit	Assignment
k_0	260	32		s^{-1}	^{3}LLCT$_{1,2*}$ → S$_0$
k_1	0	fixed		s^{-1}	^{3}LLCT$_{3*}$ → S$_0$
k_2	4825	343		s^{-1}	^{3}LC → S$_0$
k_3	0	fixed		s^{-1}	^{1}LLCT → S$_0$
k_4	$9.4 \cdot 10^8$	$4.94 \cdot 10^9$		s^{-1}	^{1}MLCT → S$_0$
E_1	3.3	2.9	0.09	meV	^{3}LLCT zero field splitting
E_2	**28.5**	**fixed**	28.5	meV	^{3}LC → ^{3}LLCT
E_3	**52.2**	**fixed**	52.2	meV	^{1}LLCT → ^{3}LLCT
E_4	240.2	102.1	470.3	meV	^{1}MLCT → ^{3}LLCT
χ^2	0.027				

*Sublevels of ^{3}LLCT are marked with the corresponding subscripts (1-3).

Table S7.26. Obtained fit parameters from temperature-dependent delayed luminescence decay of **2b** in milliseconds according to eq. (2). Fit is depicted as a dashed green line in Figure 7.29D.

2b	Fit	Standard error	Theory (77 K)	Unit	Assignment
k_0	339	630		s^{-1}	^{3}LLCT$_{1,2}$ → S$_0$
k_1	0	1305		s^{-1}	^{3}LLCT$_3$ → S$_0$
k_2	4158	12256		s^{-1}	^{3}LC → S$_0$
k_3	12333	25168		s^{-1}	^{1}LLCT → S$_0$
k_4	$1.26 \cdot 10^{14}$	$1.48 \cdot 10^{14}$		s^{-1}	^{1}MLCT → S$_0$
E_1	**0.09**	**fixed**	0.09	meV	^{3}LLCT zero field splitting
E_2	**28.5**	**fixed**	28.5	meV	^{3}LC → ^{3}LLCT
E_3	**52.2**	**fixed**	52.2	meV	^{1}LLCT → ^{3}LLCT
E_4	**470.3**	**fixed**	470.3	meV	^{1}MLCT → ^{3}LLCT
χ^2	0.075				

Table S7.27. Zero-point vibrational energy corrected adiabatic energies of **2b**.

State	E (0-0) [eV]	ZFS [cm^{-1}]
S$_0$	0.00	
^{1}LLCT	2.47	
^{3}LLCT	2.42	0.35
^{1}MLCT	2.89	
^{3}LC	2.45	0.26

Temperature dependence of delayed luminescence decay times in microseconds of **3b** was also approximated according to eq. (2). For more details, see section 7.3.5 (Experimental and Theoretical Procedures). Fit results are presented in Table S7.28. Zero field splitting of ^{3}MLCT has no effect on Boltzmann factor.

Table S7.28. Obtained fit parameters from temperature-dependent delayed luminescence decay of **3b** in microseconds according to eq. (2). Fit is depicted as a green line in Figure 7.36D.

	Fit		**Theory**		
3b	$\boldsymbol{k_r + k_{nr}}$[a]	**Standard error**	$\boldsymbol{k_r}$ **(77 K)**	**Unit**	**Assignment**
k_0	0	$2.46\cdot10^3$	$1.4\cdot10^4$	s^{-1}	^{3}LLCT$_{1,2}$ → S$_0$
k_1	$1.09\cdot10^5$	$6.72\cdot10^3$		s^{-1}	^{3}LLCT$_3$ → S$_0$
k_2	$6.39\cdot10^4$	$4.36\cdot10^3$	$7.9\cdot10^3$	s^{-1}	^{3}MLCT → S$_0$
k_3	0	$2.14\cdot10^4$	$4.2\cdot10^5$	s^{-1}	^{1}LLCT → S$_0$
k_4	$3.65\cdot10^7$	$2.32\cdot10^6$	$2.6\cdot10^6$	s^{-1}	^{1}MLCT → S$_0$
	Energy differences		**Energy differences**		
E_1	**0.6**	**fixed**	0.6	meV	^{3}LLCT zero field splitting
E_2	**19.2**	**fixed**	19.2	meV	^{3}MLCT → ^{3}LLCT
E_3	**62.2**	**fixed**	62.2	meV	^{1}LLCT → ^{3}LLCT
E_4	**114.2**	**fixed**	114.2	meV	^{1}MLCT → ^{3}LLCT
χ^2	0.311				

[a] k_{nr} adds a displacement by approximately one order a magnitude to theoretical k_r values.

Time-resolved luminescence decays in cyclohexane in milliseconds

Decay-associated spectra at 10 K of the linear formyl lutidine complex 2b

Decay-associated spectra at 10 K in the millisecond time regime were recorded to determine the spectral properties of each lifetime species. Four lifetimes were used for global fitting: τ_1 = 0.7 ms, τ_2 = 1.9 ms, τ_3 = 5.6 ms, and τ_4 = 20.0 ms. The amplitudes A_3 and A_4 resemble the spectral properties of the free ligand (Figure S7.72A) shown in Figure 7.28B. At a detection wavelength of 460 nm, the lifetime of 5.6 ms assigned to the free ligand contributes to a substantial fraction of the total emission, accounting for 63% of the emission intensity. In contrast, the very long lifetime of 20.0 ms represents only 6% of the total emission at the same wavelength. The situation changes when the detection wavelength is shifted to the detection maximum of the compound, 540 nm. At this wavelength, the lifetime of 5.6 ms contributes only 2% of the total emission, while the lifetime of 20.0 ms contributes a mere 0.1% of the total emission. This indicates that the majority of the emission in the millisecond time regime, detected at 540 nm, originates from complex **2b** and not from the free ligand (Figure S7.72B).

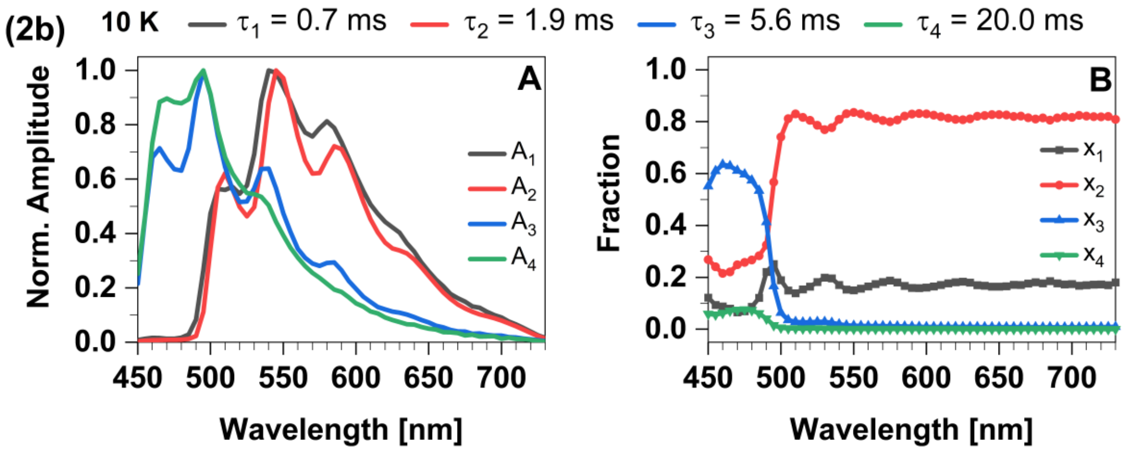

Figure S7.72. Decay-associated spectra of **2b** in cyclohexane suspension at 10 K in the millisecond time range. The lifetimes used for global fitting were τ_1 = 0.7 ms, τ_2 = 1.9 ms, τ_3 = 5.6 ms, and τ_4 = 20.0 ms. **A.** Spectral properties of each lifetime species with their normalized amplitudes. **B.** Fraction dependence on the wavelength.

Decay-associated spectra at 10 K of the trigonal formyl pyridine complex 3b

A small portion of the total luminescence signal is detected in the millisecond time regime at all temperatures, in particular below 100 K. By integrating the histogram spike at 10 K, which contains shorter lifetime components, we identified the spectrum of the compound. However, the integration of the histogram tail at the same temperature, revealed the spectrum of the free ligand (Figure S7.73A). Additionally, we constructed the decay-associated spectra at 10 K using individual lifetimes, and it is evident that all these spectra originate from the dissociated ligand (Figure S7.73B). The structured band, appearing also at the short wavelength tail of the steady-state emission spectrum at temperatures below 100 K (Figure 7.34A), is assigned to luminescence from the nπ* state of the free 4-formyl pyridine ligand. The millisecond emission was not observed in solid-state measurements as there is no ligand dissociation in the powder sample.

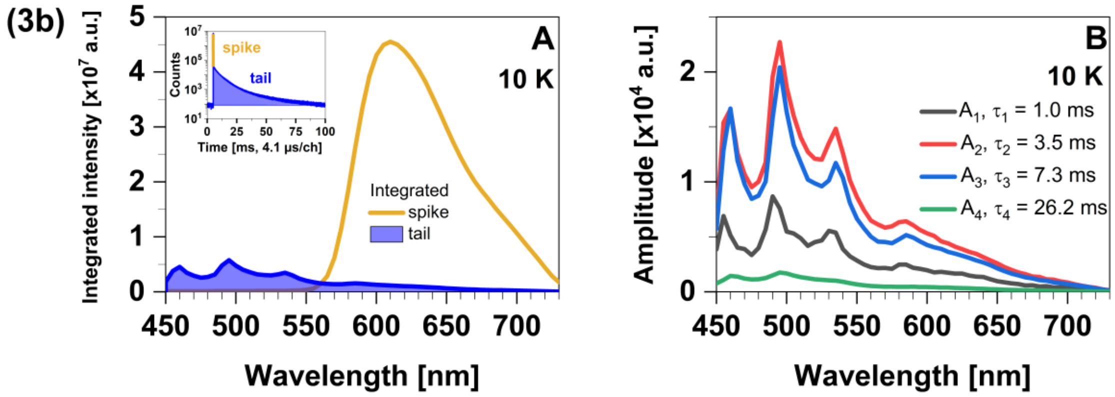

Figure S7.73. Time-resolved measurements of **3b** in cyclohexane suspension in the millisecond time regime. **A.** Time-resolved emission spectra constructed by the integration of the spike and tail of the decay histogram in the millisecond time range at 10 K. Inset: Decay recorded at 10 K with marked integrated areas. **B.** Decay-associated spectra at 10 K reveal that all four lifetime components have the same spectral properties that match the free ligand emission.

Time-resolved luminescence of the free ligand in cyclohexane solution

Free ligand of compound 2b: 4-formyl-2,6-lutidine

The complicated multi-exponential behaviour of **2b** observed in the millisecond time range can be attributed to the emission of two distinct species: compound **2b** and its free ligand (4-formyl-2,6-lutidine). The ligand does not interfere with the emission of the compound in nanoseconds and microseconds, as it remains non-emissive in these time regimes (Figure S7.74, A and B). However, it contributes to the emission observed in the millisecond time range (Figure S7.74C). The lifetime constants and their fractions are presented in Table S7.29.

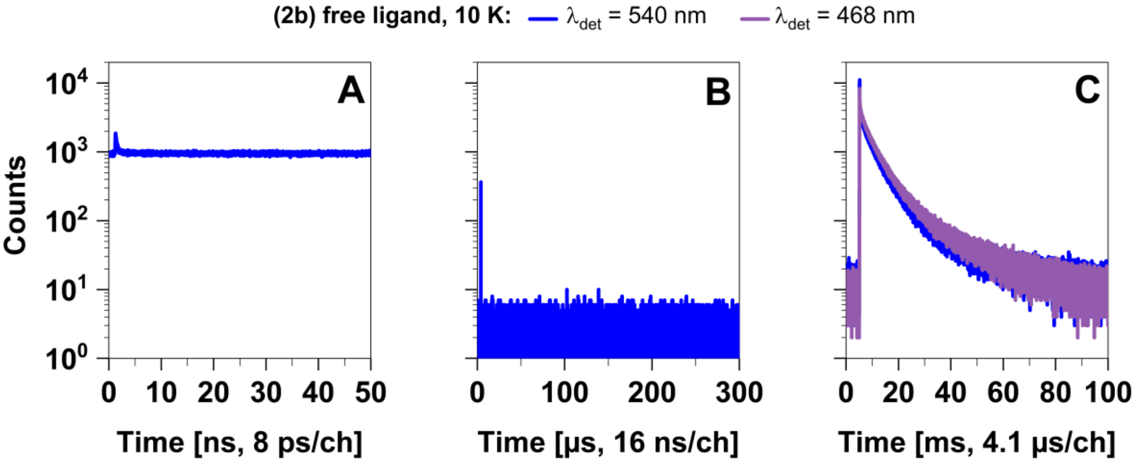

Figure S7.74. Time-resolved measurements of **2b** free ligand (4-formyl-2,6-lutidine) in cyclohexane solution at 10 K in three time regimes: **A.** nanoseconds; **B.** microseconds; and **C.** milliseconds.

Table S7.29. Free ligand (4-formyl-2,6-lutidine) in cyclohexane solution in milliseconds at 10 K. The decays were recorded at two detection wavelengths: 540 nm (emission maximum of the compound) and 468 nm (emission maximum of the free ligand).

λ_{det}	x_1	**τ_1 [ms]**	x_2	**τ_2 [ms]**	x_3	**τ_3 [ms]**	x_4	**τ_4 [ms]**	$\langle\tau\rangle_I$ [ms]	χ_r^2
468	0.02	**31.96**	0.30	**7.39**	0.36	**3.09**	0.31	**0.39**	9.82	1.05
540	0.02	**26.18**	0.37	**6.28**	0.29	**2.34**	0.32	**0.31**	8.50	1.04

Free ligand of compound 3b: 4-formyl pyridine

The free ligand of **3b** complex, 4-formyl pyridine, has an emission maximum at 465 nm. The emission band features strong vibronic coupling at very low temperatures (10-80 K). Time-resolved measurements are conducted at 10 K at the detection maximum of the free ligand (465 nm). As for **2b**, the ligand does not obscure the emission of the compound in the nanosecond and microsecond time regimes, but it affects the millisecond time regime (Figure S7.75). In the millisecond time regime, the decays were recorded at 465 nm and at the detection maximum of the compound, 595 nm. Similar lifetime constants were obtained at both detection wavelengths (Table S7.30), indicating the emission of a single species in this time regime.

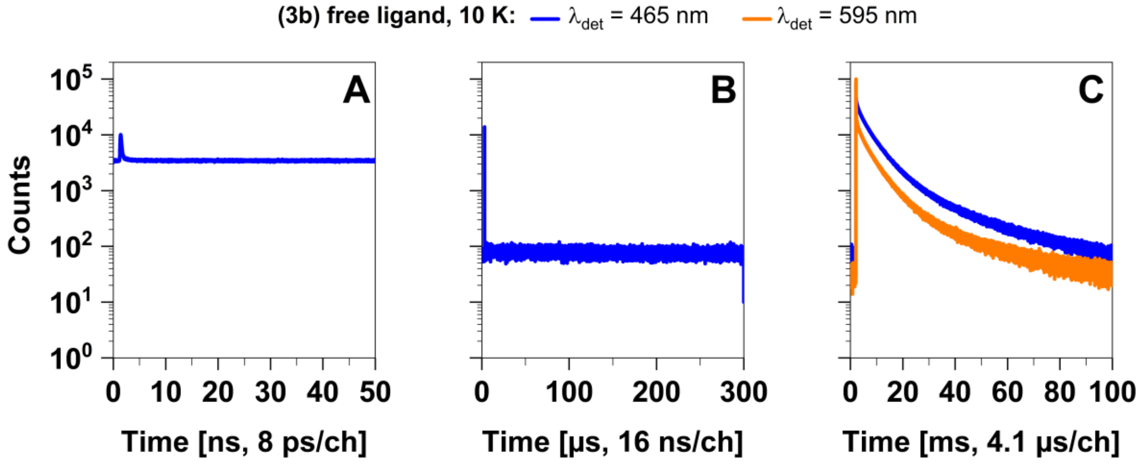

Figure S7.75. Time-resolved measurements of **3b** free ligand (4-formyl pyridine) in cyclohexane solution at 10 K in three time regimes: **A.** nanoseconds; **B.** microseconds; and **C.** milliseconds.

Table S7.30. Free ligand (4-formyl pyridine) in cyclohexane solution in the millisecond time regime at 10 K. The decays were recorded at two detection wavelengths: 465 nm (emission maximum of the free ligand) and 595 nm (emission maximum of the compound).

λ_{det}	x_1	**τ_1 [ms]**	x_2	**τ_2 [ms]**	x_3	**τ_3 [ms]**	x_4	**τ_4 [ms]**	$\langle\tau\rangle_I$ [ms]	χ_r^2
465	0.02	**36.65**	0.26	**8.49**	0.46	**3.64**	0.26	**0.56**	10.96	1.13
595	0.01	**42.69**	0.26	**7.80**	0.43	**3.29**	0.30	**0.47**	10.39	1.07

Time-resolved measurements of powdered samples

Table S7.31. Summary of the lifetime fit results of powdered **2a**, **2b**, **3a** and **3b.**

Compound	**T [K]**	x_1	τ_1	x_2	τ_2	x_3	τ_3	$\langle\tau\rangle_x$	$\langle\tau\rangle_I$	**unit**	χ_r^2
2a	298	0.40	**2.09**	0.60	**1.22**	-	-	1.57	1.69	**ns**	1.17
		0.89	**1.27**	0.11	**0.56**	-	-	1.19	1.23	**ms**	1.19
	80	0.99	**5.76**	<0.01	**1.73**	-	-	5.79	5.85	**ns**	3.21
		0.88	**2.28**	0.12	**1.22**	-	-	2.15	2.21	**ms**	1.14
2b	298	0.01	**11.84**	0.40	**2.88**	0.59	**1.21**	2.11	3.51	**ns**	1.27
		<0.01	**24.03**	<0.01	**6.22**	0.99	**0.35**	0.39	1.67	**µs**	1.05
	80	0.04	**42.33**	0.15	**4.68**	0.81	**1.21**	3.36	22.28	**ns**	1.03
		<0.01	**1.45**	<0.01	**0.47**	0.99	**0.02**	0.02	0.04	**ms**	1.12
3a	298	<0.01	**7.28**	0.56	**0.44**	0.44	**0.24**	0.36	0.40	**ms**	1.22
	80	0.32	**1.70**	0.39	**0.98**	0.29	**0.20**	0.98	1.32	**ms**	1.13
3b	298	1.00	**7.58**	-	**-**	-	**-**	7.58	7.58	**µs**	1.07
	80	<0.01	**130.37**	0.77	**28.76**	0.23	**12.96**	25.18	27.42	**µs**	1.11

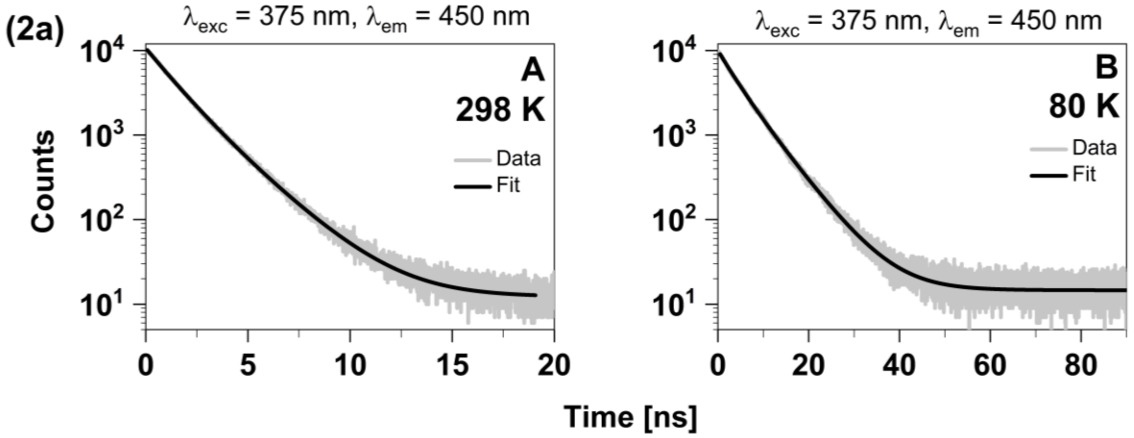

Figure S7.76. Time-resolved decays of **2a** (powdered sample) in the nanosecond range at two different temperatures: **A.** 298 K and **B.** 80 K.

(2a)

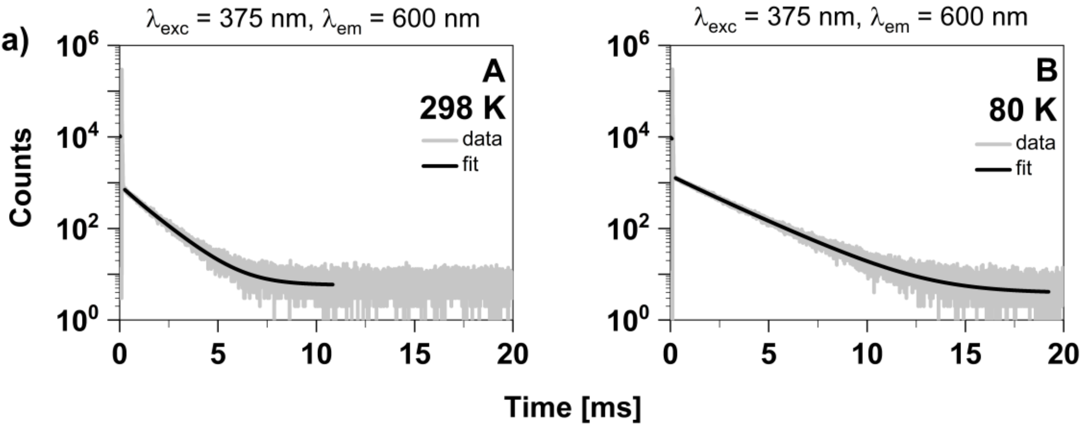

Figure S7.77. Time-resolved decays of **2a** (powdered sample) in the millisecond range at two different temperatures: **A.** 298 K and **B.** 80 K.

(2b)

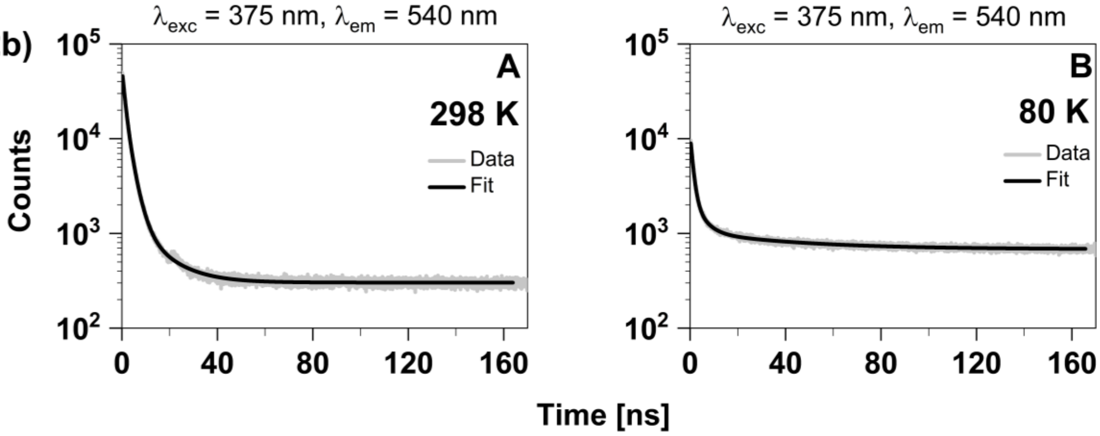

Figure S7.78. Time-resolved decays of **2b** (powdered sample) in the nanosecond range at two different temperatures: **A.** 298 K and **B.** 80 K.

(2b)

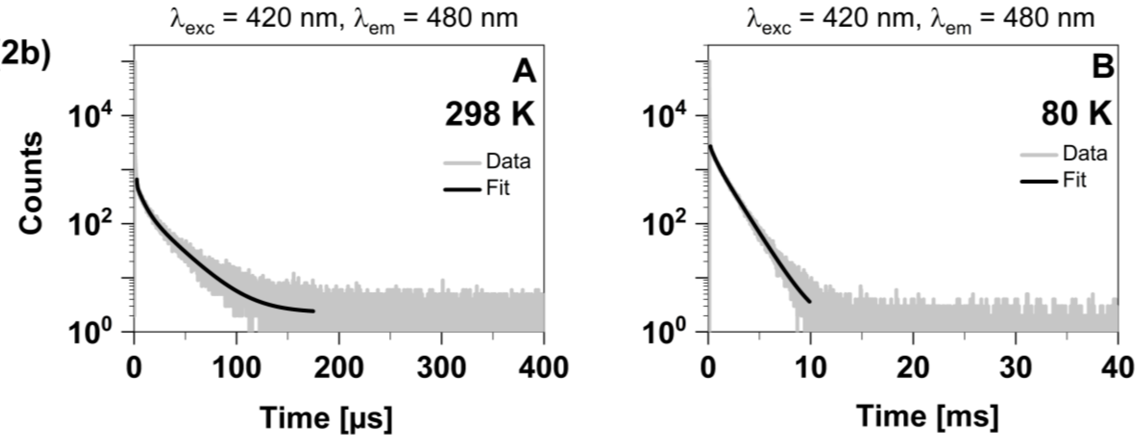

Figure S7.79. Time-resolved decays of **2b** (powdered sample) in two different time ranges and at two different temperatures: **A.** microseconds, 298 K and **B.** milliseconds, 80 K.

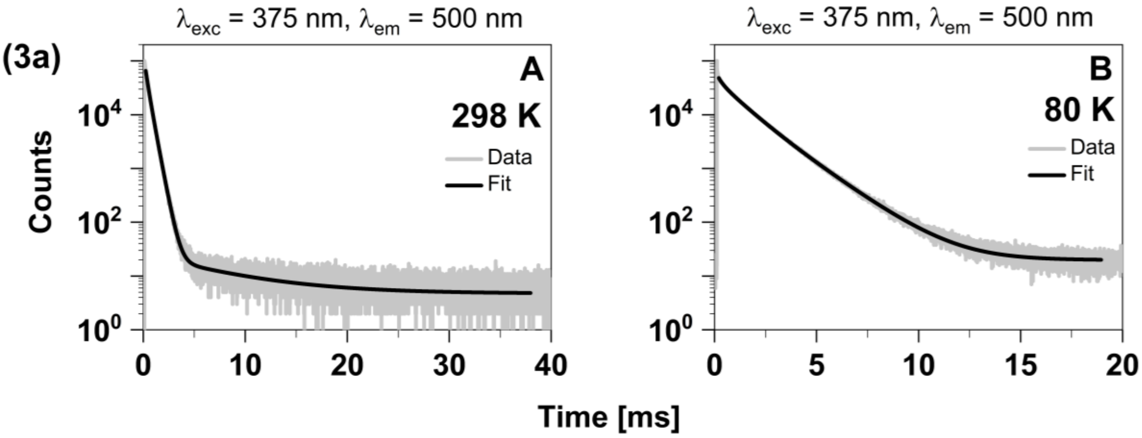

Figure S7.80. Time-resolved decays of **3a** (powdered sample) in the millisecond range at two different temperatures: **A.** 298 K and **B.** 80 K.

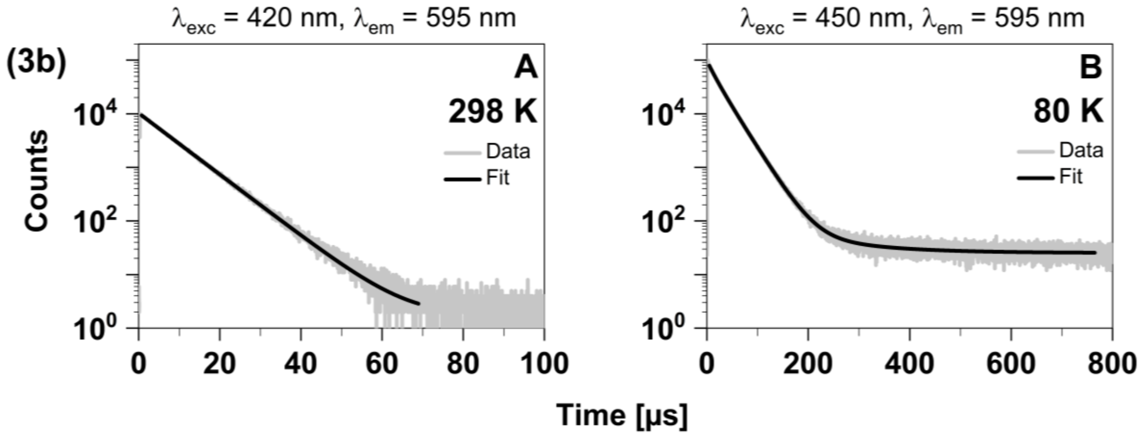

Figure S7.81. Time-resolved decays of **3b** (powdered sample) in the microsecond range at two different temperatures: **A.** 298 K and **B.** 80 K.

Detailed Computational results

Computed photophysical data

Table S7.32. Extended calculated photophysical data of the complexes **2a**, **3b**, **3a**, **3b**.

Property	Compound			
	2a	**2b**	**3a**	**3b**
$\Delta E_{0\text{-}0}$ [eV]	0.582 (LC)	0.052 (LLCT) -0.023 (^{1}LLCT-^{3}LC)	0.463 (LC)	0.062 (LLCT) 0.095 (MLCT)
$\lambda_{\text{aem,adia}}$ [nm]	409 (^{1}LC) ^{b} 519 (^{3}LC)	497 (^{1}LLCT) 507 (^{3}LLCT) 497 (^{3}LC)	372(^{1}LLCT) 389(^{1}MLCT) 391(^{1}LC) 405 (^{3}MLCT) 459 (^{3}LC)	516 (^{1}LLCT) 529 (^{3}LLCT) 519 (^{1}MLCT) 541 (^{3}MLCT)
$\lambda_{\text{em,vert}}$ ^{a} [nm]	443 (^{1}LC)^{b} 664 (^{3}LC)	563 (^{1}LLCT) 591 (^{3}LLCT) 615 (^{3}LC)	422 (^{1}LLCT) 485 (^{1}MLCT) 606 (^{1}LC) 525 (^{3}MLCT) 665 (^{3}LC)	704 (^{1}LLCT) 728 (^{3}LLCT) 707 (^{1}MLCT) 748 (^{3}MLCT)
λ_{abs} (S_1) [nm]	349 (LC/LLCT)	412 (LLCT)	329 (LLCT/MLCT(d_{xz}))	452 (LLCT/MLCT(d_{xz}))
λ_{abs} (T_1) [nm]	390 (LC)	426 (LLCT+LC)	347 (LC)	465 (LLCT+MLCT)
f_{abs} (S_1)	0.09251	0.03057	0.00916	0.01507
k_F (298 K) [s^{-1}]	4.0×10^{7} (^{1}LC)^{b}	6.3×10^{6} (^{1}LLCT)	5.9×10^{6} (^{1}LLCT) 1.0×10^{7} (^{1}MLCT) 1.0×10^{7} (SLC)	4.2×10^{5} (^{1}LLCT) 2.6×10^{6} (^{1}MLCT)
k_P (77 K) [s^{-1}]	1.1×10^{1} (^{3}LC)	7.6×10^{1} (^{3}LLCT) 2.7×10^{1} (^{3}LC)	9.5×10^{3} (^{3}MLCT) 8.6×10^{1} (TLC)	1.4×10^{4} (^{3}LLCT) 7.9×10^{3} (^{3}MLCT)
kISC (298 K) [s^{-1}]	8.0×10^{7} (^{1}LC - ^{3}LC)^{b}	2.7×10^{6} (^{1}LLCT - ^{3}LLCT) 8.5×10^{5} (^{1}LLCT - ^{3}LC)	1.5×10^{9} (^{1}LC - ^{3}LC) 5.8×10^{9}(^{1}MLCT - ^{3}MLCT) 7.2×10^{9} (^{1}LLCT - ^{3}MLCT)	2.3×10^{7} (^{1}LLCT - ^{3}LLCT) 9.1×10^{10} (^{1}LLCT - ^{3}MLCT) 2.7×10^{10} (^{1}MLCT - ^{3}MLCT) 2.8×10^{11} (^{1}MLCT - ^{3}LLCT)
krISC (298 K) [s^{-1}]	-	1.0×10^{5} (^{3}LLCT - ^{1}LLCT) 1.8×10^{3} (^{3}LC - ^{1}LLCT)	5.1×10^{-2} (^{3}LC - ^{1}LC) 4.4×10^{8} (^{3}MLCT - ^{1}MLCT) -	3.1×10^{5} (^{3}LLCT - ^{1}LLCT) 2.1×10^{9} (^{3}MLCT - ^{3}LLCT) 5.7×10^{8} (^{3}MLCT - ^{1}MLCT) 2.4×10^{8} (^{3}LLCT - ^{1}MLCT)
kISC (77 K) [s^{-1}]	1.7×10^{7} (^{1}LC - ^{3}LC)^{b}	3.4×10^{6} (^{1}LLCT - ^{3}LLCT) 6.2×10^{5} (^{1}LLCT - ^{3}LC)	1.4×10^{9} (^{1}LC - ^{3}LC) 4.7×10^{9} (^{1}MLCT - ^{3}MLCT) 1.2×10^{10} (^{1}LLCT - ^{3}MLCT)	5.8×10^{6} (^{1}LLCT - ^{3}LLCT) 1.8×10^{11} (^{1}LLCT - ^{3}MLCT) 1.5×10^{10}(^{3}MLCT - ^{3}MLCT 1.4×10^{12} (^{3}MLCT - ^{3}LLCT)
krISC (77 K) [s^{-1}]	-	4.9×10^{2} (^{3}LLCT - ^{1}LLCT) 5.1×10^{2} (^{3}LC - ^{1}LLCT)	- - -	8.9×10^{1} (^{3}LLCT - ^{1}LLCT) 1.8×10^{7} (^{3}MLCT - ^{1}LLCT) 8.8×10^{3} (^{3}MLCT - ^{1}MLCT) 9.4×10^{3} (^{3}LLCT - ^{1}MLCT)

a: Multiple entries indicate that more than one minimum was found on the S_1 or T_1 potential energy hypersurface, respectively. Adiabatic excitation energies and photophysical properties at these minima are given in the ESI.

b: The ^{1}LC state was optimized with the constrained inter-ligand dihedral angle of the ^{3}LC state. It does not constitute a proper minimum on the S_1 potential energy hypersurface. A proper minimum could not be obtained with the PBE0 functional.

Vibes parameters

Table S7.33. Parameters utilized in the computation of the intersystem crossing rates with the VIBES program. If the rate is not mentioned in the table below, an interval of 3000 fs and a damping (eta) of 10 cm^{-1} were used.

Compound	from	to	T [K]	Interval [fs]	Eta [cm^{-1}]
2b	SLLCT	TLC	298	1000	10
	SLLCT	TLC	77	1000	10
	TLC	SLLCT	298	1000	10
3a	TLC	SLC	298	3000	1
	SLLCT	TMLCT	298	500	10
	SLLCT	TMLCT	77	500	10
	TLLCT	SLLCT	77	1000	10
3b	SLLCT	TMLCT	298	300	10
	SLLCT	TMLCT	77	1000	20
	TMLCT	SLLCT	298	100	10
	TMLCT	SLLCT	77	300	10
	TLLCT	SMLCT	298	1000	10
	TLLCT	SMLCT	77	1000	10

The linear lutidine complex 2a

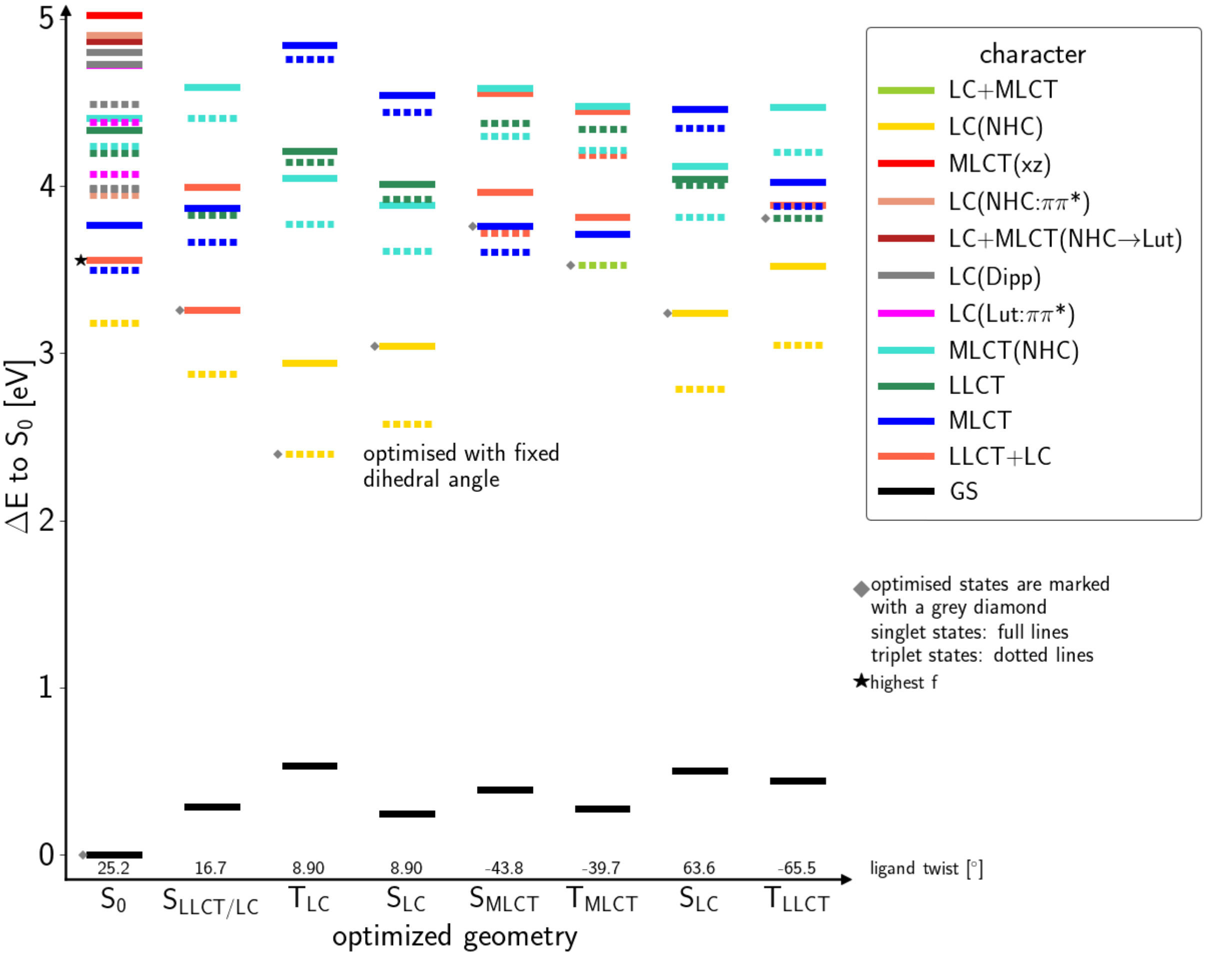

Figure S7.82. Energy state diagram of **2a** for selected optimized geometries.

Table S7.34. Singlet states and their properties at the ground state geometry of **2a**.

State	E [eV]	λ_{abs} [nm]	f	|μ| [D]	Character
S0	0			19.21	S0
S1	3.557	349	0.09251	4.79	LLCT+LC
S2	3.767	329	0.02394	14.76	MLCT
S3	4.333	286	0.00585	6.41	LLCT
S4	4.408	281	0.00218	15.07	MLCT(NHC)
S5	4.726	262	0.09399	18.05	LC(Lut:ππ*)
S6	4.728	262	0.00529	17.22	LC(Dipp)
S7	4.804	258	0.00483	19.16	LC(Dipp)
S8	4.866	255	0.01983	12.71	LC+MLCT(NHC→Lut)
S9	4.902	253	0.05730	12.21	LC(NHC:ππ*)
S10	5.021	247	0.10468	13.32	MLCT(xz)

Table S7.35. Triplet states and their properties at the ground state geometry of **2a**.

State	E [eV]	-	-	|µ| [D]	Character
T1	3.180			8.06	LC(NHC)
T2	3.5499			17.80	MLCT
T3	3.947			16.48	LC(NHC:ππ*)
T4	3.981			19.23	LC(Dipp)
T5	3.987			19.17	LC(Dipp)
T6	4.073			19.44	LC(Lut:ππ*)
T7	4.296			4.81	LLCT
T8	4.239			12.00	MLCT(NHC)
T9	4.382			13.79	LC(Lut:ππ*)
T10	4.490			18.95	LC(Dipp)

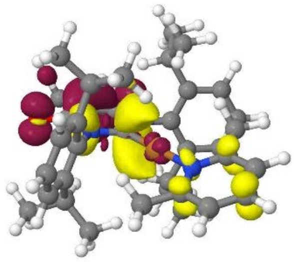

Figure S7.83. S1-S0 difference density at the **2a** GS.

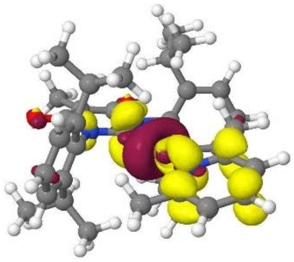

Figure S7.84. S2-S0 difference density at the **2a** GS.

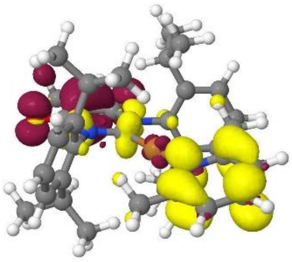

Figure S7.85. S3-S0 difference density at the **2a** GS.

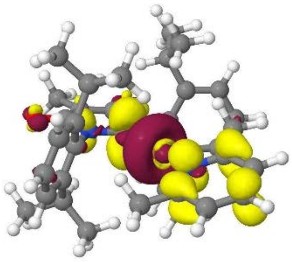

Figure S7.86. S4-S0 difference density at the **2a** GS.

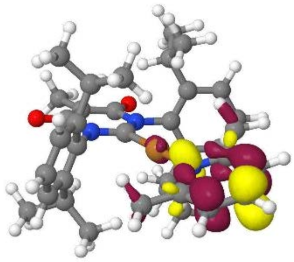

Figure S7.87. S5-S0 difference density at the **2a** GS.

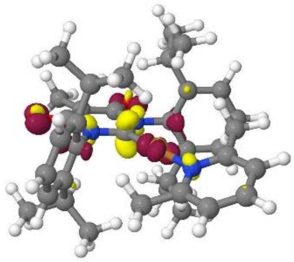

Figure S7.88. S6-S0 difference density at the **2a** GS.

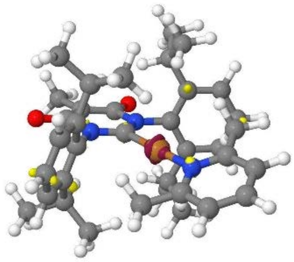

Figure S7.89. S7-S0 difference density at the **2a** GS.

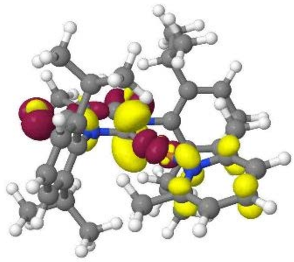

Figure S7.90. S8-S0 difference density at the **2a** GS.

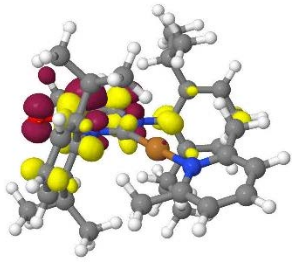

Figure S7.91. S9-S0 difference density at the **2a** GS.

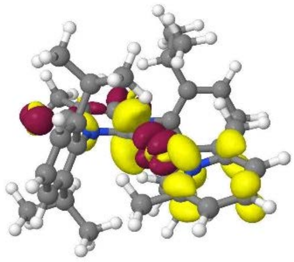

Figure S7.92. S10-S0 difference density at the **2a** GS.

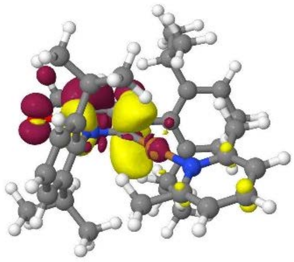

Figure S7.93. T1-S0 difference density at the **2a** GS.

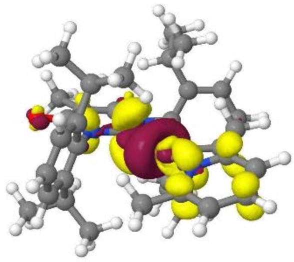

Figure S7.94. T2-S0 difference density at the **2a** GS.

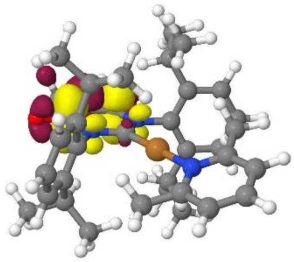

Figure S7.95. T3-S0 difference density at the **2a** GS.

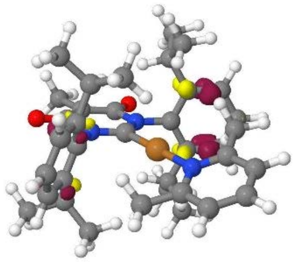

Figure S7.96. T4-S0 difference density at the **2a** GS.

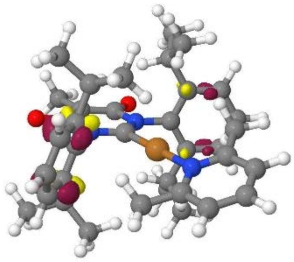

Figure S7.97. T5-S0 difference density at the **2a** GS.

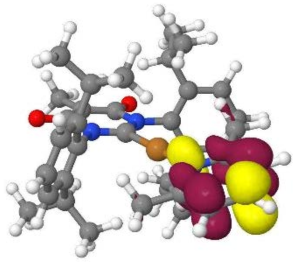

Figure S7.98. T6-S0 difference density at the **2a** GS.

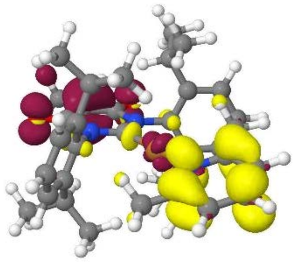

Figure S7.99. T7-S0 difference density at the **2a** GS.

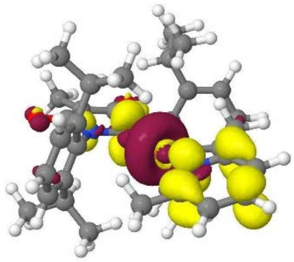

Figure S7.100. T8-S0 difference density at the **2a** GS.

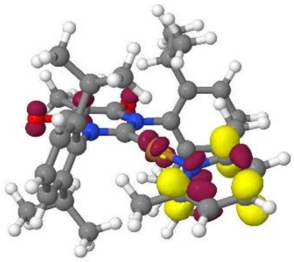

Figure S7.101. T9-S0 difference density at the **2a** GS.

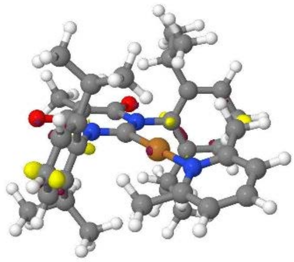

Figure S7.102. T10-S0 difference density at the **2a** GS.

Table S7.36. Energies [eV] of relevant excited states of **2a** at the optimized geometries of different states.

State	Optimized geometry							
	S0	SLC-8.9	TLC	SMLCT	TMLCT	TLLCT	SLC/LLCT	SLC-65.6
S0	0.000	0.246	0.531	0.387	0.278	0.445	0.287	0.505
SLC	3.557	3.042	2.943	4.554	3.815	3.521	3.261	3.239
TLC	3.180	2.579	2.397	3.720	4.184	3.050	2.8875	2.7854
SMLCT	3.767	4.550	4.841	3.760	3.711	4.025	3.868	4.459
TMLCT	3.499	4.440	4.760	3.606	3.526	3.879	3.663	4.357
SLLCT	4.333	4.009	4.209	3.963	4.173	3.888	3.994	4.041
TLLCT	4.196	3.923	4.143	4.374	4.185	3.812	3.824	4.001
SMLCT(NHC)	4.408	3.885	4.048	4.588	4.479	4.469	4.594	4.120
TMLCT(NHC)	4.239	3.610	3.771	4.297	4.216	4.205	4.404	3.8112

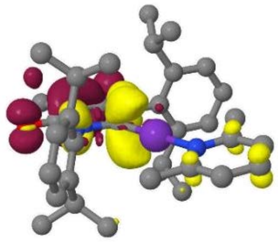

Figure S7.103. S1-S0 (LC(NHC)) difference density at the **2a** SLC-8.9geometry.

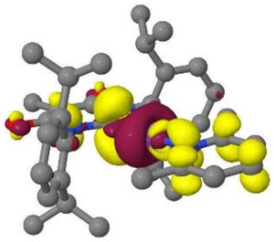

Figure S7.104. S2-S0 (MLCT(NHC)) difference density at the **2a** SLC-8.9 geometry.

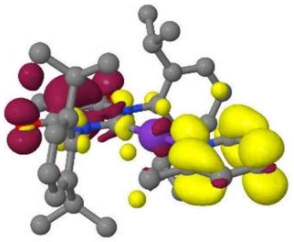

Figure S7.105. S3-S0 (LLCT) difference density at the **2a** SLC-8.9 geometry.

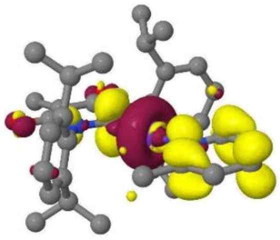

Figure S7.106. S5-S0 (MLCT) difference density at the **2a** SLC-8.9 geometry.

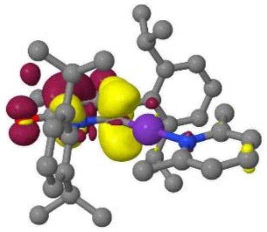

Figure S7.107. T1-S0 (LC(NHC)) difference density at the **2a** SLC-8.9 geometry.

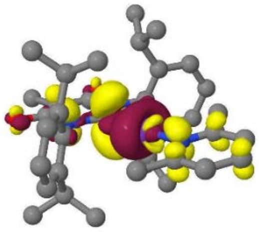

Figure S7.108. T2-S0 (MLCT(NHC)) difference density at the **2a** SLC-8.9 geometry.

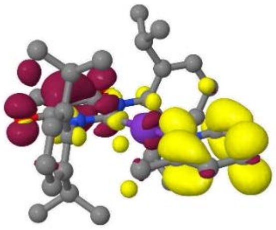

Figure S7.109. T3-S0 (LLCT) difference density at the **2a** SLC-8.9 geometry.

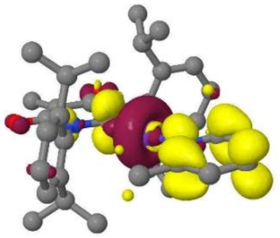

Figure S7.110. T9-S0 (MLCT) difference density at the **2a** SLC-8.9 geometry.

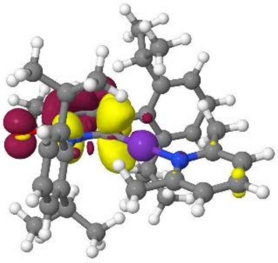

Figure S7.111. S1-S0 (LC(NHC)) difference density at the **2a** TLC geometry.

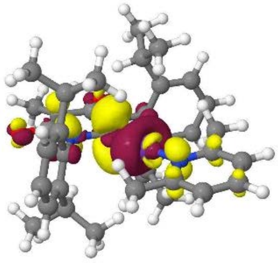

Figure S7.112. S2-S0 (MLCT(NHC)) difference density at the **2a** TLC geometry.

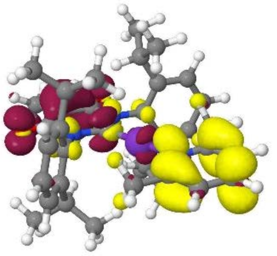

Figure S7.113. S3-S0 (LLCT) difference density at the **2a** TLC geometry.

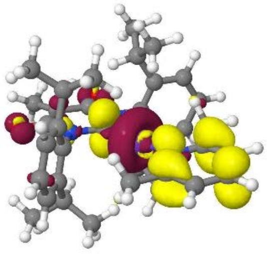

Figure S7.114. S5-S0 (MLCT) difference density at the **2a** TLC geometry.

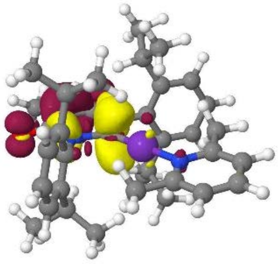

Figure S7.115. T1-S0 (LC(NHC)) difference density at the **2a** TLC geometry.

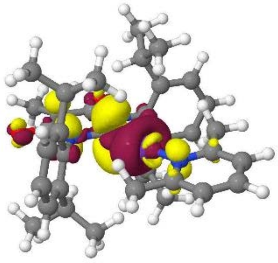

Figure S7.116. T2-S0 (MLCT(NHC)) difference density at the **2a** TLC geometry.

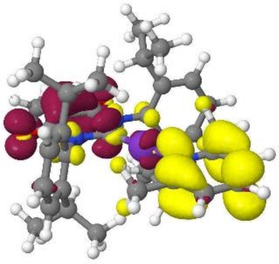

Figure S7.117. T3-S0 (LLCT) difference density at the **2a** TLC geometry.

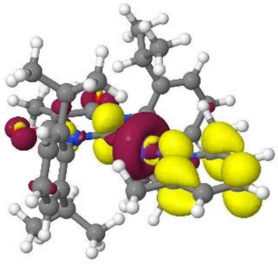

Figure S7.118. T9-S0 (MLCT) difference density at the **2a** TLC geometry.

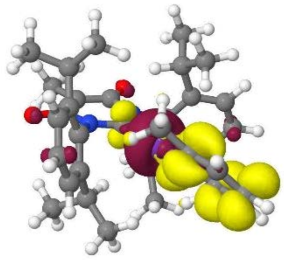

Figure S7.119. S1-S0 (MLCT) difference density at the **2a** SMLCT geometry.

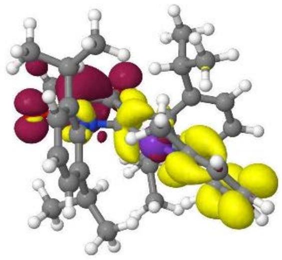

Figure S7.120. S2-S0 (LLCT) difference density at the **2a** SMLCT geometry.

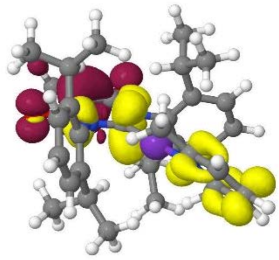

Figure S7.121. S3-S0 (LC(NHC)) difference density at the **2a** SMLCT geometry.

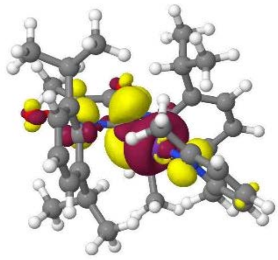

Figure S7.122. S4-S0 (MLCT(NHC)) difference density at the **2a** SMLCT geometry.

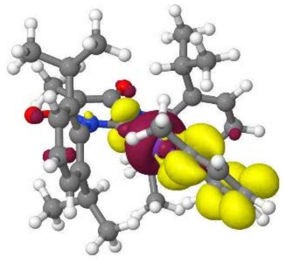

Figure S7.123. T1-S0 (MLCT) difference density at the **2a** SMLCT geometry.

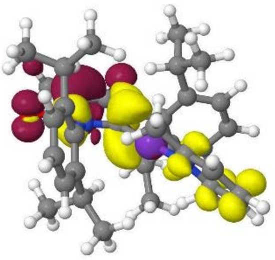

Figure S7.124. T2-S0 (LC(NHC)) difference density at the **2a** SMLCT geometry.

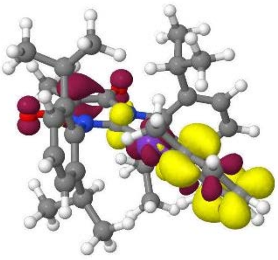

Figure S7.125. T3-S0 (LLCT) difference density at the **2a** SMLCT geometry.

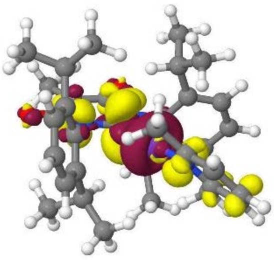

Figure S7.126. T5-S0 (MLCT(NHC)) difference density at the **2a** SMLCT geometry.

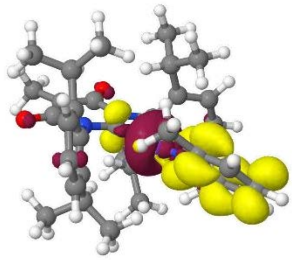

Figure S7.127. S1-S0 (MLCT) difference density at the **2a** TMLCT geometry.

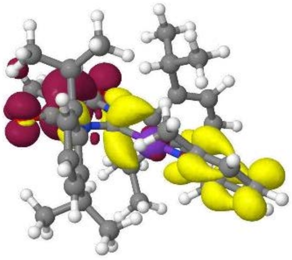

Figure S7.128. S2-S0 (LC/LLCT) difference density at the **2a** TMLCT geometry.

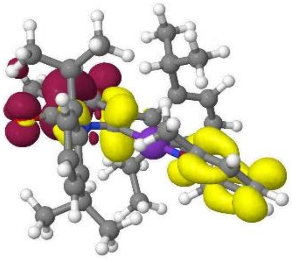

Figure S7.129. S3-S0 (LC/LLCT) difference density at the **2a** TMLCT geometry.

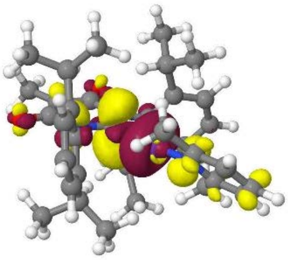

Figure S7.130. S4-S0 (MLCT(NHC)) difference density at the **2a** TMLCT geometry.

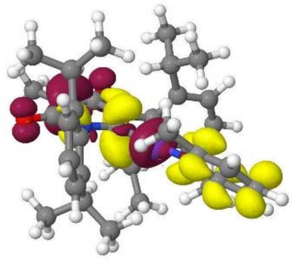

Figure S7.131. T1-S0 (LC/MLCT) difference density at the **2a** TMLCT geometry.

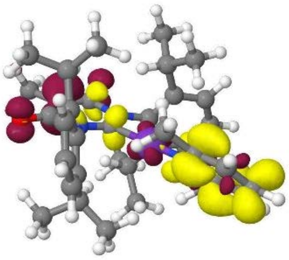

Figure S7.132. T4-S0 (LC/LLCT) difference density at the **2a** TMLCT geometry.

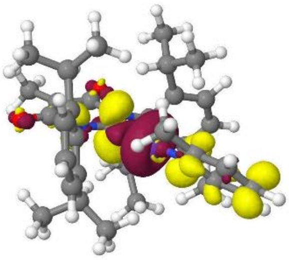

Figure S7.133. T5-S0 (MLCT(NHC)) difference density at the **2a** TMLCT geometry.

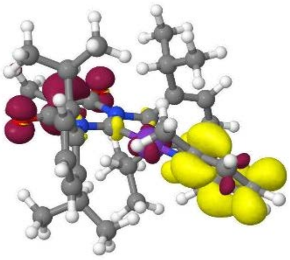

Figure S7.134. T9-S0 (LLCT) difference density at the **2a** TMLCT geometry.

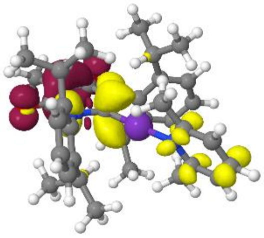

Figure S7.135. S1-S0 (LC) difference density at the **2a** TLLCT geometry.

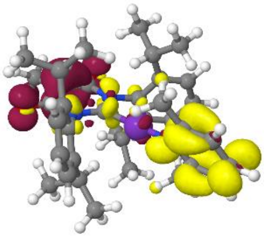

Figure S7.136. S2-S0 (LLCT) difference density at the **2a** TLLCT geometry.

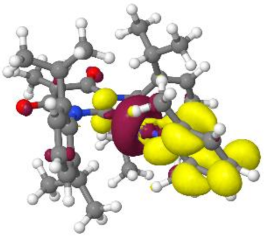

Figure S7.137. S3-S0 (MLCT) difference density at the **2a** TLLCT geometry.

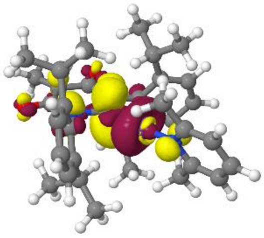

Figure S7.138. S4-S0 (MLCT(NHC)) difference density at the **2a** TLLCT geometry.

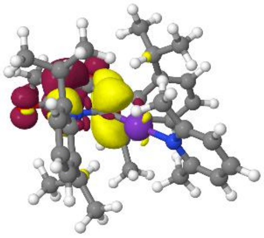

Figure S7.139. T1-S0 (LC) difference density at the **2a** TLLCT geometry.

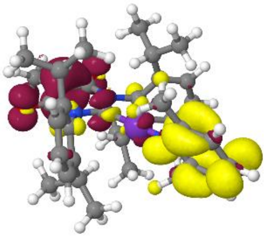

Figure S7.140. T2-S0 (LLCT) difference density at the **2a** TLLCT geometry.

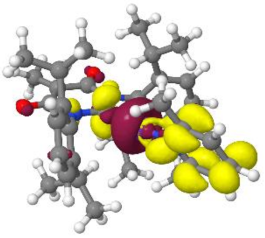

Figure S7.141. T3-S0 (MLCT) difference density at the **2a** TLLCT geometry.

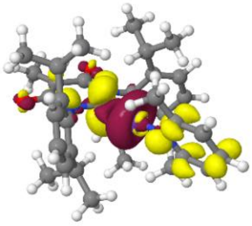

Figure S7.142. T4-S0 (MLCT(NHC)) difference density at the **2a** TLLCT geometry.

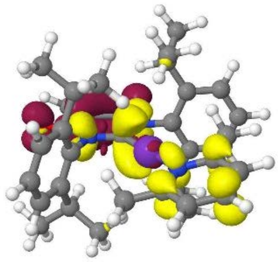

Figure S7.143. S1-S0 (LC/LLCT) difference density at the **2a** SLC/LLCT geometry.

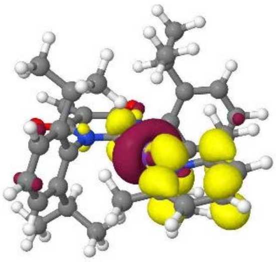

Figure S7.144. S2-S0 (MLCT) difference density at the **2a** SLC/LLCT geometry.

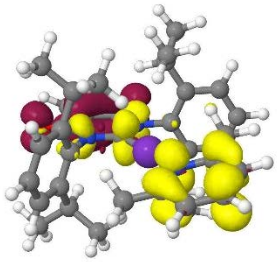

Figure S7.145. S3-S0 (LLCT/LC) difference density at the **2a** SLLCT/LC geometry.

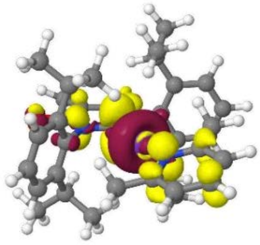

Figure S7.146. S4-S0 (MLCT(NHC)) difference density at the **2a** SLC/LLCT geometry.

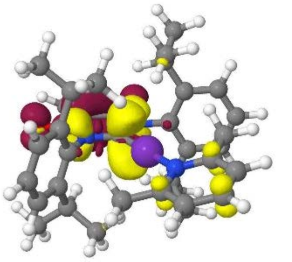

Figure S7.147. T1-S0 (LC) difference density at the **2a** SLC/LLCT geometry.

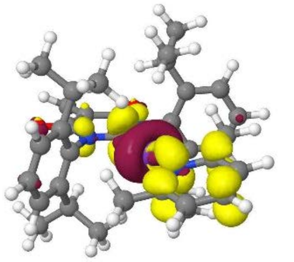

Figure S7.148. T2-S0 (MLCT) difference density at the **2a** SLC/LLCT geometry.

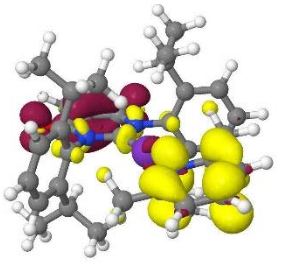

Figure S7.149. T3-S0 (LLCT) difference density at the **2a** SLC/LLCT geometry.

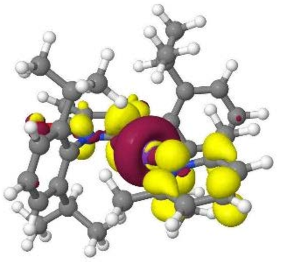

Figure S7.150. T9-S0 (MLCT(NHC)) difference density at the **2a** SLC/LLCT geometry.

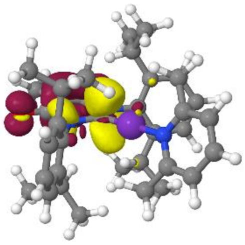

Figure S7.151. S1-S0 (LC) difference density at the **2a** SLC-65.6 geometry.

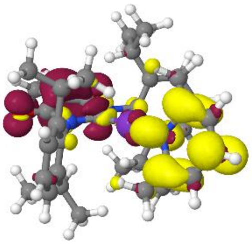

Figure S7.152. S2-S0 (LLCT) difference density at the **2a** SLC-65.6 geometry.

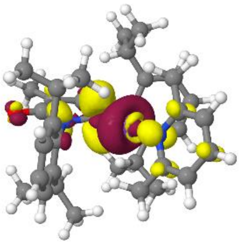

Figure S7.153. S3-S0 (MLCT(NHC)) difference density at the **2a** SLC-65.6 geometry.

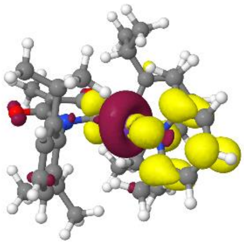

Figure S7.154. S4-S0 (MLCT) difference density at the **2a** SLC-65.6 geometry.

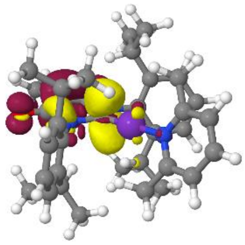

Figure S7.155. T1-S0 (LC) difference density at the **2a** SLC-65.6 geometry.

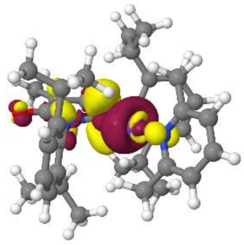

Figure S7.156. T2-S0 (MLCT(NHC)) difference density at the **2a** SLC-65.6geometry.

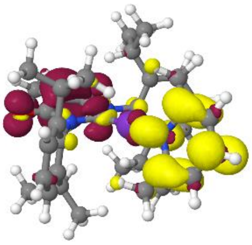

Figure S7.157. T3-S0 (LLCT) difference density at the **2a** SLC-65.6 geometry.

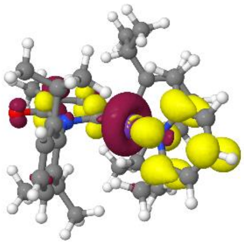

Figure S7.158. T4-S0 (MLCT) difference density at the **2a** SLC-65.6 geometry.

The linear formyl lutidine complex 2b

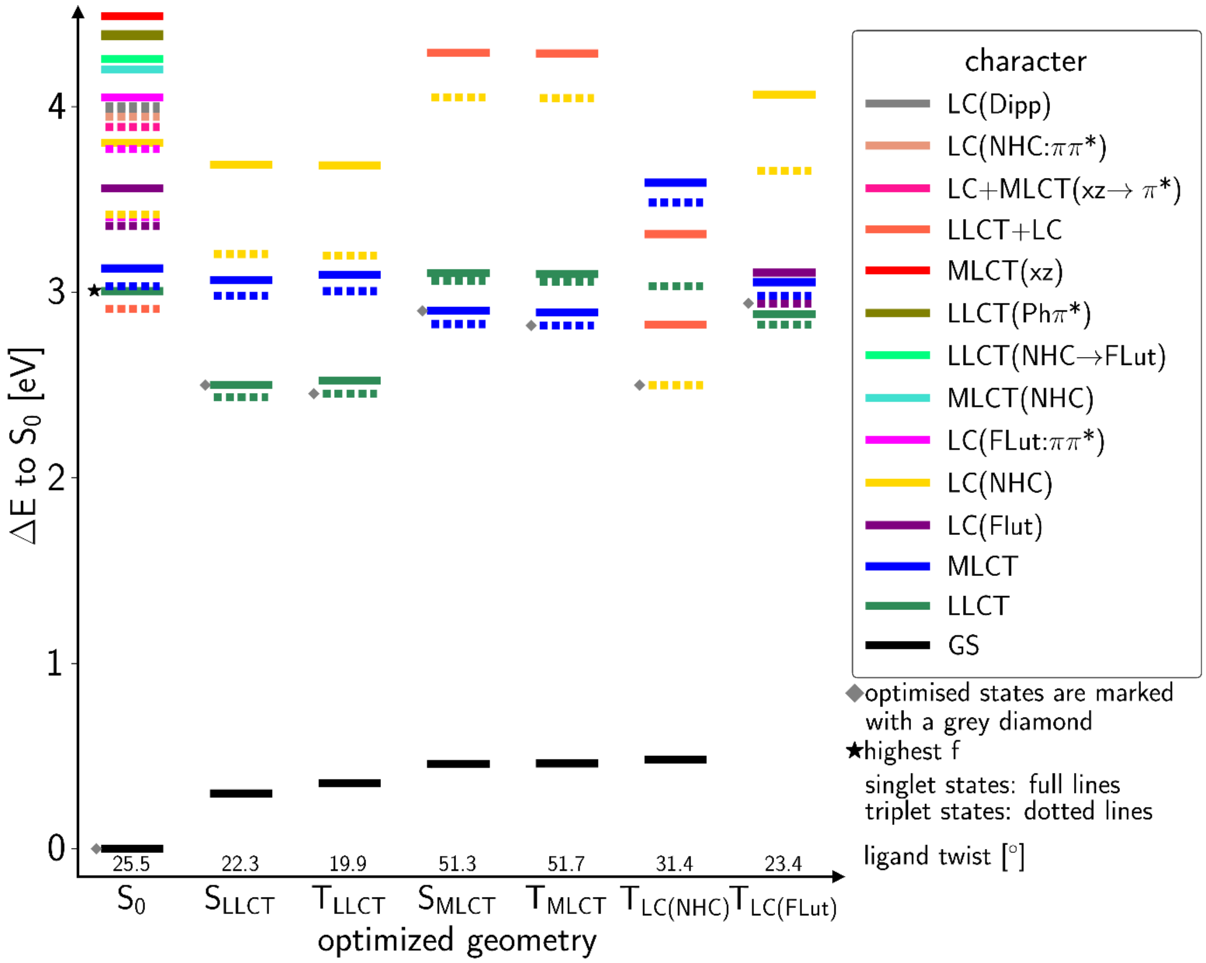

Figure S7.159. Energy state diagram of **2b** for selected optimized geometries.

Table S7.37. Singlet states and their properties at the ground state geometry of **2b**.

State	E [eV]	λ_{abs} [nm]	f	|μ| [D]	Character
S0	0			16.40	S0
S1	3.008	412	0.03057	16.47	LLCT
S2	3.130	396	0.00801	2.48	MLCT
S3	3.562	348	0	21.42	LC(FLut)
S4	3.815	326	0.08037	4.030	LC(NHC)
S5	4.051	306	0.0951	11.46	LC(FLut:ππ*)
S6	4.200	295	0.01486	18.55	MLCT(NHC)
S7	4.570	291	0.04309	4.65	LLCT
S8	4.380	283	0.02636	9.06	LLC(Phπ*)
S9	4.392	282	0.01382	13.36	LLC(Phπ*)
S10	4.489	276	0.07359	1.96	MLCT(xz)

Table S7.38. Triplet states and their properties at the ground state geometry of **2b**.

State	E [eV]	-	-	|μ| [D]	Character
T1	2.913			16.40	LLCT
T2	3.033			16.47	MLCT
T3	3.356			2.48	LC(FLut)
T4	3.404			21.42	LC(FLut:ππ*)
T5	3.421			4.03	LC(NHC)
T6	3.773			11.46	LC(FLut:ππ*)
T7	3.893			18.55	MLCT(NHC)
T8	3.945			4.65	LC(NHC:ππ*)
T9	3.991			9.06	LC(Dipp)
T10	4.004			13.36	LC(Dipp)

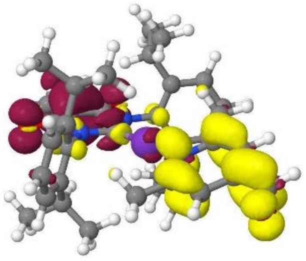

Figure S7.160. S1-S0 difference density at the GS of **2b**.

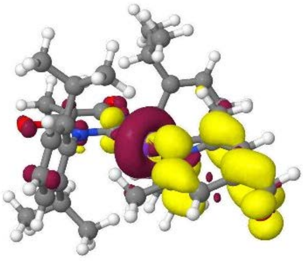

Figure S7.161. S2-S0 difference density at the GS of **2b**.

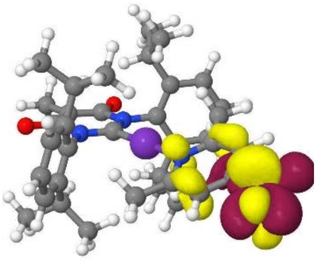

Figure S7.162. S3-S0 difference density at the GS of **2b**.

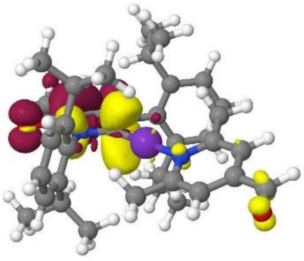

Figure S7.163. S4-S0 difference density at the GS of **2b**.

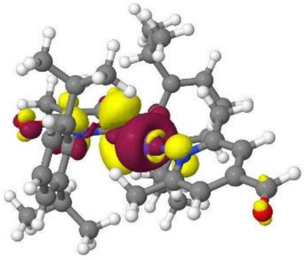

Figure S7.164. S5-S0 difference density at the GS of **2b**.

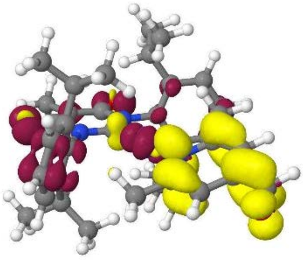

Figure S7.165. S6-S0 difference density at the GS of **2b**.

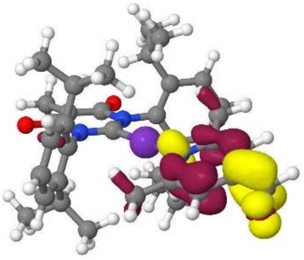

Figure S7.166. S7-S0 difference density at the GS of **2b**.

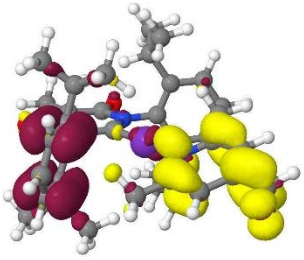

Figure S7.167. S8-S0 difference density at the GS of **2b**.

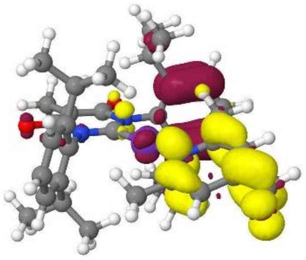

Figure S7.168. S9-S0 difference density at the GS of **2b**.

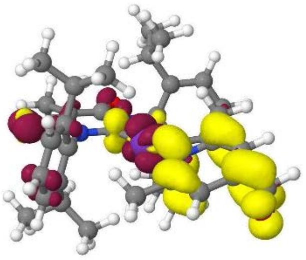

Figure S7.169. S10-S0 difference density at the GS of **2b**.

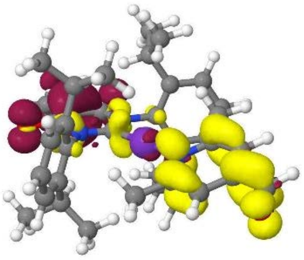

Figure S7.170. T1-S0 difference density at the GS of **2b**.

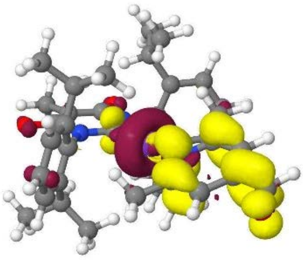

Figure S7.171. T2-S0 difference density at the GS of **2b**.

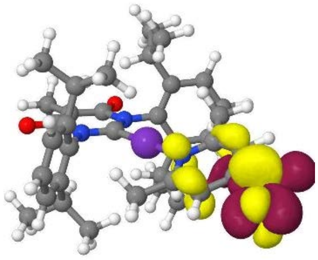

Figure S7.172. T3-S0 difference density at the GS of **2b**.

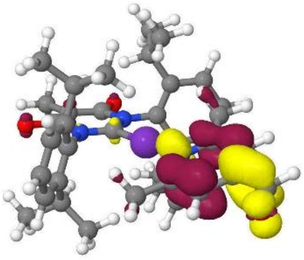

Figure S7.173. T4-S0 difference density at the GS of **2b**.

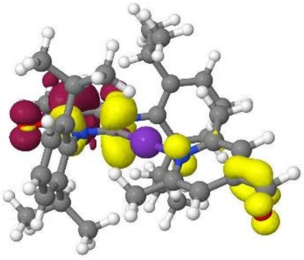

Figure S7.174. T5-S0 difference density at the GS of **2b**.

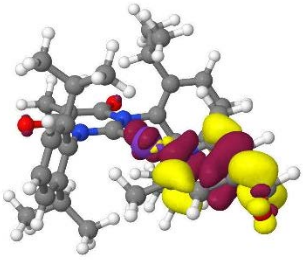

Figure S7.175. T6-S0 difference density at the GS of **2b**.

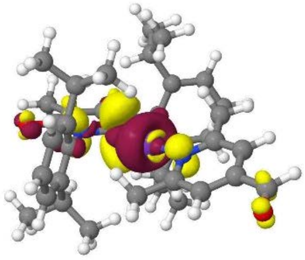

Figure S7.176. T7-S0 difference density at the GS of **2b**.

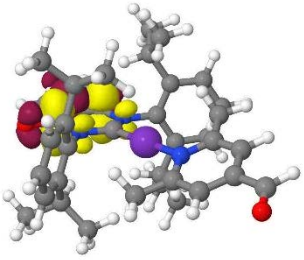

Figure S7.177. T8-S0 difference density at the GS of **2b**.

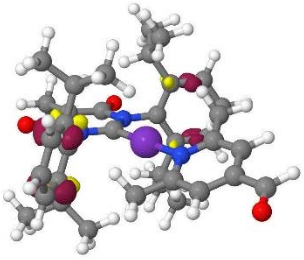

Figure S7.178. T9-S0 difference density at the GS of **2b**.

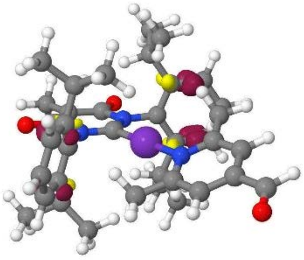

Figure S7.179. T10-S0 difference density at the GS of **2b**.

Table S7.39. Energies [eV] of relevant excited states of **2b** at the optimized geometries of different states.

State	Optimized geometry						
	S0	SLLCT	TLLCT	SMLCT	TMLCT	TLC(NHC)	TLC(FLut)
S0	0.000	0.300	0.355	0.459	0.460	0.482	0.303
SLLCT	3.008	2.500	2.525	3.104	3.098	2.827	2.882
TLLCT	2.913	2.436	2.454	3.062	3.057	3.035	2.825
SMLCT	3.130	3.067	3.094	2.900	2.892	3.592	3.055
TMLCT	3.033	2.437	3.008	2.829	2.821	3.484	2.981
TLC	4.380	3.206	3.199	4.052	4.048	2.499	3.657
Tnπ	3.357	3.217	3.267	3.328	3.330	3.713	2.940

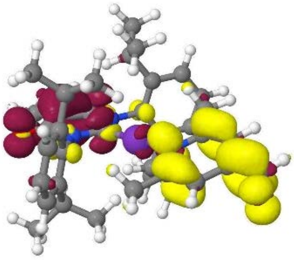

Figure S7.180. S1-S0 (LLCT) difference density at the **2b** SLLCT geometry.

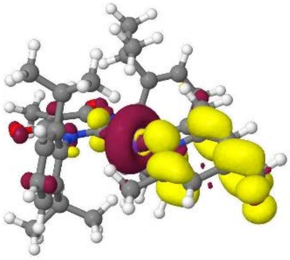

Figure S7.181. S2-S0 (MLCT) difference density at the **2b** SLLCT geometry.

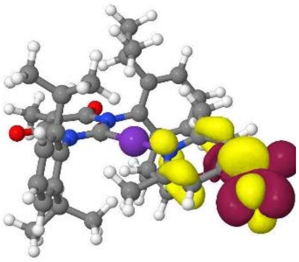

Figure S7.182. S3-S0 (LC(FLut)) difference density at the **2b** SLLCT geometry.

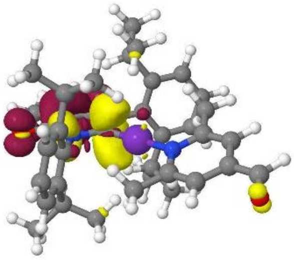

Figure S7.183. S4-S0 (LC(NHC)) difference density at the **2b** SLLCT geometry.

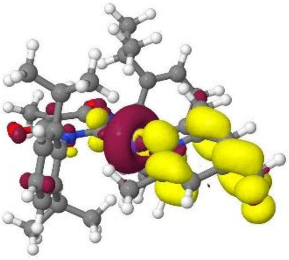

Figure S7.184. T1-S0 (LLCT) difference density at the **2b** SLLCT geometry.

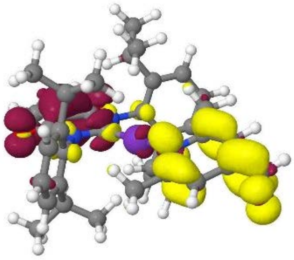

Figure S7.185. T2-S0 (MLCT) difference density at the **2b** SLLCT geometry.

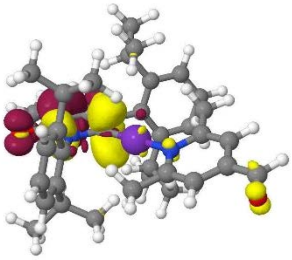

Figure S7.186. T3-S0 (LC(NHC)) difference density at the **2b** SLLCT geometry.

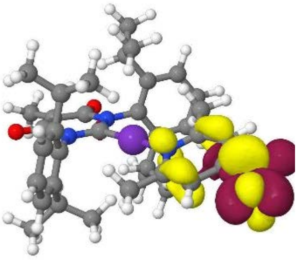

Figure S7.187. T4-S0 (LC(FLut)) difference density at the **2b** SLLCT geometry.

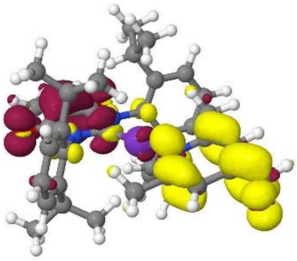

Figure S7.188. S1-S0 (LLCT) difference density at the **2b** TLLCT geometry.

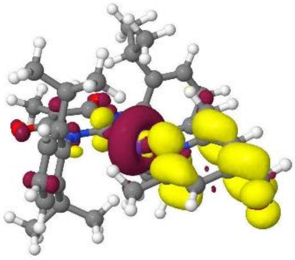

Figure S7.189. S2-S0 (MLCT) difference density at the **2b** TLLCT geometry.

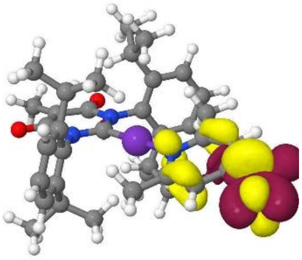

Figure S7.190. S3-S0 (LC(FLut)) difference density at the **2b** TLLCT geometry.

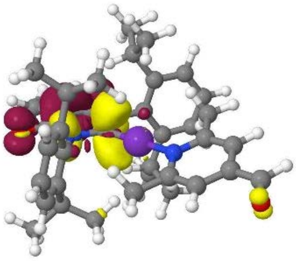

Figure S7.191. S4-S0 (LC(NHC)) difference density at the **2b** TLLCT geometry.

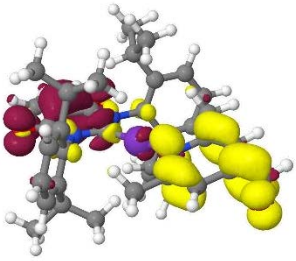

Figure S7.192. T1-S0 (LLCT) difference density at the **2b** TLLCT geometry.

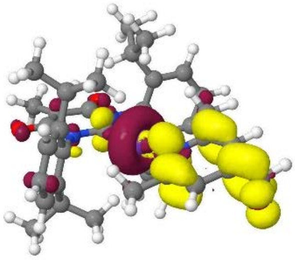

Figure S7.193. T2-S0 (MLCT) difference density at the **2b** TLLCT geometry.

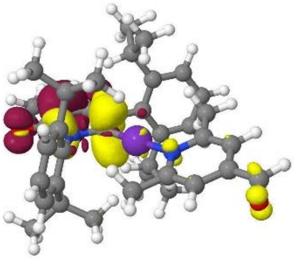

Figure S7.194. T3-S0 (LC(NHC)) difference density at the **2b** TLLCT geometry.

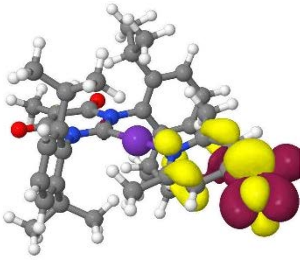

Figure S7.195. T4-S0 (LC(FLut)) difference density at the **2b** TLLCT geometry.

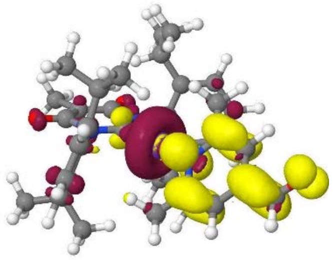

Figure S7.196. S1-S0 (MLCT) difference density at the **2b** SMLCT geometry.

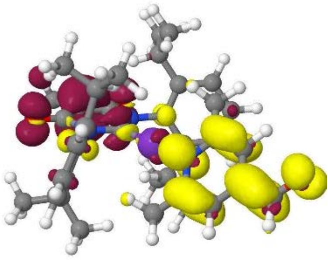

Figure S7.197. S2-S0 (LLCT) difference density at the **2b** SMLCT geometry.

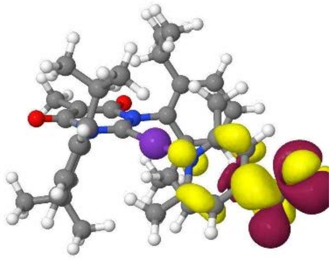

Figure S7.198. S3-S0 (LC(FLut)) difference density at the **2b** SMLCT geometry.

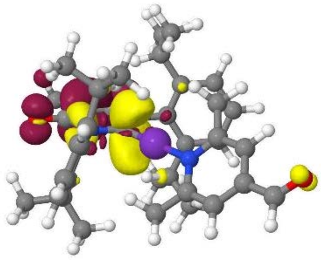

Figure S7.199. S9-S0 (LC(NHC)) difference density at the **2b** SMLCT geometry.

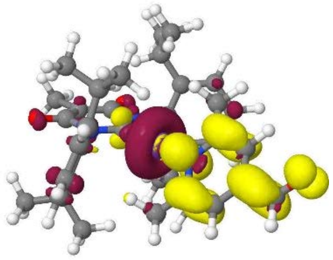

Figure S7.200. T1-S0 (MLCT) difference density at the **2b** SMLCT geometry.

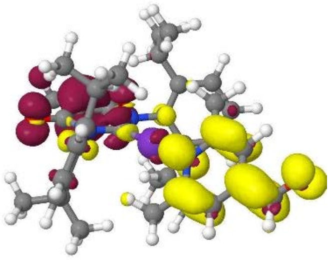

Figure S7.201. T2-S0 (LLCT) difference density at the **2b** SMLCT geometry.

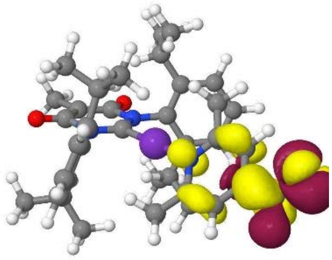

Figure S7.202. T3-S0 (LC(FLut)) difference density at the **2b** SMLCT geometry.

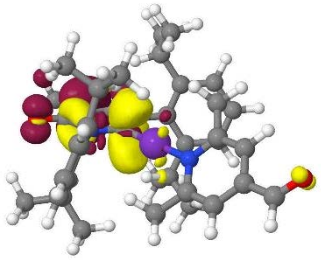

Figure S7.203. T6-S0 (LC(NHC)) difference density at the **2b** SMLCT geometry.

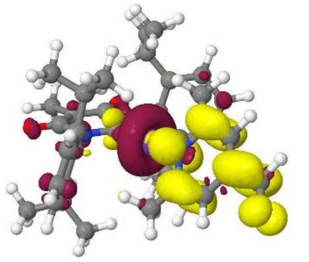

Figure S7.204. S1-S0 (MLCT) difference density at the **2b** TMLCT geometry.

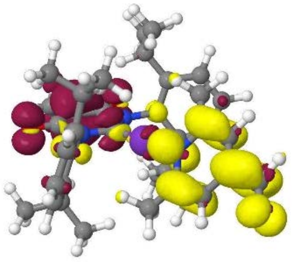

Figure S7.205. S2-S0 (LLCT) difference density at the **2b** TMLCT geometry.

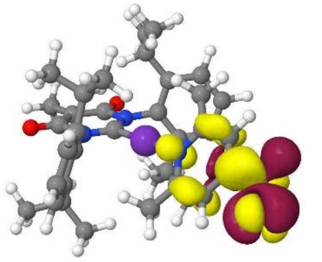

Figure S7.206. S3-S0 (FLut) difference density at the **2b** TMLCT geometry.

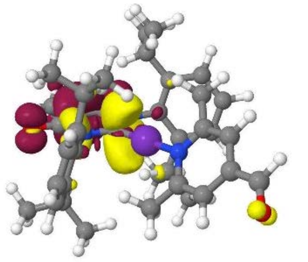

Figure S7.207. S9-S0 (LC(NHC)) difference density at the **2b** TMLCT geometry.

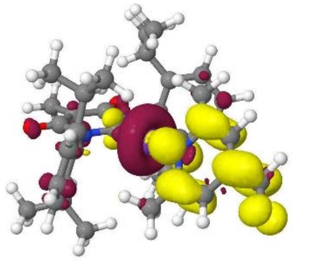

Figure S7.208. T1-S0 (MLCT) difference density at the **2b** TMLCT geometry.

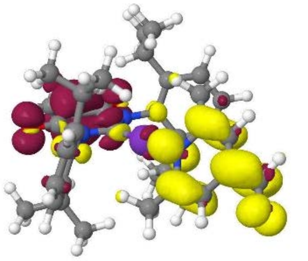

Figure S7.209. T2-S0 (LLCT) difference density at the **2b** TMLCT geometry.

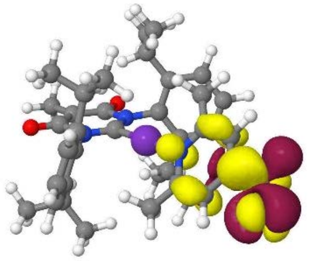

Figure S7.210. T3-S0 (LC(FLut)) difference density at the **2b** TMLCT geometry.

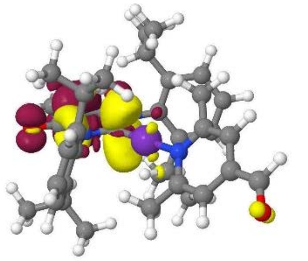

Figure S7.211. T6-S0 (LC(NHC)) difference density at the **2b** TMLCT geometry.

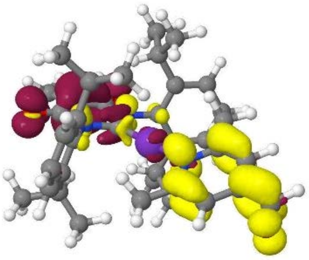

Figure S7.212. S1-S0 (LLCT) difference density at the **2b** TLC(NHC) geometry.

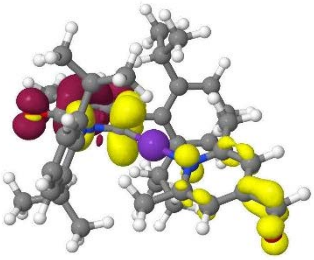

Figure S7.213. S2-S0 (LC(NHC)) difference density at the **2b** TLC(NHC) geometry.

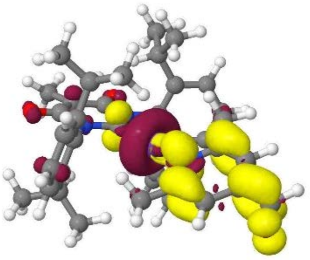

Figure S7.214. S3-S0 (MLCT) difference density at the **2b** TLC(NHC) geometry.

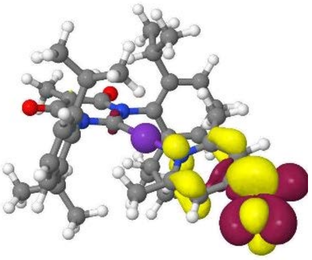

Figure S7.215. S1-S0 (LC(FLut)) difference density at the **2b** TLC(NHC) geometry.

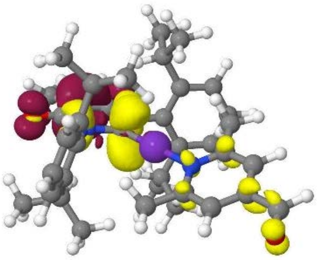

Figure S7.216. T1-S0 (LLCT) difference density at the **2b** TLC(NHC) geometry.

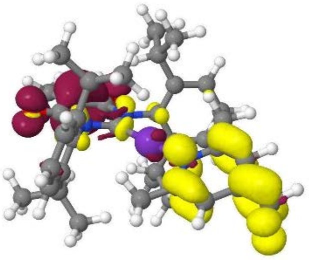

Figure S7.217. T2-S0 (LLCT) difference density at the **2b** TLC(NHC) geometry.

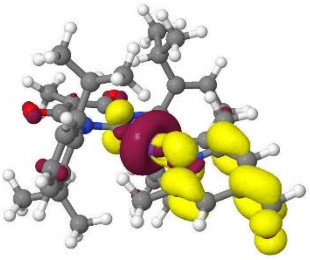

Figure S7.218. T3-S0 (MLCT) difference density at the **2b** TLC(NHC) geometry.

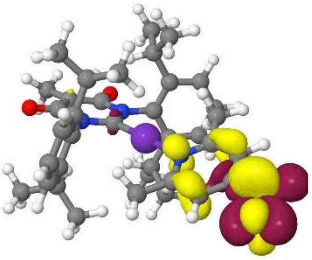

Figure S7.219. T4-S0 (LC(FLut)) difference density at the **2b** TLC(NHC) geometry.

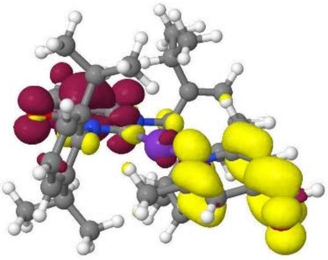

Figure S7.220. S4-S0 (LLCT) difference density at the **2b** TLC(FLut) geometry.

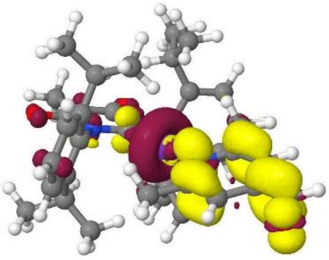

Figure S7.221. S4-S0 (MLCT) difference density at the **2b** TLC(FLut) geometry.

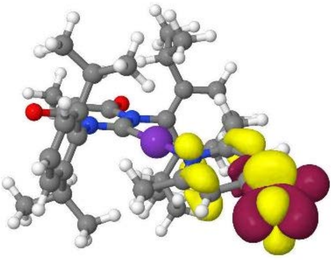

Figure S7.222. S4-S0 (LC(FLut)) difference density at the **2b** TLC(FLut) geometry.

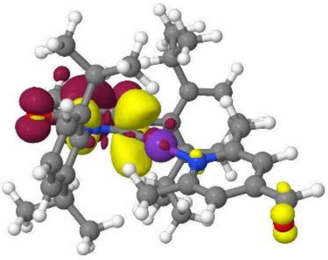

Figure S7.223. S4-S0 (LC(NHC)) difference density at the **2b** TLC(FLut) geometry.

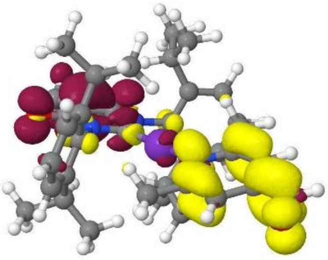

Figure S7.224. T1-S0 (LLCT) difference density at the **2b** TLC(FLut) geometry.

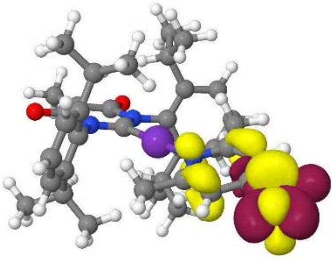

Figure S7.225. T2-S0 (LC(FLut)) difference density at the **2b** TLC(FLut) geometry.

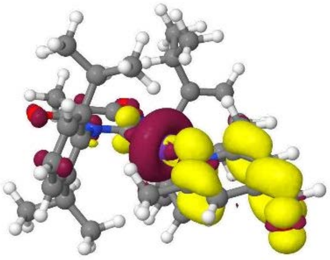

Figure S7.226. T3-S0 (MLCT) difference density at the **2b** TLC(FLut) geometry.

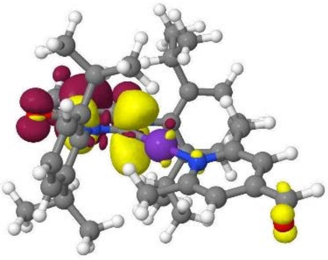

Figure S7.227. T4-S0 (LC(NHC)) difference density at the **2b** TLC(FLut) geometry.

The trigonal pyridine complex 3a

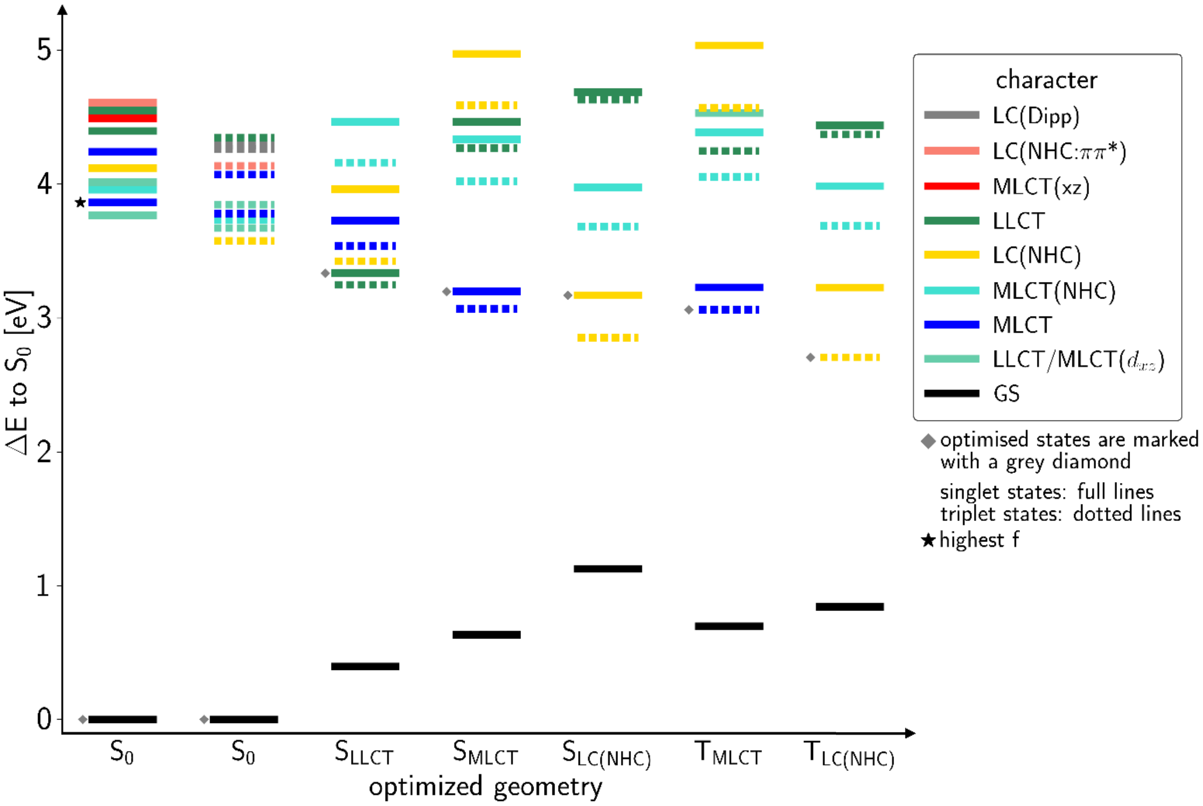

Figure S7.228. Energy state diagram of **3a** for selected optimized geometries.

Table S7.40. Singlet states and their properties at the ground state geometry of **3a**.

State	E [eV]	λ_{abs} [nm]	f	|μ| [D]	Character
S0	0			23.01	S0
S1	3.767	329	0.00916	9.41	LLCT/MLCT(xz)
S2	3.862	321	0.14889	12.74	MLCT
S3	3.957	313	0.05833	21.73	MLCT(NHC)
S4	4.014	309	0.08989	10.29	LLCT/MLCT(xz)
S5	4.120	301	0.02919	13.10	LC(NHC)
S6	4.241	292	0.01188	18.09	MLCT
S7	4.395	282	0.00707	0.49	LLCT
S8	4.491	276	0.00007	8.07	MLCT(dxz)
S9	4.555	273	0.01124	3.71	LLCT
S10	4.606	269	0.00258	12.72	LC(NHC:ππ*)

Table S7.41. Triplet states and their properties at the ground state geometry of **3a**.

State	E [eV]			|μ| [D]	Character
T1	3.574			23.01	LC(NHC)
T2	3.671			9.41	LLCT/MLCT(dxz)
T3	3.731			12.74	MLCT(NHC)
T4	3.778			21.73	MLCT
T5	3.846			10.29	LLCT/MLCT(dxz)
T6	4.070			13.10	MLCT
T7	4.135			18.09	LC(NHC:ππ*)
T8	4.263			0.49	LC(Dipp)
T9	4.287			8.07	LC(Dipp)
T10	4.344			3.71	LLCT

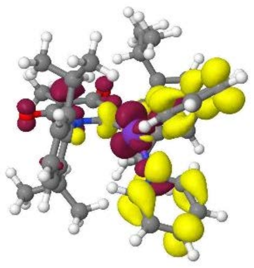

Figure S7.229. S1 difference density at the GS of **3a**.

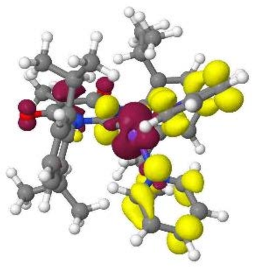

Figure S7.230. S2 difference density at the GS of **3a**.

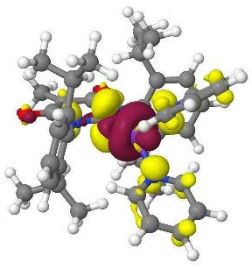

Figure S7.231. S3 difference density at the GS of **3a**.

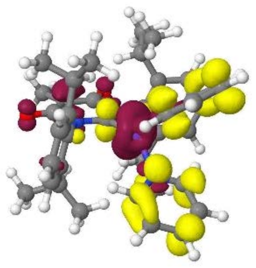

Figure S7.232. S4 difference density at the GS of **3a**.

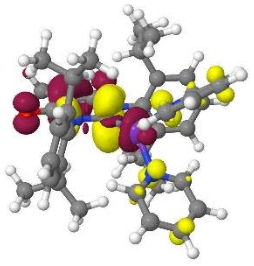

Figure S7.233. S5 difference density at the GS of **3a**.

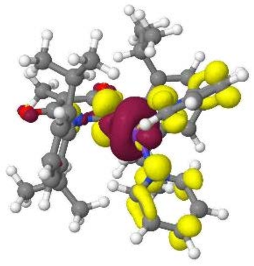

Figure S7.234. S6 difference density at the GS of **3a**.

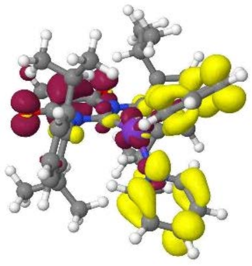

Figure S7.235. S7 difference density at the GS of **3a**.

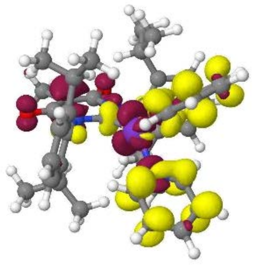

Figure S7.236. S8 difference density at the GS of **3a**.

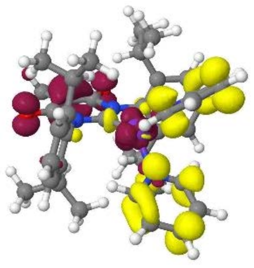

Figure S7.237. S9 difference density at the GS of **3a**.

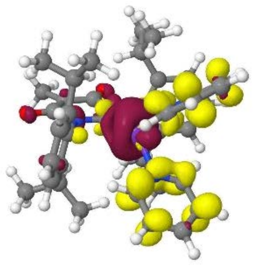

Figure S7.238. S10 difference density at the GS of **3a**.

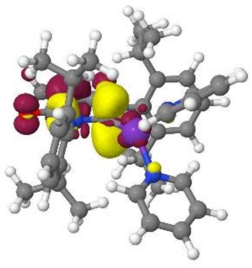

Figure S7.239. T1 difference density at the GS of **3a**.

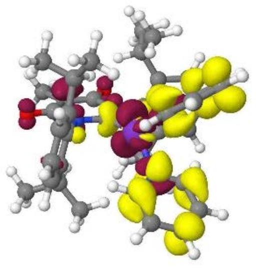

Figure S7.240. T2 difference density at the GS of **3a**.

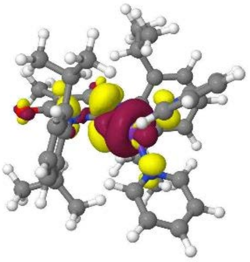

Figure S7.241. T3 difference density at the GS of **3a**.

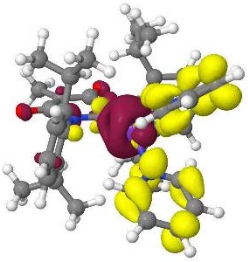

Figure S7.242. T4 difference density at the GS of **3a**.

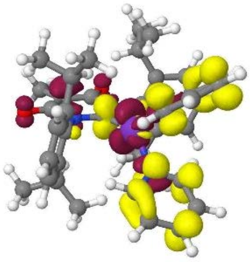

Figure S7.243. T5 difference density at the GS of **3a**.

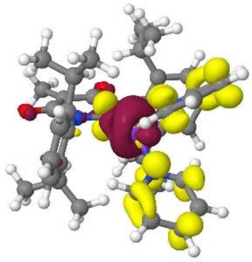

Figure S7.244. T6 difference density at the GS of **3a**.

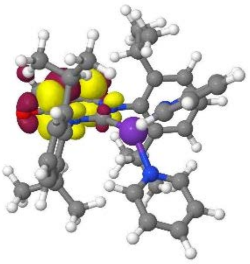

Figure S7.245. T7 difference density at the GS of **3a**.

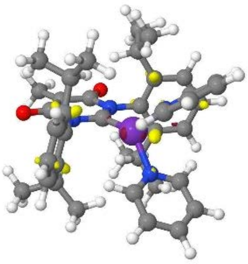

Figure S7.246. T8 difference density at the GS of **3a**.

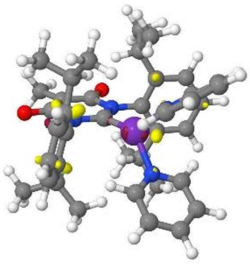

Figure S7.247. T9 difference density at the GS of **3a**.

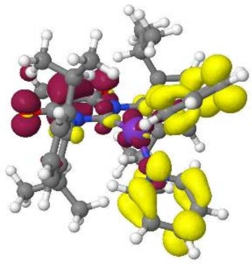

Figure S7.248. T10 difference density at the GS of **3a**.

Table S7.42. Energies [eV] of relevant excited states of **3a** at the optimized geometries of different states.

State	Optimized geometry					
	S0	SLLCT	SMLCT	TMLCT	SLC	TLC
S0	0.000	0.398	0.634	0.698	1.127	0.843
SLLCT	3.767	3.335	4.451	4.531	4.685	4.438
TLLCT	3.574	3.247	4.228	4.2459	4.630	4.438
SMLCT	3.862	3.728	3.197	3.228	-	-
TMLCT	3.778	3.538	3.068	3.061	-	-
SLC	3.862	3.960	4.950	5.034	3.170	3.227
TLC	3.574	3.424	4.557	4.567	2.853	2.706
SMLCT(NHC)	3.957	4.463	4.317	4.383	3.975	3.984
TMLCT(NHC)	3.731	4.159	3.977	4.052	3.683	3.688

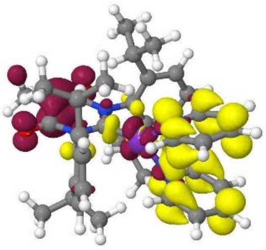

Figure S7.249. S1-S0 (LLCT) difference density at the **3a** SLLCT geometry.

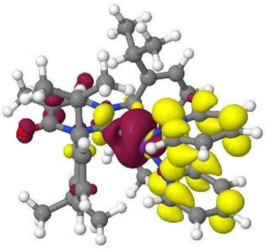

Figure S7.250. S2-S0 (MLCT) difference density at the **3a** SLLCT geometry.

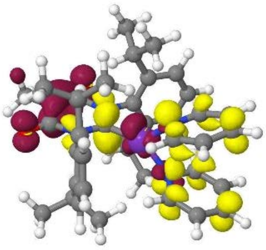

Figure S7.251. S4-S0 (LC(NHC)) difference density at the **3a** SLLCT geometry.

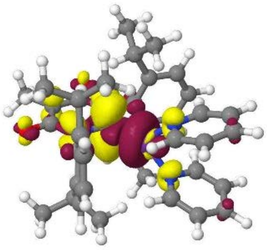

Figure S7.252. S7-S0 (MLCT(NHC)) difference density at the **3a** SLLCT geometry.

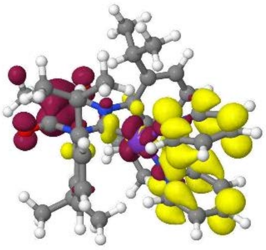

Figure S7.253. T1-S0 (LLCT) difference density at the **3a** SLLCT geometry.

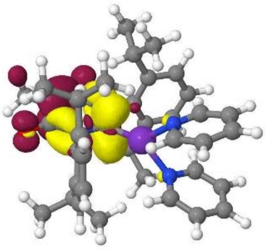

Figure S7.254. T2-S0 (LC(NHC)) difference density at the **3a** SLLCT geometry.

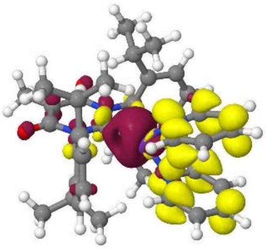

Figure S7.255. T3-S0 (MLCT) difference density at the **3a** SLLCT geometry.

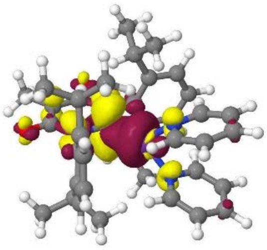

Figure S7.256. T5-S0 (MLCT(NHC)) difference density at the **3a** SLLCT geometry.

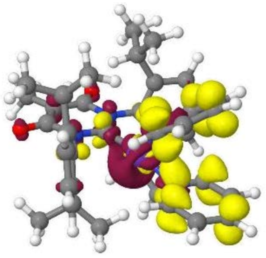

Figure S7.257. S1-S0 (MLCT) difference density at the **3a** SMLCT geometry.

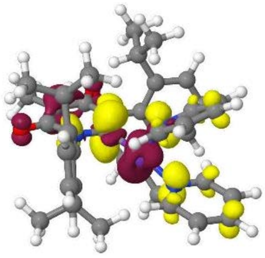

Figure S7.258. S4-S0 (MLCT(NHC)) difference density at the **3a** SMLCT geometry.

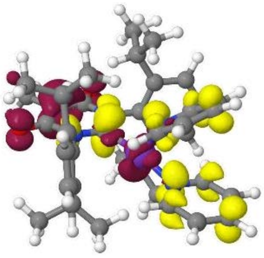

Figure S7.259. S5-S0 (LLCT) difference density at the **3a** SMLCT geometry.

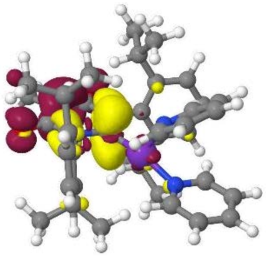

Figure S7.260. S9-S0 (LC(NHC)) difference density at the **3a** SMLCT geometry.

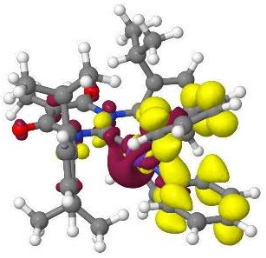

Figure S7.261. T1-S0 (MLCT) difference density at the **3a** SMLCT geometry.

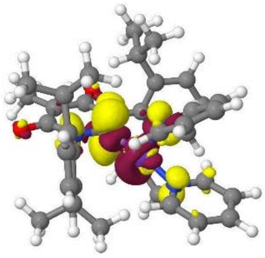

Figure S7.262. T3-S0 (MLCT(NHC)) difference density at the **3a** SMLCT geometry.

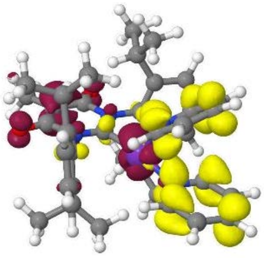

Figure S7.263. T5-S0 (LLCT) difference density at the **3a** SMLCT geometry.

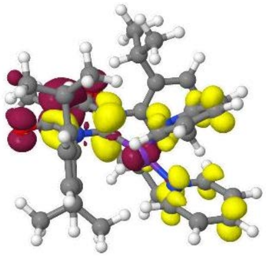

Figure S7.264. T7-S0 (LC(NHC)) difference density at the **3a** SMLCT geometry.

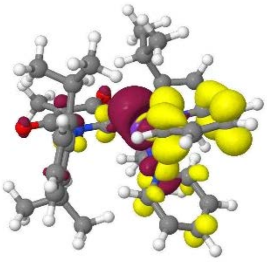

Figure S7.265. S1-S0 (MLCT) difference density at the **3a** TMLCT geometry.

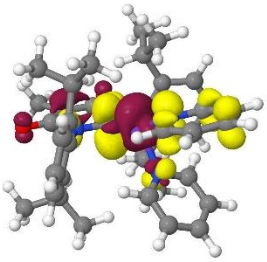

Figure S7.266. S4-S0 (MLCT(NHC)) difference density at the **3a** TMLCT geometry.

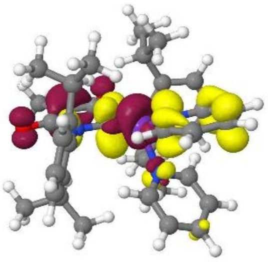

Figure S7.267. S5-S0 (LLCT) difference density at the **3a** TMLCT geometry.

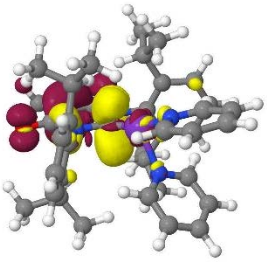

Figure S7.268. S9-S0 (LC(NHC)) difference density at the **3a** TMLCT geometry.

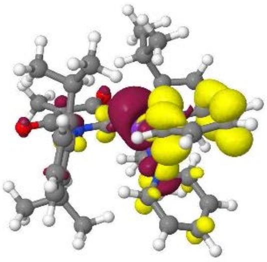

Figure S7.269. T2-S0 (MLCT) difference density at the **3a** TMLCT geometry.

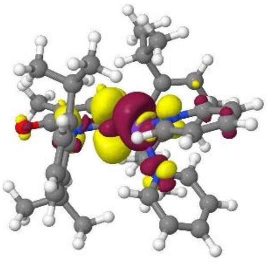

Figure S7.270. T3-S0 (MLCT(NHC)) difference density at the **3a** TMLCT geometry.

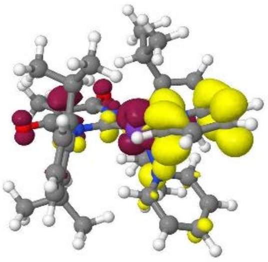

Figure S7.271. T5-S0 (LLCT) difference density at the **3a** TMLCT geometry.

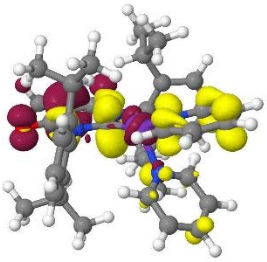

Figure S7.272. T6-S0 (LC(NHC)) difference density at the **3a** TMLCT geometry.

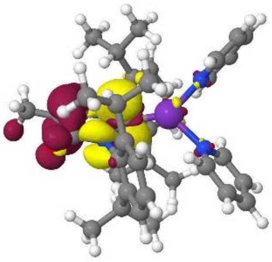

Figure S7.273. S1-S0 (LC(NHC)) difference density at the **3a** SLC(NHC) geometry.

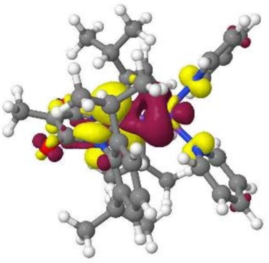

Figure S7.274. S2-S0 (MLCT(NHC)) difference density at the **3a** SLC(NHC) geometry.

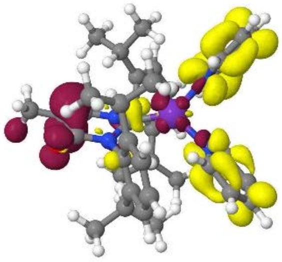

Figure S7.275. S4-S0 (LLCT) difference density at the **3a** SLC(NHC) geometry.

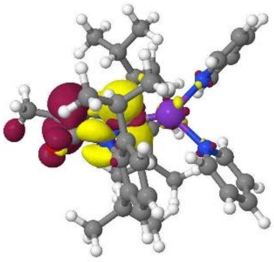

Figure S7.276. S1-S0 (LC(NHC)) difference density at the **3a** SLC(NHC) geometry.

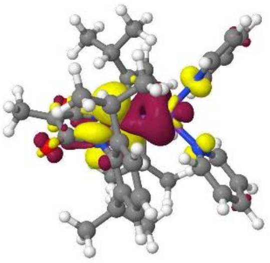

Figure S7.277. S2-S0 (MLCT(NHC)) difference density at the **3a** SLC(NHC) geometry.

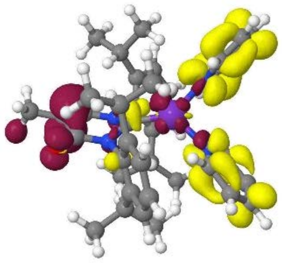

Figure S7.278. S4-S0 (LLCT) difference density at the **3a** SLC(NHC) geometry.

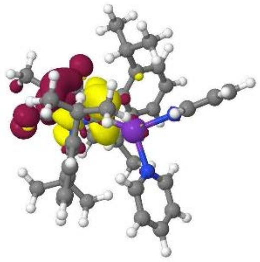

Figure S7.279. S1-S0 (LC(NHC)) difference density at the **3a** TLC(NHC) geometry.

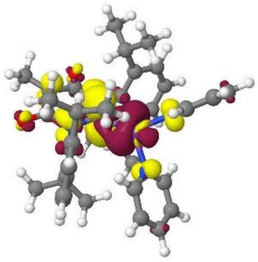

Figure S7.280. S2-S0 (MLCT) difference density at the **3a** TLC(NHC) geometry.

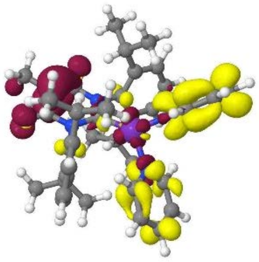

Figure S7.281. S4-S0 (LLCT) difference density at the **3a** TLC(NHC) geometry.

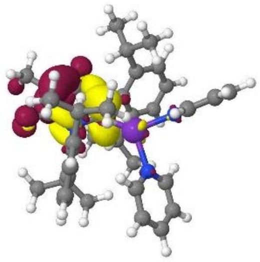

Figure S7.282. T1-S0 (LC(NHC)) difference density at the **3a** TLC(NHC) geometry.

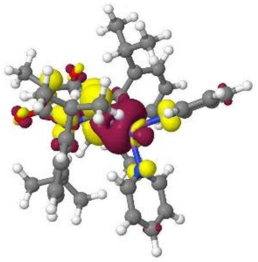

Figure S7.283. T2-S0 (MLCT(NHC)) difference density at the **3a** TLC(NHC) geometry.

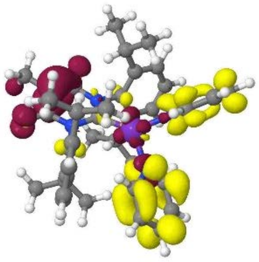

Figure S7.284. T5-S0 (LLCT) difference density at the **3a** TLC(NHC) geometry.

State interconversion in 3a

For many pairs of states, vibrational, a vibrational overlap could not be calculated in harmonic approximation due to the large difference in structure. The sum of the SOCME^2 values permit an idea of the transition strengths in-between the states.

Table S7.43. SOCME^2 values [cm^{-2}] in-between the optimized state to other low-lying excited states in **3a**. No MLCT(d_{z2}) was found at the optimized geometries of the S_{LC} and T_{LC} states.

State	Optimized geometry				
	SLLCT	SMLCT	SLC	TMLCT	TLC
LLCT	99.2	137268	1721.8	15322.4	1106.9
MLCT	95483.8	282.3	-	2112	-
LC	107.2	4055.5	10.8	2218.2	1.5

T1 absorption in 3a

Experimentally, the emission spectra were obtained while exciting at 375 nm. The first excited singlet state lies at 329 nm and is not very bright (f = 0.00916). The first triplet state is a T_{LC} at 349 nm. Due to intensity borrowing, which is elaborated below, the first triplet state possesses a non-zero oscillator strengths. Light at 375 nm could thus only excite the first triplet.

The T_{LC} consists of a sizeable admixture of a MLCT from the d_{z^2}-orbital to the antibonding carbene orbital. It can be expected, that this contribution is the major component of the (S_0-T_1) transition dipole moment.

Table S7.44. Admixture coefficients towards the T_{LC} and transition dipole moment components of the S_n and the T_{LC} with the S_0 at different geometries for **3a**.

opt. geo	Coupled state	Σ SOCME^2 [cm^{-2}] $\langle T_{LC} \lvert \hat{H}_{SO} \rvert S_n \rangle$	admixture coeff.	μ(S_n-S_0)-component [ea_0]		
				x	y	z
T_{LC}	S_2: MLCT(NHC)	11703	0.01009	0.43358	-0.01796	-0.02132
T_{LC}	Total μ(T_{LC}-S_0)			-0.00468	-0.00085	-0.00400
S_0	S_3: MLCT(NHC)	40942	0.06505	0.77498	-0.01337	-0.29250
S_0	S_1: LLCT	637	0.01662	-0.30765	-0.05540	0.03992
S_0	Total dipole of T_{LC}			-0.04855	-0.00037	0.00000

The different admixture strength may be caused by the different energy difference:

Table S7.45. Energy differences in **3a**.

States @ opt geo	T_1-S_3 @ S0	T_1-S_1 @ S0	T_1-S_2 @ TLC
ΔE [eV]	0.384	0.1936	1.245

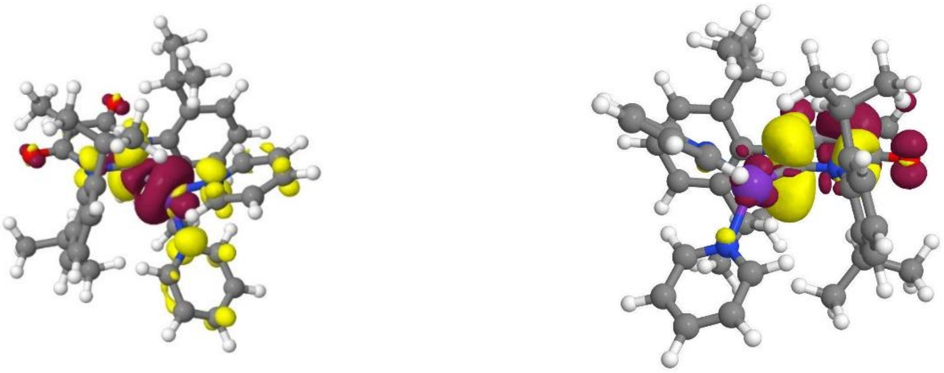

Figure S7.285. Difference densities of the S_3 @ S0 (left) and the T_1 @ S0 (right).

The comparison towards the Lutidine-bearing complex **2a** can be drawn. In **2a**, the MLCT(NHC) has a non-zero transition dipole moment to the S_0 as-well. It seems, that the S_{MLCT}-admixture is however not sufficient to facilitate a sizeable transition dipole moment to the GS.

Table S7.46. Admixture coefficients towards the T_{LC} and transition dipole moment components of the S_n and the T_{LC} with the S_0 at different geometries for **2a**.

opt. geo	Coupled state	Σ SOCME² [cm⁻²] $\langle T_{LC} \vert \hat{H}_{SO} \vert S_0 \rangle$	admixture coeff.	μ(S_n-S_0)-component [*e*a₀]		
				x	x	x
T_{LC}	S_2: MLCT(NHC)	3609	0.00444	0.47254	-0.00257	-0.07628
T_{LC}	Total μ(T_{LC}-S_0)			0.00222	0.00000	-0.00035
S_0	S_2 MLCT(NHC)	2871	-0.01159	0.47582	0.17412	0.051667
S_0	Total dipole of TLC			-0.00989	0.00157	0.00126

Table S7.47. Energy differences in **2a**.

States @ opt geo	T_1-S_2 @ S0	T_1-S_2 @ T_{LC}
ΔE [eV]	0.587	1.650

The trigonal formyl pyridine complex 3b

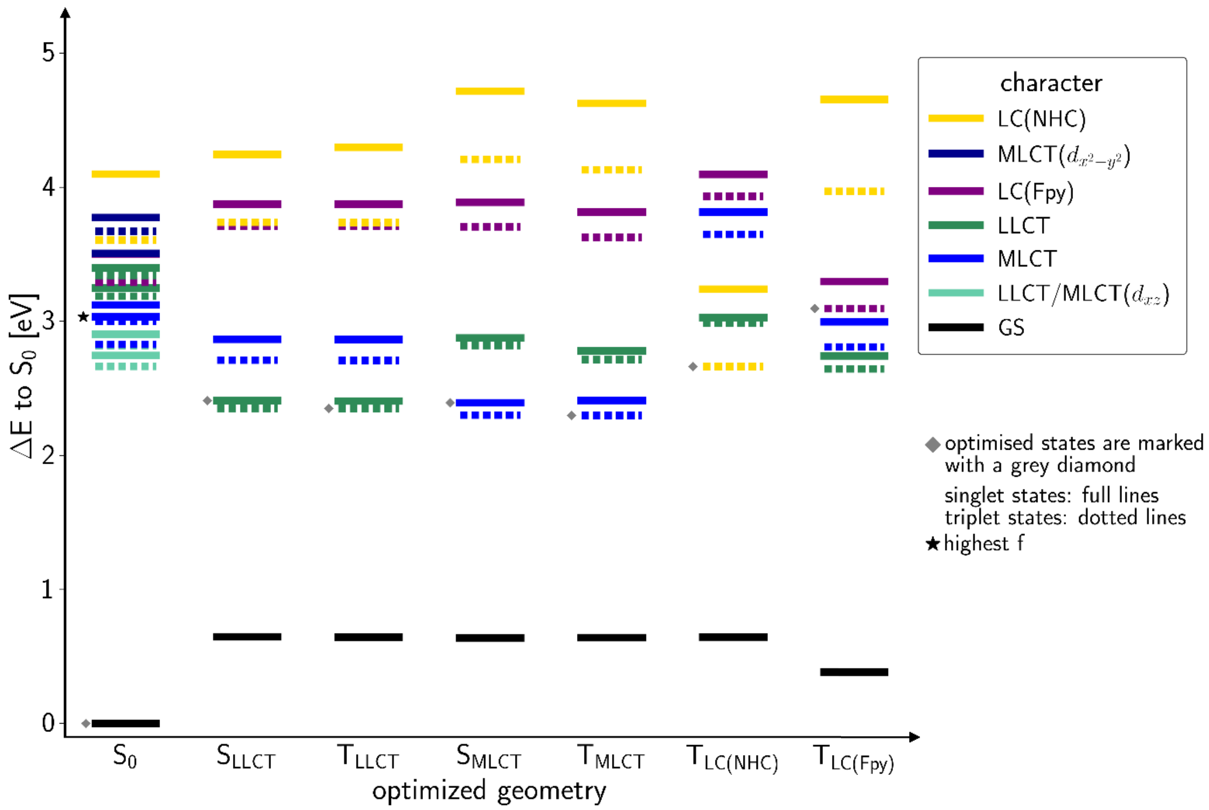

Figure S7.286. Energy state diagram of **3b** for selected optimized geometries.

Table S7.48. Singlet states and their properties at the ground state geometry of **3b**.

State	E [eV]	λ_{abs} [nm]	f	|μ| [D]	Character
S0	0			18.94	S0
S1	2.745	452	0.01507	3.87	LLCT/MLCT(xz)
S2	2.905	427	0.00305	-1.30	LLCT/MLCT(xz)
S3	3.034	409	0.13578	-10.02	MLCT
S4	3.122	397	0.07613	-11.11	MLCT
S5	3.250	381	0.01202	1.91	LLCT
S6	3.399	365	0.00421	4.44	LLCT
S7	3.504	354	0.00043	-10.09	LC(Fpy)
S8	3.508	353	0.00126	-11.15	LC(Fpy)
S9	3.774	329	0.04002	-3.19	MLCT(x2-y2)
S10	3.927	316	0.02047	16.57	MLCT(x2-y2)
S11	4.098	303	0.11954	9.59	LC(NHC)

Table S7.49. Triplet states and their properties at the ground state geometry of **3b**.

State	E [eV]			|μ| [D]	Character
T1	2.665			1.05	LLCT/MLCT(xz)
T2	2.818			2.61	LLCT/MLCT(xz)
T3	2.828			3.72	MLCT
T4	3.002			5.47	MLCT
T5	3.187			5.82	LLCT
T6	3.230			16.52	LC(Fpy)
T7	3.303			22.12	LC(Fpy)
T8	3.342			0.58	LLCT
T9	3.605			11.05	LC(NHC)
T10	3.670			6.24	MLCT(x2-y2)

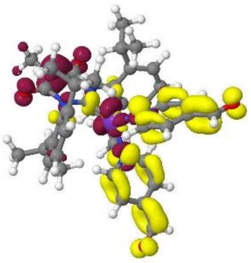

Figure S7.287. S1-S0 difference density at the GS of **3b**.

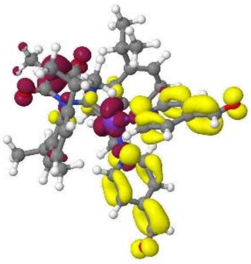

Figure S7.288. S2-S0 difference density at the GS of **3b**.

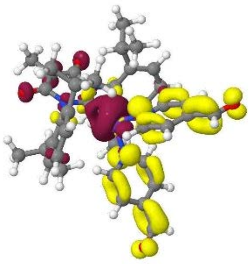

Figure S7.289. S3-S0 difference density at the GS of **3b**.

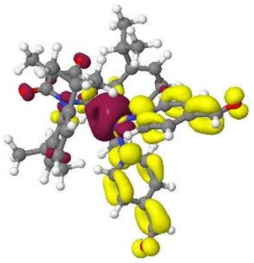

Figure S7.290. S4-S0 difference density at the GS of **3b**.

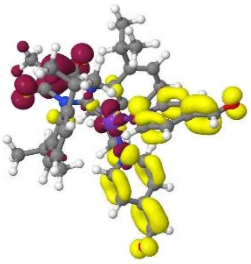

Figure S7.291. S5-S0 difference density at the GS of **3b**.

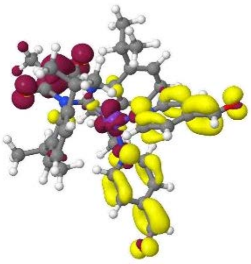

Figure S7.292. S6-S0 difference density at the GS of **3b**.

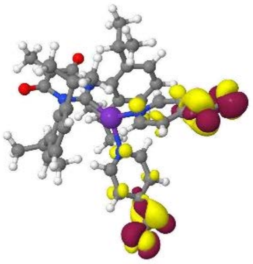

Figure S7.293. S7-S0 difference density at the GS of **3b**.

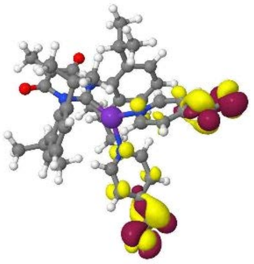

Figure S7.294. S8-S0 difference density at the GS of **3b**.

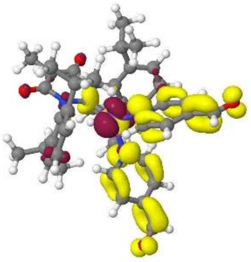

Figure S7.295. S9-S0 difference density at the GS of **3b**.

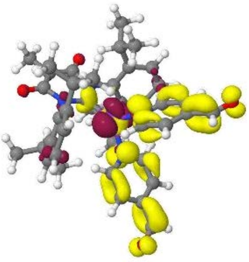

Figure S7.296. S10-S0 difference density at the GS of **3b**.

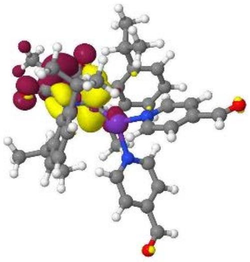

Figure S7.297. S11-S0 difference density at the GS of **3b**.

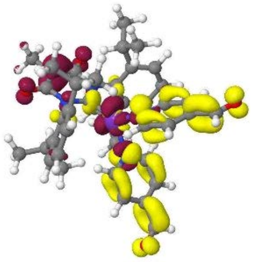

Figure S7.298. T1-S0 difference density at the GS of **3b**.

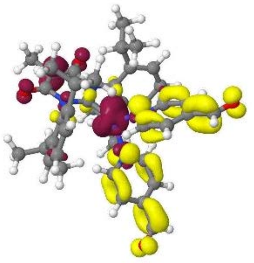

Figure S7.299. T2-S0 difference density at the GS of **3b**.

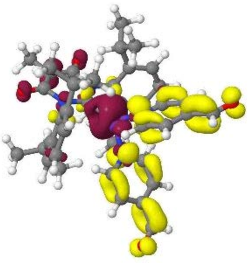

Figure S7.300. T3-S0 difference density at the GS of **3b**.

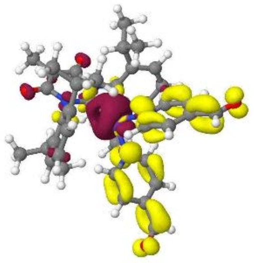

Figure S7.301. T4-S0 difference density at the GS of **3b**.

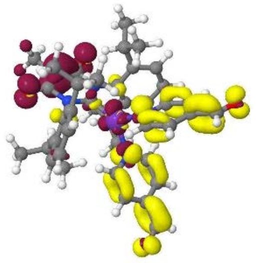

Figure S7.302. T5-S0 difference density at the GS of **3b**.

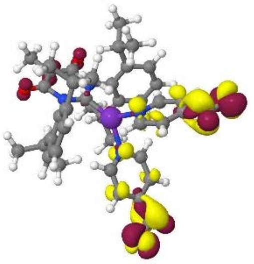

Figure S7.303. T6-S0 difference density at the GS of **3b**.

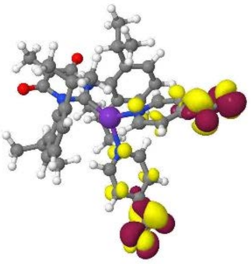

Figure S7.304. T7-S0 difference density at the GS of **3b**.

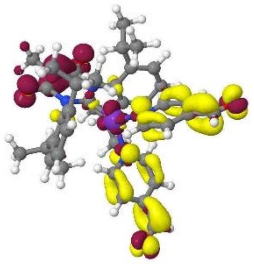

Figure S7.305. T8-S0 difference density at the GS of **3b**.

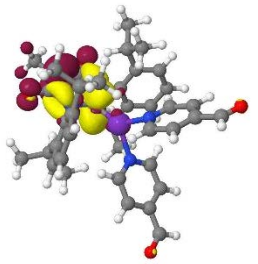

Figure S7.306. T9-S0 difference density at the GS of **3b**.

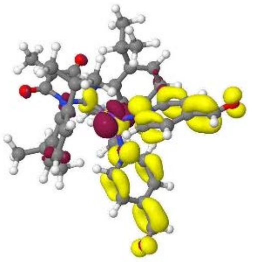

Figure S7.307. T10-S0 difference density at the GS of **3b**.

Table S7.50. Energies [eV] of relevant excited states of **3b** at the optimized geometries of different states.

State	Optimized geometry						
	S0	SLLCT	TLLCT	SMLCT	TMLCT	TLC(NHC)	TLC(Fpy)
S0	0.000	0.648	0.646	0.640	0.642	0.647	0.383
SLLCT	2.745	2.408	2.406	2.875	2.782	3.029	2.742
TLLCT	2.665	2.352	2.350	2.820	2.714	2.990	2.645
SMLCT	3.034	2.866	2.865	2.393	2.411	3.815	2.997
TMLCT	2.828	2.711	2.708	2.301	2.299	3.649	2.809
TLC(NHC)	3.342	3.739	3.738	4.208	4.130	2.663	3.968
TLC(Fpy)	3.303	2.711	3.710	3.706	3.627	3.931	3.095

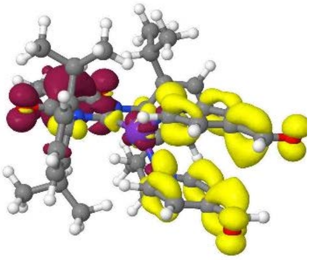

Figure S7.308. S1-S0 (LLCT) difference density at the **3b** SLLCT geometry.

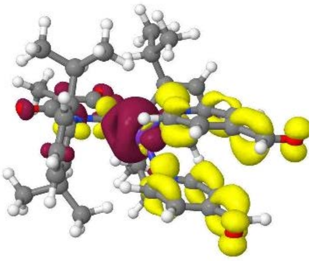

Figure S7.309. S1-S0 (MLCT) difference density at the **3b** SLLCT geometry.

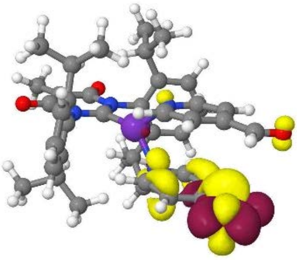

Figure S7.310. S7-S0 (LC(FLut)) difference density at the **3b** SLLCT geometry.

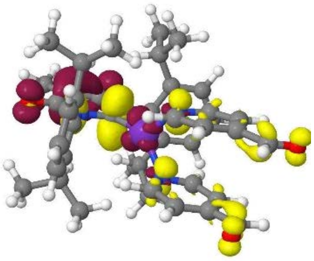

Figure S7.311. S12-S0 (LC(NHC)) difference density at the **3b** SLLCT geometry.

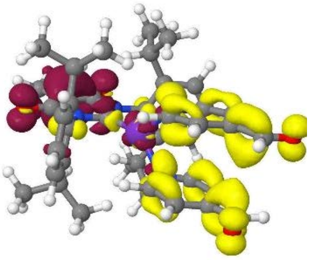

Figure S7.312. T1-S0 (LLCT) difference density at the **3b** SLLCT geometry.

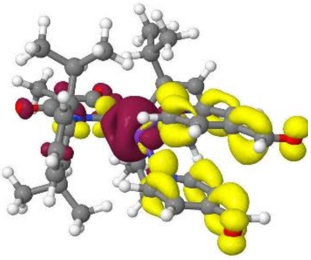

Figure S7.313. T2-S0 (MLCT) difference density at the **3b** SLLCT geometry.

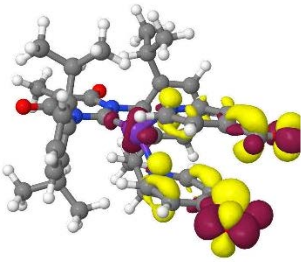

Figure S7.314. T7-S0 (LC(FLut)) difference density at the **3b** SLLCT geometry.

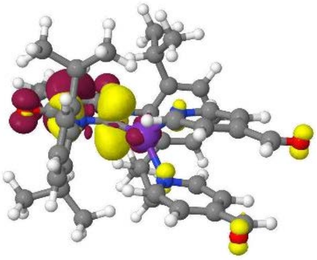

Figure S7.315. T9-S0 (LC(NHC)) difference density at the **3b** SLLCT geometry.

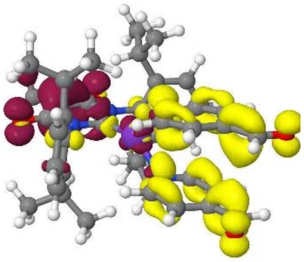

Figure S7.316. S1-S0 (LLCT) difference density at the **3b** TLLCT geometry.

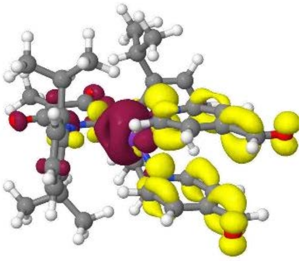

Figure S7.317. S2-S0 (MLCT) difference density at the **3b** TLLCT geometry.

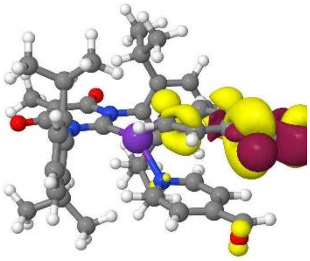

Figure S7.318. S7-S0 (LC(FLut)) difference density at the **3b** TLLCT geometry.

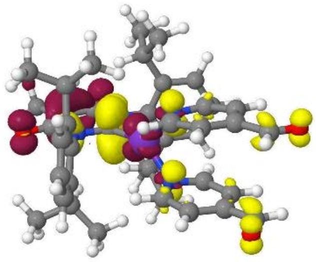

Figure S7.319. S1-S14 (LC(NHC)) difference density at the **3b** TLLCT geometry.

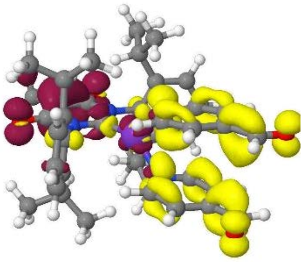

Figure S7.320. T1-S0 (LLCT) difference density at the **3b** TLLCT geometry.

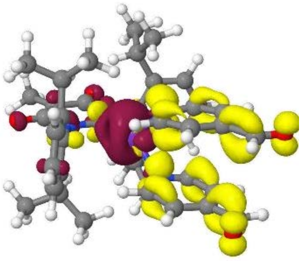

Figure S7.321. T2-S0 (MLCT) difference density at the **3b** TLLCT geometry.

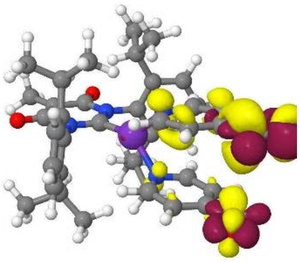

Figure S7.322. T7-S0 (LC(FLut)) difference density at the **3b** TLLCT geometry.

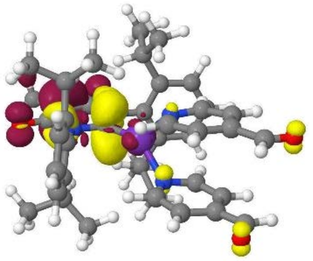

Figure S7.323. T9-S0 (LC(NHC)) difference density at the **3b** TLLCT geometry.

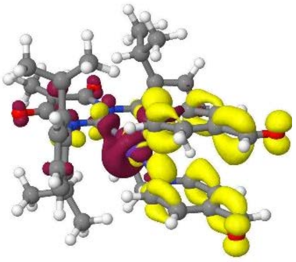

Figure S7.324. S1-S0 (MLCT) difference density at the **3b** SMLCT geometry.

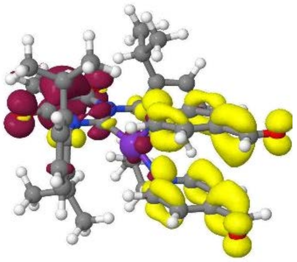

Figure S7.325. S1-S0 (LLCT) difference density at the **3b** SMLCT geometry.

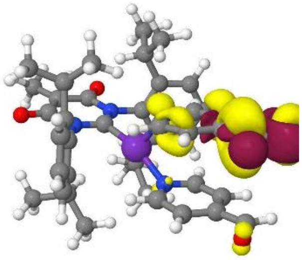

Figure S7.326. S7-S0 (LC(FLut)) difference density at the **3b** SMLCT geometry.

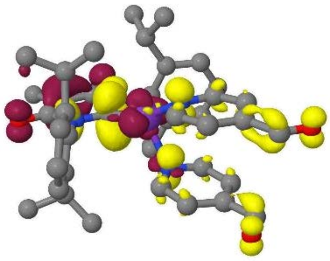

Figure S7.327. S20-S0 (LC(NHC) difference density at the **3b** SMLCT geometry.

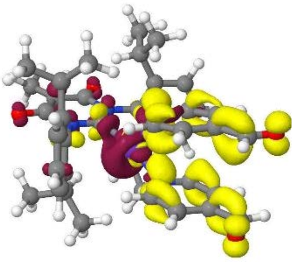

Figure S7.328. T1-S0 (MLCT) difference density at the **3b** SMLCT geometry.

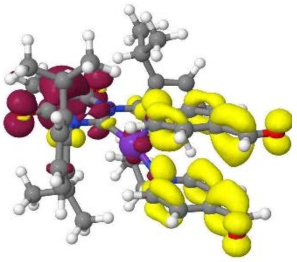

Figure S7.329. T2-S0 (LLCT) difference density at the **3b** SMLCT geometry.

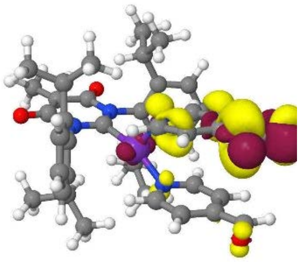

Figure S7.330. T6-S0 (LC(FLut)) difference density at the **3b** SMLCT geometry.

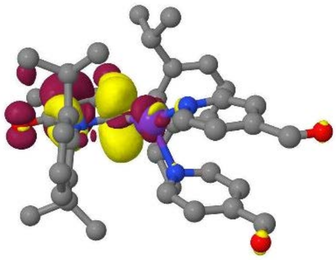

Figure S7.331. T14-S0 (LC(NHC)) difference density at the **3b** SMLCT geometry.

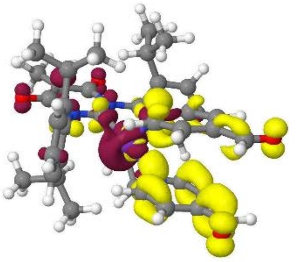

Figure S7.332. S1-S0 (MLCT) difference density at the **3b** TMLCT geometry.

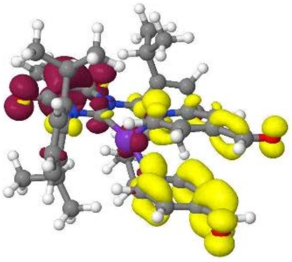

Figure S7.333. S2-S0 (LLCT) difference density at the **3b** TMLCT geometry.

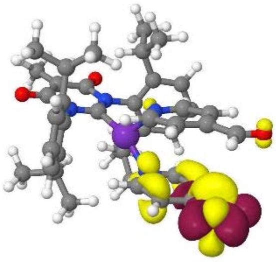

Figure S7.334. S7-S0 (LC(FLut)) difference density at the **3b** TMLCT geometry.

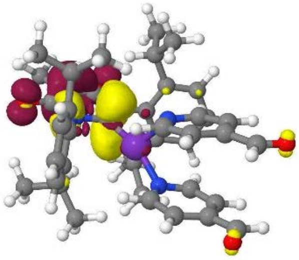

Figure S7.335. S19-S0 (LC(NHC)) difference density at the **3b** TMLCT geometry.

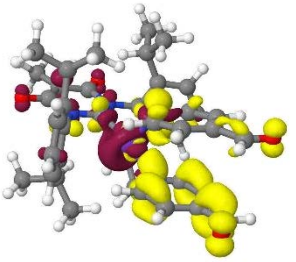

Figure S7.336. T1-S0 (MLCT) difference density at the **3b** TMLCT geometry.

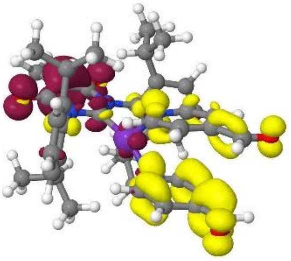

Figure S7.337. T2-S0 (LLCT) difference density at the **3b** TMLCT geometry.

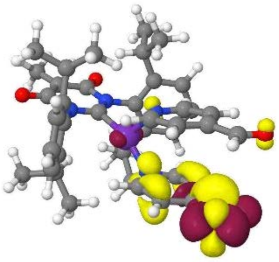

Figure S7.338. T6-S0 (LC(FLut)) difference density at the **3b** TMLCT geometry.

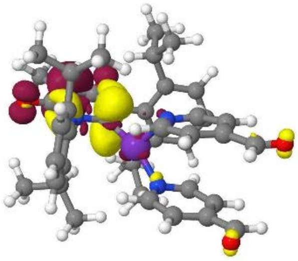

Figure S7.339. T14-S0 (LC(NHC)) difference density at the **3b** TMLCT geometry.

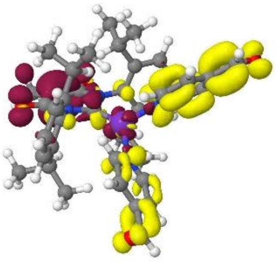

Figure S7.340. S1-S0 (LLCT) difference density at the **3b** TLC(NHC) geometry.

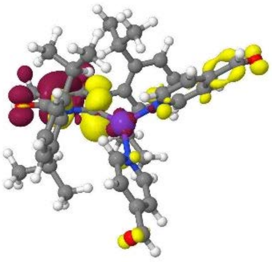

Figure S7.341. S3-S0 (LC(NHC)) difference density at the **3b** TLC(NHC) geometry.

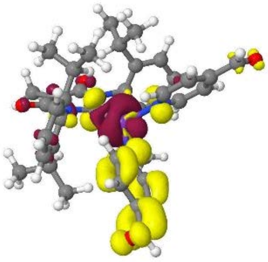

Figure S7.342. S6-S0 (MLCT(NHC)) difference density at the **3b** TLC(NHC) geometry.

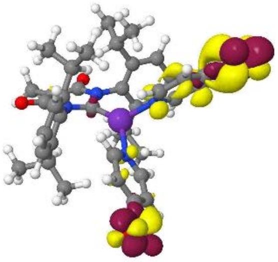

Figure S7.343. S8-S0 (LC(FLut)) difference density at the **3b** TLC(NHC) geometry.

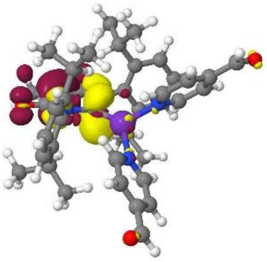

Figure S7.344. T1-S0 (LC(NHC)) difference density at the **3b** TLC(NHC) geometry.

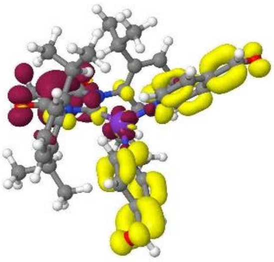

Figure S7.345. T2-S0 (LLCT) difference density at the **3b** TLC(NHC) geometry.

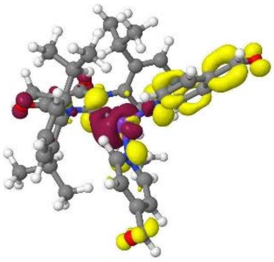

Figure S7.346. T5-S0 (MLCT) difference density at the **3b** TLC(NHC) geometry.

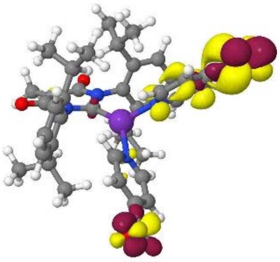

Figure S7.347. T9-S0 (LC(FLut)) difference density at the **3b** TLC(NHC) geometry.

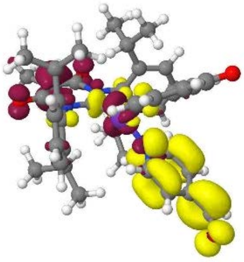

Figure S7.348. S1-S0 (LC(FLut)) difference density at the **3b** TLC(Fpy) geometry.

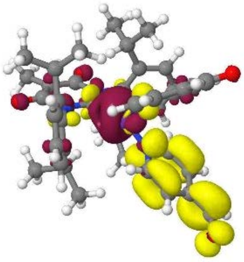

Figure S7.349. S2-S0 (LC(FLut)) difference density at the **3b** TLC(Fpy) geometry.

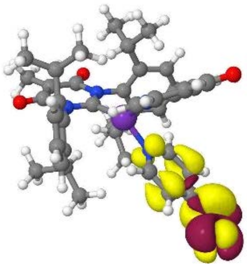

Figure S7.350. S5-S0 (LC(FLut)) difference density at the **3b** TLC(Fpy) geometry.

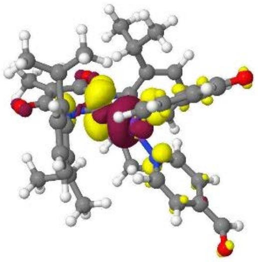

Figure S7.351. S17-S0 (LC(FLut)) difference density at the **3b** TLC(Fpy) geometry.

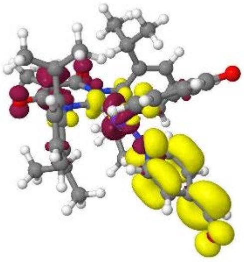

Figure S7.352. T1-S0 (LC(FLut)) difference density at the **3b** TLC(Fpy) geometry.

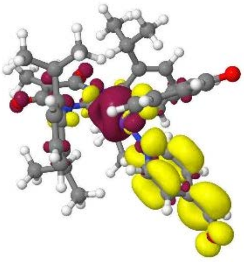

Figure S7.353. T2-S0 (LC(FLut)) difference density at the **3b** TLC(Fpy) geometry.

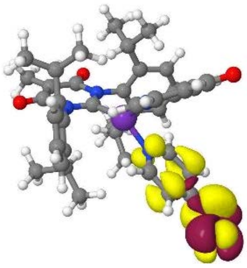

Figure S7.354. T3-S0 (LC(FLut)) difference density at the **3b** TLC(Fpy) geometry.

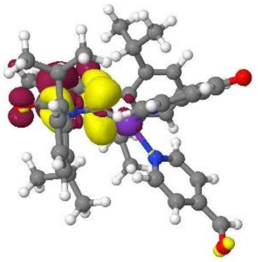

Figure S7.355. T11-S0 (LC(FLut)) difference density at the **3b** TLC(Fpy) geometry.

7.3.7 References

[1] C. W. Tang, S. A. VanSlyke, *Appl. Phys. Lett.* **1987**, *51*, 913.

[2] M. A. Baldo, D. F. O'Brien, Y. You, A. Shoustikov, S. Sibley, M. E. Thompson, S. R. Forrest, *Nature* **1998**, *395*, 151–154.

[3] H. Uoyoma, K. Goushi, K. Shizu, H. Nomura, C. Adachi, *Nature* **2012**, *492*, 234–238.

[4] H. Nakanotani, T. Higuchi, T. Furukawa, K. Masui, K. Morimoto, M. Numata, H. Tanaka, Y. Sagara, T. Yasuda, C. Adachi, *Nat. Commun.* **2014**, *5*, 4016–4022.

[5] G. Hong, X. Gan, C. Leonhardt, Z. Zhang, J. Seibert, J. M. Busch, S. Bräse, *Adv. Mater.* **2021**, *33*, 2005630.

[6] C. Adachi, A. S. D. Sandanayaka, *CCS Chem.* **2020**, *2*, 1203–1216.

[7] Y. Zhang, J. Lee, S. R. Forrest, *Nat. Commun.* **2014**, *5*:*5008*.

[8] R. Czerwieniec, M. J. Leitl, H. H. H. Homeier, H. Yersin, *Coord. Chem. Rev.* **2016**, *325*, 2-28.

[9] E. Cariati, E. Lucenti, C. Botta, U. Giovanella, D. Marinotto, S. Righetto, *Coord. Chem. Rev.* **2016**, *306*, 566 – 614.

[10] A. Steffen, B. Hupp, in *Comprehensive Coordination Chemistry III*, eds. E. C. Constable, G. Parkin, L. Jr Que, Elsevier, **2021**, pp. 466-502.

[11] P. S. Wagenknecht, P. C. Ford, *Coord. Chem. Rev.* **2011**, *255*, 591 – 616.

[12] A. Liske, L. Wallbaum, T. Hölzel, J. Föller, M. Gernert, B. Hupp, C. Ganter, C. M. Marian, A. Steffen, *Inorg. Chem.* **2019**, *58*, 5433–5445.

[13] J. Föller, C. Ganter, A. Steffen, C. M. Marian. *Inorg. Chem.* **2019**, *58*, 5446–5456.

[14] C. M. Marian, *Annu. Rev. Phys. Chem.* **2021**, *72*, 617-640.

[15] J. P. Zobel, A. M. Wernbacher, L. González, *Angew. Chem. Int. Ed.* **2023**, *62*, e202217620.

[16] Z. A. Siddique, Y. Yamamoto, T. Ohno, K. Nozaki, *Inorg. Chem.* **2003**, *42*, 6366-6378.

[17] L. Bergmann, G. J. Hedley, T. Baumann, S. Bräse, I. D. W. Samuel, *Sci. Adv.* **2016**, *2*, e1500889.

[18] M. Grupe, F. Bäppler, M. Theiß, J. M. Busch, F. Dietrich, D. Volz, M. Gerhards, S. Bräse, R. Diller, *Phys. Chem. Chem. Phys.* **2020**, *22*, 14187–14200.

[19] N. Lüdtke, J. Föller, C. M. Marian, *Phys. Chem. Chem. Phys.* **2020**, *22*, 23530–23544.

[20] J. Föller, M. Kleinschmidt and C. M. Marian, *Inorg. Chem.* **2016**, *55*, 7508-7516.

[21] R. Hamze, S. Shi, S. C. Kapper, D. S. Muthiah Ravinson, L. Estergreen, M.-C. Jung, A. C. Tadle, R. Haiges, P. I. Djurovich, J. L. Peltier, R. Jazzar, G. Bertrand, S. E. Bradforth, M. E. Thompson, *J. Am. Chem. Soc.* **2019**, *141*, 8616–8626.

[22] R. Hamze, J. L. Peltier, D. Sylvinson, M. Jung, J. Cardenas, R. Haiges, M. Soleilhavoup, R. Jazzar, P. I. Djurovich, G. Bertrand, M. E. Thompson, *Science* **2019**, *363 (6427)*, 601–606.

[23] T. Y. Li, D. S. Muthiah Ravinson, R. Haiges, P. I. Djurovich, M. E. Thompson, *J. Am. Chem. Soc.* **2020**, *142*, 6158–6172.

[24] M. J. Leitl, V. A. Krylova, P. I. Djurovich, M. E. Thompson, H. Yersin, *J. Am. Chem Soc.* **2014**, *136*, 16032-16038.

[25] A. S. Romanov, D. Di, L. Yang, J. Fernandez-Cestau, C. R. Becker, C. E. James, B. Zhu, M. Linnolahti, D. Credgington, M. Bochmann, *Chem. Commun.* **2016**, *52*, 6379-6382.

[26] R. Hamze, R. Jazzar, M. Soleilhavoup, P. I. Djurovich, G. Bertrand, M. E. Thompson, *Chem. Commun.* **2017**, *53*, 9008-9011.

[27] D. Di, A. S. Romanov, L. Yang, J. M. Richter, J. P. H. Rivett, S. Jones, T. H. Thomas, M. Abdi Jalebi, R. H. Friend, M. Linnolahti, M. Bochmann, D. Credgington, *Science* **2017**, *356 (6334)*, 159–163.

[28] M. Gernert, L. Balles-Wolf, F. Kerner, U. Müller, A. Schmiedel, M. Holzapfel, C. M. Marian, J. Pflaum, C. Lambert, A. Steffen, *J. Am. Chem. Soc.* **2020**, *142*, 8897–8909.

[29] R. Hamze, M. Idris, D. S. Muthiah Ravinson, M. C. Jung, R. Haiges, P. I. Djurovich, M. E. Thompson, *Front. Chem.* **2020**, *8, 401.*

[30] S. Shi, M. C. Jung, C. Coburn, A. Tadle, D. S. Muthiah Ravinson, P. I. Djurovich, S. R. Forrest, M. E. Thompson, *J. Am. Chem. Soc.* **2019**, *141*, 3576–3588.

[31] J. Li, L. Wang, Z. Zhao, X. Li, X. Yu, P. Huo, Q. Jin, Z. Liu, Z. Bian, C. Huang, *Angew. Chem. Int. Ed.* **2020**, *59*, 8210-8217.

[32] A. Ruduss, B. Turovska, S. Belyakov, K. A. Stucere, A. Vembris, K. Traskovskis, *Inorg. Chem.* **2022**, *61*, 2174-2185.

[33] J. Föller, C. M. Marian, *J. Phys. Chem. Lett.* **2017**, *8*, 5643-5647.

[34] S. Thompson, J. Eng, T. J. Penfold, *J. Chem. Phys.* **2018**, *149*, 014304.

[35] C. R. Hall, A. S. Romanov, M. Bochmann, S. R. Meech, *J. Phys. Chem. Lett.* **2018**, *9*, 5873-5876.

[36] J. Eng, S. Thompson, H. Goodwin, D. Credgington, T. J. Penfold, *Phys. Chem. Chem. Phys.* **2020**, *22*, 4659–4667.

[37] X.-F. Song, Z.-W. Li, W.-K. Chen, Y.-J. Gao, G. Cui, *Inorg. Chem.* **2022**, *61*, 7673-7681.

[38] T. Hölzel, A. Belyaev, M. Terzi, L. Stenzel, M. Gernert, C. M. Marian, A. Steffen, C. Ganter, *Inorg. Chem.* **2021**, *60*, 18529-18543.

[39] F. Chotard, A. S. Romanov, D. L. Hughes, M. Linnolahti, M. Bochmann, *Eur. J. Inorg. Chem.* **2019**, 4234–4240.

[40] J. Guhl, Master Thesis, Heinrich-Heine University Düsseldorf, **2022**, https://www.theochem.hhu.de/en/theses/master-und-diplomarbeiten

[41] M. Gernert, U. Müller, M. Haehnel, J. Pflaum, A. Steffen, *Chem. Eur. J.* **2017**, *23*, 2206-2216.

[42] O. Nolden, J. Kremper, W. Haselbach, M. Morshedi, J. Guhl, P. Schmeinck, C. M. Marian, C. Ganter, P. Gilch. *ChemPhotoChem* **2023**, *7,* 4, e202200231.

[43] P. Schmeinck, D. Sretenović, J. Guhl, R. Kühnemuth, C. A. M. Seidel, C. M. Marian, M. Suta, C. Ganter, *Eur. J. Inorg. Chem.* **2023**, *26*, e202300416.

[44] M. A. El-Sayed, *J. Chem. Phys.* **1963**, *38*, 2834-2838.

[45] V. César, C. Barthes, Y. C. Farré, S. V. Cuisiat, B. Y. Vacher, R. Brousses, N. Lugan, G. Lavigne, *Dalton Trans.* **2013**, *42*, 7373–7385.

[46] R. Graaff, J. G. Aarnoudse, J. R. Zijp, P. M. A. Sloot, F. F. M. de Mul, J. Greve, M. H. Koelink, *Appl. Opt.* **1992**, *31*, 1370-1376.

[47] G. D. Hager, G. A. Crosby, *J. Am. Chem. Soc.* **1975**, *97*, 7031-7037.

[48] T. Azumi, C. M. O'Donnell, S. P. McGlynn, *J. Chem. Phys.* **1996**, *45*, 2735-2742.

[49] T.-O. Peulen, O. Opanasyuk, C. A. M. Seidel, *J. Phys. Chem. B* **2017**, *121*, 8211-8241.

[50] Gaussian 16, Revision A.03, M. J. Frisch, G. W. Trucks, H. B. Schlegel, G. E. Scuseria, M. A. Robb, J. R. Cheeseman, G. Scalmani, V. Barone, G. A. Petersson, H. Nakatsuji, X. Li, M. Caricato, A. V. Marenich, J. Bloino, B. G. Janesko, R. Gomperts, B. Mennucci, H. P. Hratchian, J. V. Ortiz, A. F. Izmaylov, J. L. Sonnenberg, D. Williams-Young, F. Ding, F. Lipparini, F. Egidi, J. Goings, B. Peng, A. Petrone, T. Henderson, D. Ranasinghe, V. G. Zakrzewski, J. Gao, N. Rega, G. Zheng, W. Liang, M. Hada, M. Ehara, K. Toyota, R. Fukuda, J. Hasegawa, M. Ishida, T. Nakajima, Y. Honda, O. Kitao, H. Nakai, T. Vreven, K. Throssell, J. A. Montgomery Jr., J. E. Peralta, F. Ogliaro, M. J. Bearpark, J. J. Heyd, E. N. Brothers, K. N. Kudin, V. N. Staroverov, T. A. Keith, R. Kobayashi, J. Normand, K. Raghavachari, A. P. Rendell, J. C. Burant, S. S. Iyengar, J. Tomasi, M. Cossi, J. M. Millam, M. Klene, C. Adamo, R. Cammi, J. W. Ochterski, R. L. Martin, K. Morokuma, O. Farkas, J. B. Foresman, D. J. Fox, Gaussian Inc., Wallingford CT, **2016**.

[51] E. Cancès, B. Mennucci, J. Tomasi, *J. Chem. Phys.* **1997**, *107*, 3032-3041.

[52] B. Mennucci, E. Cancès, J. Tomasi, *J. Phys. Chem. B* **1997**, *101*, 10506-10517.

[53] S. Grimme, M. Waletzke, *J. Chem. Phys.* **1999**, *111*, 5645-5655.

[54] C. M. Marian, A. Heil, M. Kleinschmidt, *WIREs Comput. Mol. Sci.* **2019**, *9*, 1.

[55] A. Heil, M. Kleinschmidt, C. M. Marian, *J. Chem. Phys.* **2018**, *149*, 164106.

[56] M. Kleinschmidt, J. Tatchen, C. M. Marian, *J. Comput. Chem.* **2002**, *23*, 824-833.

[57] D. Figgen, G. Rauhut, M. Dolg, H. Stoll, *Chem. Phys.* **2005**, *311*, 227-244.

[58] M. Etinski, J. Tatchen, C. M. Marian, *J. Chem. Phys.* **2011**, *134*, 154105.

[59] M. Etinski, J. Tatchen, C. M. Marian, *Phys. Chem. Chem. Phys.* **2014**, *16*, 4740-4751.

[60] M. Kleinschmidt, J. Tatchen, C. M. Marian, *J. Chem. Phys.* **2006**, *124*, 124101.

7.4 Compound Class C – Fluorinated Flavins

Increasing the Fluorescence Quantum Yield and Lifetime of the Flavin Chromophore by Rational Design

Mira K. Kubitz,[a] Wiebke Haselbach,[b] Dragana Sretenović,[c] Mario Bracker,[d] Martin Kleinschmidt,[d] Ralf Kühnemuth,[c] Claus A. M. Seidel,*[c] Peter Gilch,*[b] and Constantin Czekelius*[a]

[a] M. K. Kubitz, Prof. Dr. C. Czekelius
Institut für Organische Chemie und Makromolekulare Chemie
Heinrich Heine University Düsseldorf
Universitätsstr. 1, 40225 Düsseldorf, Germany
E-mail: Constantin.Czekelius@hhu.de

[b] W. Haselbach, Prof. Dr. P. Gilch
Institut für Physikalische Chemie
Heinrich Heine University Düsseldorf
Universitätsstr. 1, 40225 Düsseldorf, Germany
E-mail: Peter.Gilch@hhu.de

[c] D. Sretenović, Dr. R. Kühnemuth, Prof. Dr. C. A. M. Seidel
Institute für Physikalische Chemie
Heinrich Heine University Düsseldorf
Universitätsstr. 1, 40225 Düsseldorf, Germany
E-mail: cseidel@hhu.de

[d] Dr. M. Bracker, Dr. M. Kleinschmidt
Institute für Theoretische Chemie und Computerchemie
Heinrich Heine University Düsseldorf
Universitätsstr. 1, 40225 Düsseldorf, Germany
E-mail: cseidel@hhu.de

This article has been published in *ChemPhotoChem* **2023**, *7*, e202200334.

DOI: 10.1002/cptc.202200334.

7.4.1 Abstract

A previous quantum chemical study (M. Bracker et al., *Phys. Chem. Chem. Phys.* **2019**, *21*, 9912-9923) on the excited state properties of fluorinated derivatives of the flavin chromophore promised an increased fluorescence performance of the derivative 7,8-difluoro-10-methyl-isoalloxazine (**7,8-dF-MIA**). Here, we describe the synthesis of **7,8-dF-MIA**, its ribityl derivative, and for reason of comparison **9-F-MIA**. The compounds dissolved in water (H_2O and D_2O) were characterized by steady state, time resolved, and fluorescence correlation spectroscopy. The experiments confirm the increase of the fluorescence quantum yield of **7,8-dF-MIA** (0.42 in H_2O) compared to **MIA** (0.22) predicted by quantum chemistry. The anticipated reduction of the fluorescence quantum yield for **9-F-MIA** is also confirmed experimentally. The quantum chemical computations as well as the spectroscopic observations attribute the increased fluorescence quantum yield of **7,8-dF-MIA** predominantly to a decrease of the rate constant of intersystem crossing. Switching from H_2O to D_2O as a solvent is shown to increase fluorescence quantum yields (0.53 for **7,8-dF-MIA**) and lifetimes of all fluorinated **MIA** derivatives. This can be attributed to a Förster type energy transfer from the excited chromophore to vibrational overtones of water and further water-mediated deactivation processes.

7.4.2 Introduction

Flavins, a class of yellow redox-active chromophores, are an essential moiety of many photoreceptor proteins like cryptochromes, phototropins or photoactivated adenylyl cyclase.[1-7] Upon absorption of blue light, photochemical processes of biological importance are induced. Among others, the circadian rhythm or the induction of flowering are related to flavin compounds.[1,3-10] Flavin derivatives bound to these proteins are most often flavin mononucleotide (FMN) or flavin adenine dinucleotide (FAD).[1,3-10] Both are ubiquitous in nature and are also known to act as cofactors in enzyme catalysis. Due to their redox activity, they can participate in both one- and two-electron transfer processes and have therefore been employed in photo-redox catalysis.[4-6,10-18]

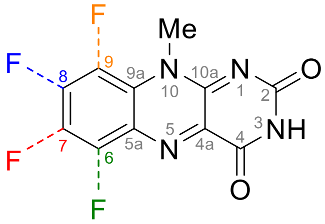

Figure 7.39. Chemical structure of 10-methylisoalloxazine **(MIA)**. Fluorine substitution positions are color coded, and the coding was continued from the reference[19] and is used throughout the paper.

By modifying the isoalloxazine core system, their photophysical properties can be altered.[19-22] If the fluorescence quantum yield Φ_{fl} and peak absorption coefficient of the first transition (1st ε_{max}) are maximized, application areas like optical imaging, where a high sensitivity (1st $\varepsilon_{max} \times \Phi_{fl}$) is needed, will benefit while high triplet quantum yields could be useful in terms of singlet oxygen production, photodynamic therapy and photochemically induced radical reactions.[23-25]

Fluorine substituents are highly suited for electronic modifications as they exert a strong electron-withdrawing effect.[26-27] When they are introduced at different positions of the core system, shifts of absorption as well as an increase/decrease of fluorescence and triplet quantum yields are observed.[19-21] At the same time, the sterical impact on protein binding and associated biological activity should be comparably small.[28-30]

As shown in our previous studies,[19] substitution of hydrogen with fluorine substituents at the left A-ring of the 10-methy-isoalloxazine **(MIA)** core system (6-, 7- and 8-position) led to a distinct impact on the photophysical properties, depending on the position of fluorination (Figure 7.39). In particular, for **6-F-** as well as **7-F-MIA** bathochromic and for **8-F-MIA** hypsochromic shifts of up to 500 cm^{-1} were observed. The derivative with fluorine in 7-position proved particularly interesting due to its 50% increased fluorescence quantum yield compared to the non-fluorinated **MIA**. These experimental observations were reproduced by quantum chemical computations.[20]

According to this study the S_1 state of $\pi\pi^*$ character is separated from its triplet counterpart T_1 by ca. 0.5 eV in **MIA** and its fluorinated derivatives in aqueous medium. Intersystem crossing to this triplet state is El-Sayed-forbidden and the large energetic separation also leads to slow vibronic ISC rate constants (ca. $5 \cdot 10^6$ s^{-1}). In vacuum, the second triplet state T_2 is of $n\pi^*$ character, energetically below the S_1 state and ISC to this state is El-Sayed-allowed and fast (ca. $2 \cdot 10^9$ s^{-1}), but in aqueous medium, this state is so strongly destabilized that it plays no role for radiationless deactivation of the S_1 state anymore. The next triplet state T_3 is of $\pi\pi^*$ character again. In water, it is shifted energetically below the T_2 state and also slightly below the S_1 state (0.0-0.2 eV depending on the mono-fluorination pattern). ISC to this state is also El-Sayed-forbidden, but the close energetic vicinity of the S_1 state as well as of the T_2 state (causing admixture of $n\pi^*$ character by out-of-plane vibrations) leads to considerable vibronic ISC rate constants (ca. $3 \cdot 10^8$ s^{-1}). The T_3 state is considered to be decisive for non-radiative decay by intersystem crossing (ISC). Therefore, the energetic upshift of the T_3 state above the S_1 state decreases the non-radiative decay and increases the fluorescence yield.

Fluorination in 7- and 8-position both cause a blue shift of this T_3 state. For vertical energies, it was shown that the effect of multiple fluorination on the photophysical properties can be predicted by simply adding the shifts of the mono-fluorinated derivatives.[20] According to this analysis, it is expected that di-fluorination in 7- and 8-position will bring the T_3 state energetically above the S_1 state, effectively hindering ISC und thus increasing fluorescence quantum yield. The computational study also predicts a decrease in fluorescence quantum yield for **9-F-MIA**, a derivative that was not previously available and is also considered in this paper.

In this work, **7,8-dF-MIA** as well as **9-F-MIA** were synthesized and their photophysical properties were investigated experimentally to compare them with computational ones. This demonstrates that the spectroscopic properties of chromophores can be tuned using a rational design approach. Following the work of Klehs et al.,[31] we tested whether the fluorescence properties of all fluorinated **MIA** derivatives can be increased even further by using heavy water (D_2O) as a solvent. For potential applications in fluorescence microscopy in analogy to riboflavin, the corresponding equivalent 7,8-difluoro-10-ribityl-isoalloxazin (**7,8-dF-RIA**) was synthesized and its fluorescence properties were also characterized.

7.4.3 Results and Discussion

Synthesis

Following the reported synthesis route,[19,32-33] **9-F-MIA (3)** was obtained starting from the corresponding fluorinated nitroaniline. As illustrated in Scheme 7.6, nitroaniline **1** was methylated in a two-step-one-pot reaction. Then, reduction of the nitro group and condensation with alloxan monohydrate gave **9-F-MIA (3)** in an overall yield of 43%. For spectroscopic measurements particular high purity of material is mandatory. Due to the generally low solubility of **MIA** derivatives, recrystallization methods often employ solvents such as formic acid or acetic acid. However, the concomitant formation of alloxazines by demethylation, which is commonly observed upon heating with traces of acid, renders the purification quite challenging. By screening other solvents trifluoroethanol proved to be highly suitable as it is very polar and not particularly acidic or nucleophilic.

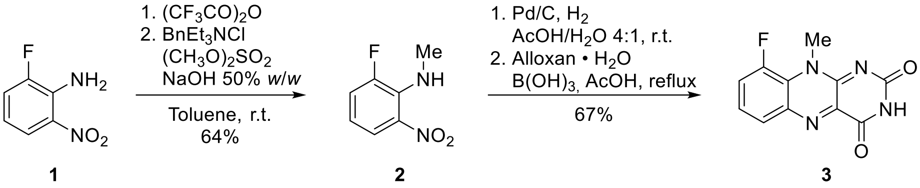

Scheme 7.6. Synthesis route to 9-F-methylisoalloxazine **(3)**.

In contrast to the monofluorinated derivatives, methylation of 4,5-Difluoro-*N*-methyl-2-nitroaniline **(4)** following the one-pot procedure shown above[32] proved to be troublesome due to a high propensity for fluorine substitution in *para*-position to the nitro group. Therefore, a modified synthesis route via Boc-protection and alkylation with methyl *p*-toluenesulfonate was developed.[34] Finally, reduction of the nitro group and condensation with alloxan monohydrate[19,33] gave **7,8-dF-MIA (8)** as the main product in a mixture with the corresponding alloxazine **(9)** in a ratio of 1:0.4 (Scheme 7.7).

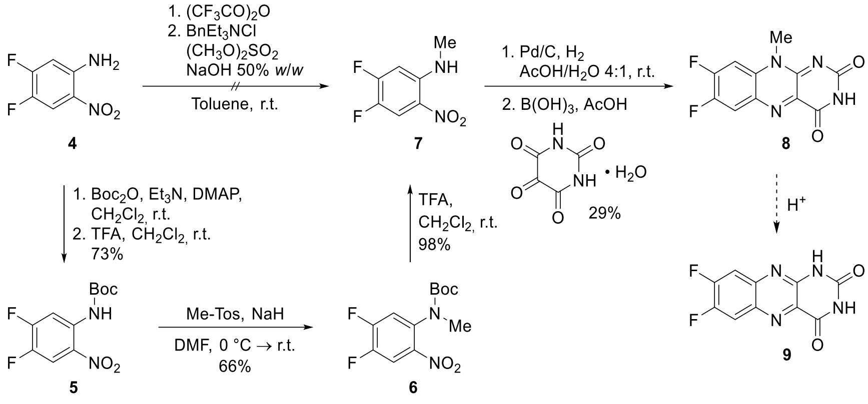

Scheme 7.7. Synthesis route to 7,8-dF-methylisoalloxazine **(8)** and formation of alloxazine by-product **(9)**.

The already mentioned formation of the alloxazine by-product turned out to be very problematic for the purification of this **MIA** derivative. Since alloxazines are less soluble than methylisoalloxazines, recrystallization was again the first choice. However, slow precipitation and fast formation of alloxazine by-product **(9)** during recrystallization were observed along with substantial degradation by nucleophilic fluorine substitution. Finally, using a combination of optimized reaction conditions[35] and work-up and purification methods, spectroscopically pure product was obtained (see Supporting Information for details). Specifically, heating should be avoided in general for this delicate compound and solvents evaporated only under high vacuum conditions. It was further found that a flash chromatography method applying the raw product as a solution in trifluoroethanol/methanol proved to be essential for purification.

7,8-Difluoro-10-ribityl-isoalloxazin (referred to as **7,8-dF-RIA**, **13**) was synthesized following a modified protocol by Mansurova et al.[36] as illustrated in Scheme 7.8. To avoid nucleophilic substitution of fluorine substituents, the nitro group was reduced first. Since the diamine was highly air-sensitive, Boc-protection was performed in situ to give the less sensitive protected derivative **10**. Ribitylated diamine **11** was obtained via reductive amination with D-ribose. Boc-deprotection was followed by condensation with alloxan monohydrate which is best performed under inert conditions in order to prevent fast oxidation of the 1,2-diaminobenzene derivative. Additionally, **7,8-dF-RIA 13** showed pronounced light sensitivity which made its purification in combination with the well-known continuous formation of poorly soluble alloxazines and the sensitivity of the fluorine substituents towards nucleophiles even more challenging. Therefore, it was renounced to heat the product at any point due to a very fast formation of side products. Instead, the solvent of the reaction mixture was solely removed at ambient temperature using high vacuum conditions. Multiple recrystallizations from different solvents led to a pre-purified product, which was finally purified by HPLC.

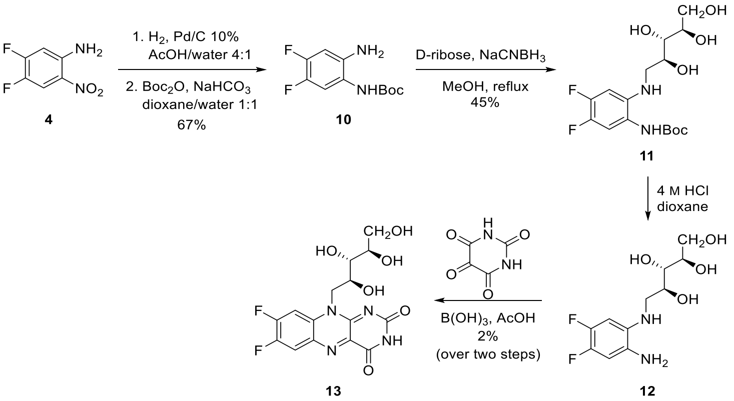

Scheme 7.8. Synthesis route to 7,8-difluor-10-ribityl-isoalloxazin (**7,8-dF-RIA**, **13**).

Spectroscopy

Steady state spectroscopy

First, we studied the impact of the fluorine substitution pattern on the optical properties of the two fluorinated derivatives **9-F-MIA** and **7,8-dF-MIA** in water. The absorption spectra exhibit two strong bands in the visible and near UV region (Figure 7.40 and Table 7.13). The position of these bands is close to the ones of **MIA**.[19-20,37] For **MIA**, the lowest-energy absorption maxima were reported at 431 nm (absorption coefficient ε_{431} = 8470 M^{-1}cm^{-1})[19] and 345 nm (ε_{345} = 6250 M^{-1} cm^{-1}).[19] Quantum chemical calculations predict the first excited state to be unaltered upon fluorination in the 9- and 7,8-positions.[20] Experimentally, a slight redshift of -54 cm^{-1} for **9-F-MIA** is observed compared to **MIA**, the absorption coefficient decreases by ~21%. For **7,8-dF-MIA**, the peak wavelength of 431 nm is retained and the absorption strength for the lowest energy absorption increases by ~31%.

For **MIA**, the emission peak is at 524 nm.[19] **7,8-dF-MIA** has a higher energy for the fluorescence peak (519 nm) and **9-F-MIA** has a lower energy (535 nm) compared to **MIA**. This translates into a lower Stokes shift for **7,8-dF-MIA** and a higher one for **9-F-MIA**.

As shown in the previous work by Reiffers et al.[19] and Bracker et al.,[20] fluorination also has an effect on the fluorescence quantum yields Φ_{fl}. The yield was determined using coumarin 153 in ethanol as a reference (Φ^{r}_{fl} = 0.544)[38] and is clearly the highest for **7,8-dF-MIA** (0.42) of all fluorinated derivatives studied so far. The yield decreases with fluorination at position 9 (0.12) compared to **MIA** (0.22). This finding was predicted by quantum chemical computations.[20]

Values for the 0-0 energies $\tilde{\nu}_{00}$, Stokes shifts $\Delta\tilde{\nu}_S$ and radiative rate constants $k_{\mathrm{rad}}^{\mathrm{SB}}$ were derived from the steady-state spectra. For the 0-0 energies, absorption and fluorescence were redrawn as a function of wavenumber $\tilde{\nu}$ to arrive at the transition dipole representation.[39] In this representation, the absorption spectrum is redrawn according to $\varepsilon(\tilde{\nu})/\tilde{\nu}$ and the fluorescence spectrum according to $S(\tilde{\nu})/\tilde{\nu}^3$. These spectra were then normalized to their maximum. The intersection of these spectra was taken as the experimentally measured value for the 0-0 energy (here reported in wavenumber units, $\tilde{\nu}_{00}$, see Table 7.13). The 0-0 energy of **9-F-MIA** obtained in this fashion is shifted by -357 cm^{-1} compared to the one of **MIA**. **7,8-dF-MIA** exhibits an upshift of +144 cm^{-1}. Shifts of these magnitudes and signs were predicted quantum chemically.[20] The Stokes shift $\Delta\tilde{\nu}_S$ of **9-F-MIA** is larger than the one of **MIA**, and it is the other way around for **7,8-dF-MIA**. Quantum chemical computations predict a smaller Stokes shift for **9-F-MIA** (4436 cm^{-1}) and **7,8-dF-MIA** (4033 cm^{-1}).

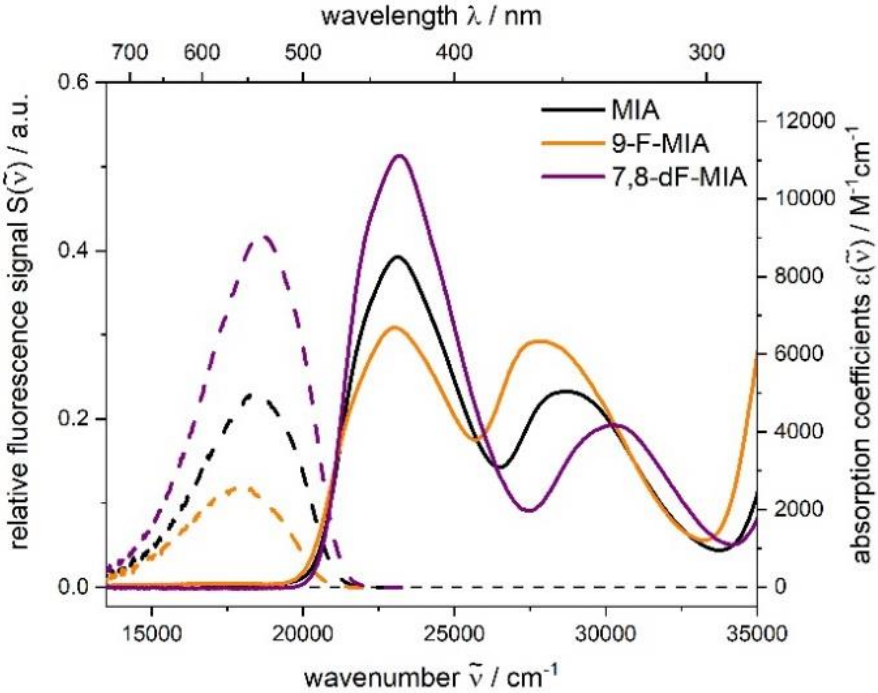

Figure 7.40. Absorption (absorption coefficients) and fluorescence emission spectra (recorded with constant wavelength bandpass and converted to constant wavenumber bandpass) of **9-F-MIA** and **7,8-dF-MIA** in water. For the fluorescence emission spectra, the excitation was tuned to 420 nm. The corresponding spectra of **MIA** in water[19] are shown for comparison. The fluorescence spectra are scaled according to their fluorescence quantum yield.

The radiative rate constants $k_{\mathrm{rad}}^{\mathrm{SB}}$ were determined from the spectra using the Strickler-Berg approach.[39-40] In this analysis, an integral needs to be computed that covers the lowest electronic transition in the absorption spectrum. A procedure requiring the use of the respective fluorescence spectrum was used here (see ref.[39,41] for details). According to this analysis, all derivatives feature rate constants of ~$5 \cdot 10^7$ s^{-1}. The one of **7,8-dF-MIA** ($5.94 \cdot 10^7$ s^{-1}) is higher compared to **MIA** ($4.45 \cdot 10^7$ s^{-1}), whereas **9-F-MIA** ($3.51 \cdot 10^7$ s^{-1}) has a lower one. The quantum chemical computation for **7,8-dF-MIA** ($5.87 \cdot 10^7$ s^{-1}) is in excellent agreement.

The computed value for **9-F-MIA** ($4.01 \cdot 10^7$ s^{-1}) deviates by only 14% from the experimental one. Together with the fluorescence quantum yield, the radiative rate constants allow predictions for the fluorescence lifetime $\tau_{\mathrm{fl}}^{\mathrm{SB}}$ using $\tau_{\mathrm{fl}}^{\mathrm{SB}} = \Phi_{\mathrm{fl}} / k_{\mathrm{rad}}^{\mathrm{SB}}$. The corresponding fluorescence lifetimes are expected in the range of 3-7 ns.

Table 7.13. Spectroscopic and photophysical parameters for **MIA** and various fluorinated **MIA** derivatives in H_2O.[a]

Parameters	**MIA**[19]	**6-F-MIA**[19]	**7-F-MIA**[19]	**8-F-MIA**[19]	**9-F-MIA**	**7,8-dF-MIA**
1st $\boldsymbol{\lambda_{max}}$ [nm]	431	430	441	422	432	431
1st $\boldsymbol{\varepsilon_{max}}$ [M^{-1} cm^{-1}]	8470	7880	9400	10220	6669	11117
1st $\boldsymbol{f}$	-	-	-	-	0.185	0.251
$\boldsymbol{\lambda_{em}}$ [nm]	524	524	533	534	535	519
2nd $\boldsymbol{\lambda_{max}}$ [nm]	345	364	331	348	357	328
2nd $\boldsymbol{\varepsilon_{max}}$ [M^{-1} cm^{-1}]	6250	8630	6640	5420	7679	5468
$\boldsymbol{\tilde{\nu}_{00}}$ [cm^{-1}]	20750	20590	20300	21320	20393	20894
$\boldsymbol{\Delta\tilde{\nu}_s}$ [cm^{-1}]	4640	5030	4520	4740	4900	4150
$\boldsymbol{\Phi_{fl}}$ (± 5%)	0.22	0.12	0.38 [c]	0.24	0.12	0.42
1st $\varepsilon_{max} \times \Phi_{fl}$ [M^{-1} cm^{-1}]	1863	946	3572	2453	800	4669
$\boldsymbol{k_{rad}^{SB}}$ [10^7 s^{-1}] (± 5%)	4.45	3.94	4.66	5.94	3.51	5.94
$\boldsymbol{\tau_{fl}^{SB}}$ [ns] (± 10%)	4.94	3.04	7.08	4.04	3.40	7.01
$\boldsymbol{\tau_{fl}}$ [ns][d] (± < 10%)	5.00	3.56	7.74	4.46	3.64	7.31
$\boldsymbol{\Phi_T}$ (± 20%)	0.5	0.4	0.2	0.5	0.4	0.3
$\boldsymbol{k_{ISC}}$ [10^7 s^{-1}] (± 20%)[b]	10.0	11.2	2.6	11.2	11.0	4.1
$\boldsymbol{\Phi_{IC}}$ (± 20%)	0.3	0.5	0.4	0.3	0.5	0.3
$\boldsymbol{k_{IC}}$ [10^7 s^{-1}] (± 20%)[b]	5.6	13.5	5.2	5.8	13.2	3.8
$\boldsymbol{\tau_T}$ [µs] (± 10%)[e]	5 (0.5); 39 (0.5)	11 (0.5); 44 (0.5)	44 (1)	10 (0.5); 47 (0.5)	21 (1)	43 (1)

[a] Wavelength maximum for the 1st and 2nd bands with the lowest absorption energies and the fluorescence maximum were determined via a Gaussian fit. The values given refer to spectra in the wavelength domain. The wavelength for absorption and emission were received from measurements with constant wavelength bandpass. Stokes shifts $\Delta\tilde{\nu}_s$ and 0-0 excitation energies $\tilde{\nu}_{00}$ are derived from spectra redrawn according to the transient dipole representation.[39] Fluorescence quantum yields Φ_{fl} were determined using coumarin 153 in ethanol as a reference ($\Phi_{fl}^r = 0.544$).[38] Radiative rate constants k_{rad}^{SB} were obtained from Strickler-Berg analysis.[39-40] A prediction of the fluorescence lifetime τ_{fl}^{SB} can be achieved via $\tau_{fl}^{SB} = \Phi_{fl}/k_{rad}^{SB}$ and compared to the $\boldsymbol{\tau_{fl}}$ measured by TCSPC. Triplet yields Φ_T were obtained from nanosecond transient absorption measurements with thioxanthone in methanol as a reference.

[b] The values were calculated by using $k_{ISC} = \Phi_T / \tau_{fl}$ and $k_{IC} = \Phi_{IC} / \tau_{fl}$ and the specified Φ_T. Using the yields Φ_{fl} and Φ_{ICS}, intersystem crossing rate constants k_{ISC} and internal conversion quantum yields Φ_{IC} could be determined.

[c] The value was updated by measurements in this study.

[d] The fluorescence lifetime measurements have an average precision < 0.05% and an accuracy given by instrument calibration and linearity < 1%.

[e] The relative amplitudes for the respective compounds are given for 550 nm.

Time-resolved spectroscopy

The fluorescence lifetimes were measured experimentally by time-correlated single photon counting (TCSPC) (Figure 7.41). A single exponential fit function including a constant offset to account for detector dark counts and afterpulsing is applied to the data to obtain the fluorescence lifetime of a sample. Fitting was performed with ChiSurf.[42] The instrument response function (IRF) full width at half maximum is around 100 ps, and it was taken into account in the fit via convolution. Measured decays are characterized by a single-exponential function and obtained fluorescence lifetimes τ_{fl} are given in Table 7.13.

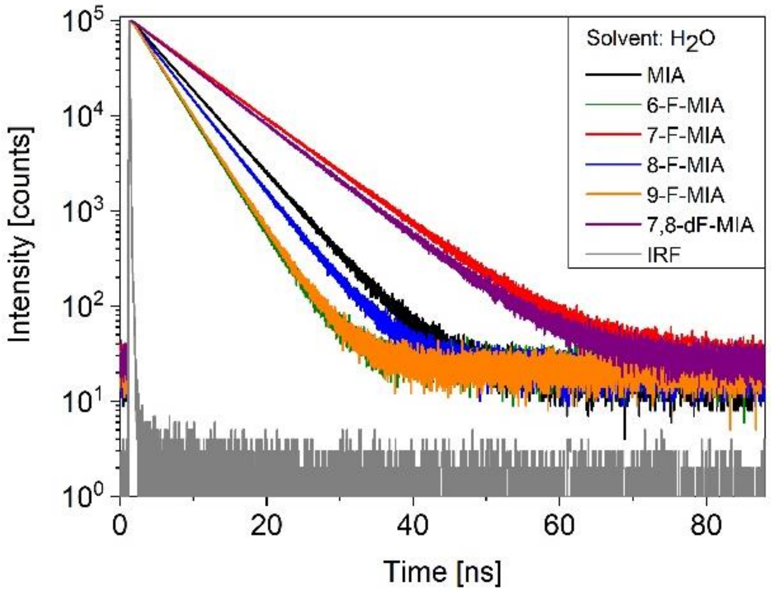

Figure 7.41. Fluorescence decays in H_2O measured by TCSPC. The corresponding decays in D_2O are shown in Figure S7.356.

The lifetimes measured by TCSPC are longer than the ones calculated via the Strickler-Berg method, but the deviations are rather small (< 10%). Together with previously[19] reported values we see a characteristic influence of the fluorination substitution. For **6-F-MIA**, **8-F-MIA** and **9-F-MIA** the fluorescence lifetime is reduced and for **7-F-MIA** is prolonged in comparison to **MIA** (5.00 ns). Interestingly, the fluorescence lifetime of the difluorinated derivative **7,8-dF-MIA** is prolonged. It is in between its mono-fluorinated counterparts, but it is closer to **7-F-MIA** than to **8-F-MIA**.

For all **MIA** derivatives studied, the fluorescence quantum yields are well below one. Therefore, the non-radiative decay processes dominate. To specify the type of non-radiative decay (ISC or internal conversion (IC)), measurements were performed on a nanosecond transient absorption instrument. From these experiments, the triplet quantum yields Φ_T and hence the rate constants for ISC can be derived. The effects of fluorination on triplet yields were investigated using a relative method detailed in ref. [19]. The difference absorption signals at time zero of the sample ($\Delta A_\mathrm{t=0}(\lambda_\mathrm{Pr})$) and a reference ($\Delta A^\mathrm{r}_\mathrm{t=0}(\lambda_\mathrm{Pr})$) (see Supporting Information, Figure S7.358) were recorded. Thioxanthone in methanol served as a reference. The respective difference absorption coefficient spectra $\Delta\varepsilon_\mathrm{T}(\lambda_\mathrm{Pr})$ and $\Delta\varepsilon^\mathrm{r}_\mathrm{T}(\lambda_\mathrm{Pr})$ of the sample and reference were obtained from the signals $\Delta A_\mathrm{t=0}(\lambda_\mathrm{Pr})$ as well as $\Delta A^\mathrm{r}_\mathrm{t=0}(\lambda_\mathrm{Pr})$ and the respective ground state bleaches (see Figure S7.359). With these inputs and the triplet quantum yield of the reference $\Phi^\mathrm{r}_\mathrm{T}$, the yield was calculated via Eq. (1):

$$\Phi_\mathrm{T} = \frac{\Delta A_\mathrm{t=0}(\lambda_\mathrm{Pr})}{\Delta\varepsilon_\mathrm{T}(\lambda_\mathrm{Pr})} \frac{\Delta\varepsilon^\mathrm{r}_\mathrm{T}(\lambda_\mathrm{Pr})}{\Delta A^\mathrm{r}_\mathrm{t=0}(\lambda_\mathrm{Pr})} \Phi^\mathrm{r}_\mathrm{T} \tag{1}$$

The triplet yields Φ_T obtained in this fashion are lower for **9-F-MIA** (0.4) and **7,8-dF-MIA** (0.3) compared to **MIA** (0.5).

By using the triplet quantum yields and fluorescence lifetimes, the rate constants for ISC (k_ISC) can be computed via $k_\mathrm{ISC} = \Phi_\mathrm{T} / \tau_\mathrm{fl}$. For **9-F-MIA** ($11.0\cdot10^7$ s^{-1}), a higher rate constant was computed than for **MIA** ($10.0\cdot10^7$ s^{-1}), **7,8-dF-MIA** ($4.1\cdot10^7$ s^{-1}) has a lower rate constant. The magnitude ~10^8 s^{-1} of the ISC rate constants match the previously published data of Bracker et al.[20]

For the fluorinated **MIA** derivatives studied, the determined quantum yields of fluorescence and triplet do not sum up to one. Thus, the derivatives also undergo the IC process in competition with the radiative decays and the ISC process. The IC quantum yield derived from $\Phi_\mathrm{IC} = 1 - \Phi_\mathrm{fl} - \Phi_\mathrm{T}$ is larger for **9-F-MIA** (0.5) compared to **MIA** (0.3) and comparable for **7,8-dF-MIA** (0.3). Using the relation $k_\mathrm{IC} = \Phi_\mathrm{IC} / \tau_\mathrm{fl}$, the respective IC rate constants can be determined. **9-F-MIA** ($13.2\cdot10^7$ s^{-1}) has a higher IC rate constant compared to **MIA** ($5.6\cdot10^7$ s^{-1}), while **7,8-dF-MIA** ($3.8\cdot10^7$ s^{-1}) has a lower one.

Finally, we want to discuss the experimental sensitivity[43] (1st $\varepsilon_\mathrm{max} \times \Phi_\mathrm{fl}$) in potential bioanalytical applications that is governed by the product of the absorption coefficient 1st ε_max and the fluorescence quantum yield Φ_fl. According to Table 7.13, fluorine substitution at the positions 7 and 8 of **MIA** result in increased absorption coefficients. This effect is even additive, so that **7,8-dF-MIA** has the largest value 1st $\varepsilon_\mathrm{max} = 11117$ M^{-1} cm^{-1}. At the same time, the fluorescence quantum yield stays very high due to the small rate constant of intersystem crossing. Altogether, the newly designed derivative **7,8-dF-MIA** has the highest sensitivity of 4669 M^{-1} cm^{-1} of all **MIA** and flavin derivatives studied in this work.

Impact of the deuterated solvent D_2O on the fluorescence

Next, we measured the fluorescence lifetimes in both H_2O and D_2O with a very high precision (< 0.05%) to characterize the non-radiative deactivation processes in more detail. Similar to Maillard et al.,[44] we observed longer fluorescence lifetimes in D_2O for all **MIA** derivatives (Table 7.14) which indicates that the **MIA** derivatives are between 13 to 33% brighter, while the absorption and fluorescence spectra as well as the absorption coefficients remain unchanged. For **7-F-MIA** and **7,8-dF-MIA** the fluorescence enhancement in D_2O is largest so that their fluorescence quantum yields are raised to 0.51 and 0.53, respectively.

To analyse the nature of the quenching reaction by H_2O in more detail, we consider H_2O molecules as quenchers with an effective pseudo-first order rate constant k_{qw} of the bulk (given by water concentration). The fluorophores dissolved in D_2O are considered as "unquenched". The measured fluorescence lifetime τ_{fl} in H_2O and D_2O relate to all deactivation processes [Eq. (2)]:

$$\tau_{\mathrm{fl}}^{(\mathrm{H_2O})} = \frac{1}{k_{\mathrm{rad}} + k_{\mathrm{ISC}}^{(\mathrm{H_2O})} + k_{\mathrm{IC}}^{(\mathrm{H_2O})} + k_{\mathrm{qw}}}$$

and

$$\tau_{\mathrm{fl}}^{(\mathrm{D_2O})} = \frac{1}{k_{\mathrm{rad}} + k_{\mathrm{ISC}}^{(\mathrm{D_2O})} + k_{\mathrm{IC}}^{(\mathrm{D_2O})}} \tag{2}$$

As absorption and fluorescence spectra are not affected by switching from H_2O to D_2O, the same radiative rate constant k_{rad} applies for both situations. This allows us to compute k_{qw} and the corresponding quenching yields, Φ_{qw}, according to eq. (3) for all compounds.

$$k_{\mathrm{qw}} = 1/\tau_{\mathrm{fl}}^{(\mathrm{H_2O})} - 1/\tau_{\mathrm{fl}}^{(\mathrm{D_2O})}$$

and

$$\Phi_{\mathrm{qw}} = k_{\mathrm{qw}} \cdot \tau_{\mathrm{fl}}^{(\mathrm{H_2O})} \tag{3}$$

Table 7.14. Fluorescence lifetimes τ_{fl} in H_2O and D_2O measured by TCSPC.

Parameters	**MIA**	**6-F-MIA**	**7-F-MIA**	**8-F-MIA**	**9-F-MIA**	**7,8-dF-MIA**
$\tau_{\mathrm{fl}}^{(\mathrm{H_2O})}$ [ns][a]	5.00	3.56	7.74	4.46	3.64	7.31
$\tau_{\mathrm{fl}}^{(\mathrm{D_2O})}$ [ns][a]	5.76	4.20	10.32	5.01	4.24	9.29
$\Phi_{\mathrm{fl}}^{(\mathrm{D_2O})}$	0.25	0.14	0.51	0.27	0.14	0.53
Φ_{qw} [b]	0.13	0.15	0.25	0.11	0.14	0.21
k_{qw} [10^7 s^{-1}][c]	2.6	4.3	3.2	2.5	3.9	2.9

[a] The fluorescence lifetime measurements have an average precision < 0.05% and an accuracy given by instrument calibration and linearity < 1%.

[b] The water quenching yields [Eq. (3)] have an average precision < 0.15% and an accuracy given by the fluorescence lifetime measurement < 1%.

[c] The quenching constant of water k_{qw} was computed by Eq. (3) with a precision of < 0.15%.

We became interested, to which extent the quenching constant has a systematic dependency and whether this is a universal feature[44] for all fluorinated **MIA** derivatives. Therefore, we formulate a Stern-Volmer correlation like Equation (4) with an average quenching constant $\overline{k_{\mathrm{qw}}}$, which is equivalent to Equation (3).

$$\tau_{\mathrm{fl}}^{(\mathrm{D_2O})} / \tau_{\mathrm{fl}}^{(\mathrm{H_2O})} = 1 + \overline{k_{\mathrm{qw}}} \cdot \tau_{\mathrm{fl}}^{(\mathrm{D_2O})}$$

assuming

$$\frac{k_{\mathrm{rad}} + k_{\mathrm{ISC}}^{(\mathrm{D_2O})} + k_{\mathrm{IC}}^{(\mathrm{D_2O})}}{k_{\mathrm{rad}} + k_{\mathrm{ISC}}^{(\mathrm{H_2O})} + k_{\mathrm{IC}}^{(\mathrm{H_2O})}} = 1 \tag{4}$$

Here, we also implicitly test the validity of the underlying assumption that the ratio of the sums for the internal radiative and non-radiative rate constants in H_2O and D_2O is unity for the distinct derivatives. In the following, we apply Eq. (4) to the **MIA** derivatives (a) to (f) (filled dots in Figure 7.42). Indeed, in Figure 7.42 we observe a linear relation with an average quenching constant $\overline{k_{\mathrm{qw}}} = 0.029$ ns^{-1} and an intercept, which is very close to unity. This value is in good agreement with the mean value of the individual quenching constants for **MIA** and its fluorinated derivatives of 0.033 ns^{-1} (see Table 7.14). Notably, the small deviations from linearity confirm our approximation in Eq. 3 and at the same time display its limits. From this we can conclude that, although the water quenching rate constants are quite similar ($\overline{k_{\mathrm{qw}}}$ = 2.9·10^7 s^{-1} ± 19%) for all **MIA** derivatives, the resulting water quenching yields Φ_{qw} = 0.17 ± 27% and the corresponding enhancement factors in D_2O vary slightly more because of the different fluorescence lifetimes.

Our analysis confirms the hypothesis that the quenching reaction of water is roughly comparable for all fluorinated **MIA** compounds and that the quenching yields depend on the specific S_1 lifetimes. This result is in very good agreement with studies of Maillard et al.[44] on the universal quenching by water and alcohols for 42 common organic fluorophores emitting in over the whole visible spectrum. Considering dyes with similar singlet energies of $\tilde{\nu}_{00} \approx$ 20500 cm^{-1} (2.5 eV), the authors report values of k_{qw} in the range of (3 ± 1) · 10^7 s^{-1}, that excellently agree with our values in Table 7.14.

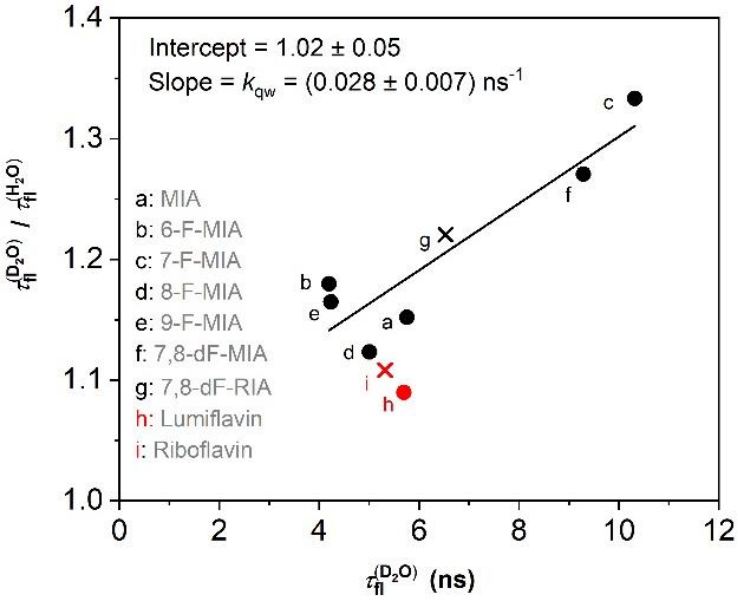

Figure 7.42. Stern-Volmer plot: The ratio of fluorescence lifetimes in D_2O over H_2O against the lifetimes in D_2O. Compounds with a methyl group at position 10 of the isoalloxazine are depicted as dots and compounds with a ribityl group with the cross. The symbols of fluorinated compounds are displayed in black and the compounds with the naturally occurring 7,8-dimethyl-isoalloxazine (flavin) core are displayed in red. The linear regression is only applied to compounds of **MIA** family (**a** to **f**, filled dots). The slope corresponds to an average quenching constant in water, $\overline{k_{\mathrm{qw}}}$ = 0.028 ns^{-1}. The standard errors were not shown as they are smaller than the symbol size.

In view of the structural diversity of the studied fluorophores, we tested the hypothesis that the universal quenching process by water is majorly mediated by internal conversion[45] and that intersystem crossing can be modulated to a minor extent (visible by the observed small deviations that are larger than our experimental uncertainties). Therefore, we applied full fluorescence correlation spectroscopy (FCS)[46-48] to study the influence of H_2O and D_2O on the stationary triplet population T_{eq} and characteristic triplet relaxation time t_T of **7-F-MIA**. We selected **7-F-MIA** for several reasons: (1) very high brightness, (2) a strong fluorescence enhancement in D_2O, and (3) the rate constants k_{qw} and k_{ISC} are approximately equal in H_2O, so that a potential change of intersystem crossing in D_2O could be detected with high sensitivity. The normalized full correlation curves $G(t_c)$ of **7-F-MIA** are displayed as a function of the correlation time t_c in Figure 7.43.

In both solvents, the correlation curves exhibit similar distinctive features in the three characteristic time regimes: antibunching, triplet and translational diffusion. The rise term in D_2O is slower because the excited state lifetime is prolonged. Notably, the triplet terms in H_2O and D_2O are quite similar in air-saturated solution. Thus, a significant difference of the underlying key triplet parameters, rate constant for intersystem crossing k_{ISC} and triplet depopulation k_T, can be excluded. The value of k_{ISC} of $2.58 \cdot 10^7$ s^{-1} recovered by FCS for both conditions excellently agrees with result obtained by transient absorption spectroscopy in Table 7.13. The triplet decay is faster in the FCS experiment due to oxygen from air. The kinetic scheme (Figure 7.45) and a detailed description of analysis procedure for determining the triplet parameters is given in the experimental section. The final decay of $G(t_c)$ due to translational diffusion is slightly longer in D_2O, because its viscosity is approximately 25% higher.[49-50] To conclude, our FCS measurements show that the triplet properties of **7-F-MIA** are not majorly changed in D_2O, i.e. FCS confirms our hypothesis that the fluorescence enhancement in D_2O cannot be caused by a reduction of rate of intersystem crossing but by a reduction of internal conversion.

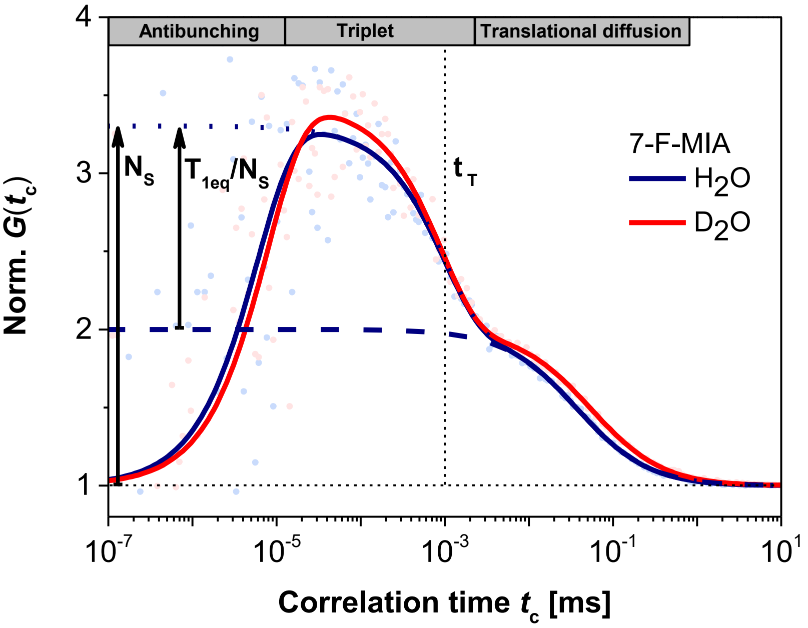

Figure 7.43. Normalized and averaged full correlation curves $G(t_c)$ of **7-F-MIA** in air-saturated H_2O and D_2O at nanomolar concentrations. The detailed analysis and the fitted model function [solid lines, Equations (6), (7)] are described in the experimental section. The overall and unnormalized amplitude of $G(t_c)$ is related to the inverse number of bright molecules in the singlet state N_S. The obtained triplet parameters were the triplet fraction $T_{1eq} = 0.56 \pm 0.01$ and the triplet relaxation time $t_T = (1.02 \pm 0.06)$ µs for H_2O and $T_{1eq} = 0.59 \pm 0.01$ and $t_T = (0.92 \pm 0.07)$ µs for D_2O. The dashed lines represent the contributions of the translational diffusion and triplet term to the fitted model function [Eq. (6)] with the following additional parameters: $t_d = 37$ µs, $z_0/\omega_0 = 6$ (fixed), $AB = 1$ (fixed), $t_{AB} = 6.0$ ns for H_2O and $t_d = 54$ µs, $z_0/\omega_0 = 6$ (fixed), $AB = 1$ (fixed), $t_{AB} = 8.1$ ns for D_2O.

Impact of the ribityl group

Finally, we studied the effect of the ribityl residue at position 10 of the isoalloxazine ring. For this, we compared the fluorescence lifetimes of **7,8-dF-RIA** (**13**) with the natural analogue riboflavin and studied the accord with the corresponding derivatives incorporating a methyl group at position 10 (7,8,10-trimethyl-isoalloxine referred to as lumiflavin) (Table 7.15). In both ribityl derivatives, the fluorescence lifetime in H_2O is reduced and the quenching constant of water k_{qw} is increased by approx. 20% as compared to the corresponding methyl-substituted compounds **7,8-dF-MIA** and lumiflavin (Table 7.15). Moreover, from the comparison between the 10-ribityl- and 10-methyl derivatives, it obvious that the ribityl substitution leads to a reduction of fluorescence with the rate constant k_{qRib} that has a similar order of magnitude as water quenching k_{qw} and is solvent independent. It is remarkable that both quenching constants k_{qw} and k_{qRib} are three times smaller for non-fluorinated flavin derivatives as compared to fluorinated derivatives. Notably, the significantly lower fluorescence reduction of non-fluorinated flavin derivatives by the ribityl substituent is also visible in the Stern-Volmer analysis in Figure 7.42 (red symbols).

Again, we applied FCS to investigate which non-radiative deactivation process is influenced by the ribityl substituent. The analysis of the correlation functions of **7,8-dF-MIA** and **7,8-dF-RIA** in D_2O (see Supporting Information) shows that k_{ISC} ($1.54\cdot 10^7$ s^{-1} ± 21%) of **7,8-dF-RIA** is not increased with respect to **7,8-dF-MIA**. Thus, the reduction of the fluorescence lifetime by the ribityl substituent is caused by additional internal conversion processes.

Table 7.15. Fluorescence lifetimes τ_{fl} of **7,8-dF-RIA** in relation to flavins in H_2O and D_2O measured by TCSPC.

Parameters	**7,8-dF-MIA**	**7,8-dF-RIA**	**Lumiflavin**	**Riboflavin**
$\tau_{\text{fl}}^{(\text{H}_2\text{O})}$ [ns][a]	7.31	5.35	5.23	4.80
$\tau_{\text{fl}}^{(D_2O)}$ [ns][a]	9.29	6.53	5.70	5.32
Φ_{qw} [b]	0.21	0.18	0.07	0.08
k_{qw} [10^7 s^{-1}][c]	2.9	3.4	1.6	2.0
$k_{\text{qRib}}^{(\text{H}_2\text{O})}$ [10^7 s^{-1}][d]		5.0		1.7
$k_{\text{qRib}}^{(\text{D}_2\text{O})}$ [10^7 s^{-1}][d]		4.6		1.3

[a] The fluorescence lifetime measurements have an average precision < 0.05% and an accuracy given by instrument calibration and linearity < 1%.

[b] The water quenching yields [Eq. (1)] have an average precision < 0.15% and an accuracy given by the fluorescence lifetime measurement < 1%.

[c] The quenching constant of water k_{qw} was computed by Eq. (3) with a precision of < 0.15%.

[d] The quenching constant of the ribityl chain k_{qRib} was computed by

$k_{\text{qRib}} = 1/\tau_{\text{fl}}^{(\text{Rib-derivative})} - 1/\tau_{\text{fl}}^{(\text{Me-derivative})}$ with a precision of < 0.15%.

7.4.4 Conclusion

To develop bright fluorophores, it is essential to minimize non-radiative deactivation processes that compete with fluorescence.

In previous work,[19-20] we have demonstrated that rational design regarding the photophysical properties of new flavin derivatives using quantum chemical calculations works to predict state energies as well as radiative and ISC rate constants. To find even brighter **MIA** derivatives, we had applied these methodologies and computed the properties of the electronic states of further **MIA** compounds, **9-F-MIA** and **7,8-dF-MIA**. Here, these derivatives were also synthesized and characterized experimentally. The predicted similarity of **9-F-MIA** with **6-F-MIA** was reproduced experimentally. Moreover, the predicted high fluorescence quantum yield of **7,8-dF-MIA** was also experimentally confirmed. The small rate constant of intersystem crossing due to a higher energy of the $^3\pi\pi^{*u}$ state can be rationalized by the additivity of the energy shifts of both **7-F-MIA** and **8-F-MIA** (Figure 7.44).

This shows that quantum chemical calculations are already on a very high level to make tailor design of fluorescence probes for microscopy feasible. Additionally, the fluorinated flavin derivative **7,8-dF-RIA** as a first example of a fluorescent probe for analytical applications and fluorescence microscopy was synthesized. The fluorescence lifetime measurements of **7,8-dF-RIA** revealed that the incorporation of the ribityl group reduces its fluorescence by 27%, so that its fluorescence quantum yield drops to 0.31 (Table 7.15). Nevertheless, it is still brighter than natural flavin with $\Phi_{\text{fl}} = 0.20$.[51] The fluorescence enhancement of all **MIA** derivatives in D_2O demonstrates that the quenching by protic solvents is also significant. The FCS measurements of **7-F-MIA** in H_2O and D_2O (Figure 7.43) reveal that internal conversion is the main process caused by water quenching. Millard et al.[44] studied the fluorescence quenching of 42 distinct dyes by protic solvents in detail. For dyes with $E_{0,0} < 2.1$ eV, they suggest that an efficient universal deactivation by dipolar coupling between the fluorophore and water by Förster resonance energy transfer from the electronic (vibronic) excited fluorophore state and isoenergetic vibrational oscillators of the solvent. For other fluorophores and our flavin derivatives with $E_{0,0} \approx 2,6$ eV, the predicted rate constant of FRET quenching drops to $\approx 2 \cdot 10^6$ s^{-1} so that additional solvent-mediated deactivation processes are proposed.[44-45]

Altogether, we predicted and synthesized the new **MIA** derivative **7,8-dF-MIA** that has the highest sensitivity (1^{st} $\varepsilon_{\max} \times \Phi_{\text{fl}}$) = 4669 M^{-1} cm^{-1} of all **MIA** and flavin derivatives studied in this work. Its fluorescence quantum yield is enhanced even further in D_2O ($\phi_{\text{fl}}^{(D_2O)} = 0.53$)

in concord with a very long fluorescence lifetime ($\tau_{\mathrm{fl}}^{(\mathrm{D_2O})} = 9.3\ ns$) that makes **7,8-dF-MIA** a promising probe for bioanalytical applications.

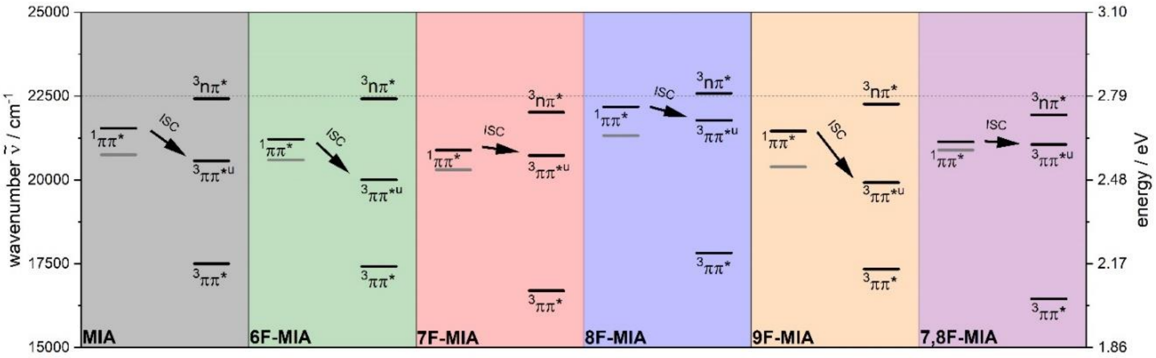

Figure 7.44. Schematic representation of experimental and calculated adiabatic energies for **MIA** as reference and the fluorinated derivatives in aqueous solution.[20] Gray bars represent experimental 0-0 energies of the singlet states for the respective compounds. Black bars represent the quantum chemical ones.[20] The values include zero-point vibrational energy (ZPVE) corrections for the equilibrium geometries.[20] Note that the changes in the rate constant of the intersystem crossing correlate with the energetic transition between the $^1\pi\pi^*$ and $^3\pi\pi^{*u}$ states in the mono-fluorinated derivatives. The additive behaviour of the energy shifts explains the small rate constant of the intersystem crossing in the di-fluorinated compound.

7.4.5 Experimental Section

Steady-state measurements

Absorption spectra were carried out with a two-beam absorption spectrometer from PerkinElmer (Lambda 19). Steady-state fluorescence measurements were carried out using a HORIBA Scientific instrument (FluoroMax-4). The spectral sensitivity of the instrument as well as the solvent background were corrected. Absorbance was adjusted for all fluorescence measurements to be less than 0.05 per cm at the excitation wavelength (420 nm) to avoid inner filter effects.

Time-correlated single photon counting

Time-correlated single photon counting (TCSPC) was performed using a fluorescence lifetime and steady-state spectrometer (FT300 with hybrid PMT detector, PicoQuant, Germany). Excitation was achieved with a supercontinuum laser excitation source (EXW-12 with EXTEND-UV spectral extension unit, NKT Photonics, Denmark) running at a repetition rate of 11.1 MHz. Excitation wavelengths were set by tuning the frequency doubler. They were selected to match the absorption maxima. **MIA**, **6-F-MIA**, **9-F-MIA** and **7,8-dF-MIA** were excited at 430 nm, **7-F-MIA** at 440 nm, and **8-F-MIA** at 420 nm. Emission was detected under magic angle conditions (excitation polarizer 0° - emission polarizer 54.7°). Input and output slit widths were set to 1000 µm which corresponds to a detection bandpass of 5.4 nm. Detection wavelengths were selected to match the fluorescence maxima, i.e. 525 nm, 530 nm, 535 nm, 510 nm, 540 nm, and 520 nm for **MIA**, **6-F-MIA**, **7-F-MIA**, **8-F-MIA**, **9-F-MIA**, and **7,8-dF-MIA** respectively. Measurements were performed at 20 °C. All samples were measured in Quartz Macro Cell type 111-QS cuvettes (Hellma) with a light path of 1 cm and a sample volume of 3 ml. As solvents, double-distilled water (H_2O) and heavy water (D_2O) from Aldrich (99.9 atom % D) were used. The concentration of the sample was in the range of 10^{-6} to 10^{-5} M in all measurements. For the instrument response function (IRF), Ludox HS-30 colloidal silica water suspension (Aldrich) with a zero lifetime was used.

Nanosecond transient absorption spectrometer

Nanosecond transient absorption data were acquired using a transient absorption spectrometer from Edinburgh Instruments in a right-angle geometry (LP980).[52] The excitation source was a Nd:YAG laser (Spitlight 600, InnoLas, repetition rate 5 Hz, pulse duration of 12 ns (FWHM), diameter of the pump beam ~8 mm) with an excitation wavelength of 355 nm which was generated by frequency-tripling. The average pulse energy amounted to 0.5 mJ. A pulsed xenon lamp (Osram XBO 150 W/CR OFR) was used as a probe beam. Fused silica flow-through cuvettes from the manufacturer Hellma were used, with a path length of 5 mm in the pump and 10 mm in the probe direction. The absorption was adjusted to 0.65 per cm at the excitation wavelength. The transmitted probe light was dispersed with a grating monochromator and detected by using a Hamamatsu photomultiplier covering the UV/Vis spectral range (PMT-900). To acquire transient spectra, kinetic traces were recorded every 5 nm and averaged over 80 acquisitions. Typical data are shown in Figure S7.358 and Figure S7.359. The nanosecond transient absorption data $\Delta A(\lambda, \mathrm{t})$ were analysed by global multi-exponential fit function via Eq. (5).[53-54]

$$\Delta A(\lambda, \mathrm{t}) = \mathrm{IRF} \otimes \sum_{\mathrm{i}=1}^{\mathrm{n}} \Delta A_{\mathrm{i}}(\lambda) \mathrm{e}^{-\mathrm{t}/\tau_{\mathrm{i}}} \quad (5)$$

The exponential decay functions were convoluted with the response function (IRF) of the instrument (FWHM; 12 ns). $\Delta A_{\mathrm{i}}(\lambda)$ stand for the decay associated difference spectra with the respective time constants τ_i.

Fluorescence correlation spectroscopy (FCS)

Fluorescence correlation spectroscopy (FCS) measurements were performed using a confocal fluorescence microscope (FV1000, Olympus) with extension for time-resolved experiments.[55] The samples were excited by a laser diode at 440 nm (LDH-D-C 440, PicoQuant) in continuous wave mode. The laser beam was directed by a dichroic beam splitter into the microscope objective (Olympus 60X, NA 1.20, water immersion) and focused in the sample close to the diffraction limit. The emitted light was separated into polarisations parallel and perpendicular relative to the excitation beam (PBS 101, Thorlabs). In each channel the light, after passing a dichroic beam splitter (BS 560, AHF) and a bandpass filter (HC520/35, AHF) was focused on a single photon sensitive detector (PDM50-CTC, Micro Photon Devices). The photon trace was recorded by a TCSPC module (HydraHarp 400, PicoQuant). Custom software (LabVIEW based) was used to analyse the received data. The full correlation curves were measured in air at nanomolar concentrations of **7-F-MIA** at 23 °C for 30 minutes and repeated four times each.

The setup was calibrated measuring the translational diffusion times of Rhodamine 110 in H_2O and D_2O (t_{d} = 45 μs and 56 μs, respectively). To this end, the following model function was fitted to the FCS curves [Equation (6)]:

$$G(t_\mathrm{c}) = \mathrm{offset} + \frac{1}{N_\mathrm{S}} \cdot \frac{1}{1 + \frac{t_\mathrm{c}}{|t_\mathrm{d}|}} \cdot \frac{1}{\sqrt{\left(1 + \frac{t_\mathrm{c}}{\left(\frac{z_0}{\omega_0}\right)^2 \cdot |t_\mathrm{d}|}\right)}} \cdot \left(1 - |T_\mathrm{1eq}| + |T_\mathrm{1eq}| \cdot e^{-\left(\frac{t_\mathrm{c}}{|t_\mathrm{T}|}\right)}\right) \cdot \left(1 - |AB| \cdot e^{-\left(\frac{t_\mathrm{c}}{|t_\mathrm{AB}|}\right)}\right) \tag{6}$$

with the number of bright molecules in the singlet state N_S, their translational diffusion time t_d, the axial ratio of the detection volume element z_0/ω_0 and T_1eq, t_T, AB and t_AB the amplitude and relaxation time corresponding to the triplet kinetics and the antibunching, respectively.

The known diffusion coefficient of Rhodamine 110 of $4.3 \cdot 10^{-6}$ cm^2 s^{-1} at 22.5 °C in water[56] was rescaled to the experimental conditions using Stokes-Einstein equation and the temperature-dependent viscosity of the two solvents (H_2O: 0.9321 mPa·s at 23 °C;[49] D_2O: 1.1562 mPa·s at 23 °C[50]). A constant hydrodynamic radius of R110 was assumed. This way the radial extension of the confocal detection volume element ω_0 = 0.276 µm was confirmed to be identical within the experimental error (± 5%) in both cases.

We used the reported absorption coefficient of ε = 9400 M^{-1} cm^{-1} at 441 nm[19] to compute excitation rate k_{01} in the next step. In agreement with Maillard et al.[44], we find no differences for the absorption spectra and absorption coefficients of **7-F-MIA** between H_2O and D_2O.

To avoid losses by reflection, we measured the laser power P at the sample with an immersion power meter: P = 65 µW. Widengren et al.[46] showed that the size of the confocal observation volume defined by the pinhole slightly affects the effective value for the average irradiance I_av in the top hat approximation. As lower limit for the mean irradiance, we estimate $I_\mathrm{av} = 1.2\, P/(\pi\, \omega_0^2) = 32.6$ kW/cm^2 for H_2O and D_2O, which results in an excitation rate constant of k_{01} = $0.26 \cdot 10^7$ s^{-1}. This is a slight underestimation of the absolute value of I_av, since a confocal aperture of about 1.5 AU was used to collect photons most efficiently. Thus, we compute also an upper limit for the mean irradiance by I_av = $1.6\, P/(\pi\, \omega_0^2)$ = 43.5 kW/cm^2, which results in an excitation rate of k_{01} = $0.35 \cdot 10^7$ s^{-1}. The characteristic rise time of the antibunching term t_AB describing the population of the S_1 state is related to the whole kinetic scheme according to Eq. (9). The time regime of the antibunching was too noisy to give reproducible results but served to stabilize the fit.

To relate the FCS observables, the amplitude connected to the triplet fraction T_1eq and the triplet relaxation time t_T, the kinetic scheme (left side) with the corresponding rate matrix (right) must be solved.

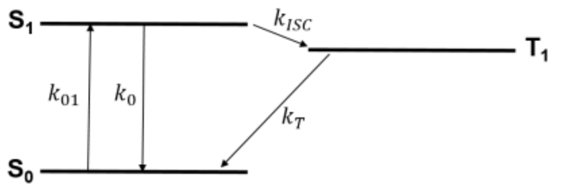

$$\begin{pmatrix} -k_{01} & k_0 & k_{\mathrm{T}} \\ k_{01} & -(k_0 + k_{\mathrm{ISC}}) & 0 \\ 0 & k_{\mathrm{ISC}} & -k_{\mathrm{T}} \end{pmatrix}$$

Figure 7.45. Assumed kinetic scheme (left) and the rate matrix (right). The solution of the kinetic scheme is given in Equations (7)-(9).

$$T_{1eq} = \frac{k_{ISC}}{k_T} S_{1eq} = \frac{k_{ISC} \cdot k_{01}}{k_{01} \cdot (k_{ISC} + k_T) + k_T \cdot (k_0 + k_{ISC})} \tag{7}$$

$$\frac{1}{t_T} = \frac{1}{2}\left(-\sqrt{(k_0 + k_{01} + k_{ISC} + k_T)^2 - 4(k_0 k_T + k_{01} k_{ISC} + k_{01} k_T + k_{ISC} k_T)} + k_0 + k_{01} + k_{ISC} + k_T\right) \tag{8}$$

$$\frac{1}{t_{\mathrm{AB}}} = \frac{1}{2}\left(\sqrt{(k_0 + k_{01} + k_{ISC} + k_T)^2 - 4(k_0 k_T + k_{01} k_{ISC} + k_{01} k_T + k_{ISC} k_T)} + k_0 + k_{01} + k_{ISC} + k_T\right) \tag{9}$$

Considering the independently measured fluorescence lifetimes ($= 1/k_0$) of 7.74 ns (H_2O) and 10.32 ns (D_2O), the experimental results are consistent with an intersystem crossing rate of $k_{\mathrm{ISC}} = 2.58 \cdot 10^7\ \mathrm{s}^{-1}$ and a triplet depopulation rate of $k_{\mathrm{T}} = 0.043 \cdot 10^7\ \mathrm{s}^{-1}$ for both cases, assuming excitation rates $k_{01} = 0.34 \cdot 10^7\ \mathrm{s}^{-1}$ (H_2O) and $k_{01} = 0.31 \cdot 10^7\ \mathrm{s}^{-1}$ (D_2O). This would correspond to a 10% smaller focal area in H_2O, well within the experimental error. A significant difference in triplet depopulations has not been observed for the two solvents.

7.4.6 Supplementary Information

Synthesis

General description

Chemicals and equipment

In all experiments, chemicals by the companies Merck, Acros, Fluka, Sigma Aldrich, TCI, Fluorochem, J&K, Eurisotop, Apollo Scientific, Carbolution and BLDPharm were used and if necessary purified by recrystallisation or distillation before use. The solvents n-hexane, ethyl acetate, dichloromethane and acetone for work-up and purification were purchased in technical purity and distilled before use by a rotary evaporator Rotavapor R-210 by the company Büchi and diaphragm pumps by vacuubrand. All other solvents as well as those used for syntheses were purchased in analytical purity, dried over molecular sieve if necessary and used without further purification. Dry solvents like dichloromethane and toluene were taken from a solvent drying system MBraun MB SPS-800.

Air-sensitive reactions were carried out under exclusion of oxygen and water on a combined vacuum-nitrogen line using conventional Schlenk techniques. Glass appliances were dried in a compartment dryer overnight at 120 °C and then additionally heated under high vacuum with a heat gun by Meterk. High vacuum was generated by a rotary vane oil pump by vacuubrand. Nitrogen was dried by molecular sieve (3 Å) and orange gel before use and nitrogen flow was checked by a bubble counter. Liquids were transferred by syringe through a septum and solids were added to the reaction flask in nitrogen countercurrent. If necessary, reaction mixtures or solvents were degassed by purging nitrogen through or by freeze-pump-thaw method.

For stirring, a PTFE-coated stirring bar and magnetic stirrers with heating plates by IKA RCT or Heidolph MR were used, which were equipped with a thermometer and a silicone oil bath. Room temperature reactions are considered within a range of 18-30 °C. An ice-water bath and an acetone dry ice bath were used to generate temperatures of 0 °C and -78 °C, respectively. The rotary evaporator Rotavapor R-210 by Büchi and a diaphragm pump by vacuubrand were used to remove solvents *in vacuo*.

Chromatography

Thin layer chromatography was performed on Alugram® Xtra SIL G/UV254 standard silica aluminum plates by Macherey-Nagel to check the progress of reactions and flash chromatography. The spots were detected by means of UV light (254 nm) and/or by staining with a potassium permanganate solution of the composition 3.0 g $KMnO_4$, 20 g K_2CO_3, 5.0 ml 5% NaOH and 300 ml H_2O and then developed with a heat gun by Meterk. For flash chromatography silica gel 60M by Macherey-Nagel was used. Flash chromatography was either performed manually with nitrogen pressure or by using a MPLC system by Büchi including a Control Unit C-620, a Fraction Collector C-660, a UV Photometer C-640 and Pump Modules C-605. Reversed Phase HPLC was performed using the following devices: Knauer HPLC Pump 64, Merck-Hitachi L-6250 Intelligent Pump, Knauer Dynamic Mixing Chamber, Knauer Automatic HPLC Valve, Latek HMV-P, Knauer Variable Wavelength Monitor, Merck-Hitachi L-4000 UV Detector, Erma Degasser ERC-3510, Waters Fraction Collector II, LiChrospher® 100 RP-18 (5 µm) Sorbent Lot No. HX391811 Hibar® RT 250-25, Knauer Eurospher 100-C18 (5 µm), 4.0 mmID. For data processing, the program Clarity was used.

Analytics

For NMR-spectroscopy chloroform-*d*, methanol-d_4 and dimethylsulfoxide-d_6 were used. The standardization of the NMR spectra was performed using the following (residual) proton signals of the solvents:[57]

Chloroform-*d*:	^{1}H-NMR	$\delta = 7.26$ ppm.
	^{13}C-NMR	$\delta = 77.16$ ppm.
Methanol-d_4:	^{1}H-NMR	$\delta = 3.31$ ppm.
	^{13}C-NMR	$\delta = 49.00$ ppm.
DMSO-d_6:	^{1}H-NMR	$\delta = 2.50$ ppm.
	^{13}C-NMR	$\delta = 39.52$ ppm.

For evaluation, the multiplicities of the NMR-Signals were abbreviated as follows: singlet = s, doublet = d, triplet = t, quartet = q and multiplet = m and combinations of these. Coupling constants J are given in Hertz (Hz) and chemical shifts δ in ppm. The following devices were used for recording of the NMR-spectra:

NMR-Spectroscopy	^{1}H-NMR	Bruker Avance III – 300, 300 MHz
		Bruker Avance III – 600, 600 MHz
	^{13}C-NMR	Bruker Avance III – 300, 75 MHz
		Bruker Avance III – 600, 151 MHz

For IR-spectroscopy a Jasco FT/IR-6200 spectrometer was used. Infrared spectra were recorded from samples as a film on a sodium chloride single crystal or on a diamond plate. For evaluation, the intensities of the absorption bands were designated with the following abbreviations: very strong = vs, strong = s, medium = m and weak = w.

Melting points were measured on a Büchi B-540 melting point apparatus and are uncorrected. For mass spectra (HRMS) a Bruker Daltonics UHR-QTOF maXis 4G spectrometer was used.

Experimental details

1) Synthesis of 9-F-MIA (3)

9-F-MIA was synthesized *via* the following route (Scheme S7.1).

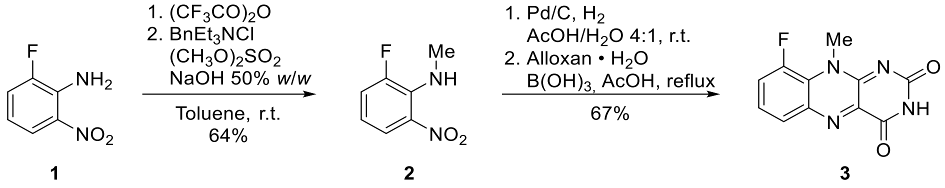

Scheme S7.1. Synthesis route to **9-F-MIA**.

2-Fluoro-N-methyl-6-nitroaniline (2)

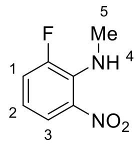

Analogous to the method by Brown and Rizzo,[32] 6-fluoro-2-nitroaniline (**1**) (1.02 g, 6.55 mmol) was suspended in toluene (15.0 mL) and the mixture cooled down to 0 °C. Trifluoroacetic anhydride (1.80 mL, 2.72 g, 12.9 mmol, 2.0 eq) was added and the reaction mixture stirred for 80 min at r.t. resulting in formation of colourless crystals. To the mixture were successively added benzyltriethylammonium chloride (1.50 g, 6.57 mmol, 1.0 eq) and dimethyl sulphate (0.780 mL, 1.04 g, 8.24 mmol, 1.3 eq) and the mixture stirred for 25 min before 50% *w/w* NaOH (6.60 mL) was added. The mixture was stirred for 3 d at r.t. before sat. NH_4Cl-solution (30 mL) and CH_2Cl_2 (20 mL) were added. The layers were separated and the aqueous layer extracted with CH_2Cl_2 (4 x 20 mL). The combined organic layers were dried over Na_2SO_4, filtered and the solvent removed *in vacuo*. Purification via flash chromatography (n-hexane, then n-hexane/EtOAc 6:4) gave the product as red crystals (715 mg, 4.20 mmol, 64%). The spectroscopic data are in agreement with the literature[58]: **^{1}H-NMR** (300 MHz, $CDCl_3$) δ

7.94 (dt, J = 8.8, 1.6, 1.6 Hz, 1H, H-3), 7.83 (s, 1H, H-4), 7.17 (dddd, J = 13.9, 7.8, 1.6, 0.6 Hz, 1H, H-1), 6.55 (ddd, J = 8.8, 7.8, 4.5 Hz, 1H, H-2), 3.25 (dd, J = 7.5, 5.5 Hz, 3H, H-5) ppm.

9-Fluoro-10-methylbenzo[g]pteridine-2,4(3H,10H)-dione (3)

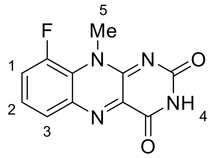

Analogous to the method by Gilch and Czekelius et al.[19] and Averill et al.,[33] a solution of nitroaniline **2** (499 mg, 2.93 mmol) in AcOH/H_2O 4:1 (14.0 mL) was degassed by purging N_2 for 30 min. Pd/C 10% (40.5 mg, 38.1 mmol, 0.01 eq related to Pd) was added and the mixture stirred vigorously under H_2 atmosphere overnight. Then, it was filtered through a syringe filter directly into a degassed (30 min) mixture of alloxan monohydrate (611 mg, 3.81 mmol, 1.3 eq) and $B(OH)_3$ (1.14 g, 18.5 mmol, 6.3 eq) in AcOH (37.0 mL). After refluxing for 1 h, the product was obtained by filtration. Addition of water (150 mL) in this step turned out to be helpful for precipitation. The raw product was obtained as a green powder (494 mg, 1.97 mmol, 67%) with a purity of 98% and 2% of AcOH incorporated. **mp:** Decomposition >280 °C. **^{1}H-NMR** (300 MHz, DMSO-*d₆*) δ 11.49 (s, 1H, H-4), 7.97 (dt, J = 8.1, 1.2 Hz, 1H, H-3), 7.83 (ddd, J = 14.4, 8.2, 1.5 Hz, 1H, H-1), 7.60 (td, J = 8.2, 4.8 Hz, 1H, H-2), 4.09 (d, J = 7.2 Hz, 3H, H-5) ppm. **^{13}C{^{1}H}-NMR** (151 MHz, DMSO-d_6) δ 158.53, 154.48, 151.13, 149.71 (d, J = 250.3 Hz), 138.83, 135.97, 127.66 (d, J = 3.6 Hz), 125.06 (d, J = 8.9 Hz), 122.80 (d, J = 6.2 Hz), 120.75 (d, J = 23.2 Hz), 35.41 (d, J = 15.9 Hz) ppm. **^{19}F{^{1}H}-NMR** (282 MHz, DMSO-d_6) δ -120.48 ppm. **IR (Film):** $\tilde{\upsilon}$ [cm^{-1}] 3186 (w), 3067 (w), 1665 (m), 1614 (w), 1582 (m), 1547 (m), 1508 (m), 1466 (s), 1400 (m), 1271 (m), 1246 (m), 1204 (s), 1065 (w), 1022 (w). **HRMS (ESI):** m/z = 247.0626 [M+H$^+$] (calculated: 247.0626).

Purification procedure for photophysical measurements:

The raw product (198 mg) was dissolved in CF_3CH_2OH (90 mL) by heating to 80 °C and the solution filtered hot through a Büchner funnel. The filtrate was cooled to 0 °C for 7 days before the product was filtered off through a Büchner funnel giving a pre-purified product (118 mg). Then, this material was again dissolved in CF_3CH_2OH (40 mL) by heating to 80 °C, EtOAc (10 mL) was layered on top, and the two-layer system stored at 0 °C overnight. The product was filtered off, giving the product in >99% purity as a green powder with <1% CF_3CH_2OH incorporated (59.8 mg).

2) Synthesis of 7,8-dF-MIA (8)

7,8-dF-MIA was synthesized *via* the following route (Scheme S7.2):

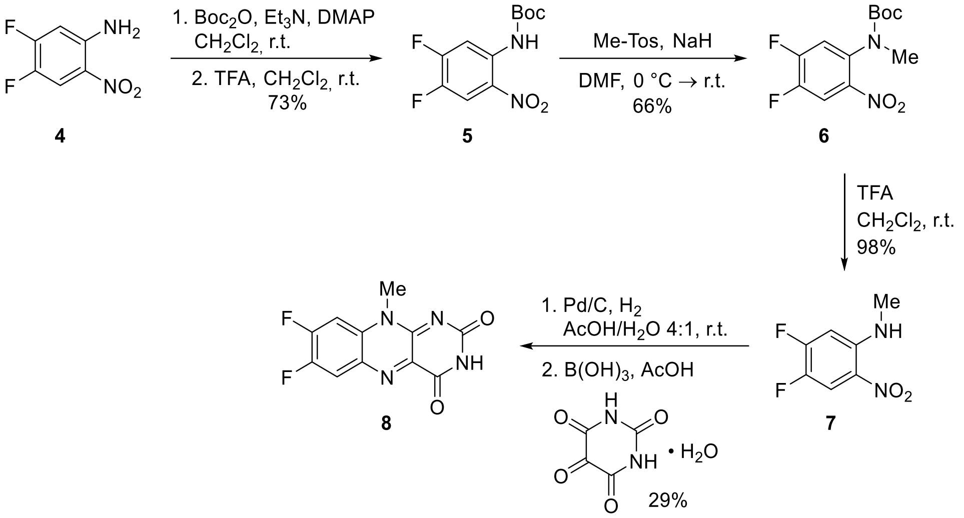

Scheme S7.2. Synthesis route to **7,8-dF-MIA** (**8**).

tert-Butyl (4,5-difluoro-2-nitrophenyl)carbamate (5)

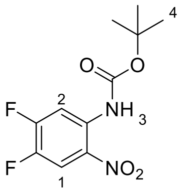

Analogous to the protocol by Xie and Liao et al.[34] 4,5-fluoro-2-nitroaniline (**4**) (296 mg (1.70 mmol) was dissolved in CH_2Cl_2 (4.20 mL) and Boc_2O (830 µL, 789 mg, 3.61 mmol, 2.1 eq) as well as NET_3 (360 µL, 261 mg, 2.58 mmol, 1.5 eq) were added dropwise. The mixture was stirred at r.t. for 5 min before addition of DMAP (20.8 mg, 170 µmol, 0.1 eq) and stirring for 35 min continued. Then, the solvent was evaporated and the residue dissolved in CH_2Cl_2 (780 µL). To the solution cooled to 0 °C TFA (200 µL, 298 mg, 2.61 mmol, 1.5 eq) was added slowly and the mixture stirred at 0 °C for 5 min and at r.t. for 2 h. To complete conversion, additional TFA (200 µL, 298 mg, 2.61 mmol, 1.5 eq) was added, and the mixture stirred at r.t. for 10 min. Then, sat. Na_2CO_3-solution (6.00 mL) was added, the phases separated, and the aqueous phase extracted with CH_2Cl_2 (4 x 3 mL). The combined organic phases were dried over Na_2SO_4, filtered and the solvent removed *in vacuo*. Purification **via** flash chromatography (n-hexane/EtOAc 99:1) gave the product as a yellow powder 339 mg (1.24 mmol, 73%). **m.p.** 94.5 – 97.3 °C. **^{1}H-NMR** (600 MHz, $CDCl_3$) δ 9.76 (s, 1H, H-3), 8.59 (dd, J = 13.0, 7.5 Hz, 1H, H-1), 8.09 (dd, J = 10.1, 8.0 Hz, 1H, H-2), 1.54 (s, 9H, H-4) ppm. **^{13}C{^{1}H}-NMR** (151 MHz, $CDCl_3$) δ 155.02 (dd, J = 259.4, 12.9 Hz), 152.03, 144.28 (dd, J =

249.2, 14.3 Hz), 134.65 – 134.28 (m), 130.97, 114.96 (dd, J = 22.5, 3.2 Hz), 109.29 (d, J = 25.4 Hz), 82.80, 28.28 ppm. **^{19}F{^{1}H}-NMR** (565 MHz, $CDCl_3$) δ -121.14 (d, J = 23.0 Hz), -141.64 (d, J = 23.0 Hz) ppm. **IR (Film):** $\tilde{\upsilon}$ [cm^{-1}] 3366 (m), 3104 (w), 3088 (w), 2983 (m), 2936 (w), 1739 (vs), 1599 (s), 1530 (vs), 1456 (s), 1343 (s), 1312 (s), 1285 (vs), 1232 (s), 1148 (vs), 1069 (m). **HRMS (ESI):** m/z = 297.0653 [M+Na$^+$] (calculated: 297.0657).

tert-Butyl (4,5-difluoro-2-nitrophenyl)(methyl)carbamate (6)

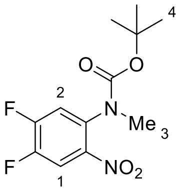

The reaction was done analogous to the method by Xie and Liao et al.[34]: To a pre-cooled (0 °C) solution of Boc-protected amine **5** (4.91 g, 17.9 mmol) in DMF (90.0 mL) NaH, 60% dispersion in mineral oil (1.47 g, 36.8 mmol, 2.1 eq) was added. The mixture was stirred for 10 min at 0 °C before methyl p-toluenesulfonate (3.00 mL, 3.70 g, 19.9 mmol, 1.1 eq) was added and the mixture stirred for another 10 min at 0 °C before being stirred at r.t. for 5 h. Finally, ice was added in small portions followed by water (180 mL) and EtOAc (80 mL). The phases were separated and the aqueous phase extracted with EtOAc (2 x 80 mL). The combined organic layers were dried over Na_2SO_4, filtered, and the solvent removed *in vacuo*. Purification *via* flash chromatography (n-hexane/EtOAc 99:1 – 9:1) gave the product as a yellow powder (3.41 g, 11.8 mmol, 66%). **m.p.** 75.2 – 76.5 °C. **^{1}H-NMR** (300 MHz, $CDCl_3$) δ 7.83 (t, J = 8.6 Hz, 1H, H-1), 7.18 (dd, J = 10.2, 7.1 Hz, 1H, H-2), 3.25 (s, 3H, H-3), 1.55 – 1.20 (m, 9H, H-4) ppm. **^{13}C{^{1}H}-NMR** (75 MHz, $CDCl_3$) δ 152.80 (dd, J = 260.0, 13.6 Hz), 152.79, 147.76 (dd, J = 254.0, 13.6 Hz), 142.11, 135.15, 118.06 (d, J = 19.2 Hz), 114.86 (d, J = 22.2 Hz), 82.26, 37.58 (d, J = 33.4 Hz), 28.06 (d, J = 32.5 Hz) ppm. **^{19}F{^{1}H}-NMR** (282 MHz, $CDCl_3$) δ -126.15 (dd, J = 84.8, 21.6 Hz), -135.07 (dd, J = 89.6, 21.7 Hz) ppm. **IR (Film):** $\tilde{\upsilon}$ [cm^{-1}] 2979 (w), 2362 (w), 1714 (s), 1605 (w), 1543 (s), 1346 (s), 1263 (m), 1153 (m). **HRMS (ESI):** m/z = 289.0994 [M+H$^+$] (calculated: 289.0990).

4,5-Difluoro-N-methyl-2-nitroaniline (7)

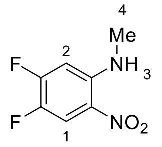

The reaction was done analogous to the method by Xie and Liao et al.[34]: To a pre-cooled (0 °C) solution of methylated Boc-protected amine **6** (603 mg, 2.09 mmol) in CH_2Cl_2 (1.00 mL) TFA (250 µL, 372 mg, 3.26 mmol, 1.6 eq) was added and the mixture stirred at r.t. for 3.5 h. Then, additional TFA (120 µL, 179 mg, 1.57 mmol, 0.8 eq) was added and the mixture stirred at r.t. for 2.5 h. Sat. Na_2CO_3-solution (10 mL) was added, the phases separated, and the aqueous phase extracted with CH_2Cl_2 (5 x 3 mL). The combined organic layers were dried over Na_2SO_4, filtered, and the solvent removed *in vacuo*. Purification *via* flash chromatography (n-hexane/EtOAc 99:1) gave the product as a yellow powder (386 mg, 2.05 mmol, 98%). **m.p.** 114.6 – 116.0 °C. **^{1}H-NMR** (300 MHz, $CDCl_3$) δ 8.05 (m, 2H, H-1,3), 6.60 (dd, J = 12.5, 6.7 Hz, 1H, H-2), 3.00 (d, J = 5.1 Hz, 3H, H-4) ppm. **^{13}C{^{1}H}-NMR** (75 MHz, $CDCl_3$) δ 156.50 (dd, J = 259.4, 14.5 Hz), 144.89 (d, J = 11.0 Hz), 140.88 (dd, J = 241.8, 14.8 Hz), 126.60 (m), 115.25 (dd, J = 21.6, 3.7 Hz), 100.95 (d, J = 22.6 Hz), 30.22 ppm. **^{19}F{^{1}H}-NMR** (282 MHz, $CDCl_3$) δ -121.86 (d, J = 23.2 Hz), -150.91 (d, J = 23.9 Hz) ppm. **IR (Film):** $\tilde{\upsilon}$ [cm^{-1}] 3384 (m), 3074 (w), 1648 (m), 1578 (s), 1527 (vs), 1457 (m), 1407 (s), 1310 (m), 1262 (s), 1235 (s), 1028 (s). **HRMS (ESI):** m/z = 189.0469 [M+H$^+$] (calculated: 189.0470).

7,8-Difluoro-10-methylbenzo[*g*]pteridine-2,4(3H,10H)-dione (8)

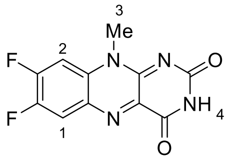

The reaction was done following the method by Gilch and Czekelius et al.[19] and Averill et al.[33]: A solution of *N*-methyl-nitroaniline **7** (1.39 g, 7.39 mmol) in AcOH (36.0 mL) and water (9.00 mL) was degassed by purging N_2 for 20 min. Then, Pd/C (10%, 111 mg, 105 µmol, 0.01 eq) was added, the reaction vessel set under H_2-atmosphere and the mixture stirred at r.t. overnight. The colourless mixture was filtered through a syringe filter directly into a degassed mixture (N_2-purge for 30 min) of alloxan monohydrate (1.53 g, 9.56 mmol, 1.3 eq) and $B(OH)_3$ (2.88 g, 46.5 mmol, 6.3 eq) in AcOH (90.0 mL). It was stirred for 1 h at r.t. before the solution was concentrated using high vacuum to 5-10 mL. The residue was suspended with cold water and filtered using a glass frit. The precipitate was washed with cold water and cold

EtOH in small portions giving the raw product as a green powder (2.26 g). NMR-spectroscopy showed a mixture of product, alloxazine and unknown monofluorinated side product 1:0.4:0.2. A fraction of the raw material (1.93 g) was submitted to the optimized purification protocol (see below) and the yield of pure product calculated accordingly (482 mg, 1.82 mmol, 29% orange-yellow powder). **m.p.** decomposition >200 °C. **^{1}H-NMR** (300 MHz, DMSO-*d$_6$*) δ 11.45 (s, 1H, H-4), 8.35 (dd, J = 10.5, 8.4 Hz, 1H, H-1), 8.18 (dd, J = 12.5, 7.4 Hz, 1H, H-2), 3.93 (s, 3H, H-3) ppm. **^{13}C{^{1}H}-NMR** (75 MHz, DMSO-*d$_6$*) 159.40, 155.38, 153.59 (dd, J = 271.1, 14.4 Hz), 150.84, 147.55 (dd, J = 248.3, 15.3 Hz), 139.08 (d, J = 3.7 Hz), 131.64 (d, J = 10.7 Hz), 131.33 (d, J = 10.7 Hz), 118.77 (d, J = 17.7 Hz), 105.61 (d, J = 24.0 Hz), 32.68 ppm. **^{19}F{^{1}H}-NMR** (282 MHz, DMSO-*d$_6$*) δ -124.56 (d, J = 23.6 Hz), -139.03 (d, J = 23.8 Hz) ppm. **IR (Film):** $\tilde{\upsilon}$ [cm^{-1}] 3028 (w), 1712 (m), 1643 (m), 1547 (s), 1537 (s), 1504 (s), 1395 (m), 1298 (m), 1275 (s) 1238 (vs), 1211 (s). **HRMS (ESI):** m/z = 265.0532 [M+H$^+$] (calculated: 265.0532).

*Purification procedure of **7,8-dF-MIA (8)** for photophysical measurements:*

1.93 g of raw product **8** was subsequently suspended in ca. 5 mL CF_3CH_2OH and ca. 5 mL MeOH and the supernatant solution applied onto a prepacked column (silica gel). Flash chromatography was performed with EtOAc/MeOH 95:5 as eluent. The undissolved residue of material was dried *in vacuo* and suspended again in CF_3CH_2OH and MeOH, respectively. With this procedure 15 consecutive flash chromatographies were performed giving a total yield of 482 mg product with a purity of >99% and <1% CF_3CH_2OH incorporated.

2) Synthesis of 7,8-dF-riboflavin (13)

7,8-dF-Riboflavin (**7,8-dF-RIA**) was synthesized following a modified protocol by Gärtner et al.[36] according to the synthesis route shown in Scheme S7.3.

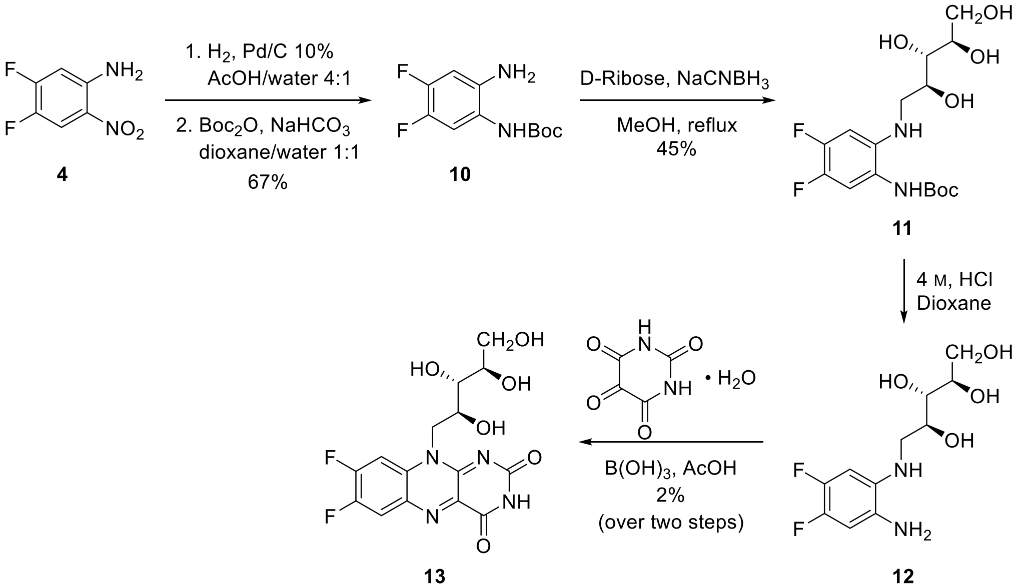

Scheme S7.3. Synthesis route to **7,8-dF-RIA** (**13**).

tert-Butyl(2-amino-4,5-difluorophenyl)carbamate (10)

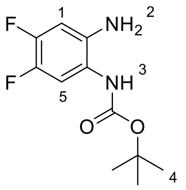

Nitroaniline **4** (3.00 g, 17.2 mmol) was dissolved in a mixture of AcOH (85.0 mL) and water (21 mL) and Pd/C (10%, 246 mg, 231 µmol, 0.01 eq) was added. The mixture was degassed by purging N_2 through for 30 min before purging with H_2 for 5 min and finally setting the flask under H_2 atmosphere. After stirring at r.t. for 5.5 h, the flask was set under nitrogen atmosphere overnight. The mixture was filtered through a syringe filter into a new flask and the solvent was removed under inert conditions using high vacuum. Dissolving the residue in a degassed mixture of dioxane (120 mL) and water (120 mL) was followed by addition of $NaHCO_3$ (1.45 g, 17.3 mmol, 1.0 eq) and Boc_2O (4.00 mL, 3.80 g, 17.4 mmol, 1.0 eq). After stirring at r.t. for 24 h and 42 h additional Boc_2O (1st: 1.50 mL, 1.43 g, 6.53 mmol, 0.38 eq; 2nd: 1.00 mL, 950 mg, 4.35 mmol, 0.25 eq) was added. After stirring for 44 h altogether, water (210 mL) was added and the product extracted with 3 x 150 mL CH_2Cl_2. The combined organic phases were washed with 100 mL sat. $NaHCO_3$-solution and 100 mL brine, dried over Na_2SO_4, filtered, and the solvent removed *in vacuo*. Flash chromatography (n-hexane/EtOAc 9:1 – 6:4) furnished carbamate 10 as a beige powder (2.81 g, 11.5 mmol, 67%). **m.p.** 142.2 – 144.9°C. **^{1}H-NMR** (300 MHz, $CDCl_3$) δ 7.31 – 7.18 (m, 1H, H-5), 6.57 (dd, J = 11.4, 7.6 Hz, 1H, H-1), 6.15 (brs, 1H, H-3), 3.59 (brs, 2H, H-2), 1.51 (s, 9H, H-4) ppm. **^{13}C{^{1}H}-NMR** (75 MHz, $CDCl_3$) δ 153.69, 147.98 (dd, J = 244.5, 13.4 Hz), 143.64 (dd, J = 239.1, 13.4 Hz), 136.13, 120.85, 113.43 (d, J = 20.3 Hz), 105.96 (d, J = 20.1 Hz), 81.22, 28.40 ppm. **^{19}F{^{1}H}-NMR** (282 MHz, $CDCl_3$) δ -141.22, -148.31 ppm. **IR (Film):** $\tilde{\upsilon}$ [cm^{-1}] 3440 (m), 3361 (m), 3290 (s), 3049 (w), 2993 (m), 1677 (vs), 1508 (vs), 1439 (s), 1369 (m), 1282 (m), 1221 (m), 1156 (m). **HRMS (ESI):** m/z = 245.1099 [M+H^{+}] (calculated: 245.1096).

tert-Butyl(4,5-difluoro-2-(((2S,3S,4R)-2,3,4,5-tetrahydroxypentyl)amino)phenyl) carbamate (11)

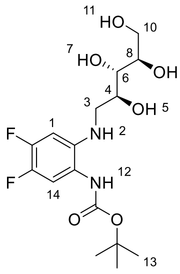

Boc-protected aniline **10** (1.43 g, 5.85 mmol) was dissolved in MeOH (120 mL) and D-ribose (3.43 g, 22.9 mmol, 3.9 eq) and $NaCNBH_3$ (1.47 g, 23.4 mmol, 4.0 eq) were added. The mixture was purged with N_2 for 30 min and refluxed overnight before evaporation of the solvent. To the residue was slowly added 1 m HCl (60 mL) until gas formation stopped and subsequently neutralized using sat. $NaHCO_3$-solution. After extraction with 4 x 90 mL EtOAc were the combined organic phases dried over Na_2SO_4, filtered and the solvent removed *in vacuo*. Flash chromatography (CH_2Cl_2/MeOH 95:5 – 9:1) gave the desired riboaniline **11** as a white powder (1.01 g, 2.66 mmol, 45%; recovery starting material: 423 mg, 1.73 mmol, 30%). **m.p.** 49.8 – 53.4 °C. **^{1}H-NMR** (300 MHz, MeOD) δ 7.09 (dd, J = 11.6, 8.4 Hz, 1H, H-14), 6.62 (dd, J = 13.3, 7.8 Hz, 1H, H-1), 3.93 (ddd, J = 7.6, 6.1, 3.3 Hz, 1H, H-4), 3.84 – 3.57 (m, 4H, H-6,8,10), 3.38 (dd, J = 12.9, 3.4 Hz, 1H, H-3), 3.16 (dd, J = 12.8, 7.7 Hz, 1H, H-3'), 1.50 (s, 9H, H-13) ppm. **^{13}C{^{1}H}-NMR** (75 MHz, MeOD) δ 156.68, 149.97 (dd, J = 241.3, 12.9 Hz), 142.50 (dd, J = 234.6, 13.7 Hz), 142.07, 120.60 (dd, J = 7.5, 3.0 Hz), 115.96 (d, J = 19.6 Hz), 101.06 (d, J = 22.3 Hz), 81.41, 74.47, 74.38, 71.87, 64.64, 47.32, 28.65 ppm. **^{19}F-NMR** (282 MHz, MeOD) δ -142.89 (d, J = 22.3 Hz), -155.70 (d, J = 22.5 Hz) ppm. **IR (Film):** $\tilde{\upsilon}$ [cm^{-1}] 3312 (w), 2972 (w), 1685 (m), 1525 (s), 1368 (m), 1233 (m), 1155 (s), 1051 (s). **HRMS (ESI):** m/z = 379.1682 [M+H^{+}] (calculated: 379.1675).

7,8-Difluoro-10-((2S,3S,4R)-2,3,4,5-tetrahydroxypentyl)benzo[*g*]pteridine-2,4-(3*H*,10*H*)-dione (13)

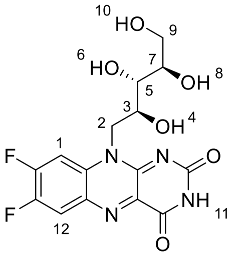

Boc-protected riboaniline **11** (500 mg, 1.32 mmol) was dissolved in dioxane (15.0 mL) and conc. HCl (7.50 mL) was added slowly. The mixture was degassed by purging N_2 through for 15 min and then stirred at r.t. under N_2 atmosphere for 2.5 h. The solvent was removed *in vacuo*, the residue dissolved in water (150 mL) and extracted with 3 x 30 mL ET_2O. The aqueous phase was lyophilized and the ribitylated aniline **12** as the residue directly dissolved in AcOH/water 4:1 (11 mL). Alloxan monohydrate (40.7 mg, 254 µmol, 3.6 eq) and $B(OH)_3$ (16.4 mg, 265 µmol, 3.8 eq) were added, the mixture degassed by purging N_2 through for 30 min and stirred at r.t. overnight. The solvent was removed *in vacuo* and the residue suspended in toluene/water 1:1 (20 mL). It was stirred for 10 min before removal of the solvent *in vacuo* to give 337 mg raw product. A fraction of the raw material (80.0 mg) was submitted to the optimized purification protocol (see below) and the yield of pure product calculated accordingly (11.0 mg, 28.5 µmol, 2.2% yellow powder). **^{1}H-NMR** (300 MHz, MeOD) δ 8.13 (dd, J = 12.4, 7.4 Hz, 1H, H-12), 8.01 (dd, J = 10.0, 8.3 Hz, 1H, H-1), 4.93 – 4.77 (m, 2H, CHOH), 4.32 (dt, J = 9.0, 3.7 Hz, 1H, CHOH), 3.81 – 3.52 (m, 4H, H-2,9) ppm. **^{19}F{^{1}H}-NMR** (282 MHz, MeOD) δ -124.22 (d, J = 21.7 Hz), -139.10 (d, J = 21.8 Hz) ppm. **HRMS (ESI):** m/z = 385.0954 [M+H$^+$] (calculated: 385.0954).

Purification method for photophysical measurements:

80.0 mg raw product was dissolved in water (150 mL) and the solution concentrated at max. 38 °C stepwise in a 50 mL flask to an amount of ~5 mL. The residue was stored in a fridge overnight. The precipitate was filtered off using a glass frit. The filtrate was disposed and the solid (54.5 mg) redissolved in water (50 mL). Evaporation of water was performed following the described procedure and the concentrate (~4 mL) stored in the fridge until precipitation occurred. The solvent was removed via pipette and retained (filtrate 1). The precipitate was dissolved again in water (30 mL), evaporated to ~4 mL and stored in the fridge until precipitation occurred. The solvent was removed via pipette, combined with filtrate 1 and the solvent was removed *in vacuo*. The residue was dissolved in MeOH (6 mL), filtered and the solvent removed *in vacuo* before dissolving in MeOH (4 mL) again and addition of ET_2O (80 mL) in one batch. The solvent was removed via pipette and the residue dissolved in 8.0 mL CF_3CH_2OH, filtered, and evaporated. The residue was dissolved in MeOH (2 mL) and purified via two separate HPLC runs with water/MeOH 95:5 – 9:1 (60 min). The product was obtained in pure form as a yellow powder (2.6 mg).

Impact of the deuterated solvent D_2O on the fluorescence

Fluorescence lifetimes were measured by time-correlated single photon counting (TCSPC) in both H_2O and D_2O. All the investigated dyes have significantly longer fluorescence lifetimes in D_2O. Fluorescence decays in D_2O are shown in Figure S7.356.

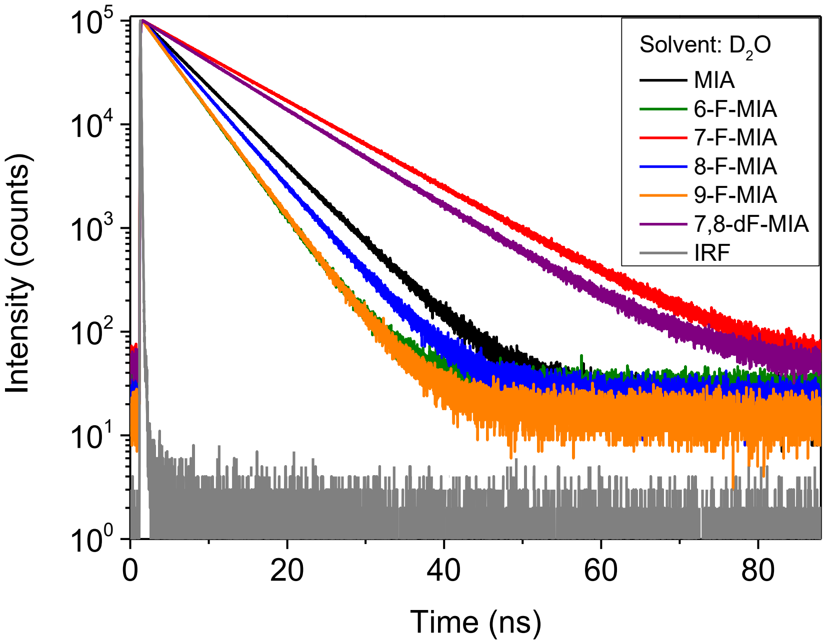

Figure S7.356. Fluorescence decays in D_2O measured by TCSPC.

In order to elucidate the impact of the deuterated solvent D_2O on the fluorescence lifetimes, we need to introduce a quenching constant in water, k_{qw}. Since we are interested in a systematic dependency for all **MIA** derivatives, we assume that all the derivatives have the same quenching constant and therefore, the term average quenching constant, $\overline{k_{qw}}$ is used. Assuming that quenching is present in water, the rate constants of S_1 depopulation k_{S1} in H_2O and D_2O differ by the quenching constant:

$$k_{S1}^{(H_2O)} = k_{rad}^{(H_2O)} + k_{IC}^{(H_2O)} + k_{ISC}^{(H_2O)} + \overline{k_{qw}} \tag{S1}$$

$$k_{S1}^{(D_2O)} = k_{rad}^{(D_2O)} + k_{IC}^{(D_2O)} + k_{ISC}^{(D_2O)} \tag{S2}$$

The solvent is marked in the superscript. The radiative rate constant k_{rad} is obtained from the Strickler-Berg analysis and presents the rate constant for the emitter with no non-radiative transitions. The internal conversion and intersystem crossing rates are given in Table 7.13, and for the sake of simplicity, a non-radiative rate constant is introduced as a sum of these two constants (eq. S3).

$$k_{nr} = k_{IC} + k_{ISC} \tag{S3}$$

Finally, the respective lifetimes in H_2O and D_2O can be expressed as following using the experimental observation that the shape of the spectra in H_2O an D_2O does change, i.e.

$$k_{rad}^{(H_2O)} = k_{rad}^{(D_2O)} = k_{rad}$$

$$\tau_{fl}^{(H_2O)} = \frac{1}{k_{S1}^{(H_2O)}} = \frac{1}{k_{rad} + k_{nr}^{(H_2O)} + \overline{k_{qw}}} \tag{S4}$$

$$\tau_{fl}^{(D_2O)} = \frac{1}{k_{S1}^{(D_2O)}} = \frac{1}{k_{rad} + k_{nr}^{(D_2O)}} \tag{S5}$$

Their ratio is equal to:

$$\frac{\tau_{fl}^{(D_2O)}}{\tau_{fl}^{(H_2O)}} = \frac{k_{rad} + k_{nr}^{(H_2O)} + \overline{k_{qw}}}{k_{rad} + k_{nr}^{(D_2O)}}. \tag{S6}$$

Taking into account the following assumption:

$$k_{rad} + k_{nr}^{(D_2O)} = k_{rad} + k_{nr}^{(H_2O)}, \tag{S7}$$

we gain:

$$\frac{\tau_{fl}^{(D_2O)}}{\tau_{fl}^{(H_2O)}} = 1 + \frac{\overline{k_{qw}}}{k_{rad} + k_{nr}^{(D_2O)}}. \tag{S8}$$

This equation can be rewritten as a Stern-Volmer type equation:

$$\frac{\tau_{fl}^{(D_2O)}}{\tau_{fl}^{(H_2O)}} = 1 + \overline{k_{qw}} \cdot \tau_{fl}^{(D_2O)} \tag{S9}$$

The dependency $\tau_{fl}^{(D_2O)}/\tau_{fl}^{(H_2O)}$ against $\tau_{fl}^{(D_2O)}$ is called the Stern-Volmer plot, and it is shown in Figure 7.42 in the main text of the manuscript. The average quenching constant in water $\overline{k_{qw}}$ is obtained as the slope of the linear regression.

Impact of the ribityl group

7,8-dF-MIA and **7,8-dF-RIA** in D_2O were measured at 20.5 °C, excited with P = 96 µW and detected employing Hybrid PMTs (HPM-100-40, Becker&Hickl) under otherwise identical conditions as **7-F-MIA**. Besides the formal fit [combination of Equations (1)-(4)] was fit to the averaged FCS-curves using a custom script in ORIGIN 8.6 (OriginLab Corporation) to directly yield the rate constants corresponding to the kinetic model in Figure 7.45. In these fits the fluorescence rate constants k_0 were fixed using the independently measured fluorescence lifetimes in D_2O (**7,8-dF-MIA**: τ_{fl} = 9.29 ns, **7,8-dF-RIA**: τ_{fl} = 6.53 ns). Due to the high correlation between the fit parameters also the excitation rate needed to be approximated and fixed in the fit. To that end, the best fit of the excitation rate from **7-F-MIA** measured in D_2O was scaled for the different excitation power and the different extinction coefficient (ε = 10560 $M^{-1}cm^{-1}$ at 440 nm for **7,8-dF-MIA** in H_2O, the ratio for the two molecules is assumed to be identical in D_2O and H_2O). Thus, an excitation rate for **7,8-dF-MIA** of $k_{01} = 0.51 \cdot 10^7$ s^{-1} is estimated. This assumption yields an intersystem crossing rate of $k_{ISC} = 2.3 \cdot 10^7$ s^{-1} (± 13%) and a triplet depopulation rate of $k_T = 0.039 \cdot 10^7$ s^{-1} (± 10%) for **7,8-dF-MIA** in D_2O. Under our measurement conditions, we observe a high triplet fraction of **7,8-dF-MIA**, so that the signal in the centre of the detection volume is saturated. This results in a broadened correlation function and a systematically smaller k_{ISC}[46] Under these circumstances the values of k_{ISC} obtained by FCS and transient absorption spectroscopy (Table 7.13) are consistent. Notably, FCS obtains very similar values of **7-F-MIA** in water $k_{ISC} = 2.58 \cdot 10^7$ s^{-1}. Assuming the same excitation rate for **7,8-dF-RIA** in D_2O, $k_{ISC} = 1.54 \cdot 10^7$ s^{-1} (± 21%) and $k_T = 0.051 \cdot 10^7$ s^{-1} (± 17%) are obtained. Error bars are standard errors of the fit and do not include possible systematic errors due to uncertainties in the excitation rate or the inhomogeneous illumination profile (see description in Methods). The corresponding quantum yields for intersystem crossing for **7,8-dF-MIA** and **7,8-dF-RIA** in D_2O are $\Phi_{ISC} = 0.22$ and $\Phi_{ISC} = 0.10$, respectively.

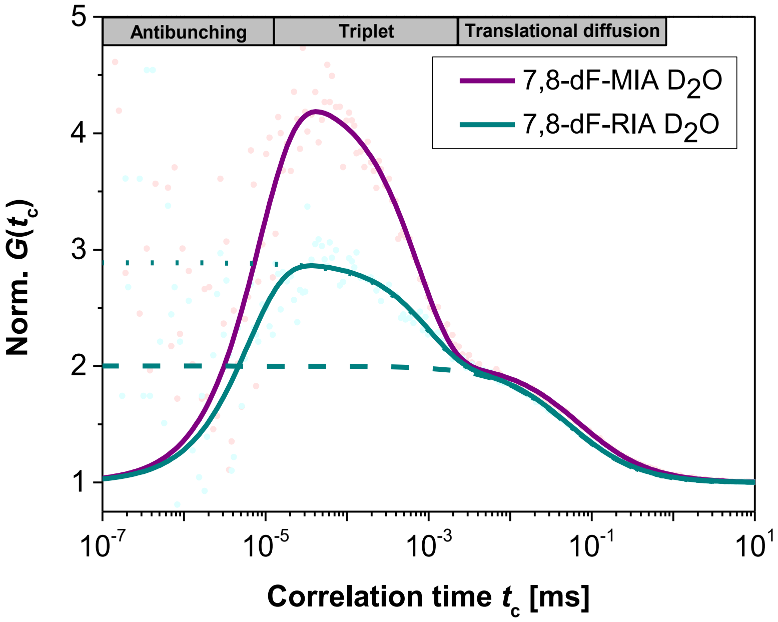

Figure S7.357. Normalized and averaged full correlation curves G(t_c) of **7,8-dF-MIA** and **7,8-dF-RIA** in D_2O. The dashed lines represent the contributions of the translational diffusion and triplet term to the fitted model function [Eq. (6)] with additional parameters listed in Table S7.51.

Table S7.51. Parameters of formal fits [Eq. (6)] to the averaged curves

Sample	N_s	t_d / µs	z_0 / ω_0	T_{1eq}	t_T / µs	AB	t_{AB} / ns
7,8-dF-MIA / D_2O	25.1	70[a]	10 (fixed)	0.69	0.75	1 (fixed)	8.7
7,8-dF-RIA / D_2O	3.5	52	10 (fixed)	0.47	1.01	1 (fixed)	6.2

[a] due to the high triplet fraction, the signal is saturated that results in a broadened correlation function with increased apparent diffusion time t_d. Due to the smaller fluorescence quantum yield of **7,8-dF-RIA**, the triplet population is significantly smaller, so that G(t_c) is much less saturated.

Triplet quantum yield (relative method)

Nanosecond transient absorption data were acquired as described in the methods section. Typical data are shown in Figure S7.358 and Figure S7.359.

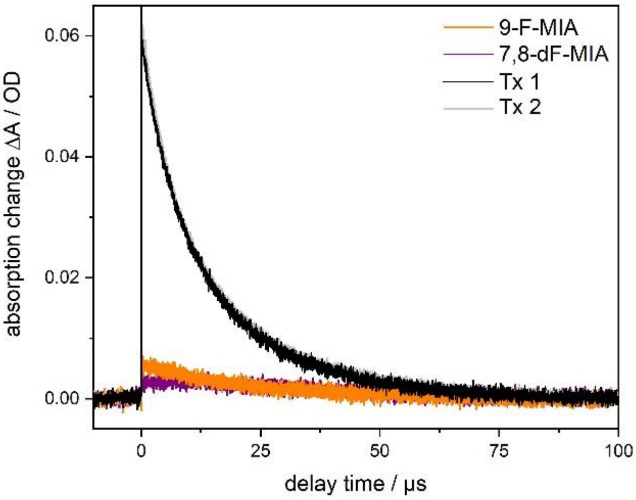

Figure S7.358. Nanosecond transient absorption time trace at 600 nm for the samples and the reference. The recorded time zero signals of the samples ($\Delta A_{\mathrm{t=0}}(\lambda_{\mathrm{Pr}})$) and the reference ($\Delta A^{\mathrm{r}}_{\mathrm{t=0}}(\lambda_{\mathrm{Pr}})$) were on the order of ~5 mOD and 60 mOD, respectively. The sample solutions (nitrogen-purged water) as well as the reference (thioxanthone (Tx)) solution (nitrogen-purged methanol) were excited at 355 nm. Tx was measured before the sample solutions (Tx 1) and afterwards (Tx 2).

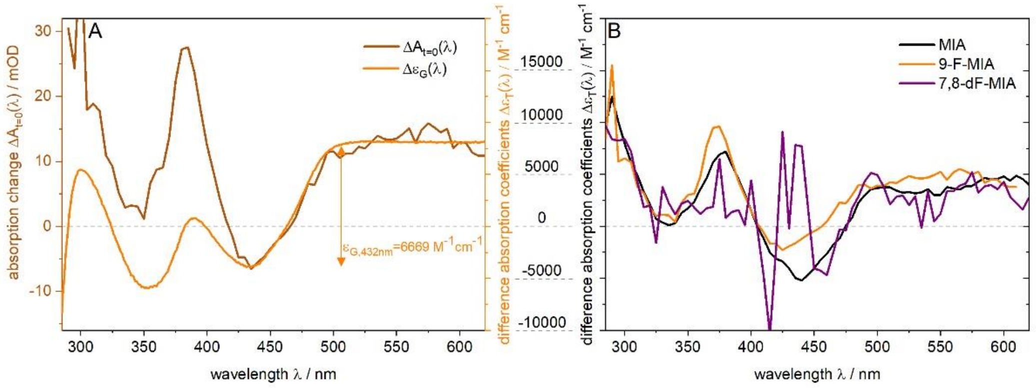

Figure S7.359. Relative method for determining difference absorption coefficients $\Delta\varepsilon_{\mathrm{T}}(\lambda)$. **A:** The ground state bleach of the time zero spectrum $\Delta A_{\mathrm{t=0}}(\lambda)$ (dark orange) is aligned with the ground state absorption spectrum (orange), respectively, exemplified for **9-F-MIA**. **B:** Triplet difference absorption coefficients $\Delta\varepsilon_{\mathrm{T}}(\lambda)$ for all **MIA** derivatives studied in this paper.

Spectra

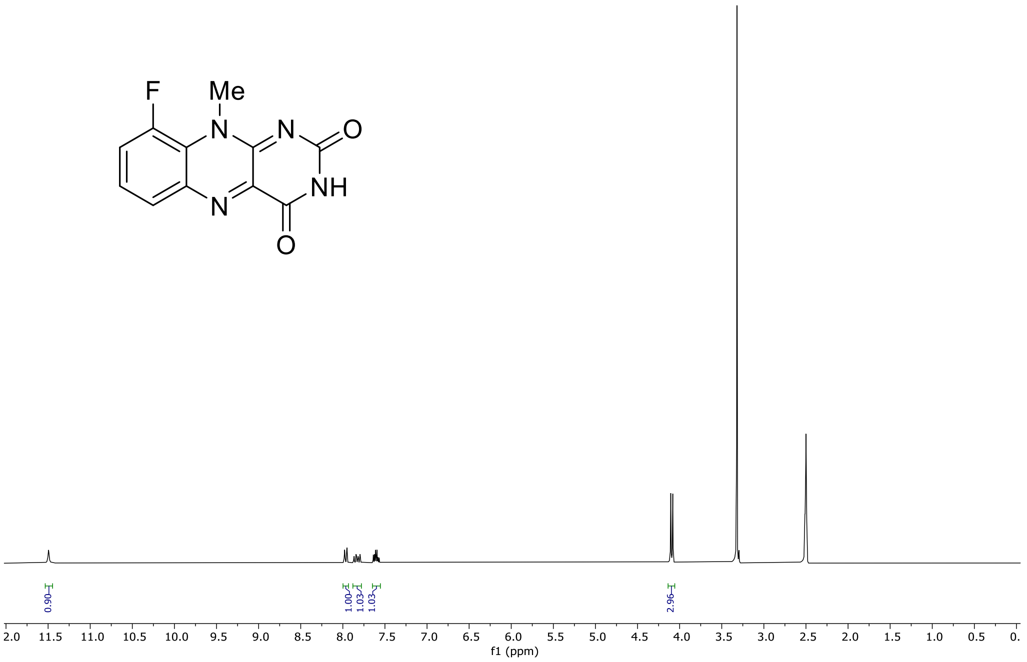

Figure S7.360. ^{1}H-NMR spectrum (300 MHz, DMSO-d_6) of 9-fluoro-10-methylbenzo[*g*]pteridine-2,4(3*H*,10*H*)-dione (**3**).

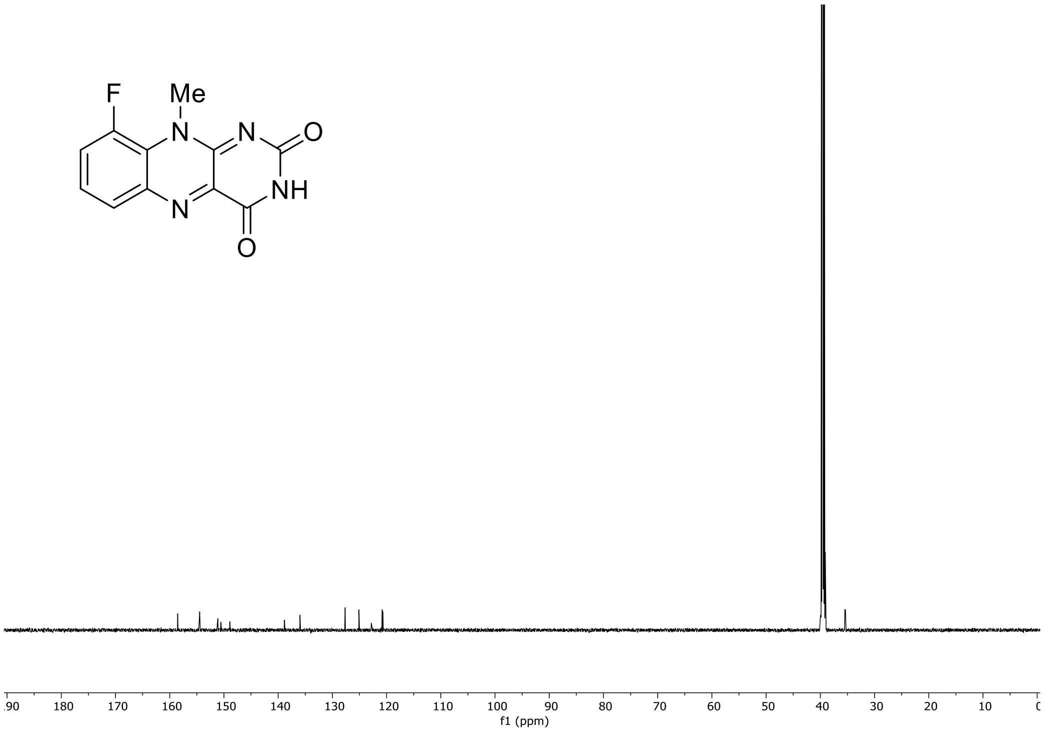

Figure S7.361. ^{13}C{^{1}H}-NMR spectrum (151 MHz, DMSO-d_6) of 9-fluoro-10-methylbenzo[*g*]pteridine-2,4(3*H*,10*H*)-dione (**3**).

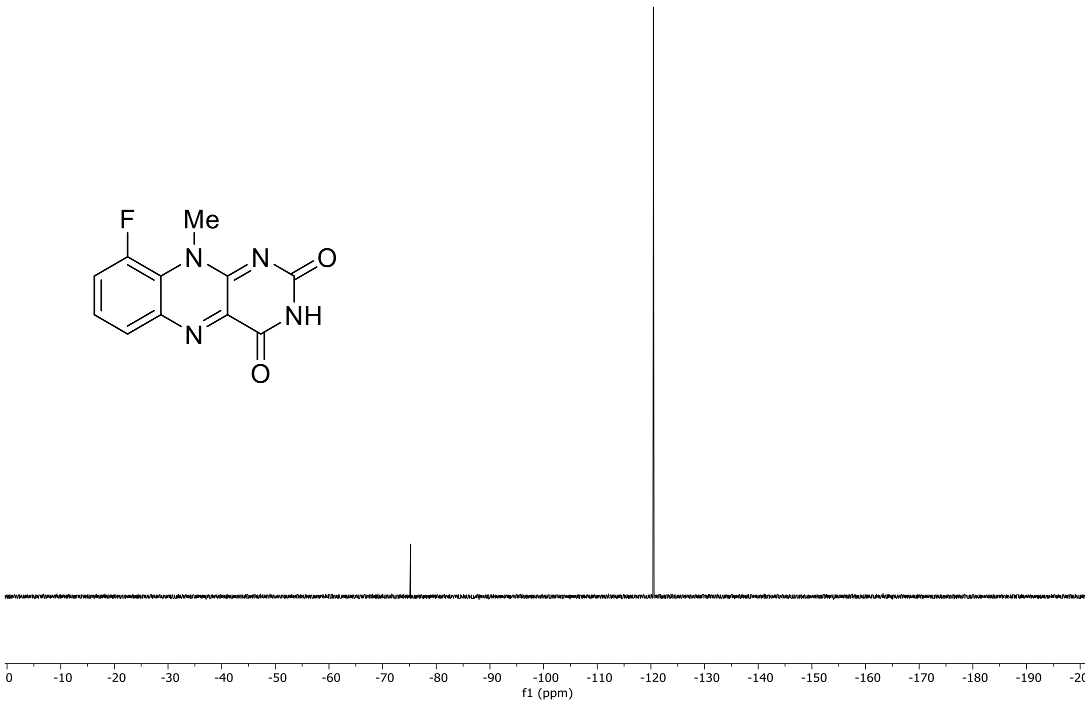

Figure S7.362. $^{19}F\{^{1}H\}$-NMR spectrum (282 MHz, DMSO-d_6) of 9-fluoro-10-methylbenzo[*g*]pteridine-2,4(3*H*,10*H*)-dione (**3**).

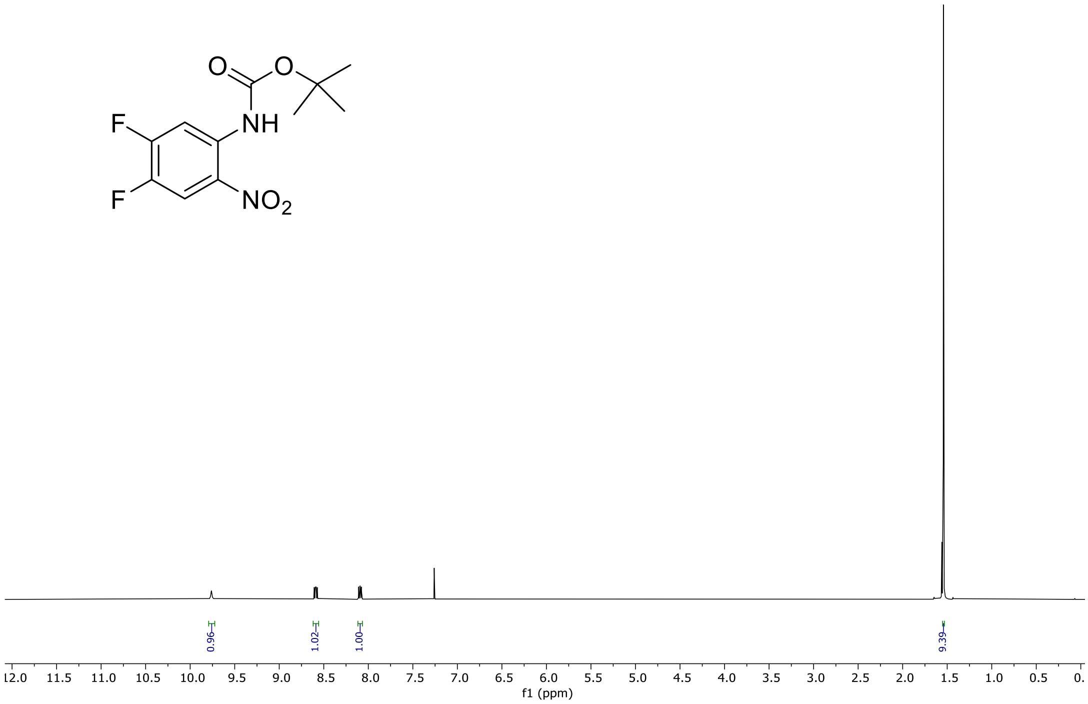

Figure S7.363. ^{1}H-NMR spectrum (600 MHz, $CDCl_3$) of *tert*-butyl (4,5-difluoro-2-nitrophenyl)carbamate (**5**).

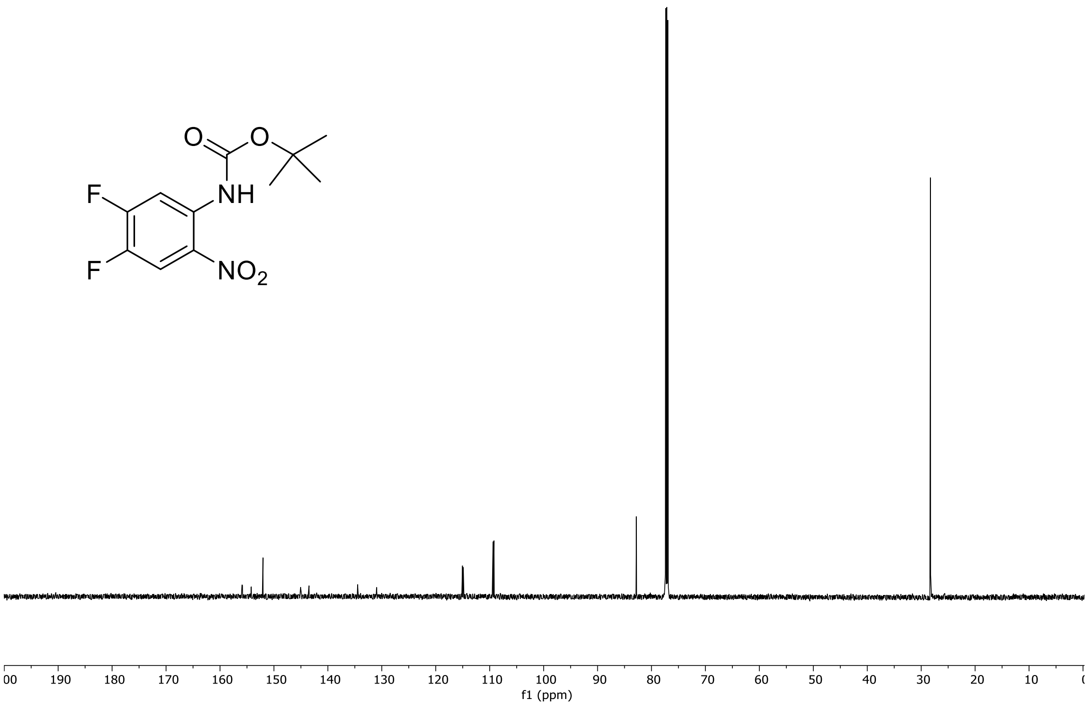

Figure S7.364. $^{13}C\{^{1}H\}$-NMR spectrum (151 MHz, $CDCl_3$) of *tert*-butyl (4,5-difluoro-2-nitrophenyl)carbamate (**5**).

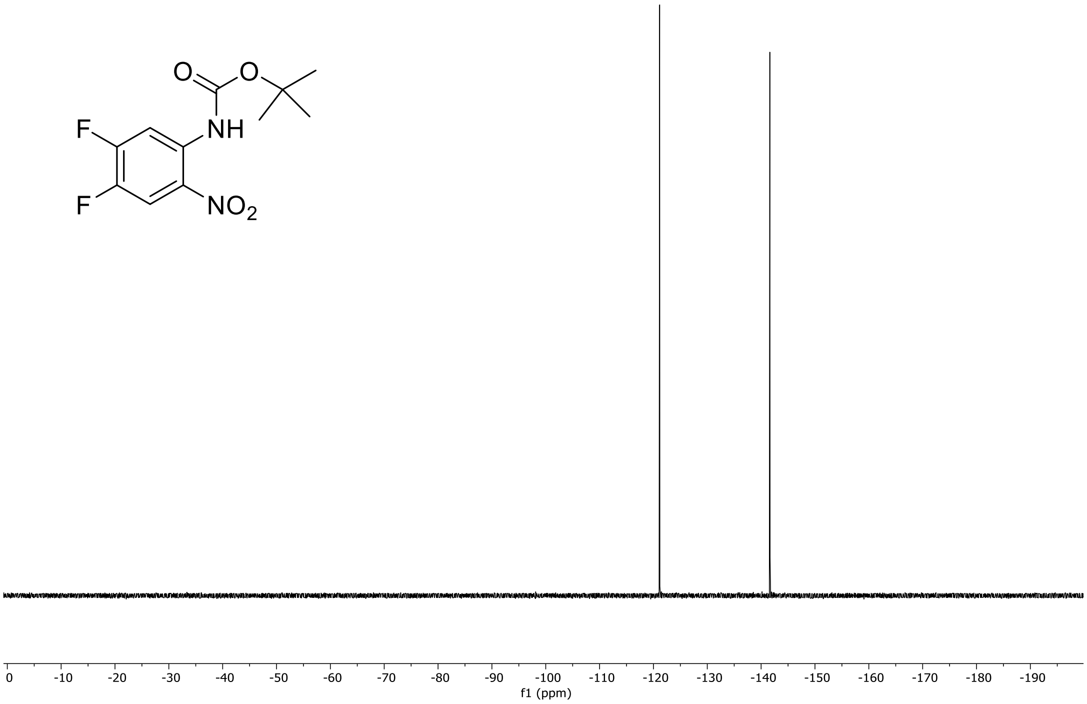

Figure S7.365. $^{19}F\{^{1}H\}$-NMR spectrum (565 MHz, $CDCl_3$) of *tert*-butyl (4,5-difluoro-2-nitrophenyl)carbamate (**5**).

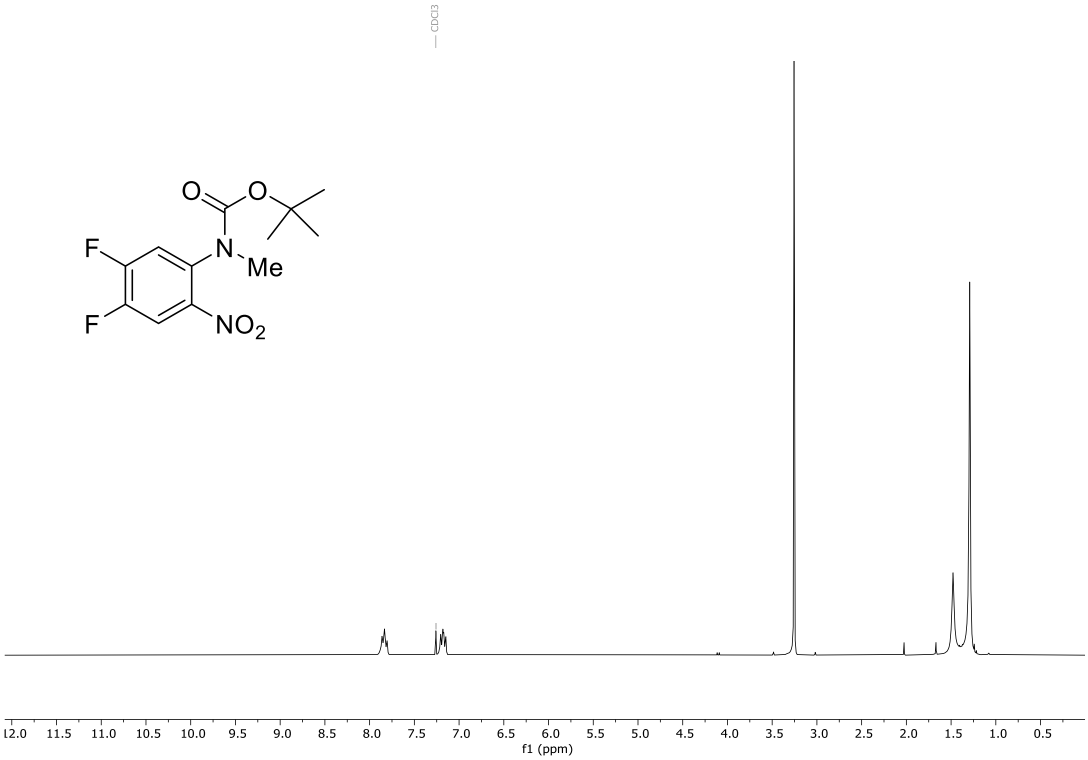

Figure S7.366. ^{1}H-NMR spectrum (300 MHz, $CDCl_3$) of *tert*-butyl (4,5-difluoro-2-nitrophenyl)(methyl)carbamate (**6**).

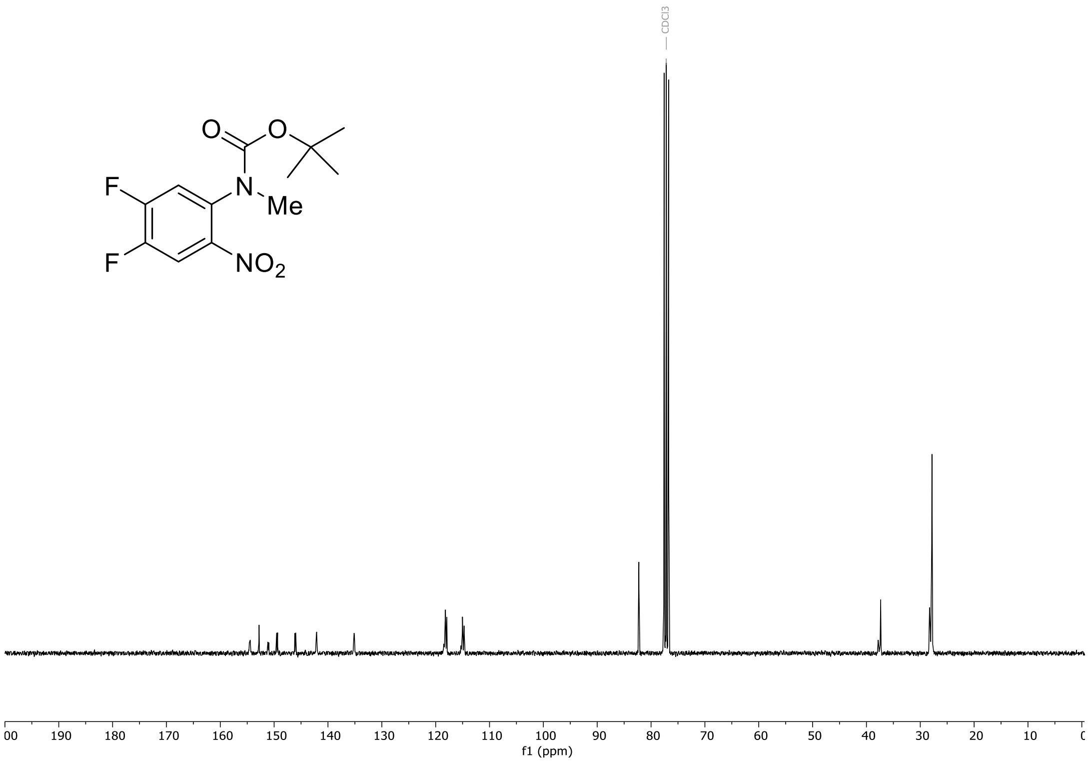

Figure S7.367. $^{13}C\{^1H\}$-NMR spectrum (75 MHz, $CDCl_3$) of *tert*-butyl (4,5-difluoro-2-nitrophenyl)(methyl)carbamate (**6**).

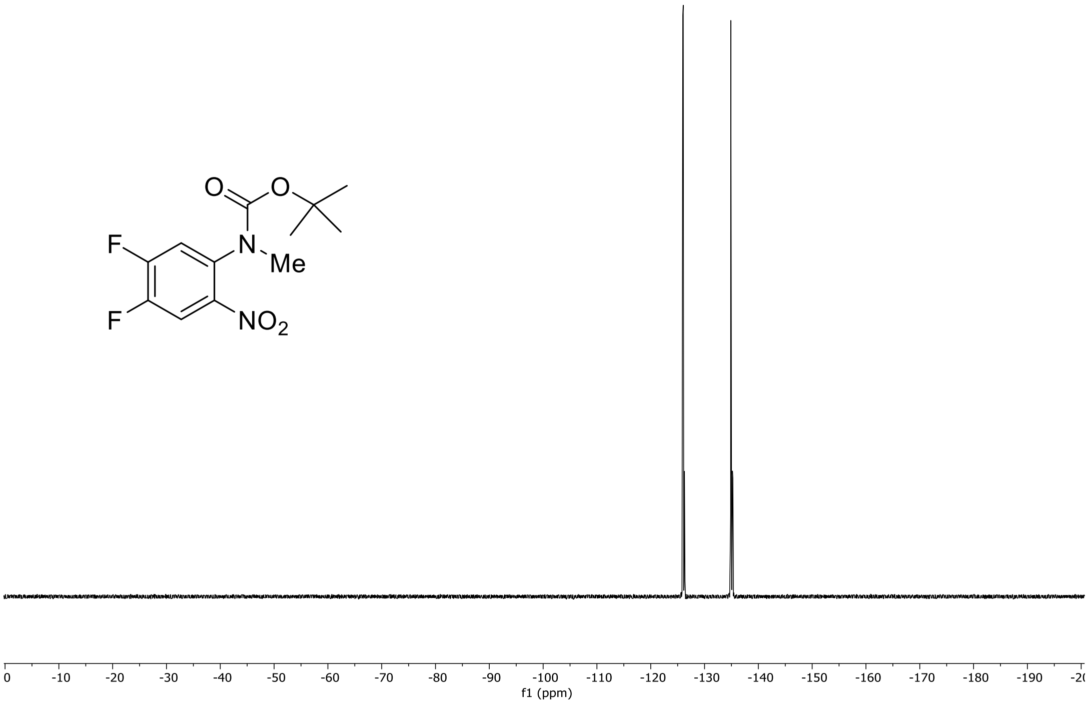

Figure S7.368. $^{19}F\{^1H\}$-NMR spectrum (282 MHz, $CDCl_3$) of *tert*-butyl (4,5-difluoro-2-nitrophenyl)(methyl)carbamate (**6**).

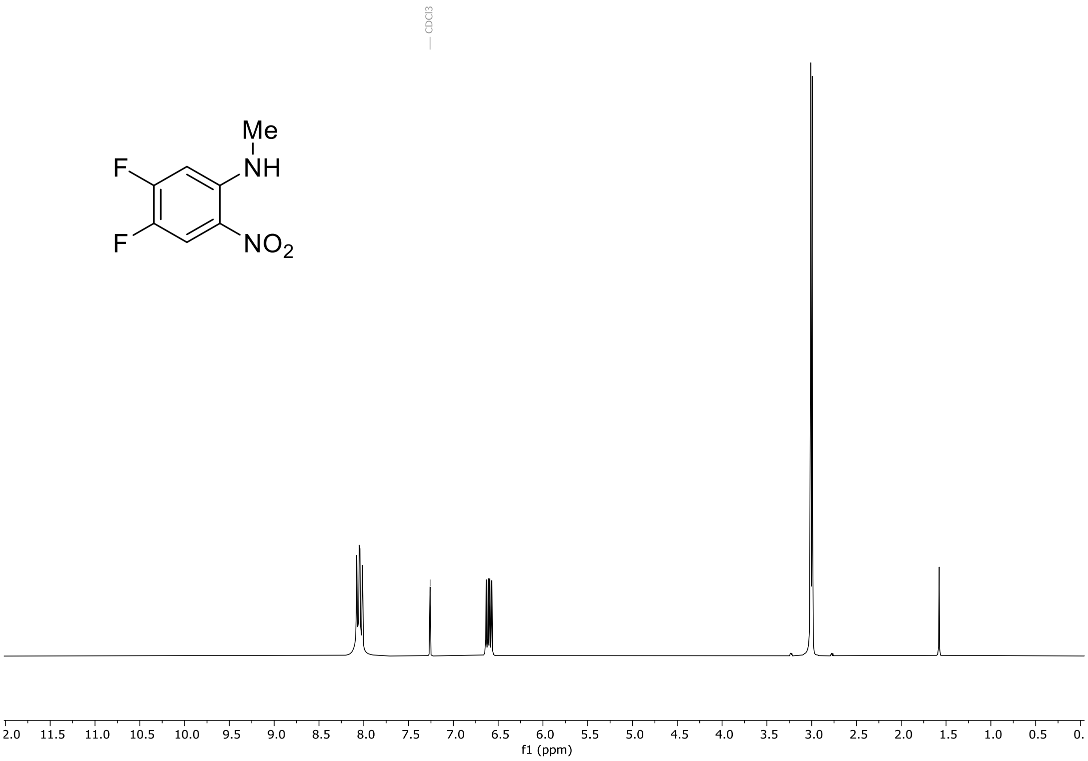

Figure S7.369. ^1H-NMR spectrum (300 MHz, $CDCl_3$) of 4,5-difluoro-N-methyl-2-nitroaniline (**7**).

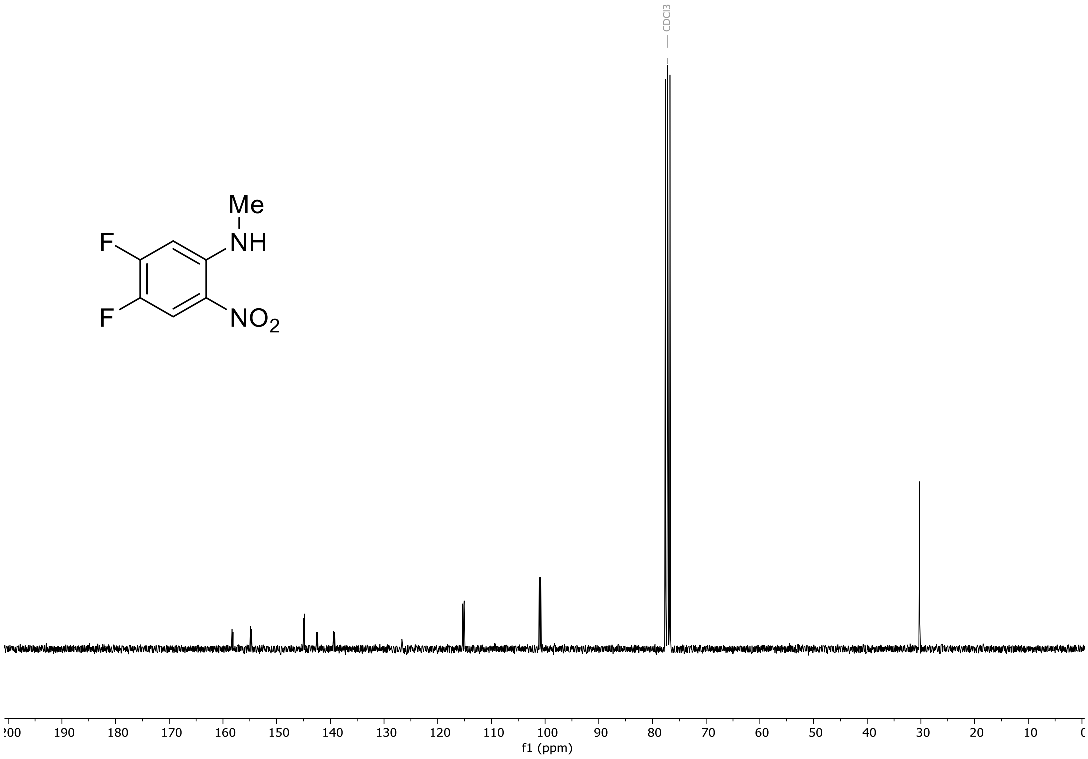

Figure S7.370. $^{13}C\{^1H\}$-NMR spectrum (75 MHz, $CDCl_3$) of 4,5-difluoro-N-methyl-2-nitroaniline (**7**).

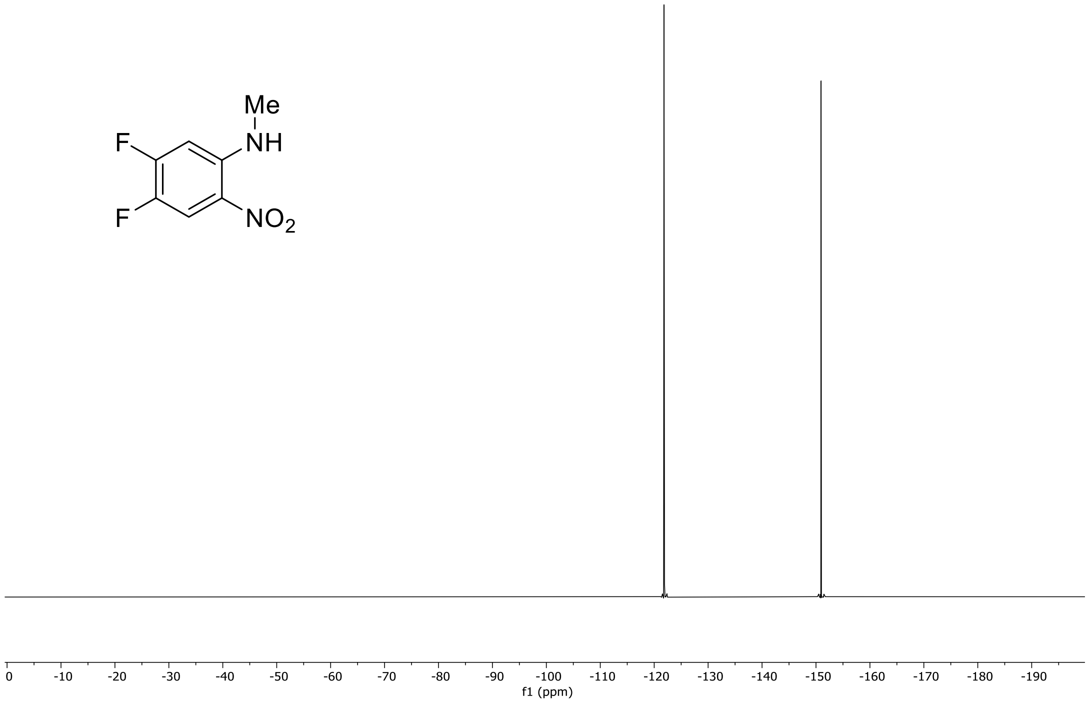

Figure S7.371. $^{19}F\{^1H\}$-NMR spectrum (282 MHz, $CDCl_3$) of 4,5-difluoro-N-methyl-2-nitroaniline (**7**).

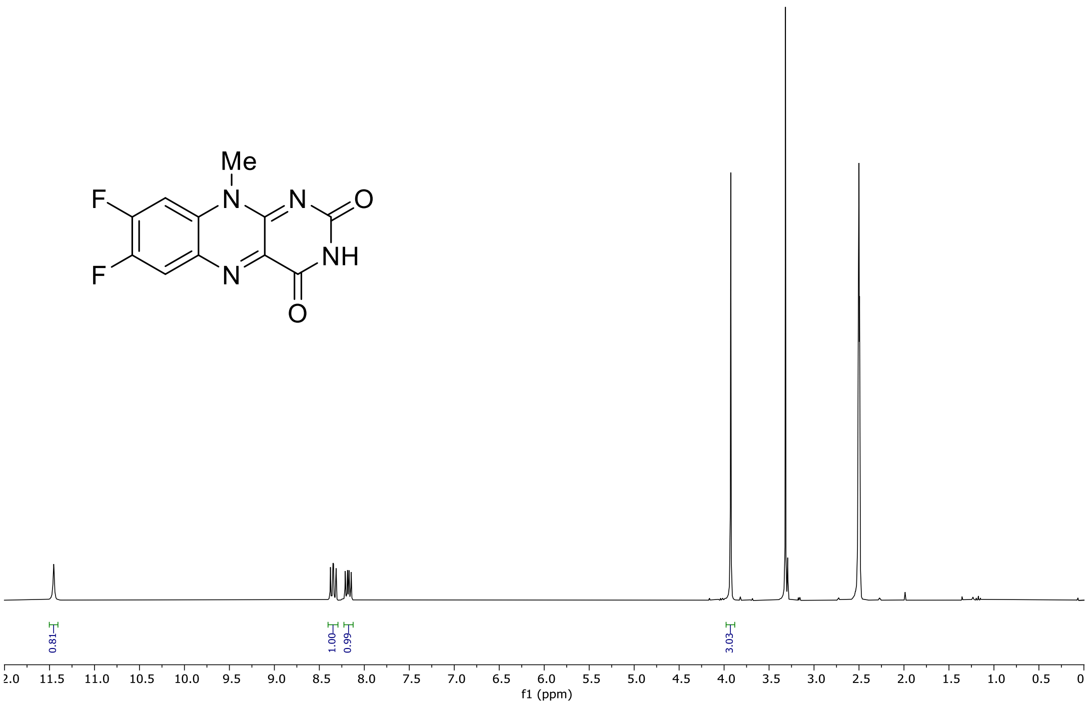

Figure S7.372. ^{1}H-NMR-spectrum (300 MHz, DMSO-d_6) of 7,8-difluoro-10-methylbenzo[*g*]pteridine-2,4(3H,10H)-dione (**8**).

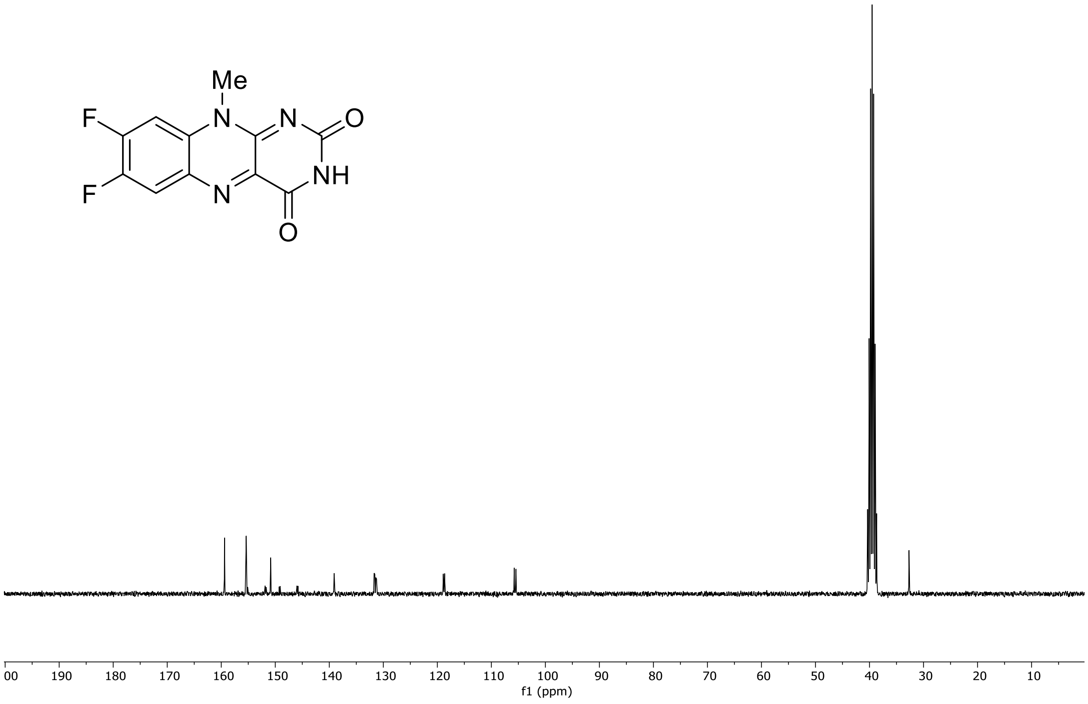

Figure S7.373. ^{13}C{^{1}H}-NMR-spectrum (75 MHz, DMSO-d_6) of 7,8-difluoro-10-methylbenzo[*g*]pteridine-2,4(3H,10H)-dione (**8**).

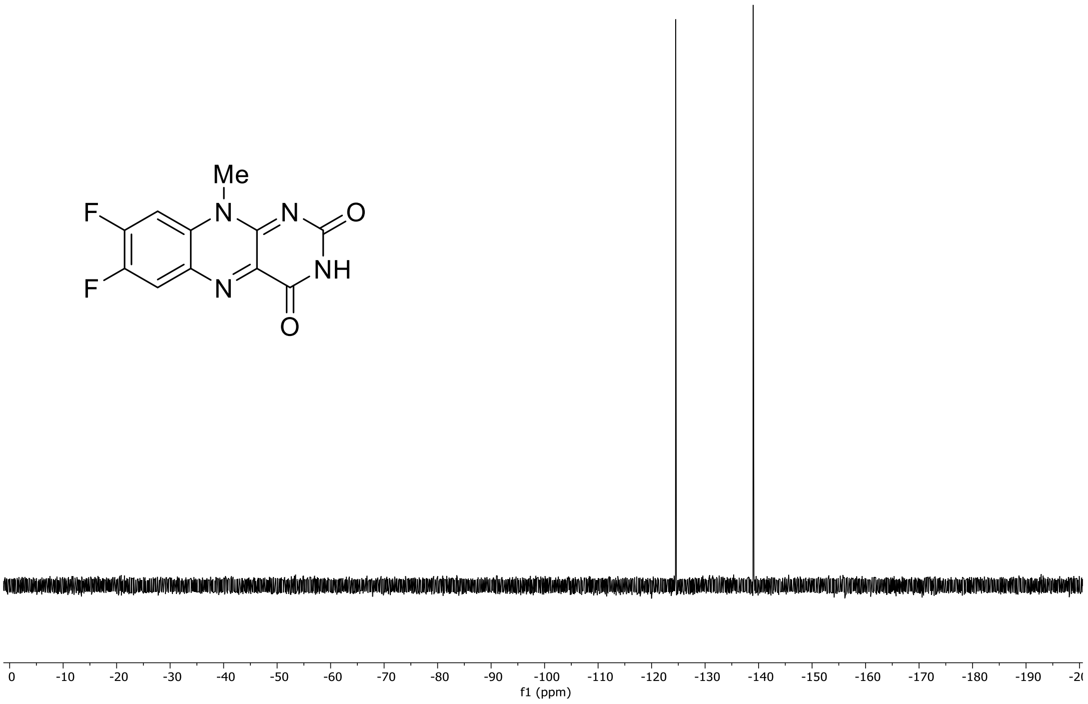

Figure S7.374. $^{19}F\{^1H\}$-NMR-spectrum (282 MHz, DMSO-d_6) of 7,8-difluoro-10-methylbenzo[*g*]pteridine-2,4(3H,10H)-dione (**8**).

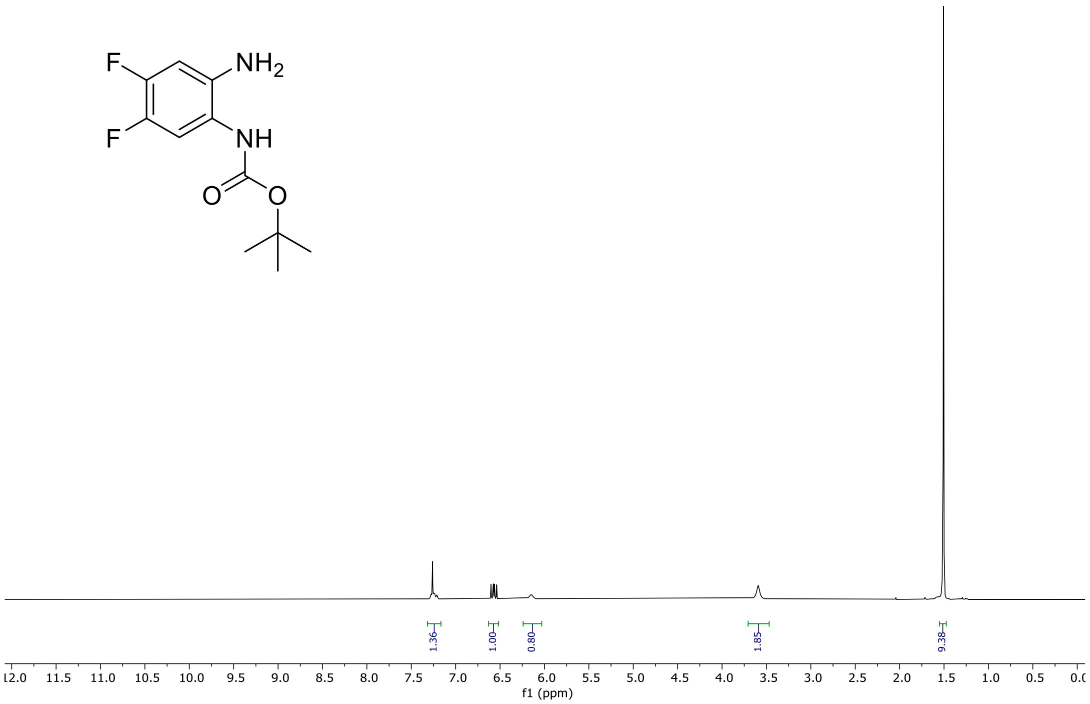

Figure S7.375. ^1H-NMR spectrum (300 MHz, $CDCl_3$) of *tert*-butyl(2-amino-4,5-difluorophenyl)carbamate (**10**).

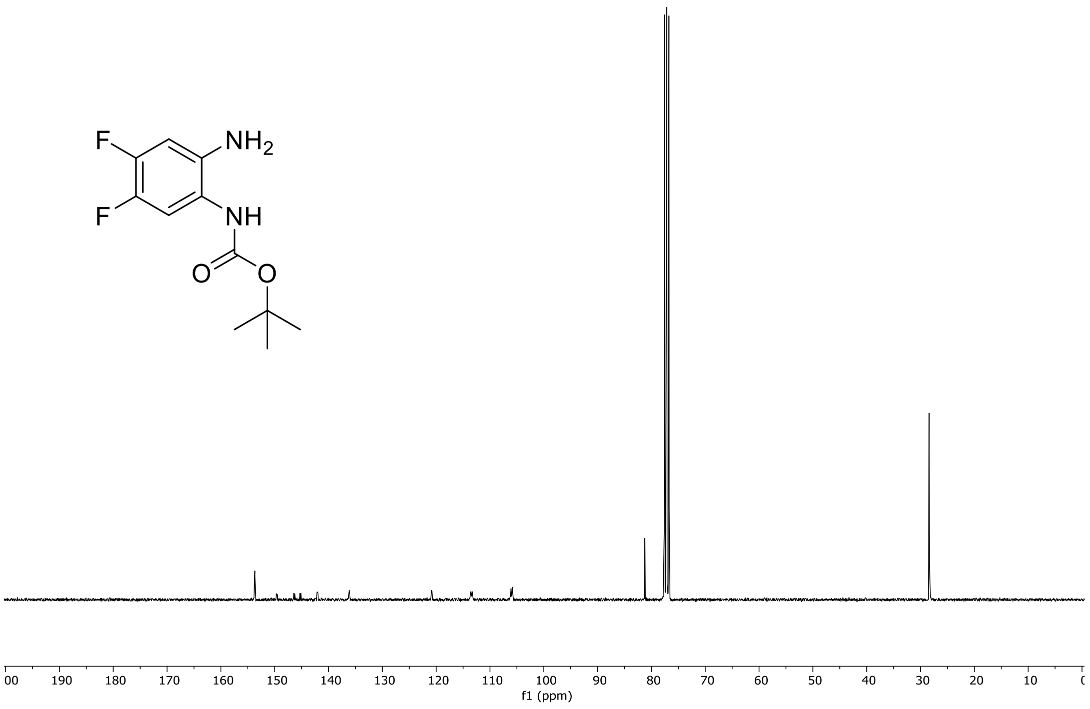

Figure S7.376. $^{13}C\{^{1}H\}$-NMR spectrum (75 MHz, $CDCl_3$) of *tert*-butyl(2-amino-4,5-difluorophenyl)carbamate (**10**).

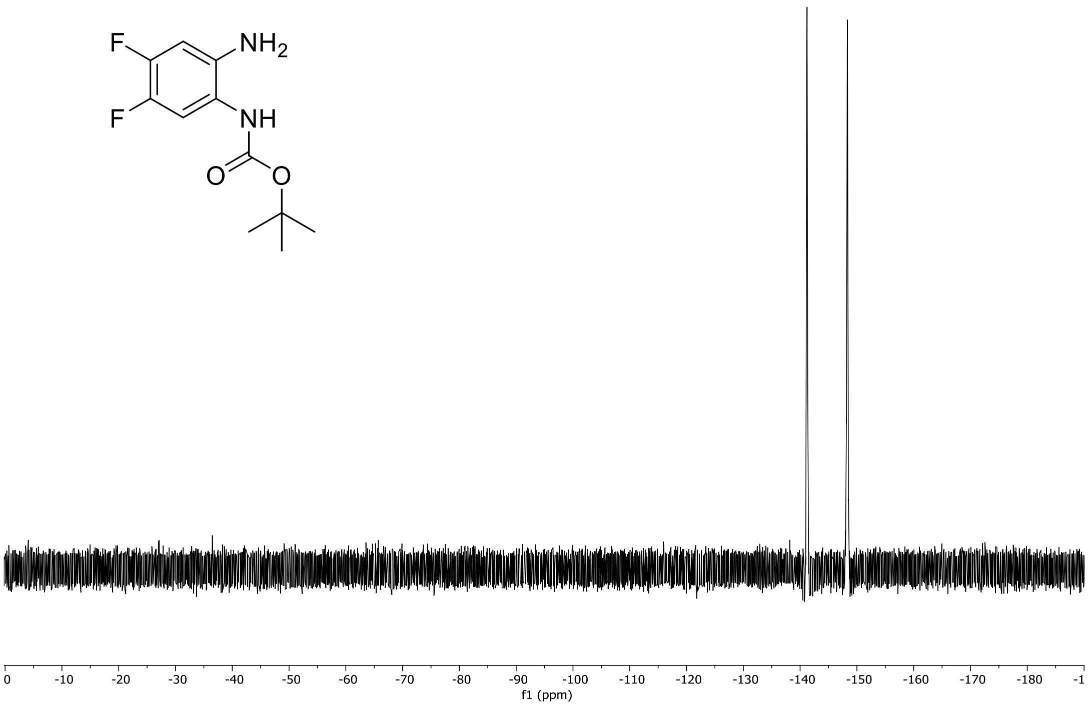

Figure S7.377. $^{19}F\{^{1}H\}$-NMR spectrum (282 MHz, $CDCl_3$) of *tert*-butyl(2-amino-4,5-difluorophenyl)carbamate (**10**).

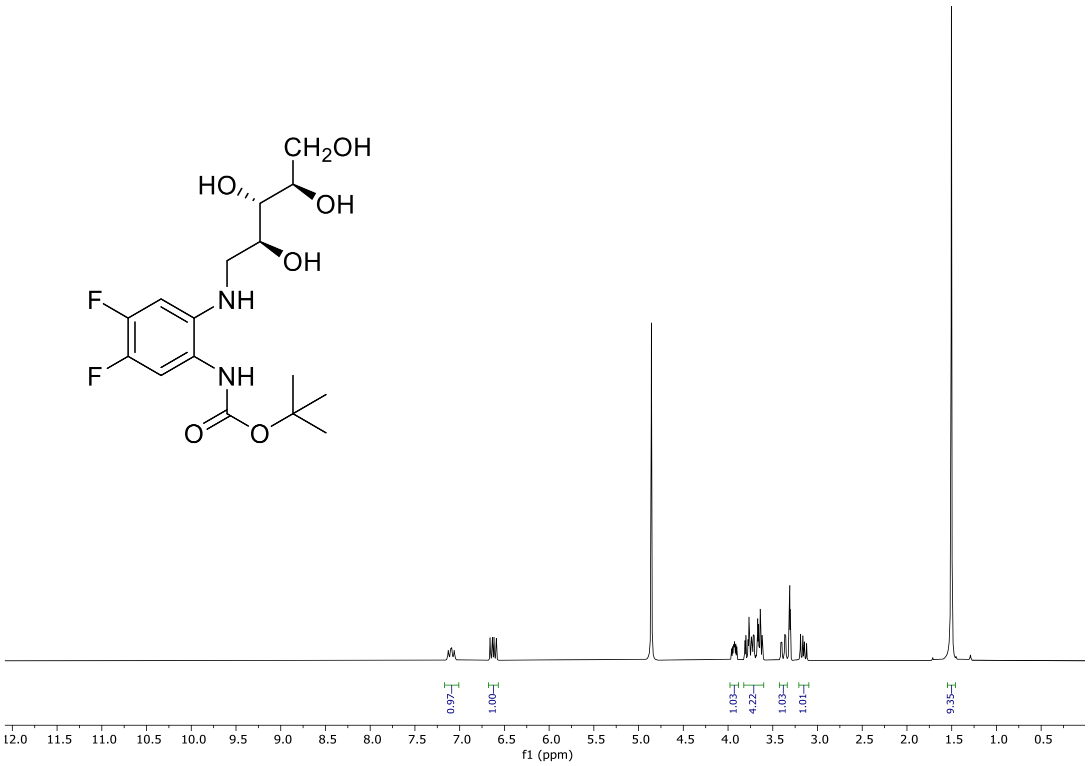

Figure S7.378. ^{1}H-NMR spectrum (300 MHz, MeOD) of *tert*-butyl(4,5-difluoro-2-(((*2S*,*3S*,*4R*)-2,3,4,5-tetrahyroxypentyl)amino)phenyl)carbamate (**11**).

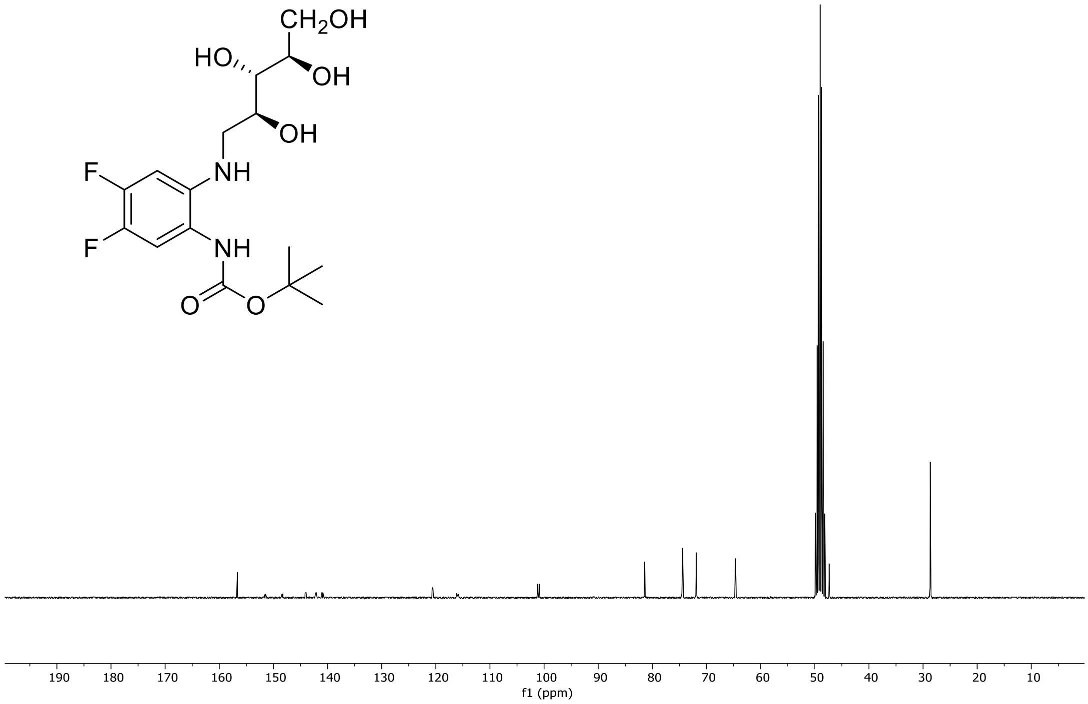

Figure S7.379. ^{13}C{^{1}H}-NMR spectrum (75 MHz, MeOD) of *tert*-butyl(4,5-difluoro-2-(((*2S*,*3S*,*4R*)-2,3,4,5-tetrahydroxypentyl)amino)phenyl)carbamate (**11**).

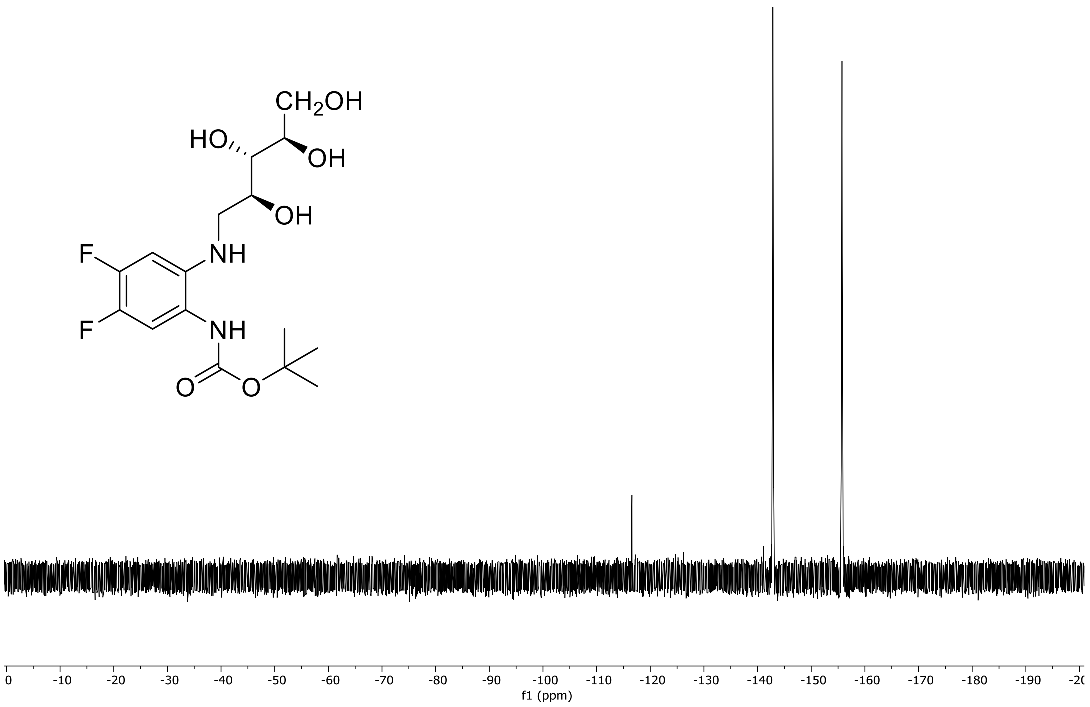

Figure S7.380. $^{19}F\{^{1}H\}$-NMR spectrum (282 MHz, MeOD) of *tert*-butyl(4,5-difluoro-2-(((*2S*,*3S*,*4R*)-2,3,4,5-tetrahydroxypentyl)amino)phenyl)carbamate (**11**).

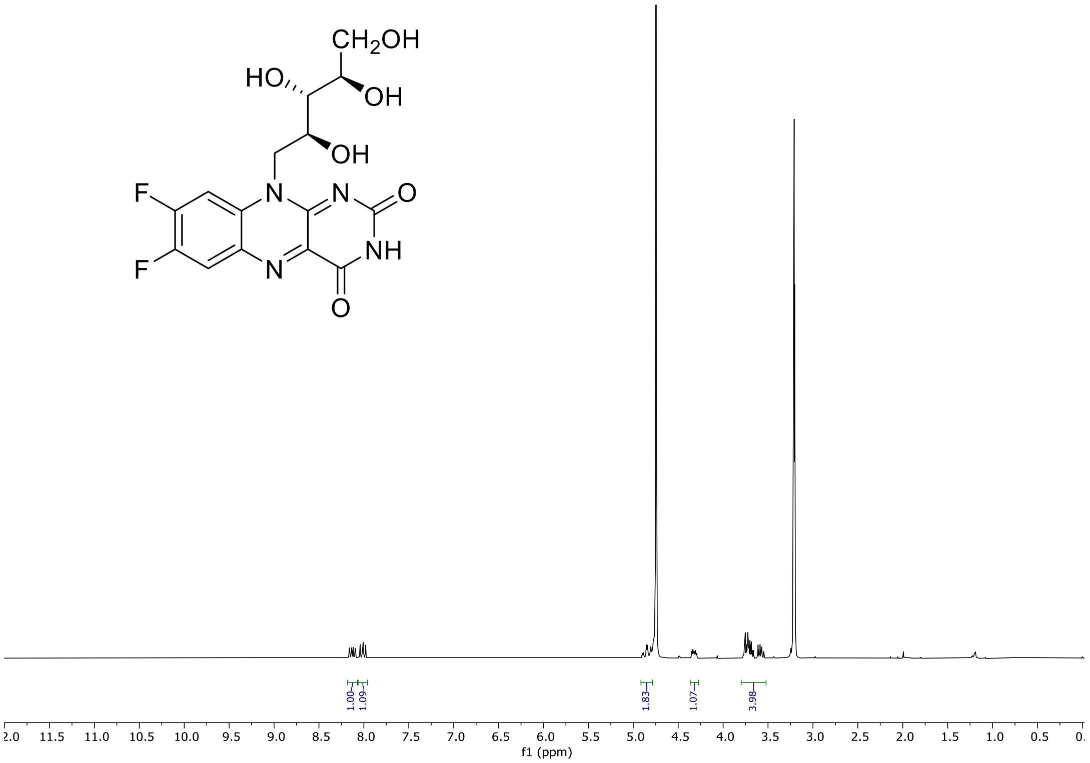

Figure S7.381. ^{1}H-NMR spectrum (300 MHz, MeOD) of 7,8-difluoro-10-((*2S*,*3S*,*4R*)-2,3,4,5-tetrahydroxypentyl)benzo[*g*]pteridine-2,4(3H,10H)-dione (**13**).

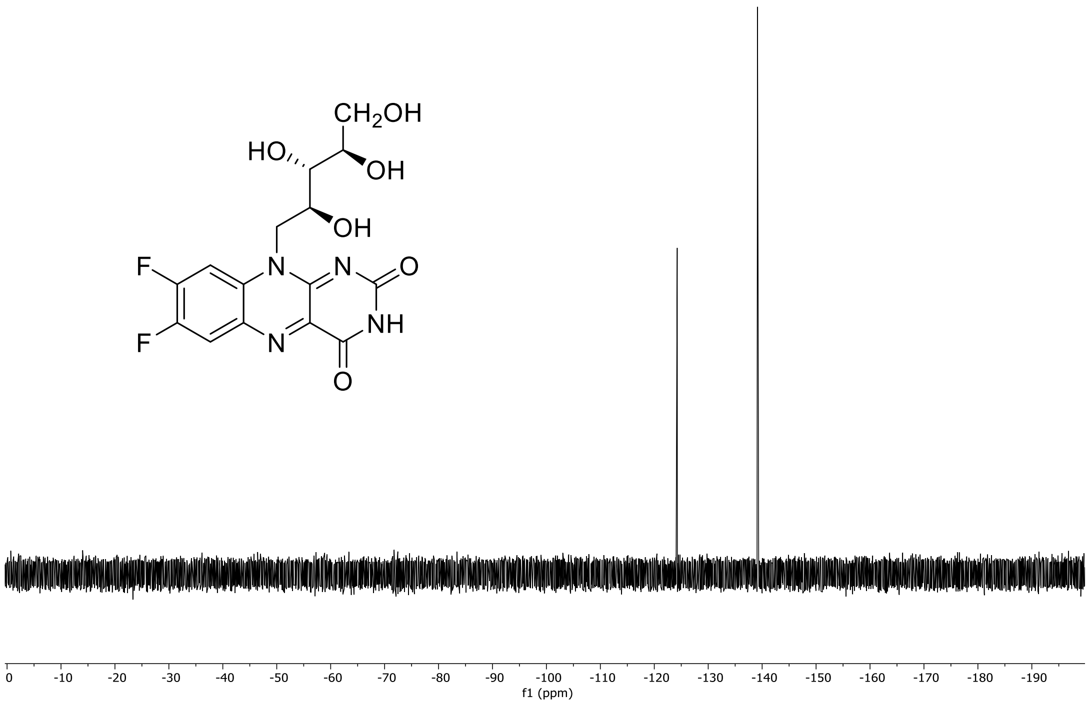

Figure S7.382. ^{19}F{^{1}H}-NMR spectrum (282 MHz, MeOD) of 7,8-difluoro-10-((*2S*,*3S*,*4R*)-2,3,4,5-tetrahydroxypentyl)benzo[*g*]pteridine-2,4(3H,10H)-dione (**13**).

7.4.7 References

[1] A. Losi, *Photochem. Photobiol.* **2007**, *83*, 1283-1300.

[2] L. O. Björn Photobiology: *The Science of Life and Light*; Springer: New York **2007**.

[3] M. A. van der Horst, K. J. Hellingwerf, *Acc. Chem. Res.* **2004**, *37*, 13-20.

[4] E. Silva, A. M. Edwards Flavins: *Photochemistry and Photobiology*; The Royal Society of Chemistry: Cambridge, UK, **2006**.

[5] A. R. Cashmore, J. A. Jarillo, Y.-J. Wu, D. Liu, *Science* **1999**, *284*, 760-765.

[6] R. Banerjee, A. Batschauer, *Planta* **2005**, *220*, 498-502.

[7] A. Losi, W. Gärtner, *Annu. Rev. Plant Biol.* **2012**, *63*, 49-72.

[8] R. P. Sinha, D.-P. Häder, *Photochem. Photobiol. Sci.* **2002**, *1*, 225-236.

[9] W. R. Briggs, J. M. Christie, *Trends Plant Sci.* **2002**, *7*, 204-210.

[10] E. Liscum, D. W. Hodgson, T. J. Campbell, *Plant Physiol.* **2003**, *133*, 1429-1436.

[11] T. Pavlovska, R. Cibulka, *Structure and Properties of Flavins. In Flavin-Based Catalysis*, **2021**, S. 1-27.

[12] V. Massey, *Biochem. Soc. Trans.* **2000**, *28*, 283-296.

[13] J. Svoboda, H. Schmaderer, B. König, *Chem. Eur. J.* **2008**, *14*, 1854-1865.

[14] N. A. Romero, D. A. Nicewicz, *Chem. Rev.* **2016**, *116*, 10075-10166.

[15] T. Hering, B. Mühldorf, R. Wolf, B. König, *Angew. Chem. Int. Ed.* **2016**, *55*, 5342-5345.; *Angew. Chem.* **2016**, *128*, 5428-5431.

[16] S. Fukuzumi, K. Tanii, T. Tanaka, *J. Chem. Soc. Perk. Trans. 2* **1989**, 2103-2108.

[17] A. Rehpenn, A. Walter, G. Storch, *Synthesis* **2021**, *53*, 2583-2593.

[18] A. Kormányos, M. S. Hossain, G. Ghadimkhani, J. J. Johnson, C. Janáky, N. R. de Tacconi, F. W. Foss Jr., Y. Paz, K. Rajeshwar, *Chem. Eur. J.* **2016**, *22*, 9209-9217.

[19] A. Reiffers, C. Torres Ziegenbein, A. Engelhardt, R. Kühnemuth, P. Gilch, C. Czekelius, *Photochem. Photobiol.* **2018**, *94*, 667-676.

[20] M. Bracker, F. Dinkelbach, O. Weingart, M. Kleinschmidt, *Phys. Chem. Chem. Phys.* **2019**, *21*, 9912-9923.

[21] M. Bracker, M. K. Kubitz, C. Czekelius, C. M. Marian, M. Kleinschmidt, *ChemPhotoChem* **2022**, e202200040.

[22] M. Mansurova, J. Simon, S. Salzmann, C. M. Marian, W. Gärtner, *ChemBioChem* **2013**, *14*, 645-654.

[23] L. Jullien, A. Gautier, *Methods Appl. Fluoresc.* **2015**, *3*, 042007.

[24] T. Drepper, T. Eggert, F. Circolone, A. Heck, U. Krauß, J.-K. Guterl, M. Wendorff, A. Losi, W. Gärtner, K.-E. Jaeger, *Nat. Biotechnol.* **2007**, *25*, 443-445.

[25] X. Shu, V. Lev-Ram, T. J. Deerinck, Y. Qi, E. B. Ramko, M. W. Davidson, Y. Jin, M. H. Ellisman, R. Y. Tsien, *PLoS Biol.* **2011**, *9*, e1001041.

[26] B. M. Medina, D. Beljonne, H.-J. Egelhaaf, J. Gierschner, *J. Chem. Phys.* **2007**, *126*, 111101.

[27] B. E. Smart, *J. Fluorine Chem.* **2001**, *109*, 3-11.

[28] A. Bondi, *J. Phys. Chem.* **1964**, *68*, 441-451.

[29] J. C. Biffinger, H. W. Kim, S. G. DiMagno, *ChemBioChem* **2004**, *5*, 622-627.

[30] B. Cordero, V. Gómez, A. E. Platero-Prats, M. Revés, J. Echeverría, E. Cremades, F. Barragán, S. Alvarez, *Dalton Trans.* **2008**, 2832-2838.

[31] K. Klehs, C. Spahn, U. Endesfelder, S. F. Lee, A. Fürstenberg, M. Heilemann, *ChemPhysChem* **2014**, *15*, 637-641.

[32] S. A. Brown, C. J. Rizzo, *Synth. Commun.* **1996**, *26*, 4065-4080.

[33] V. Kumar, K. A. Woode, R. F. Bryan, B. A. Averill, *J. Am. Chem. Soc.* **1986**, *108*, 490-496.

[34] K. Cheng, S. Li, X. Lv, Y. Tian, H. Kong, X. Huang, Y. Duan, J. Han, Z. Xie, C. Liao, *Bioorg. Med. Chem. Lett.* **2019**, *29*, 1012-1018.

[35] J. J. Hasford, C. J. Rizzo, *J. Am. Chem. Soc.* **1998**, *120*, 2251-2255.

[36] M. Mansurova, M. S. Koay, W. Gärtner, *Eur. J. Org. Chem.* **2008**, *2008*, 5401-5406.

[37] S. Salzmann, J. Tatchen, C. M. Marian, *J. Photochem. Photobiol. A* **2008**, 198, 221-231.

[38] K. Rurack, M. Spieles, *Anal. Chem.* **2011**, *83*, 1232-1242.

[39] W. W. Parson, *Modern optical spectroscopy*, *Vol. 2*, Springer, **2007**.

[40] S. J. Strickler, R. A. Berg, *J. Chem. Phys.* **1962**, *37*, 814-822.

[41] J. Mooney, P. Kambhampati, *J. Phys. Chem. Lett.* **2013**, *4*, 3316-3318.

[42] T.-O. Peulen, O. Opanasyuk, C. A. M. Seidel, *J. Phys. Chem. B* **2017**, *121*, 8211-8241.

[43] C. R. Cantor, P. R. Schimmel, *Biophysical Chemistry*, *Part II*: *Techniques for the study of biological structure and function*, Freeman and Company, New York, **1980**, S. 443.

[44] J. Maillard, K. Klehs, C. Rumble, E. Vauthey, M. Heilemann, A. Fürstenberg, *Chem. Sci.* **2021**, *12*, 1352-1362.

[45] P. Fita, M. Fedoseeva, E. Vauthey, *J. Phys. Chem. A* **2011**, *115*, 2465-2470.

[46] J. Widengren, U. Mets, R. Rigler, *J. Phys. Chem.* **1995**, *99*, 13368-13379.

[47] S. Felekyan, R. Kühnemuth, V. Kudryavtsev, C. Sandhagen, W. Becker, C. A. M. Seidel, *Rev. Sci. Instrum.* **2005**, *76*, 083104.

[48] P. A. W. van den Berg, J. Widengren, M. A. Hink, R. Rigler, A. J. W. G. Visser, *Spectrochim. Acta Part A* **2001**, *57*, 2135-2144.

[49] M. L. Huber, R. A. Perkins, A. Laesecke, D. G. Friend, J. V. Sengers, M. J. Assael, I. N. Metaxa, E. Vogel, R. Mareš, K. Miyagawa, *J. Phys. Chem. Ref. Data* **2009**, *38*, 101-125.

[50] M. J. Assael, S. A. Monogenidou, M. L. Huber, R. A. Perkins, J. V. Sengers, *J. Phys. Chem. Ref. Data* **2021**, *50*, 033102.

[51] A. Kotaki, K. Yagi, *J. Biochem.* **1970**, *68*, 509-516.

[52] W. Haselbach, J. M. Kaminski, L. N. Kloeters, T. J. J. Müller, O. Weingart, C. M. Marian, P. Gilch, B. E. Nogueira de Faria, *Chem. Eur. J.* **2023**, *29*, e202202809.

[53] H. Satzger, W. Zinth, *Chem. Phys.* **2003**, *295*, 287-295.

[54] I. H. M. van Stokkum, D. S. Larsen, R. van Grondelle, *Biochim. Biophys. Acta Bioenerg.* **2004**, *1657*, 82-104.

[55] S. Weidtkamp-Peters, S. Felekyan, A. Bleckmann, R. Simon, W. Becker, R. Kühnemuth, C. A. M. Seidel, *Photochem. Photobiol. Sci.* **2009**, *8*, 470-480.

[56] P. O. Gendron, F. Avaltroni, K. J. Wilkinson, *J. Fluoresc.* **2008**, *18*, 1093-1101.

[57] G. R. Fulmer, A. J. M. Miller, N. H. Sherden, H. E. Gottlieb, A. Nudelman, B. M. Stoltz, J. E. Bercaw, K. I. Goldberg, *Organometallics* **2010**, *29*, 2176-2179.

[58] N. E. Kanitz, T. Lindel, Z. *Naturforsch., B: Chem. Sci.* **2016**, *71*, 1287-1300.